Abril - Junio
Volumen 63
Número 2

April - June
Volume 63
Number 2

Geofísica Internacional

Revista Trimestral Publicada por el Instituto de Geofísica de la Universidad Nacional Autónoma de México
Quarterly Journal Published by the Institute of Geophysics of the National Autonomous University of Mexico

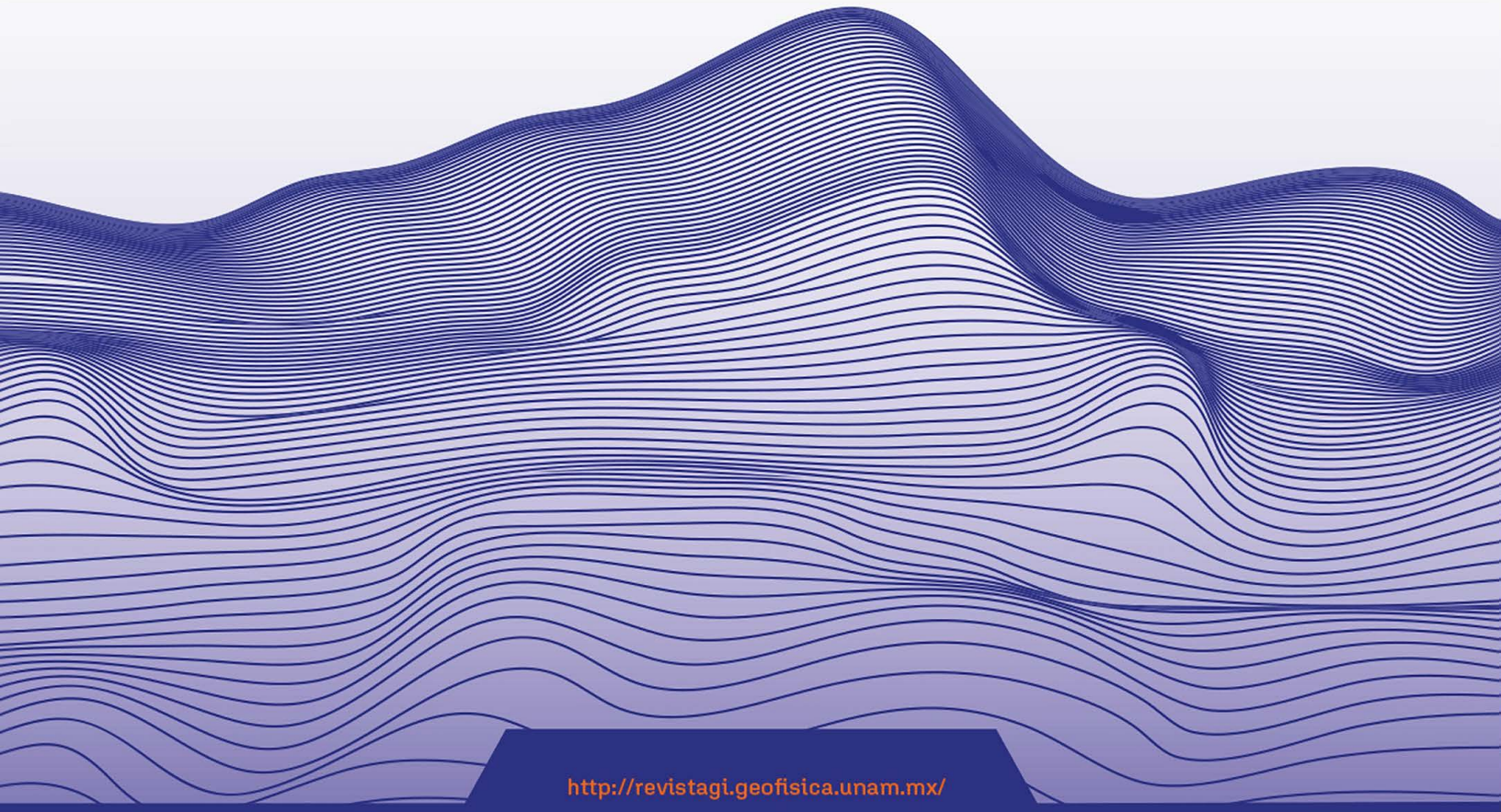

http://revistagi.geofisica.unam.mx/

ISSN 2954-436X

MÉXICO MEXICO

— Geofísica Internacional —

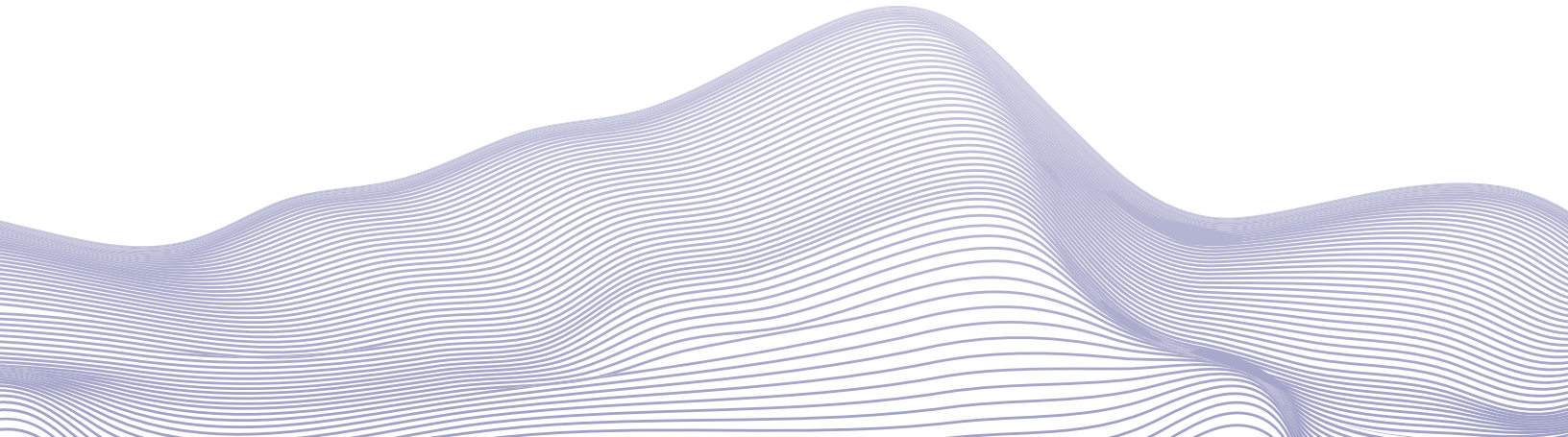

GEOFÍSICA INTERNACIONAL, Año 63, Vol. 63, Núm. 2, abril - junio de 2024 es una publicación trimestral, editada por la Universidad Nacional Autónoma de México, Ciudad Universitaria, Alcaldía Coyoacán, C.P. 04510, Ciudad de México, a través del Instituto de Geofísica, Circuito de la Investigación Científica s/n, Ciudad Universitaria, Alcaldía Coyoacán, C.P. 04510, Ciudad de México, Tel. (55)56 22 40 36. URL: http://revistagi.geofisica.unam.mx, correo electrónico: revistagi@igeofisica.unam.mx. Editor responsable: Saúl Armendáriz Sánchez. Certificado de Reserva de Derechos al uso Exclusivo del Título: 04-2022-081610251200-102, eISSN: 2954-436X, otorgados por el Instituto Nacional del Derecho de Autor (INDAUTOR). Responsable de la última actualización, Minerva Castro Escamilla Editora Técnica. Fecha de la última modificación: 1 de abril de 2024, Circuito de la Investigación Científica s/n, Ciudad Universitaria, Alcaldía Coyoacán, C.P. 04510, Ciudad de México.

https://doi.org/10.22201/igeof.2954436xe.2024.63.2

Geofísica Internacional
Vol. 63, Núm. 2, abril - junio de 2024

Contents

Mexico City Earthquake of 11 May 2023 (Mw3.2)
L. Quintanar, S. K. Singh, V. H. Espíndola, A. Iglesias, D.I. Bello-Segura and D. Arroyo
749

A Source and Ground Motion Study of the Veracruz Earthquakes of 29 October 2009 (Mw5.7) and 4 August 2021 (Mw4.8): Evidence of Strong Azimutual Variation of Attenuation
A. Iglesias, S. K. Singh, D. Arroyo, X. Pérez-Campos, V. H. Espíndola, A. Vargas4, F. Córdoba-Montiel and Deni M. González-López
763

Prediction of Fourier Amplitude Spectrum of Ground Motion in Mexico City from Subduction Thrust Earthquakes
Danny Arroyo, Mario Ordaz and Shri K. Singh
783

Site effect evaluation for Culiacan, Sinaloa, Mexico
Domínguez Reyes Tonatiuh and Rodríguez Lozoya Héctor
803

Forward modeling of spectral gamma-ray (SGR) logging in sedimentary formations
Lechuga-Lagos F.M., Aquino-López A., Valdez-Grijalva M.A. and Campos-Enriquez J.O.
817

Vertical Electrical Sounding Technique as an Efficient and Rapid Tool for Groundwater Investigation in a Basaltic Environment at Kodana Station for the Shami goats. Case Study from Southern Syria
Jamal Asfahani
835

Geofísica Internacional

Vol. 63, Núm. 2, abril - junio de 2024

The use of in situ Gamma-Ray Spectrometry to Assess the Environmental Impacts of Intensive Agriculture in terms of Geochemical Mobility in soil and waters

Matheus Felipe Stanfoca Casagrande, César Augusto Moreira, Lucas Moreira Furlan and Vania Rosolen

851

Investigation of Salanda Fault Zone, between Yesiloz and Gumuskent (Nevsehir-Turkey) with PSInSAR

Ramazan Demircioğlu and Osman Oktar

865

La erupción del volcán Irazú 1917-1921 (Costa Rica): dinámica y entorno social

Mauricio M. Mora, Giovanni Peraldo Huertas and Gerardo J. Soto

881

Sección especial

Introducción

Marie-Noëlle Guilbaud

911

The 2020 and 2021 Seismic Swarms in the Tancítaro-Paricutín Area (Uruapan-Michoacán, México) Evidence Magma Intrusion in an Area with High Density of Monogenetic Cones

Gema V. Caballero-Jiménez, Ma. Cristina Zarazúa-Carbajal, Ana Teresa Mendoza-Rosas and Servando De La Cruz- Reyna

913

Quarrying volcanic landscapes: territory and strategies of metate production in Turícuaro (Michoacán, México)

Caroline Hamon, Gregory Pereira, Laurent Aubry, Oryaëlle Chevrel, Claus Siebe, Osiris Quezada and Nanci Reyes-Guzmán

929

Geofísica Internacional (2024) **63-2**: 749 - 762

Mexico City Earthquake of 11 May 2023 (Mw3.2)

L. Quintanar[1], S. K. Singh[1], V. H. Espíndola[1], A. Iglesias[1], D.I. Bello-Segura[1] and D. Arroyo[2]

Abstract

On 11 May 2023 a local earthquake in Mexico City was felt very strongly in Mixcoac, San Angel, and Coyoacán. The event was part of a seismic sequence that had begun about 6 months earlier. Peak Ground Acceleration (PGA) at the closest station (distance ~ 1 km), located in the hill zone, was ~ 0.18 g. Although the response spectrum at short periods at this station exceeded the design spectrum specified in the Mexico City´s Building Code, no structural damage was reported. Moment tensor inversion of bandpass filtered (0.08 – 0.24 Hz) displacement records yields $M_0 = 6.8\times10^{13}$ N-m (M_w 3.2), H = 0.7 km, and the likely fault plane characterized by $\varphi = 270^0$, $\delta = 76^0$, $\lambda = -75^0$. These source characteristics are very similar to those estimated for the 17 July 2019 earthquake which occurred during a swarm-like seismic activity about 5 km to the north. Spectral analysis of recordings at 19 sites in the hill zone, 14 in the transition zone, and 41 in the lake-bed zone reveals great variability of the ground motion within each of the zones. Estimated stress drop, $\Delta\sigma$, is 0.5 MPa. A large disparity is found between the observed source spectrum and theoretical source spectrum; their ratio provides an estimation of the amplification of seismic waves as they travel through the layers of decreasing velocity at shallower depth. We denote this ratio as the site effect. Predicted PGA and PGV for an M_w 3.2 earthquake, computed using stochastic technique (Boore 1983, 2003), assuming a Brune ω^{-2} source, $\Delta\sigma = 0.5$ MPa and including the site effect, are in reasonable agreement with the observations. Expected PGA and PGV at the epicenter of a postulated M_w 5 earthquake are 0.6 g and 60 cm/s at a generic hill-zone site; the expected values are twice as large in the lake-bed zone. These predictions should, however, be taken with caution as they are based on several approximations.

Key words: Earthquakes in Mexico City, Moment Tensor Inversion, Peak Ground Acceleration.

Resumen

El 11 de mayo de 2023, un sismo local en la Ciudad de México se sintió fuertemente en Mixcoac, San Angel y Coyoacán. El evento fue parte de una secuencia sísmica que inició aproximadamente 6 meses antes. Las aceleraciones pico del suelo (PGA) en la estación más cercana (distancia ~ 1 km) localizada en zona de lomas, fue de ~ 0.18 g. Aunque el espectro de respuesta a períodos cortos en esta estación excedió el espectro de diseño especificado en el Reglamento de Construcción de la Ciudad de México, no se reportaron daños estructurales. La inversion del Tensor de Momento a partir de los registros de desplazamiento filtrados (0.08 – 0.24 Hz) arrojan valores de $M_0 = 6.8\times10^{13}$ N-m (M_w 3.2), H = 0.7 km, con un probable plano de falla caracterizado por $\varphi = 270^0$, $\delta = 76^0$, $\lambda = -75^0$. Estas características focales son muy similares a las estimadas para el sismo del 17 de Julio de 2019 durante un enjambre sísmico ocurrido aproximadamente 5 km al norte. El análisis spectral de los registros en 19 sitios de la zona de lomas, 14 en zona de transición y 41 en zona de lago, revela una gran variabilidad en el movimiento del suelo en cada una de estas zonas. La caída de esfuerzos estimada $\Delta\sigma$, es de 0.5 MPa. Se encontró una gran disparidad entre los espectros de la fuente observados con los teóricos; su relación nos da una estimación de la amplificación de las ondas sísmicas al viajar a través de capas someras con velocidades decrecientes; identificamos a esta relación como el efecto de sitio. Los valores predichos de PGA y PGV para un sismo de M_w 3.2, calculados usando la técnica Estocástica (Boore 1983, 2003), suponiendo un modelo de focal de Brune, $\Delta\sigma = 0.5$ MPa e incluyendo el efecto de sitio, concuerdan razonablemente con las observaciones. Los valores esperados de PGA y PGV en el epicentro de un sismo postulado de M_w 5, son de 0.6 g and 60 cm/s respectivamente en un sitio de lomas genérico; los valores esperados en zona de lago serían del doble. Estas predicciones sin embargo, deben tomarse con precaución dado que están basadas en varias aproximaciones.

Palabras clave: Sismos en la Ciudad de México, Inversión del Tensor de Momento, Aceleraciones pico del suelo.

Received: November 14, 2023; Accepted: February 27, 2023; Published on-line: April 1, 2024.

Editorial responsibility: Dr. Quetzalcóatl Rodríguez-Pérez

* Corresponding author: L. Quintanar, luisq@igeofisica.unam.mx
[1] Universidad Nacional Autónoma de México, Instituto de Geofísica, CDMX-México
[2] Universidad Autónoma Metropolitana, Unidad Azcapotzalco, CDMX-México

https://doi.org/10.22201/igeof.2954436xe.2024.63.2.1757

1. Introduction

Valley of Mexico lies in the central part of Trans-Mexican Volcanic Belt (TMVB) which is an E-W oriented, Miocene to Quaternary, calc-alkaline volcanic arc related to the subduction of Rivera and Cocos plates below Mexico. It is traversed by faults which are parallel as well as orthogonal to its axis (Pasquaré *et al.*, 1987; Johnson and Harrison, 1990) (Figure 1). The stress regime of the TMVB is transtensional (Mooser, 1972; Suter *et al.*, 1992; Ego and Ansan, 2002).

The valley is surrounded by volcanic ranges of andesitic and dacitic composition (Figure 1). Numerous normal faults trending E-W and NE-SW have been mapped in the region. Although the Valley of Mexico and Mexico Basin may refer to distinct areas, here we shall use the terms interchangeably; Mexico City is situated within the valley (Figure 1). Based on geotechnical characteristics of the near-surface layers, the city is divided in three zones: (1) the hill zone with surface layer of volcanic tuffs or lava flows, (2) the lake-bed zone consisting of 10 to >100 m of clays underlain by sandy and silty layers, and (3) the transition zone composed of alluvial sandy and silty layers, with occasional clay layers (Marsal and Mazari, 1969). Seismic waves suffer dramatic amplification in the lake-bed and transition zones with respect to hill zone at the natural frequency of the site, which lies between 0.2 and 0.7 Hz (Singh *et al.*, 1988a, 1988b; Reinoso and Ordaz, 1999).

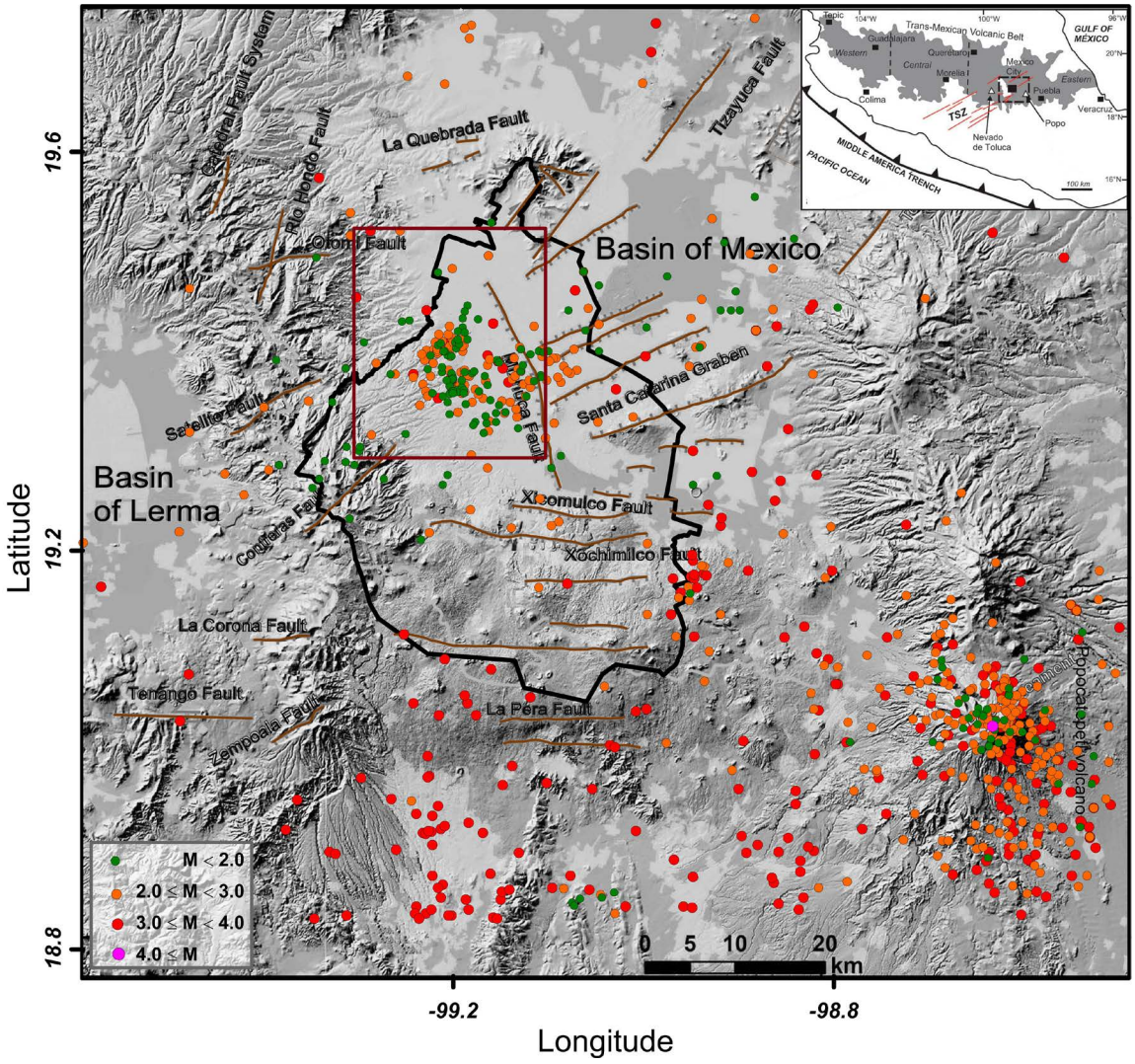

Figure 1. Digital elevation model of the Mexico Basin area showing faults in the region (modified from Arce *et al.*, 2019). Inset: Map of central Mexico in which the thick dashed rectangle indicates the area covered by the figure. Heart-shaped black contour is Mexico City. Seismicity in the region for 2010 - May 2023 is shown by color-coded dots. Note the concentration of earthquakes within a rectangular area in the west of the city, in Milpa Alta to the south-east, and in the area of currently-active Popocatepetl Volcano. An enlarged map of the rectangular area is shown in Figure 2.

Local earthquakes in the Valley of Mexico, though small in magnitude, cause great panic in the population living in the epicentral zone. Seismicity often occurs in swarm-like sequences (Figueroa, 1971; Manzanilla, 1986). As can be seen in Figure 1, the recent events are concentrated in a rectangular area to the west, as well as at Milpa Alta to the southeast, and the area of currently-active Popocatepetl Volcano. Because of scarcity of seismic instrumentation in the Valley of Mexico, until recently only a few local earthquakes could be studied in detail. Among the well-studied events is a swarm-like activity that occurred near the seismological station of Tacubaya (TAC) in 1981 (Figure 2a) (Havskov, 1982). The swarm lasted from 4 to 15 February 1981; the largest event, M_L 3.3, occurred on 4 February. This figure also shows other events well recorded in this area.

The disaster suffered by Mexico City during the great Michoacán earthquake of 1985 (M_w 8.0) and, more recently, from the Puebla-Oaxaca inslab earthquake of 2017 (M_w 7.0), along with the frequently-occurring local events, have produced a rapid increase in the number of seismographs and accelerographs in the valley, installed and maintained by different institutions (Quintanar *et al.*, 2018). For this reason, the swarm-like activity that occurred in the city in June-August 2019 was extensively recorded. This sequence also occurred close to TAC, about 4 km north of the 1981 sequence (Figure 2a). The largest event of the 2019 sequence, an M_w 3.2 earthquake on 17 July (Figure 2c), caused great panic in some of the neighborhoods of the city, and produced peak ground acceleration (PGA) exceeding 0.3 g at the closest station about 1 km away. Analysis of the large dataset produced by the sequence presented unusual difficulties (Singh *et al.*, 2020) owing to the complex upper crust and highly-variable superficial layers of the Valley of Mexico.

On 11 May 2023 a local earthquake in the city was felt very strongly in Mixcoac, San Angel, and Coyoacán neighborhoods. The earthquake was preceded and followed by events that were also alarming to the population (Figure 2b). The events in the 2023 sequence were located about 5 km south of the 2019 sequence, most events occurring within 2 km of the 1981 sequence (Figure 2a). The 11 May 2023 earthquake produced a PGA triplet of (152, 139, 178 cm/s^2) on the NS, EW, and Z components.

This paper presents an analysis of the 2023 sequence. We focus on the source characteristics of the main event and the recorded ground motions in the three geotechnical zones in which the city is divided. The study closely follows that of the 2019 sequence and draws on several of the results derived therein. Although there is no evidence of the magnitude of a local earthquake exceeding 4.2 since 1910, larger events can´t be ruled out as there are several mapped normal faults in the valley which exceed 20 km in length (Figure 1). Also, the TMVB has experienced many significant earthquakes in the last 450 years (Suárez *et al.*, 2019). This emphasizes the need of careful analyses of small earthquakes in Mexico City as it may help us understand what might happen during postulated, larger earthquakes.

2. Crustal Model, Location of Events, and Moment Tensor Inversion of the Main Event

In locating the events, we only used phase data from stations at epicentral distance (Δ) $\leq$ 20 km. Including farther stations increases the residuals at closer stations, no doubt due to the complex and heterogeneous shallow crustal structure. (S-P) time at the nearest station ENP8 for the main event is 0.44 s, suggesting that it was a shallow earthquake, similar to those that occurred during the nearby sequences of 1981 and 2019.

The crustal model used in locating the events and in moment tensor (MT) inversion is the same as given in Singh *et al.* (2020) which is reproduced in Table 1. The model was developed from those reported by Havskov (1982), Cruz-Atienza *et al.* (2010), and Espíndola *et al.* (2017). P-wave velocity, α, of top two layers was taken from a refraction study (Havskov and Singh, 1978). For the near-source data analyzed here, the waves mostly traverse through the first two layers. From P and S arrival times from the 2019 earthquake sequence and construction of the Wadati diagram, Singh *et al.* (2020) estimated $\alpha/\beta = 1.84$, hence β in the first layer of 1.58 km/s. The low β of the first layer may be consequence of high-water content of the rocks. For other layers α/β was fixed at 1.73. Density (ρ) and S-and P-wave quality factors (Q_β and Q_α), listed in the Table 1, have been chosen in agreement with values reported by Havskov (1982) for that zone of the city; MT inversion is not sensitive to an accurated value of these parameters.

Table 1. Crustal Model (from Singh *et al.*, 2020)

Layer	Thickness, km	α, km/s	β, km/s	ρ, gm/cm^3	Q_β[1]
1	2	2.90	1.58	2.50	50
2	2	4.70	2.72	2.76	50
3	26	6.60	3.81	2.82	50
4	5	7.10	4.10	3.03	50
5	∞	8.10	4.68	3.14	150

[1] $Q\alpha = 2\ Q_\beta$

Seismograms of some selected events of the sequence at the closest station ENP8 are displayed in Figure 3. Clearly, the recording of the main event is contaminated by a smaller

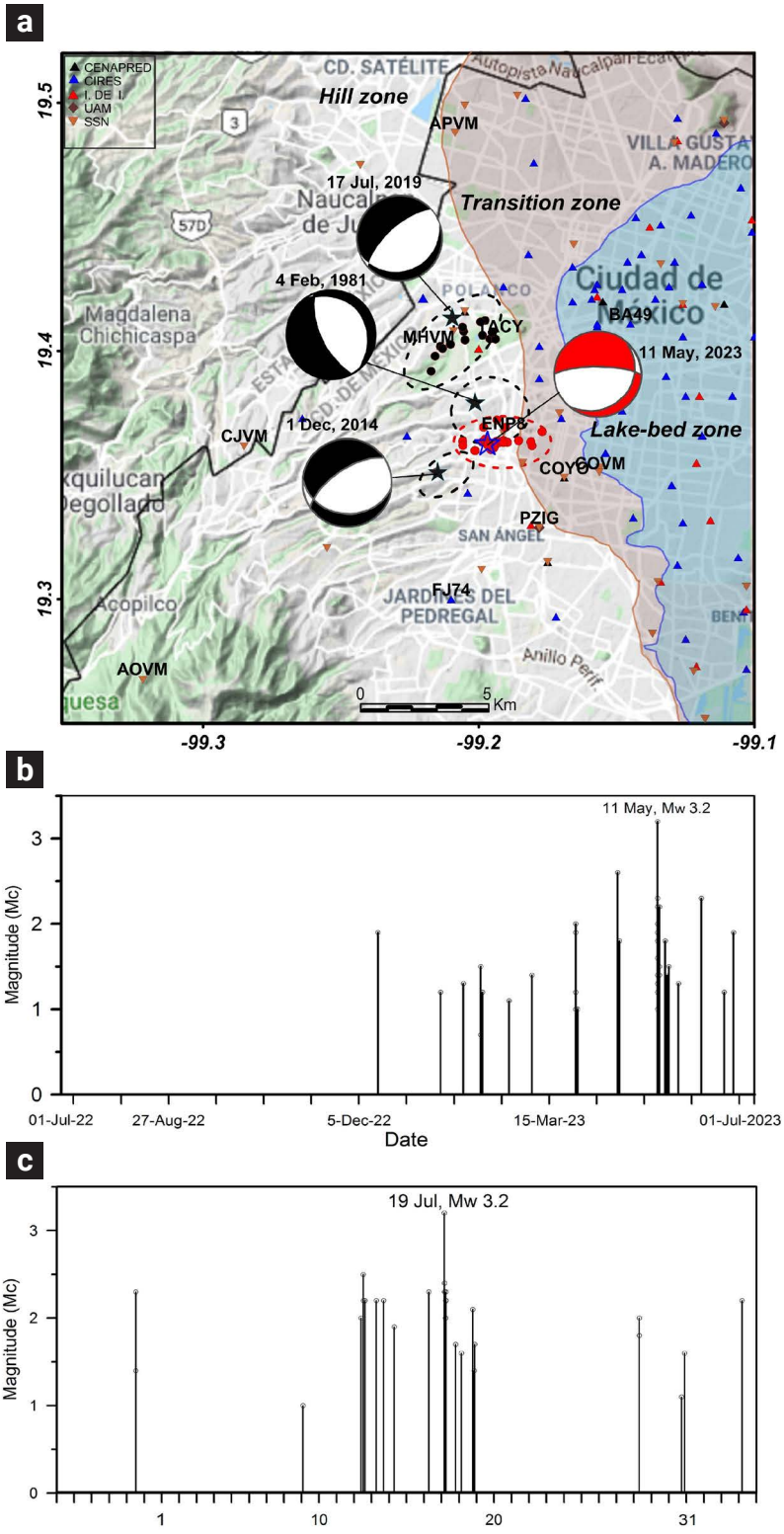

Figure 2. a) Enlarged view of the rectangular area marked in Figure 1. Hill, lake-bed, and transition zones are delineated in the figure. Dashed contours enclose seismic activity during the seismic sequence of 1981, 2014, 2019, and 2023. Star: mainshock location. Beach ball: focal mechanism. For the 2023 event the locations of the aftershocks are shown. Although recordings from 74 stations (19 in the hill zone, 14 in the transition zone, and 41 in the lake-bed zone) are analyzed in this study, only stations that are mentioned in the text are identified in the figure. b) Coda-wave magnitude versus time of events within a radius of 5 km from the epicenter of the earthquake of 11 May 2023, during a period of one year, from 1 July 2022 to 30 June 2023. Total number events = 45. Note the absence of activity during the first half of the period. c) Coda-wave magnitude versus time of events during the 2019 sequence. Much of the activity was concentrated between 12 -19 July 2019.

earthquake which occurred 2.7 s earlier (top trace). This made reading of the first motions difficult. The contamination also affects the MT inversion of the main event as the signal includes contribution from both events. A few other events were also preceded by a smaller event (Figure 3).

The events were located using SEISAN program (Havskov and Ottemöller, 1999). The hypocentral parameters of the main event are: 19.364°N, 99.197°W, H = 0.8 km, origin time 04:20:19.4, residual 0.37 s. Although the aftershock activity was intense, only 30 of these events were large enough to be located; the hypocenters of 22 of these could be determined using the double-difference technique (Waldhauser and Ellsworth, 2000). The locations are shown in Figure 2a.

Moment tensor inversion for the mainshock was performed using algorithm ISOLA (Sokos and Zahradnik, 2008). The algorithm allows for the inversion of complete regional and local waveforms. The moment tensor is retrieved through a least-squares inversion, whereas the position and origin time of the point sources are grid searched with a correlation coefficient greater than 90%. Green's functions, which includes near-field contribution, are calculated using the discrete wavenumber method (Bouchon, 1981; Coutant, 1989).

ISOLA has different error parameters that quantify the uncertainty of each solution. Each one of these parameters is not significant on its own; a joint interpretation of all the parameters is recommended (Sokos and Zahradnik, 2013). A useful indicator of solution quality is the Focal-Mechanism Variability Index, (FMVAR), defined as the mean K-angle (Kagan, 1991) of all acceptable solutions (as specified by the user-defined correlation threshold) with respect to the best-fit solution. A large value of FMVAR indicates that the moment tensor is unstable; conversely, when the focal mechanism is stable in the neighborhood of a source with maximum correlation, FMVAR will have a small value (Sokos and Zahradnik, 2013).

After many trials with different sets of stations, we used band-passed (0.08 – 0.24 Hz) displacement seismograms at stations COVM, MHVM, CJVM, APVM, and AOVM (Figure 4) in the inversion. The epicenter was fixed at the location obtained from the phase data. The Green's functions were generated using the crustal model given in Table 1. Observed and synthetic wave-

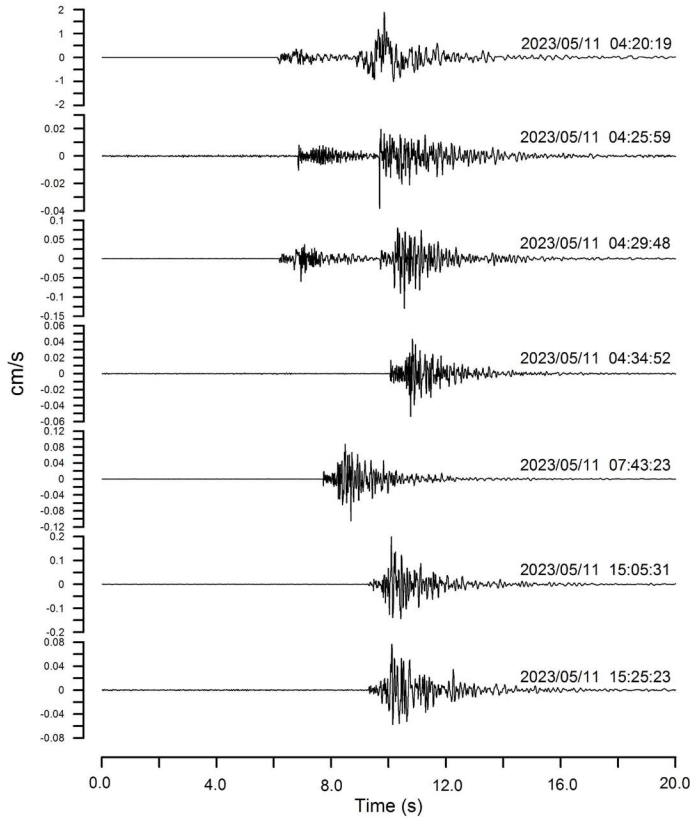

Figure 3. Velocity seismograms (cm/s) of the mainshock and some of the aftershocks at the closest station ENP8 (Z component). The mainshock (top trace) was preceded by a relatively small event that occurred 2.7 s earlier. A few other events were also preceded by a small event (second and third traces from the top).

forms are shown in the figure. The retrieved source parameters are: $M_0 = 6.79 \times 10^{13}$ Nm (M_w 3.2), H = 0.7 km, and NP1: φ = 270°, δ = 76°, λ = −75°; NP2: φ = 42°, δ = 20°, λ = −136°. The quality of the solution is moderate as seen from the fit of the synthetic seismograms to observed ones and by the FMVAR value of 22±21. The moderate quality of the solution is partly due to the contamination of the signal by an event that preceded the main event and partly due to the inadequacy of the 1-D crustal model to represent the real complex 3-D crustal structure. Based on the orientation of the faults mapped in the valley (Figure 1) and focal mechanisms of other events in the vicinity (Figure 2a), our preferred fault plane is NP1.

3. Source Spectrum, Variability of Ground Motion, and Site Effect

A theoretical source spectrum of the 11 May 2023 earthquake may be constructed from the seismic moment, M_0, estimated from the MT inversion, and an estimate of the stress drop, $\Delta\sigma$. To predict ground motion from future earthquakes it is important to know if the source spectrum computed from the observed recordings agree with the theoretical source spectrum. We first briefly present the procedure we have used to compute the source spectrum from the observed data.

The Fourier acceleration spectrum, $A(f, R)$, of horizontal component of *S*-wave group at a site in the far-field may be written as:

$$A(f, R) = C \times G(R) \times [\{f^2 M_0(f)\}] \times [Site(f) \times e^{-\pi\kappa f} \times B(f, f_m) \times e^{-\pi f R / \beta Q(f)}] \quad (1a)$$

$$C = FPR_{\theta\varphi} / (4\pi\rho\beta^3), \quad (1b)$$

where $\dot{M}_0(f)$ is the source displacement spectrum (also called the moment rate spectrum) so that $\dot{M}_0(f) \rightarrow M_0$ as $f \rightarrow 0$, R = hypocentral distance, $R_{\theta c\varphi}$= average radiation pattern (0.55), F = free surface amplification (2.0), P takes into account the partitioning of energy in the two horizontal components ($1/\sqrt{2}$), β = shear-wave velocity at the source, and ρ= density in the focal region. $G(R)$ in equation (1a) is the geometrical spreading term, often taken as $1/R$ for $R < R_x$ and $1/(R_x R)^{0.5}$ for $R \geq R_x$. The shape of the observed acceleration spectrum, $A(f, R)$, depends on the source acceleration spectrum, $f^2\dot{M}_0(f)$, modified by terms in the second square bracket of equation (1a). In this bracket, $Q(f)$ is the quality factor which includes both inelastic absorption and scattering, and κ and Butterworth filter $B(f, fm)$ account for attenuation in the near-surface layers and the finite bandwidth of the observed spectrum imposed by the sampling rate (Singh *et al.* 1982; Boore, 1983; Anderson and Hough 1984). $Site(f)$ represents spectral amplification due to local site effect; it includes the amplification resulting from lower velocities of the shallow layers, not accounted for in the simple half-space model which is the basis of equation 1a. As formulated above, $Site(f) = 1$ implies the absence of site effect. Often either $B(f, fm)$ or κ is sufficient to model the high-frequency fall off of the observed spectrum. Henceforth, we take $B(f, fm) = 1$. Following Singh *et al.* (2020), where details are given, we take β=1.58 km/s, ρ= 2.50 gm/cm^3, Rx = 3 km, $Q(f) = 13.2f^{0.83}$, and κ = 0.04 s. We note that for a Brune ω^{-2} source model (Brune, 1970):

$$\dot{M}_0(f) = M_0 f_c^2 / (f^2 + f_c^2) \quad (2a)$$

where f_c is the corner frequency. In Brune source model the stress drop, $\Delta\sigma$, is related to M_0 and f_c by (Brune, 1970):

$$\Delta\sigma = 8.47\, M_0\, (f_c/\beta)^3 \quad (2b)$$

4. Corner Frequency and Stress Drop

It is difficult to estimate the corner frequency f_c (hence, $\Delta\sigma$ from equation 2b) from the source spectrum because of the distortion caused by site effect. Yet, a knowledge of $\Delta\sigma$ is critical to gauge the strength of the relatively shallow faults (H ~ 1 km) in the Valley of Mexico. It is also a crucial parameter in the estimation of ground motion from postulated earthquakes.

An alternative method to estimate f_c is from the ratio of spectrum of a small event to that of the mainshock. The small event and mainshock should be collocated and should have the same focal mechanism. We could find only one suitable small event, an earthquake that occurred on 21 April 2023 (M_c 2.6). It was well recorded at stations PZIG, COVM, and COYO (Figure 2a). Figures 5a,b,c show the ratios of the NS, EW, and Z components as well as the geometric mean of the ratios of the three components at each of these stations. All nine spectral ratios and their geometric mean curve are displayed in Figure 5d. Each frame includes the theoretical spectral ratio corresponding to an ω^{-2}, constant $\Delta\sigma$, source model, a moment ratio of 10^{-2}, and corner frequencies, f_c, of 1.44 Hz ($\Delta\sigma$ = 0.5 MPa) and 0.84 Hz ($\Delta\sigma$ = 0.1 MPa). Short vertical lines in the figure mark f_c of 1.44 and 0.84 Hz. The observed ratios point to f_c = 1.44 Hz ($\Delta\sigma$ = 0.5 MPa) for the mainshock *albeit* with considerable uncertainty.

5. Source Spectrum and Site Effect

We correct the Fourier acceleration spectrum, $A(f, R)$, at each station according to equation 1 and solve for $[f^2\dot{M}_0(f)$

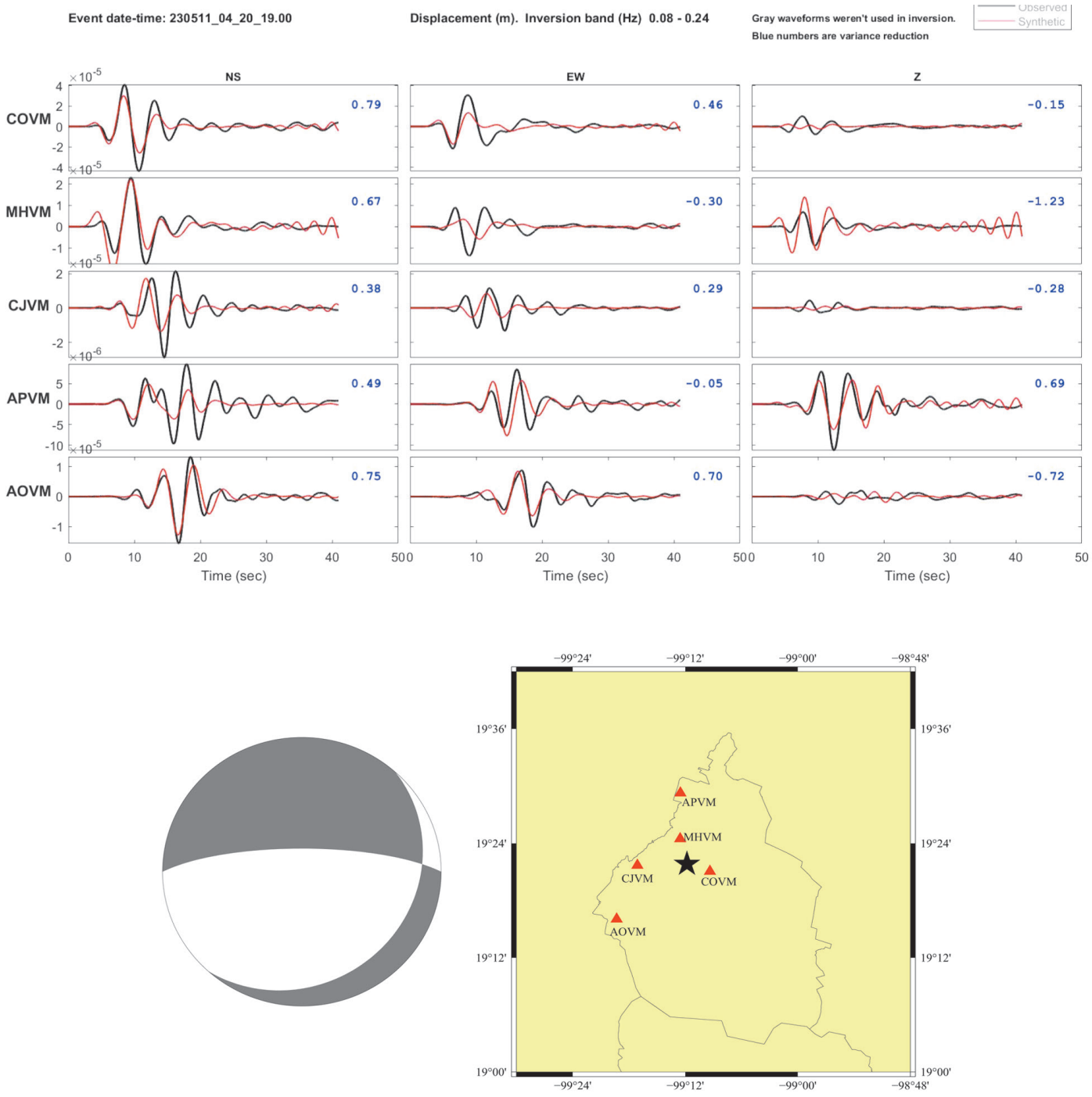

Figure 4. Observed and synthetic displacement waveforms band-passed 0.08–0.24 Hz from ISOLA moment tensor (MT) inversion of the mainshock. Also shown are the double couple focal mechanism and the stations used in the inversion.

Site(f)] which we call the observed acceleration source spectrum, *OASS(f)*. Since M_0 and f_c are known, the theoretical source spectrum, [$f^2\dot{M}_0(f)$], is constructed assuming a Brune ω^{-2} source model (equation 2a). *OASS(f)* curves of the mainshock computed at 19 stations in the hill zone, 14 stations in the transition zone, and 41 stations in the lake-bed zone are illustrated in Figures 6a,b,c, respectively. The plots show remarkable variability of ground motion in each of the three geotechnical zones. Figures 6a,b,c include the geometric mean and ± one standard deviation curves. Figure 6d illustrates geometric mean curves for the sites in the hill, transition, and lake-bed zones. The figure also shows the curve at CU which is often used as a reference site. Theoretical curve for an ω^{-2}-Brune source with $\Delta\sigma$ of 0.5 MPa is plotted in Figures 6a,b,c,d. Ratios of the *OASS*(f) geometric mean curve for each zone to the theoretical [$f^2\dot{M}0$ (f)] (equation 2a) are illustrated in Figure 6e. The ratio gives *Site(f)*, which includes amplification of the seismic waves caused by low-velocity layers above the source. For comparison, *Site(f)* in the hill zone, reported previously from a similar analysis of the recordings from the earthquake of 17 July 2019 earthquake (Singh *et al.*, 2020), is also shown in Figure 6e. The difference in the two site effects is partly because the stations and their total amount were not the same in the two analyses. Note that a deviation of the source from the assumed theoretical source model and error in the estimated $\Delta\sigma$ are mapped in the site effect.

Large site effect even in the hill zone of the Valley of Mexico is not unexpected. It was previously reported by Ordaz and Singh (1992) and Singh *et al.* (1995) based on seismograms from coastal earthquakes recorded in the valley.

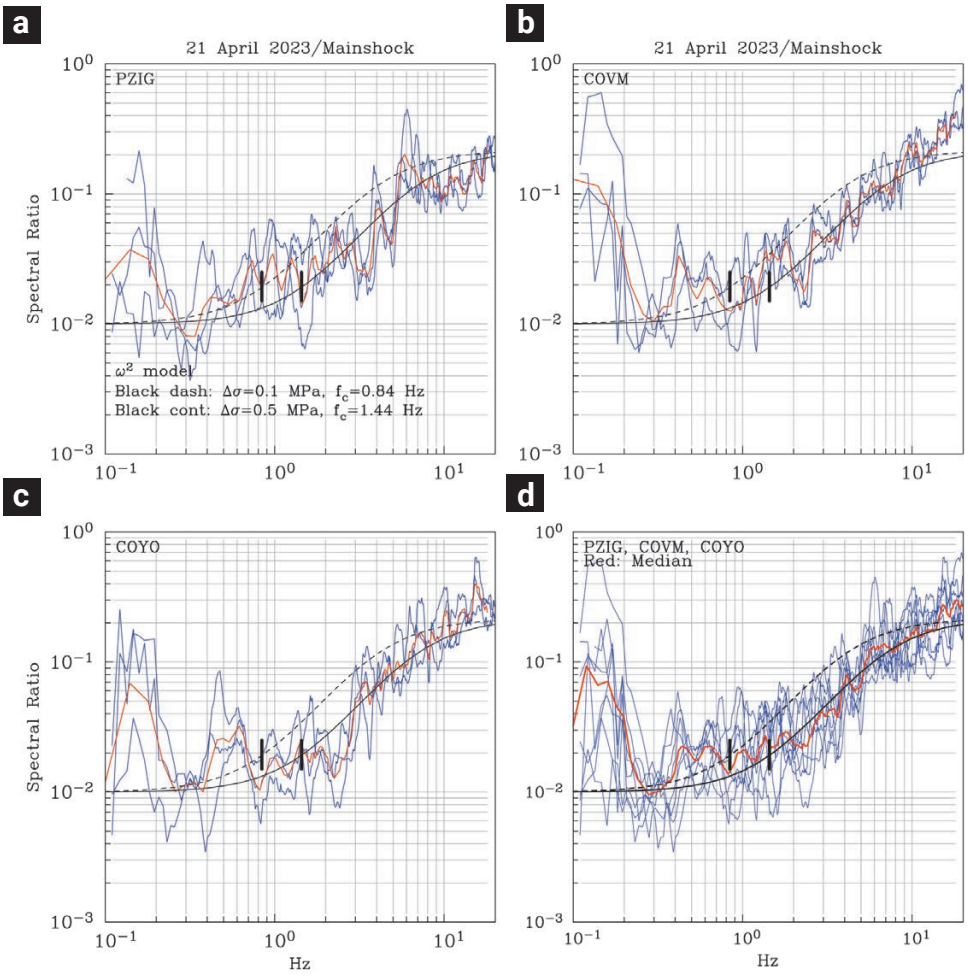

Figure 5. Spectral ratios of the earthquake of 21 April 2023 to the mainshock of 11 May 2023 at a) PZIG, b) COVM, c) COYO. Red curve is the geometric mean of NS, EW, and Z ratios. d) Geometric mean curve (in red) of spectral ratios at PZIG, COVM, and COYO. Each frame shows theoretical spectral ratio corresponding to an ω^{-2}, constant $\Delta\sigma$ source model, a moment ratio of 10^{-2}, and corner frequency, f_c, of 1.44 Hz ($\Delta\sigma$ = 0.5 MPa) (black smooth curve) and 0.84 Hz ($\Delta\sigma$ = 0.1 MPa) (black, dashed, smooth curve). Short vertical lines mark f_c of 1.44 and 0.84 Hz. Observed ratios suggest fc = 1.44 Hz ($\Delta\sigma$ = 0.5 MPa) for the mainshock.

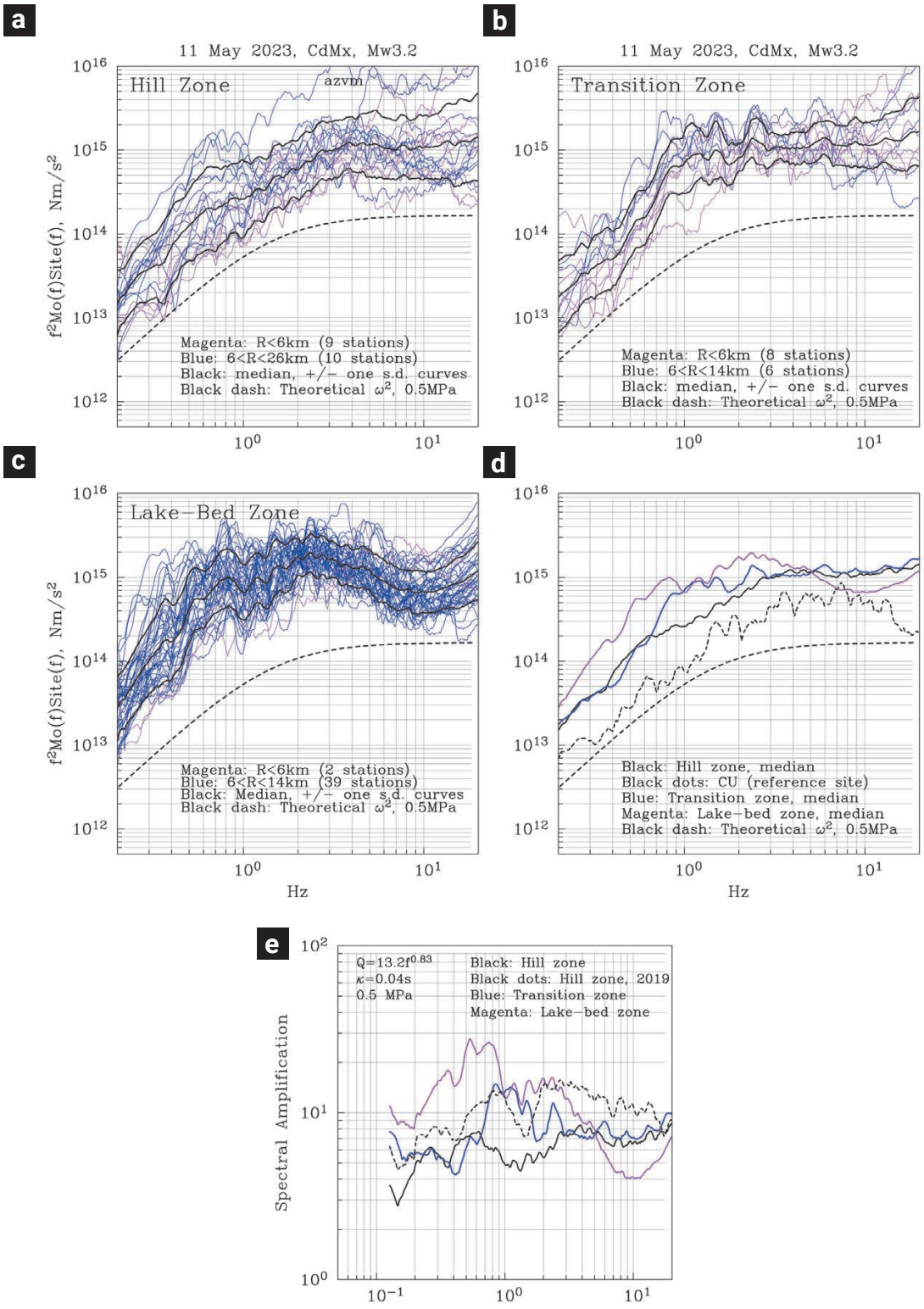

Figure 6. $[f^2\dot{M}_0\,(f)Site(f)]$ curves of the mainshock estimated at a) 19 individual stations in the hill zone, b) 14 stations in the transition zone, and c) 41 stations in the lake-bed zone. Plots show remarkable variability of ground motion in each of the three geotechnical zones. Geometric mean and ± one standard deviation curves are shown in black. d) Geometric mean curves for the sites in the hill, transition, and lake-bed zones. Also shown is the curve at CU which is often used as a reference site (dotted black line). Theoretical curve for an ω^{-2}-Brune source with $\Delta\sigma$ of 0.5 MPa is shown in a) to d). e) Ratios of the observed $[f^2\dot{M}_0\,(f)]$ geometric mean curve for each zone to the theoretical $[f^2\dot{M}_0\,(f)]$ curve predicted by the ω^{-2}-Brune source model. The ratio yields $Site(f)$, the site effect. For comparison, the site effect in the hill zone reported previously from a similar analysis of the recordings from the earthquake of 17 July 2019 earthquake (Singh *et al.*, 2020) is also shown.

6. Observed and Predicted PGA and PGV

As discussed above, the estimation of the generic site effect in the different geotechnical zones of the Valley of Mexico depends on $\Delta\sigma$. However, in the present case, the estimation of ground motion from postulated events *via* stochastic method (Boore, 1983) does not require a knowledge of true $\Delta\sigma$ provided that the postulated earthquake also follows the ω^{-2} source model, and $\Delta\sigma$ is the same as that of the M_w 3.2 event. In this case, the predicted Fourier amplitude spectrum at a generic site from the postulated earthquake and, hence, also the predicted ground motion parameters remain the same irrespective of $\Delta\sigma$. We take advantage of this possibility and compute PGA and PGV for M_w 3.2 and 5.0 earthquakes. Predictions for an M_w 3.2 earthquake permit comparison with the observed data, while those for an M_w 5.0 event provide an estimate of ground motions from a reasonable scenario earthquake.

We recapitulate the assumptions made and parameters used in the application of the stochastic method: Brune ω^{-2} source; $\Delta\sigma = 0.5$ MPa; $\beta = 1.58$ km/s; $\rho = 2.50$ gm/cm^3; $\kappa = 0.04$ s; $Rx = 3$ km; $Q(f)=13.2f^{0.83}$. Generic *Site(f)* for the three zones are shown in Figure 6e. Application of the stochastic method also requires an estimation of the effective duration, T_d, of the ground motion; we use the relation $(T_d - 1/f_c) = 0.93\,\Delta$, where Δ is the epicentral distance; this relation was derived for the hill zone in the previous study of the 2019 sequence (Singh *et al.*, 2020); we assume that this relation holds for all three zones. Figures 7a,b show predicted PGA and PGV curves as a function of R for an M_w 3.2 earthquake superimposed on the observed values. Predicted PGA curves for the three zones are nearly the same. The observed PGA values in the hill zone are in good agreement with the prediction but not in the transition and lake-bed zones where they are somewhat greater than the predicted ones. Unlike predicted PGA curves, the PGV curves for the three zones differ substantially. Both the observations and the predictions are greater for the lake-bed zone than for the transition zone which, in turn, are greater than for the hill zone. There is large scatter in the observed PGA and PGV data which is consistent with great variability of the source spectrum seen in Figures 6a,b,c.

7. Ground Motion from a Scenario M_w 5.0 Earthquake

We consider a scenario local earthquake of M_w 5.0 although larger earthquakes are certainly plausible because there are several mapped normal faults in the Valley of Mexico exceeding 20 km in length (Figure 1). There is, however, no evidence of an M > 4.2 local earthquake in Mexico City in the available seismograms recorded in the city (at Tacubaya for the period 1910 – 1973; at other stations since then). We estimate ground motions from the scenario earthquake by applying the stochastic technique. The technique assumes that the far-field, point source approximation is valid, *i.e.*, distance to station, R, is much greater than both the source dimension as well the wavelength of interest. Expected rupture length of an M_w 5.0 earthquake is about 3 to 4 km (Wells and Coppersmith, 1994). The period of interest in Mexico City is less than about 2.5 s, so that, for $\beta = 1.58$ km/s, the wavelength of interest is < 4.0 km. It follows that for far-field approximation to be valid R should be much greater than 4.0 km. Although we present expected ground motions at shorter distances, the results for $R < 6.0$ km are likely to be approximate. Furthermore, the rupture of an M_w 5.0 earthquake may reach 3 to 4 km in depth while the parameters we have used in the simulations were estimated from shallower sources. With these limitations in mind, the expected PGA and PGV at the epicenter of a postulated M_w 5 earthquake are 0.6 g and 60 cm/s at a typical hill site; at lake-bed site the expected values are twice as large (Figures 7c,d). We note that the simulated PGA values at soft sites for an M_w 5.0 earthquake are greater than at hard sites by a factor greater than those observed during the M_w 3.2 mainshock (compare Figures 7a and 7c). It is further accentuated for PGV (compare Figures 7b and 7d). This implies that the scaling of PGA and PGV with M_w differs for hard and soft sites. It is confirmed from Figures 7e and 7f which show the scaling of PGA and PGV with M_w at generic sites in the hill and lake-bed zones with R fixed at 7.5 km. The figures show greater dependence of PGA and PGV on M_w at the soft site. We also computed expected PGA and PGV at $R = 7.5$ km as a function M_w using the recordings at the hill-zone station of FJ74 ($R = 7.2$ km) and lake-zone station of BA49 ($R = 7.5$ km) as empirical Green´s functions (EGFs). A scheme of random summation of EGF introduced by Ordaz *et al.* (1995) was used in the simulation. A stress drop of 0.5 MPa was assumed for both the EGF and target events. The predicted values from the EGF technique are superimposed in Figures 7e,f. While the stochastic predictions at hill zone and lake-bed zone differ significantly, the EGF predictions are nearly the same. This is because the predictions using EGF technique are site specific (for FJ74 and BA49) while those obtained from stochastic method are for a generic site.

Numerical modelling of wave propagation in Mexico City from local earthquakes has been the topic of two recent studies (Cruz-Atienza *et al.*, 2016; Hernandez-Aguirre *et al.*, 2023). These studies shed light on the cause of long coda observed in the seismograms of lake-bed zone and on the nature of the wavefield. Hernandez-Aguirre *et al.* (2023) computed synthetic seismograms (low-pass filtered at 1.3 Hz) from the 17 July 2019 M_w 3.2 earthquake. Although the complex 3D structure of the valley is still poorly known, Hernandez-Aguirre *et al.* (2023)

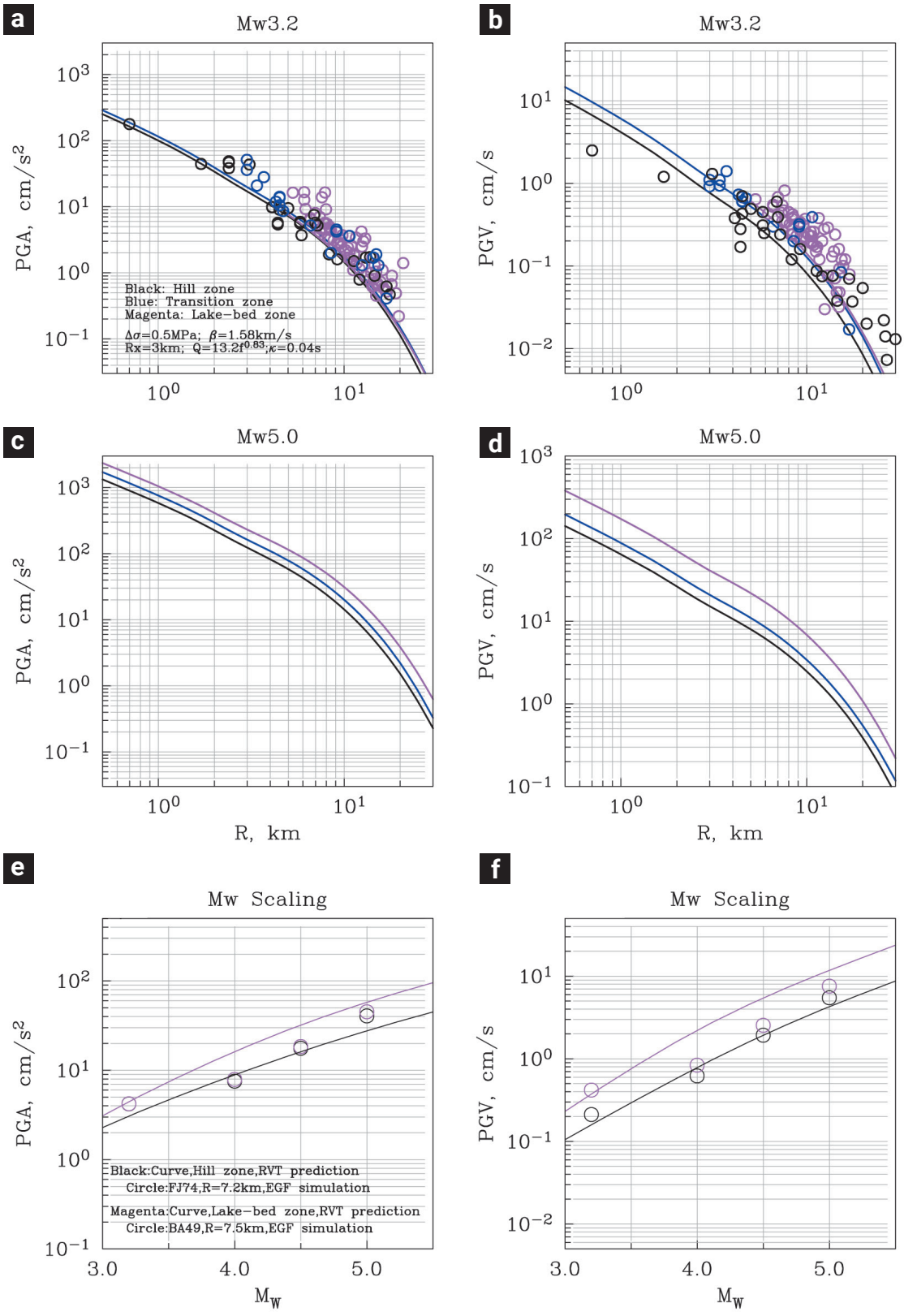

Figure 7. a), b) Predicted PGA and PGV curves for an M_w 3.2 earthquake for the three geotechnical zones computed via the stochastic method superimposed on the observed values during the 2023 mainshock. c), d) Predicted PGA and PGV curves for a postulated M_w 5.0 earthquake applying the stochastic technique. e), f) Predicted PGA and PGV curves as function of M_w at R = 7.5 km at a generic site in the hill-zone zone and lake-bed zone using the stochastic method. Superimposed are estimated values at FJ74 (in the hill zone) and BA49 (in the lake-bed zone) using an EGF technique. Stations are located at nearly the same distance (R = 7.5 km). EGFs are the 2023 mainshock recordings at these two stations.

find good agreement between simulated and observed velocity records. As our knowledge of the structure improves, it will become possible to synthesize ground motions from postulated, larger earthquakes.

8. High PGA in the Epicentral Area but No Damage

As mentioned earlier, the PGA triplet on the NS, EW, and Z components during the 2023 earthquake at the epicentral station of ENP8 was (152, 139, 178 cm/s^2). The corresponding triplet during the 2019 earthquake at the nearest station of MHVM was (101, 314, 305 cm/s^2). No wonder these earthquakes were very strongly felt in the epicentral area. Yet, surprisingly, no building damage was reported. The epicenter of the 2019 event coincides with a cemetery. Thus, it may be argued that the absence of damage was due to the lack of structures in the epicentral region. However, no structural damage was reported during the 2023 event either although the epicentral region was located within a highly-populated zone with many one- to two-stories structures that, in principle, were susceptible to the short-period ground motion. A relevant question is whether the observed *SA* (pseudo response spectra, 5% damping) during the two earthquakes exceeded the design spectrum for the hill zone as prescribed in the Mexico City Building Code. Figure 8 shows the comparison. Clearly, the observed *SA* at short periods exceeded the design spectrum, (see also Ordaz *et al.*, 2023). Further studies are warranted to understand the cause of the lack of structural damage during the 2019 and 2023 M_w3.2 earthquakes.

9. Discussion and Conclusions

The earthquake of 11 May 2023 occurred in the west of Mexico City during a seismic sequence that had initiated 5 months earlier. The events in the sequence were shallow (H ~ 1 km). The earthquake was felt very strongly in Mixcoac, San Angel, and Coyoacán. The PGA at the closest station was ~ 0.18 g.

Moment tensor inversion of bandpass filtered (0.08 – 0.24 Hz) displacement records of the 2023 earthquake yields $M_0 = 6.8\times10^{13}$ N-m (M_w3.2), H = 0.7 km, and the likely fault plane characterized by $\varphi = 270^0$, $\delta = 76^0$, $\lambda = -75^0$.

Spectral analysis of the recordings reveals great variability of ground motion within each of the three geotechnical zones in which Mexico City is divided. The cause of this variability is clearly the complex, 3D structure of the superficial layers; hence, the parameters needed to correct the spectra of observed ground motion in Mexico City to estimate the source spectrum are not well constrained. Using those that were derived from the analysis of the earthquake of 17 July 2019, we determined the source spectrum of the 2023 event. We find a large disparity between the observed source spectrum and theoretical source spectrum (computed for an ω^{-2} source with $\Delta\sigma = 0.5$ MPa). Although we attribute this disparity to the amplification of seismic waves as they travel upwards from the source through layers of decreasing velocity, the uncertainty in the parameters used may also partly be responsible. Predicted PGA and PGV for an M_w 3.2 earthquake, computed using stochastic technique, assuming a Brune ω^{-2} source, $\Delta\sigma = 0.5$ MPa and including the site effect, are in reasonable agreement with the observations.

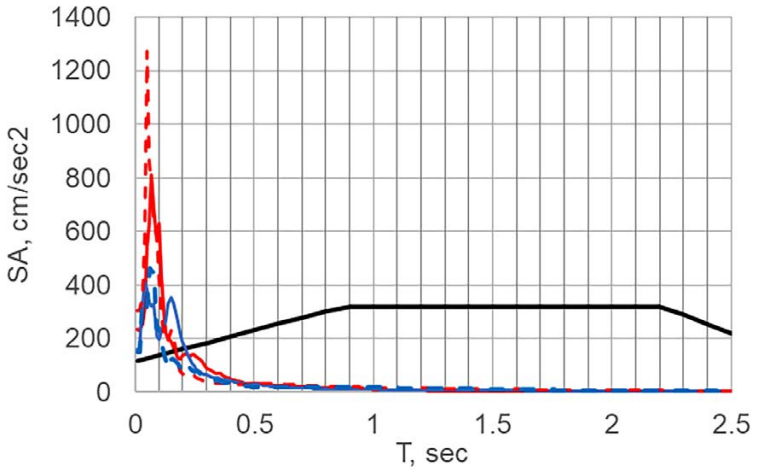

Figure 8. Comparison of recorded SAs during the 2019 and 2023 M_w 3.2 earthquakes at the closest station with the design spectrum prescribed in the Mexico City Building Code for the region. The quadratic mean of the SA of the two horizontal components and the SA of the vertical component are plotted with continuous and dashed curves (blue: 2023 earthquake; red: 2019 earthquake). Continuous black line is the horizontal design spectrum according to the Mexico City Building Code.

Expected PGA and PGV at the epicenter of a postulated M_w 5 earthquake, under several assumptions, are 0.6 g and 60 cm/s at a generic hill site; at lake-bed site the expected values are twice as large.

In many respects the Mexico City earthquakes of 11 May 2023 and 17 July 2019 were very similar: (1) They occurred in the same part of the city, both were shallow (H ~ 1 km), and had the same magnitudes, M_w 3.2. (2) Both earthquakes were part of a swarm-like activity. (3) They were strongly felt by the population living in the epicentral area, causing panic, and producing high PGA (0.18 g in 2023; 0.3 g in 2019). (4) The response spectrum of both events at the closest station exceeded the City´s design spectrum at short periods. Even so, neither of the two events caused structural damage although there were many one- and two-story buildings in the epicentral zone (at least during the 2023 event; the epicenter of the 2019 earthquake fell in a cemetery) susceptible to ground motion at short periods. (5) As expected from transtensional stress regime of the central TMVB, both events had predominantly normal-faulting focal mechanism. (6) Stress drop of both events was low which is reasonable for these shallow events; $\Delta\sigma$ estimate, however, is poorly constrained. A reliable estimate of $\Delta\sigma$ of these shallow earthquakes is most desirable. (7) A large disparity between observed and theoretical source spectra is found during both earthquakes. We have attributed this to a site effect. The cause, however, could partly be the error in the parameters used in correcting the spectra.

Not all the seismicity in the Valley of Mexico is shallow. SSN earthquake catalog and examination of seismograms suggest that it extends up to a depth of ~ 15 km. These relatively deep earthquakes have yet to produce extensive recordings. Once such recordings become available it will be interesting to compare these events with the shallower ones.

10. Data and Resources

Data used in this study were obtained by the National Seismological Service (SSN; **http://www.ssn.unam.mx/doi/networks/mx/**), Instituto de Geofísica, UNAM; the Strong Ground Motion Database System (**http://aplicaciones.iingen.unam.mx/AcelerogramasRSM/**); and the Centro de Instrumentación y Registro Sísmico (CIRES; **http://cires.org.mx/registro_es.php**), Mexico City.

11. Acknowledgments

We thank Juan M. Gómez-González for guiding us in the use of ISOLA software. The dedication of the personnel of National Seismological Service (SSN), Instituto de Geofísica, UNAM; Seismic Instrumentation Group of Instituto de Ingeniería, UNAM; and Centro de Instrumentación y Registro Sísmico (CIRES) in station maintenance, and data acquisition and distribution is acknowledged. The research was partly supported by DGAPA UNAM projects IN109423 (S.K.S.) and IN116423 (L.Q.).

12. References

Anderson, J. G. and S. E. Hough (1984). A model for the shape of the Fourier amplitude spectrum of acceleration at high frequencies, *Bull. Seism. Soc. Am.* 74, 1969-1994.

Arce, J. L., P. W. Layer, J. L. Macías, E. Morales-Casique, A. García-Palomo, F. J. Jiménez-Domínguez, J. Benowitz, and A. Vásquez-Serrano (2019). Geology and stratigraphy of the Mexico Basin (Mexico City), Central Trans-Mexican Volcanic Belt, *Journal of Maps*, doi: **https://doi.org/10.1080/17445647.2019.1593251**

Boore, D. M. (1983). Stochastic simulation of high-frequency ground motions based on seismological models of the radiated spectra, *Bull. Seism. Soc. Am.* 73, 1865-1894.

Boore, D.M. (2003). Simulation of Ground Motion Using the Stochastic Method, *Pure Appl. Geophys*. 160, 635–676.

Bouchon, M. (1981). A simple method to calculate Green's functions for elastic layered media, *Bull. Seism. Soc. Am.* 71, 959-971. doi: **https://doi.org/10.1785/BSSA0710040959**

Brune, J.N. (1970). Tectonic stress and the spectra of seismic shear waves from earthquakes, *J. Geophys. Res.* 75, 4997-5009.

Coutant, O. (1989). Program of numerical simulation AXITRA, Tech. Rep., LGIT, Grenoble, France (in French).

Cruz-Atienza, V. M., A. Iglesias, J. F. Pacheco, N. M. Shapiro, and S. K. Singh (2010). Crustal structure below the Valley of Mexico estimated from receiver functions, *Bull. Seism. Soc. Am.* 100, 3304–3311, doi: **https://doi.org/10.1785/01201000051**

Cruz-Atienza, V.M., J. Tago, J.D. Sanabria-Gómez, E. Chaljub, V. Etienne, J. Virieux, and L. Quintanar (2016). Long duration of ground motion in the paradigmatic Valley of Mexico. *Scientific Reports* 6, 38807. doi: **https://doi.org/10.1038/srep38807**

Ego F. and V. Ansan, (2002). Why is the Central Trans-Mexican Volcanic Belt (102°–99°W) in transtensive deformation?, *Tectonophysics* 359, 189 – 208. doi: **https://doi.org/10.1016/S0040-1951(02)00511-5**

Espíndola V. H., L. Quintanar, and J. M. Espíndola (2017). Crustal Structure beneath Mexico from Receiver Functions, *Bull. Seism. Soc. Am.* 107, 2427-2442. doi: **https://doi.org/10.1785/0120160152**

Figueroa, J. (1971). Sismicidad en la Cuenca del Valle de México, *Serie de Investigación No. 289*, Instituto de Ingeniería, UNAM, 12 pp. (in Spanish).

Havskov J. (1982). The Earthquake Swarm of February 1981 in Mexico City, *Geofís. Int.* 21 no. 2, 157-175. doi: **https://doi.org/10.22201/igeof.00167169p.1982.21.2.909**

Havskov, J. and S.K. Singh (1978). Shallow crustal structure below Mexico City, *Geofís. Int.* 17, no. 2, 223-229. doi: **https://doi.org/10.22201/igeof.00167169p.1978.17.2.935**

Havskov, J. and L. Ottemöller (1999). Electronic seismologist: SeisAn earthquake analysis software, *Seism. Res. Lett.* 70, 532-534.

Hernández-Aguirre, V. M., R. Paolucci, F. J. Sánchez-Sesma, and I. Mazzieri (2023). Three-dimensional numerical modeling of ground motion in the Valley of Mexico: A case study from the Mw3.2 earthquake of July 17, 2019, *Earthquake Spectra*, doi: **https://doi.org/10.1177/87552930231192463**

Johnson, C.A. and C. G. A.Harrison, C.G.A. (1990). Neotectonics in Central Mexico, *Phys. Earth Planet. Inter.* 64, 187-210. doi: **https://doi.org/10.1016/0031-9201(90)90037-X**

Kagan, Y. Y. (1991). 3-D rotation of double-couple earthquake sources, *Geophys. J. Int.* 106, 709–716, doi: **https://doi.org/10.1111/j.1365-246X.1991.tb06343.x**

Manzanilla, L. (1986). Relación de los sismos ocurridos en la ciudad de México y sus efectos, *Revista Mexicana de Sociología* 4, No. 2, 265-282 (in Spanish).

Marsal, R.J., Mazari, M. (1969). El subsuelo de la Ciudad de México. Instituto de Ingeniería, UNAM, México, ISBN: 9786070281969. pp 456.

Mooser, F. (1972). The Mexican volcanic belt structure and tectonics, *Geofís. Int*. 12, 55–70. doi: **https://doi.org/10.22201/igeof.00167169p.1972.12.2.1024**

Ordaz, M. and S.K. Singh (1992). Source Spectra and Spectral Attenuation of Seismic waves from Mexican Earthquakes, and Evidence of Amplification in the hill zone of Mexico City, *Bull. Seism. Soc. Am.* 82, 24-43.

Ordaz, M, J. Arboleda, and S.K. Singh (1995). A scheme of random summation of an empirical Green's function to estimate ground motions from future large earthquakes, *Bull. Seism. Soc. Am.* 85, 1635–1647.

Ordaz, M., Danny Arroyo, Shri K. Singh, Luis Quintanar, (2023); Microsismos en la CDMX; *Revista del Colegio de Ingenieros Civiles de México A.C.*; No. 646, Año LXXIII, pp. 20-23, octubre 2023.

Pasquaré, G., L. Vezzoli and A. Zanchi (1987). Morphological and structural model of Mexican Volcanic Belt. *Geofís. Int.* 26 no. 6, 159-176. doi: **https://doi.org/10.22201/igeof.00167169p.1987.26.2.1107**

Quintanar, L., A. Cárdenas-Ramírez, D. I. Bello-Segura, V. H. Espíndola, J. A. Pérez-Santana, C. Cárdenas-Monroy, A. L. Carmona-Gallegos and I. Rodríguez-Rasilla (2018). A seismic network for the Valley of Mexico: present status and perspectives, *Seismol. Res. Lett.* 89, no. 2A, 356-362, doi: **https://doi.org/10.1785/0220170198**

Reinoso, E., M. Ordaz (1999). Spectral ratios for Mexico City from free-field recordings, *Earthquake Spectra* 15, 273-295.

Singh, S. K., R. Apsel, J. Fried, and J. N. Brune (1982). Spectral attenuation of SH waves along the Imperial fault, *Bull. Seism. Soc. Am.* 72, 2003-2016. doi: **https://doi.org/10.1785/BSSA07206A2003**

Singh, S. K., E. Mena, and R. Castro (1988a). Some aspects of source characteristics of 19 September 1985 Michoacán earthquake and ground motion amplification in and near Mexico City from the strong motion data, *Bull. Seism. Soc. Am.* 78, 451-477.

Singh, S. K., J. Lermo, T. Domínguez, M. Ordaz, J.M. Espinosa, E. Mena, and R. Quaas (1988b). A study of amplification of seismic waves in the Valley of Mexico with respect to a hill zone site (CU), *Earthquake Spectra* 4, 653-674.

Singh S.K., R. Quaas, M. Ordaz, F. Mooser, D. Almora, M. Torres, and R. Vásquez (1995). Is there truly a "hard" rock site in the Valley of Mexico?, *Geophys. Res. Lett.* 22, no. 4, 481-484. doi: **https://doi.org/10.1029/94GL03298**

Singh, S. K., J. G. Anderson, and M. Rodríguez (1998). Triggered seismicity in the Valley of Mexico from major Mexican earthquakes, *Geofís. Int.* 37 no. 1, 1-11. doi: **https://doi.org/10.22201/igeof.00167169p.1998.37.1.2155**

Singh, S. K., L. Quintanar-Robles, D. Arroyo, V. M. Cruz-Atienza, V. H. Espíndola, D. I. Bello-Segura, and M. Ordaz (2020). Lessons from a small local earthquake (Mw 3.2) that produced the highest acceleration ever recorded in Mexico City, *Seismol. Res. Lett.* 91, 3391–3406, doi: **https://doi.org/10.1785/0220200123**

Sokos, E. and J. Zahradnik (2008). ISOLA-A Fortran code and a Matlab GUI to perform multiple-point source inversion of seismic data, *Comput. Geosci.* 34, 967-977. doi: **https://doi.org/10.1016/j.cageo.2007.07.005**

Sokos, E. and J. Zahradnik (2013). Evaluating Centroid-Moment-Tensor uncertainty in the new version of ISOLA software, *Seismol. Res. Lett.* 84, 656–665. doi: **https://doi.org/10.1785/0220130002**

Suárez, G., G.V. Caballero-Jiménez, D.A. Novelo-Casanova (2019). Active crustal deformation in the Trans-Mexican Volcanic Belt as evidenced by historical earthquakes during the last 450 years, *Tectonics*, doi: **https://doi.org/10.1029/2019TC005601**

Suter, M., O. Quintero, and C. Johnson (1992). Active faults and state of stress in the central part of the Trans-Mexican Volcanic Belt. 1. The Venta de Bravo fault, *J. Geophys. Res.* 97, 11,983–11,994. doi: **https://doi.org/10.1029/91JB00428**

Waldhauser, F. and W.L. Ellsworth (2000). A double-difference earthquake location algorithm: method and application to the northern Hayward fault, California, *Bull. Seism. Soc. Am.* 90, 1353–1368. doi: **https://doi.org/10.1785/0120000006**

Wells, D.L. and K. J. Coppersmith (1994). New empirical relationships among magnitude, rupture length, rupture width, rupture area, and surface displacement, *Bull. Seism. Soc. Am.* 84, 974–1002. doi: **https://doi.org/10.1785/BSSA0840040974**

Geofísica Internacional (2024) **63-2**: 763 - 781

A Source and Ground Motion Study of the Veracruz Earthquakes of 29 October 2009 (Mw5.7) and 4 August 2021 (Mw4.8): Evidence of Strong Azimutual Variation of Attenuation

A. Iglesias[1], S. K. Singh[1], D. Arroyo[2], X. Pérez-Campos[1,3], V. H. Espíndola[1], A. Vargas[4], F. Córdoba-Montiel[5] and Deni M. González-López[6]

Abstract

We study two moderate earthquakes that occurred offshore the State of Veracruz, in the southwestern Gulf of Mexico, on 29 October 2009 (M_w 5.7) and 4 August 2021 (M_w 4.8). The former was located near the town of Alvarado and latter near the city of Veracruz. The events were well recorded by accelerographs and seismographs at local and regional distances. *W*-phase regional centroid moment tensor inversion reveals that they had reverse-faulting mechanism, similar to several other earthquakes in the southwestern Gulf of Mexico. Of the seven focal mechanisms now available along the southwestern margin, two are strike slip and the rest are of thrust type, suggesting a heterogeneous stress regime. We take advantage of local and regional recordings produced by these two earthquakes to study the characteristics of the ground motion. Source spectra computed at each station separately (without correcting for the site effect), assuming a reasonable geometrical spreading and $Q = 141f^{0.63}$, show remarkably high variability due to difference in path and local site effects. The geometric mean apparent source spectrum (source spectrum including site effects) of both earthquakes may be modeled by an ω^2-Brune source model with a stress drop, $\Delta\sigma$, of 40 MPa. These source spectra, along with the application of stochastic method, yield peak ground acceleration (*PGA*) and velocity (*PGV*) as a function of distance in general agreement with the observations. Of greater practical importance is the ground motion at sedimentary sites in the city of Veracruz and at the Laguna Verde Nuclear Power Plant (LVNPP) site, especially from a postulated M_w 6.5 earthquake which is a reasonable scenario event for the region. For the city of Veracruz and LVNPP we estimate site effect with respect to the ω^2-Brune source with $\Delta\sigma$ of 2 MPa. There is some support for this $\Delta\sigma$. We apply both stochastic and empirical Green's functions (*EGF*) techniques in the estimation of the ground motion. The recording of the 2021 earthquake is taken as the *EGF*, and $\Delta\sigma$ of the *EGF* and the target event are assumed to be the same and equal to 2 MPa. The predicted *PGA* and *PGV* at sedimentary sites in the city of Veracruz and LVNPP above the hypocenter (depth = 20 km) from the postulated M_w 6.5 earthquake are 0.2 g and 10 cm/s and 0.18 g and 3 cm/s, respectively. These results are preliminary as they are based on several assumptions.

Key words: Veracruz Earthquakes, Site Effect, Empirical Green Functions.

Resumen

En este trabajo estudiamos dos sismos de magnitud moderada que ocurrieron frente a las costas del Estado de Veracruz, en el suroeste del Golfo de México, el 29 de octubre de 2009 (M_w 5.7) y el 4 de agosto de 2021 (M_w 4.8). El primero estaba ubicado cerca de Alvarado, Ver. y el segunda cerca de la ciudad de Veracruz, Ver. Ambos eventos fueron bien registrados mediante acelerógrafos y sismógrafos a distancias locales y regionales. La inversión del tensor de momento con fase W muestra mecanismos de falla inversa, similar a otros sismos en el suroeste del Golfo de México. De los siete mecanismos focales disponibles a lo largo del margen suroeste, dos muestran fallas de deslizamiento lateral y el resto de muestran mecanismos de tipo inverso, lo que sugiere un régimen de tensiones heterogéneo. Con base en los registros locales y regionales de estos dos sismos, en este trabajo, estudiamos las características del movimiento del suelo. Los espectros de la fuente calculados en cada estación por separado (sin corregir el efecto de sitio), suponiendo una dispersión geométrica razonable y $Q = 141f^{0.63}$, muestran una variabilidad notablemente alta debido a la diferencia en los efectos de la trayectoria y del sitio. La media geométrica del espectro de fuente aparente (espectro de fuente que incluye los efectos del sitio) de ambos terremotos puede modelarse mediante un modelo de fuente ω^2-Brune con una caída de esfuerzos, $\Delta\sigma$, de 40 MPa. A través de un método estocástico, los espectros de la fuente producen aceleraciones máximas del suelo (PGA) y velocidades máximas (PGV), con respecto de la distancia, que en general están de acuerdo con las observaciones. De importancia relevante son las aceleraciones en sitios en la ciudad de Veracruz y en el sitio de la Central Nuclear Laguna Verde (LVNPP), especialmente suponiendo un terremoto postulado de M_w 6.5, lo cual es un escenario razonable para la región. Para la ciudad de Veracruz y LVNPP estimamos los efectos de sitio asumiendo una fuente ω^2-Brune con $\Delta\sigma$ de 2 MPa, caída de esfuerzos que tiene cierto soporte. En este trabajo fueron aplicados métodos tanto de funciones de Green (EGF) estocásticas como empíricas en la estimación del movimiento del suelo. El registro del sismo de 2021 se toma como EGF, y se supone que las $\Delta\sigma$'s del EGF y el evento objetivo son las mismas e iguales a 2 MPa. Los PGA y PGV pronosticados en sitios sedimentarios en la ciudad de Veracruz y la LVNPP sobre el hipocentro (profundidad = 20 km) del sismo postulado de M_w 6.5 son 0.2 g y 10 cm/s y 0.18 g y 3cm/s, respectivamente. Estos resultados son preliminares ya que se basan en varios supuestos.

Palabras clave: Sismos en Veracruz, Efectos de sitio, Funciones de Green Empíricas.

Received: July 6, 2023 ; Accepted: March 15, 2024 ; Published on-line: April 1, 2024.

Editorial responsibility: Dr. Raúl Valenzuela Wong

* Corresponding author: Arturo Iglesias, arturo@igeofisica.unam.mx
[1] Instituto de Geofísica, Universidad Nacional Autónoma de México, Mexico City, Mexico.
[2] Departamento de Materiales, Universidad Autónoma Metropolitana, Mexico City, Mexico.
[3] CTBTO Preparatory Comission, Vienna, Austria.
[4] Instituto de Ingeniería, Universidad Veracruzana, Veracruz, Veracruz, Mexico.
[5] Centro de Ciencias de la Tierra, Universidad Veracruzana, Xalapa, Veracruz, Mexico.
[6] Posgrado en Ciencias de la Tierra, UNAM, Mexico City, Mexico.

https://doi.org/10.22201/igeof.2954436xe.2024.63.2.1726

Introduction

Seismicity in the central and northern Gulf of Mexico is low. Consequently, there are only a few studies that deal with this topic. An earthquake on 24 July 1978 (m_b 5), which occurred in this part of the gulf, was analyzed by Frohlich (1982). A sequence of three earthquakes (M_w 4.6, 5.2, 5.9) that occurred in 2006 near the 1978 event was studied by Nettles (2006) and Gangopadhyay and Sen (2008). Location and focal mechanism of the 1978 and 10 September 2006 (M_w 5.9) earthquakes are shown in Figure 1. Origin of these earthquakes has been attributed to the stress caused of deposition of sediments carried by the Missisipi river (Frohlich, 1982; Gangopadhyay and Sen, 2008).

Seismicity is more abundant along the southwestern margin of the gulf (Suárez and López, 2015). The largest known earthquake in this region, the Jaltipan earthquake, occurred on 26 August 1959 (M_w 6.4) causing serious damage to the towns of Jaltipan, Coatzacoalcos, and Minatitlan (Figueroa, 1964; Rosenblueth, 1964; Reséndiz, 1964). As seen in Figure 1, the southwestern gulf earthquakes have either a thrust faulting or a strike-slip focal mechanism. Trend of *P* axes of the thrust earthquakes has been explained by strong coupling along the subduction plate interface offshore Tehuantepec and absolute motion of the north American plate (e.g., Dewey and Suárez, 1991; Suárez, 2000; Suárez and López, 2015; Singh *et al.*, 2015). The strike-slip earthquake of 15 February 2017 (M_w 4.3) whose mechanism was also determined in this study (Appendix A) may be related to left-lateral movement on the Neogene Veracruz fault studied in detail by Adreani *et al.* (2008). However, there is no structure with which we can relate the strike-slip event of 23 May 2007 (M_w 5.7).

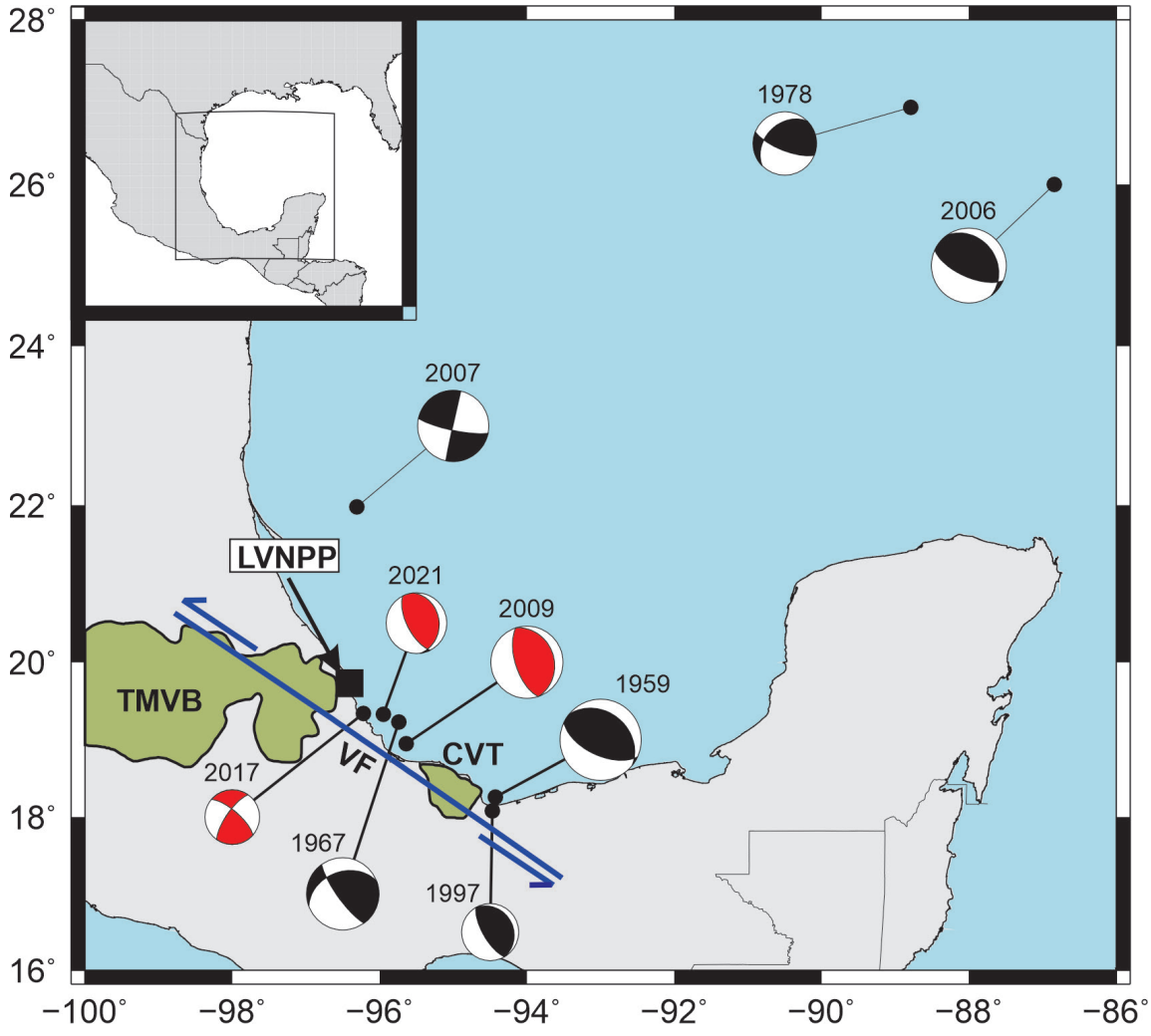

Figure 1. Map of Gulf of Mexico showing location of earthquakes with known focal mechanism. Red and white beach balls are focal mechanisms obtained in this study using local and regional recordings. LVNPP: Laguna Verde Nuclear Power Plant. VF: Veracruz fault (Adreani *et al.*, 2008). Focal mechanism of 2017 event is consistent with the geologically-mapped sense of motion on the Veracruz fault. Note that the earthquakes along the southwest margin of the gulf have thrust as well as strike-slip mechanism.

As more focal mechanisms have become available, our understanding of the current deformation and the geodynamics of the gulf has improved. However, there is still no study dealing with expected ground motion from postulated local and regional earthquakes, occurring at the southwestern margin of the gulf, mostly because of the scarcity of recordings. This is an important shortcoming as there are several important cities and towns along the coast of southwestern Gulf of Mexico (e.g., Veracruz, Alvarado, Coatzacoalcos, and Minatitlan), as well as hydrocarbon exploration and production facilities, and the Laguna Verde Nuclear Power Plant (LVNPP) (Figure 1). The region is exposed to seismic hazard from intraslab earthquakes in the subducted Cocos plate and those that occur along the southwestern margin of the gulf. Indeed, in the seismic design of the LVNPP, the ground motion from a migrating M_w 6.5 earthquake was of primary concern. In view of the 1959 Jaltipan event, an M_w 6.5 earthquake near the coast of the gulf is a likely scenario event for the region.

Seismic instrumentation in the state of Veracruz presently consists of stations of the Servicio Sismológico Nacional (SSN, National Seismological Service, Mexico) at the LVNPP (named LVIG) and Tuzandepetl (named TUIG). They are equipped with broadband seismograph and accelerograph. These stations have been in operation since 1996 (LVIG) and 1992 (TUIG). Federal Electricity Commission (CFE) maintains accelerographs and seismographs in and near the LVNPP and Universidad Veracruzana (UV) operates a few accelerographs and seismographs in and near the city of Veracruz (Figures 2 and 3).

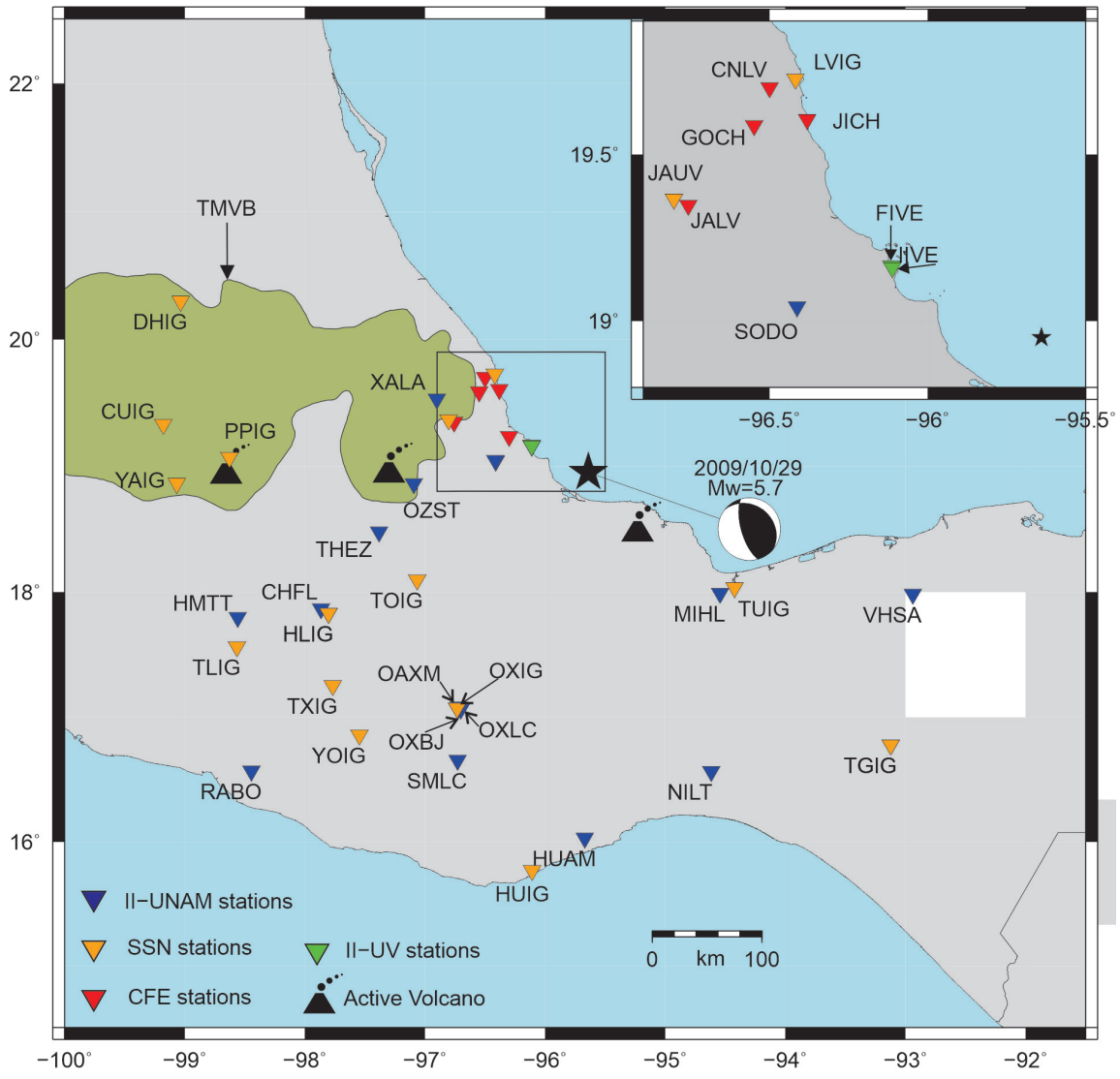

Figure 2. Location and focal mechanism of the 2009 Alvarado earthquake and stations whose recordings are analyzed in this study. Black triagle: active volcano. Green area: Trans Mexican Volcanic Belt. Inset: an enlarged area near the source.

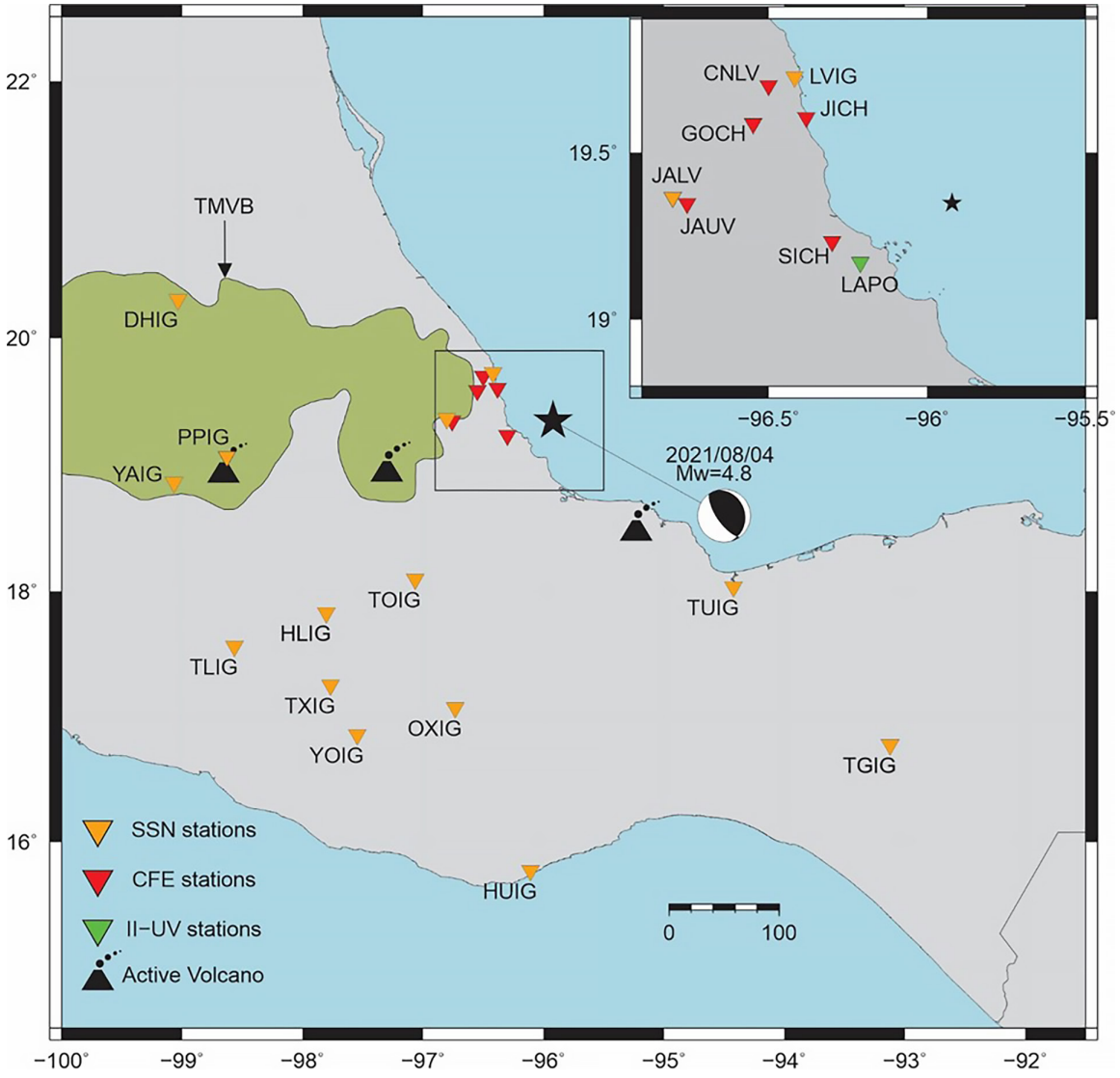

Figure 3. Location and focal mechanism of the 2021 Veracruz earthquake and stations whose recordings are analyzed in this study. Black triagle: active volcano. Green area: Trans Mexican Volcanic Belt. Inset: an enlarged area near the source.

Recently, two moderate earthquakes have been fairly-well recorded, permitting us to determine their source parameters and to obtain a preliminary estimate of ground motion from postulated earthquakes based on the analysis of the local and regional recordings. Alvarado earthquake of 29 October 2009 (M_w5.7) was recorded by 3 accelerographs in and near the city of Veracruz (distance < 100 km), many stations of the SSN network, and the accelerographic network operated by Instituto de Ingeniería, UNAM at farther distances (Figure 2). Veracruz earthquake of 4 August 2021 was recorded by 8 near-source stations (distance < 100 km) and by many stations at regional distances (Figure 3). The accelerograms were corrected for instrument response by multiplication with a constant whereas the broadband seismograms were corrected using information on poles and zeros. We use the recordings of the two earthquakes to perform *W*- phase centroid moment tensor inversion. Both earthquakes involved reverse faulting. The recordings of the events (distance ≤ 400 km) reveal a surprisingly large variability of the ground motion, suggesting dramatic difference in the path to individual stations and the local site effect. We investigate whether the geometric mean of the apparent source spectrum (source spectrum including the site effect) of both events may be modelled by an ω^2-Brune source (Brune, 1968) and whether PGA and PGV estimated from the application of stochastic method are in reasonable agreement with the observations. We focus on the important and practical issue of the estimation of ground motion at sedimentary sites in and near the city of Veracruz and at LVNPP site from postulated earthquakes along the southwestern margin of the gulf, applying stochastic and empirical Green´s function techniques. We pay special atten-

tion to the expected motions from a future M_w 6.5 earthquake, a scenario event for the region.

Location of the Earthquakes

The velocity model used in locating the 2009 and 2021 earthquakes is given in Table 2. In this model, the *P* wave velocities and depths of the layers above Moho are taken from Singh *et al.* (2015) where appropriate references are given. The velocities and depths of the layers below Moho are taken from the model routinely used by the SSN. The depth of the events in the location were unstable. In locating the 2009 earthquake we fixed the depth at 27 km. This depth was determined by Suárez and López (2015) from the inversion of teleseismic *P* waves. For the 2021 earthquake the depth was fixed at 16 km which was obtained from *W*-phase inversion (see next section). Table 1 gives the location of the events. We also located an event which occurred on 15 February 2017 near the 2021 earthquakes. A detailed analysis of the event is given in Appendix A.

Table 1. Source parameters of earthquakes in and near Gulf of Mexico.

No.	Date	Location	Depth	M_w		Focal Mechanism		
		°N	°W	km		φ °	δ °	λ °
1	26 Aug 1959[a]	18.26	94.43	21	6.4	309	32	102
2	11 Mar 1967[b]	19.23	95.74	26	5.7	250	39	20
3	24 Jul 1978[c]	26.49	88.79	15	5.0	225	49	111
						240	63	52
4	06 Sep 1997[d]	18.08	94.47	30	4.5	330	20	90
5	10 Sep 2006	26.32	86.84	30	5.9	324	28	117[e]
6	23 May 2007	21.98	96.31	24	5.6	102	80	-1[e]
		(22.02 (21.98 (22.0	96.27 96.14 96.3	11 44 6.7	5.6 5.5 5.6	95 106 97	71 83 80	-16)[f] 8)[g] 3)[h]
7	29 Oct 2009	19.005 (19.14 (18.9	95.602 95.58 95.8	27 17 16	5.7 5.7 4.8	162 164 153	64 69 65	90[i] 10)[e] 81

[a] Location from ISS; depth, focal mechanism, and M_w from Suárez (2000).
[b] Location from ISC; depth, focal mechanism, and M_w from Suárez (2000).
[c] Location, depth, and focal mechanism from Frohlich (1982). The two mechanisms are extreme types consistent with first-motion data.
[d] Singh *et al.* (2015).
[e] Global CMT catalog.
[f] Source parameters listed in **http://www.eas.slu.edu/eqc/eqc_mt/MECH.NA/20070523190916/index.html**
[g] Franco *et al.* (2013).
[h] Suárez and López (2015).
[i] All parameters from this study; location from phase data with depth fixed at 27 km; M_w and focal mechanism from *W*-phase inversion.
[j] All parameters from this study; location from phase data; M_w and focal mechanism from regional centroid moment tensor inversion (see Appendix A).
[k] All parameters from this study; location from phase data with depth fixed at 16 km; M_w and focal mechanism from *W*-phase inversion.

Table 2. Crustal model used in the location of 2009 Alvarado and 2021 Veracruz earthquakes. Ratio of *P*-wave to *S*-wave speed has been taken as 1.78.

Layer	Thickness, km	*P*-wave speed α, km/s
1	1.8	2.80
2	15.6	4.25
3	15.6	6.5
4	67.0	7.25
5	∞	7.95

Centroid Moment Tensor Inversion

Since 2014, the SSN has implemented a routine calculation of M_w through *W*-phase inversion (Kanamori and Rivera, 2008). It uses an algorithm modified for moderate magnitude earthquakes by Hayes *et al.* (2009) and revised by Duputel *et al.* (2012). The algorithm is automatically triggered for $M \geq 5.2$ earthquakes ten minutes after the origin time and uses the broadband data from stations of the SSN (Pérez-Campos *et al.*, 2019). It starts with the SSN location and magnitude, and looks for the best half duration and then the best location. Later, the solution is manually revised to eliminate data with problems (e.g., inverse polarity or glitches) or a bad fit given the preferred solution.

Figure 4 shows the revised *W*-phase solution for the 29 October 2009 (M_w 5.7) and the 4 April 2021 (M_w 4.8) events and the fit of the inversion. For these events, 28 and 13 channels, filtered from 0.0067 to 0.02 Hz, were used in the inversions. The corresponding stations were located between 185 and 810 km

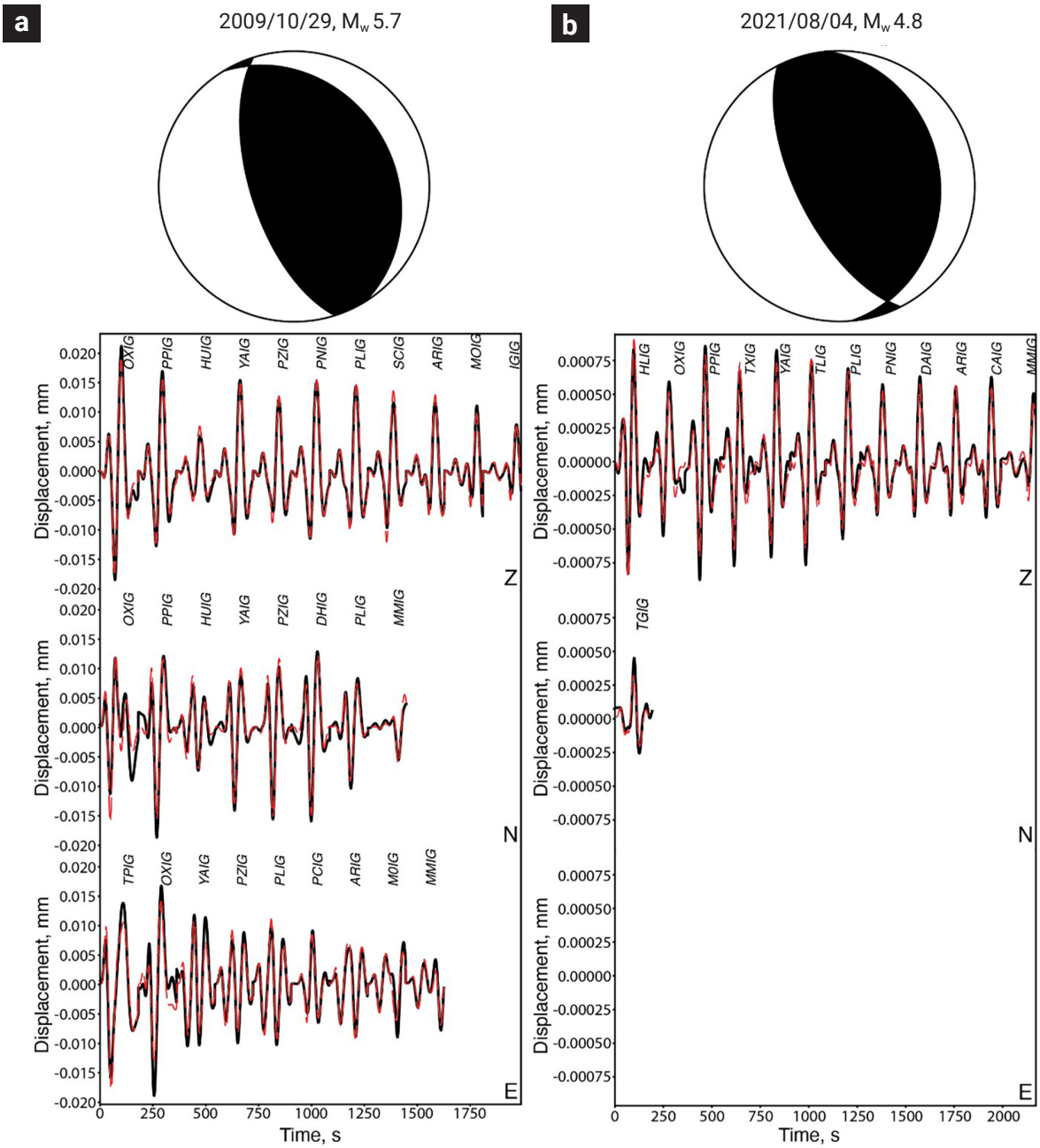

Figure 4. *W*-phase solution of a) 29 October 2009, M_w 5.7 and b) 4 August 2021, M_w 4.8 earthquakes. Top: Focal mechanism solution. Bottom: *W*-phase fit for the three components (Z = vertical; N = North; E = East). The black and red dashed traces correspond to the synthetic *W* phase for the preferred solution and the observed *W* phase, respectively.

from the epicenter for the 2009 earthquake, and 240 and 775 km for the 2021 event. The depths of the 2009 and 2021 events returned by the *W*-phase inversion are 19.5 km and 15.5 km, respectively. The seismic moments are $M_0 = 5.07 \times 10^{17}$ Nm and $M_0 = 1.93 \times 10^{16}$ Nm. The focal mechanisms, which in both cases correspond to an reverse-faulting, are listed below:

2009 earthquake
Nodal plane 1: $\varphi_1 = 328.7°$, $\delta_1 = 26.8°$, $\lambda_1 = 77.7°$
Nodal plane 2: $\varphi_2 = 162.4°$, $\delta_2 = 63.9°$, $\lambda_2 = 90.2°$
2021 earthquake
Nodal plane 1: $\varphi_1 = 354.6°$, $\delta_1 = 26.5°$, $\lambda_1 = 109.3°$
Nodal plane 2: $\varphi_2 = 153.2°$, $\delta_2 = 65.1°$, $\lambda_2 = 80.7°$

The focal mechanisms of the 2009 and 2021 events are very similar. While *W*-phase mechanism of the 2009 event is also similar to that reported in the Global CMT catalog, it differs considerably from that reported by Suárez and López (2015) (Table 1).

Centroid moment tensor inversion of the relatively small earthquake (M_w 4.3) of 15 February 2017 is discussed in Appendix A.

Source Spectrum

Moment rate spectrum, $\dot{M}_0(f)$, of an earthquake can be estimated from the Fourier amplitude spectrum of the recorded ground motion. The method requires corrections for the diminution and amplification of seismic waves as they travel from the source to the recording site. Ideally, $\dot{M}_0(f)$ estimated at different stations should be similar. Generally, however, they differ because the corrections are inadequate to account for the complex and varying path and local site effects. On the other hand if $\dot{M}_0(f)$ is known or specified, then the Fourier spectrum at any site can be estimated. The stochastic method may, then, be applied to estimate ground-motion parameters useful in earthquake engineering (e.g., Boore, 1983).

A brief description of the theory follows. Under far-field, point-source approximation, Fourier amplitude spectrum of the horizontal component of acceleration of an event at a distance *R*, $A(f, R)$, may be written as:

$$A(f, R) = C \cdot G(R)\ [\{f^2 \dot{M}_0\ (f)\} S(f)][\ e^{-\pi f R/\beta Q(f)}] \quad (1)$$

where,

$$S(f) = Site(f)\ e^{-\pi \kappa f} B(f), \quad (2)$$

$$C = FPR_{\theta\varphi}(2\pi)^2/(4\pi\rho\beta^3) \quad (3)$$

In equations above, $\dot{M}_0\ (f) \rightarrow M_0$ as $f \rightarrow 0$, R = hypocentral distance, $R_{\theta\phi}$= average radiation pattern (0.55), F = free surface amplification (2.0), P takes into account the partitioning of energy in the two horizontal components ($1/\sqrt{2}$), β= shear-wave velocity at the source, ρ = density in the focal region, and $Q(f)$ = quality factor, which includes both anelastic absorption and scattering. The attenuation in the near-surface layer and the finite bandwidth of the observed spectrum are accounted by the parameter κ (Singh *et al.*, 1982; Anderson and Hough, 1984) and/or the Butterworth filter, B(f) (Boore, 1983). Often either κ or $B(f)$ is sufficient to explain the high-frequency falloff of the spectrum. We assume the geometrical spreading term, $G(R)$, in equation (1) as $1/R$ for $R \leq 100$ km and $1\ /\ (100R)^{0.5}$ for $R > 100$ km.

We take $Q(f) = 141 f^{0.63}$ estimated for the eastern and central Trans Mexican Volcanic Belt (Canas, 1986; Singh *et al.*, 2017). β and ρ in the source region are assumed to be 3.75 km/s and 2.85 gm/cm^3, respectively. We take logarithm of equation (1):

$$log\ [A(f, R)] = log\ C + log\ G(R) + log\ [f^2 \dot{M}_0(f)\ S(f)] - [1.36\{Rf/\beta Q(f)\}]$$

and compute $log\ [f^2 \dot{M}_0(f) S(f)]$ at each station. Plots of $[f^2 \dot{M}_0(f)\ S(f)]$ at each station for the earthquakes of 2009 are shown in Figure 5a. The corresponding geometric mean and $\pm$ one standard deviation curves are plotted in Figure 5b. The spectra, grouped in three distance ranges, $62 < R < 160$ km, $165 < R < 285$ km, and $290 < R < 390$ km, are illustrated in Figures 5c,d, and e. These figures reveal surprisingly large variability of ground motion (especially at $f \geq 3$ Hz), suggesting large difference in $S(f)$ of each site. The variability persists in each distance group. The sites with especially anomalous spectrum are identified in the figure. These sites are LVNPP, PPIG (Popocatépetl volcano) and DHIG (Demacu) (Figure 2).

As it is not possible to determine $S(f)$ at each site, we do not attempt to separate $S(f)$ from $[f^2 \dot{M}_0(f) S(f)]$. Our goal here is not to determine the true source spectrum; we seek a spectrum that can be used in the estimation of ground motion from future earthquakes via the stochastic method. For this purpose, the path- and site-affected source acceleration spectrum, $[f^2 \dot{M}_0(f)\ S(f)]$, henceforth also called the apparent source acceleration spectrum, *ASAS(f)*, suffices. $S(f)$ in equation 2 may be written as:

$$S(f) = ASAS(f)\ /\ f^2 \dot{M}_0 S(f) \quad (4)$$

We interpret the geometric mean *ASAS(f)* by the ω^2-source model of Brune (1970). Figure 5b shows theoretical source

spectra corresponding to M_0 of 5.07×10^{18} Nm (M_w 5.7) and of 40, 10, and 2 MPa. The observed geometric mean *ASAS(f)* is well approximated by a $\Delta\sigma$ of 40 MPa. We reiterate that this is not the true stress drop but one that fits the *ASAS(f)*.

Figure 6 is similar to Figure 5 but for the 2021 Alvarado earthquake. Similar to 2009 earthquake, it also reveals large variability of *ASAS(f)* at individual sites (Figure 6a) that persists in each of the three distance ranges (Figures 6c,d, and e). There are some sites with especially anomalous spectrum e.g., IIVE, FIVE, LVIG, PPIG, TUIG, DHIG. The sites with especially anomalous spectrum for the 2021 event show the same tendency as observed for the 2009 earthquake. The geometric mean of *ASAS(f)* is, again, reasonably well fit by the ω^2-source model with M_0 of 1.93×10^{16} Nm (M_w 4.8) and M_0 of 40 MPa (Figure 6b).

Clearly, we need more recordings at local and regional distances of the earthquakes that occur near the coast of Veracruz to learn whether the ω^2-source model with $\Delta\sigma$ of 40 MPa is good approximation to *ASAS(f)* of most of such events. Lacking such dataset, we shall assume that this is so. Replacing $[f^2\dot{M}_0(f)S(f)]$ in equation 1 by the Brune ω^2-source model with M_0 of 40 MPa, we may estimate the Fourier acceleration spectrum at an "average" site ($R \leq 400$ km).

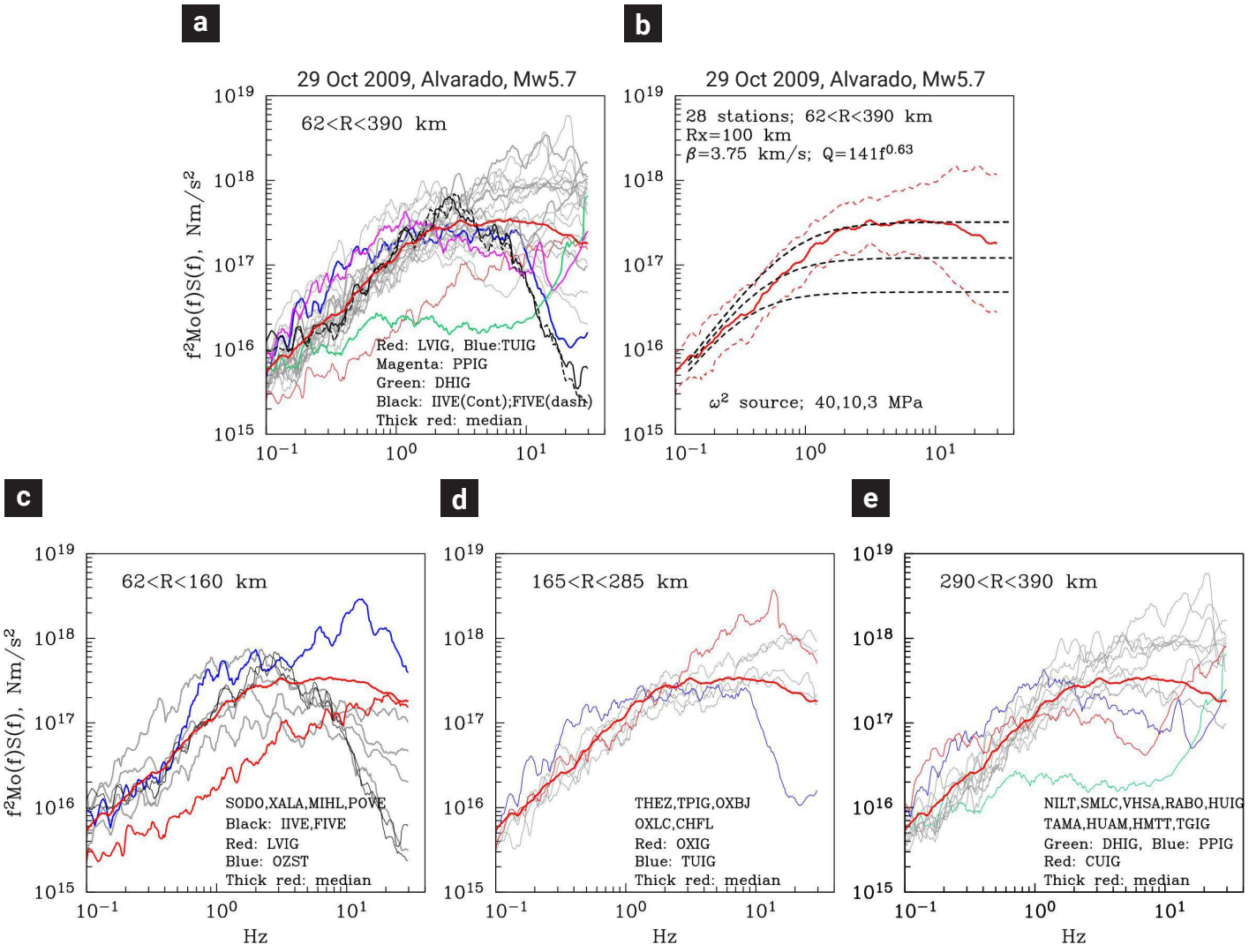

Figure 5. a) $ASAS(f) = [f^2\dot{M}_0(f)S(f)]$ curves of the 2009 earthquake estimated at individual stations. The plot shows remarkable variability. Especially anomalous sites (IIVE, FIVE, OXIG, OZST, LVIG, PPIG, and DHIG) are identified. Thick red curve shows the plot of the geometric mean. b) Geometric mean and ± one standard curves. Superimposed are theoretical curves for an ω^2-Brune source model with $\Delta\sigma$ of 40, 10, and 3 MPa. The observed geometric mean curve is well fit with $\Delta\sigma$ of 40 MPa. c), d), e) *ASAS(f)* curves with stations grouped in three distant ranges. For reference, each frame shows the geometric mean curve (Figure 5b).

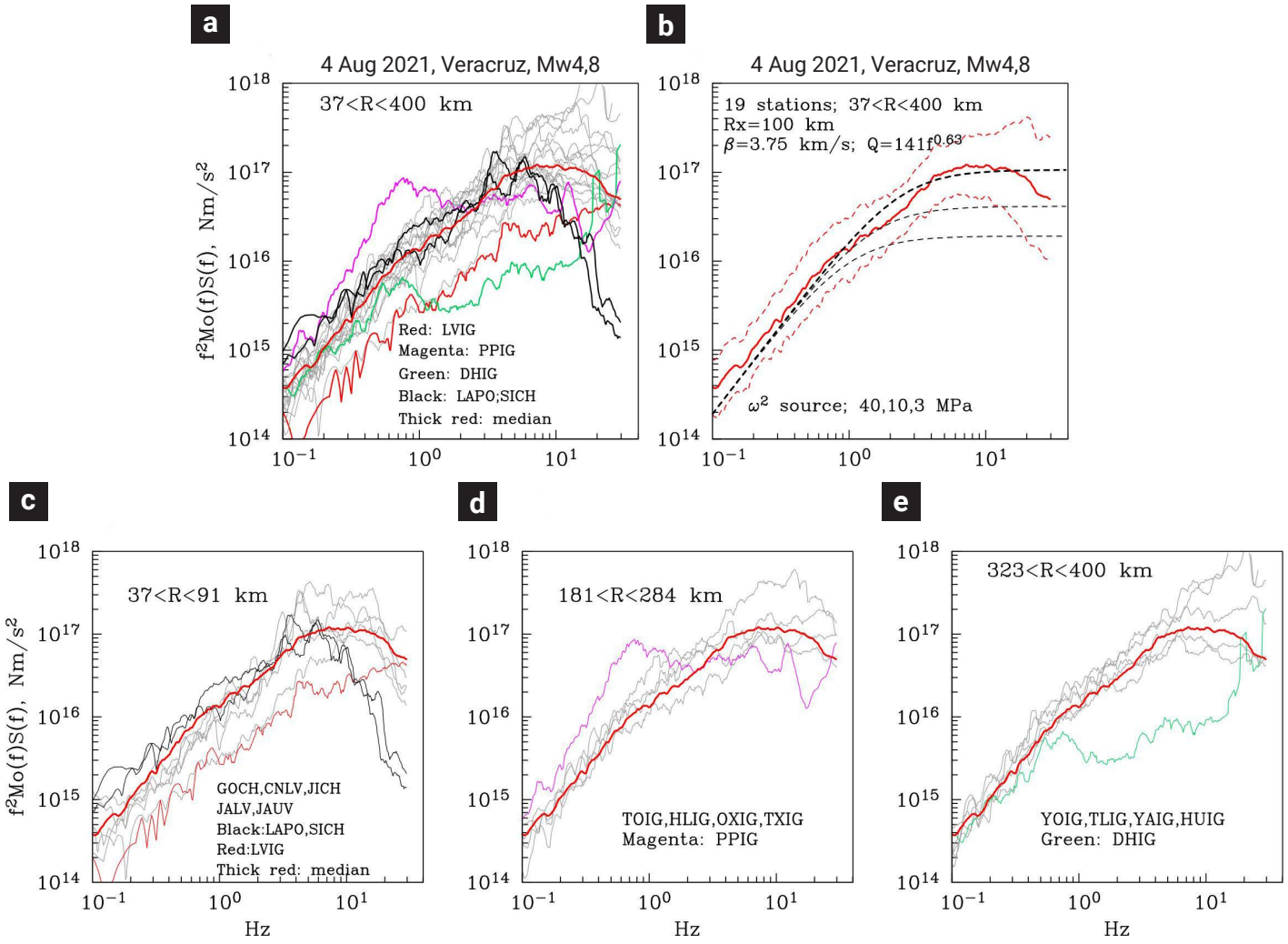

Figure 6. Same as Figure 5 but for the 2021 earthquake. Anomalous sites in this case are LAPO and SICH, and, similar to the 2009 event, the sites of LVIG, PPIG, and DHIG. Similar to the 2009 earthquake, the observed geometric mean curve of the 2009 event is well fit by an ω^2-Brune source with $\Delta\sigma$ of 40 MPa. For reference, each frame shows the geometric mean curve (Figure 6b).

Observed and Predicted Ground Motions from the Two Veracruz Earthquakes

We verify whether $A(f,R)$ computed for a Brune source with $\Delta\sigma$ of 40 MPa , along with the application of the stochastic method, gives *PGA* and *PGV* values consistent with those observed during the 2009 and 2021 earthquakes. A parameter needed in the application of the method is the duration of intense part of the ground motion, T, which we take as $T = 1/f_c + 0.05R + C$, where R is in km, f_c is the corner frequency, and C is a constant. This relation was originally proposed by Herrmann (1985) with C equals 0. For the Brune source model $f_c = 0.49\ \beta\ (\Delta\sigma/M_0)^{1/3}$. $\Delta\sigma$ is taken as 40 MPa. Based on an earlier analysis of a sequence of small earthquakes in Morelia, Mexico (Singh *et al.*, 2012) we set $C = 3$ sec. The predicted curves and observed *PGA* and *PGV* values of the two earthquakes (Tables 3 and 4) are shown in Figure 7. We note that the values at site DHIG are especially low. Ignoring DHIG, the predicted *PGA* and *PGV* curves fit the observed values reasonbly well. Most of the values fall within a factor of two of the predicted curves. Presumably, the same set of parameters and application of the stochastic method would produce reasonable PGA and PGV curves for postulated earthquakes. To keep the work to a manageable level, we abstained from testing the sensitivity of the results to other choices of the parameters. We did, however, test the sensitivity of the predictions to the critical parameter of stress drop. We performed calculations with twice and half of the stress drop of 40 Mpa: 80 MPa and 20 MPa. The values, with respect to those for 40 MPa, were greater by a factor of ~1.5 and smaller by a factor of ~1/1.5 for higher and lower stress drops, respectively.

Table 3. PGA and PGV, Alvarado Earthquake, 29 October 2009, M_w5.7.

Station	R,km	PGA, cm/s²			PGV, cm/s			Site
		NS	EW	Z	NS	EW	Z	
IIVE	62	22.8	19.1	10.6	9.86E-01	1.19	3.63E-01	S
FIVE	63	23.9	19.2	16.2	1.41	1.03	6.74E-01	S
SODO	90	4.87	4.68	5.35	2.23E-01	2.47E-01	1.71E-01	A
LVIG	120	2.68	4.17	2.58	7.30E-02	7.77E-02	4.60E-02	H
XALA	150	2.02	1.93	1.61	1.21E-01	1.20E-01	7.48E-02	H
OZST	160	15.5	11.6	8.07	2.48E-01	2.23E-01	1.73E-01	S
MIHL	161.3	3.28	3.27	1.46	3.73E-01	3.45E-01	1.44E-01	S
TUIG	167	1.98	1.87	8.65E-01	1.66E-01	1.38E-01	7.30E-02	S
THEZ	199	2.23	2.93	2.48	1.17E-01	1.47E-01	6.24E-02	H
TPIG	199	1.51	1.37	1.71	8.69E-02	8.62E-02	7.17E-02	H
OXIG	246	2.7	4.06	2.47	7.21E-02	1.26E-01	5.59E-02	H
OXBJ	246	1.63	1.19	1.83	4.18E-02	3.48E-02	4.77E-02	H
OXLC	246	1.38	1.63	7.62E-01	6.07E-02	7.44E-02	3.97E-02	H
OAXM	246	6.33	5.5	3.72	1.73E-01	2.11E-01	9.37E-02	A
CHFL	271.3	4.52E-01	4.57E-01	3.42E-01	2.39E-02	2.91E-02	2.88E-02	H
SMLC	287.3	1.05	1.08	6.68E-01	7.22E-02	4.78E-02	3.78E-02	H
NILT	291	2.05	1.86	6.15E-01	5.89E-02	8.65E-02	3.39E-02	H
VHSA	304.2	1.22	9.86E-01	3.28E-01	8.79E-02	4.73E-02	1.94E-02	S
RABO	305.2	2.87E-01	4.22E-01	3.54E-01	2.12E-02	2.40E-02	2.19E-02	H
PPIG	314	2.96E-01	3.11E-01	2.09E-01	4.71E-02	4.64E-02	2.01E-02	H
TAMA	322.1	5.52E-01	5.17E-01	3.52E-01	3.08E-02	3.62E-02	2.78E-02	H
HUAM	330.2	6.85E-01	6.20E-01	5.39E-01	2.89E-02	2.91E-02	2.14E-02	H
TLIG	340	4.74E-01	3.35E-01	3.37E-01	2.37E-02	1.77E-02	2.11E-02	H
HMTT	341.1	4.44E-01	5.41E-01	3.93E-01	3.60E-02	3.66E-02	4.14E-02	H
TGIG	361	1.42	8.91E-01	5.20E-01	8.89E-02	6.96E-02	4.43E-02	H
HUIG	363	4.18E-01	3.02E-01	2.41E-01	1.73E-02	1.12E-02	1.40E-02	H
CUIG	379	6.40E-02	6.48E-02	5.76E-02	1.95E-02	2.19E-02	1.25E-02	H
DHIG	389	1.48E-02	1.28E-02	1.84E-02	5.16E-03	5.05E-03	5.93E-03	H

Site S: soft, A: Alluvium, H: rock

Table 4. PGA and PGV, Veracruz Earthquake, 4 August 2021, M_w4.8

Station	R,km	PGA, cm/s²	PGV, cm/s	Site				
		NS	EW	Z	NS	EW	Z	
LAPO	36.6	29.5	23.7	20.8	7.65E-01	1.25E+00	4.13E-01	S
SICH	41.7	21.2	13.1	7.64	7.89E-01	6.00E-01	1.89E-01	S
JICH	56.8	5.99	2.67	4.48	1.06E-01	7.03E-02	1.23E-01	H
LVIG	67.7	2.2	2.78	4.84	2.75E-02	4.14E-02	3.12E-02	H
GOCH	70.8	18.1	14.9	5.45	3.12E-01	3.51E-01	1.00E-01	H
CNLV	72.6	7.19	5.59	9.34	7.25E-02	5.34E-02	8.06E-02	H
JALV	86.5	6.69	11.5	10.5	2.01E-01	3.11E-01	1.63E-01	H
JAUV	91.2	19.4	11.7	8.26	5.28E-01	2.37E-01	1.66E-01	H
TOIG	181.5	1.14E+00	9.08E-01	1.03E+00	2.66E-02	2.37E-02	3.75E-02	H
TUIG	216.6	1.76E-01	1.24E-01	1.48E-01	5.30E-03	5.19E-03	2.78E-01	S
HLIG	257.5	1.44E-01	1.63E-01	1.38E-01	4.74E-03	5.74E-03	4.31E-03	H
OXIG	264.7	4.87E-01	7.13E-01	4.85E-01	1.38E-02	3.06E-02	1.16E-02	H
TXIG	282	1.58E-01	1.72E-01	1.43E-01	9.93E-03	8.48E-03	6.31E-03	H
PPIG	283.5	1.09E-01	9.76E-02	4.70E-02	1.71E-02	1.39E-02	6.20E-03	H
YOIG	323	9.12E-02	8.70E-02	7.10E-02	5.03E-03	5.58E-03	4.01E-03	H
YAIG	332.3	5.90E-02	5.23E-02	3.57E-02	3.89E-03	3.25E-03	2.34E-03	H
TLIG	339.3	1.07E-01	9.44E-02	9.13E-02	4.28E-03	5.15E-03	5.57E-03	H
DHIG	340.8	8.30E-03	6.33E-03	7.66E-03	1.27E-03	1.16E-03	1.00E-03	H
HUIG	396.3	9.43E-02	8.51E-02	5.34E-02	2.69E-03	2.73E-03	2.43E-03	H

Site S: soft, A: Alluvium, H: rock

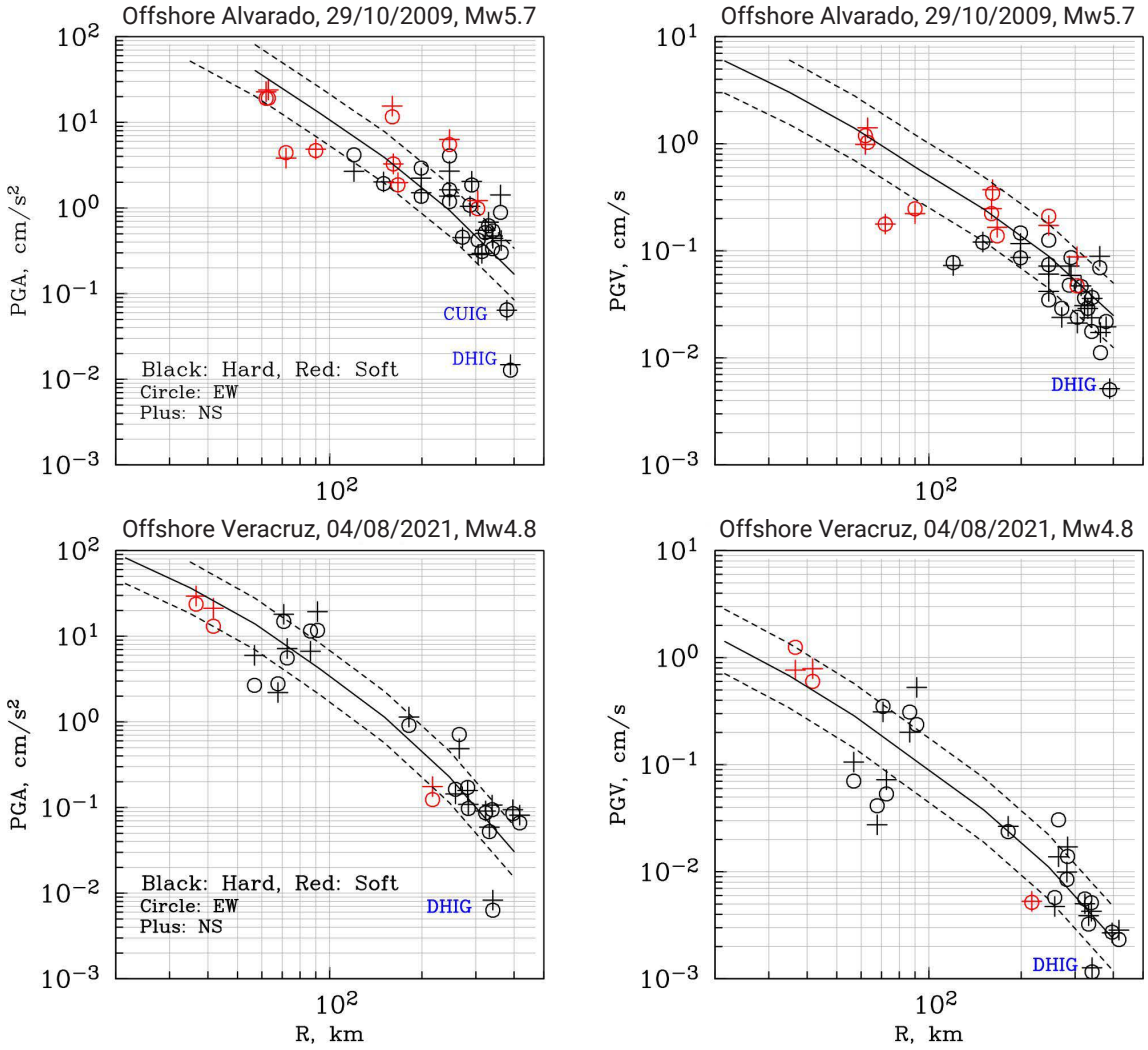

Figure 7. Comparison of observed and stochastically simulated PGA and PGV values for the 2009 Alvarado earthquake (top two frames) and the 2021 Veracruz earthquake (bottom two frames).

Ground Motion in the city of Veracruz and Laguna Verde Nuclear Power Plant from Postulated Earthquakes

The stochastic predictions above are for an "average" site located at $R \leq 400$ km. Of practical interest, however, is the ground motion in the near-source region, especially at sedimentary sites in and near the city of Veracruz and at the LVNPP. We focus our attention to these sites and take recourse to both empirical Green function (EGF) and stochastic methods.

a) EGF Method

We synthsize ground motion from an M_w 6.5 event using the recordings of 2021 earthquake (M_w 4.8) as empirical Green's functions (EGF). A method proposed by Ordaz *et al.* (1995) is used in the synthesis. It is based on adding N scaled EGF records, each differed in time by a random delay. The probability distribution of the delays is such that, on an average, the simulations follow an ω^2-spectral scaling at all frequencies. The method requires specification of the seismic moment, M_0, and the stress drop, $\Delta\sigma$, of both the EGF and the target earthquakes. In our case, M_0 of the EGF is 1.93×10^{15} N-m (M_w 4.8) and that of the target event is 7.08×10^{18} N-m (M_w 6.5). Unfortunately, the site effect distorts the source spectrum so that it is difficult to estimate the corner frequency, f_c, hence $\Delta\sigma$, of the EGF.

We explored the possibility of estimating f_c of the 2021 earthquake from the spectral ratios of the aftershocks to the mainshock, thus eliminating the site effect. The aftershocks of the 2021 earthquake were not large enough to produce useful recordings. However, we could find an aftershock of the 2009 earthquake

which was well recorded at four broadband stations (LVIG, TPIG, OXIG, PPIG) (Figure 2). The source parameters of this aftershock, listed in SSN catalog, are: 29/10/2009; 23:25:20.3; 18.95^{0}N, -95.71^{0}E; depth = 24 km; M 4.3. The location of the aftershock is close to that of the 2009 mainshock. The focal mechanism of the aftershock could not be determined because of complex crustal structure and poor signal at long period. Here we assume that the aftershock and mainshock were collocated and had similar mechanism. Under these assumptions, the spectral ratio of the aftershock to mainshock at the same station provides the ratio of the source spectra. These ratios are shown in Figures 8 where all three components are plotted. At $f \leq 1$ Hz the ratios are ~10-2, *i.e.*, M_0 of the aftershock is 5.07×10^{15} Nm (M_w 4.4). Superimposed on the observed spectral ratios are theoretical ratios corresponding to the ω^2-source model (see Chael, 1987 for the equation of theoretical ratio) and $f_c = 0.3$ Hz ($\Delta\sigma = 2$ MPa) and $f_c = 0.5$ Hz ($\Delta\sigma = 10$ MPa). Two relationships between $\Delta\sigma$ and M_0 are considered: (1) $\Delta\sigma$ is constant, and (2) $\Delta\sigma$ increases with M_0 such that $\Delta\sigma$ is proportional to $M_0^{1/4}$ (a scaling proposed by Nuttli, 1983 for mid-plate earthquakes; see

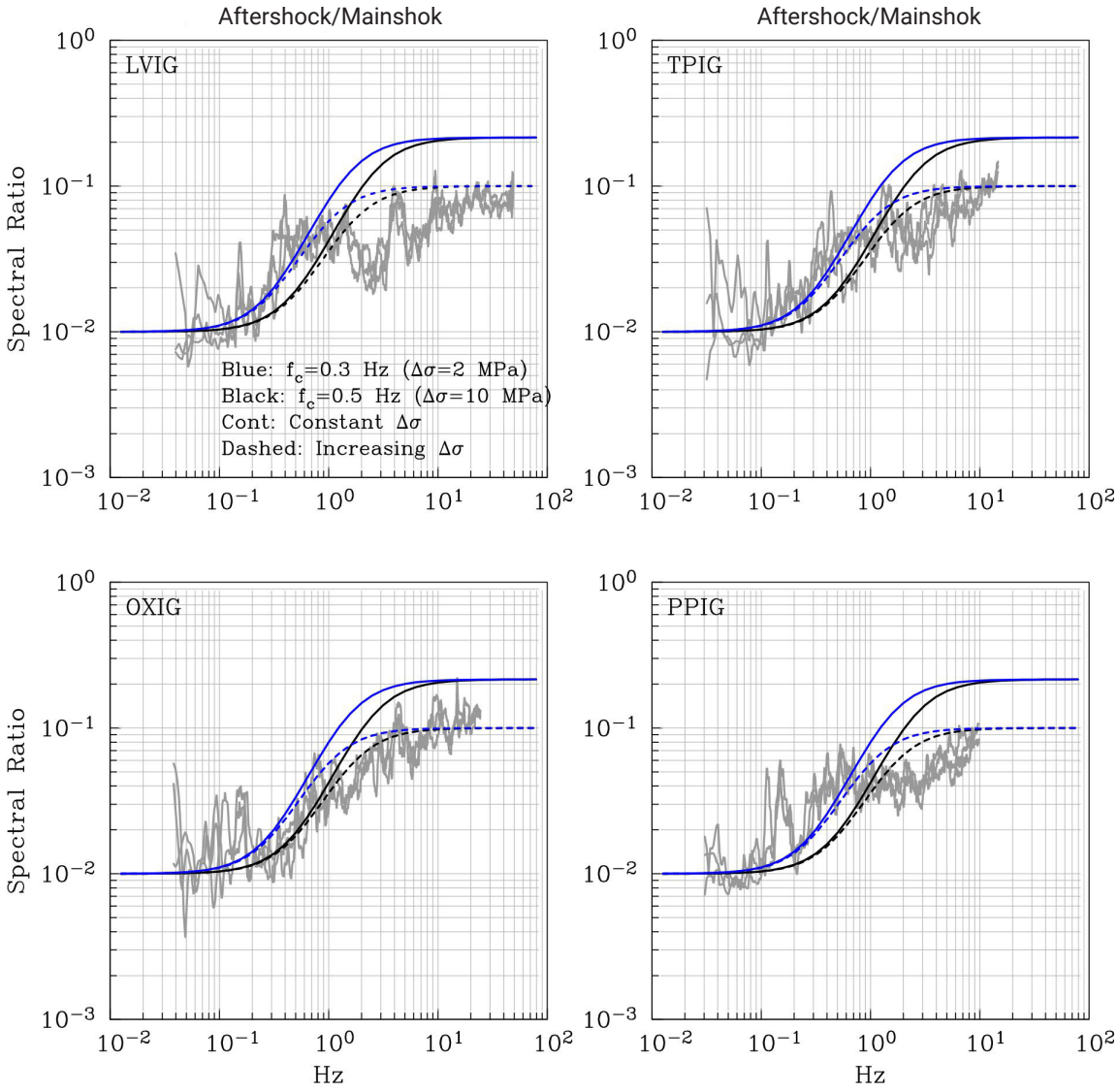

Figure 8. Spectral ratios of an aftershock to the 2009 Alvarado mainshock at the same station. All three components are plotted. At $f \leq 1$ Hz the ratios are ~10^{-2}, *i.e.*, M_0 of the aftershock is 5.07×10^{15} Nm (M_w 4.4). Superimposed on the observed spectral ratios are theoretical ratios corresponding to the ω^2-source model and $f_c = 0.3$ Hz ($\Delta\sigma = 2$ MPa) and $f_c = 0.5$ Hz ($\Delta\sigma = 10$ MPa). Two relationships between $\Delta\sigma$ and M_0 are considered: 1) $\Delta\sigma$ is constant, and 2) $\Delta\sigma$ increases with M_0 such that $\Delta\sigma$ is proportional to $M_0^{1/4}$. Theoretical ratios for $f_c = 0.3$ Hz better fit the observed spectral ratios at $f < 0.5$ Hz at LVIG, TPIG, and PPIG irrespective of the $\Delta\sigma$ - M_0 relationship. However, at OXIG, $f_c = 0.5$ Hz is preferable.

also Chael, 1987). Theoretical ratios for $f_c = 0.3$ Hz better fit the observed spectral ratios at $f < 0.5$ Hz at LVIG, TPIG, and PPIG irrespective of the $\Delta\sigma$- M_0 relationship. However, at OXIG, $f_c =$ 0.5 Hz is preferable. Perhaps, a source directivity is the cause of the greater fc at OXIG. At $f > 1$ Hz the theoretical ratios for constant approximate the observed ratios very poorly; increasing stress drop model does a better job. Figure 8 and the discussion above support $f_c = 0.3$ Hz ($\Delta\sigma = 2$ MPa); certainly $f_c \geq 0.5$ Hz ($\Delta\sigma \geq 10$ MPa) appears unlikely. Stress drop of 2 MPa is close to median stress drop of 4 MPa reported by Allman and Shearer (2009) in a global study of stress drop variation. We shall further assume that $\Delta\sigma$ of the EGF earthquake of 2021 and the target earthquake (M_w 6.5) is the same as that of the 2009 mainshock, i.e., 2 MPa. With these assumptions, *PGA* and *PGV* values were synthesized for the target event at the near-source sites where the 2021 earthquake was recorded using the EGF method. The results, along with those obtained from the stochastic method, are presented in the next section.

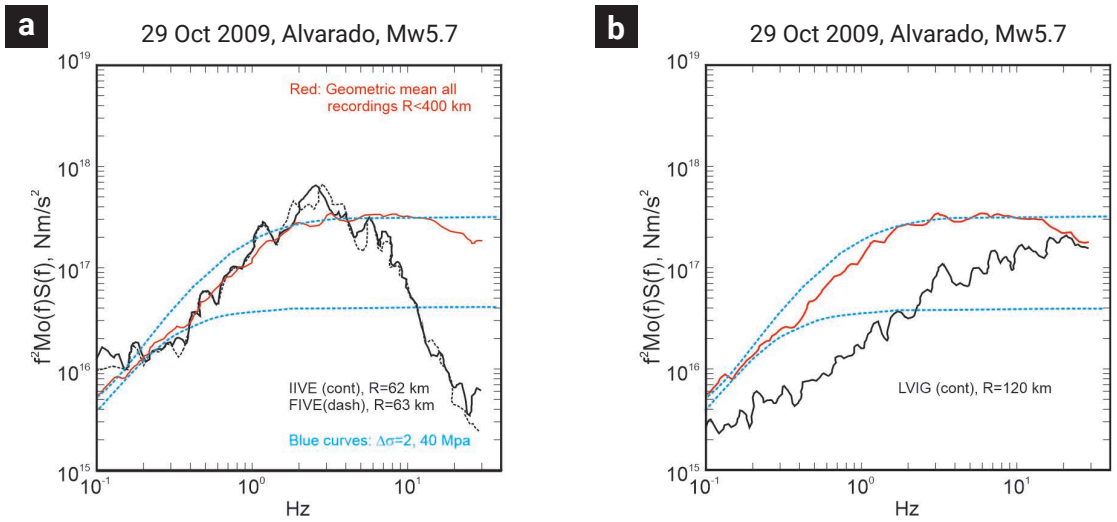

Figure 9. a) *ASAS*(*f*) of the 2009 earthquake at near-source sedimentary sites of IIVE and FIVE located in the city of Veracruz. b) Same as a) but for LVIG located in the LVNPP. Theoretical source spectra for an ω^2-Brune source with $\Delta\sigma$ of 40, and 2 MPa are shown for reference. Also shown in the figure is the geometric mean *ASAS*(*f*) computed from all recordings (R < 400 km) from Figure 5b.

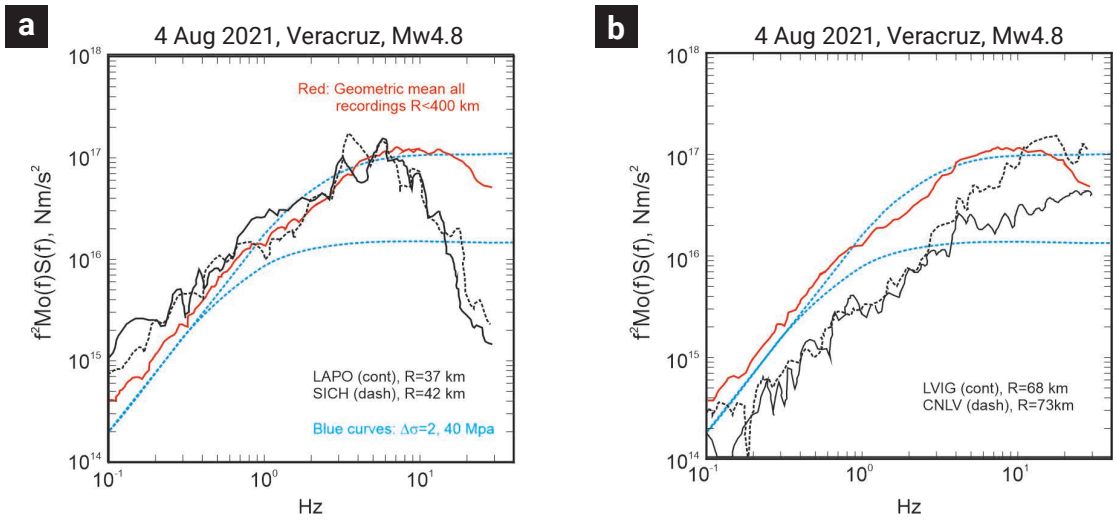

Figure 10. Same as Figure 9 but for the 2021 earthquake. LAPO and SICH are the sedimentary sites in the city of Veracruz. CNLV is a site in the LVNPP, near LVIG. The geometric mean *ASAS*(*f*) computed from all recordings (R < 400 km) is from Figure 6b.

b) Stochastic Method

Figure 9a shows the *ASAS(f)* of the 2009 earthquake at near-source sedimentary sites of IIVE and FIVE located in the city of Veracruz. Figure 9b illustrates a similar plot for LVIG located in the LVNPP. Theoretical source spectra for an ω^2 Brune source with $\Delta\sigma$ of 40, and 2 MPa are shown for reference. Also included in the figure is the geometric mean *ASAS(f)* computed from all recordings (Figure 5b). This spectrum fits those at IIVE and FIVE at f less than about 3 Hz; the spectra, however, rapidly falloff above 3 Hz. We attribute the falloff to unaccounted attenuation of seismic waves in the sedimentary upper layers.

The spectrum at LVIG is remarkable; it is lower than at other sites, except DHIG (Figure 5); it is also lower than the theoretical source spectrum corresponding to $\Delta\sigma = 2$ MPa. The expected merger of theoretical and LVIG spectra at low frequencies (~ 0.1 Hz) does not occur and there is no spectral falloff at least till $f = 20$ Hz.

Figure 10 is similar to Figure 9 but for the 2021 earthquake. LAPO and SICH are the near-source stations on sedimentary sites in the city of Veracruz. Similar to 2009 earthquake, the source spectra at these sites rapidly falloff at frequencies greater than 3 Hz. At LVNPP, the earthquake was recorded at LVIG and a nearby site CNLV. The *ASAS(f)* at LVIG and CNLV are similar at $f < 4$ Hz; both are lower than the theoretical spectrum corresponding to $\Delta\sigma = 2$ MPa. Above 4 Hz, the CNLV spectrum deviates from the LVIG spectrum; the former becomes greater than the latter, most probably as a consequence of low-velocity superficial layer. We address the peculiar nature of the spectra at LVIG and CNLV in a later section.

Assuming that the true source spectrum is given by the theoretical ω^2-source model with $\Delta\sigma$ of 2 MPa, the deviation of the observed *ASAS(f)* from this spectrum may be attributed to $S(f)$. Figure 11a shows geometric mean of the *ASAS(f)* at IIVE and FIVE for the 2009 earthquake and the corresponding theoretical spectrum. Figure 11b illustrates the observed *ASAS(f)* at LVIG as well as the theoretical source spectrum. Figures 11c, and d give similar plots for the 2021 earthquake. From equation 4, $S(f)$ during the earthquakes of 2009 and 2021 at sedimentary sites in the city of Veracruz and sites at LVPP are given in Figures 11e and f, respectively. It may be noted that the $S(f)$ of the two earthquakes are fairly similar. Knowing $[f^2\dot{M}_0(f)S(f)]$, the acceleration spectrum, $A(f, R)$, may be computed (equation 1) and the stochastic method may be used to obtain ground motion parameters.

Predicted *PGA* curves, using the stochastic method, for M_w 4.5, 5.5, and 6.5, as function of R, for sedimentary Veracruz sites and LVNPP sites are illustrated in Figures 12a and c, respectively. The corresponding *PGV* curves are given in Figures 12b and d. Observed *PGA* and *PGV* values during the 2009 (red plusses) and 2021 earthquakes (blue plusses) are superimposed on these figures. For the LVNPP sites, the synthesized *PGA* and *PGV* values for a scenario M_w 6.5 earthquake, using the recordings of the 2021 (M_w 4.8) earthquake as EGFs, are very similar to the stochastically predicted ones. For the sedimentary sites in the city of Veracruz, the EGF predictions are greater than the stochastic ones. We checked the stochastic predictions for stress drops of 4 and10 MPa instead of 2 MPa. A 5 times increase in $\Delta\sigma$ produces ~ 3 time increase in PGA and PGV values. A two-fold increase in $\Delta\sigma$ produces ~ 1.6 time increase in PGA and PGV values while a five times greater $\Delta\sigma$ produces ~ 3 times larger PGA and PGV values. This shows the sensitivity of the results to the stress drop of the postulated earthquake. In as much as $\Delta\sigma$ of the postulated event is uncertain by a factor of at least 2 or 3 of 2 MPa, the predicted values of PGA and PGV values corresponding to $\Delta\sigma$ of 2 MPa may be off by a factor of 2 or more.

As mentioned earlier, the estimation of ground motion from a scenario M_w6.5 earthquake is of great practical interest, especially above the hypocenter (R ~ 20 km). For such an event the stochastically predicted *PGA* and *PGV* at sedimentary coastal sites above the hypocenter are 0.18 g and 10 cm/s. At LVNPP, the corresponding predicted motions are 0.2 g and 3 cm/s. As mentioned above, the values may be off by a factor of atleast 2.

Unusual Recordings at DHIG and LVIG Sites

Two sites where *ASAS(f)* is unusually low are DHIG and LVIG (Figures 2 and 3). Here we briefly discuss the cause of this extraordinary observation.

Shapiro *et al.* (2000) noted that the amplitude of seismic waves traversing the active Popocatépetl volcano before reaching Mexico City is diminished by a factor of about one-third at frequencies greater than 1 Hz as compared to those that do not cross it. The higher attenuation below the volcano was attributed to the presence of magma and partial melting of rocks. DHIG is a limestone site at the northern end of the Mexican Volcanic Belt (MVB) (Figures 2 and 3). The wavepaths from 2009 and 2021 earthquakes to DHIG do not cross any active volcano but travel about 300 km in the MVB (Figures 2 and 3). Greatly reduced *ASAS(f)* at DHIG is very likely a consequence low Q along the path. Relatively low Q in the MVB has been reported by Singh *et al.* (2007).

Singh *et al.* (2006) documented a relative diminution of amplitude of seismic waves recorded at LVIG during certain group of earthquakes. They associated the diminution to wavepath through low-Q mantle wedge. LVIG, situated in the LVNPP facility, is located on basaltic flows underlain by vulcanites that

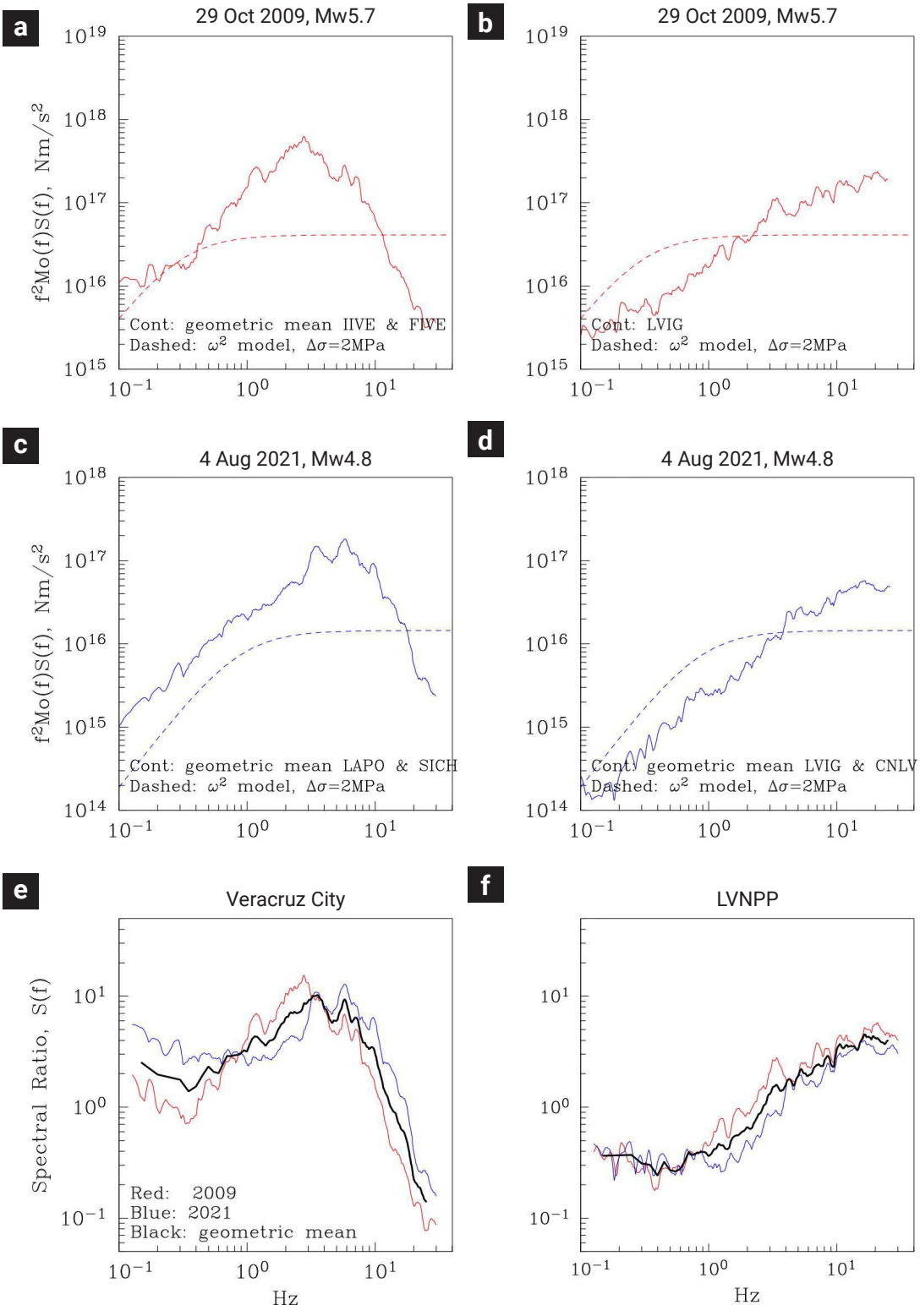

Figure 11. Geometric mean of *ASAS*(*f*) for the 2009 earthquake a) at the sedimentary Veracruz sites of IIVE and FIVE, b) at LVIG. Geometric mean of *ASAS*(*f*) for the 2021 earthquake c) at sedimentary Veracruz sites of LAPO and SICH, d) at LVIG and CNLV. Theoretical spectrum for ω^2 source model with $\Delta\sigma$ of 2 MPa are shown in a), b), c), and d). *S*(*f*), the ratio of geometric mean of *ASAS*(*f*) to the theoretical spectrum, for the sedimentary sites in the city of Veracruz and sites in the LVNPP are shown in d) and f), respectively.

overlie a granitic inclusion. It is probably one of the harder sites of the national seismological and accelereographic networks. The low *ASAS(f)* at LVIG during the 2009 and 2021 earthquakes, of course, can not be attributed to mantle wedge. It is most likely due to the highly competent rock site where the station is situated. For certain group of events both low-Q mantle wedge and hard LVIG site may be responsible for low observed spectrum and lower than expected *PGA* and *PGV*. We searched for $Q(f)$ which will bring the source spectra retrieved from the LVNPP recordings to theoretical source spectra (Figure 11). As intuitively expected, it requires low $Q(f)$, ~50f, for f < 2.5 Hz, and high $Q(f)$, ~300f, for f ≥2.5 Hz. A thorough study is warranted to pin point the cause of the abnormal spectra at LVNPP. This is beyond the scope of this paper.

Conclusions

The 2009 Alvarado (M_w5.7) and 2021 Veracruz (M_w4.8) earthquakes are the first two moderate events to occur near the margin of southwest Gulf of Mexico that were well-recorded at local and regional distances. This permitted us to perform centroid moment tensor inversion using the *W*-phase which yielded reverse-faulting focal mechanism for both events. This

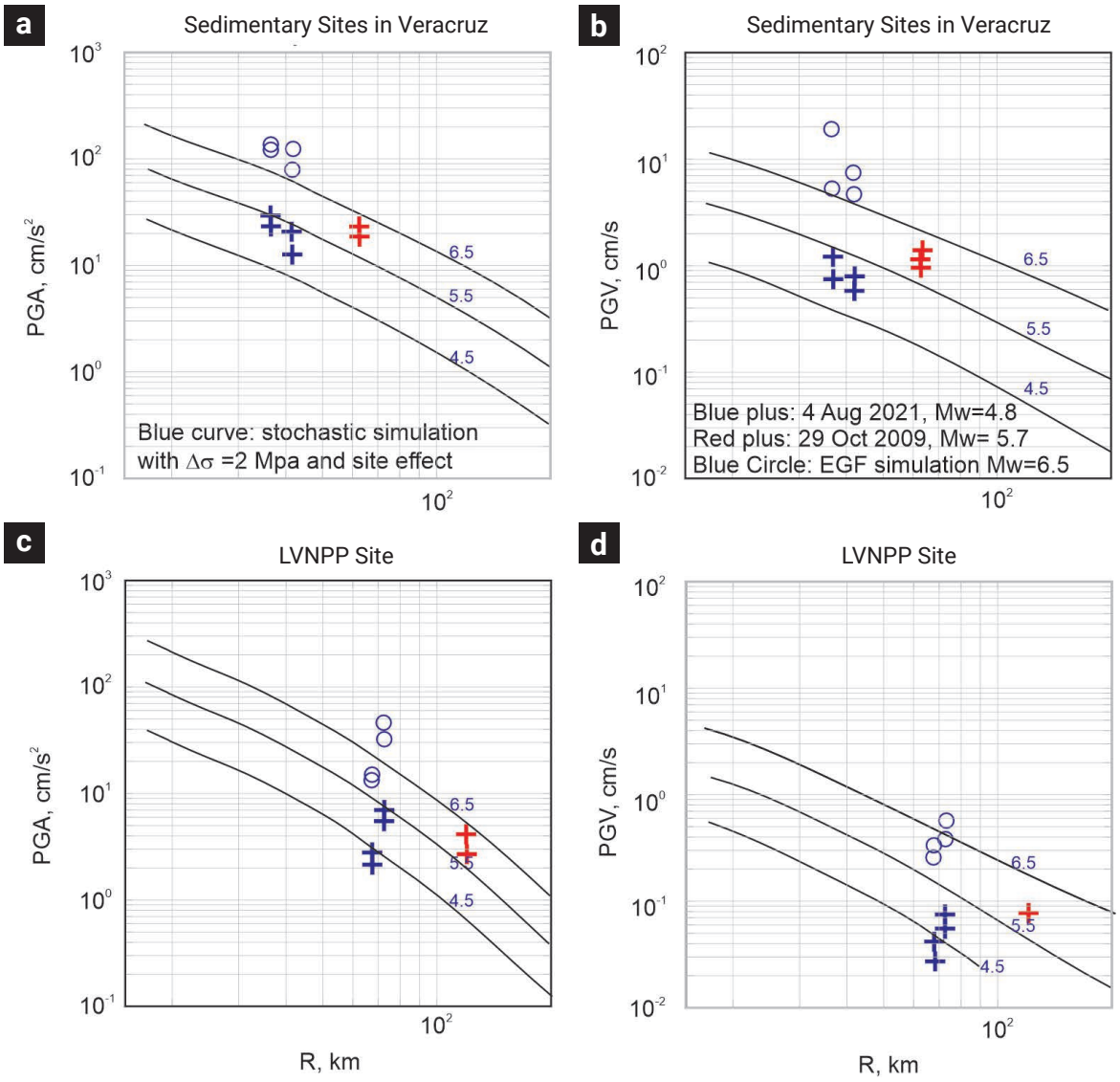

Figure 12. Predicted *PGA* curves from stochastic method for M_w 4.5, 5.5, and 6.5 earthquakes as function of R at a) sedimentary Veracruz sites, and c) LVNPP sites The corresponding *PGV* curves are given in b) and d). Observed values during the 2009 (red plusses) and 2021 earthquakes (blue plusses) are superimposed on these figures. Synthesized *PGA* and *PGV* values for an M_w 6.5 earthquake from the EGF technique are shown by circles.

mechanism is similar to those of three other earthquakes in the southwestern Gulf of Mexico. We also determined the focal mechanism of another earthquake (15 Feb 2017, M_w 4.3) with epicenter near the 2021 event. The mechanism of this event, strike slip, is consistent with left-lateral, strike-slip Veracruz fault on which it may have occurred. Presently, focal mechanisms of seven earthquakes along the southwestern margin of the gulf is known; of these two are strike-slip and the rest are thrust type. Thus, the stress regime near the southwest margin of the gulf appears to be more heterogeneous than previously thought.

The recordings of the 2009 and 2021 earthquakes also permitted us to estimate ground motion from future earthquakes occurring in the southwest margin of the gulf, critical for seismic risk assessment of the region but still lacking at present. In particular, the estimation of ground motion from a "migrating" M_w 6.5 earthquake has been of great concern in the seismic design of the Laguna Verde Nuclear Power Plant (LVNPP). Source spectrum computed at each station (distance $\leq$ 400 km) individually by applying reasonable Q and geometric spreading corrections, exhibits remarkably high variability due to difference in the path and local site effects. The geometric mean apparent source spectrum of both earthquakes may be modeled by an ω^2 -Brune source with $\Delta\sigma = 40$ MPa. This source spectrum, along with the application of the stochastic method, yields *PGA* and velocity *PGV* as a function of distance in general agreement with the observations.

Of greater, practical importance is the estimation of ground motion at near-source sedimentary sites in the city of Veracruz and at the LVNPP. We used both EGF and stochastic methods in the estimation. The recordings of the 2021 earthquake were taken as EGFs and $\Delta\sigma$ of 2 Mpa for the EGF and target events was assumed in the simulation. While this stress drop is reasonable, it is weakly constrained by the data. In the application of stochastic method, we estimated the site effect in the city of Veracruz and at LVNPP from the spectral ratio of observed apparent source spectrum to theoretical source spectrum corresponding to the ω^2 - Brune source with $\Delta\sigma = 2$ MPa.

For an M_w 6.5 earthquake, the predicted *PGA* and *PGV* at sedimentary coastal sites above the hypocenter ($R = 20$ km) are 0.18 g and 10 cm/s. At LVNPP, the corresponding predicted motions are 0.21 g and 3 cm/s. These values may be off by a factor of 2 or more due to uncertainty in the stress drop of the postulated event. It is worth remembering that the estimates are based on few data presently available and several assumptions, e.g., ω^2 - Brune source with $\Delta\sigma = 2$ MPa is valid for all earthquakes and farfield, point source approximation holds even for an M_w 6.5 earthquake at a distance of 20 km. Thus, the estimated motions are necessarily preliminary that would be revised and modified as more near-source recordings become available. The present study brings in to focus the need for more intensive instrumentation in the region and lays ground for future work.

Acknowledgements

Data used in this study were provided by the Servicio Sismológico Nacional (SSN, Mexican National Seismological Service), Red Acelerográfica del Instituto de Ingeniería (IING), Universidad Nacional Autónoma de México (UNAM, National Autonomous University of Mexico), Comisión Federal de Electricidad (CFE) and Instituto de Ingeniería of Universidad Veracuzana (IIUV). We thank personnel of these institutions for station maintenance, data acquisition and distribution. Conversations with Juan Manual Espindola regarding stress regime along the southwestern margin of Gulf of Mexico are acknowdged. Comments and suggestions by the revewer resulted in an improved manuscript. The research was partially supported by UNAM, PAPIIT projects IN108221 and IN109423 (S.K.S.).

The views expressed herein are those of the authors and do not necessarily reflect the views of the CTBTO Preparatory Commission.

References

Allmann, B. P., and P. M. Shearer (2009). Global variations of stress drop for moderate to large earthquakes, *J. Geophys. Res.*, 114, B01310. doi: **https://doi.org/10.1029/2008JB005821**

Andreani, L., Rangin, C., Martinez-Reyes, J., Le Roy, C., Aranda-Garcia, M., Le Pichon, X., Peterson-Rodriguez, R. (2008). The Neogene Veracruz Fault: evidences for left-lateral slip along the Southern Mexico Block, *Bulletin de la Société Géologique de France*, 179, 195-208. doi: **https://doi.org/10.2113/gssgfbull.179.2.195**

Boore, D. M. (1983). Stochastic simulation of high-frequency ground motions based on seismological models of radiated spectra. *Bulletin of Seismological Society of America*, 73, 1865-1884. **https://doi.org/10.1785/BSSA07306A1865**

Boore, D.M. (2003). Simulation of ground motion using the stochastic method. Pure and Applied Geophysics, 160, 635-676. **https://link.springer.com/article/10.1007/PL00012553**

Brune, J. N. (1970). Tectonic stress and the spectra of seismic shear waves from earthquakes. *Journal of Geophysical Research*, 75(26), 4997-5009. doi: **https://doi.org/10.1029/jb075i026p04997**

Canas, J. A. (1986). Estudio de factor inelástico Q de la coda de los terremotos correspondientes a las regiones central y oriental del eje volcánico de México, *Geofísica Internacional*, 25, 503-520. doi: **https://doi.org/10.22201/igeof.00167169p.1986.25.4.775**

Chael, E. P. (1987). Spectral scaling of earthquakes in the Miramichi region of New Brunswick. *Bulletin of the Seismological Society of*

America, 77(2), 347-365. doi: **https://doi.org/10.1785/bssa0770020347**

Dewey, J.W., Suárez, G. (1991). Seismotectonics of middle America, in Slemmons, D.B., Engdahl, E.R., Zoback, M.D., and Blackwell, D.D., eds., Neotectonicas of North America, Boulder, Colorado, *Geological Society of America*, Decade Map, V. 1, 309-321. doi: **https://doi.org/10.1130/DNAG-CSMS-NEO.309**

Dreger, D.S., 2003, TDMT_INV: time domain seismic moment tensor inversion, in Lee, W.H.K., Kanamori, H., Jennings, P.C., Kisslinger, C. (eds.), *International handbook of earthquake and engineering seismology*, B: London, U.K. Academic Press, 1627.

Dreger, D. S., Helmberger, D. V. (1993). Determination of source parameters at regional distances with three-component sparse network data. *Journal of Geophysical Research: Solid Earth, 98*(B5), 8107-8125. doi: **https://doi.org/10.1029/93jb00023**

Duputel, Z., Rivera, L., Kanamori, H., Hayes, G. (2012). W-phase fast source inversion for moderate to large earthquakes (1990 - 2010). *Geophysical Journal International*, 189(2), 1125-1147. doi: **https://doi.org/10.1111/j.1365-246X.2012.05419.x**

Figueroa, J. (1964). El macrosismo de Jáltipan. 1. Sismologia. Ingeniería, July, 357-362.

Franco, S. I., Canet, C., Iglesias, A., Valdés-González, C. (2013). Seismic activity in the Gulf of Mexico. A preliminary analysis. *Boletín de la Sociedad Geologíca Mexicana*, 65, 447-455. ISSN: 1405-3322.

Frohlich, C. A. (1982). Seismicity of the central Gulf of Mexico. *Geology*, 10(2), 103. doi: **https://doi.org/10.1130/0091-7613(1982)10**

Fukuyama, E., Dreger, D. S. (2000). Performance test of an automated moment tensor determination system for the future "Tokai" earthquake. *Earth, Planets and Space, 52*(6), 383-392. doi: **https://doi.org/10.1186/bf03352250**

Hayes, G. P., Rivera, L., Kanamori, H. (2009). Source Inversion of the W-Phase: Real-time Implementation and Extension to Low Magnitudes. Seismological Research Letters, 80(5), 817-822. doi: **https://doi.org/10.1785/gssrl.80.5.817**

Herrmann, R. B. (1985). An extension of random vibration theory estimates of strong ground motion at large distances. *Bull. Seism. Soc. Am., 75*, 1447-1453. doi: **https://doi.org/10.1785/BSSA0750051447**

Kanamori, H., Rivera, L. (2008). Source inversion of W phase: speeding up seismic tsunami warning. *Geophysical Journal International, 175*(1), 222-238. doi: **https://doi.org/10.1111/j.1365-246x.2008.03887.x**

Nuttli, O. W. (1983). Average seismic source-parameter relations for mid-plate earthquakes. *Bulletin of the Seismological Society of America, 73*(2), 519-535. doi: **https://doi.org/10.1785/bssa0730020519**

Ordaz, M., Arboleda, J., Singh, S.K. (1995). A scheme of random summation of an empirical Green´s function to estimate ground motions from future large earthquakes. *Bull. Seism. Soc. Am.*, 85, 1635-1647. doi: **https://doi.org/10.1785/BSSA0850061635**

Pérez-Campos, X., Espíndola, V. H., Pérez, J. *et al.* (2019). Servicio Sismológico Nacional, Mexico. *Summary of the Bulletin of the International Seismological Centre, 53*(II), 29-40. doi: **https://doi.org/10.31905/sz7rybtm**

Reséndiz, D. (1964). El macrosismo de Jáltipan. 2. Suelos. *Ingeniería,* July, 362-379.

Rosenblueth, E. (1964). El macrosismo de Jáltipan. Introducción. Ingeniería, July, 357.

Shapiro, N. M., Singh, S. K., Iglesias-Mendoza, A., Cruz-Atienza, V. M., Pacheco, J. F. (2000). Evidence of low Q below Popocatépetl Volcano, and its implication to seismic hazard in Mexico City. *Geophysical Research Letters, 27*(17), 2753-2756. doi: **https://doi.org/10.1029/1999gl011232**

Singh, S.K., Pacheco, J.F., Garcia, D., Iglesias, A. (2006). An estimate of shear-vave Q of the mantle wedge in Mexico, *Bulletin of the Seismological Society of America*, 96, 176–187, doi: **https://doi.org/10.1785/0120050001**

Singh, S. K., Iglesias, A., García, D., Pacheco, J. F., Ordaz, M. (2007). Q of Lg Waves in the Central Mexican Volcanic Belt. *Bulletin of the Seismological Society of America*, 97(4), 1259-1266. doi: **https://doi.org/10.1785/0120060171**

Singh, S.K., Pacheco, J. F., Pérez-Campos, X., Ordaz, M., Reinoso, E. (2015). The 6 September 1997 (Mw4.5) Coatzacoalcos-Minatitlan, Veracruz, Mexico earthquake: implications for tectonics and seismic hazard of the region, *Geofísica International*, 54, 289-298. doi: **https://doi.org/10.1016/j.gi.2015.08.001**

Singh, S.K., Arroyo, D., Pérez-Campos, X., Iglesias, A., Espíndola, V.H., Ramírez, L. (2017). Guadalajara, Mexico, earthquake sequence of December 2015 and May 2016: source, Q, and ground motions, *Geofísica Internacional*, 56-2, 173-186. doi: **https://doi.org/10.22201/igeof.00167169p.2017.56.2.1764**

Suárez, G., López, A. C. G. (2015). Seismicity in the southwestern Gulf of Mexico: evidence of active back arc deformation. *Revista Mexicana de Ciencias Geológicas*, 32(1), 77-83. **http://www.redalyc.org/pdf/572/57237105007.pdf**

Suárez, G. (2000). Reverse faulting in the Isthmus of Tehuantepec: Back-arc deformation induced by the subduction of the Tehuantepec ridge, in Delgado, H., Aguirre, G., Stock, J., (eds), Cenozoic Tectonics and Volcanism of Mexico, *Geological Society of. America Special Paper*, 334, 263-268. doi: **https://doi.org/10.1130/0-8137-2334-5.263**

Appendix A

Location and moment tensor inversion of the 15 February 2017 earthquake

The 2017 earthquake was located using phase data and crustal structure given in Table 2 and varying the depth (H). Residuals as a function of H, illustrated in Figure Aa, suggest a depth between 15 and 21 km.

An Automated Moment Tensor Determination (AMTD) algorithm, developed at the Berkeley Seismological Laboratory (Fukuyama and Dreger, 2000; Dreger, 2003) and implemented at UNAM using realtime data from SSN stations (Franco *et al.*, 2013) was used to determine moment tensor of the 2017 event. Full three-component broadband displacement waveforms were inverted to obtain the moment tensor solution (Dreger and Helmberger, 1993). The algorithm searches for the H that provides the best fit between the observed and synthetic seismograms, i.e., that H which provides greatest variance reduction (VR). VR as a function of H is shown in Figure Ab. We note that the focal mechanism remains stable for sources at H between 10 km and 40 km and VR is relatively insensitive to H between 20 and 35 km. Thus, from AMTD a depth between 20 and 35 km is acceptable. Since H = 20 km is in agreement with the location output, we take this to be depth of the 2017 event. Figure Ac compares the observed and synthetic displacements (H = 18 km) at 4 stations. The fit is good. M_0 is 2.15×10^{15} Nm (M_w4.3) and the focal mechanism is given by:

Nodal plane 1: $\varphi_1 = 3090$, $\delta_1 = 74^0$, $\lambda_1 = 23^0$
Nodal plane 2: $\varphi_2 = 2120$, $\delta_2 = 67^0$, $\lambda_2 = 163^0$

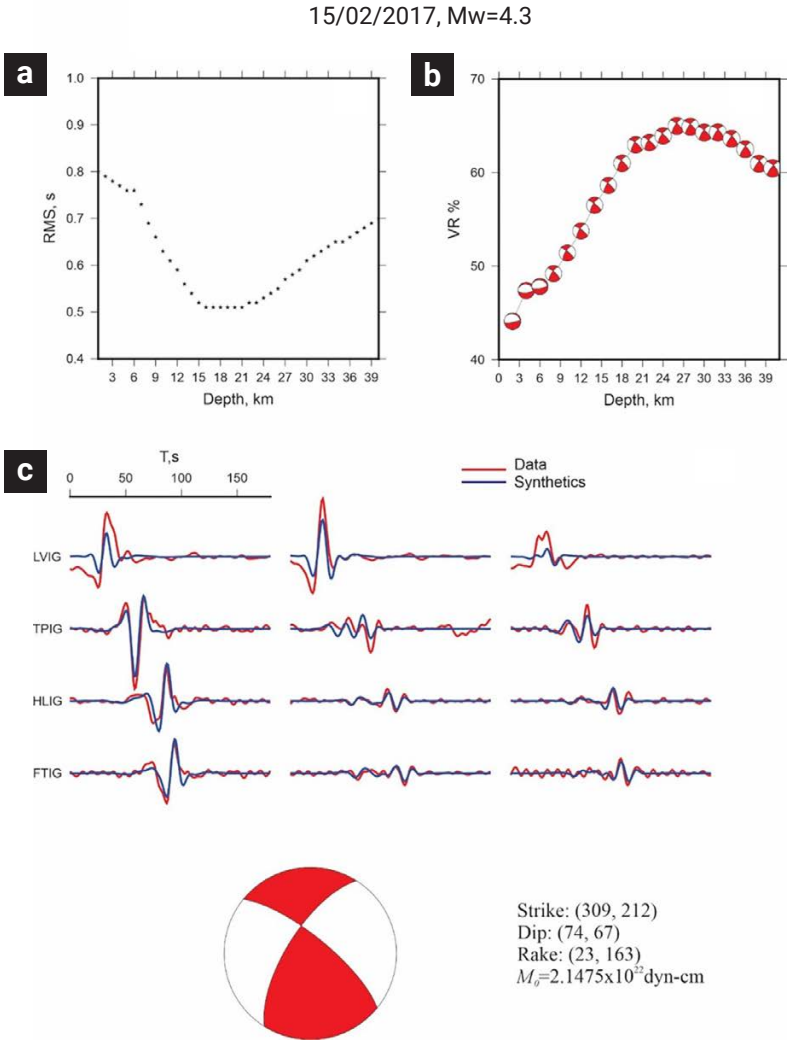

Figure A. a) RMS error as a function of depth, *H*, from earthquake location program. Minimum in the plot suggests *H* between 15 and 21 km. b) Variance reduction (*VR*) as a function of *H*. Although the focal mechanism is stable, *H* is poorly resolved from VR. c) Observed (red) and synthetic (blue) (*H* = 20 km) displacements at four broadband stations. Red and white beach ball shows the focal mechanism of the 2017 earthquake.

Geofísica Internacional (2024) **63-2**: 783 - 801

Prediction of Fourier Amplitude Spectrum of Ground Motion in Mexico City from Subduction Thrust Earthquakes

Danny Arroyo[*1], Mario Ordaz[2] and Shri K. Singh[3]

Abstract

Mexico City, one of the largest cities in the world, experiences frequent, devastating interplate earthquakes that originate on the subduction thrust along the Pacific coast of Mexico more than 250 km away. A notorious example is the 19 September 1985 Michoacán earthquake (M_w 8.0) which killed ~ 10,000 persons and caused wide-spread destruction in the city. The main cause of seismic damage in Mexico City is its subsoil that amplifies the ground motion. In view of the seismic hazard faced by the city, a reliable estimation of ground motion during future earthquakes is of vital importance. We present a new ground motion prediction equation (GMPE) for the Fourier amplitude acceleration spectrum (*FAS*) from subduction thrust earthquakes along the Pacific coast of Mexico at the reference station, CU, located in the firm zone of Mexico City. The GMPE is derived *via* Bayesian regression analysis and is based on an enlarged set of recordings (1965-2020; 40 earthquakes; $250 \leq R \leq 500$ km; $5 \leq M_w \leq 8.0$). An important feature of the new GMPE is that it includes a term to model different attenuation along different ray paths. The inclusion of this term leads to a reduction in the aleatory variability of the GMPE, particularly at high frequencies. Since spectral amplification of seismic waves with respect to CU is known at many sites in the city, the *FAS* at these sites can be computed if it is known at CU. The new GMPE has been incorporated in a fully Fourier-based probabilistic seismic hazard analysis of Mexico City.

Key words: GMPE, FAS, subduction earthquakes, Bayesian analysis.

Resumen

La CDMX, una de las ciudades más grandes del mundo, ha sufrido continuamente sismos destructivos que se originan en la interfaz de la zona de subducción en la costa del Pacífico a más de 250 km de distancia. Un ejemplo notable es el gran sismo de Michoacán del 19 de septiembre de 1985 el cual devasto la ciudad y provocó más de 10,000 víctimas. La causa principal de los daños es la gran amplificación del movimiento del suelo que se presenta en la CDMX. En vista del nivel de peligro sísmico a que está expuesta la ciudad es necesario contar con estimaciones precisas del movimiento del suelo durante eventos sísmicos futuros. Se presenta un modelo de atenuación (GMPE) del espectro de amplitudes de Fourier de la aceleración (FAS) del movimiento del suelo, en la estación de Ciudad Universitaria (CU) en la CDMX, durante sismos en la interfaz de subducción a lo largo de la Costa del Pacífico Mexicano con mecanismo de falla inverso. Se consideran registros entre 1965 a 2020 durante 40 sismos con magnitudes entre 5 y 8 a distancias entre 250 km y 500 km, lo cual representa un incremento considerable de registros respecto a los estudios previos. Como método de regresión se utilizó un esquema de regresión Bayesiano. Una característica importante del modelo propuesto es que incluye términos para modelar la atenuación a lo largo de diferentes trayectorias, se observó que la inclusión de estos términos conduce a una reducción en la variabilidad aleatoria del GMPE, particularmente en altas frecuencias. Dado que la amplificación de las ondas sísmicas con respecto a la estación CU se conoce en muchos sitios instrumentados en la CDMX es posible estimar el FAS en estos sitios si se conoce el FAS en la estación CU. El modelo propuesto ha sido incorporado en un análisis de peligro sísmico basado en el uso de FAS y ha dado lugar a los espectros de diseño sísmico de la nueva versión del Reglamento de Construcciones de la CDMX.

Palabras clave: Modelo de atenuación, espectro de amplitud de Fourier, sismos de subducción, análisis de regresión Bayesiano.

Received: June 21, 2023; Accepted: January 20, 2024; Published on-line: April 1, 2024.

Editorial responsibility: Dr. Sreenath Vemula

* Corresponding author: Arroyo, Danny. E-mail: aresda@azc.uam.mx
[1] Departamento de Materiales. Universidad Autónoma Metropolitana.
[2] Instituto de Ingeniería. Universidad Nacional Autónoma de México.
[3] Instituto de Geofísica. Universidad Nacional Autónoma de México.

https://doi.org/10.22201/igeof.2954436xe.2024.63.2.1717

1. Introduction

Mexico City and the surrounding metropolitan area, home of nation´s 40% population, experiences frequent, devastating interplate earthquakes that originate on the subduction thrust along the Pacific coast of Mexico more than 250 km away. A notorious example is the 19 September 1985 Michoacán earthquake (M_w 8.0) which killed ~ 10,000 persons and caused wide-spread destruction in the city (Anderson *et al.*, 1986). The city is also prey to intraslab, normal-faulting earthquakes in the subducted Cocos plate that may occur at hypocentral distances as close as 120 km. A recent example of this type of event is the 19 September 2017 Puebla-Morelos earthquake (M_w 7.1) which caused severe damage to the city and death of about 220 persons (Singh *et al.*, 2018). Additionally, the city is exposed to seismic hazard from local and regional earthquakes in the Trans-Mexican Volcanic Belt within which Mexico City is situated.

The main cause of damage in Mexico City from interplate and intraslab earthquakes is its subsoil that amplifies the ground motion (Rosenblueth, 1953; Anderson *et al.*, 1986; Celebi *et al.*, 1987; Singh *et al.*, 1988a, 1988b; Ordaz and Singh, 1992). From geotechnical perspective the subsoil is divided in three zones: the lake-bed zone (consisting of 30 to 80 m deposit of highly-compressible, high-water content clay underlain by resistant sands); the hill zone (comprising of a surface layer of lava flows and volcanic tuffs); and the transition zone (composed of alluvial sandy and silty layers with occasional intervals of clay layers). Seismic waves trapped in the soft layers of the transition and lake-bed zones are greatly amplified at frequencies between 0.2 to 1 Hz. The buildings whose natural periods coincide with the dominant period of the subsoil are highly vulnerable to earthquake ground motion.

In view of the seismic hazard faced by the city, a reliable estimation of ground motion during future earthquakes is of vital importance. Following the 1985 Michoacán earthquake, the occurrence of a great earthquake, $M_w \geq 8$, in the Guerrero seismic gap became a major concern of seismologists and earthquake engineers. Ordaz *et al.* (1993) applied a technique of summation of empirical Green's function (EGF) (Joyner and Boore 1986) to estimate ground motions in Mexico City from a postulated M_w 8.2 earthquake in the gap. Later, Ordaz *et al.* (1995) developed an improved scheme of random summation of EGF and re-estimated the ground motions. Kanamori *et al.* (1993) used several recordings as EGFs and, assuming different rupture scenarios and ω^2-source model, estimated ground motion at a site in Mexico City from an M_w 8.0 earthquake. While the EGF technique is very powerful since it automatically accounts for path and site effects, its application is limited by the availability of adequate EGFs.

An alternative approach that has been pursued is to estimate *FAS* at sites in Mexico City. This is facilitated by the fact that a strong-motion station, CU, located on basalt lava flows at the main campus of National Autonomous University of Mexico (UNAM) in Mexico City, has been in continuous operation since 1964, recording earthquakes during the past 59 years. The extensive recorded dataset has been used to derive ground motion prediction equation (GMPE) for *FAS* at CU (Castro *et al.* 1988, Ordaz *et al.*, 1994). On the other hand, spectral amplifications of ground motion at other sites in the city have been computed with respect to the recordings at CU (Ordaz *et al.*, 1988; Singh *et al.*, 1988b; Reinoso and Ordaz, 1999). To a first order, the spectral amplification at a site in the lake-bed or the transition zone is independent of the magnitude, epicentral distance, depth, and azimuth of the source. Thus, if the *FAS* of the ground motion of an earthquake at CU is known (either from its recording or from the GMPE), then the spectrum can be estimated at all sites in the city whose spectral amplification is known. An application of stochastic theory (Boore, 2003), along with an estimation of the duration of the intense part of the ground motion, then yields the expected ground motion parameters in the city. This empirical approach has been validated for the Valley of Mexico by Ordaz *et al.* (1988) and Reinoso and Ordaz (2001). The approach is very useful in practical applications (Ordaz *et al.*, 2017); it also circumvents the complex wave-propagation phenomenon of seismic waves in a poorly known shallow crustal structure of the valley (Cruz-Atienza *et al.*, 2016).

Since 1994 when the last GMPE for *FAS* at CU was derived, the quality and quantity of useful strong motion (SM) recordings at this station have significantly improved. Because the *FAS* at CU plays such an important role in practical applications, we take advantage of the enlarged dataset to construct a new GMPE. Similar to Ordaz *et al.* (1994) we follow the Bayesian approach in the regression analysis which allows for inclusion of knowledge not directly derived from observed data. Analysis based on the enlarged and improved dataset results in a significant reduction of aleatory variability of the GMPE with respect to the previous GMPE (Ordaz *et al.*, 1994). Guided by the observed residuals, we further modify the model to include the variation of attenuation along different ray paths. We find that this simple modification leads to a reduction in the aleatory variability of the GMPE, especially at frequencies greater than 1 Hz.

2. Data

We searched for SM recordings at CU from shallow-dipping thrust faulting earthquakes on the plate interface. Near-trench earthquakes which are known to be deficient in high-frequency

radiation (Shapiro *et al.*, 1998; Iglesias *et al.*, 2003; Singh *et al.*, 2016), were excluded from the analysis. The remaining dataset comprises of 40 earthquakes recorded between 1965 and 2020. They are listed in Table 1 along with their magnitude (M_w), depth (H) and epicenter. These parameters were taken from published papers if available; otherwise M_w and H were obtained from the Global CMT catalog (**https://www.globalcmt.org**) and the epicentral location was taken from the catalog of National Seismological Service (SSN; **http://www.ssn.unam.mx/doi/networks/mx/**). Table 1 also lists the closest distance from CU

Table 1. List of earthquakes analyzed in this study. Last 3 earthquakes were not used in the regression analysis

Date	Latitude	Longitude	M_w	Depth, km	R_{rup}, km
23/08/1965	16.28	-96.02	7.45	16	446
03/02/1968	16.67	-99.39	5.9	16	292
02/08/1968	16.25	-98.08	7.2	16	339
01/02/1976	17.15	-100.23	5.6	16	263
07/06/1976	17.45	-101.46	6.4	29	311
07/06/1976	17.036	-99.745	6.6	11	251
29/11/1978	16.00	-96.69	7.6	16.1	419
14/03/1979	17.46	-101.46	7.55	26.7	285
07/06/1982	16.516	-98.339	6.9	18.6	310
07/06/1982	16.424	-98.253	6.9	10.7	322
19/09/1985	18.073	-102.754	8.0	21.3	300
21/09/1985	17.62	-101.82	7.6	20.8	302
30/04/1986	18.361	-103.045	7.0	20.7	403
08/02/1988	17.4	-101.22	5.9	16	299
25/04/1989	16.795	-99.275	6.9	15	266
11/05/1990	17.14	-100.8	5.6	15	294
31/05/1990	17.14	-100.86	5.9	26	297
14/09/1995	16.752	-98.667	7.4	21.8	264
16/12/1997	15.70	-99.04	6.0	16	398
03/02/1998	15.69	-96.37	6.3	24	495
11/07/1998	17.25	-101.54	5.5	24.1	337
12/07/1998	16.83	-100.44	5.5	15	305
22/01/2003	18.60	-104.22	7.5	26	505
01/01/2004	17.30	-101.36	5.7	20.4	319
01/01/2004	17.34	-101.42	6.1	15	318
31/01/2009	17.66	-101.94	5.2	12	343
30/06/2010	16.24	-97.99	6.3	17.8	358
20/03/2012	16.264	-98.457	7.5	15.4	318
11/04/2012	17.9217	-103.068	6.7	20.5	426
21/08/2013	16.7527	-99.5812	6.2	23.3	283
18/04/2014	17.15	-100.845	7.3	18.9	275
08/05/2014	17.163	-100.819	6.5	21.3	287
10/05/2014	17.15	-100.845	6.1	20.7	294
24/05/2014	16.2002	-98.4073	5.7	16.2	354
08/05/2016	16.323	-97.8773	5.9	23.9	357
27/06/2016	16.208	-98.003	5.6	21.3	366
16/02/2018	16.218	-98.0135	7.2	20	345
17/02/2018	15.8438	-97.9887	6.0	16.7	402
19/02/2018	16.2477	-97.775	5.9	23.8	369
23/06/2020	15.8033	-96.1337	7.4	21.5	480
08/09/2021	16.767	-99.951	7.0	15.0	276
19/09/2022	18.220	-103.290	7.6	15.0	453
22/09/2022	18.050	-103.120	6.7	12.0	453

to the rupture area (R_{rup}). M_w of the dataset ranges between 5.0 and 8.0 and R_{rup} between 250 km and 500 km. Figure 1 shows the magnitude-distance plot. The figure identifies events included in the previous study (Ordaz *et al.*, 1994) while Figure 2 shows the corresponding M_w and R_{rup} histograms

The recent Acapulco earthquake of 08/09/2021 (M_w 7.0) and Michoacán - Colima earthquakes of 19/09/2022 (M_w 7.6) and 22/09/2022 (M_w 6.7), which are listed in Table 1, were not included in the regression analysis. They were used to check the validity of the new model. Figure 3 gives a map showing epicenters and magnitudes of all earthquakes, and their ray paths to CU.

SM recordings before 1985 were made by analog accelerographs. The digitized and processed data of these events are available at 50 sps. Beginning 1985 the earthquakes were recorded by digital accelerographs at 100 sps and/or 250 sps. All recordings were baseline corrected and bandpass filtered between 0.1 and 10 Hz. A 5% cosine taper is applied before computing the spectrum which is then smoothed by a 1/6 octave filter. *FAS* used in the regression is the quadratic mean of the two horizontal components as has been considered in previous GMPE studies in Mexico (Garcia *et al.* 2005, Arroyo *et al.* 2010).

3. The Model

Similar to Ordaz *et al.* (1994), our starting model is based on the solution of a point dislocation in an infinite space. Under far-field approximation and in the presence of anelastic attenuation and site effect, the Fourier acceleration amplitude spectrum, *FAS*, of the ground motion of an earthquake of seismic moment M_0 (moment magnitude M_w) at distance R_{rup} may be written as:

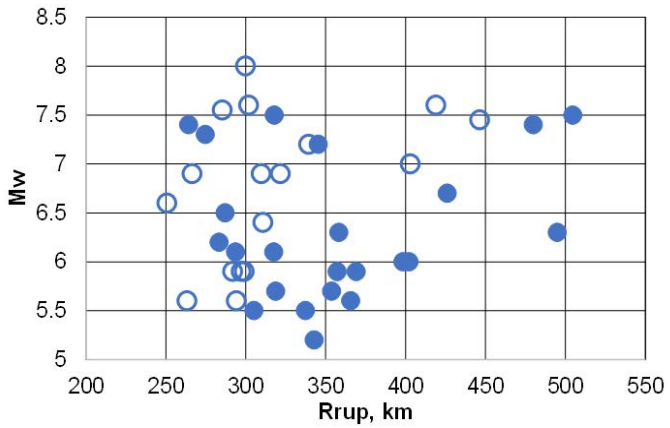

Figure 1. M_w - R_{rup} distribution of the data analyzed in this study. Open circles identify the events considered by Ordaz *et al.* (1994).

$$FAS(M_0, R_{rup}, f) = CG(R_{rup})\left\{f^2 \mathrm{M}_0(f)\right\}\left\{e\frac{-\pi f R_{rup}}{\beta Q(f)}\right\} \quad (1)$$

where C is a constant, *Site(f)* accounts for the site effect, Q(*f*) is the quality factor. $G(R_{rup})$ is the geometric spreading function defined by:

$$G\left(R_{rup}\right) = \begin{cases} \dfrac{1}{R_{rup}} & if\ R_{rup} \le R_x \\ \dfrac{1}{R_x}\left(\dfrac{R_{rup}}{R_x}\right)^{-0.5} & if\ R_{rup} \le R_x \end{cases}$$

In common with previous studies in the region, we set $R_x = 100$ km. $\dot{M}_0$ (*f*) in equation 1 is the moment rate function. For Brune ω^2-source model (Brune, 1970), $\dot{M}_0(f) = M_0 f_c^2 / (f^2 + f_c^2)$, and $f_c = 4.9\text{x}10^6 \beta(\Delta\sigma/M_0)^{1/3}$ where M_0 is in dyne-cm, β is shear-wave velocity at the source in km/sec, and $\Delta\sigma$ is the stress drop in bar. M_w is related to M_0 by $M_w = 2/3 \log M_0$ -10.71. For regression analysis we recast equation 1 in the following function form:

$$\ln(FAS) = a_1 + a_2 M_w + \ln\left(G\left(R_{rup}\right)\right) + a_3 R_{rup} \quad (2)$$

where a_1, a_2 and a_3 are coefficients to be determined by regression an}alysis. The functional form in equation (2) is based on the Brune's point-source model and it lacks terms that account for near source effects. However, given that the earthquakes analyzed herein are always generated at sources located at distances larger than 200 km we found that the functional form in equation (2) leads to reasonable results.

The regression analysis uses the Bayesian technique in which the regression coefficients and standard deviation of the residuals are considered random variables whose prior probability density is known and the prior densities are updated with observations using Bayes' theorem. A detailed discussion of the Bayesian framework can be found elsewhere (e.g., Broemling, 1985; Ordaz *et al.*, 1994). The prior information required by the Bayesian scheme was set as follows. It is assumed that regression coefficients follow a multivariate normal distribution with parameters μ (vector location) and Σ (covariance matrix). In addition, we supposed that the precision of the residuals follows a Gamma distribution with parameters λ (rate) and k (shape).

The elements of the vector location parameter are the prior mean value of the regression coefficients and they were set as follows: for a_1 we set its prior mean value to 1 to set the prior mean value of a_2 we generated a set of synthetic *FAS* from the Brune source model with $\beta = 3.5$ km/s and $\Delta\sigma$=100 bar for

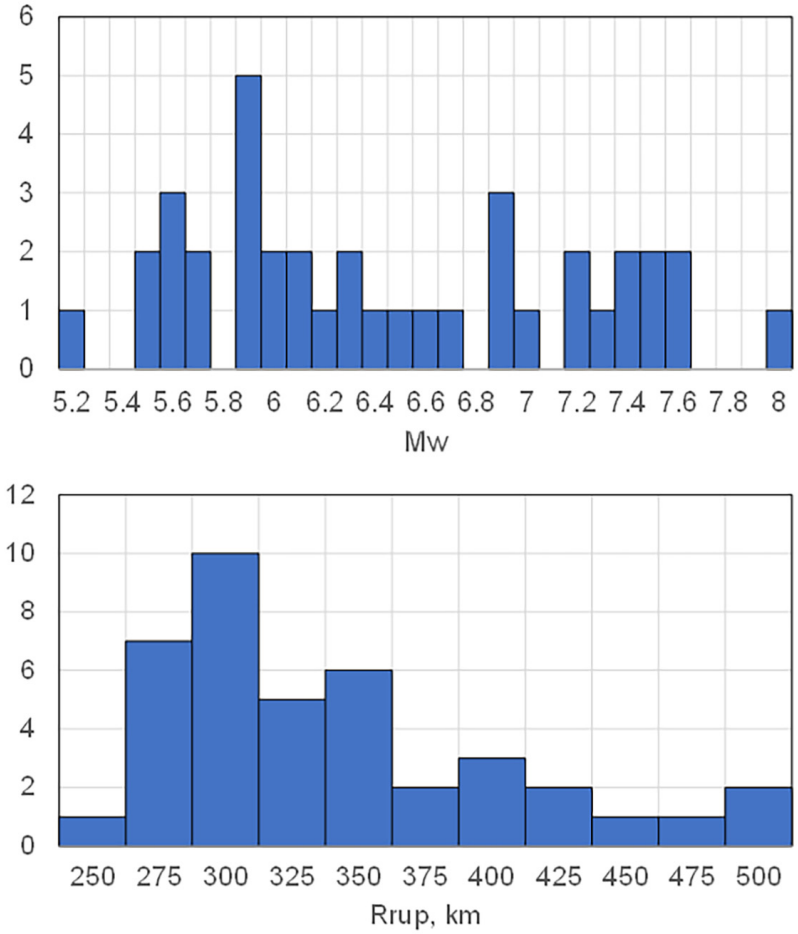

Figure 2. M_w and R histograms for the dataset in Figure 1.

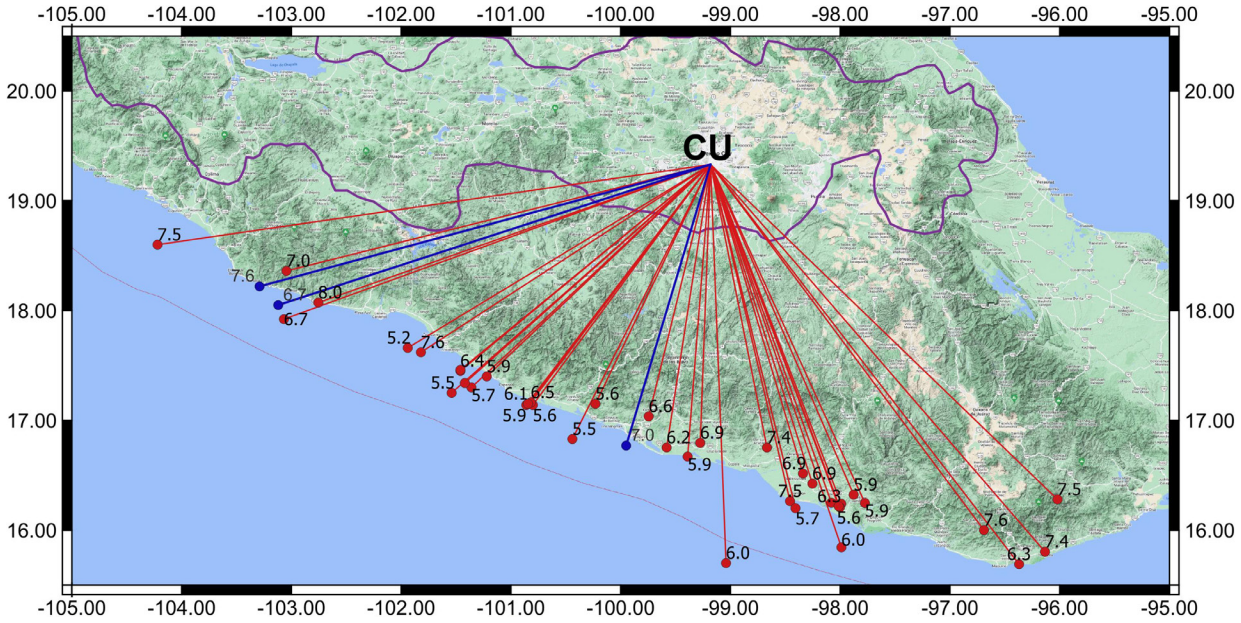

Figure 3. Map showing epicenters and magnitudes of the earthquakes considered in this study. Raypaths to CU are shown in straight lines. Blue dots are 3 recent events which were not included in the regression analysis. Violet contour encloses the Trans Mexican Volcanic Belt.

different M_w and R_{rup} combinations and performed a regression analysis to define the prior mean values a_2,The prior mean value of the coefficient a_3 was obtained from:

$$a_3^{'} = \frac{-\pi f}{\beta Q(f)} \quad (3)$$

where $a_3^{'}$ is the prior mean value of a_3. We take $Q(f)=273\, f^{0.66}$ reported for the region by Ordaz and Singh (1992).

The elements of the covariance matrix were set as follows: we suppose that, a priori, the regression coefficients are uncorrelated then the covariance matrix was set as a diagonal matrix. The elements in the diagonal of the covariance matrix are the variance of each regression coefficient, we assigned a large variance to a_1 because we decided to let it free during the regression analysis, to define the variance of a_2 we suppose a coefficient of variation equal to 0.3 and to define the variance of a_3 we suppose a coefficient of variation equal to 0.7.

The method also requires the parameters of the prior density of the precision of the residuals ($1/\sigma^2$), we suppose that the prior mean value of σ was equal to 0.7, a value commonly reported in the literature of GMPEs, and we assumed a variance equal to unity, from the properties of the gamma distribution this leads to λ=2.23 and k=0.606.

We emphasize that the prior information for our model comes from a physical model. This is an important characteristic of the model since this assures that in regions of scarce data the predictions will be close to a reasonable physical model.

We performed the regression analysis at 84 frequencies between 0.1 and 10 Hz. We examined the normalized residuals (*i.e.*, the ratio of residuals to their standard deviation) for this model and we noted that the model systematically overestimated or underestimated observations for certain ray paths as shown in Figure 4 (although not shown, similar trends were observed at other frequencies). To study the dependence of the residuals on the ray path, we grouped the events in 5 bins of 300 each. The angles defining the bins are illustrated in Figure 5. The average normalized residual was computed for each bin. The results are summarized in Figure 6 which reveal that for a given frequency the residuals for some paths may be systematically different than residuals for other ray paths. We attribute these trends to the difference in the anelastic attenuation along different ray paths. To account for this variation, we modified the initial functional form in equation 2 to a new one:

$$\ln(FAS) = a_1 + a_2 M_w + \ln(G(R_{rup})) + \sum_{i=1}^{5} d_i c_i R_{rup} \quad (4)$$

where a_1, a_2, and c_i are now the coefficients to be determined by regression analysis and d_1 is a dummy variable which equals 1 if $0° \leq \theta < 30°$, 0 otherwise, d_2 is a dummy variable which equals 1 if $30° \leq \theta < 60°$, 0 otherwise, and so on. We tried different number of bins in our analysis and noted that as the number of bins increases the σ values decrease but the regression tends to be unstable because overfitting. We decided to set the number of bins to five because we obtain a model that yields realistic predictions, since many bins lead to extreme variation in the predictions that are physically unrealistic.

We set the prior mean value of c_i equal to $a_3^{'}$ (equation 3). For set the covariance matrix we assign a coefficient of variation equal to 0.5 for c_1 and c_3 and a value of 0.8 to the coefficient of variation for c_2, c_4 and c_5. We set different prior coefficients of variation to c_i to leave them as free as possible during the regression analysis but avoiding positive values that are physically untenable.

The coefficients of the proposed model and the standard deviation of the residuals in natural logarithmic units (σ) are given in Table 2. In Figures 7, 8 and 9 we compare prior probability density functions and posterior probability density functions for the regression parameters for f=0.5, 1 and 5 Hz. The effect of the data on the updating of the prior densities is evident. Figures 10 and 11 show normalized residuals for different frequencies as a function of M_w and R_{rup}. We show a linear trendline for the residuals. As the small values of the slope of the trendline reveal, the residuals tend to be unbiased with respect to M_w and R_{rup}. Figure 12 show similar maps to those in Figure 4 but for the proposed model. In Figure 13 we compare average normalized residuals for different θ bins. As expected, the residuals are nearly independent of θ. For the proposed model the mean residual in the bins is not reduced to zero because, as mentioned earlier, the coefficients c_i are not free during the regression analysis; their values are controlled by the prior mean value in some degree to avoid overfitting. Although some bias persists for some bins at frequencies < 1 Hz, our model yields realistic predictions, because differences in predictions among different bins are physically realistic.

In future, as the number of recordings increases, it would be possible to let the coefficients free during the regression to correct the bias for all bins in the entire frequency range.

In Figure 14 we compare the parameters obtained from the regression analysis and the prior mean values used in the analysis. As expected, the data significantly change the prior information for a_1 while the parameters a_2 and c_i are close to the prior mean value. Figure 15 shows plot of the source scaling term, $a_1 + a_2 M_w$, as a function of frequency and M_w. Note that the proposed model has the expected theoretical scaling since the scaling term is proportional to M_w for f >0.5 Hz (i.e., above the corner frequency of most events in the dataset) as expected from the ω^2-source model. Note that the corner frequency in the source scaling term plots shift to lower frequencies as M_w increases as

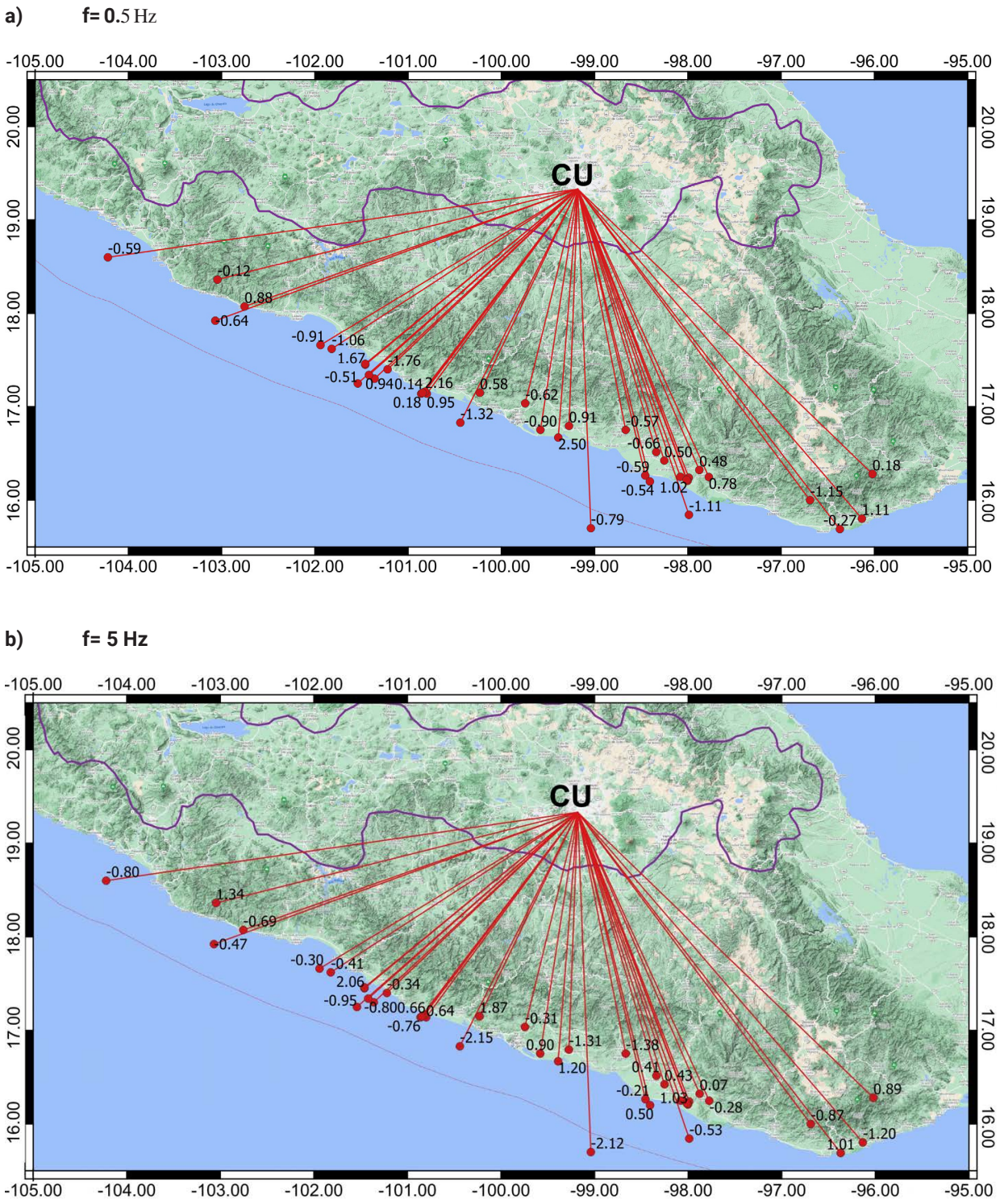

Figure 4. Map showing normalized residuals for the model defined in equation 2 at f = 0.5 Hz and f= 5 Hz.

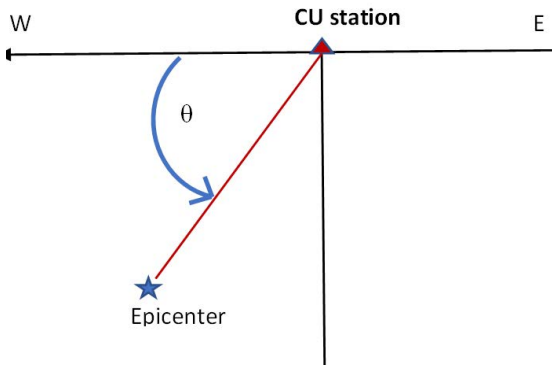

Figure 5. Definition of angle θ used in grouping events in bins.

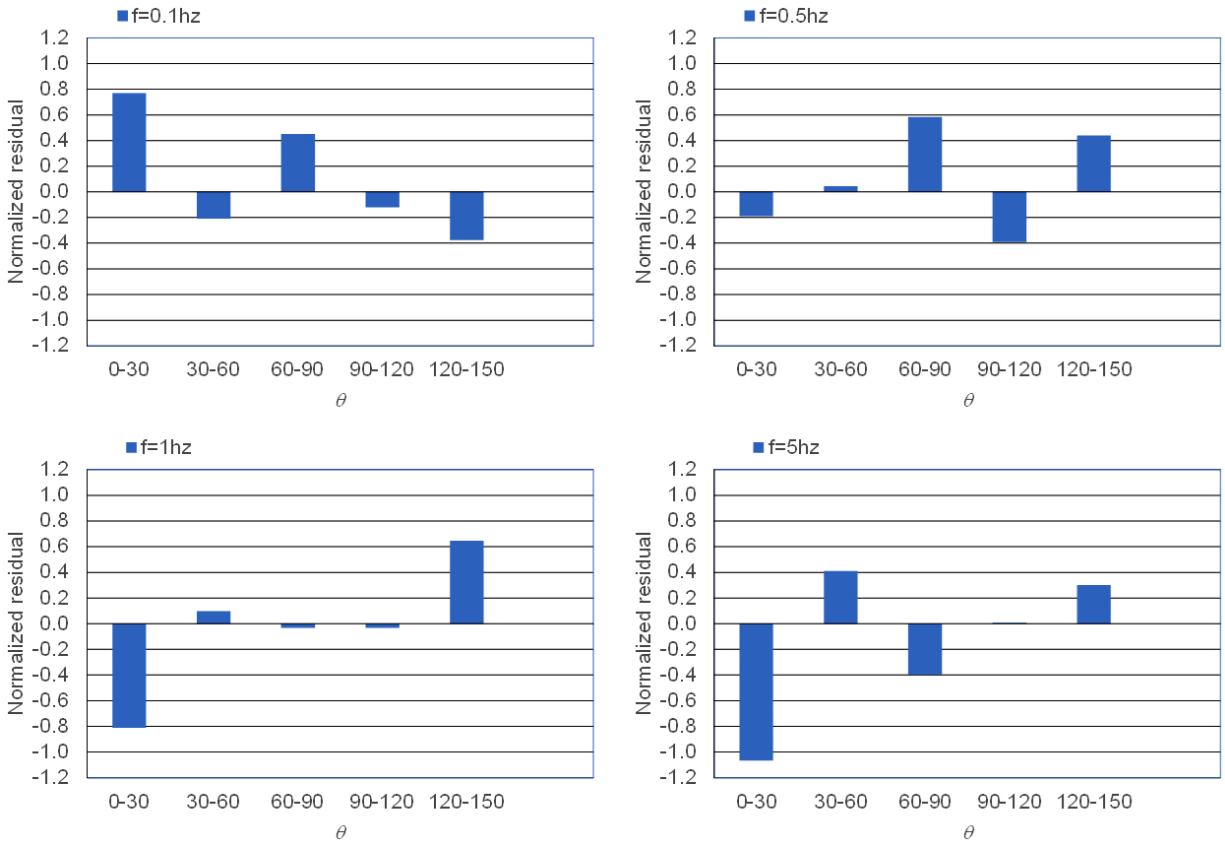

Figure 6. Variation of normalized residuals for the initial model defined in equation 2 with θ at selected frequencies.

Table 2. Coefficients for the proposed model in equation 4.

f, Hz	a_1	a_2	c_1	c_2	c_3	c_4	c_5	σ
0.1	-7.4403	1.8508	-9.844E-04	-2.319E-03	-1.256E-03	-2.006E-03	-2.016E-03	0.717
0.11	-6.6177	1.7604	-8.730E-04	-2.394E-03	-1.357E-03	-2.066E-03	-2.256E-03	0.810
0.12	-6.7245	1.7985	-1.250E-03	-2.447E-03	-1.400E-03	-1.950E-03	-1.689E-03	0.762
0.13	-6.5159	1.7784	-1.525E-03	-2.497E-03	-1.403E-03	-1.533E-03	-1.790E-03	0.780
0.14	-6.3751	1.7715	-1.576E-03	-2.377E-03	-1.478E-03	-1.842E-03	-1.854E-03	0.755
0.15	-6.2226	1.7695	-1.261E-03	-2.518E-03	-1.742E-03	-1.685E-03	-1.650E-03	0.763
0.16	-6.2697	1.7921	-8.633E-04	-2.371E-03	-1.936E-03	-1.873E-03	-1.720E-03	0.797
0.17	-5.6027	1.7178	-7.225E-04	-2.968E-03	-2.158E-03	-1.430E-03	-9.503E-04	0.726
0.18	-5.2066	1.6711	-6.889E-04	-2.830E-03	-2.241E-03	-1.576E-03	-8.807E-04	0.797
0.19	-5.3646	1.7045	-9.875E-04	-2.771E-03	-2.223E-03	-1.579E-03	-1.098E-03	0.732
0.2	-4.7847	1.6192	-1.251E-03	-2.701E-03	-2.273E-03	-1.380E-03	-1.124E-03	0.744
0.21	-5.1450	1.6794	-1.501E-03	-2.144E-03	-2.239E-03	-1.326E-03	-1.537E-03	0.821
0.22	-5.5076	1.7561	-1.512E-03	-2.240E-03	-2.305E-03	-1.552E-03	-1.610E-03	0.702
0.24	-5.8537	1.8409	-1.586E-03	-2.336E-03	-2.246E-03	-2.219E-03	-1.530E-03	0.756
0.25	-6.0724	1.8843	-1.868E-03	-1.982E-03	-2.199E-03	-2.225E-03	-1.724E-03	0.753
0.26	-5.9307	1.8729	-2.346E-03	-1.751E-03	-2.208E-03	-2.191E-03	-1.245E-03	0.741
0.28	-5.2897	1.8310	-2.367E-03	-2.718E-03	-1.848E-03	-2.569E-03	-1.713E-03	0.643
0.29	-4.8379	1.7914	-2.285E-03	-2.878E-03	-1.899E-03	-2.647E-03	-2.110E-03	0.643
0.31	-5.0406	1.8565	-2.541E-03	-3.260E-03	-1.607E-03	-2.704E-03	-2.521E-03	0.600
0.33	-4.7300	1.8132	-2.796E-03	-3.411E-03	-1.704E-03	-2.185E-03	-2.809E-03	0.605
0.34	-4.5670	1.7881	-2.993E-03	-3.039E-03	-1.734E-03	-2.441E-03	-2.713E-03	0.662
0.36	-3.4665	1.6521	-2.719E-03	-3.426E-03	-1.716E-03	-3.336E-03	-2.920E-03	0.663
0.38	-3.1641	1.6241	-2.427E-03	-2.794E-03	-1.859E-03	-4.184E-03	-3.207E-03	0.694
0.4	-2.5956	1.5449	-2.286E-03	-3.277E-03	-1.534E-03	-4.323E-03	-3.352E-03	0.588
0.43	-2.4008	1.5016	-2.221E-03	-3.095E-03	-1.929E-03	-3.694E-03	-3.131E-03	0.566
0.45	-2.7788	1.5527	-2.240E-03	-3.113E-03	-2.411E-03	-3.593E-03	-2.443E-03	0.600
0.47	-2.4767	1.5077	-2.368E-03	-3.117E-03	-2.458E-03	-3.747E-03	-2.375E-03	0.601
0.5	-2.9118	1.6002	-3.300E-03	-2.884E-03	-1.994E-03	-3.667E-03	-2.621E-03	0.569
0.53	-2.0368	1.4916	-3.371E-03	-2.909E-03	-2.186E-03	-2.952E-03	-2.912E-03	0.621
0.56	-1.8736	1.4671	-3.029E-03	-3.383E-03	-2.377E-03	-2.368E-03	-3.194E-03	0.585
0.59	-1.5293	1.4160	-3.062E-03	-2.975E-03	-2.567E-03	-2.495E-03	-3.259E-03	0.527
0.62	-1.3190	1.3743	-3.369E-03	-2.870E-03	-2.337E-03	-2.588E-03	-3.378E-03	0.512
0.65	-1.2948	1.3627	-3.391E-03	-3.182E-03	-2.246E-03	-3.272E-03	-2.798E-03	0.556
0.69	-1.6501	1.3735	-3.787E-03	-2.866E-03	-2.243E-03	-2.972E-03	-2.688E-03	0.535
0.73	-1.0105	1.2993	-3.449E-03	-3.486E-03	-2.314E-03	-3.504E-03	-2.759E-03	0.438
0.77	-0.7145	1.2444	-3.961E-03	-3.163E-03	-2.615E-03	-3.573E-03	-3.169E-03	0.471
0.81	-0.6925	1.2456	-3.602E-03	-3.376E-03	-2.551E-03	-3.708E-03	-3.175E-03	0.483
0.85	-0.8940	1.2795	-3.288E-03	-3.776E-03	-2.800E-03	-3.513E-03	-3.437E-03	0.474
0.9	-0.7983	1.2449	-3.979E-03	-3.725E-03	-2.767E-03	-3.259E-03	-3.044E-03	0.476
0.95	-0.4314	1.1998	-3.708E-03	-3.570E-03	-2.986E-03	-3.256E-03	-2.391E-03	0.361
1	-0.3724	1.1938	-3.955E-03	-3.099E-03	-3.238E-03	-3.252E-03	-2.731E-03	0.379

1.06	-0.1406	1.1717	-3.648E-03	-3.673E-03	-3.548E-03	-3.222E-03	-2.896E-03	0.398
1.11	-0.5983	1.2292	-3.565E-03	-3.349E-03	-3.539E-03	-3.404E-03	-3.413E-03	0.396
1.18	-0.2920	1.1622	-3.999E-03	-3.526E-03	-3.595E-03	-3.271E-03	-3.673E-03	0.451
1.24	-0.3533	1.1848	-3.977E-03	-3.493E-03	-3.431E-03	-3.560E-03	-3.718E-03	0.393
1.31	-0.5841	1.1985	-4.070E-03	-3.581E-03	-3.533E-03	-3.783E-03	-3.818E-03	0.456
1.38	-0.6549	1.1979	-3.858E-03	-3.728E-03	-3.666E-03	-3.897E-03	-3.705E-03	0.434
1.46	-0.8558	1.2217	-4.194E-03	-3.718E-03	-3.529E-03	-3.915E-03	-4.109E-03	0.414
1.54	-0.6812	1.1945	-3.884E-03	-3.470E-03	-3.673E-03	-4.726E-03	-4.420E-03	0.456
1.62	0.4512	1.0231	-4.288E-03	-3.613E-03	-4.056E-03	-4.718E-03	-4.090E-03	0.495
1.71	-0.2807	1.1240	-4.115E-03	-3.489E-03	-4.163E-03	-4.821E-03	-4.049E-03	0.373
1.8	-0.4060	1.1424	-4.485E-03	-3.690E-03	-4.100E-03	-4.655E-03	-4.898E-03	0.439
1.9	-0.7700	1.1910	-4.929E-03	-3.749E-03	-4.168E-03	-4.314E-03	-4.778E-03	0.380
2.01	-0.2678	1.1171	-5.186E-03	-3.610E-03	-3.986E-03	-4.504E-03	-4.276E-03	0.438
2.12	-0.2912	1.0843	-5.061E-03	-3.231E-03	-4.426E-03	-4.227E-03	-4.528E-03	0.431
2.23	-0.6453	1.1221	-5.192E-03	-3.410E-03	-4.386E-03	-4.028E-03	-4.426E-03	0.371
2.36	-0.3661	1.0843	-5.480E-03	-4.149E-03	-4.235E-03	-4.962E-03	-4.993E-03	0.381
2.49	-0.6866	1.1225	-5.665E-03	-4.018E-03	-4.536E-03	-4.951E-03	-4.831E-03	0.421
2.62	-0.9134	1.1475	-5.405E-03	-3.765E-03	-4.652E-03	-5.326E-03	-4.713E-03	0.417
2.77	-0.6502	1.1277	-5.887E-03	-4.296E-03	-4.704E-03	-5.005E-03	-5.433E-03	0.392
2.92	-0.4173	1.0842	-5.601E-03	-4.124E-03	-5.225E-03	-4.838E-03	-5.671E-03	0.401
3.08	-0.3605	1.0667	-5.800E-03	-4.240E-03	-4.829E-03	-5.237E-03	-5.258E-03	0.358
3.25	0.1369	0.9903	-6.171E-03	-4.410E-03	-5.109E-03	-4.768E-03	-5.365E-03	0.405
3.43	-0.1349	1.0454	-6.304E-03	-4.588E-03	-5.269E-03	-5.265E-03	-6.139E-03	0.382
3.62	-0.2889	1.0658	-6.490E-03	-4.720E-03	-5.257E-03	-5.746E-03	-5.929E-03	0.388
3.82	-0.3401	1.0517	-6.582E-03	-4.094E-03	-5.673E-03	-5.468E-03	-5.547E-03	0.398
4.03	0.0017	1.0012	-6.596E-03	-4.563E-03	-5.656E-03	-5.255E-03	-5.680E-03	0.415
4.25	-0.3213	1.0429	-6.893E-03	-4.280E-03	-5.660E-03	-5.675E-03	-6.245E-03	0.367
4.48	-0.2932	1.0474	-7.330E-03	-4.691E-03	-5.839E-03	-5.906E-03	-6.115E-03	0.411
4.73	-0.3853	1.0211	-7.217E-03	-4.323E-03	-5.916E-03	-5.589E-03	-5.765E-03	0.421
4.99	-0.5101	1.0355	-7.464E-03	-4.736E-03	-5.567E-03	-5.778E-03	-6.352E-03	0.406
5.26	-0.1366	0.9754	-7.762E-03	-5.065E-03	-6.244E-03	-5.803E-03	-6.244E-03	0.439
5.55	-0.2660	0.9927	-7.611E-03	-5.219E-03	-6.527E-03	-6.515E-03	-6.453E-03	0.482
5.86	-0.5841	1.0228	-8.059E-03	-5.499E-03	-6.308E-03	-6.966E-03	-6.549E-03	0.434
6.18	-0.5244	1.0129	-8.025E-03	-5.508E-03	-6.664E-03	-7.343E-03	-6.865E-03	0.450
6.52	-0.3751	0.9996	-8.122E-03	-5.897E-03	-7.004E-03	-7.470E-03	-7.275E-03	0.466
6.88	-0.5177	0.9992	-8.224E-03	-5.907E-03	-6.991E-03	-7.160E-03	-6.878E-03	0.485
7.25	-0.5989	1.0180	-8.417E-03	-6.332E-03	-7.224E-03	-7.461E-03	-7.169E-03	0.495
7.65	-0.6367	1.0047	-8.463E-03	-6.498E-03	-7.386E-03	-7.704E-03	-7.225E-03	0.504
8.07	-0.9273	1.0164	-8.332E-03	-6.726E-03	-7.417E-03	-7.686E-03	-7.268E-03	0.513
8.52	-1.4988	1.0681	-8.046E-03	-6.836E-03	-7.468E-03	-7.487E-03	-7.398E-03	0.533
8.98	-1.2225	1.0085	-7.988E-03	-7.000E-03	-7.878E-03	-8.107E-03	-7.757E-03	0.560
9.48	-1.3279	1.0133	-8.033E-03	-7.878E-03	-8.087E-03	-8.469E-03	-7.988E-03	0.609
10	-1.3478	0.9877	-7.601E-03	-8.019E-03	-8.359E-03	-8.733E-03	-8.032E-03	0.667

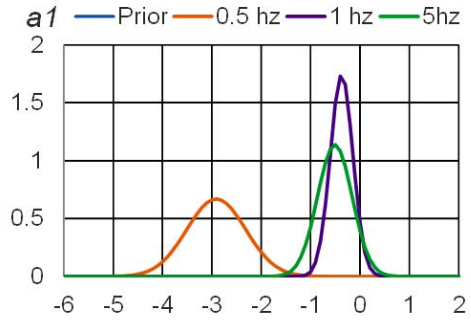

Figure 7. Comparison of posterior probability density functions for parameter a_1 for f=0.5, 1 and 5 Hz. The prior probability density function was a normal density with a very large variance for all frequencies, therefore it is not visible in the figure because of the scale.

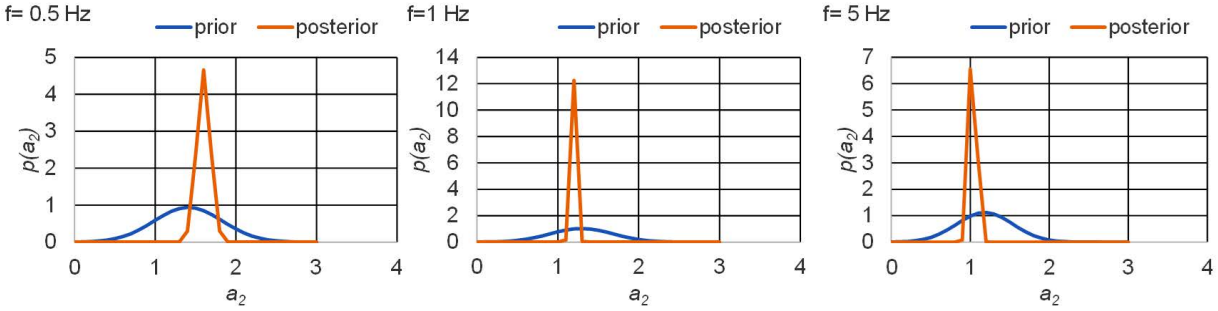

Figure 8. Prior and posterior probability density functions for a_2 parameter for f=0.5, 1 and 5 Hz.

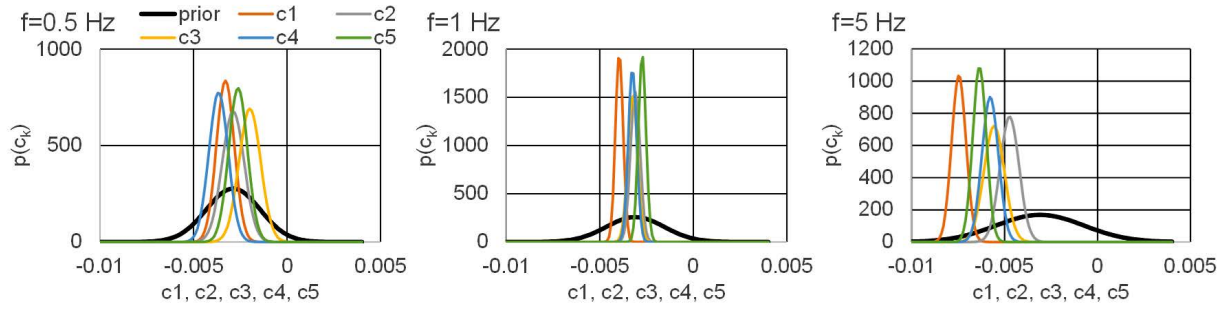

Figure 9. Prior and posterior probability density functions for c_1, c_2, c_3, c_4 and c_5 parameters for f=0.5, 1 and 5 Hz.

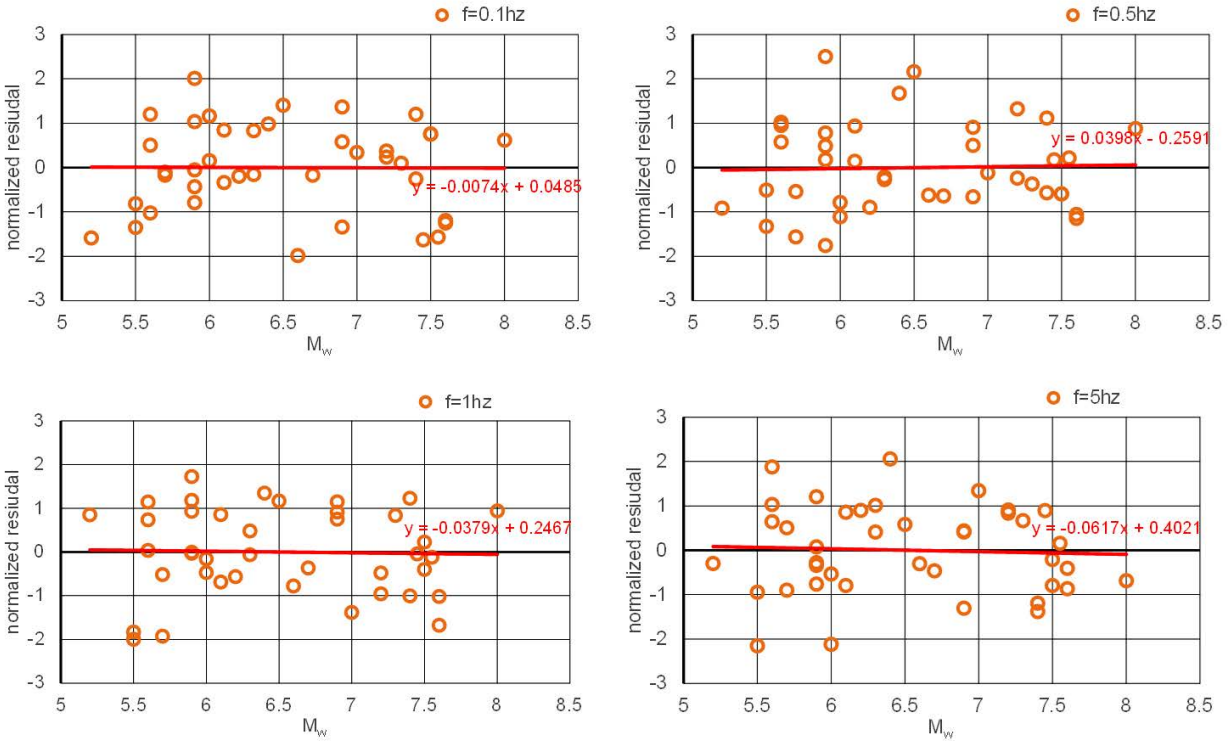

Figure 10. Normalized residuals as a function of M_w for the proposed model (equation 4).

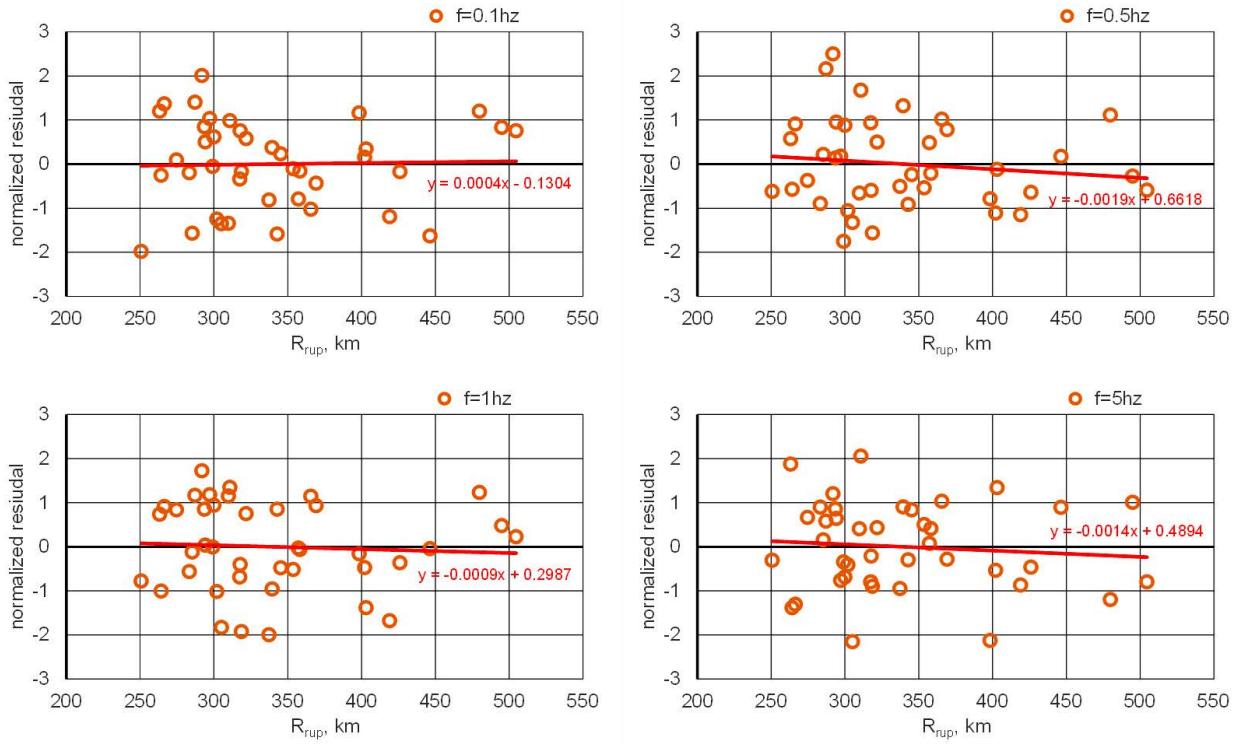

Figure 11. Normalized residuals as a function of R_{rup} for the proposed model (equation 4).

a) f= 0.5 Hz

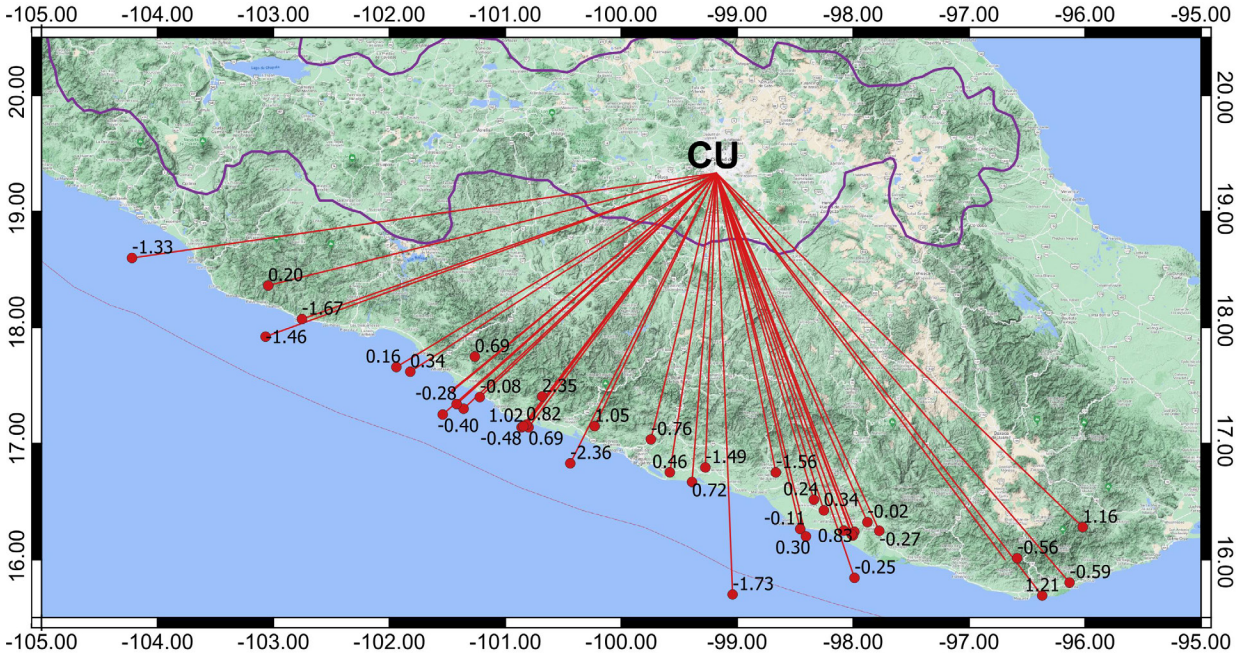

b) f= 5 Hz

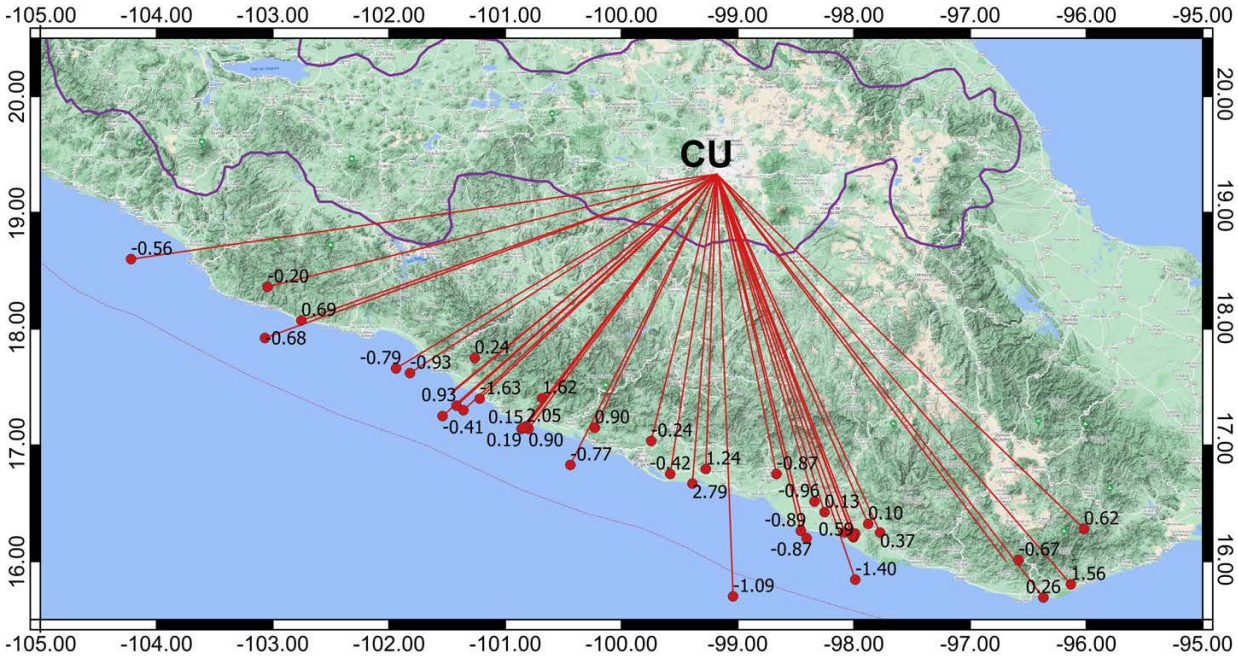

Figure 12. Map showing normalized residuals for the proposed model (equation 4) at $f = 0.5$ Hz and $f = 5$ Hz.

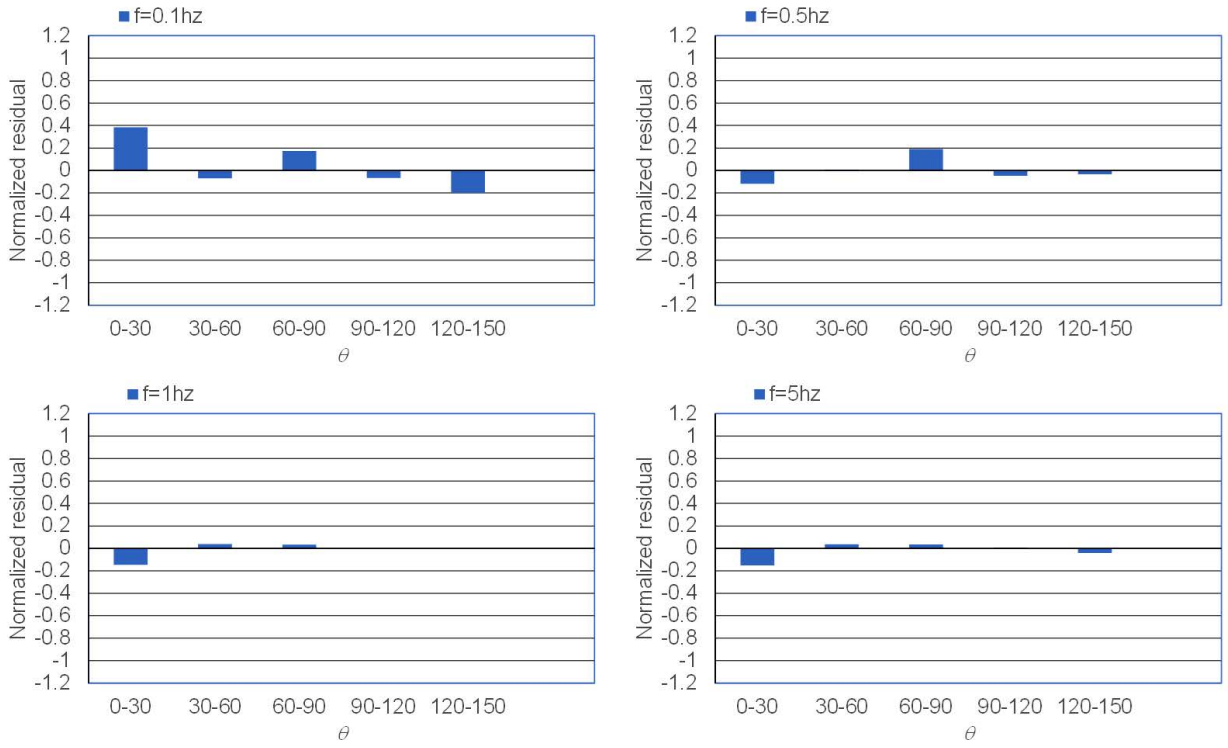

Figure 13. Variation of normalized residuals for the proposed model (equation 4) with θ at selected frequencies.

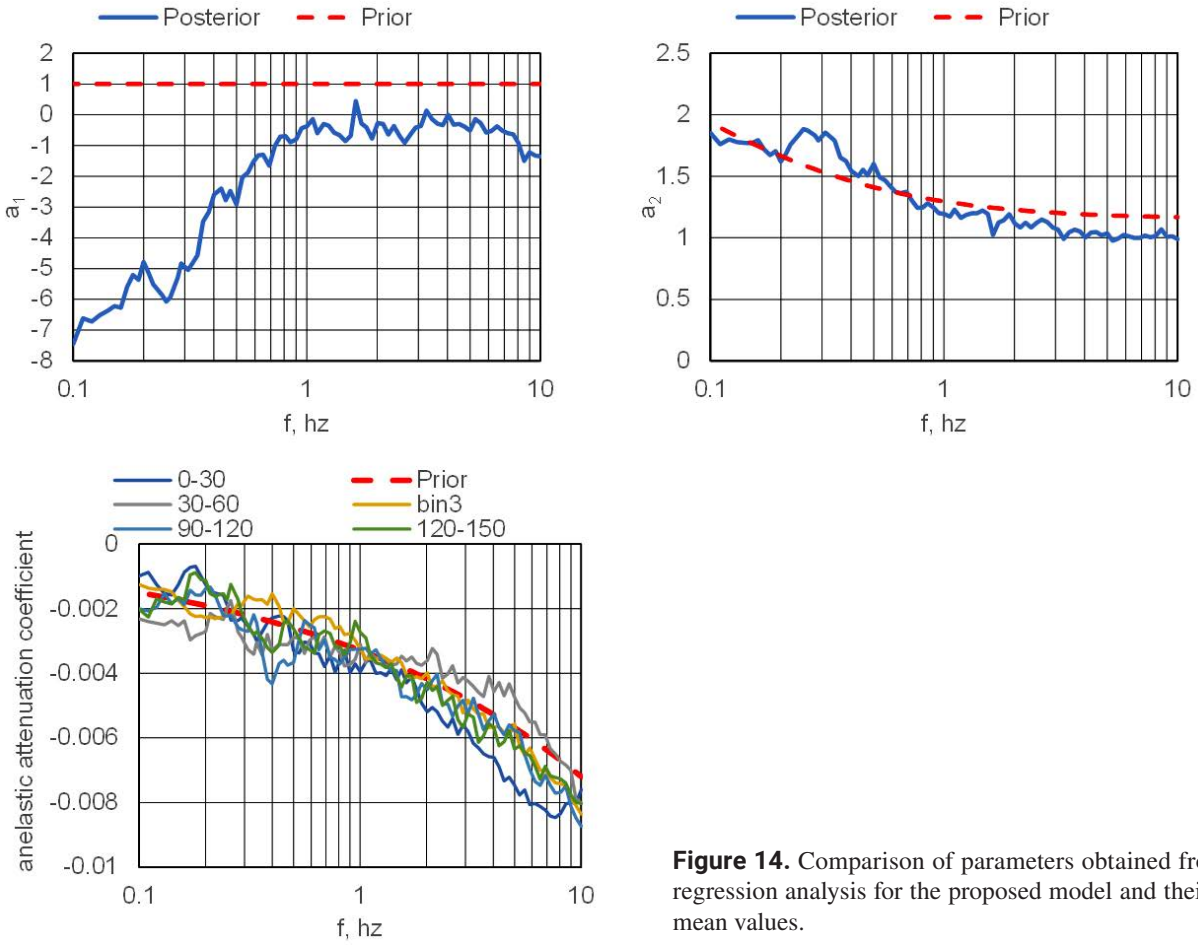

Figure 14. Comparison of parameters obtained from the regression analysis for the proposed model and their prior mean values.

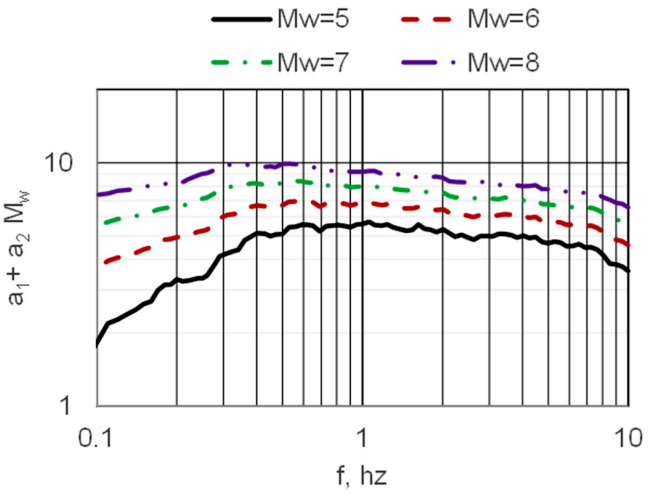

Figure 15. Source scaling term ($a_1 + a_2 M_w$) as function of frequency and M_w for the proposed model (equation 4). Note that the scaling term is roughly proportional to M_w for $f > 0.5$ Hz (i.e., above the corner frequency of most events in the dataset) as expected from the ω^2-source model.

expected from the seismological theory. In Figure 16 we show the magnitude scaling of *FAS* predictions for a distance of 300 km, note that magnitude scaling is the same for all distances according to the proposed model. However, in view that earthquakes being analyzed herein always happen at distances larger than 200 km the magnitude scaling in Figure 16 seems reasonable.

In Figure 17 we compare σ values reported by Ordaz *et al.* (1994) (based on the model given in equation 2), and those obtained in this study (based on the proposed model given in equation 4). Clearly a significant reduction in σ values is obtained with the proposed model. This is a valuable characteristic of the proposed model because it leads to a better estimation of seismic hazard. The reduction in σ values partly comes from the increase in the quality and quantity of records and partly from the functional form that we used to model different anelastic attenuation along different ray paths.

Figure 17 also shows σ values for the model in equation 2 but including the new data. The significant reduction in σ for the model in equation 2 with respect to the model of Ordaz *et al.* (1994) is produced due to the increase in the quality and quantity of the dataset, while the reduction in σ for the proposed model with respect to the model in equation 2 is the result of the modeling of different attenuation along different ray paths. Note that the reduction in σ for the proposed model with respect to the model in equation 2 is present for all frequencies but is slightly more pronounced at higher frequencies. Finally, we note that a simple modification to the functional form leads to a reduction in the aleatory variability of the GMPE. As discussed before on important application of the model is to estimate the value of seismic intensities during future earthquakes (i.e. PGA, PGV and SA). Therefore, we performed several test and we identified that for the ground motions in Mexico City the range of frequencies considered in the model is sufficient to estimate the seismic intensities in the framework of random vibration theory.

4. Comparison of Observations and Predictions from the Proposed GMPE

In Figure 18 we show a comparison of the observed and predicted *FAS* for some of the earthquakes in the dataset. In general, the GMPE curves fit the observed *FAS* well. Two of the exceptions are the observed *FAS* for the Guerrero earthquakes of 08/05/2014 (M_w 6.5) and10/05/2014 (M_w 6.1) which are greater than the predicted *FAS*. This agrees with the strong directivity towards Mexico City during these two earthquakes documented by Singh *et al.* (2019). Figure 18 also includes the Acapulco earthquake of 08/09/2021 (M_w 7.0), and Michoacán - Colima earthquakes of 19/09/2022 (M_w 7.6) and 22/09/2022 (M_w 6.7) which were not included in the regression analysis. The model fits well the 19/09/2022 (M_w 7.6) earthquake but underestimates the earthquakes of 08/09/2021 (M_w 7.0) and 22/09/2022 (M_w 6.7) both of which are known to have ruptured towards Mexico City (Iglesias *et al.* 2022; Singh *et al.*, 2023).

Figure 19 shows a comparison of *FAS* at CU for a postulated M_w 8.0 earthquake at R_{rup}=300 km located in different θ bins.

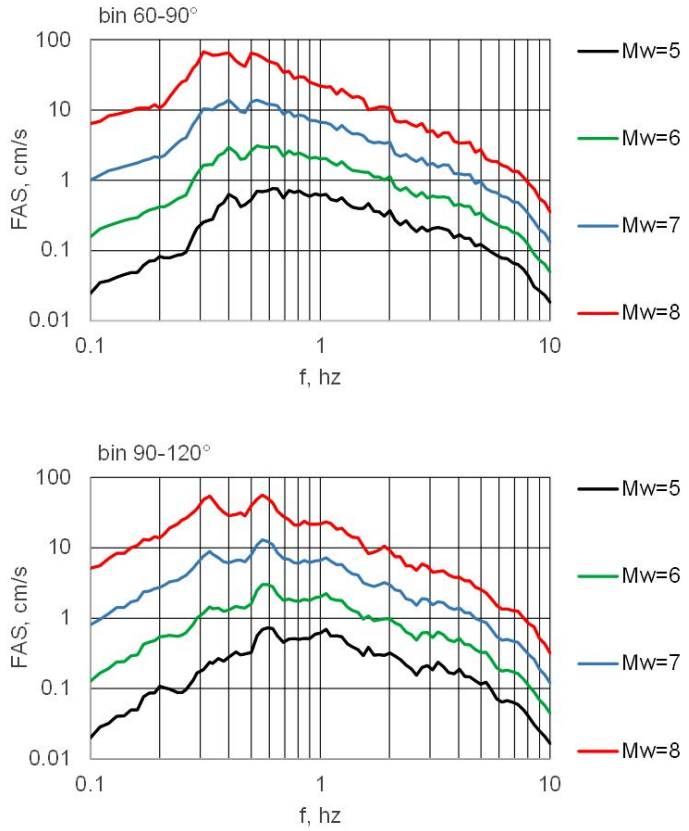

Figure 16. Scaling for *FAS* predictions with M_w for a distance of 300 km.

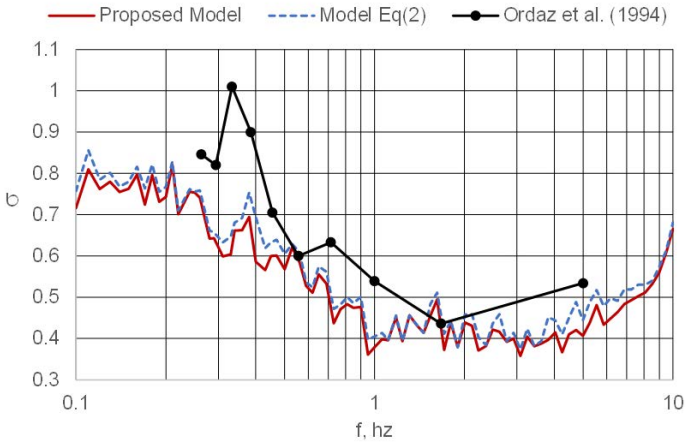

Figure 17. Comparison of σ for different models. σ for the proposed model (equation 4) is less than for the initial model (equation 2) which, in turn, is smaller than for the model of Ordaz *et al.* (1994).

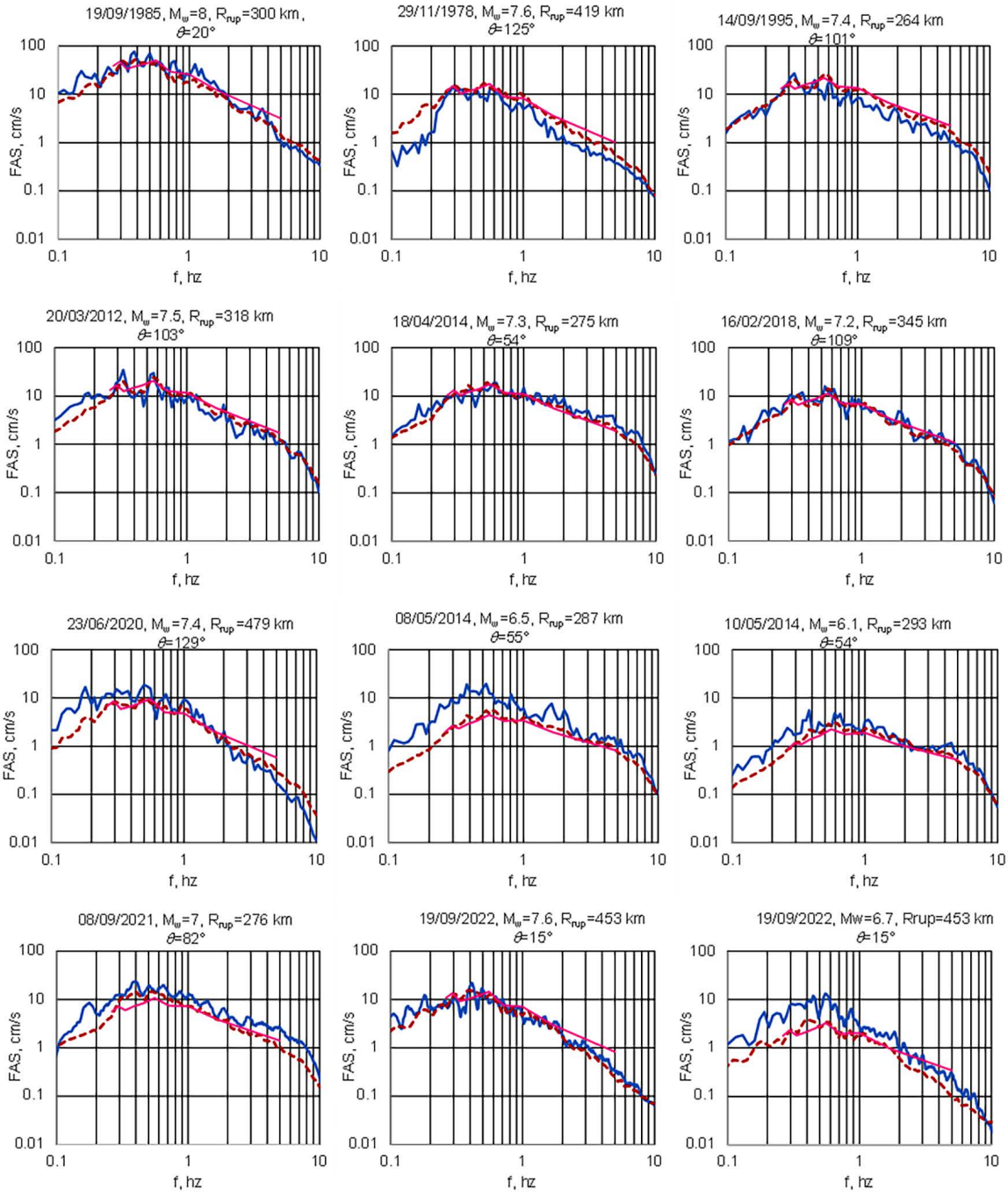

Figure 18. Comparison of observed (continuous curves), predicted (dashed red curves) *FAS* from the proposed model and predicted (pink continuous line) *FAS* from the Ordaz *et al.* (1994) GMPE for some of the earthquakes in the dataset. Predicted *FAS* are from the new model (equation 4). Note that the recent Acapulco earthquake of 08/09/2021 (M_w 7.0) and Michoacán - Colima earthquakes of 19/09/2022 (M_w 7.6) and 22/09/2022 (M_w 6.7) were not used in the regression analysis for the proposed model. While only the recordings during the 19/09/1985 (Mw8) and the 29/11/1978 (M_w 7.6) earthquakes were used in the regression analysis for the Ordaz *et al.* (1994) model.

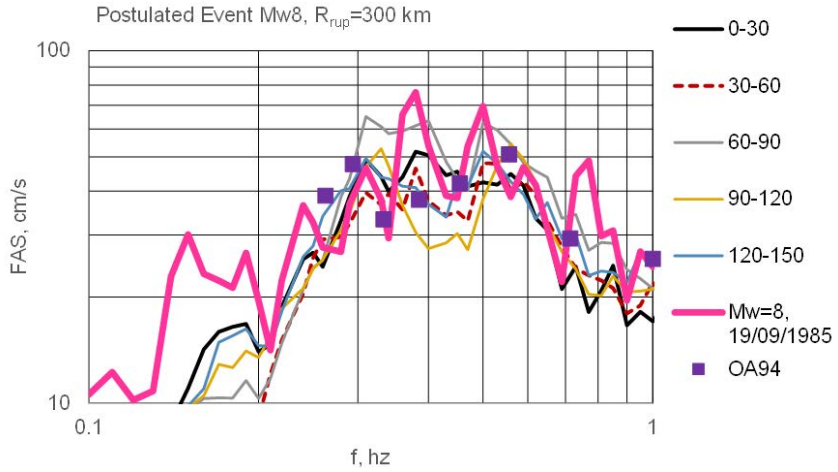

Figure 19. Predicted *FAS* at CU from an M_w 8.0 earthquake at R_{rup} = 300 km located in different θ bins. For comparison, the observed *FAS* of the 1985 Michoacán earthquake, M_w 8.0, R_{rup} = 300 km (θ =20°) is shown. The purple squares are predictions from the Ordaz *et al.* (1994) GMPE.

The model predicts larger intensities from earthquakes from the 60°-90° bin, a region that includes San Marcos and Papanoa seismic sources, and from the 0°-30° bin, a region that includes Michoacán seismic source. Unfortunately, our study suggest that such regions have the potential to produce SM at Mexico City comparable to ground motions observed during the deadly 1985 M_w 8.0 Michoacán earthquake.

5. Conclusions

The estimation of strong ground motion at CU from future earthquakes is crucial for seismic hazard assessment of Mexico City. In this study, we have taken advantage of the recent increase in the number of earthquakes that have produced recordings at CU to derive a site-specific GMPE for *FAS* from subduction thrust faulting interface earthquakes. The dataset is composed of 40 earthquakes ($5 \leq M_w \leq 8$) at distances between 250 and 500 km. We used a functional form based on a point-source model but included a modification to model different attenuation along different ray paths. We show that this simple modification leads to a significant reduction in the aleatory variability of the GMPE particularly at frequencies greater than 1 Hz. The model is applicable to *FAS* in CU station in Mexico City during thrust faulting interface earthquakes with M_w between 5 and 8 and distances in the range between 250 and 500 km. The proposed model has been incorporated in a fully Fourier-based PSHA for Mexico City leading to earthquake design spectra in the 2023 version of the Mexico City Building Code.

6. Acknowledgments

A functional form similar to equation 4 was proposed many years ago by Eduardo Pérez-Rocha and others. This study was supported by Instituto para la Seguridad de las Construcciones de la CDMX and by DGAPA, UNAM project IN109423 (S.K.S.). Authors thank also the two reviewers who provided constructive criticism for the initial version of this manuscript that allowed its improvement.

7. References

Anderson, J. G., P. Bodin, J. Brune, J. Prince, S. K. Singh, R. Quass, and M. Oñate. (1986). Strong ground motion from the Michoacan, Mexico earthquake, Science 233, 1043-1049. doi: **https://doi.org/10.1126/science.233.4768.1043**

Arroyo, D., García, D., Ordaz, M., Mora, M. A., & Singh, S. K. (2010). Strong ground-motion relations for Mexican interplate earthquakes. Journal of Seismology, 14, 769-785. Doi: **https://doi.org/10.1007/s10950-010-9200-0**

Boore, D.M. (2003). Simulation of ground motion using the stochastic method, *Pageoph* 160, 635-676. doi: **https://doi.org/10.1007/PL00012553**

Broemling, L.D., (1985). *Bayesian Analysis of Linear Models*, Marcel Dekker, Inc., New York. doi: **https://doi.org/10.1201/9781315138145**

Brune, J.N (1970). Tectonic stress and the spectra of seismic shear waves from earthquakes, *J. Geophys. Res*. 75, 4997-5009. doi: **https://doi.org/10.1029/jb075i026p04997**

Castro, R., S. K. Singh, and E. Mena (1988). An empirical model to

predict Fourier amplitude spectra of horizontal ground motion, *Earthquake Spectra 4*, 675-686. doi: **https://doi.org/10.1193/1.1585497**

Celebi, M., J. Prince, C. Dietel, M. Oñate, and G. Chavez (1987). The culprit in Mexico City-amplification of motions, *Earthquake Spectra 3*, 315-328. doi: **https://doi.org/10.1193/1.1585431**

Cruz-Atienza, V. M. *et al.* (2016). Long duration of ground motion in the paradigmatic Valley of Mexico, *Sci. Rep. 6*, 38807. doi: **https://doi.org/10.1038/srep38807**

García, D., Singh, S. K., Herráiz, M., Ordaz, M., & Pacheco, J. F. (2005). Inslab earthquakes of central Mexico: peak ground-motion parameters and response spectra. Bulletin of the Seismological Society of America, 95(6), 2272-2282. doi: **https://doi.org/10.1785/0120050072**

Iglesias, A., S.K. Singh, J.F. Pacheco, L. Alcántara, M. Ortiz, and M. Ordaz (2003), Near-trench Mexican earthquakes have anomalously low peak accelerations, *Bull. Seism.Soc. Am.*, 93, 953-959. doi: **https://doi.org/10.1785/0120020168**

Joyner, W. J. and D. M. Boore (1986). On simulation of large earthquakes by Green´s functions addition of small earthquakes. In Das S, Boatwright J, Scholtz C H (ed) Earthquake Source Mechanics, (Maurice Ewing Series 6). *American Geophysical Union Monograph 37*, Washington, D.C., 269-274. doi: **https://doi.org/10.1029/GM037p0269**

Kanamori H, P. C. Jennings, S. K. Singh, and L. Astiz (1993). Estimation of strong ground motions in Mexico City expected for large earthquakes in the Guerrero seismic gap. *Bull Seism Soc. Am.* 93, 811-829. doi: **https://doi.org/10.1785/BSSA0830030811**

Ordaz, M. and Singh, S.K., (1992). Source spectra and spectral attenuation of seismic waves from Mexican earthquakes, and evidence of amplification in the hill zone of Mexico City, *Bull Seism Soc. Am.* 82, 24-43. doi: **https://doi.org/10.1785/BSSA0820010024**

Ordaz, M., S. K. Singh, and A. Arciniega (1994). Bayesian attenuation regressions: an application to Mexico City, *Geophys. J. Int.*, 177, 335- 344. doi: **https://doi.org/10.1111/j.1365-246X.1994.tb03936.x**

Ordaz, M., J. Arboleda, and S. K. Singh (1995). A scheme of random summation of an empirical Green's function to estimate ground motions from future large earthquakes. *Bull Seism Soc. Am.* 85, 1635-1647. doi: **https://doi.org/10.1785/BSSA0850061635**

Ordaz, M., E. Reinoso, M. A. Jaimes, L. Alcántara, and C. Pérez (2017). High-resolution early earthquake damage assessment system for Mexico City based on a single-station, *Geofísica Internacional*. 56, 117-135. doi: **https://doi.org/10.22201/igeof.00167169p.2017.56.1.1751**

Rosenblueth, E. (1953). *Teoria del diseño sismico sobre mantos blandos*, Ediciones ICA, Serie B, No. 14, 3-12.

Shapiro, N.M., S.K. Singh, and J.F. Pacheco (1998). A fast and simple diagnostic method for identifying tsunamigenic earthquakes, *Geophys. Res. Lett.* 25, 3911-3914. doi: **https://doi.org/10.1029/1998GL900015**

Singh, S. K., J. Lermo, T. Domínguez, M. Ordaz, J. M. Espinosa, E. Mena, and R. Quaas (1988a). A study of relative amplification of seismic waves in the Valley of Mexico with respect to a hill zone site (CU), *Earthquake Spectra 4*, 653-674. doi: **https://doi.org/10.1193/1.1585496**

Singh, S. K., E. Mena, and R. Castro (1988b). Some aspects of source characteristics of 19 September 1985 Michoacan earthquake and ground motion amplification in and near Mexico City from the strong motion data, *Bull. Seism. Soc. Am.* 78, 451-477. doi: **https://doi.org/10.1785/BSSA0780020451**

Singh, S.K., Arroyo, D., Pérez-Campos, X., Rodríguez, Q, and Iglesias, A. (2016). Fast identification of near-trench earthquakes along the Mexican subduction zone based on characteristics of ground motion in Mexico City, *Bull. Seism. Soc. Am.* 106, 2071-2080, doi: **https://doi.org/10.1785/0120160003**

Singh, S.K., E. Reinoso, D. Arroyo, M. Ordaz, V. Cruz-Atienza, X. Pérez-Campos, A. Iglesias, and V. Hjörleifsdóttir (2018). Deadly intraslab Mexico earthquake of 19 September 2017 (Mw7.1): Ground motion and damage pattern in Mexico City, *Seism. Res. Lett.* 89, 2193-2203, doi: **https://doi.org/10.1785/0220180159**

Singh, S.K., Plata-Martínez, R., Pérez-Campos, X., Espíndola, V., Arroyo, D. and Iglesias, A. (2019). Evidence of directivity during the earthquakes of 8 and 10 May 2014 (Mw 6.5, 6.1) in the Guerrero, Mexico seismic gap and some implications, *J. Seism.* 23, 683-697.

Singh, S. K., Iglesias Mendoza, A., Arroyo, D., Pérez-Campos, X., Ordaz, M., Mendoza, C., Corona-Fernández, R. D., Espíndola, V. H., González-Ávila, D., Martínez-López, R., Castro-Artola, O., Santoyo, M. A., & Franco, S. I. (2023). A Seismological study of the Michoacán-Colima, Mexico, Earthquake of 19 September 2022 (Mw7.6). *Geofísica Internacional*, 62(2), 445-465. doi: **https://doi.org/10.22201/igeof.2954436xe.2023.62.2.1453**

Geofísica Internacional (2024) **63-2**: 803 - 815

Site effect evaluation for Culiacan, Sinaloa, Mexico

Domínguez Reyes Tonatiuh[*1] and Rodríguez Lozoya Héctor[2]

Abstract

Using the spectral ratio technique (HVSR), we performed an analysis of 120 seismic noise records obtained at different points distributed throughout the city of Culiacán, Sinaloa, México. The results show a clear relationship of dominant periods between 0.2 to 0.7 for the alluvium zone in the central and western area of the city and minor periods for points near outcrops of igneous rocks south and southeast of the city. The higher relative amplitudes were found along the riverbed, in the transition zone of conglomerate deposits to alluvium. We performed a multichannel analysis (station arrays) at some points in which we also measured H/V. Afterward, we produced velocity profiles were obtained and transfer functions were calculated. Five of these values were compared with the HVSR technique. Three of them could be compared with the surficial startigraphy obtained in soil mechanics studies to which access was granted.

Key words: site effect, ambient noise, dominant period, surface waves, transfer functions.

Resumen

Usando la técnica de relación espectral (HVSR), realizamos un análisis de 120 registros de ruido sísmico obtenidos en diferentes puntos distribuidos a lo largo de la ciudad de Culiacán, Sinaloa, México. Los resultados muestran una clara relación de períodos dominantes entre 0,2 y 0,7 para la zona de aluvión en la zona central y occidental de la ciudad y períodos menores para puntos cercanos a afloramientos de rocas ígneas al sur y sureste de la ciudad. Las mayores amplitudes relativas se encontraron a lo largo del lecho del río, en la zona de transición de los depósitos de conglomerado al aluvión. Realizamos un análisis multicanal (arreglos de estaciones) en algunos puntos donde se realizó la medición H/V. Se obtuvieron perfiles de velocidad y se calcularon las funciones de transferencia. Se corroboraron los valores de período dominante obtenidos con la técnica HVSR. Tres de ellos pudieron compararse con la estratigrafía superficial obtenida en estudios de mecánica de suelos a los que se tuvo acceso.

Palabras clave: efecto de sitio, ruido sísmico, periodos dominantes, ondas superficiales, funciones de transferencia.

Received: May 3, 2023 ; Accepted: February 1, 2024; Published on-line: April 1, 2024.

Editorial responsibility: Dr. Carlos Miguel Valdés-González

[*] Corresponding author: Domínguez Reyes, Tonatiuh.E-mail: tonatiuh@ucol.mx
[1] Centro Universitario de Estudios Vulcanológicos. Universidad de Colima. Av. Universidad 333 Colonia Las Víboras, Colima Col., 28040.
[2] Facultad de Ingeniería Civil. Universidad Autónoma de Sinaloa. Ciudad Universitaria, Culiacán Sinaloa México, 80000. rolohe@uas.edu.mx

https://doi.org/10.22201/igeof.2954436xe.2024.63.2.1631

1. Introduction

Among the most harmful natural phenomena for mankind are earthquakes. One way to mitigate those damages is through prevention. Building regulations have precisely that function. For the elaboration of a realistic regulation for a certain locality, the observations of local damages occurred during earthquakes must be taken into account or, in the other hand, measurements of the mechanical characteristics of the soil in different parts of the city. The distribution of damage during large earthquakes often depends on so-called site effects. Subsurface impedance contrasts can significantly amplify the ground motion, as well as increase ground motion duration. Mapping of places with site effect also called microzoning, has been carried out in large cities around the world (Pergalani et al, 2020, Keil *et al.* 2020, Zalbuin et al, 2021). A large number of these types of studies have relied on ambient vibration records given the ease and low cost with which the data can be obtained. Seismic noise is also used to measure the structural health of buildings in the face of possible loss of rigidity due to the occurrence of earthquakes by measuring changes in its natural frequency of vibration and amplitude (Godinez K., 2022, Vargas-Luque & Del Carpio, 2021). In early studies, site resonance frequency was deduced from spectral proportions of seismic noise records (Kagami *et al.*, 1986; Seo, 1992), or taken as the peak frequency of the horizontal component Fourier amplitude spectrum (Kobayashi *et al.*, 1986; Gutierrez and Singh, 1992). More recently, what has been used are the spectral ratios calculated between horizontal components relative to the simultaneously recorded vertical component (HVSR, Nakamura, 1989; Lermo and Chavez-Garcıa, 1994; Field and Jacob, 1995, among many others). It is now recognized that the HVSR technique generally provides a reliable estimate of the resonant frequency.

When we observe an amplification due to a large impedance contrast between a soft soil layer and the basement, the use of HVSR is clearly reliable (Chavez et al, 2007). A more complex

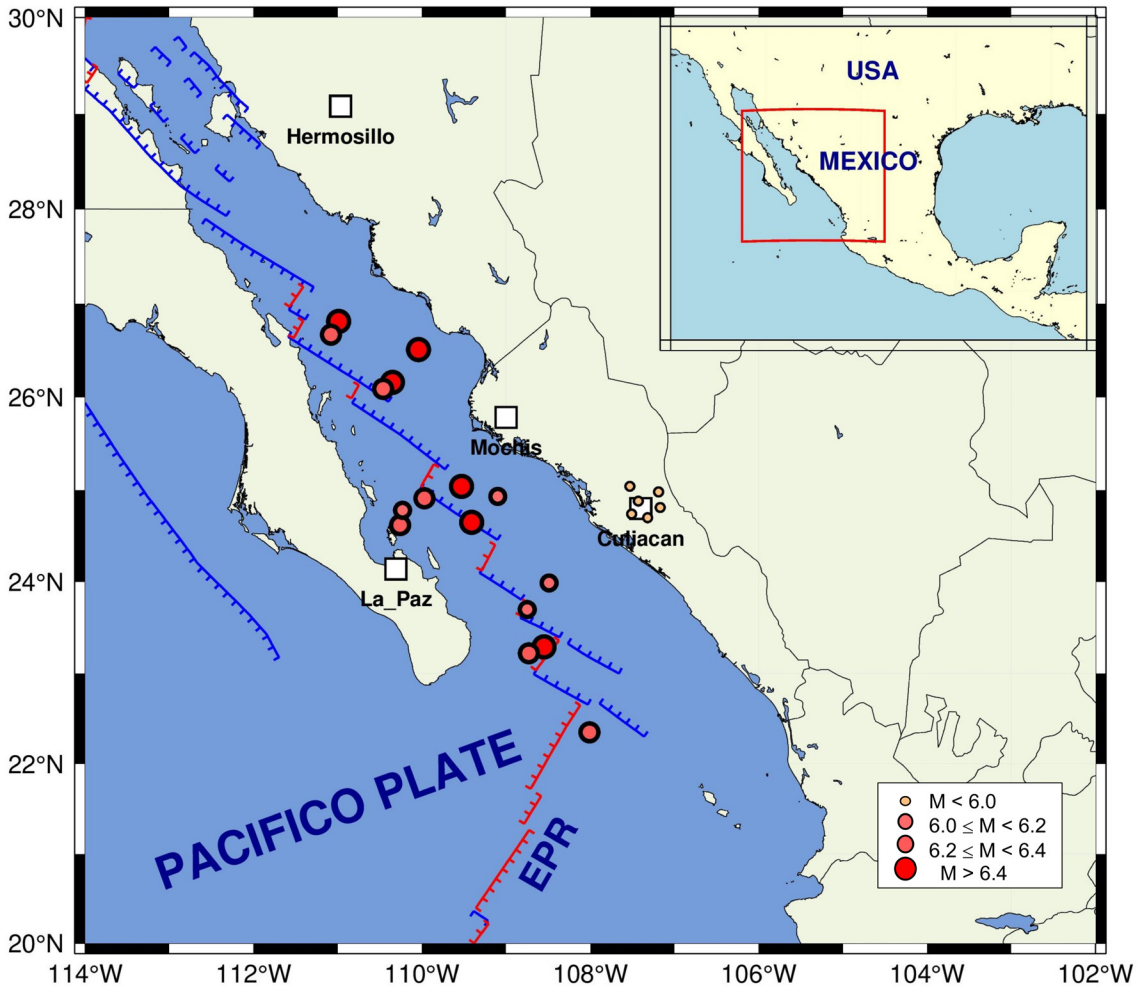

Figure 1. Regional tectonics of the area of study. Circles are epicenters. Main cities are represented by squares

local geology, however, raises the question of its reliability. It is important to understand the limitations of such a technique.

The goal of this work is to present a dynamic characterization of the city of Culiacán using the HVSR technique, reinforcing it with direct observations obtained from soil mechanics studies and multichannel analysis carried out in different points of the city.

It is important to recall the need of updating the local building regulation, attaching information related to the dynamic behavior of the soil along with stratigraphy when possible.

2. Background

2.1 Regional tectonics

Gulf of California, in front of which the state of Sinaloa is located, is a divergent boundary between the North American and Pacific plates. This boundary consists of a series of transform faults and small dispersion centers creating ridges and basins along the entire gulf and ending in the south, at the East Pacific Ridge (EPR) that marks the boundary of the Rivera plate (Fenby and Gastil, 1991; Nagy and Stock, 2000, Figure 1).

Displacement speed of one tectonic plate with respect to the other in this region is estimated to be between 41 and 54 millimeters per year (Plattner *et al.*, 2007). The southern region of the Gulf of California is an area of high seismicity. Most of the earthquakes that are generated there, are mainly related to the transform faults of right lateral behavior.

Culiacán region, has experienced the effects of earthquakes. Sixteen earthquakes with Mw≥ 6 have occurred in Gulf of California in front of Sinaloa State since 1980. The strongest, occurred on November 13, 2015 (Mw=6.6), and its epicenter was located 216 km northwest of Culiacán.

There are some active faults in the region of hills and foothills, parallel to the coastline that have caused low magnitude earthquakes (SSN, 2023; SGM, 1999). According to SSN catalog, at least six small events within a radius of 30 km from the city have occurred in the last 40 years. The most recently, on August 12, 2021 (Mw=3.8, Figure 1).

2.2 Geology

Mountain ranges at the east of the city consist of volcanic rocks, essentially of rhyolitic composition. Some settlements begin to occur on the slopes of these hills that rise at more than 300 m altitude. The Cerro El Tule, southeast of the city is formed from volcanic rocks of basaltic composition of Pleistocene age. It represents the last manifestation of volcanism in the region.

Most of the urban area of the city of Culiacán is settled on fluvioaluvial and lacustrine materials of very recent ages. They are composed of clastic elements of various sizes, well rounded, of diverse composition, packed in an incipiently cemented sandy matrix where small and thin levels of medium-grained sands are occasionally interspersed. They are massive sediments, with no visible stratification nor faulting, at least apparently.

Southern and NE areas of the city are settled on a sequence of conglomerates and sandstones, compact well consolidated, paleogene, reddish coloration. The most recent urban developments are based on these materials.

Towards the NE and SE of Culiacán city, spills of lavas of andesitic composition of neogene age can be observed. They are compact rocks, although fractured and partially altered, which constitute consolidated flat terrain (SGM, 1999).

The Tamazula and Humaya rivers that converge in the city of Culiacán and later from the Culiacán River, have produced diverse deposits along their courses and floodplains. These materials constitute a very particular area of clastic materials (gravel, sand, silt and clay) that constitute unconsolidated and saturated terrains (Figure 2).

Buildings of heights exceeding 40 m have been recently built in areas adjacent to the aforementioned rivers, which makes site effects studies, have an importance from an engineering and a civil protection point of view.

3. Analysis and results

3.1 HVSR method

Spectral ratios of horizontal components relative to the vertical recorded simultaneously have been widely used to determine site response from ambient-vibration records. The records of 113 sites within the urban area of Culiacán (triangles in Fig. 3) were analyzed. A Kinemetrics ETNA recorder with triaxial accelerometers and a sampling rate of 100 samples per second was used.

At each site we obtained two or more ambient vibration records with durations of 1 to 3 minutes. In each record, we selected a window which showed the fewest transient signals and the noise appeared more stationary. We calculate the spectral relationship between horizontal and vertical movement from the selected window. These relationships produced HVSR graphs where a peak could be clearly be identified from which a dominant period value and maximum amplification was determined. Geopsy (Geophysical Signal Database for Noise array Processing) software (Wathelet et al, 2020) was used for this analysis.

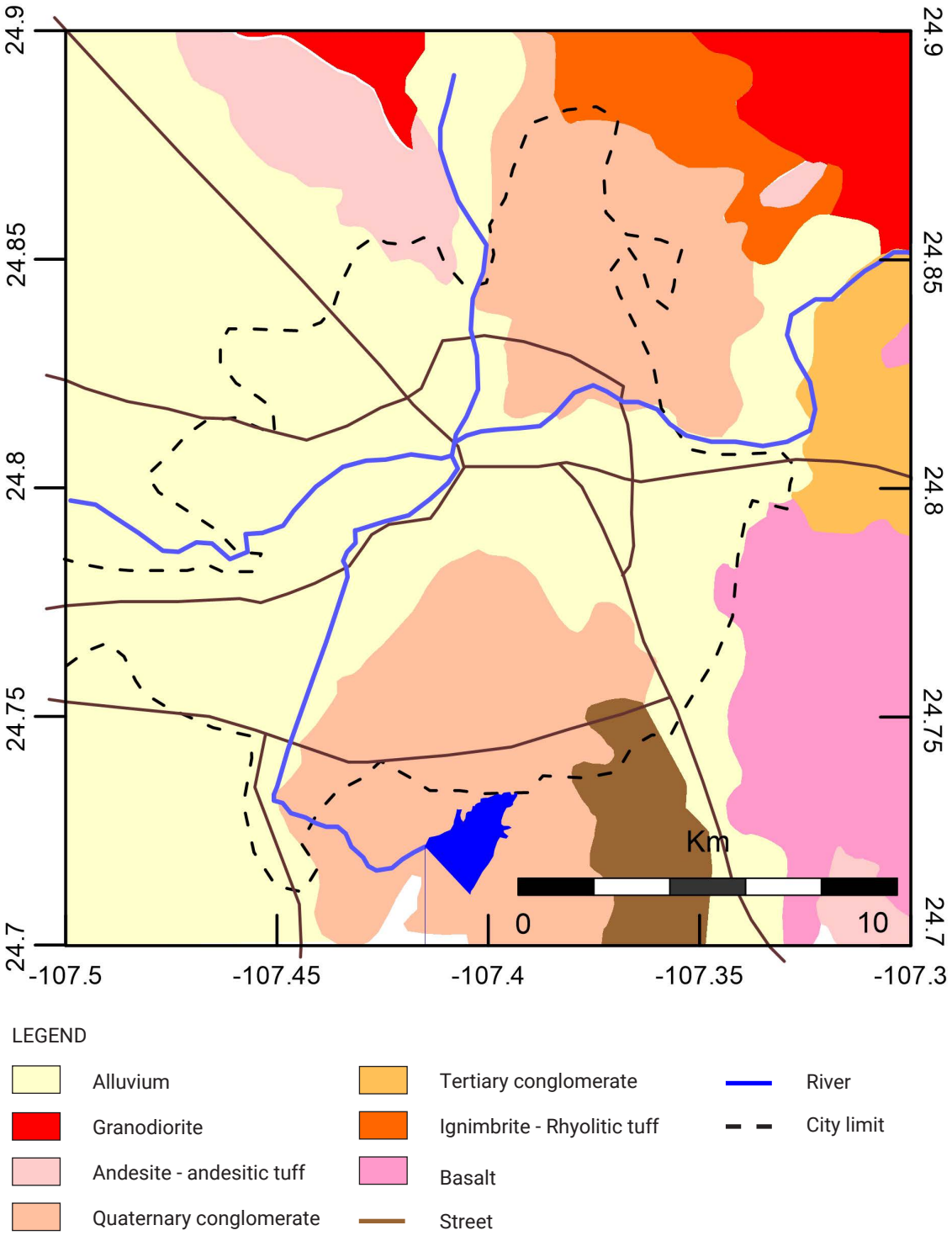

Figure 2. Geological map of the Culiacán (Modified after SGM, 1999). Dotted line indicates the boundary of the urban sprawl. The brown lines represent the most important avenues across the city.

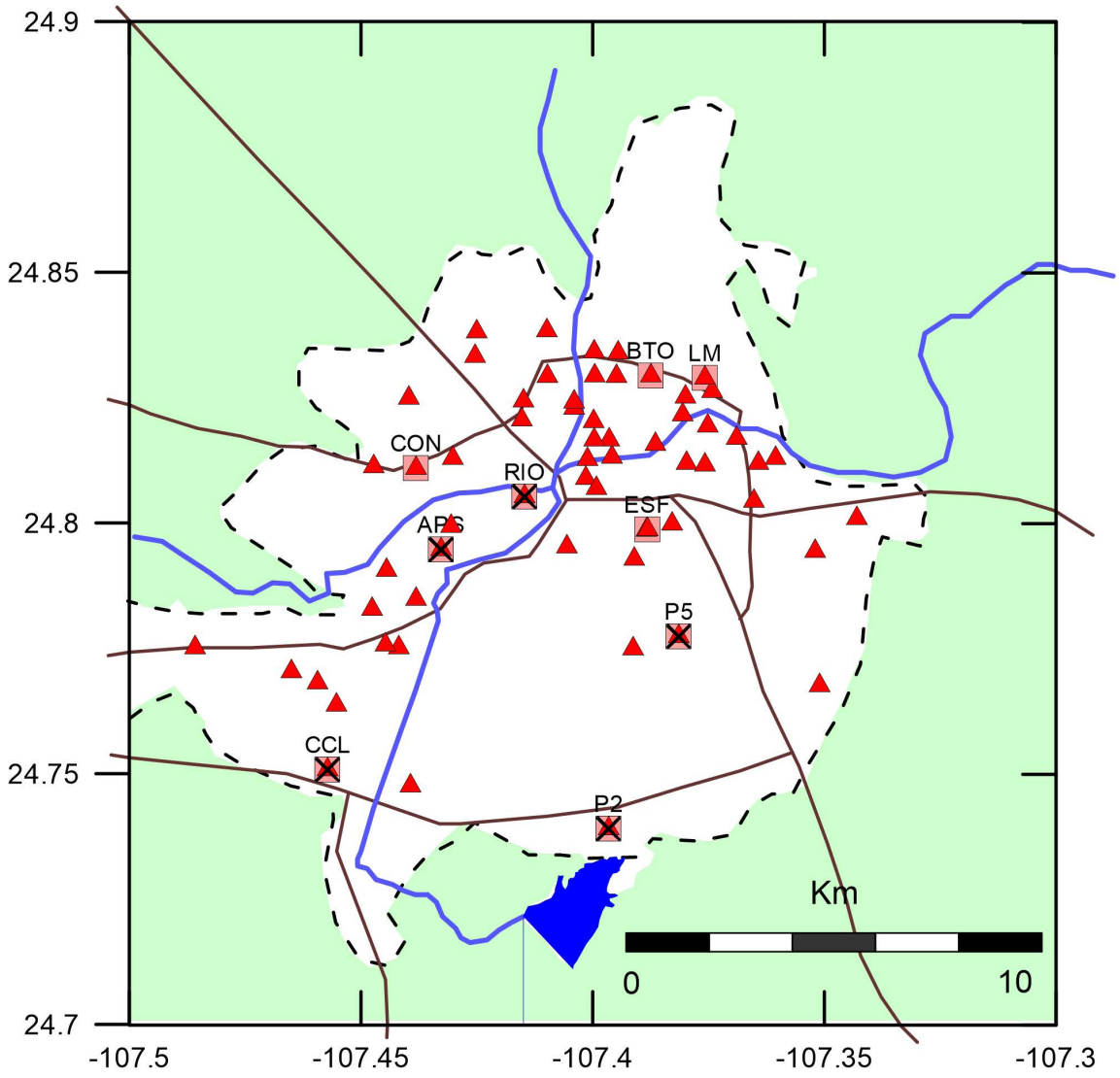

Figure 3. Location of HVSR measuring points (triangles). The white zone represents the urban sprawl of the city. Main streets and rivers are shown. Labeled squares indicate the sites where multi-channel measurements were made and velocity profiles were obtained. Crosses indicate places for which soil mechanics information is available.

Figure 4 shows an example of a 3 components record, the used window and their respective HVSR with a clear peak.

From the 113 records, only 61 produced HVSR with clear peaks from which a value of dominant period and maximum amplification could be determined. We attribute these results to the physical conditions when each measure was taken as they are not grouped in specific areas.

Once the dominant periods for all the 61 points were estimated, they were used to build a contour map using the Kriging spatial inference method in the context of surface geology as shown in Figure 5. The city boundary is also shown, as well as the main streets and rivers.

A correlation between the dominant periods distribution and the surface geology can be observed. The alluvial zone has periods between 0.2 and 0.7 and decreases in transitions to another type of soil. Conglomerates to the northeast and south, andesite to the northwest and andesite and conglomerates to the east.

Figure 6, on the other hand, shows the amplitude distribution

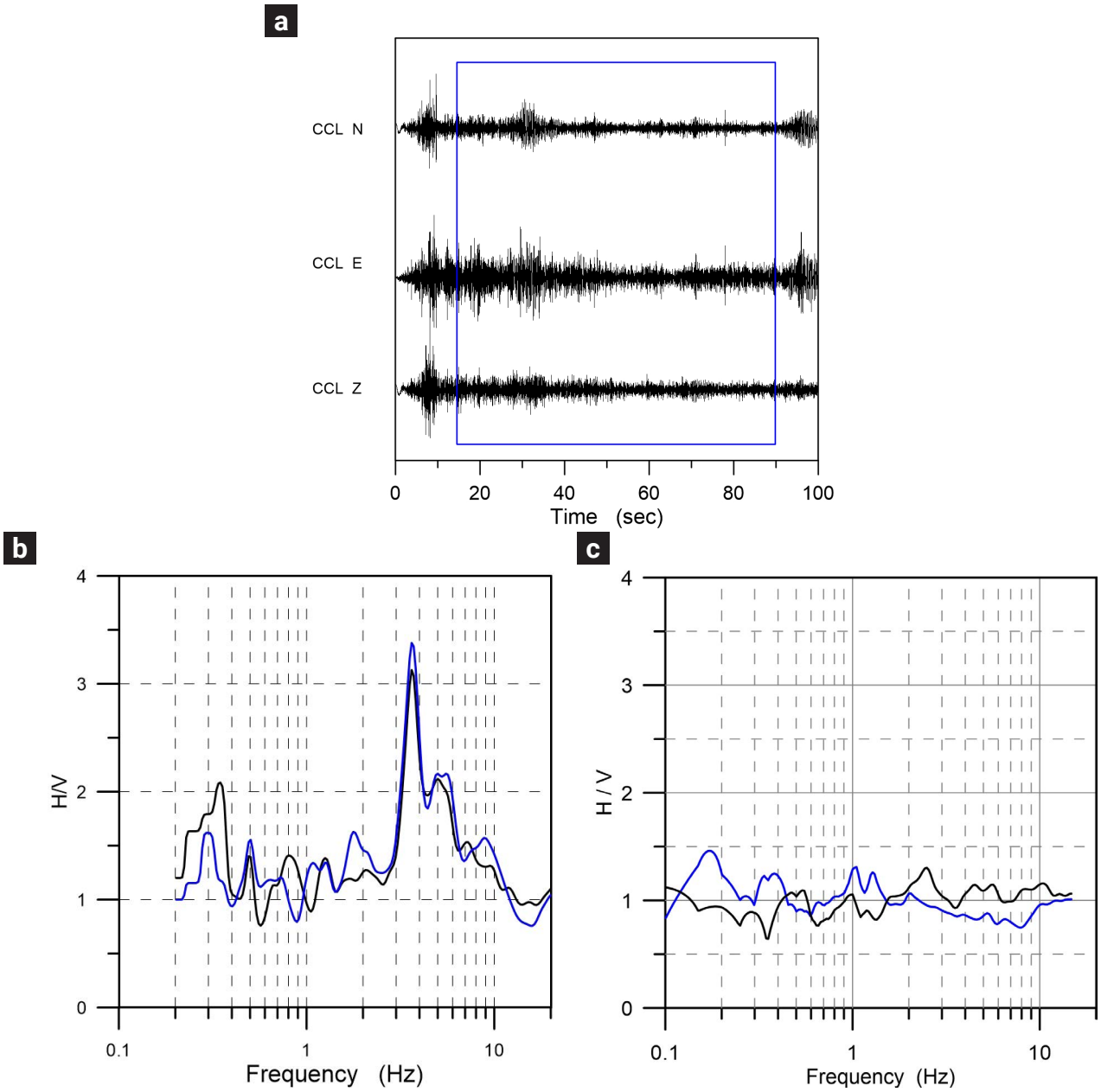

Figure 4. Example of a 3-component record a). The box in the traces indicates the window used for analysis. b) H/V spectrum with a clear peak. c) H/V spectrum where no significant peak was observed. Blue and black curves are the different estimates of H/V from different records at each site.

Amplitudes between 2 and 4 can be observed. The maximum found, are located along the riverbed, in the transition zone from conglomerate deposits to alluvium.

3.2 Multichannel Analysis of Surface Waves

3.2.1 Microtremor Array Method (MAM)

In order to reinforce observations made with the HVSR technique, multichannel measurements were made at some points, velocity profiles were obtained and transfer functions calculated by means of a multichannel analysis of surface waves. Specifically using the microtremor Array Method (MAM).

Ambient vibration recorded at a measuring point is produced by different sources which arrive from different directions which makes the vibration field essentially a random field. If we correlate records from different points, we can observe a wave travelling through the surface. A surface wave.

The principle underlying the Multichannel Analysis of Surface Waves method is the dispersive nature of Rayleigh waves when

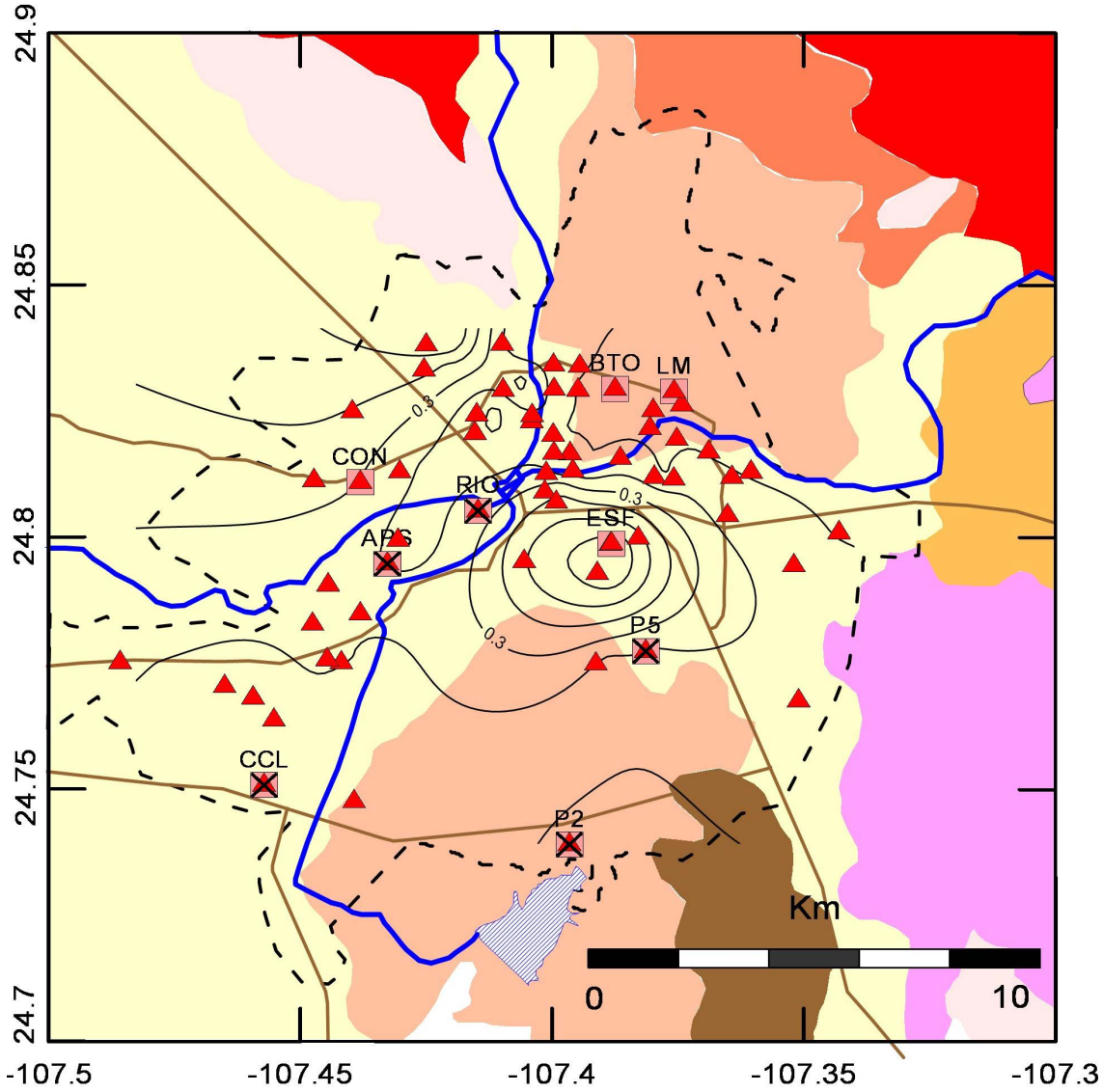

Figure 5. Contour map of dominant periods for Culiacán city. The dotted line indicates the boundary of urban sprawl.

they travel in a stratified medium. Different frequencies travel at different speeds. By calculating phase velocities at different wavelengths (frequencies), we can build a dispersion curve (Park et al, 1999). For an array of sensors, phase velocities are obtained by comparing the amplitude spectra of each pair of sensors.

With this multichannel approach, an image is constructed where the dispersion trend is identified from the energy accumulation pattern. The dispersion curve is extracted following the trends in the image.

We carried out measurements at nine locations throughout the city (shown as squares in Fig. 3, coinciding with single-station measurements sites). We used a PASI GEA24 exploration seismograph with a 24-bit dynamic range and a line of 24, vertical-component, 4 Hz natural frequency geophones. The sampling rate was 8 msec. This system had a flat response for velocity between 4.5 and 250 Hz. At each location, the geophones were installed with a 5-m distance between them, giving a total length of 120 m, and five time windows of about 60 sec of ambient vibration were recorded. Data is recorded in seg2 format so it can be directly read by the seisimager analysis software (test version).

The process begins with the transformation of all the records of the array, from the time-space domain (t-x), to the frequency-wave number domain (F-K) and from there, to the frequency-phase velocity domain (F-C) from which the dispersion curve of the maximum energy accumulation is obtained as shown in figure 7.

Surficial stratigraphy in terms of velocities can be estimated from the inversion of the dispersion curve by applying some

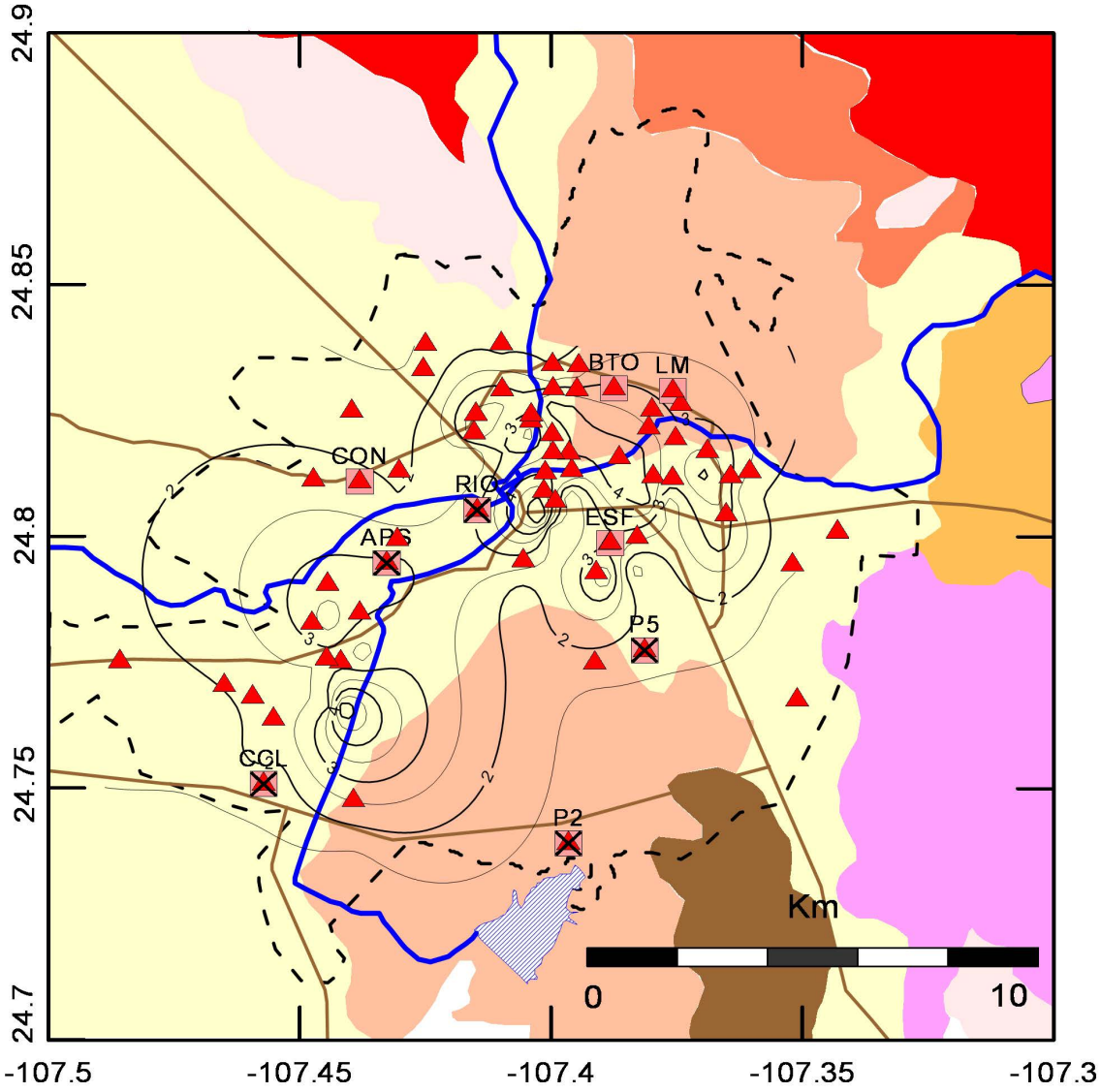

Figure 6. Contour map of amplitudes for Culiacán city. The dotted line indicates the boundary of urban sprawl.

standard algorithm, for example Herrmann's algorithm in which, the nonlinear inversion is replaced by a stochastic least squares procedure in which successive iterations are made until the differences between the theoretical dispersion curve obtained from the iterated model and the observed dispersion curve is small enough (Herrmann, 1973, Figure 8).

For the determination of dispersion curves, the seisimager software was used. Velocity models were obtained with the Computer Programs in Seismology Software (Herrmann & Ammon, 2002).

Frequency range that could be observed in the dispersion maps, from which the dispersion curves were obtained, indicate that the velocity profiles are reliable up to 30 to 40 m depths. We compared some the obtained profiles with direct measurements of soil mechanics carried out in other specific studies. Three of them could be corroborated up to 20 m depth, one up to 30 m and one profile only up to 10 m. (Figure 9).

Direct comparison shows good agreement in all the cases which gives us confidence in the profiles obtained from the inversion process. It can be observed that the velocities in the first 8 meters are similar at all locations but from 12 to 18 meters, higher velocities can be observed at RIO and P5 locations compared with the other which suggests harder strata at these depths below these locations. P2 shows the higher velocity below 20 m. probably related to the nearby basalt deposit.

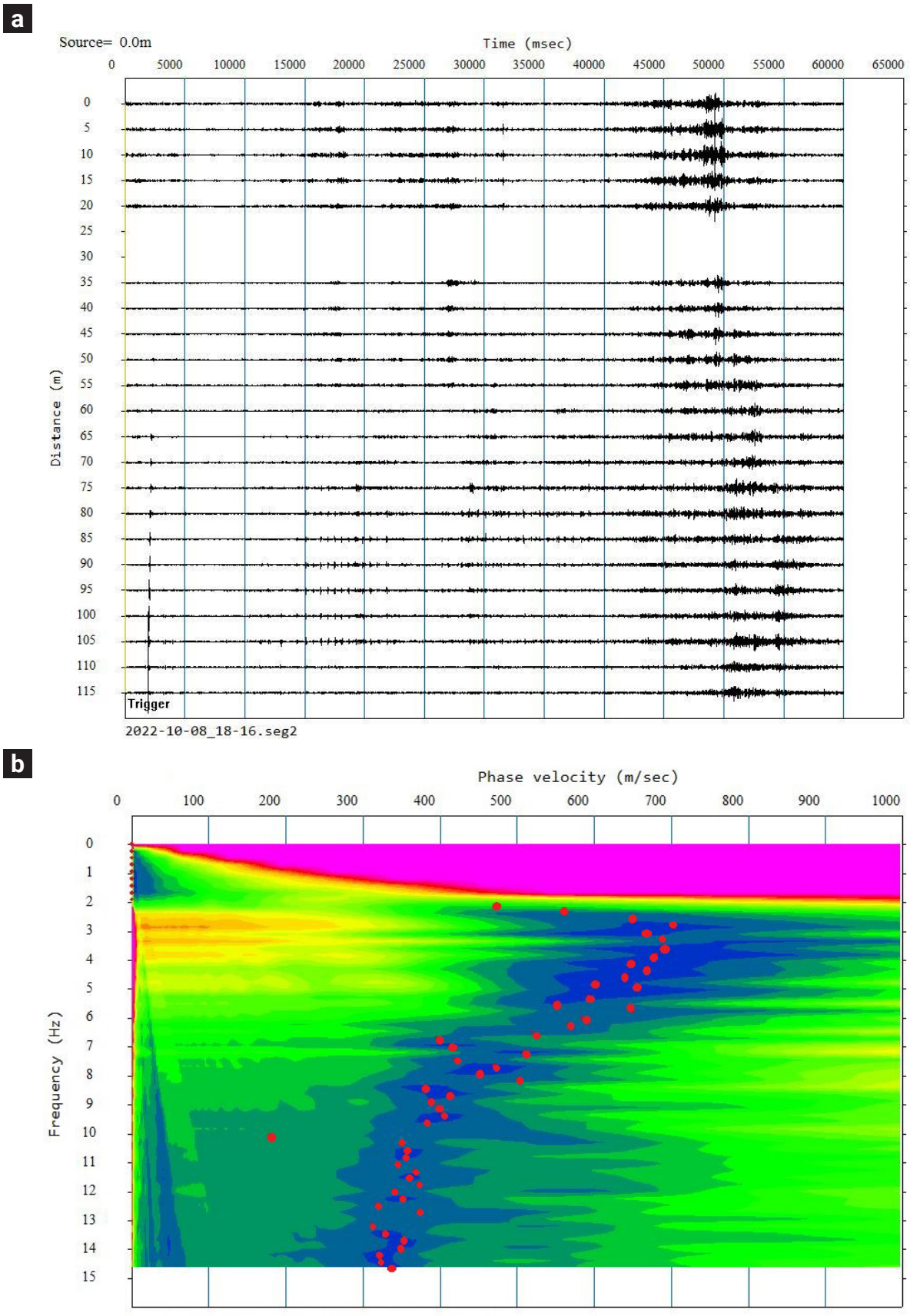

Figure 7. a) Seismic traces stacked from 4 recording windows for the RIO site. b) Estimated phase-frequency image. Red circles indicate maximum energy accumulation.

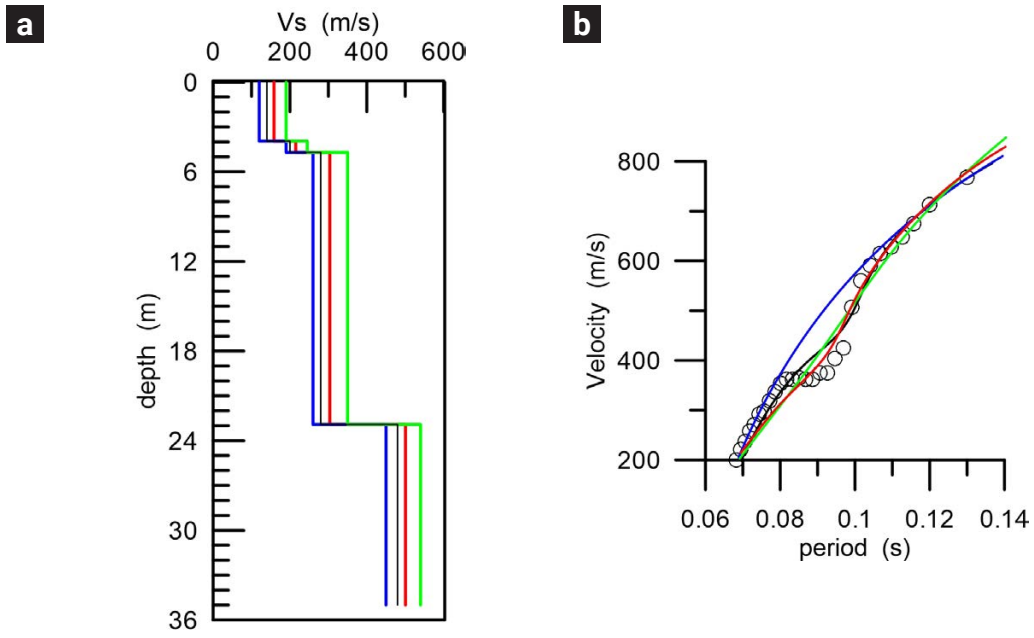

Figure 8. a) Velocity models obtained from the iterated dispersion curves. b) Iterated dispersion curves. Circles indicate the observed dispersion curve. Analysis correspond to CCL site.

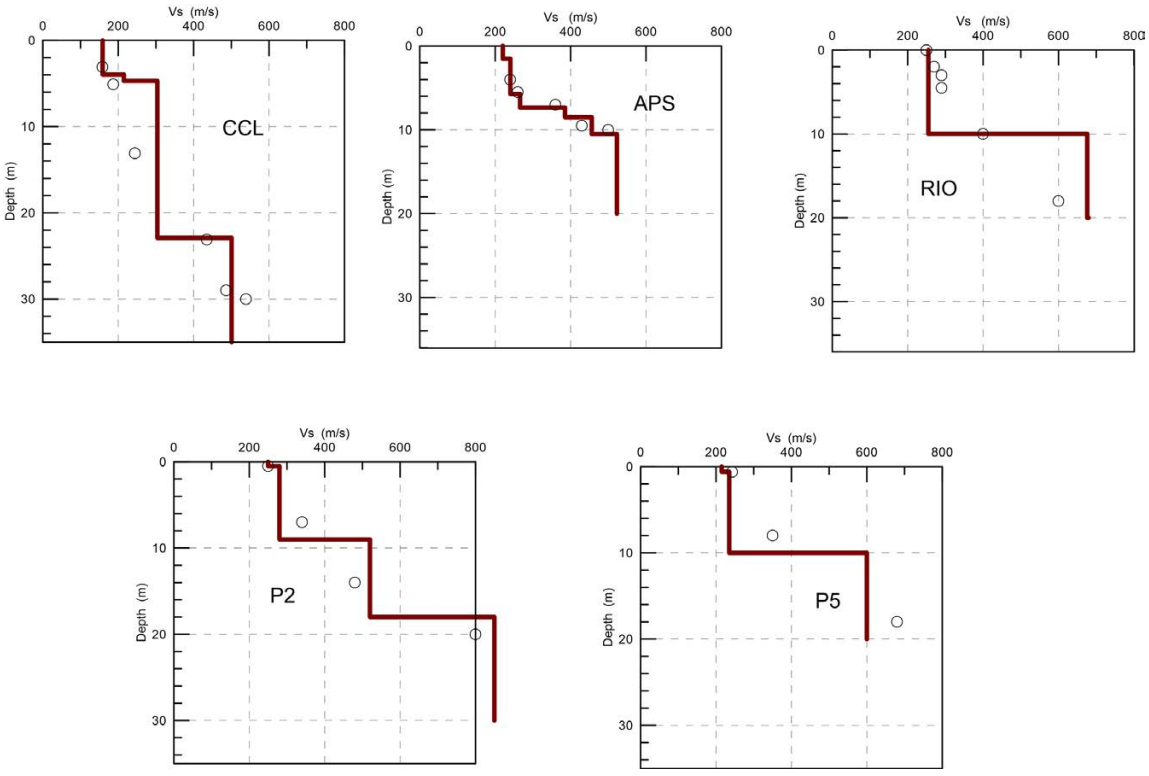

Figure 9. S-wave velocity profiles for five locations for which soil mechanics studies were available. The circles indicate the values obtained in those studies. The solid lines show the profile obtained from the inversion of the phase velocity dispersion curves observed at the corresponding location.

Shear-wave velocity profiles for the topmost 30 m for all nine sites are shown in Figure 10.

We can observe that the behavior of all profiles is similar up to approximately 8 m. The highest surface velocities can be seen in the P2 site which is located over conglomerate deposits, and the smallest at ESF site, located on alluvial soil. Between 10 and 20 m the lowest velocity is seen in CCL site which is a site over alluvium, farthest from the deposits of harder or consolidated material. In contrast, the highest speeds below 20 m are seen at BTO and P2 sites, reflecting the conglomerate deposits below these sites. In general, we can observe a correlation between the obtained velocities and the surface geology. Lower velocities in sites over alluvial soils, higher velocities in sites over harder deposits (conglomerate).

3.3 Transfer Functions

For modeling purposes, the site effect caused by a soil structure can be considered as the result of the convolution of energy (eg. seismic energy), which travels through a stratigraphic structure, and the site's own response called the transfer function. If the soil characteristics are known (the stratigraphic structure), the transfer function of the site can be estimated, and a total theoretical response can be obtained given any input signal by propagating it (Green's function) through the medium.

There are several ways to describe a medium based on its elastic properties: homogeneous medium, stratified medium, heterogeneous medium, etc. In this study we describe the medium as stratified with horizontal flat layers, characterized by its thickness, density, shear modulus and damping factor.

We computed the Transfer Function using two different tools to compare results. The Degtra software (Ordaz, 1988) and the SHAKE2000 (Ordoñez, 2012). Both use the transfer matrix originally proposed by Thompson (1950) and corrected by Haskell (1953). We used the corresponding shear-wave profile for each site. For the most superficial layers a damping factor of 5% was considered and for the intermediate and deep layers we use a value of 4%. Density in each layer was considered to be 1800 kg/m3. Both tools gave similar results. Figure 11 illustrates the transfer functions obtained for the 9 sites.

Transfer functions obtained show maximum amplifications less than or equal to 3 and fundamental frequencies between 4 and 9 Hz (0.1 to 0.25 seconds) in good agreement with dominant periods obtain by HVSR method. The greatest contribution of energy corresponds to the fundamental mode of vibration.

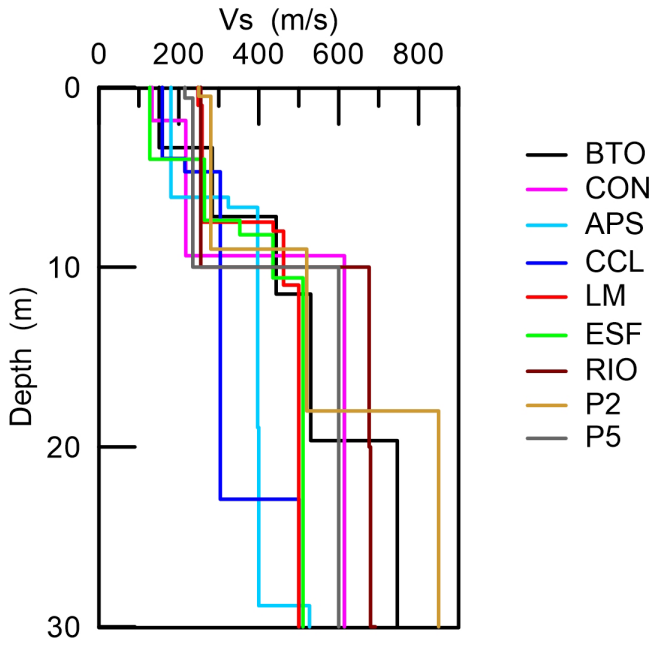

Figure 10. Shear-wave velocity profiles inverted from phase-velocity dispersion curves for the nine sites.

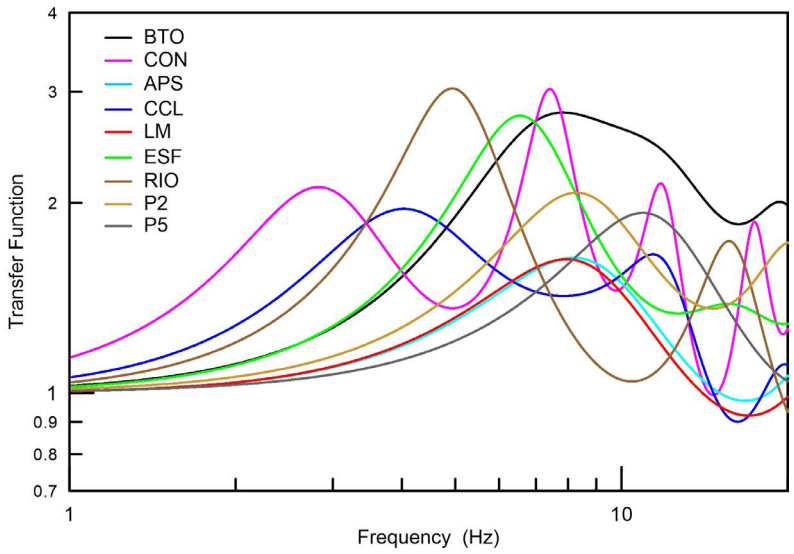

Figure 11. Transfer functions for the 9 sites of Culiacán, México.

4. Conclusions

A dynamic characterization for the soil of Culiacán, Mexico, using the HVSR technique was performed. The results show good agreement of dominant periods with the geology shown in Figure 2. Dominant periods between 0.2 to 0.7 for the alluvial zone in the central and western part of the city and lower periods for sites near igneous rock outcrops south and southeast of the city. A multichannel analysis was carried out at 7 sites where the measurement of H / V was performed using the MAM method. The phase-velocity dispersion curves were inverted and reliable speed profiles up to 30 m were obtained. Five of them could be compared with soil mechanics data. The direct comparison in all 5 cases shows agreement. Transfer functions were computed and the dominant period values obtained with the HVSR technique were similar.

Finally, direct observations such as those obtained in this study, are essential for an adequate dynamic characterization of the soil of the city of Culiacán, Sinaloa and a very important factor to consider for a future update of the building regulations of the city of Culiacán.

5. Acknowledgments

The comments by two anonymous reviewers, helped us to improve our manuscript.

6. References

Chávez, F., Domínguez, T., Rodríguez, M., Perez, F. (2007). "Site effects in a volcanic environment: A comparison between HVSR and array techniques at Colima, México". *Bull. Seis. Soc. Am.*, V97, 2, 591-604.

Fenby, S. S., Gastil, R. G., (1991). "A seismotectonic map of the Gulf of California and surrounding areas, in Dauphin, J.P., and Simoneit, B.R., eds., The Gulf and Peninsular Province of the California". *American Association of Petroleum Geologists Memoir* 47, 79-83.

Field, E. H. and Jacob, K. (1995). "A comparison and test of various site response estimation techniques, including three that are non-reference-site dependent". *Bull. Seism. Soc. Am.* 85, 1127-1143.

Godinez, Karla. (2022). "El uso del ruido sismico ambiental para el estudio de vibraciones en el sistema subsuelo-edificio". [Tesis de Licenciatura publicada]. Facultad de Ingeniería, UNAM, México.

Gutierrez, C., and Singh, S. K. (1992). "A site effect study in Acapulco, Guerrero, Mexico: comparison of results from strong motion and microtremor data". *Bull. Seism. Soc. Am.*, 82, 642-659.

Haskell, N. A., (1953). "The dispersion of surface waves on multilayered media". *Bull. Seism. Soc. Am.*, 43, 17-34.

Herrmann, R. B., (1973). "Some aspects of band-pass filtering of surface waves". Bull.Seism. Soc. Am. 63, 663-671.

Herrmann, R. B. and Ammon, C. J. (2002). *"Computer Programs in Seismology"*. Saint Louis University, 7 vols.

Kagami, H., S. Okada, K., Shiono, M. Oner, M., Dravinski, M., Mal, A. K. (1986). "Observation of 1 to 5 second microtremors and their application to earthquake engineering, part III: A two-dimensional study of site effects in S. Fernando valley". *Bull. Seism. Soc. Am.*, 76, 1801-1812.

Keil, S., Wassermann, J., Igel H. (2021). "Single-station seismic microzonation using 6C measurements", *Journal of Seismology*, 25, 103-114.

Kobayashi, H., Seo, K., Midorikawa, S. (1986). *"Estimated strong ground motions in the Mexico City due to the Michoacan, Mexico earthquake of September 19, 1985 based on characteristics of microtremor. Part 2, Report on microzoning studies of the Mexico earthquake of September 19, 1985"*. The Graduate School of Nagatsuta, Tokyo Institute of Technology, Yokohama, Japan.

Lermo, J., and Chavez-Garcia, F. J. (1994). "Are microtremors useful in site effect evaluation?". *Bull. Seism. Soc. Am.* 84, 1350-1364.

Nakamura, Y. (1989). "A method for dynamic characteristics estimation of subsurface using microtremor on the ground surface". *Q. Rep. Railway Tech. Res. Inst.*, 30, 1, 25-33.

Nagy, E.A., Stock, J.M. (2000). "Structural controls on the continent-ocean transition in the northern Gulf of California". *Journal of Geophysical Research*, 105 (B7), p.16. 25116,269.

Ordaz, M. (1988). "*Degtra V8.3*".

Ordoñez, G. (2012). *"A Computer program for the 1-D analysis of geotechnical Earthquake Engineering Problems"*. Geomotions LLC.

Park, C.B., Miller, R. D., Xia, J. (1999). "Multichannel analysis of surface waves (MASW)". *Geophysics*, 64, 800-808.

Pergalani, F., Pagliarodi, A., Bourdeau, C., Campagnoni, M., Lenti, l., Lualdi, M., Madiai, C., Martino, S., Razzano, R., Verone, C., Verrubbi V. (2020). "Seismic microzoning map: Aproaches, results and applications after the 2016-2017 Central Italy seismic sequence". *Bulletin of earthquake engineering*. 18, 5595-5629.

Plattner, C., Malservisi, R., Dixon, T.H., Lafemina, P., Sella, G. F., Fletcher, J., Suarez-Vidal, F., (2007). "New constraints on relative motion between the Pacific plate and Baja California microplate (Mexico) from GPS measurements". *Geophysical Journal International*, 170. 1373-1380, doi: **https://doi.org/10.1111/j.1365-246X.2007.03494.x**

Seo, K. (1992). "A joint work for measurements of microtremors in the Ashigara valley". Int. Symp. *Effects of Surf. Geol. on Seismic Motion*, Vol. I, ESG, Odawara, Japan, 43-52.

Thomson, W. (1950). "Transmission of elastic waves through stratified solid". *Journal of applied physics.* 21, 89-93.

Servicio Geologico Mexicano. (1999). *"Carta Geológico-Minera G13-10 Sinaloa y Durango"*.

UNAM, Instituto de Geofísica (2023). *Servicio Sismológico Nacional*, México. **http://www.ssn.unam.mx**

Thomson, W. (1950). "Transmission of elastic waves through stratified solid". *Journal of applied physics*, 21, 89-93.

Vargas-Luque, A. and Del Carpio, F. (2021). "Aplicación de la vibración ambiental a la información física de las construcciones para determinar la vulnerabilidad sísmica". *Ciencia Latina Revista Científica Multidisciplinar*. V5, No.2. P 2033. doi: **https://doi.org/10.37811/cl_rcm.v5i2.41**

Wathelet, M., Chatelain, J. L., Cornou, C., Giulio, G. D., Guillier, B., Ohrnberger, M., Savvaidis, A. (2020). "Geopsy: A User-Friendly Open-Source Tool Set for Ambient Vibration Processing". *Seismological Research Letters*, 91(3), 1878-1889, doi: **https://doi.org/10.1785/0220190360**

Zalbuin, L., Sugianto, N., Refrizon (2021). "Seismic hazard microzonation of bengKulu City, Indonesia". *Geoenvironmental Disasters.* 8, article number 5.

Geofísica Internacional (2024) **63-2**: 817 - 834

Forward modeling of spectral gamma-ray (SGR) logging in sedimentary formations

Lechuga-Lagos F.M.[1], Aquino-López A.[*2], Valdez-Grijalva M.A.[2] and Campos-Enriquez J.O.[3]

Abstract

We propose a new approach to improve spectral gamma-ray (SGR) logging forward modeling by considering the radioactive minerals present in the rock as gamma-ray sources. This is based on the radioactive attenuation theory. The assumptions are: 1) minerals with K^{40}, U^{238}, and Th^{232} content are considered radioactive sources uniformly distributed in the rock; 2) the measured radioactivity is proportional to the concentration of radioactive minerals and inversely proportional to the rock bulk density; 3) the radioactivity is only attenuated by absorption of gamma-rays. The forward modeling was tested using a synthetic case of sandstone with clay minerals and brine-saturated pores to analyze the sensitivity of SGR to changes in illite/smectite-illite/mica ratios and sandstone porosities. Finally, it was further validated with 44 core samples, of which 22 are from two shale gas and 22 from two clastic formations. The Pearson correlation coefficient applied to measure the misfit between the simulated and observed K, U, Th, and SGR data attained values of 0.82, 0.83, 0.61, and 0.57, respectively. A further improvement to 0.87, 0.85, 0.65, and 0.69 was achieved when applying joint inversion for data where illite/smectite and illite/mica ratios were not specified. The correlation between the simulated and observed data supports the viability of the proposed SGR forward modeling approach method.

Key words: Spectral gamma-ray logging, Forward modeling, Radioactive minerals, Sedimentary formations, K^{40}, U^{238}, Th^{232} radioisotopes.

Resumen

Proponemos un nuevo enfoque para mejorar el modelado directo del registro de rayos gamma espectral (SGR) al considerar los minerales radioactivos presentes en la roca como fuentes de rayos gamma. Este se basa en la teoría de la atenuación radiactiva. Los supuestos son: 1) los minerales con contenido de K^{40}, U^{238}, y Th^{232} son considerados fuentes radiactivas que están uniformemente distribuidas en la roca; 2) la radiactividad medida es proporcional a la concentración de minerales radiactivos e inversamente proporcional a la densidad aparente de la roca; 3) la radiactividad solo se atenúa por absorción de rayos gamma. El modelado directo fue probado usando un caso sintético de arenisca con minerales arcillosos y poros saturados con salmuera para analizar la sensibilidad de SGR a cambios en las relaciones de ilita/esmectita e ilita/mica y porosidades de la arenisca. Finalmente, el enfoque fue validado con 44 muestras de núcleo, siendo 22 de dos formaciones de gas en lutita y 22 de dos formaciones clásticas. El coeficiente de correlación de Pearson se aplicó para medir el desajuste entre los datos simulados y medidos de K, U, Th y SGR, obteniéndose valores de 0.82, 0.83, 0.61 y 0.57 respectivamente, y una mejora adicional de 0.87, 0.85, 0.65 y 0.69, respectivamente. Estos resultados fueron alcanzados aplicando inversión conjunta para los datos donde las relaciones ilita/esmectita e ilita/mica no fueron especificadas. La correlación lograda entre los datos simulados y observados sustenta la viabilidad del nuevo enfoque para el modelado directo propuesto de SGR.

Palabras clave: Registro de rayos gamma espectral, Modelado directo, Minerales radioactivos, Formaciones sedimentarias, Radioisótopos K^{40}, U^{238}, Th^{232}.

Received: May 16, 2023 ; Accepted: November 15, 2023; Published on-line: April 1, 2024.

Editorial responsibility: Dr. Oscar C. Valdiviezo-Mijangos

* Corresponding author: Ambrosio Aquino López. E-mail: aaquino@imp.mx
[1] Posgrado del Instituto Mexicano del Petróleo, Instituto Mexicano del Petróleo, Ciudad de México (CDMX), México.
[2] Geofísica Cuantitativa, Instituto Mexicano del Petróleo, Ciudad de México (CDMX), México.
[3] Instituto de Geofísica, Universidad Nacional Autónoma de México, Ciudad de México (CDMX), México.

Francisco Miguel Lechuga Lagos, Ambrosio Aquino López, Miguel Ángel Valdez Grijalva, José Oscar Campos Enríquez.

https://doi.org/10.22201/igeof.2954436xe.2024.63.1.1710

1. Introduction

Sedimentary rocks contain radioisotopes that emit radiation due to nuclear decay. In geophysical logging applications, the gamma-ray spectrum is of primary interest due to its high penetration into rock, which is approximately inversely proportional to the atomic number of the elements which make up the rock through which it travels, which allows gamma rays to be recorded by an instrument (Bassiouni, 1994; Schön, 2015; Serra, 1984; Owen, 1966). The radioisotopes which are significant in sedimentary rocks are K^{40} (half-life time of 4.4×10^{9} years), Th^{232} (half-life time of 1.4×10^{10} years), and U^{238} (half-life time of 1.3×10^{9} years). These decay into Ar^{40}, Pb^{208}, and Pb^{206}, emitting radiation with energies of 1.46 MeV, 2.62 MeV, and 1.76 MeV, respectively (Bassiouni, 1994; Schön, 2015; Serra, 1984).

Estimating radioactive elements is critical in rock formation evaluation since it assists lithology identification of many clay minerals (Bassiouni, 1994; Schnyder *et al.*, 2006; Ellis and Singer, 2007; Schön, 2015). SGR logging allows a quantitative evaluation of K, U, and Th concentrations by decomposing the total radioactive spectra into the three characteristic spectra (Brannon and Osoba, 1956; Lock and Hoyer, 1971; Serra *et al.*, 1980; Serra, 1984; Mathis *et al.*, 1984; Bassiouni, 1994).

The total gamma-ray contribution is obtained by the sum of the radioactivity of K, U, and Th (Bassiouni, 1994; Schön, 2015; Serra *et al.*, 1980). Assessment of the presence of these radioisotopes is helpful in the determination of lithology because they are usually concentrated in carbonate minerals, clay minerals, organic matter, potassium feldspars, and evaporites, as well as in heavy minerals (Schön, 2015; Ellis and Singer, 2007; Bassiouni, 1994; Serra *et al.*, 1980; Fertl, 1979; Russell, 1945).

SGR logging is applied in conventional formations (sandstone and carbonate rocks) to differentiate between reservoir and non-reservoir rocks, to recognize the evaporite mineral, to identify rock mineral types, and help evaluation of their concentration by either cross-plot or computation (Fertl *et al.*, 1982; Bassiouni, 1994; Schön, 2015; Serra, 1984). It also allows the identification of zones containing organic material in unconventional reservoirs (Huang *et al.*, 2015; Lüning and Kolonic, 2003; Swanson, 1960; Bohacs, 1998; Bohacs and Miskell-Gerhardt, 1998; Ge *et al.*, 2016; Jacobi *et al.*, 2008), and the identification of fractured reservoirs (Fertl, 1979; Fertl and Rieke III, 1980). Further, the Th/K or Th/U ratios are used as qualitative indicators of the principal radioactive mineral contained in the rock (Bassiouni, 1994; Serra *et al.*, 1980; Schön, 2015) and to identify sedimentary facies (Adams and Weaver, 1958; Bigelow, 2002).

Empirical equations to estimate shale content by assuming that only clay minerals emit gamma radiation (Larionov, 1969; Stieber, 1970; Clavier *et al.*, 1971) and to estimate organic material content in unconventional reservoirs considering mainly the U concentration (Wang *et al.*, 2019, 2016; Steiner *et al.*, 2016; Gonzalez *et al.*, 2013; Schmoker, 1981) were derived by different authors. However, sedimentary formations contain different radioactive minerals (Bigelow, 2002). Sandstones and carbonates can contain other radioactive minerals besides clay (Chudi and Simon, 2012; Schön, 2015). Shale gas formations exhibit a high content of K, U, and Th due to the presence of clay and plagioclase minerals (Huang *et al.*, 2015; Lüning and Kolonic, 2003; Passey *et al.*, 1990, 2010; Russell, 1945; Alharthy *et al.*, 2012). Therefore, the concentration of organic matter could be overestimated by not separating the U present in the clay and plagioclase (Lüning and Kolonic, 2003; Schnyder *et al.*, 2006). Th/K and Th/U ratios do not help as a facies discriminator if they are approximately constant in the studied lithofacies (North and Boering, 1999). Estimation of the concentration of radioactive minerals can be approximated by linearly correlating SGR signals with compressional travel time (Δt), bulk density (ρ_b), or neutron porosity (ϕ_N) logs, and it is strengthened with information from lithological and geochemical logging, Scanning Electron Microscope images (SEM), and X-ray diffraction in cores (Day-Stirrat *et al.*, 2021; Chudi and Simon, 2012; Hertzog *et al.*, 1989). The inadequate quantification of the concentration of radioactive minerals leads to increased uncertainty in the estimation of reservoirs (GaffneyCline, 2023).

We are interested in quantifying radioactive minerals from SGR signals without using empirical equations. In this context, forward modeling of natural gamma rays has been done considering multiple radioactive minerals (Serra, 1984; Bassiouni, 1994; Ellis and Singer, 2007) but is limited to modeling the total radioactivity of a given formation. SGR simulation has been applied to derive source rock characteristics and examine diagenesis by reconstructing part of the sedimentary rock history without focusing on quantifying radioactive minerals (Van der Boor, 2014).

In this work, we present an approach to SGR logging forward modeling that considers radioactive minerals present in the rock as gamma-ray sources, and it is based on radioactivity attenuation theory. The forward modeling is based on the following assumptions: 1) minerals with K^{40}, Th^{232}, and U^{238} content are considered radioactive sources uniformly distributed in the rock; 2) the measured radioactivity is proportional to the concentration of radioactive minerals and inversely proportional to the rock bulk density; 3) the radioactivity is only attenuated by absorption of gamma-rays.

Some minerals are bound together, such as illite/smectite and illite/mica, so their concentration is reported jointly in the petrographic analysis of cores without specifying the specific content of each mineral. For this reason, the SGR modeling

approach is tested through a synthetic control rock of sandstone with clay minerals of illite/smectite and illite/mica mixtures and brine-saturated pores to analyze the sensitivity of SGR to changes in illite/smectite-illite/mica ratios and sandstone porosities.

We further tested the SGR forward modeling on 44 core samples, 22 corresponding to two shale gas and 22 to two clastic formations, to validate it. Pearson correlation coefficient was applied to analyze the misfit between the simulated and observed U, K, Th, and SGR data, attaining values of 0.82, 0.83, 0.61, and 0.57, respectively. Joint inversion was applied in those cases where corresponding ratios of illite/smectite and illite/mica were unavailable, leading to an improvement of Pearson correlation coefficient of 0.87, 0.85, 0.65 and 0.69, respectively, for U, K, Th, and SGR.

2. Theoretical background

In this section, we describe the basics of SGR logging to quantify the presence of K, Th, and U; and the physical basis of the proposed modeling considering minerals as radioactive sources.

2.1 SGR logging basics

The K^{40}, Th^{232}, and U^{238} radioisotopes are abundant in sedimentary rocks and have respective half-lives of 4.4×10^{9}, 1.4×10^{10}, and 1.3×10^{9} years, respectively, so their presence in the rock is sufficiently long-lived, and they produce appreciable amounts of gamma rays (Bassiouni, 1994; Hertzog *et al.*, 1989; Bigelow, 2002; Serra, 1984; Schön, 2015). These radioisotopes are contained in different proportions in the radioactive minerals of petroleum reservoirs (Lock and Hoyer, 1971; Killeen, 1982; Serra, 1984; Bassiouni, 1994; Schön, 2015). K^{40}, Th^{232}, and U^{238} radioisotopes have characteristic energies emitted in discrete values of 1.46 MeV, 2.62 MeV, and 1.76 MeV, respectively, and they are contained in specific minerals that are assumed to be uniformly distributed in the sedimentary formation (Rhodes and Mott, 1966; Bassiouni, 1994; Serra, 1984; Schön, 2015).

Gamma-ray logging aims to measure the total number of gamma rays emitted by the rock formation per second per unitary weight (Belknap *et al.*, 1959). Its general configuration consists of a gamma ray detector, a processor, a memory, a telemetry module, and a surface acquisition system (Morys, 2020; Morys, 2021). The signal from the detector is amplified and discretized in energy levels or windows which span a specific energy band. The data is then encoded and sent to a surface acquisition system (Brannon and Osoba, 1956; Lock and Hoyer, 1971; Serra *et al.*, 1980; Serra, 1984; Mathis *et al.*, 1984; Bassiouni, 1994).

Three energy windows are associated with the characteristic energies of K^{40}, Th^{232}, and U^{238}, and their fractional abundances are computed by:

$$\sum_{i=1}^{n} r_i^2 = \sum_{i=1}^{n}\left(W_i - A_i Th^{232} - B_i \mathrm{U}^{238} - C_i \mathrm{K}^{40}\right)^2 = r^2 \quad (1)$$

where r_i is a factor representing a statistical error, W_i is the count-rate from window i, and A_i, B_i and C_i are the calibrated coefficients for the respective window i obtained by using a calibration "TUK" pit by minimizing Equation 1 (Serra, 1984, p. 120).

2.2 Physical basis of gamma radiation for radioactive minerals

This section describes the modeling of gamma-ray activity from K^{40}, U^{238}, and Th^{232}, considering them hosted in certain minerals, and that the medium (in this case, the rock) attenuates the gamma-ray flux.

In gamma radiation, a photon is emitted after a nucleus decays. The law of radioactive decay states that over a short time interval, dt, the number of decaying radioisotopes obeys the following expression (Rutherford and Soddy, 1902):

$$\frac{dN}{dt} = -\lambda N \ , \quad (2)$$

where N is the number of atoms of the radioisotope and λ (s^{-1}) is the decay constant. Integrating Equation 2 leads to the exponential relation:

$$N = N_0 e^{-\lambda t}, \quad (3)$$

where N_0 is the number of radioisotopes present at time $t = 0$. The activity A, the rate at which nuclei are decaying, is obtained by:

$$A=\lambda N \quad (4)$$

The specific activity (a) is a more widely used parameter which is defined as the net gamma counts per second measured from a gram of a radioisotope in equilibrium (s^{-1}). For the K^{40}, U^{238}, and Th^{232} series, it is obtained by summing the measured contributions from each of the radioisotopes considering only photons with energy greater than 100 keV (Belknap *et al.*, 1959; Ehsan *et al.*, 2019; Bassiouni, 1994). Their respective specific activities are: a_K=3.4 s^{-1}, a_U=2.8×10^4 s^{-1}, and a_{Th}=1.0×10^4 s^{-1} (Belknap *et al.*, 1959).

In a sedimentary rock a can be considered as (Belknap *et al.*, 1959):

$$a=a_K K+a_U U+a_{Th} Th, \quad (5)$$

being K (%), U (ppm), and Th (ppm) the fractional abundances of K^{40}, U^{238}, and Th^{232} in the rock (Serra, 1984; Ellis and Singer, 2007; Schön, 2015).

The radioactive activity of *m* minerals in a volume dV, considering them as sources, as a function of the fractional abundance of *n* radioisotopes for a control volume is obtained by:

$$dS_{ij} = \left[\sum_{i}^{m} \sum_{j}^{n} C_j \rho_i w^i_j a_j \right] dV \tag{6}$$

$C_i \left(\sum_{i=1}^{n} C_i = 1 \right)$ and ρ_i are the fractional concentration in the control volume, and density of the *i*-th mineral, respectively. w^i_j is the fractional abundance of the *j*-th radioisotope in the *i*-th mineral and a_j is the specific activity of the *j*-th radioisotope. We consider that the radioactive minerals are uniformly distributed.

Considering the radioactive attenuation theory, the total emissions are obtained by (Ellis and Singer, 2007; Evans, 1955):

$$d\phi(r) = \left[\sum_{i}^{m} \sum_{j}^{n} C_j \rho_i w^i_j a_j \right] \frac{e^{-\mu_a r}}{4\pi r^2} dV \ , \tag{7}$$

being $e^{-\mu a\, r}$ the attenuation factor and μa (cm^{-1}) the macroscopic absorption cross section (Duderstadt and Hamilton, 1976; Rhodes and Mott, 1966; Evans, 1955). The entire spherical source is obtained integrating over the solid angle Ω, thus $\int_{\Omega} dA = 4\pi r^2$. The total gamma-ray flux that reaches to the detector is given by:

$$\phi = \left[\sum_{i}^{m} \sum_{j}^{n} C_i \rho_i w^i_j a_j \right] \int_0^{\infty} e^{-\mu_a r} dr = \left[\sum_{i}^{m} \sum_{j}^{n} C_i \rho_i w^i_j a_j \right] \frac{1}{\mu_a} , \tag{8}$$

and the count rate R through (Evans, 1955):

$$R = \in \frac{\mu_a}{\rho_b} \phi \frac{\in}{\rho_b} \left[\sum_{i}^{m} \sum_{j}^{n} C_i \rho_i w^i_j a_j \right], \tag{9}$$

where ϵ is the efficiency of the gamma-ray sensor, the probability that a gamma-ray incident to the detector will produce a count (Belknap *et al.*, 1959; Rhodes and Mott, 1966), and ρ_b is the rock bulk density.

To calculate the count rate in API units and considering only the radioisotopes of our interest: K^{40}, U^{238}, and Th^{232}, Equation 9 can be simplified in the following equation:

$$SGR = \frac{\in}{\rho_b} \sum_{i}^{m} C_i \rho_i \left(K^i \eta + U^i \alpha + Th^i \beta \right), \tag{10}$$

where the coefficient η, β, and α depend on the detector and sonde design and normalized a_{Th} and a_K to a_U (the concentration of U in ppm that give the exact count rate as 1% of K and 1 ppm of Th). K_i, U_i, and Th_i are the fractional abundances of K^{40}, U^{238}, and Th^{232}, respectively, in the *i*-th mineral.

Further, Equation 10 can be rewritten in the standard form (Belknap *et al.*, 1959; Bassiouni, 1994; Ellis and Singer, 2007; Schön, 2015):

$$SGR = \epsilon(\eta K + \alpha U + \beta Th), \tag{11}$$

being K, U, and Th, the total content of K^{40}, U^{238}, and Th^{232} in the rock, respectively, and modeled as:

$$K = \frac{1}{\rho_b} \sum_{i}^{m} C_i \rho_i K^i \ , \tag{12}$$

$$U = \frac{1}{\rho_b} \sum_{i}^{m} C_i \rho_i U^i \ , \tag{13}$$

$$Th = \frac{1}{\rho_b} \sum_{i}^{m} C_i \rho_i Th^i \ . \tag{14}$$

3. SGR forward modeling

The petrophysical model underlying the proposed SGR forward modeling comprises pores, radioactive minerals, and nonradioactive minerals. The radioactive minerals have characteristic fractional abundances of K^{40}, U^{238}, and Th^{232} in specific ranges for each mineral, which were considered for forward modeling (Table 1).

The SGR forward modeling is done with Equation 10 and tested: 1) against a synthetic control rock of sandstone with clay minerals and brine-saturated pores to analyze the sensibility of the SGR to changes in illite/smectite, illite/mica ratios, and sandstone porosities; and 2) against 44 core samples of which 22 are from two shale gas formations and 22 from two clastic formations to validate it.

3.1 Synthetic case

We consider a sandstone with clay minerals and brine-saturated pores. The sandstone comprises 80% of solid grains

Table 1. Range of fractional abundances *K*, *U*, and *Th* in some radioactive minerals (Schön, 2015; Bigelow, 2002; Huntley and Baril, 1997; Yuguchi *et al.*, 2021; Sen, 1959; Lewis *et al.*, 2004). Void entries in the table indicate the absence of the respective radioisotope.

Mineral	***K* (%)**	***U* (ppm)**	***Th* (ppm)**	$\rho\left(\frac{g}{cm^3}\right)$
Quartz	< 0.15	< 0.4	< 2.0	2.648
Calcite	< 0.4	1.5 – 15	< 2.0	2.71
Dolomite	0.1 – 0.3	1.5 – 10	< 2.0	2.86
K-feldspar	11.8 – 14	0.2 – 5.0	0.01 – 7.0	2.56
Plagioclase	< 0.54	0.02 – 5.0	0.01 – 3.0	2.68
Mica (Biotite)	6.2 – 10.1	1 – 40	0.5 – 50	2.8
Illite	3.5 – 8.3	1 – 5	10 – 20	2.66
Smectite	0 – 1.5	1 – 21	6 – 44	2.2
Kaolinite	0 – 0.6	1 – 12	6 – 47	2.594
Chlorite	0 – 0.35	–	3 – 5	2.8
Kerogen	–	62.5 – 500	–	1.1 – 1.4

(quartz) and 20% of pores. To increase the clay concentration, we replaced equivalent concentrations of sandstone. Only clay minerals are radioactive.

We analyze the K, U, Th, and SGR forward modeling in two scenarios: a) a sandstone with a mixture of illite/smectite and b) a sandstone with an illite/mica mixture. Scenario a) comprised: 1) clay of 100% of illite, 2) clay of 100% of smectite, and 3) clay with a proportion of 50 to 50% of illite and smectite. Scenario b) comprised: 1) clay of 100% of illite, 2) clay of 100% of mica, and 3) clay with a proportion of 50 to 50% of illite and mica. All possible illite/smectite and illite/mica ratios are bounded by 1 and 2 in scenarios "a" and "b", respectively. The fractional abundances *K*, *U*, and *Th* and the density used for the respective radioactive minerals are shown in Table 2. The K, U, and Th content were modeled with Equations 12, 13, and 14, respectively, and SGR was modeled with Equation 10.

K content obtained from illite/smectite ratios is broader than those obtained with illite/mica ratios for each clay concentration (Figure 1). In addition, it can be observed that K values in illite/smectite mixtures are lower compared to illite/mica mixtures (Figure 1). This is evident from the reference lines depicting 50 to 50% of the illite/smectite mixture and 100% of smectite (Figure 1a), which show lower K values than the reference lines of 50 to 50% of the illite/mica mixture and 100% of mica (Figure 1b).

U content from illite/smectite and illite/mica ratios are in a similar range below 18% of clay concentration (less than 1%

Table 2. Fractional abundances *K*, *U*, and *Th* and density used for synthetic case forward modeling.

Mineral	***K* (%)**	***U* (ppm)**	***Th* (ppm)**	$\rho\left(\frac{g}{cm^3}\right)$
Illite	8.3	5	20	2.66
Smectite	1.5	21	44	2.2
Mica	6.2	16.9	27	2.8

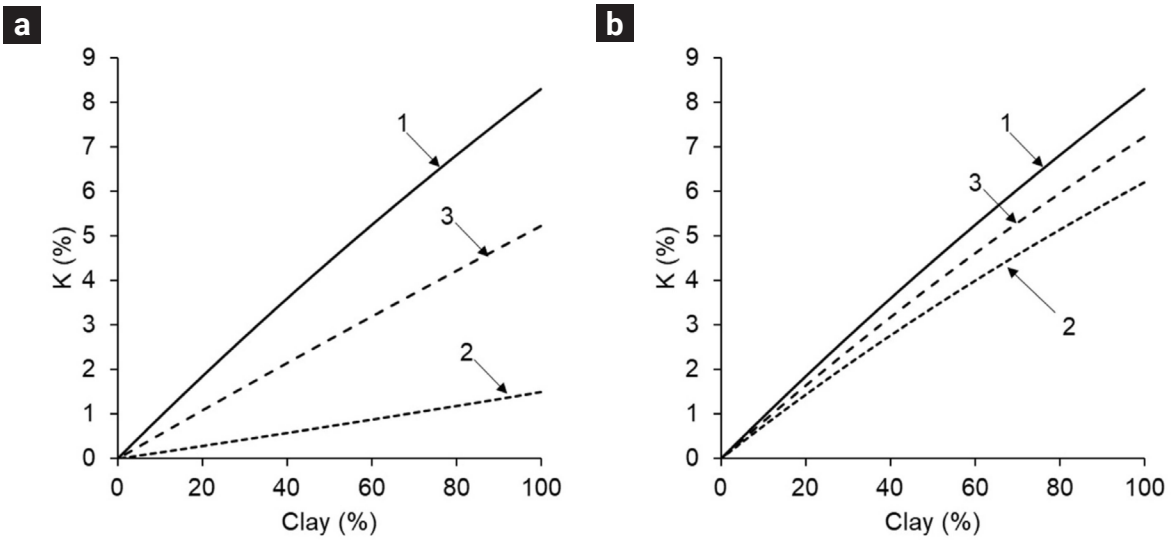

Figure 1. K content for mixtures of a) illite/smectite and b) illite/mica. a) K for clay constituted by illite (line 1), smectite (line 2), and 50 to 50% of illite/smectite (line 3). b) K for clay constituted by illite (line 1), mica (line 2), and 50 to 50% of illite/mica (line 3).

absolute difference), but above 18% are higher (Figure 2). The reference lines for 50 to 50% of the illite/smectite mixture and 100% of smectite compared to 50 to 50% of illite/mica and 100% of mica, respectively, show that the U values for scenario "a" (Figure 2a) are slightly higher than scenario "b" (Figure 2b).

Th content from illite/smectite ratios has a broader range than illite/mica ratios for each clay concentration (Figure 3). The reference lines for 50 to 50% of illite/smectite mixture and 100% of smectite (Figure 3a) give higher Th values than 50 to 50% of illite/mica mixture and 100% of mica (Figure 3b), indicating that Th values for scenario "a" are higher than scenario "b".

SGR for scenario "a" has a similar range to scenario "b" (Figure 4). The reference lines for 50 to 50% of illite/smectite mixture and 100% of smectite (Figure 4a) are slightly higher for SGR values than 50 to 50% of illite/mica mixture and 100% of mica (Figure 4b). Furthermore, the relationships between SGR and clay concentration are not linear for both scenarios due to the differences in their bulk densities.

We further analyzed the effect of porosity changes on the SGR considering sandstone porosities of 1) 45%, 2) 25%, and 3) 5% and clay with a 50 to 50 % proportion of illite/mica (Figure 5) since changes in porosities impact directly over ρ_b, which in turn affects the radioactive response. The SGR radioactive intensity is lower as the ρ_b is higher (Schmoker, 1979).

These results show that considering K, U, Th, and SGR for the presented synthetic case improve the contrast to identify mineral mixtures that only regard SGR (in this case, illite/smectite and illite/mica), and this analysis can be generalized to other mixtures of associated minerals. Further, the nonlinear trend between SGR versus clay concentration depends on the rock's bulk density.

3.2 SGR forward modeling applied to core samples

3.2.1 Sample descriptions

We applied the SGR forward modeling to 44 core samples, of which 14 are from Well A and 8 from Well G (Sabinas and Burgos provinces, respectively, in Mexico), both corresponding to shale gas formations and 19 were taken from Well N (Cordilleras Mexicanas province) and 3 from Well Q (North Sea, Netherlands), both corresponding to clastic formations. The data considered for modeling are the concentrations of porosity, quartz, calcite, dolomite, pyrite, feldspars: K-feldspar and plagioclase, total clay: proportions of illite/smectite and illite/mica, kaolinite, chlorite, and kerogen (Table 3). The porosity was obtained from the petrophysical analysis, the mineralogical concentration was provided by thin section petrography and X-ray diffraction (XRD), and the kerogen concentration was calculated through the Total Organic Carbon (TOC) reported in geochemical data, considering that the kerogen concentration is approximately twice that of the TOC (Kethireddy *et al.*, 2014; Passey *et al.*, 2010; Schmoker, 1981). We consider kerogen for the gamma-ray forward modeling even though it is not a mineral because it has a high uranium concentration (Lüning and Kolonic, 2003). The ρ_b, SGR and K, U, and Th fractional abundances for each core sample were obtained from Well logs (Table 4).

The core samples from Well A correspond to a calcareous silty shale. The porosity measured is between 2.03 to 12.26%, saturated mainly by gas. The minerals present in the rock are quartz, calcite, dolomite, pyrite, K-feldspar, plagioclase, proportions of illite/smectite and illite/mica, kaolinite, and kerogen as an organic component which is the ranges of 0.58-12.22%. The

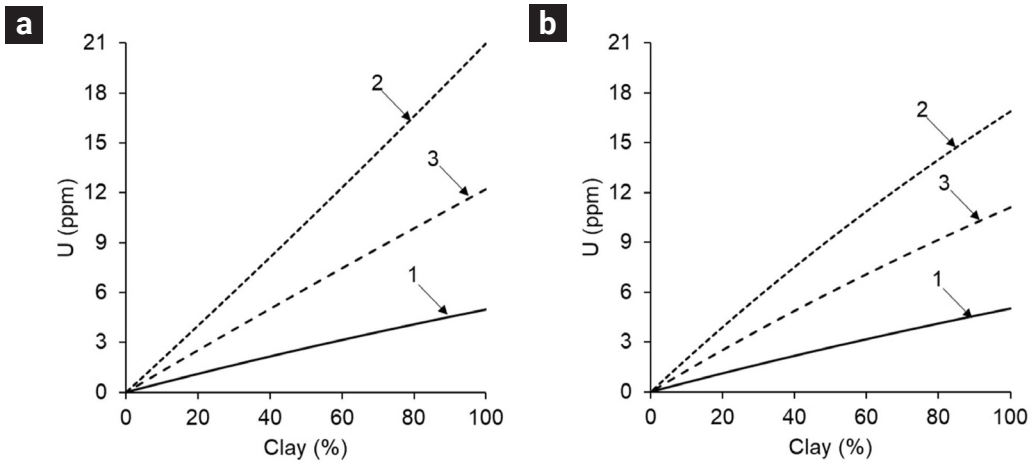

Figure 2. U content for mixtures of a) illite/smectite and b) illite/mica. a) U for the clay of illite (line 1), smectite (line 2), and 50 to 50% of illite/smectite (line 3). b) U for the clay of illite (line 1), mica (line 2), and 50 to 50% of illite/mica (line 3).

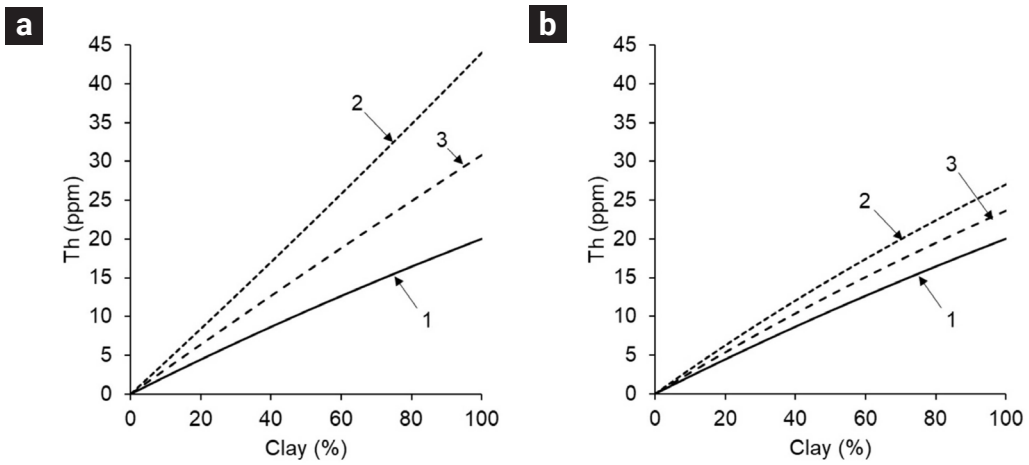

Figure 3. The content for mixtures of a) illite/smectite and b) illite/mica. a) Th for clay constituted illite (line 1), smectite (line 2), and 50 to 50% illite/smectite. b) Th for clay constituted by: illite (line 1), mica (line 2), and 50 to 50% of illite/mica (line 3).

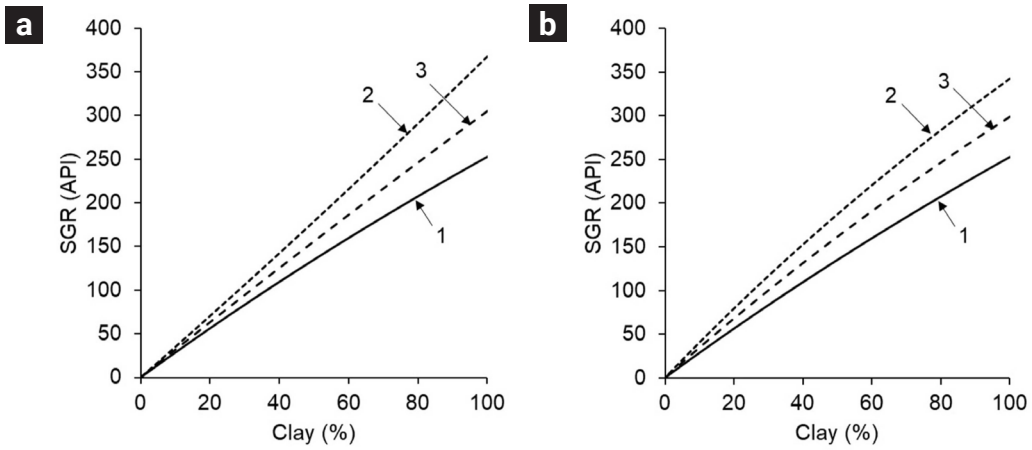

Figure 4. SGR modeled for mixtures of a) illite/smectite and b) illite/mica. a) SGR for a clay constituted by: illite (line 1), smectite (line 2), and 50 to 50% of illite/smectite (line 3). b) SGR for a clay constituted of illite (line 1), mica (line 2), and 50 to 50% of illite/mica (line 3).

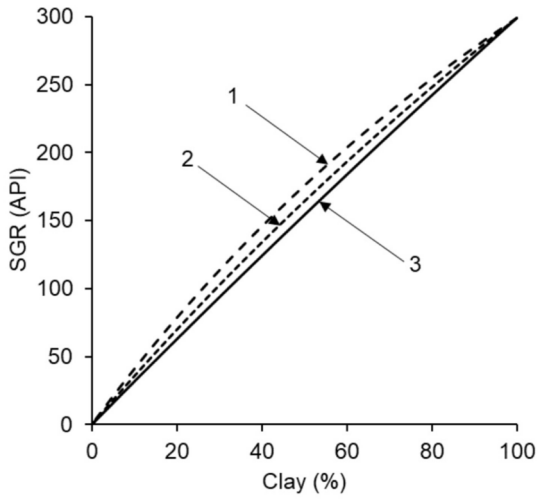

Figure 5. SGR modeled for a 50 to 50% proportion of illite/mica. Line 1: Sandstone with a density of 1.91 g/cm^3, 55% of quartz grains and 45% of pores; line 2: density range of 2.24 g/cm^3, 75% of quartz grains and 25% of pores; and line 3: a density of 2.56 g/cm^3, 95% of quartz grains and 5% of pores.

Table 3. Data from 44 core samples. Concentration in %. Void entries indicate the absence of the respective mineral.

Sample	Porosity	Quartz	Calcite	Dolomite	Pyrite	K-feldspar	Plagioclase	Illite/smectite	Illite/mica	Kaolinite	Chlorite	Total clay	Kerogen
Core from Well A													
A1	5.76	40.70	26.47	0.92	2.50	0.33	1.17	6.91	4.33	0.00	0.00	11.24	10.92
A2	2.99	3.27	83.05	0.77	0.00	0.00	0.00	2.02	2.69	4.62	0.00	9.34	0.58
A3	7.96	36.03	22.29	3.42	3.82	0.81	1.79	6.91	6.26	0.00	0.00	13.18	10.7
A5	7.520	33.72	21.51	2.67	3.07	0.32	1.62	10.43	7.60	0.00	0.00	18.03	11.54
A7	4.73	5.06	1.31	57.33	4.22	0.00	1.03	8.53	3.28	12.83	0.00	24.64	1.68
A8	2.03	6.68	78.50	0.00	1.16	0.00	0.68	4.36	3.29	2.23	0.00	9.87	1.08
A2-1	4.96	4.91	76.28	0.00	0.69	0.00	0.00	1.98	1.72	0.52	0.00	4.22	8.94
A12	7.71	39.54	17.54	0.50	3.72	1.16	2.07	10.42	7.86	0.00	0.00	18.28	9.48
A3-1	6.42	37.79	19.15	2.69	5.88	0.25	1.93	9.83	6.47	0.00	0.00	16.29	9.60
A16	8.44	42.79	12.37	1.29	3.80	0.24	1.78	9.46	9.14	0.00	0.00	18.60	10.68
A18	8.50	46.05	12.88	0.32	3.54	0.56	2.17	7.33	7.65	0.00	0.00	14.97	11.00
A4-1	12.26	47.91	10.64	0.23	2.94	0.30	1.51	5.96	6.04	0.00	0.00	12.00	12.22
A18A	6.07	36.71	12.77	10.32	6.85	0.00	1.52	8.97	7.44	0.00	0.00	16.41	9.34
A18B	10.10	47.95	10.95	2.94	2.86	0.57	1.63	8.90	5.96	0.00	0.00	14.87	8.14
Core from Well G													
G2 ET	8.83	16.56	38.85	2.61	0.87	3.49	6.10	13.07	6.97	0.00	2.61	22.65	4.04
G3 ET	9.65	14.23	51.05	0.84	0.84	1.67	2.51	10.04	2.51	0.00	0.00	12.55	6.66
G4 ET	8.60	12.81	55.52	1.71	5.12	1.71	3.42	4.27	0.85	0.00	0.00	5.12	5.98
G5 ET	9.05	14.86	49.53	0.83	1.65	0.83	3.30	5.78	4.95	0.00	0.83	11.56	8.40
G6 ET	9.57	8.32	59.94	0.00	0.83	1.66	3.33	4.99	4.19	0.00	0.00	9.16	7.18
G7 ET	9.28	23.76	40.14	1.64	1.64	1.64	3.28	6.55	2.46	0.00	0.82	9.38	8.8
G8 ET	10.08	19.72	33.92	2.37	3.16	1.58	3.94	9.47	3.16	0.00	1.58	14.20	11.04
G9 ET	9.17	15.30	36.25	0.81	4.03	1.61	4.83	12.08	4.83	0.00	0.81	17.72	10.28
Core from Well N													
N1H1A	9.31	22.49	25.12	6.53	0.27	6.53	17.87	-	-	-	-	12.06	0.00
N1H11	30.26	12.83	41.15	1.53	0.35	1.95	5.30	-	-	-	-	6.63	0.00
N1H12	29.89	14.65	37.51	2.17	0.35	1.89	6.66	-	-	-	-	6.87	0.00
N1H17	23.35	18.78	26.21	1.38	0.77	3.53	11.88	-	-	-	-	14.10	0.00
N1H18	22.72	19.39	43.36	1.93	1.24	1.47	5.33	-	-	-	-	6.57	0.00
N1H20	24.21	20.69	23.95	1.67	0.45	3.79	12.58	-	-	-	-	12.66	0.00
N1H21	23.06	20.16	26.70	1.69	0.46	3.23	11.54	-	-	-	-	13.16	0.00
N1H22	25.38	21.12	23.13	2.16	0.45	3.36	13.73	-	-	-	-	10.67	0.00
N3H2	26.48	17.35	25.00	2.35	1.25	2.06	9.19	-	-	0.59	1.91	16.32	0.00
N3H4	25.30	13.15	6.87	5.53	2.32	4.48	12.62	-	-	1.49	3.21	29.73	0.00
N3H5	24.95	20.19	7.43	8.93	1.65	6.15	16.36	-	-	0.75	1.95	14.33	0.00
N3H7	31.02	17.59	9.10	9.66	1.38	4.41	14.76	-	-	0.89	2.14	12.07	0.00
N3H8	32.05	17.06	6.18	8.15	1.36	4.28	15.08	-	-	1.01	2.25	15.83	0.00
N3H10	24.12	24.05	6.75	5.92	1.52	6.68	18.67	-	-	0.76	1.89	12.29	0.00
N3H13	23.88	26.72	7.54	6.55	1.38	6.62	17.96	-	-	0.84	2.06	8.91	0.00
N3H15	3.97	26.89	25.83	4.90	2.11	6.72	20.55	-	-	0.77	2.11	9.03	0.00
N3H16	23.09	16.46	8.00	4.92	1.69	6.54	13.61	-	-	1.00	2.70	25.69	0.00
N3H25	11.90	24.40	19.47	4.93	1.94	6.34	14.17	-	-	0.88	2.82	16.30	0.00
N3H26	13.16	19.80	16.93	5.21	1.74	7.38	16.85	-	-	0.95	2.86	18.93	0.00
Core from Well Q													
Q4V	20.80	78.41	0.00	0.00	0.00	0.00	0.00	-	-	0.00	0.00	0.79	0.00
Q38V	16.30	79.52	0.00	0.00	0.00	0.00	0.00	-	-	0.00	0.00	4.19	0.00
Q49V	18.90	77.05	0.00	0.00	0.00	0.00	0.00	-	-	0.81	0.00	4.06	0.00

Table 4. Density ρ_b, SGR, K, U and Th measured from well logs corresponding to the 44 core samples.

Sample	$\rho\left(\frac{g}{cm^3}\right)$	SGR (API)	K (%)	U (ppm)	Th (ppm)
Core from Well A					
A1	2.38	77.41	0.91	5.87	3.99
A2	2.69	48.00	0.42	3.61	3.10
A3	2.45	61.17	0.64	4.58	3.58
A5	2.44	50.58	0.37	4.57	2.04
A7	2.76	97.74	0.49	10.21	2.05
A8	2.68	144.68	0.46	14.80	4.74
A2-1	2.48	130.68	0.85	12.17	4.92
A12	2.54	91.82	1.24	6.74	4.53
A3-1	2.47	65.79	1.03	4.98	2.37
A16	2.67	95.41	1.32	6.42	5.72
A18	2.43	69.35	0.85	5.02	3.92
A4-1	2.44	88.92	0.85	7.09	4.66
A18A	2.36	92.37	1.02	9.85	3.29
A18B	2.43	65.56	0.72	5.44	2.64
Core from Well G					
G2 ET	2.76	32.93	0.88	1.39	1.95
G3 ET	2.55	62.01	1.07	3.07	5.10
G4 ET	2.50	63.47	0.70	4.24	4.57
G5 ET	2.46	64.96	0.59	4.69	4.48
G6 ET	2.45	70.29	0.68	5.14	4.57
G7 ET	2.44	70.01	0.51	5.82	3.83
G8 ET	2.48	71.24	0.54	5.94	3.80
G9 ET	2.51	59.53	0.58	3.84	4.87
Core from Well N					
N1H1A	2.29	69.04	1.70	4.21	8.78
N1H11	2.26	48.94	1.35	2.70	6.78
N1H12	2.23	58.93	1.61	3.03	8.60
N1H17	2.25	53.33	1.49	2.69	7.88
N1H18	2.24	53.23	1.65	2.35	8.53
N1H20	2.24	56.41	1.49	2.73	8.59
N1H21	2.27	49.78	1.27	2.35	7.70
N1H22	2.26	60.70	1.34	2.71	9.70
N3H2	2.24	56.18	1.97	2.73	8.50
N3H4	2.23	42.18	1.60	2.68	5.12
N3H5	2.22	40.59	1.65	2.71	4.67
N3H7	2.35	34.09	1.57	2.10	4.27
N3H8	2.38	33.18	1.48	2.01	4.22
N3H10	2.36	31.11	1.58	1.41	4.89
N3H13	2.30	39.76	1.61	1.89	6.08
N3H15	2.29	38.64	2.01	2.13	5.33
N3H16	2.39	39.82	1.98	2.52	4.84
N3H25	2.26	44.65	1.78	2.92	5.25
N3H26	2.32	44.72	1.83	2.74	5.62
Core from Well Q					
Q4V	2.29	10.03	0.17	0.52	4.73
Q38V	2.42	52.76	1.08	3.27	8.84
Q49V	2.27	10.70	0.15	0.89	0.85

percentage of smectite in the illite/smectite ratio is between 10-20% for the core samples A2, A3, A16, A18, A18A, and A18B, 70-80% for A7, A8, and A12, and is not specified for A1, A2-1, A3-1, and A4-1. The ratio for illite/mica is not set for any of the core samples.

The lithology of the core samples from Well G corresponds to silty argillaceous limestone. The rock porosity measured is between 8.6 to 10.08%. The minerals that conform to the rock are quartz, calcite, dolomite, pyrite, K-feldspar, plagioclase, proportions of illite/smectite and illite/mica, and chlorite. The presence of kerogen is in the range of 4.04-11.04%. The percentage of smectite in the illite/smectite ratio is between 30-50%, but the percentage of mica in the illite/mica ratio is not specified for all core samples.

Set data from Well N comprises two subsets: 8 core samples for N1 and 11 for N3. The lithology of both subsets corresponds to fine-grained sandstone cemented by calcareous material, and there is the presence of clay minerals. The porosity measured is between 3.97 to 32.05%. The minerals present in N1 are quartz, calcite, dolomite, pyrite, K-feldspar, plagioclase, and clay minerals, where their type is not specified. N3 has the same minerals as N1, but for clay minerals, it is reported: proportions of illite/smectite and illite/mica where the respective concentration and ratio are not specified, kaolinite and chlorite.

The lithology for the core samples from Well Q comprised sandstone, shales, silty sandstone, claystone, and sandy claystone. The porosity measured is 20.8%, 16.30%, and 18.90% for Q4V, Q38V, and Q49V, respectively. The minerals reported are quartz, clay minerals, being its type not specified, and kaolinite.

3.2.2 Core-well comparison

The data used in the forward modeling of the 44 core samples have different scales, i.e., XRD is given in microns (μm), information from thin petrographic sections is in millimeters (mm), petrophysical analysis is performed on centimeter-scale samples, and Well logs are recorded on the centimeter scale. Therefore, to analyze if the sample is representative of the entire rock due to heterogeneity of the medium, we calculate the density ρ_{bc} considering the minerals and fluid concentration in the respective core samples and their respective densities (Table 1), and we compare it with their corresponding bulk densities ρ_b obtained from Well logs. We use density as a reference point because it is an intensive and isotropic property, and the intrinsic densities of each component are not scale-dependent.

Figure 6a shows a good fit for samples A1, A2, A3, and A3-1 for Well A. For Well G, the fit is good for G4 ET, G5 ET, G6 ET, and G7 ET samples (Figure 6b). Sub-set N1 of well N, N1H12, N1H20, N1H21, and N1H22 present a minor misfit (Figure 6c) but a poor correlation for the N3 set (Figure 6d). Samples Q4V and Q49V fit well for Well Q, but Q38V mismatch (Figure 6e). The misfit between ρ_b and ρ_{bc} is a relevant factor to consider as it will affect the modeling results.

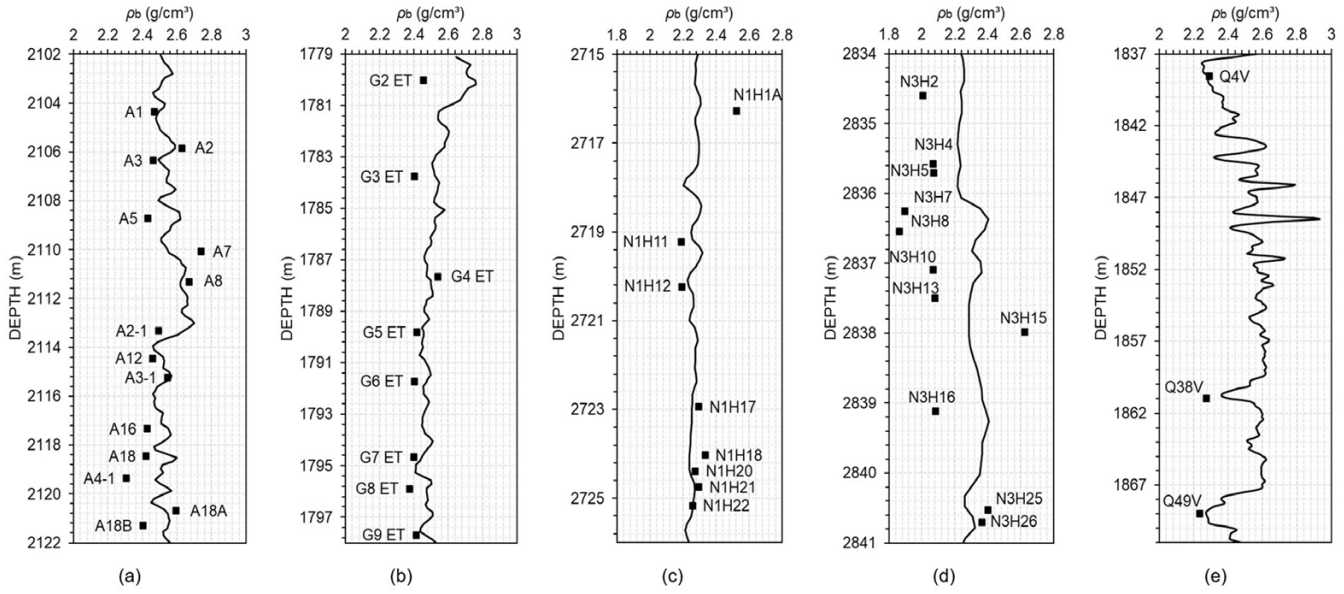

Figure 6. Misfit analysis between ρ_b from Well logs (black line) versus ρ_{bc} (squares) recalculated from core samples for the Wells: (a) A, (b) G, (c) Sub-set N1 of set N, (d) sub-set N3 of set N, and (e) Q. We consider that the misfits are associated to the variations of the sample scales and the heterogeneity of the medium.

3.2.3 Discussion

We choose for the radioactive minerals those fractional abundances of K, U, and Th that resulted in a very good fit between the simulated (K_s, U_s, Th_s, SGR_s) and the well log measured values of K_o, U_o, Th_o, and SGR_o given in Table 1.

The considered radioactive minerals from the core samples for Well A are calcite, dolomite, K-feldspar, plagioclase, mixtures of illite/smectite and illite/mica, kaolinite, and kerogen. Since the proportion of the illite/smectite mixture was unavailable for these samples, it was assumed to lie in 10% - 20% or 70% - 80%. We assigned a 50 to 50% ratio for the illite/mica mixture. For Well G, the radioactive minerals are calcite, dolomite, K-feldspar, plagioclase, illite/smectite, illite/mica, chlorite, and kerogen. Since the illite/smectite and illite/mica mixtures were not specified, we assigned 50 to 50% ratios. The radioactive considered minerals in the N1 core sample are calcite, dolomite, K-feldspar, plagioclase, and mica. For N3, the radioactive minerals considered are calcite, dolomite, K-feldspar, plagioclase, illite, smectite, kaolinite, and chlorite. The considered radioactive minerals for well Q are mica and kaolinite. We neglect quartz as a radioactive mineral in all the samples because it does not contribute significantly to the SGR modeled.

We analyze the results separately for K, U, Th, and SGR due to the scale differences of their units. We used the positive Pearson correlation coefficient (r) to measure the misfit between the simulated and observed data, where $r = 0$ means zero correlation, $0 < r <= 0.3$ represents a weak correlation, $0.3 < r <= 0.6$ is associated with a moderate correlation, $0.6 < r <= 0.9$ is a strong correlation, and $r > 0.9$ corresponds to a very high correlation (Akoglu, 2018; Taylor, 1990).

We used Equation 12 and the parameters listed in Table 5 for the respective radioactive minerals present in the five sample sets to simulate K (K_s). K observed (K_o) was established directly from the Well log (Figure 7). The relationship between K_s and K_o correlates with $r = 0.82$.

Equation 13 and the values indicated in Table 6 were used for the respective radioactive minerals present in the five sample sets to simulate U (U_s). U observed (U_o) was taken directly from the respective well logs (Figure 8). The correlation between U_s and U_o is $r = 0.83$.

We model Th (Th_s) with Equation 14 and the values indicated in Table 7 for the respective radioactive minerals in the five sample sets. Th observed (Th_o) is taken directly from the Well log (Figure 9). The misfit between Th_s and Th_o correlates with $r = 0.61$.

The correlation between SGR simulated modeled with Equation 10 (SGR_s) and SGR observed taken from the Well log (SGR_o) has a high correlation of $r = 0.57$ (Figure 10).

The forward modeling results show a strong correlation between simulated and observed data for K, U, and Th but a moderate correlation for SGR. The misfit is due not only to the difference between ρ_{bc} and ρ_c but also because we are assuming fixed concentrations and ratios for illite/smectite and illite/mica in set data A, B, and N3, and the clay is mica for N1 and Q.

Joint inversion with SGR, K, Th, and U was applied to improve the correlation by finding the concentrations of clay minerals that are not explicitly specified in the core information. The condition to be met is that the sum of the clay minerals must be equal to the total clay reported in each data set.

Joint inversion process minimizes the cost function relating to the observed and simulated data:

$$F_{min}=\|\mathbf{W}_d\,(\mathbf{d}(\mathbf{m})-\mathbf{d}_o)\|^2. \quad (15)$$

Table 5. Fractional *K* (%) abundance for the respective radioactive minerals used in the five core sample sets. Void entries indicate the absence of the mineral.

Mineral	A	G	N1	N3	Q
Calcite	1.9	1.9	1.9	1.9	-
Dolomite	0	0	0	1.5	-
K-feldspar	7	7	7	7	-
Plagioclase	3	3	3	3	-
Mica	40	1	50	20	50
Illite	15	10	-	20	-
Smectite	6	6	-	7	-
Kaolinite	20	-	-	44	50
Chlorite	-	5	-	5	-
Kerogen	0	0	-	-	-

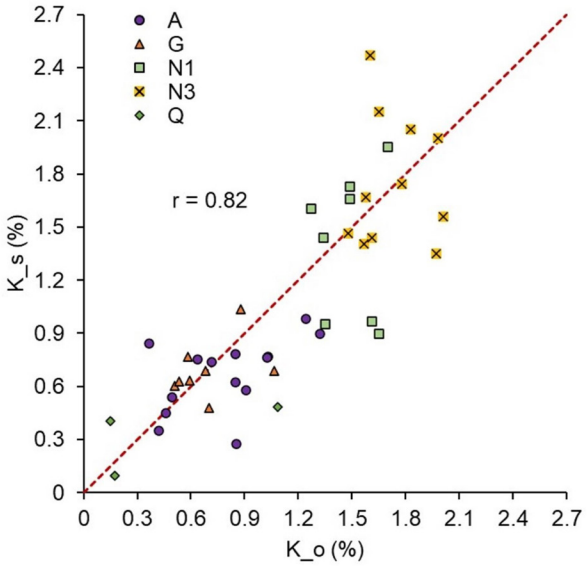

Figure 7. The general correlation between the K_s and K_o for the core samples: A (purple circles), G (red triangles), N1 (green squares), N3 (yellow squares), and Q (green diamonds). The Pearson correlation coefficient (r) is 0.82.

Table 6. Fractional *U* (ppm) abundance for the respective radioactive minerals used in the five core sample sets. Void entries indicate the absence of the mineral.

Mineral	A	G	N1	N3	Q
Calcite	10	2.5	3.5	6	-
Dolomite	10	10	8	10	-
K-feldspar	0.2	0.2	3	0.2	-
Plagioclase	0.02	0.02	5	0.02	-
Mica	5	5	5	4	40
Illite	5	1	-	3.5	-
Smectite	21	1	-	9	-
Kaolinite	1	-	-	1	1
Chlorite	-	0	-	0	-
Kerogen	66	62.5	-	-	-

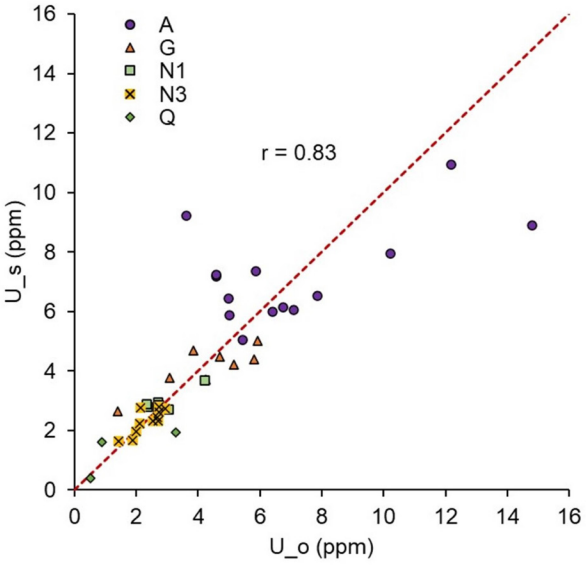

Figure 8. The general correlation between the U_s and U_o for the core sample sets: A (purple circles), G (red triangles), N1 (green squares), N3 (yellow squares), and Q (green diamonds). The Pearson correlation coefficient (r) is 0.83.

Table 7. Fractional abundance of *Th* (ppm) for the respective radioactive minerals used in the five core sample sets. Void entries indicate the absence of the mineral.

Mineral	A	G	N1	N3	Q
Calcite	1.9	1.9	1.9	1.9	-
Dolomite	0	0	0	1.5	-
K-feldspar	7	7	7	7	-
Plagioclase	3	3	3	3	-
Mica	40	1	50	20	50
Illite	15	10	-	20	-
Smectite	6	6	-	7	-
Kaolinite	20	-	-	44	50
Chlorite	-	5	-	5	-
Kerogen	0	0	-	-	-

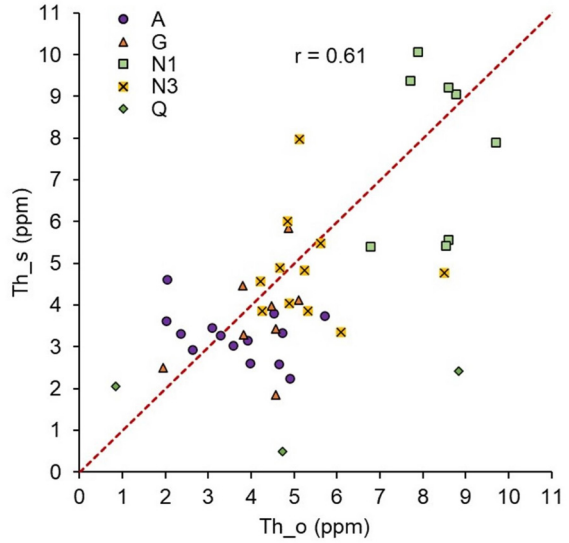

Figure 9. The general correlation between the Th_s and Th_o for the core sample sets: A (purple circles), G (red triangles), N1 (green squares), N3 (yellow squares), and Q (green diamonds). The Pearson correlation coefficient (r) is 0.61.

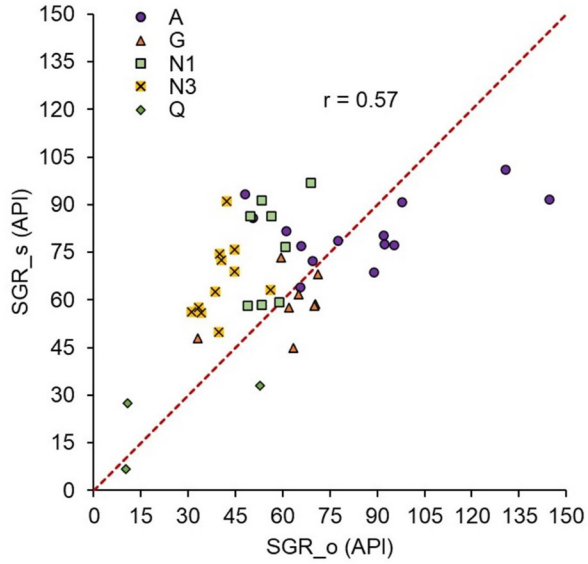

Figure 10. The general correlation between the SGR_s and SGR_o for the core sample sets: A (purple circles), G (red triangles), N1 (green squares), N3 (yellow squares), and Q (green diamonds). The Pearson correlation coefficient (r) is 0.57.

The vector $\mathbf{d}(\mathbf{m})$ contains the simulated data, and $\mathbf{d}_o$ the observed data:

$$\mathbf{d}(\mathbf{m})=[SGR\_s,K\_s,Th\_s,U\_s]^T, \quad (16)$$

$$\mathbf{d}_o=[SGR\_o,K\_o,Th\_o,U\_o]^T, \quad (17)$$

$\mathbf{W}_d$ represents the diagonal matrix of weight coefficient to account for different error scales and distribution of each input data and is calculated as the inverse of the standard deviation. The Nelder-Mead method was used to obtain the solution to the cost function optimization problem which gives a stable global minimum without the need to calculate functional derivatives (Nelder and Mead, 1965). The r improved to a strong correlation of 0.87, 0.85, 0.65, and 0.69 for K (Figure 11), U (Figure 12), Th (Figure 13), and SGR (Figure 14), respectively.

The correlation is further improved when joint inversion supports the forward modeling. Table 8 summarizes the correlation r for forward modeling with non-joint and joint inversion for the unknown mixture ratios.

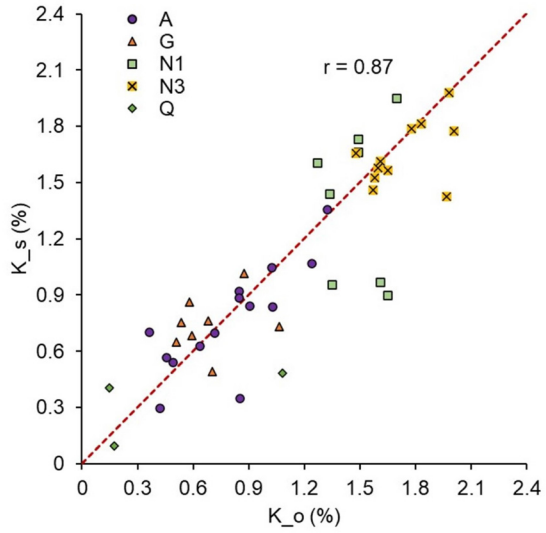

Figure 11. The correlation between the K_s and K_o improved after inverting for the unknown mixture ratios for core sample sets: A (purple circles), G (red triangles), N1 (green squares), N3 (yellow squares), and Q (green diamonds). The Pearson correlation coefficient (r) attained a value of 0.87.

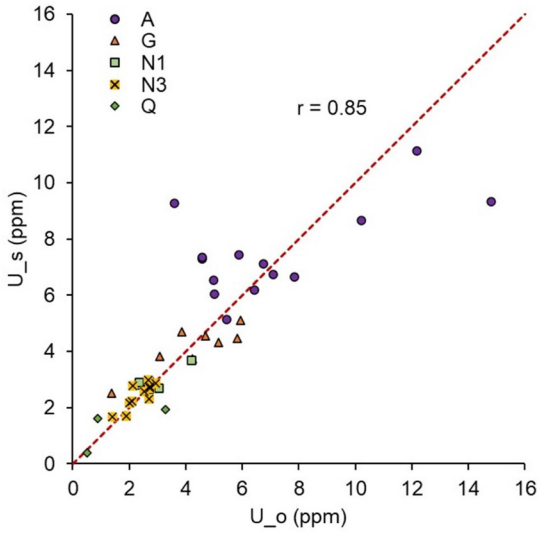

Figure 12. The correlation between the U_s and U_o improved after inverting for the unknown mixture ratios for core sample sets: A (purple circles), G (red triangles), N1 (green squares), N3 (yellow squares), and Q (green diamonds). The Pearson correlation coefficient (r) attained a value of 0.85.

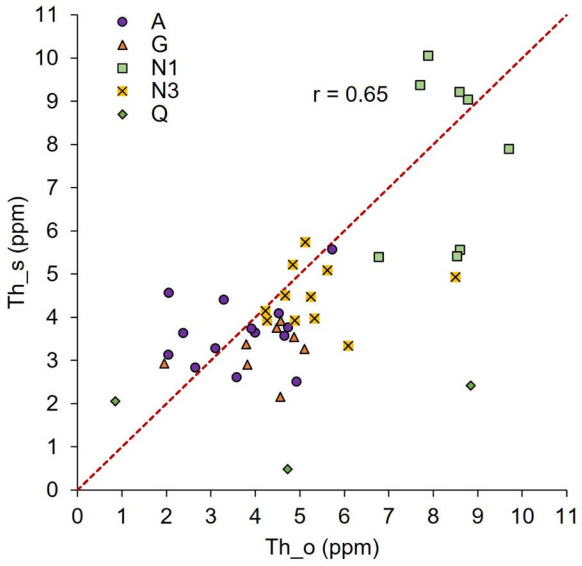

Figure 13. The correlation between the Th_s and Th_o improved after inverting for the unknown mixture ratios for core sample sets: A (purple circles), G (red triangles), N1 (green squares), N3 (yellow squares), and Q (green diamonds). The Pearson correlation coefficient (r) attained a value of 0.65.

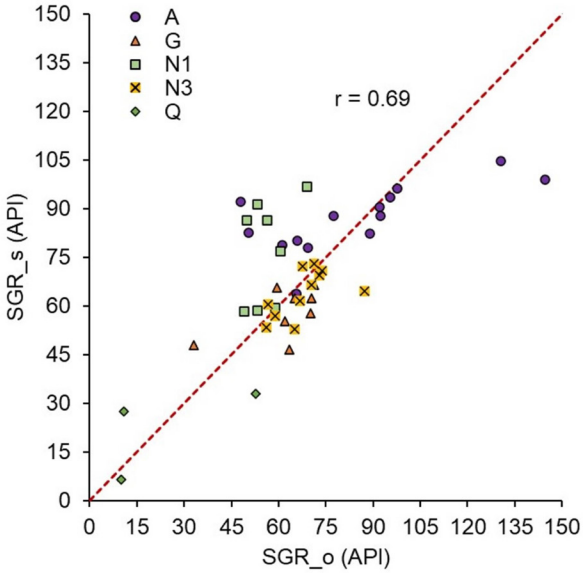

Figure 14. The correlation between the SGR_s and SGR_o improved after inverting for the unknown mixture ratios for core sample sets: A (purple circles), G (red triangles), N1 (green squares), N3 (yellow squares), and Q (green diamonds). The Pearson correlation coefficient (r) attained a value of 0.69.

Table 8. Pearson correlation coefficients (r) comparison between forward modeling with non-joint inversion and supported by the joint inversion.

	Non-joint inversion	Joint inversion
K (%)	0.82	0.87
U (ppm)	0.83	0.85
Th (ppm)	0.61	0.65
SGR (API)	0.57	0.69

4. Conclusions

We presented a new approach to improve SGR forward modeling by considering minerals with K^{40}, Th^{232}, and U^{238} content as radioactive sources that are uniformly distributed in the rock; furthermore, the measured radioactivity is proportional to the concentration of radioactive minerals, and the radioactivity is only attenuated by absorption of gamma-rays. The forward modeling approach foundation is based on radioactive attenuation theory.

The SGR forward modeling was tested in a synthetic rock of sandstone with clay minerals and brine-saturated pores to analyze the sensitivity to variations of illite/smectite and illite/mica mixtures over SGR. The results show that illite/smectite and illite/mica ratio variations impact the simulated K, U, Th, and SG. Thus, to determine the corresponding mixtures, it is recommended to include K, U, and Th in addition to SGR in the forward modeling. Moreover, the nonlinear trend between SGR versus clay concentration depends on the rock's bulk density.

Finally, we tested the proposed modeling for 44 core samples from four wells, where 22 correspond to shale gas and 22 to clastic formation. We evaluated the misfit using the Pearson correlation coefficient. For K, U, and Th, a strong correlation of 0.82, 0.83, and 0.61, respectively, is obtained, and a moderate correlation of 0.57 for SGR. However, the respective correlations improved to a strong correlation of 0.87, 0.85, 0.65, and 0.69 after joint inversion for the unknown illite/smectite and illite/mica mixtures. The strong correlation between the simulated and observed K, U, Th, and SGR support the viability of the proposed SGR forward modeling approach.

The proposed approach allows us to dispense with empirical equations and can improve petrophysical evaluations of oil reservoirs by quantifying the concentration of radioactive minerals, even distinguishing between clays and the presence of feldspars in hot sands, and the organic matter content can be calculated in formations with organic richness. Furthermore, it can be useful to identify the abundance of fractures in carbonate formations, since with the proposed approach a lower density with a higher radiative response can be modeled.

5. Acknowledgments

The author Francisco Miguel Lechuga Lagos expresses his gratitude to CONACYT for the scholarship granted to him and to the Postgraduate Program of Instituto Mexicano del Petróleo for the support provided. The authors thank Project 205862 of the SENER Hidrocarburos Sectoral Fund for allowing them to use information in developing this paper. NLOG.NL is also acknowledged for the information provided on its website. Special thanks to all the two anonymous reviewers and to Oscar C. Valdiviezo-Mijangos associated editor for their critical and constructive comments that helped to improve the manuscript quality, the anonymous reviewers and the associate editor for their important comments and technical corrections to improve this paper.

6. References

Akoglu, H. (2018). User's guide to correlation coefficients. *Turkish Journal of emergency medicine*, 18(3), 91–93. doi: 10.1016/j.tjem.2018.08.001

Adams, J. A. & Weaver, C. E. (1958). Thorium-to-uranium ratios as indicators of sedimentary processes: example of concept of geochemical facies. *AAPG Bulletin*, 42(2):387–430. doi: 10.1306/0BDA5A89-16BD-11D7-8645000102C1865D

Alharthy, N., Al Kobaisi, M., Torcuk, M. A., Kazemi, H., and Graves, R. (2012). *Physics and Modeling of Gas Flow in Shale Reservoirs*—paper presented at the Abu Dhabi International Petroleum Exhibition and Conference held in Abu Dhabi, UAE, 11-14 November 2012. doi: 10.2118/161893-MS

Bassiouni, Z. (1994). Gamma Ray Log. In Schenewerk, P. A. & Pert, D. M. (Eds.), *Theory, measurement, and interpretation of Well logs* (Vol. 4, pp. 146–158). Society of Petroleum Engineers.

Belknap, W. B., Dewan, J. T., Kirkpatrick, C., Mott, W. E., Pearson, A., and Rabson, W. (1959). Api calibration facility for nuclear logs, drilling and production practices API, reprinted in Gamma-Ray, Neutron and Density Logging: SPWLA Reprint volume (1978), Soc. Prof. Well Log Analysts, Houston, Texas (1959).

Bigelow, E. L. (2002). Determining Porosity, Formation Factor, and Shaliness. In Baker Atlas (Eds.) *Introduction to wireline log analysis* (pp. 137-184). Baker Hughes.

Bohacs, K. M. (1998). Contrasting expressions of depositional sequences in Mudrocks from Marine to non Marine Environs. In: Schieber, J., Zimmerle, W., Sethi, P. (Eds.), Shales and Mudstones (Vol. 1): Basin Studies, Sedimentology and PaleontologySchweizerbart'sche Verlagsbuchhandlung, Stuttgart, pp. 33-78

Bohacs, K. M. and Miskell-Gerhardt, K. (1998). Well-log expression of lake strata; controls of lake-basin type and provenance, contrasts with marine strata—paper presented at the AAPG Annual Meeting Expanded Abstracts, Tulsa, Oklahoma, p. A78.

Brannon, H. and Osoba, J. (1956). Spectral gamma-ray logging. Transactions of the AIME, 207(01): pp. 30-35.

Chudi, O. and Simon, R. (2012). Petrophysical characterization of radioactive sands-integrating well logs and core information: A case study in the Niger delta. Paper presented at the Nigeria Annual International Conference and Exhibition, Lagos, Nigeria, August 2012. doi: 10.2118/163020-MS

Clavier, C., Hoyle, W., and Meunier, D. (1971). Quantitative interpre-

tation of thermal neutron decay time logs: part I fundamentals and techniques. *Journal of Petroleum Technology*, 23(06): 743-755. doi: 10.2118/2658-A-PA

Day-Stirrat, R. J., Hillier, S., Nikitin, A., Hofmann, R., Mahood, R., and Mertens, G. (2021). Natural gamma-ray spectroscopy (NGS) as a proxy for the distribution of clay minerals and bitumen in the cretaceous McMurray formation, Alberta, Canada. *FUEL*, 288. doi: 10.1016/j.fuel.2020.119513

Duderstadt, J. J. and Hamilton, L. J. (1976). Neutron Transport. In Wiley (Ed.), *Nuclear reactor analysis* (pp. 103–148). John Wiley & Sons.

Ehsan, M. S., Rahman, M. F., Tabassum, N., Prodhan, M. M. H., Pervin, S., Siraz, M. M., Rahman, A. M., Yeasmin, S., & Mahal, S. F. (2019). The activity concentration of radionuclides (226ra, 232nd, and 40k) in soil samples and associated health hazards in Natore, Kushtia, and Pabna districts of Bangladesh. *Journal of Bangladesh Academy of Sciences*, 43(2):169–180. doi: 10.3329/jbas.v43i2.45738

Ellis, D. V. and Singer, J. M. (2007). Gamma Ray Devices. In Springer (Ed.) *Well logging for earth scientists* (Vol. 692, pp. 267–288). Springer.

Evans, R. D. (1955). Attenuation and Absorption of Electromagnetic Radiation. In McGraw-Hill (Ed.) *The atomic nucleus* (pp. 711–745). McGraw-Hill New York.

Fertl, W. H. (1979). Gamma ray spectral data assists in complex formation evaluation. *Petrophysics*, 20(05).

Fertl, W. H., Chilingarian, G. V., & Yen, T. (1982). Use of natural gamma ray spectral logging in evaluation of clay minerals. *Energy Sources*, 6(4):335–360. doi: 10.1080/00908318208946036

Ge, X., Fan, Y., Cao, Y., Li, J., Cai, J., Liu, J., and Wei, S. (2016). Investigation of organic related pores in unconventional reservoir and its quantitative evaluation. *Energy & Fuels*, 30(6):4699–4709. doi: 10.1021/acs.energyfuels.6b00590

Gonzalez, J., Lewis, R., Hemingway, J., Grau, J., Rylander, E., & Schmitt, R. (2013). Determination of formation organic carbon content using a new neutron-induced gamma ray spectroscopy service that directly measures carbon—paper presented at the SPWLA 54th annual logging symposium.

Hertzog, R., Colson, L., Seeman, O., O'Brien, M., Scott, H., McKeon, D., Wraight, P., Grau, J., Ellis, D., Schweitzer, J., *et al.* (1989). Geochemical logging with spectrometry tools. *SPE Formation Evaluation*, 4(02):153–162. doi: 10.2118/16792-PA

Huang, R., Wang, Y., Cheng, S., Liu, S., and Cheng, L. (2015). Selection of logging-based TOC calculation methods for shale reservoirs: A case study of the Jiaoshiba shale gas field in the Sichuan basin. *Natural Gas Industry B*, 2(2-3):155–161. doi: 10.1016/j.ngib.2015.07.004

Huntley, D. J. & Baril, M. (1997). The K content of the K-feldspars being measured in optical dating or in thermoluminescence dating. *Ancient Tl,* 15(1):11–13.

Jacobi, D. J., Gladkikh, M., LeCompte, B., Hursan, G., Mendez, F., Longo, J., Ong, S., Bratovich, M., Patton, G. L., & Shoemaker, P. (2008). Integrated petrophysical evaluation of shale gas reservoirs—paper presented at the CIPC/SPE Gas Technology Symposium 2008 Joint Conference, Calgary, Alberta, Canada, June 2008. doi: 10.2118/114925-MS

Kethireddy, N., Chen, H., & Heidari, Z. (2014). Quantifying the effect of kerogen on resistivity measurements in organic-rich mudrocks. *Petrophysics*-The SPWLA Journal of Formation Evaluation and Reservoir Description, 55(02):136–146.

Killeen, P. (1982). Gamma-ray logging and interpretation. In Fitch A. A. (Ed.) *Developments in Geophysical Exploration Methods-3* (pp. 95–150). Springer.

Larionov, W. W. (1969). Method of natural radioactivity of rocks. In Nedra (Ed.) Borehole radiometry (pp. 74-129). Nedra, Moscow

Lewis, R., Ingraham, D., Pearcy, M., Williamson, J., Sawyer, W., & Frantz, J. (2004). New evaluation techniques for gas shale reservoirs—paper presented at the Reservoir symposium, Schlumberger, Houston, July 2004.

Lock, G. and Hoyer, W. (1971). Natural gamma-ray spectral logging. Paper presented at the SPWLA 12th Annual Logging Symposium, Dallas, Texas, May 1971.

Lüning, S. & Kolonic, S. (2003). Uranium spectral gamma-ray response as a proxy for organic richness in black shales: Applicability and limitations. *Journal of petroleum geology*, 26(2):153–174. doi: 10.1111/j.1747-5457.2003.tb00023.x

Mathis, G. L., Tittle, C., Rutledge, D., Mayer, R., & Ferguson, W. (1984). A spectral gamma ray (SGR) tool—paper presented at the SPWLA 25th Annual Logging Symposium, New Orleans, Louisiana, June 1984.

North, C. P. and Boering, M. (1999). Spectral gamma-ray logging for facies discrimination in mixed fluvial-eolian successions: A cautionary tale. *AAPG Bulletin*, 83(1):155–169. doi: 10.1306/00AA9A2A-1730-11D7-8645000102C1865D

Morys, M. (2020). *Spectral Gamma Ray Downhole Logging Tool* (U.S. Patent No. US 10,670,736 B2). Nabors Drilling Technologies USA, Inc., Houston, TX (US).

Morys, M. (2021). *Spectral Gamma Ray Downhole Logging Tool* (U.S. Patent No. US 11,119,226 B2). Nabors Drilling Technologies USA, Inc., Houston, TX (US).

Owen, J. D. (1966). A review of fundamental nuclear physics applied to gamma ray spectral logging. In *The Log Analyst*, 7(03).

Passey, Q., Creaney, S., Kulla, J., Moretti, F., & Stroud, J. (1990). A practical model for organic richness from porosity and resistivity logs. *AAPG Bulletin*, 74(12):1777–1794. doi: 10.1306/0C9B25C9-1710-11D7-8645000102C1865D

Passey, Q. R., Bohacs, K., Esch, W. L., Klimentidis, R., and Sinha, S. (2010). From oil-prone source rock to gas-producing shale reservoir–geologic and petrophysical characterization of unconventional shale-gas reservoirs—paper presented at the International Oil and Gas Conference and Exhibition in China, Beijing, China, June 2010. doi: 10.2118/131350-MS

Rhodes, D. & Mott, W. (1966). Quantitative interpretation of gamma-ray spectral logs. *Geophysics*, 31(2):410–418. doi: 10.1190/1.1439785

Russell, W. L. (1945). Relation of radioactivity, organic content, and sedimentation. *AAPG Bulletin*, 29(10):1470–1493. doi: 10.1306/3D933796-16B1-11D7-8645000102C1865D

Rutherford, E., & Soddy, F. (1902). LXIV. The cause and nature of radioactivity. —Part I. *The London, Edinburgh, and Dublin Philosophical Magazine and Journal of Science*, 4(23), 569–585. doi: doi.org/10.1080/14786440209462881

Schmoker, J. W. (1979). Determination of organic content of Appalachian Devonian shales from formation-density logs: Geologic notes. *AAPG Bulletin*, 63(9):1504–1509. doi: 10.1306/2F9185D1-16CE-11D7-8645000102C1865D

Schmoker, J. W. (1981). Determination of organic-matter content of Appalachian Devonian shales from gamma-ray logs. *AAPG Bulletin*, 65(7):1285–1298. doi: 10.1306/03B5949A-16D1-11D7-8645000102C1865D

Schnyder, J., Ruffell, A., Deconinck, J.-F., and Baudin, F. (2006). Conjunctive use of spectral gamma-ray logs and clay mineralogy in defining late Jurassic–early Cretaceous palaeoclimate change (Dorset, UK). *Paleogeography, Palaeoclimatology, Palaeoecology*, 229(4):303–320. doi: 10.1016/j.palaeo.2005.06.027

Schön, J. H. (2015). Nuclear/Radioactive Properties. In Elsevier (Ed.) *Physical properties of rocks: Fundamentals and principles of petrophysics* (pp. 119 – 166). Elsevier.

Sen, S. K. (1959). Potassium content of natural plagioclases and the origin of antiperthites. The Journal of Geology, 67(5):479–495. doi: 10.1086/626602

Serra, O. (1984). Natural gamma-ray spectrometry. In Elsevier (Ed.) *Fundamentals of well-log interpretation, the acquisition of logging data* (pp. 113 – 133). Elsevier Science Pub. Co., Inc., New York, NY.

Serra, O., Baldwin, J., & Quirein, J. (1980). Theory, interpretation, and practical applications of natural gamma ray spectroscopy—paper presented at the SPWLA 21st Annual Logging Symposium, Lafayette, Louisiana, July 1980.

Steiner, S., Ahsan, S. A., Raina, I., Dasgupta, S., & Lis, G. P. (2016). Interpreting total organic carbon TOC in source rock oil plays—paper presented at the Abu Dhabi International Petroleum Exhibition & Conference, Abu Dhabi, UAE, November 2016. doi: 10.2118/183050-MS

Stieber, S. (1970). Pulsed neutron capture log evaluation-Louisiana Gulf coast—paper presented at the Fall Meeting of the Society of Petroleum Engineers of AIME, Houston, Texas, October 1970. doi: 10.2118/2961-MS

Swanson, V. E. (1960). Oil yield and uranium content of black shales. Technical report, Geological Survey, Washington, DC (USA).

Taylor, R. (1990). Interpretation of the correlation coefficient: a basic review. *Journal of diagnostic medical sonography*, 6(1), 35–39.

Tittman, J. (1966). Radiation logging: Physical Principles. Petroleum Engineering Conference. University of Kansas. In Lawson B. L. & Hoyer G. R. (Eds.) *Gamma Ray, Neutron and Density Logging* L. I. SPWLA

Van der Boor, M. (2014). Modelling the spectral gamma-ray log: The influence of provenance and selective transport: Master's thesis, Delft University of Technology.

Wang, J., Gu, D., Guo, W., Zhang, H., & Yang, D. (2019). Determination of total organic carbon content in shale formations with regression analysis. Journal of Energy Resources Technology, 141(1). doi: 10.1115/1.4040755

Wang, P., Chen, Z., Pang, X., Hu, K., Sun, M., and Chen, X. (2016). Revised models for determining TOC in shale play: Example from Devonian Duvernay shale, western Canada sedimentary basin. Marine and Petroleum Geology, 70:304–319. doi: 10.1016/j.marpetgeo.2015.11.023

Yuguchi, T., Yagi, K., Sasao, E., and Nishiyama, T. (2021). K-ar geochronology for hydrothermal k-feldspar within plagioclase in a granitic pluton: Constraints on timing and thermal condition for hydrothermal alteration. Heliyon, 7(4): e06750. doi: 10.1016/j.heliyon.2021.e06750

Geofísica Internacional (2024) **63-2**: 835 - 850

Vertical Electrical Sounding Technique as an Efficient and Rapid Tool for Groundwater Investigation in a Basaltic Environment at Kodana Station for the Shami goats. Case Study from Southern Syria.

Jamal Asfahani[*1]

Abstract

Geoelectrical survey was conducted by using vertical electrical sounding technique (*VES*) with adapting Schlumberger configuration, to locate and drill a borehole for groundwater extraction in the Kodana station for the Shami goats, Southern Syria. An integrated approach is proposed to increase the efficacy of the *VES* technique and to reduce the uncertainties and the high failures in locating and drilling a successful groundwater borehole. The approach is essentially based on analyzing the Dar-Zarrouk (D-Z) parameters with constraining several conditions to obtain the optimum hydro-geophysical model. The *1D* inversion quantitative interpretation of twelve *VES* sounding points and the (D-Z) parameters allowed the characterization of the study area in terms of depth and the Neogene pyroclastic basalt aquifer. The result showed that *VES* point (*V6*) has the optimum and favorable properties for drilling a successful borehole in the area. The *V6* has GPS coordinates of E: 3589614, N: 3301961 and Z: 770835m. The Neogene (fractured pyroclastic layer with rocks of basaltic composition) aquifer at this *V6* point is characterized by a thickness (h) of 217m, a resistivity (ρ) of 227Ωm, a transverse resistance (R) of 49259 Ωm^2, and an anisotropy parameter (λ) of 1.15. The advantages of the proposed approach are well proven and documented, in comparing with other techniques that require the combination of *VES* technique with other available geophysical techniques. The *VES* technique within the proposed approach is therefore recommended to be easily applied for groundwater investigations, and locating the suitable positions for drilling boreholes in similar worldwide basaltic environments.

Key words: *VES* technique, Groundwater, Dar-Zarrouk parameters, Shami goats station, Syria.

Resumen

Se realizó un estudio geoeléctrico utilizando la técnica de sondeo eléctrico vertical (VES), con una configuración de Schlumberger adaptativa para localizar y perforar un pozo para la extracción de agua subterránea en la estación Kodana para cabras Shami, en el sur de Siria. Se propone un enfoque integrado para aumentar la eficacia de la técnica VES y reducir la incertidumbre y errores serios en la localización y perforación del pozo. El enfoque se basa esencialmente en el análisis de los parámetros de Dar-Zarrouk (D-Z), restringiendo varias condiciones para obtener un modelo hidrogeofísico óptimo. La interpretación cuantitativa por inversión 1-D de doce puntos de sondeo VES y los parámetros D-Z permitieron caracterizar el área de estudio en términos de la profundidad de un acuífero en basaltos fracturados del Neógeno. Los resultados mostraron que el punto VES (V6) tenía las propiedades óptimas y favorables para perforar un pozo exitoso en el área. Las coordenadas GPS del V6 son E: 3589614, N: 3301961 y Z: 770m. El acuífero en la capa piroclástica fracturada con rocas de composición basáltica del Neógeno en este punto V6 tiene un espesor (h) de 217 m, una resistividad (ρ) de 227 Ωm, una resistencia transversal (R) de 49259 Ωm2 y un parámetro de anisotropía (λ) de 1.15. Las ventajas del enfoque propuesto están bien comprobadas y documentadas, comparadas con otras técnicas que requieren combinaciones de la técnica VES con otras técnicas geofísicas disponibles. Por lo tanto, se recomienda aplicar el enfoque propuesto de la técnica VES para la investigación de aguas subterráneas y para localizar los mejores sitios para perforar pozos en ambientes basálticos similares en todo el mundo.

Palabras clave: Sondeos Eléctricos Verticales *VES*, Aguas Subterráneas, Parámetros de Dar-Zarrouk, Estación de cabras Shami, Siria.

Received: November 22, 2022 ; Accepted: December 19, 2023 ; Published on-line: April 1, 2024.

Editorial responsibility: Dra. Claudia Arango-Galván

* Corresponding author: Jamal Asfahani. E-mail: **cscientific@aec.org.sy**
[1] Geology Department, Atomic Energy Commission, P.O. Box 6091, Damascus- Syria.

https://doi.org/10.22201/igeof.2954436xe.2024.63.2.1442

1. Introduction

Water is basic for agriculture domestic, industry and construction. The geoelectrical techniques are widely used to detect the aquifer saturated zone. Vertical electrical sounding technique (*VES*) with Schlumberger configuration is the favorable effective technique for groundwater investigation.

The present paper is a case study to show the application of *VES* technique for locating and drilling a successful well for groundwater water exploration at Kodana station for the Shami goats in southern Syria. The fat-tail triple purpose Awassi is the local breed in Syria and several neighboring countries in the Middle East. This breed is characterized by high adaptability and tolerance to stressful conditions and harsh environment. The Shami goat is seasonal and is native to Syria and has been introduced into some countries to improve the performance of the local breed. The locating and drilling of a borehole for groundwater in a basaltic environment is not an easy task, and surrounded by a lot of dangers if traditional *VES* technique is only applied, due to the sharp, rapid and brutal variations of basalt laterally and vertically.

Engineering geophysists in Syria have suffered a lot while groundwater exploration in basaltic environments, where high percentage failures in locating and drilling successful boreholes have been happened when applying only the traditional *VES* technique.

Internationally, all the geophysical efforts have been already concentrated and oriented towards supporting and combining the *VES* technique by another available geophysical technique.

Geoelectrical resistivity surveying techniques have been largely applied to determine the resistivity and thickness of layered structure for assessing the groundwater potential and successfully sitting boreholes in fractured unconfined aquifers (Muchingami *et al.*, 2012). This has been traditionally done in benefiting from one-dimensional (*1D*) vertical electrical sounding surveys. However, the solely use of *1D VES* do not furnish with comprehensive information for interpreting the subsurface hydro-geological features in a basaltic environments. The incorporation of two-dimensional (*2D*) geophysical techniques of electrical resistivity tomography (*ERT*) and (*VES*) for groundwater prospecting has been already proposed and often used to provide a more accurate interpretation of the basaltic subsurface hydro-geological features, from which potential successful borehole locations are identified (Muchingami *et al.*, 2012). Muchingami *et al.*, 2012 proposed the combination of *2D ERT* with *1D VES* to establish a subsurface resistivity model for evaluating the groundwater potential in the basaltic-greenstone formation of the Matsheumhlope well field in Bulawayo, Zimbabwe. Their proposed technique demonstrated its efficacy in comparing with the traditional *VES*,

in providing precise hydro-geophysical model for the study area, by which suitable borehole locations for long term groundwater prospecting were easily identified.

The combination of two geoelectrical techniques of the constant separation traversing (*CST*) and *VES* was also proposed and used to determine the occurrence of fractures as most probable borehole sites in the southwestern flank of Mt. Cameroon, under-lained by basalts. An electrical image of the subsurface can be created by such a complementary combination tools of *VES* and *CST*, to evaluate groundwater distribution in the aquifer, such as the uncertainties in subsurface exploration are considerably reduced, and the most reliable locations for groundwater exploitation are successfully determined (Lordon *et al.*, 2017).

An integrated combined geophysical approach using geoelectrical *VES* and gravity survey were recently proposed and practiced to study the effect of basement and hard rock on groundwater prospects in Mount Betung, Indonesia (Rustadi *et al.*, 2022). The presence of the hard rock (andesite and breccias) caused several drilling failures for groundwater extraction, and the misalignment of the groundwater aquifers. Such failures are basically related to the randomly scattered fractures.

Because of the difficulties mentioned and the high level of failure in locating groundwater wells in basaltic environments, we were formally assigned this challenging duty, for which *VES* technology was adopted by a new proposed integrated methodology and applied in a basaltic environment in the Kodana study area. It is to mention that the same study Kodana area, although being very small (1Km*1Km), has been previously several times surveyed by traditional *VES* technique, where negative and failure results were unfortunately obtained. The reasons behind such a repeated failure are due to the fractures randomly distributed in the study region.

The research novelty in this paper is therefore not to practice as previously the traditional *VES* technique, but to use this technique within an integrated interpretative approach, based on Dar-Zarrouk parameters, with imposing and constraining different hydro-geophysical conditions. Such a proposed integrated approach helps largely in reducing considerably the uncertainties in subsurface exploration, and in determining successfully the most suitable location drillings for groundwater exploitation. Using this *VES* approach, the hydro-geoelectrical model is established as best as possible under each *VES* point. The importance of the proposed integrated *VES* technique is related to the fact that some laboratories do not possess a variety of geophysical techniques rather than *VES* one.

The present study area consists of successive volcanic deposits ranging from fragmented to very hard. The most important characteristic of the lithological section in these areas is the clay levels with the volcanic tuff resulting from basaltic decomposition, which significantly complicates the interpretation of the *VES* data.

The main objective of this paper is therefore the followings:

1. To characterize the subsurface basaltic environment in the Kodana station through interpreting twelve VES data points within a proposed integrated approach, based on Dar-Zarrouk (D-Z) parameters of total resistance (TR), transverse resistivity (ρt), total conductance (S), longitudinal resistivity (ρl), and anisotropy (λ).
2. To determine the hydro-geophysical optimal subsurface conditions to locate and drill a successful borehole for water extraction.
3. To follow the spatial variations of different resulting hydro-geophysical parameters mentioned above.

2. Material and methods

2.1 Vertical electrical sounding (VES) Technique

Indian resistivity meter model *ACR-1* was used to measure the apparent resistivity of twelve *VES* in the study area with Schlumberger configuration.

The half-current electrode spacing *AB/2* varied from 3.0 to 500 m and half-potential electrode spacing *MN/2* varied from 0.25 to 20 m.

The apparent resistance (*Ra*) was first measured in the field, and converted later to apparent resistivity (ρa) for the Schlumberger array by using the following equation (Dobrain 1976):

$$\rho_a = G * \mathrm{R}a \tag{1}$$

Where G is the geometric factor formulated as follows:

$$G = \pi * \frac{(AB/2)^2 - (MN/2)^2}{MN} \tag{2}$$

The vertical electrical sounding curve was thereafter plotted in the next stage for each survey location, and smoothened to remove noisy signatures (Chakravarthi *et al.*, 2007; Ebong *et al.*, 2014).The curve matching technique with master curves were used firstly for interpreting the field resistivity curves to obtain an initial model including resistivities and thicknesses of the corresponding layers (initial model) (Orellana and Mooney,1966). The inversion WINRESIST software program of Velpen, 2004 is thereafter applied and practiced to interpret the parameters of the approximate model to definitely and accurately get the final optimum model, in which a goodness of fit between the field resistivity curve and the final theoretical regenerated curve was arrived (Zohdy, 1989; Zohdy and Bisdorf, 1989).

2.2 Hydro-Geoelectrical model and Dar-Zarrouk parameters

The quantitative *1D* interpretation of the *VES* allows to get the fundamental parameters describing the geoelectrical layers as the real resistivity (ρi) and thickness (*hi*) values along the study research area; where the subscript "*i*" refers to the layer position in the geoelectrical depth section. Another geoelectrical parameters can be also established from those basic resistivity and thickness parameters, such as the total transverse resistance (*TR*) and the total longitudinal conductance (*S*). Maillet (1947) *called TR* and *S* as the Dar-Zarrouk parameters, which are mathematically derived as apparent parameters:

A unit square cross-section area cut out of a group of n-layers of infinite lateral extent is taken into consideration to obtain the hydro-geoelectrical parameters.

The total transverse unit resistance *TR* is expressed by the equation:

$$TR = \sum_{i=1}^{n} h_i \rho_i \tag{3}$$

The total longitudinal conductance *S* is expressed by the equation:

$$S = \sum_{i=1}^{n} \frac{h_i}{\rho_i} \tag{4}$$

Where h_i and ρ_i are the layer thickness and resistivity of i^{th} layer in the depth section respectively.

TR and *S* of equations (3 and 4) allow to get directly the transverse resistivity (ρt) and longitudinal resistivity (ρl) respectively as indicated by equations (5 and 6).

$$\rho t(\Omega m) = \frac{\sum_{i=1}^{n} hi * \rho i}{\sum_{i=1}^{n} hi} \tag{5}$$

$$\rho l(\Omega m) = \frac{\sum_{i=1}^{n} hi}{\sum_{i=1}^{n} \frac{hi}{\rho i}} \tag{6}$$

The Dar-Zarrouk parameters are an efficient tool while interpreting the geoelectrical *VES* data oriented for groundwater exploration survey (Zohdy *et al.*, 1974).

Generally, the longitudinal resistivity (ρl) is less than the transverse resistivity (ρt) unless the medium is uniform (Flathe 1955). Keller (1988) suggested also that the more conductive layers dominate the distribution of (ρl) (in the present case study, clay and weathered/basalts even if a small fraction of resistive layers are present).

The anisotropy parameter (λ) can be also derived by the combination of equations (4 and 5) as expressed by equation (7):

$$\lambda = \sqrt{\frac{\rho t}{\rho l}} \tag{7}$$

The (D-Z) parameters are developed in the present paper in order to characterize as precisely as possible both the geoelectrical section and the pyroclastic basaltic Neogene aquifer in the Kodana station, Southern Syria. Those parameters help largely in reducing the uncertainty (Maillet 1947), during interpreting and analyzing the subsurface lithological and structural characteristics.

The anisotropy parameter plays in addition a significant role in aquifer groundwater assessment.

3. Results and discussion

The study region is related to an active volcanic area. Geologically, a distinct period of active volcanism was prevailing over most Syria territories through Miocene to Holocene times. The younger volcanic commenced with sub-aerial flood basalts in the early Miocene, mostly 20–16 Ma, and extended over most of Southern Syria, Jordan, and Saudi Arabia (Ponikarov 1966).

Twelve field *VES* points were carried out in the study area (station of Shami goats), and interpreted by using a comprehensive computer inversion program (WinResist) for characterizing the subsurface formations and identifying the water bearing one. Those twelve *VES* data are distributed on three profiles (*A*, *B*, and *C*) as indicated in Figure 1.

The quantitative interpretations in term of *1D* structure of those twelve *VES* measurements allow to get the real thicknesses and resistivities of the corresponding subsurface layers. Different geoelectrical layered models of five, six, and seven layers are shown in the study area as indicated in Table 1, and represented by different geoelectrical curves, due to the non uniformity of the study area.

Figure 2 shows the *1D* quantitative graphic results of the twelve *VES* distributed along the three profiles A, B, and C.

The *1D* quantitative interpretation results for those twelve *VES* sounding points using the inversion software of Velpen, 2004 are shown in Table 1.

The average value to the deepest interface (DI) in the 12 stratified models is about 250 m. DI varies between a minimum of 144.4m at V1 and a maximum of 379.3m at V8. The careful examination of the fits between the measured apparent resistivities and those calculated from the inverted 12 models indicates that this DI is warranted by the field geoelectrical data.

The real thicknesses and resistivities of the corresponding subsurface layers shown in Table 1 will be the base of the

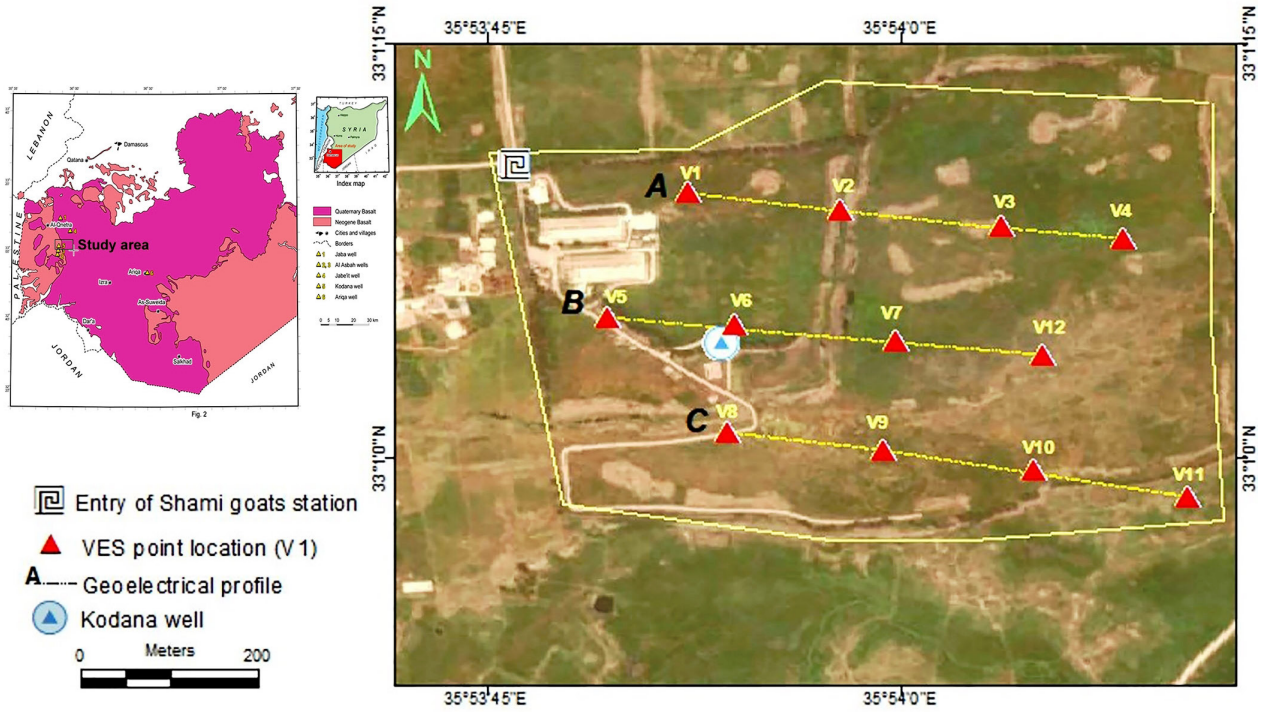

Figure 1. Vertical electrical sounding (*VES*) locations in the Kodana station, Southern Syria.

A

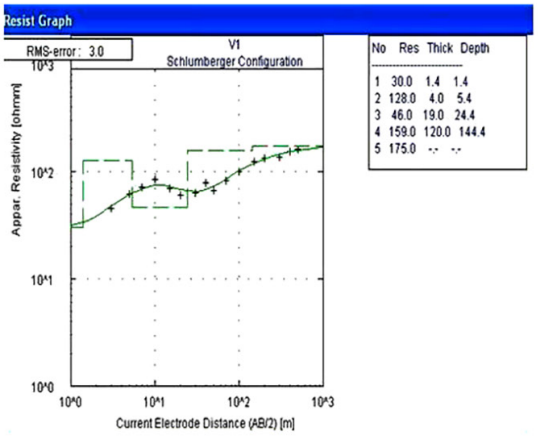
Resist Graph
RMS-error : 3.0
V1
Schlumberger Configuration
No Res Thick Depth
1 30.0 1.4 1.4
2 128.0 4.0 5.4
3 46.0 19.0 24.4
4 159.0 120.0 144.4
5 175.0 -.- -.-
Appar. Resistivity [ohmm]
Current Electrode Distance (AB/2) [m]

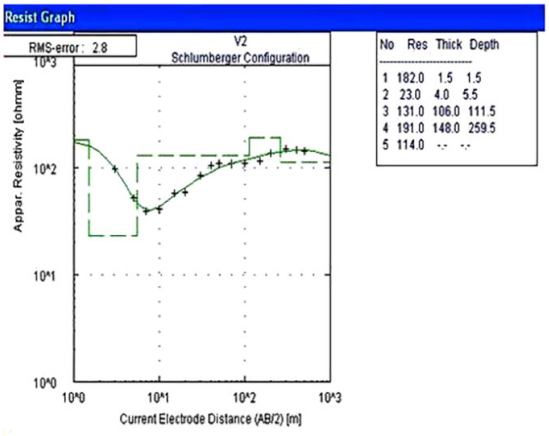
Resist Graph
RMS-error : 2.8
V2
Schlumberger Configuration
No Res Thick Depth
1 182.0 1.5 1.5
2 23.0 4.0 5.5
3 131.0 106.0 111.5
4 191.0 148.0 259.5
5 114.0 -.- -.-
Appar. Resistivity [ohmm]
Current Electrode Distance (AB/2) [m]

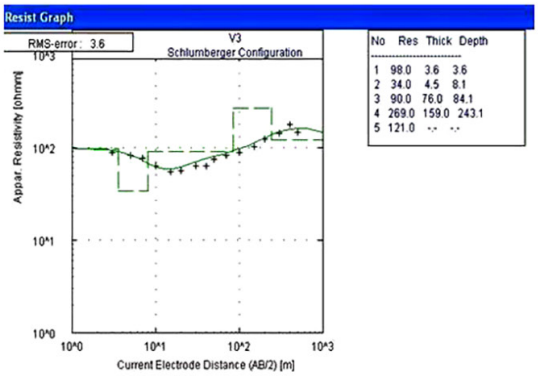
Resist Graph
RMS-error : 3.6
V3
Schlumberger Configuration
No Res Thick Depth
1 98.0 3.6 3.6
2 34.0 4.5 8.1
3 90.0 76.0 84.1
4 269.0 159.0 243.1
5 121.0 -.- -.-
Appar. Resistivity [ohmm]
Current Electrode Distance (AB/2) [m]

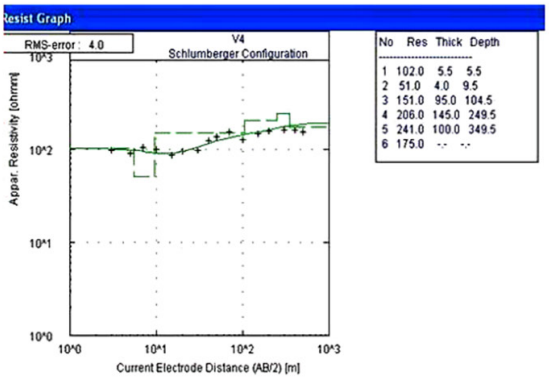
Resist Graph
RMS-error : 4.0
V4
Schlumberger Configuration
No Res Thick Depth
1 102.0 5.5 5.5
2 51.0 4.0 9.5
3 151.0 95.0 104.5
4 206.0 145.0 249.5
5 241.0 100.0 349.5
6 175.0 -.- -.-
Appar. Resistivity [ohmm]
Current Electrode Distance (AB/2) [m]

B

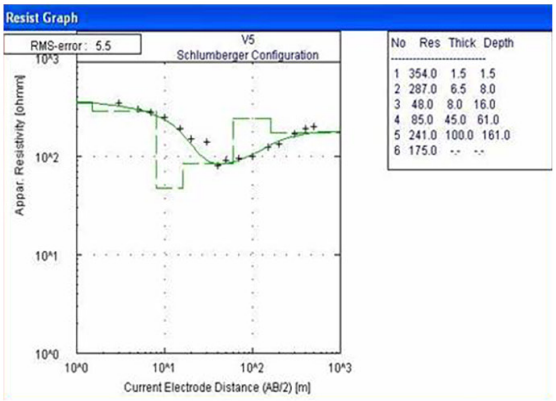
Resist Graph
RMS-error : 5.5
V5
Schlumberger Configuration
No Res Thick Depth
1 354.0 1.5 1.5
2 287.0 6.5 8.0
3 48.0 8.0 16.0
4 85.0 45.0 61.0
5 241.0 100.0 161.0
6 175.0 -.- -.-
Appar. Resistivity [ohmm]
Current Electrode Distance (AB/2) [m]

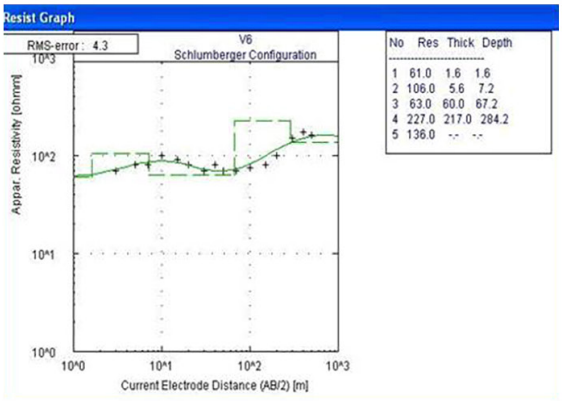
Resist Graph
RMS-error : 4.3
V6
Schlumberger Configuration
No Res Thick Depth
1 61.0 1.6 1.6
2 106.0 5.6 7.2
3 63.0 60.0 67.2
4 227.0 217.0 284.2
5 136.0 -.- -.-
Appar. Resistivity [ohmm]
Current Electrode Distance (AB/2) [m]

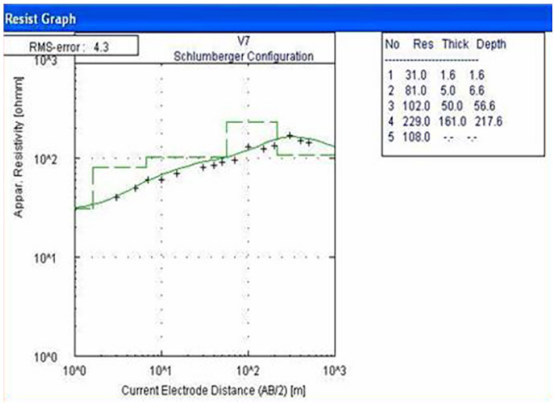
Resist Graph
RMS-error : 4.3
V7
Schlumberger Configuration
No Res Thick Depth
1 31.0 1.6 1.6
2 81.0 5.0 6.6
3 102.0 50.0 56.6
4 229.0 161.0 217.6
5 108.0 -.- -.-
Appar. Resistivity [ohmm]
Current Electrode Distance (AB/2) [m]

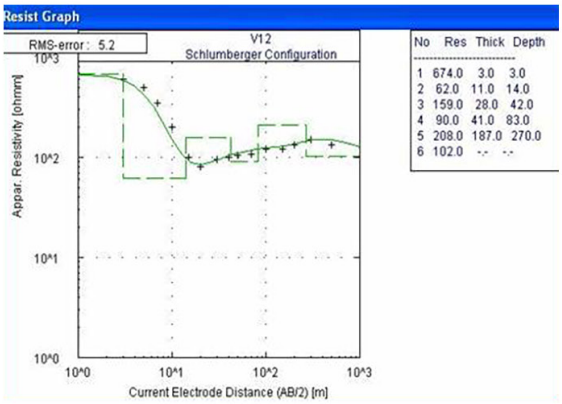
Resist Graph
RMS-error : 5.2
V12
Schlumberger Configuration
No Res Thick Depth
1 674.0 3.0 3.0
2 62.0 11.0 14.0
3 159.0 28.0 42.0
4 90.0 41.0 83.0
5 208.0 187.0 270.0
6 102.0 -.- -.-
Appar. Resistivity [ohmm]
Current Electrode Distance (AB/2) [m]

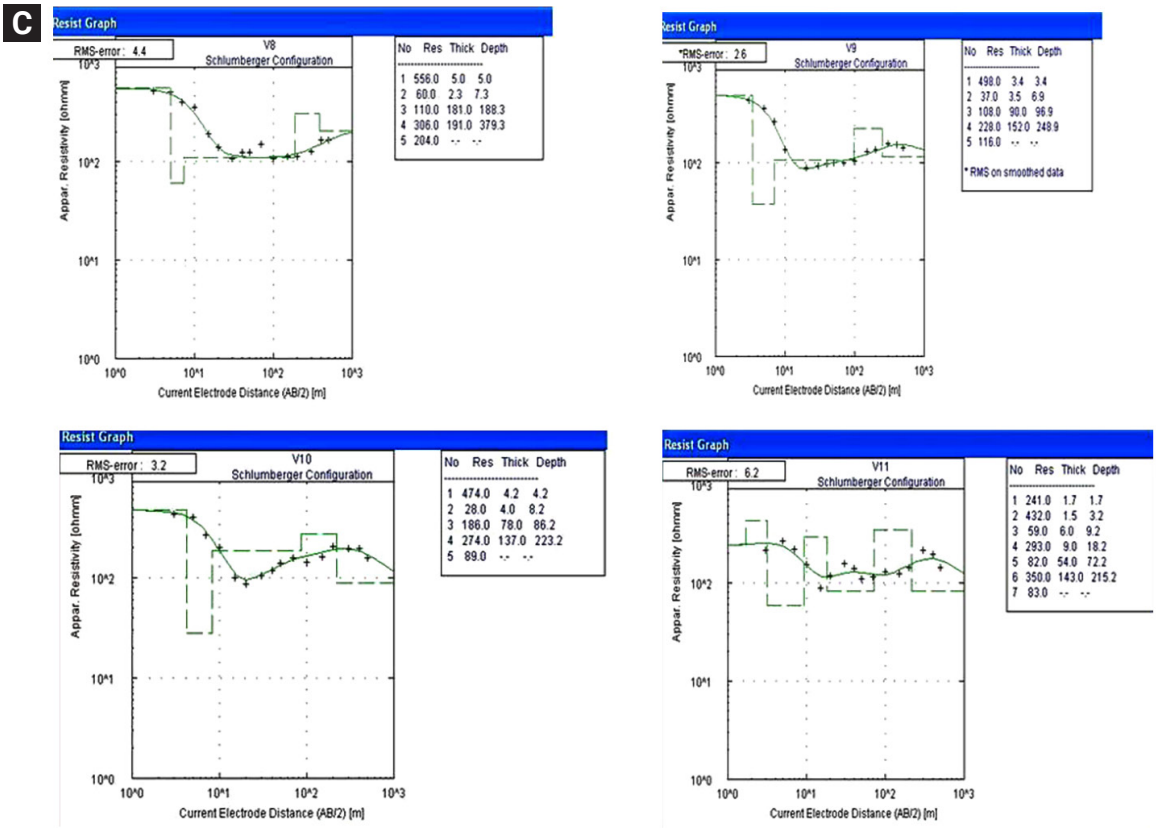

Figure 2. Twelve field *VES* measurements distributed on the three profiles (A, B, and C), their *1D* inversion quantitative interpretations, and models.

Table 1. Interpretative results related to twelve *VES* points at Kodana station of Shami goats, Southern Syria.

VES	No. layers	Resistivity of layers ρ (Ωm)							Thickness of layers *h* (m)						RMS	Curve type
		ρ_1	ρ_2	ρ_3	ρ_4	ρ_5	ρ_6	ρ_7	h_1	h_2	h_3	h_4	h_5	h_6	(%)	
V1	5	30	128	46	**159**	175	--		1.4	4	19	**120**	--	--	3	**KHA**
V2	5	182	23	131	**191**	114	--		1.5	4	106	**148**	--	--	2.8	**HAK**
V3	5	98	34	90	**269**	121	--		3.6	4.5	76	**159**	--	--	3.6	**HAK**
V4	6	102	51	151	206	**241**	175		5.5	4	95	145	**100**	--	4	**HAAK**
V5	5	354	287	48	85	**241**	175		1.5	6.5	8	45	**100**		2	**HAK**
V6	5	61	106	63	**227**	136			1.6	5.6	60	**217**	--		2.1	**KHK**
V7	5	31	81	102	**229**	108			1.6	5	50	**161**	==		2.6	**AAK**
V8	5	556	60	110	**306**	204			5	2.3	181	**191**	==	--	4.4	**HAK**
V9	5	498	37	108	**228**	116	--		3.4	3.5	90	**152**	--	--	2.6	**HAK**
V10	5	474	28	186	**274**	89	--		4.2	4	78	**137**	--	--	3.2	**HAK**
V11	7	241	432	59.	293	82	**350**	83	1.7	1.5	6	9	54	**143**	2	**KHKH**
V12	6	674	62	159	90	*208*	102		3	11	28	41	**187**		6.2	**HAK**

*: Resistivity and thickness in **bold** represent the Neogene pyroclastic basalt aquifer.

proposed integrated approach aimed at establishing the Dar-Zarrouk (D-Z) parameters as presented in Table 2.

Table 2 shows consequently the resulting (D-Z) geoelectrical data of those studied *VES* points.

The results include the *GPS* coordinates of N and E for those *VES* points, the different Dar-Zarrouk parameters discussed above, and the thickness (h), resistivity (ρ), and the transverse resistance (R) of the Neogene pyroclastic basalt aquifer.

The total transverse resistance *TR* (Ωm^2) obtained according to equation (3) varies between a minimum of 6605 Ωm^2 at V5 and a maximum of 81274 Ωm^2 at V8 (Figure 3).

The transverse resistivity ρt obtained according to equation (5) varies between a minimum of 108 Ωm at V5 and a maximum of 272 Ωm at V11(Figure 4).

The total longitudinal conductance S (Ω^{-1}) obtained according to equation (4) varies between a minimum of 0.73 Ω^{-1} at V5 and a maximum of 2.31 Ω^{-1} at V8 (Figure 5).

The longitudinal resistivity ρl obtained according to equation

Table 2. Resulting (D-Z) geoelectrical data of the 12 *VES* points.

Location	*E*	*N*	*h (m)*	*ρ (Ω.m)*	*S* (Ω^{-1})	ρ_l *(Ω.m)*	*TR* ($\Omega.m^2$)	*ρt (Ω.m)*	*λ*	*R* ($\Omega.m^2$)
V1	35.89785	33.01934	120	159	1.240	116.45	20508	142	1.10	19080
V2	35.89939	33.01916	148	191	1.750	148.3	42519	163.8	1.05	28268
V3	35.90102	33.01900	159	269	1.600	151.9	50117	206	1.16	42771
V4	35.90225	33.01887	100	241	1.88	186.2	69080	198	1.03	24100
V5	35.89704	33.01808	100	241	0.727	83.91	6605	108	1.13	24100
V6	35.89832	33.01800	217	227	1.989	142.88	53730	189	1.15	49259
V7	35.89995	33.01784	161	229	1.300	167.4	42424	195	1.08	36869
V8	35.89825	33.01692	191	306	2.310	164.00	81274	214	1.14	58446
V9	35.89983	33.01674	152	228	1.590	156.00	46199	186	1.09	34656
V10	35.90134	33.01654	137	274	1.072	208.00	54149	243	1.08	37538
V11	35.90290	33.01627	143	350	1.210	178.00	58527	272	1.24	50050
V12	35.90143	33.01770	187	208	1.710	158.00	49742	184	1.08	38896

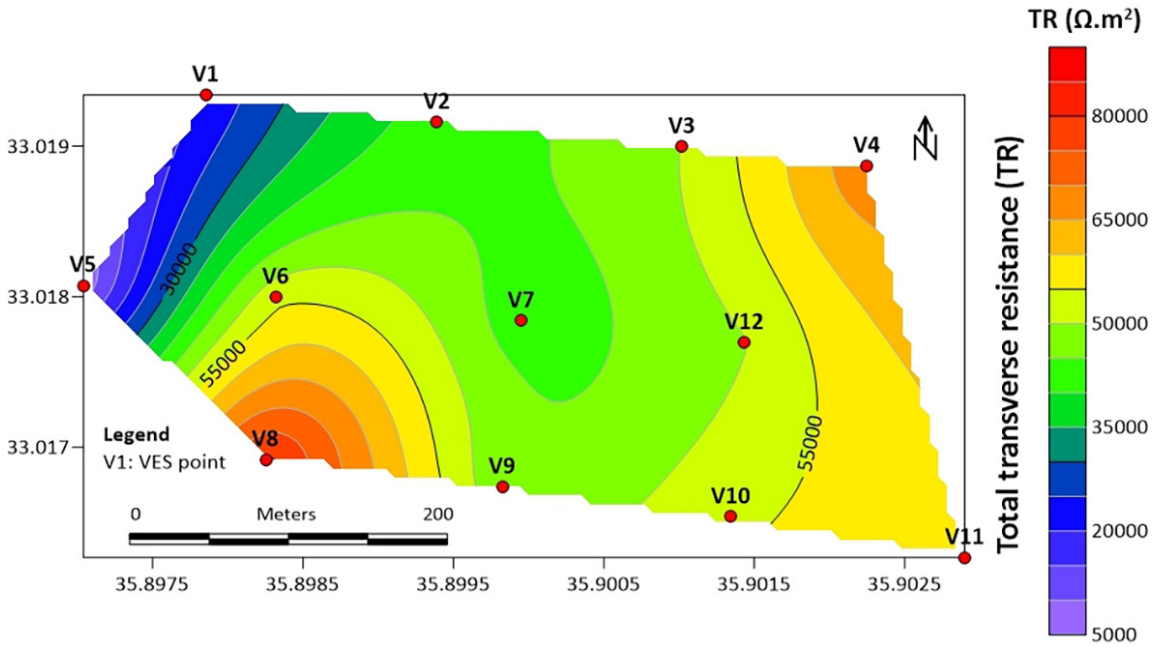

Figure 3. The distribution of the total transverse resistance of the study Kodana area, Southern Syria.

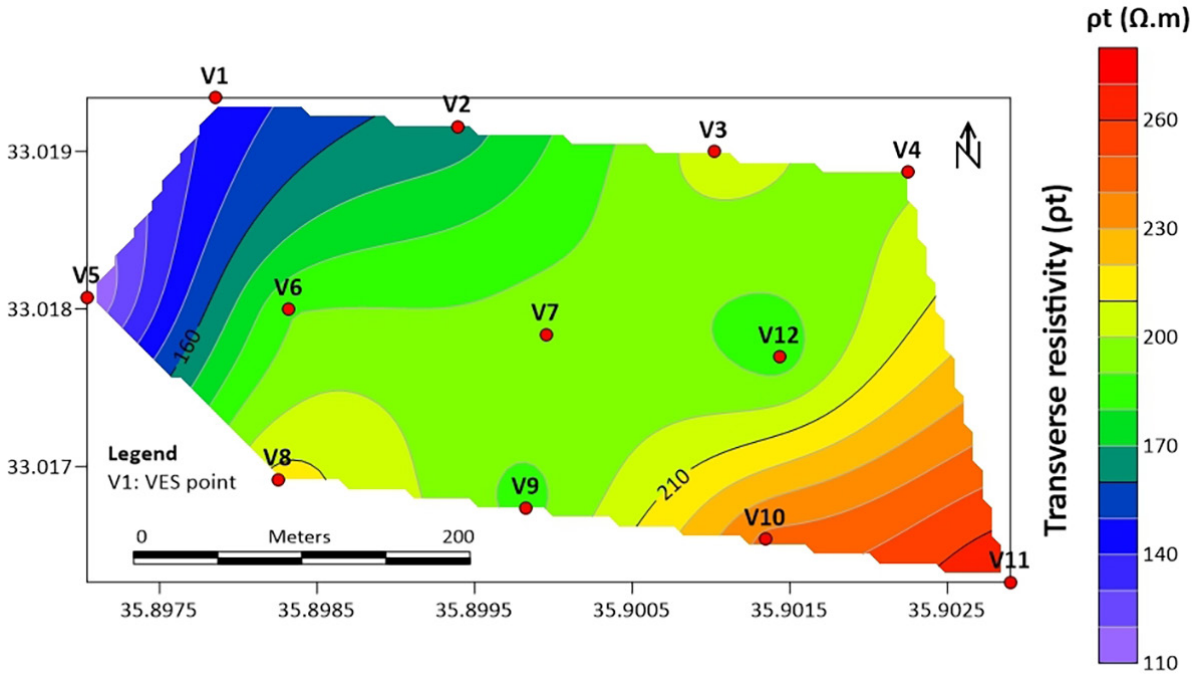

Figure 4. The distribution of the transverse resistivity of the study Kodana area, Southern Syria.

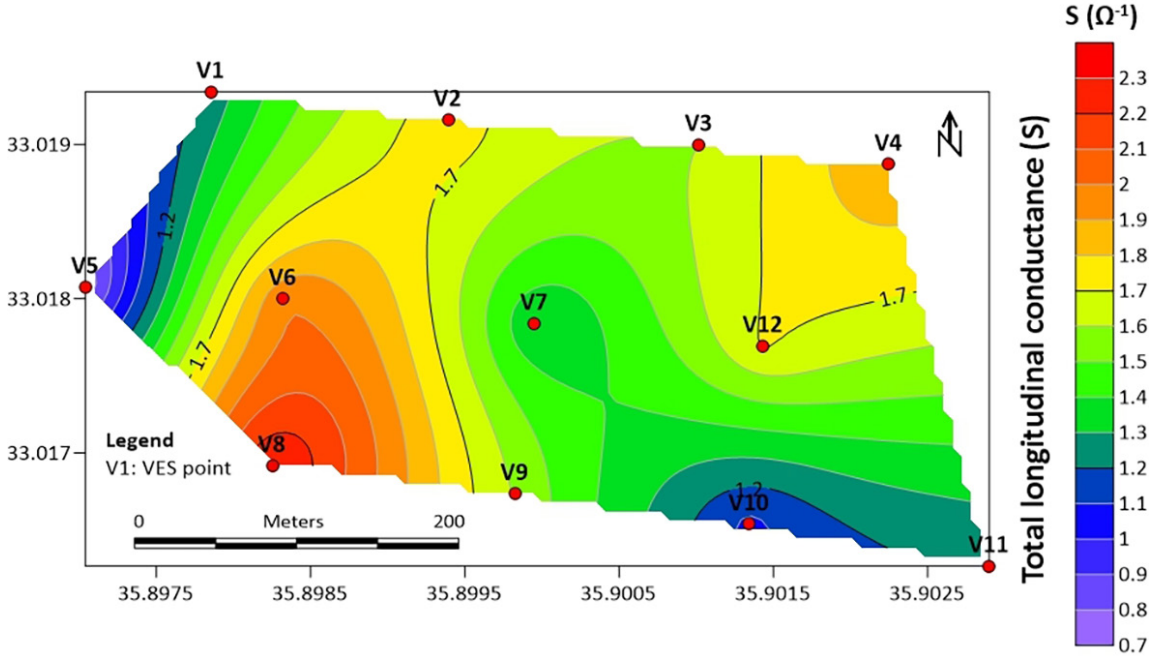

Figure 5. The distribution of the total longitudinal conductance of the study Kodana area, Southern Syria.

(6) varies between a minimum of 83.9 Ωm at V5 and a maximum of 208 Ωm at V10 (Figure 6).

The anisotropy coefficient λ obtained according to equation (7) varies between a minimum of 1.03 at V4 and a maximum of 1.24 at V11(Figure 7).

The anisotropy observed in the study region is due to the influence of the weathering, alteration processes and fracturing related to tectonic activities. Similar anisotropy results were obtained while characterizing the Quaternary fractured basalt aquifer (B1Q1) in Deir Al-Adas region, Southern Syria (Asfahani and Al-Fares, 2021). The anisotropy findings in the present case study are also in a good concordance with those obtained

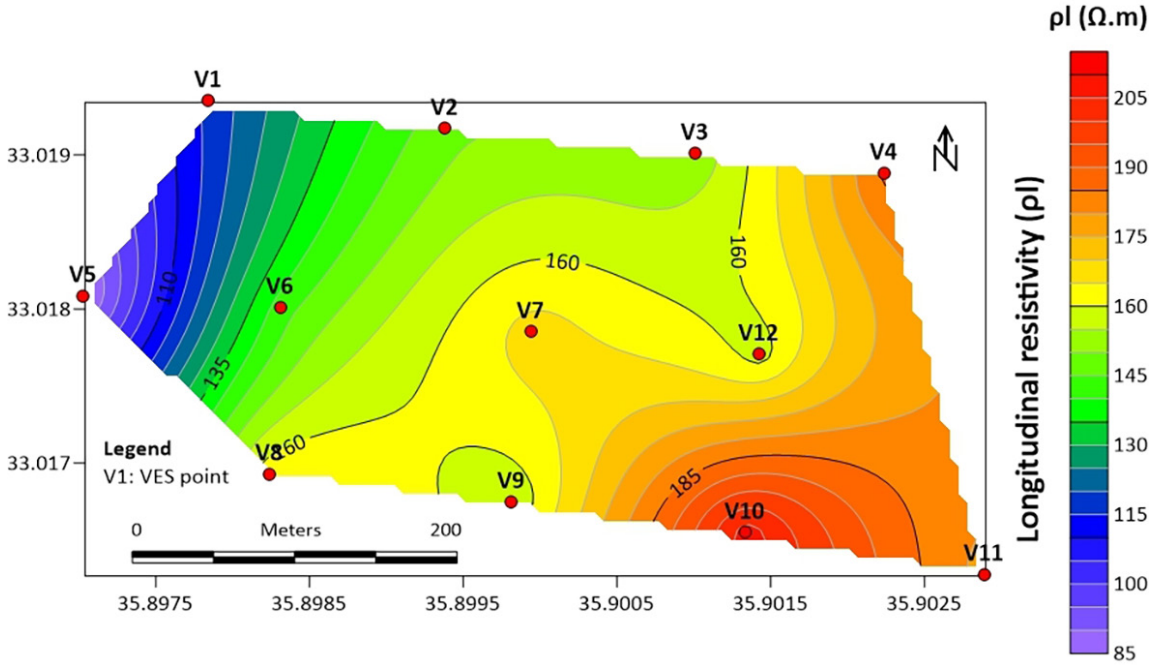

Figure 6. The distribution of longitudinal resistivity of the study Kodana area, Southern Syria.

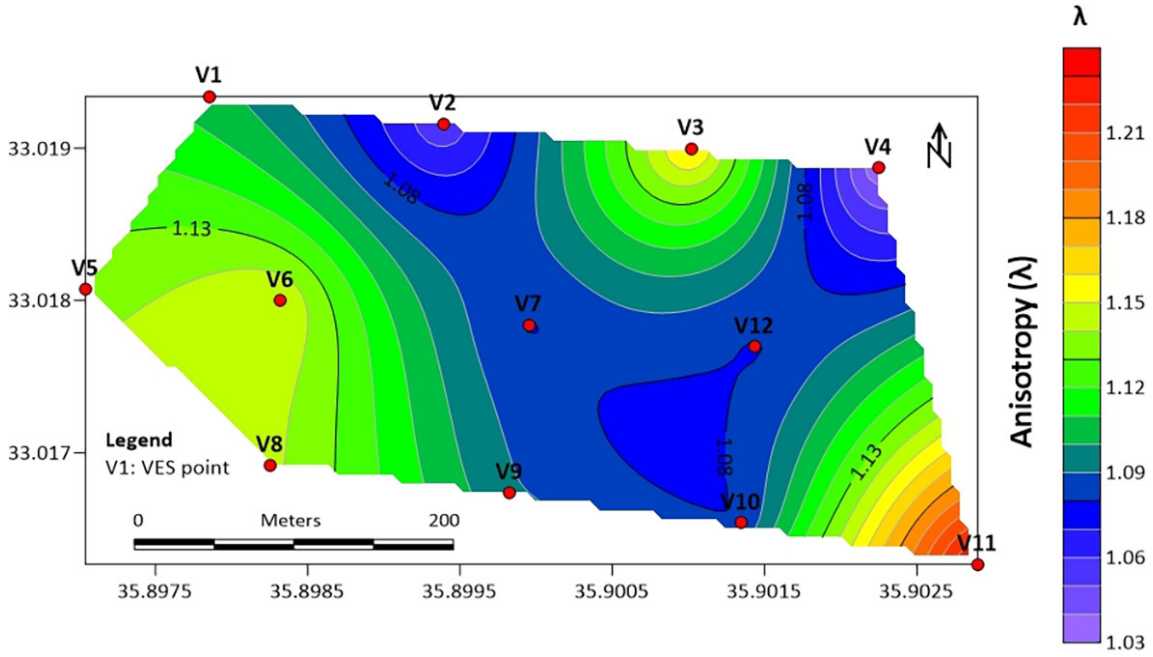

Figure7. The distribution of the anisotropy variations of the study Kodana area, Southern Syria.

by Kumar *et al.* (2014), who mentioned that the high anisotropy values indicate different degrees of fracturing with better water holding ability in hard basaltic environments.

The Neogene pyroclastic basaltic aquifer in the study area is the fourth or the fifth subsurface layer as indicated in Table 1. Its thickness varies between a minimum of 100 m at (V4 and V5), and a maximum of 217m at *V6* (Figure 8).

Its resistivity varies between a minimum of 159 Ωm at V1 and a maximum of 350 Ωm at V11 (Figure 9).

The Dar-Zarrouk (D-Z) transverse resistance parameter of this aquifer R (the product of h and ρ as indicated in Table 2) varies between a minimum of 19080 $\Omega.m^2$ at V1 and a maximum of 58446 $\Omega.m^2$ at V8 (Figure 10).

Table 3 summarizes all the (D-Z) parameters obtained in the

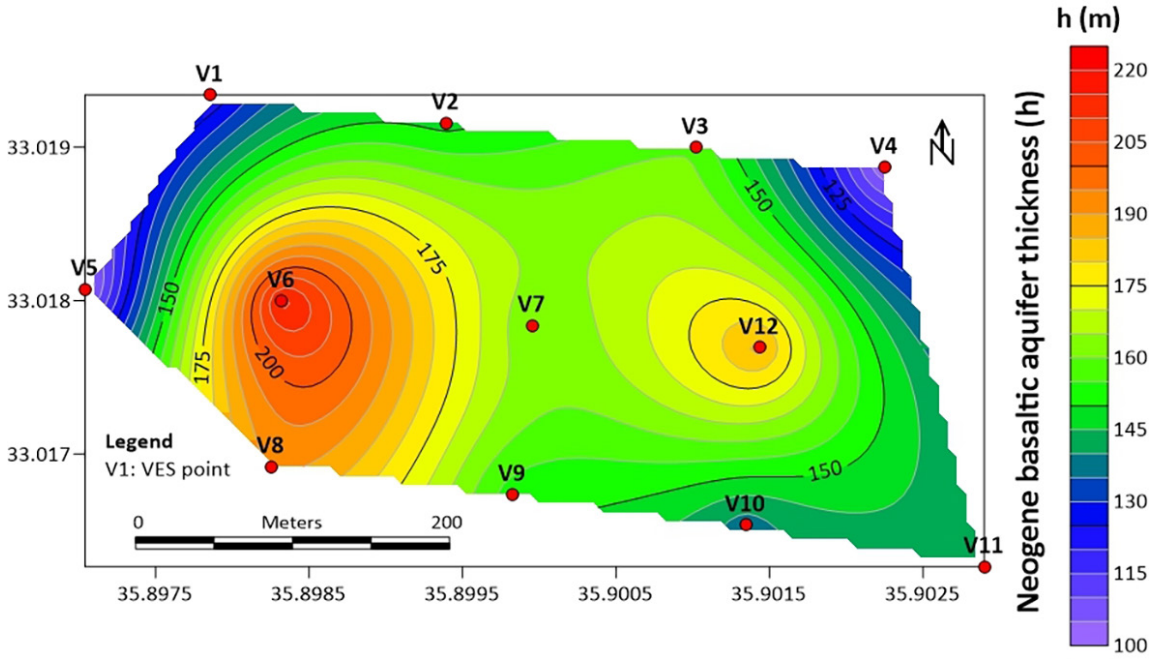

Figure 8. The distribution of the thickness of Neogene pyroclastic basalt aquifer of the study Kodana area, Southern Syria.

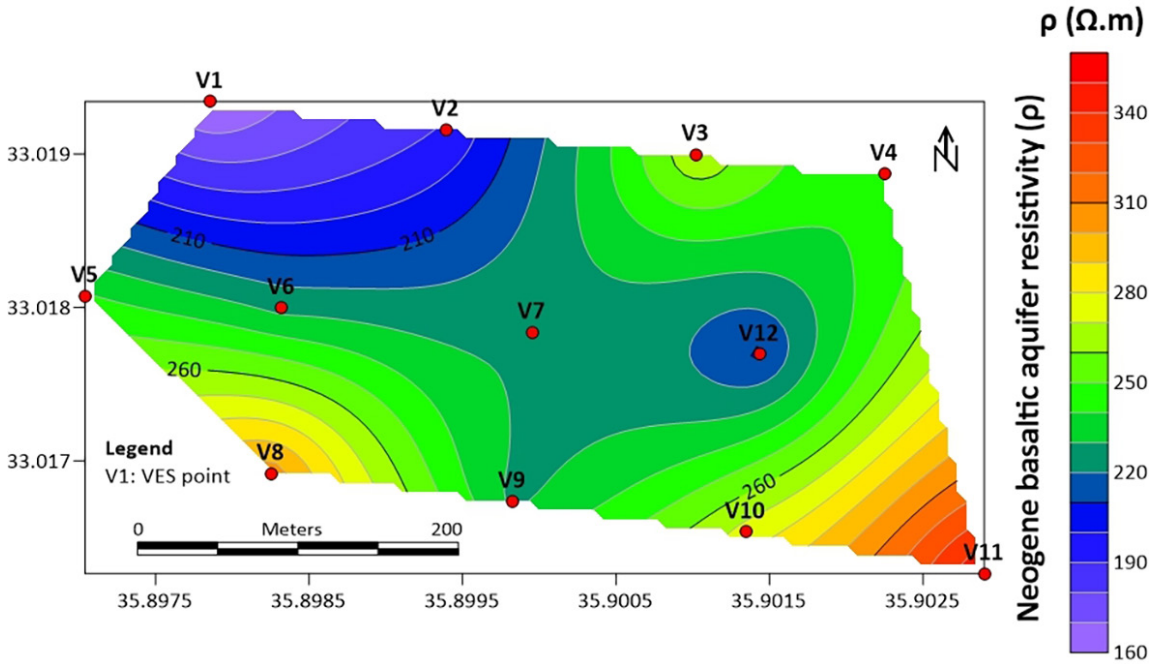

Figure 9. The distribution of the resistivity of Neogene pyroclastic basalt aquifer of the study Kodana area, Southern Syria.

study area. The last layer in all the inverted twelve *VES* models shown in Figure 2 has a resistivity ranging between 83 Ωm and 204 Ωm. The thickness of this layer is not defined for being the last. This layer is not therefore included in the computation of D-Z parameters discussed above. The resistivities and the thicknesses of the layers above this last one are well determined and defined without any ambiguity and uncertainty, and are only taken into consideration while computing D-Z parameters.

The integrated approach in this paper is based essentially on supporting the *VES* results with the different D-Z parameters as discussed above. The *1D* interpretation of *V6* shows the presence of five layers as follows:

The first top surfacial soil layer of a thickness of 1.6 m and a resistivity of 61 Ω.m, the second layer has a thickness of 5.6 m and a resistivity of 106 Ω.m, the third layer has a thickness of 60m and a resistivity of 63 Ω.m, the fourth layer (Noegene pyroclastic

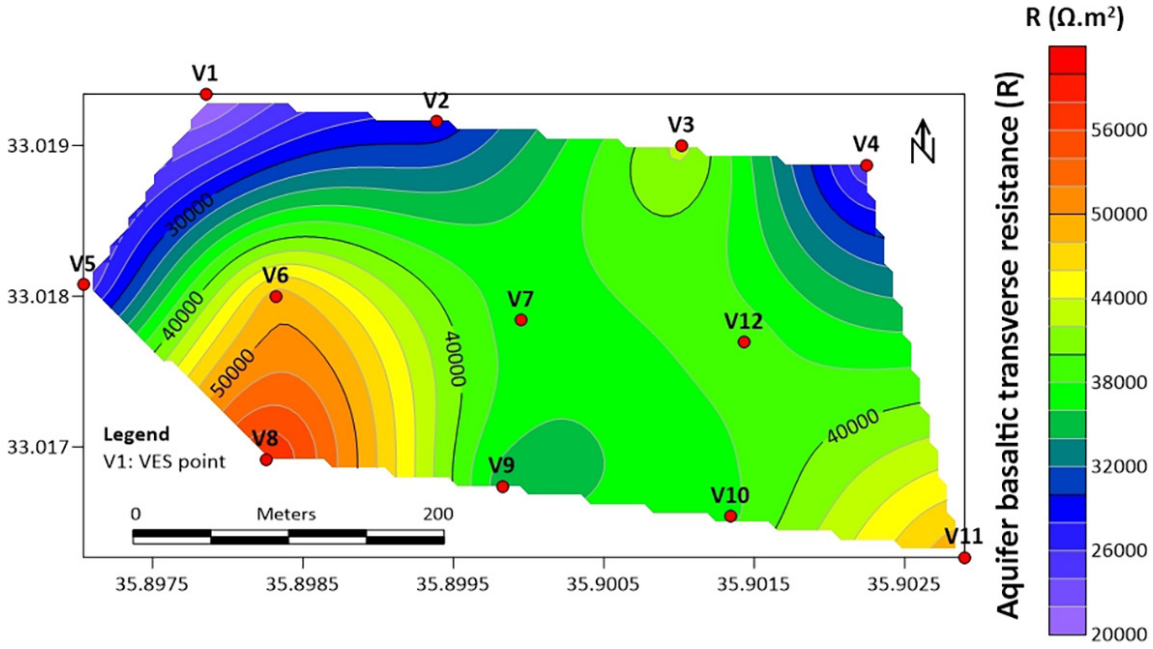

Figure 10. The distribution of the transverse resistance of Neogene pyroclastic basalt aquifer of the study Kodana area, Southern Syria.

Table 3. Statistical characteristics of the pyroclastic aquifer and its related (D-Z) parameters.

Parameter	Min	Max	Average	(σ)
***h* (m)**	100	217	151	35.5
***ρ* (Ω.m)**	159	350	243	51.1
***R* (Ωm²)**	19080	58446	37002.7	11883.6
***S* (Ω⁻¹)**	0.73	2.31	1.53	0.44
***ρl* (Ωm)**	83.9	208	155	32
***TR* (Ωm²)**	6605	81274	47906	19712
***ρt* (Ωm)**	108	272	192	43
λ	1.03	1.24	1.11	0.06

basalt aquifer) has a thickness of 217m and a resistivity of 227 Ω.m, and the last fifth layer has a resistivity of 136 Ω.m. The other 11 *VES* points show similar geoelectrical results as *V6*.

The *VES* (*V6*) point is decided through the proposed geo-electrical approach to be the favorable and best location for drilling a successful borehole for groundwater extraction for the following reasons:

1. High thickness of Neogene pyroclastic basaltic aquifer (217m),
2. High Neogene pyroclastic basaltic aquifer resistivity (227Ωm) to have less percentage clay, that prevents hydraulic conductivity connection,
3. High Neogene basaltic aquifer transverse resistance (49259 Ωm^2),
4. High anisotropy (1.15).

The four mentioned conditions are the base of the proposed integrated approach to determine and locate a suitable location for drilling successfully a groundwater borehole. Those conditions allow to get the optimum hydro-geophysical model under each of the *VES* points in the study area, and to reduce considerably the failures and uncertainties in locating and drilling a successful borehole.

It is to mention that the aquifer pyroclastic basalt layer is well determined in all the twelve studied *VES* points. This aquifer layer is located just above the last layer of resistivity changing between 83 Ωm and 204 Ωm.

Figure 11 shows geoelectrical cross section of the W-E profile. B, and the variations of the h, ρ, R, and λ parameters along this profile (Figure 1).

It is to mention that the ranges of resistivity obtained through this *1D* inversion quantitative interpretation are in a good agreement and concordance with those obtained while classifying and characterizing the long normal resistivity data of the Kodana well itself (Asfahani, 2011).

The water level and the contact between the two saturated and non saturated zones were determined in the study region through studying different nuclear neutron-porosity logs, as shown in Figure 12 (Asfahani, 2011).

Figure 13 (a and b) shows the lithological and hydrological characteristics of the well drilled at *V6*.

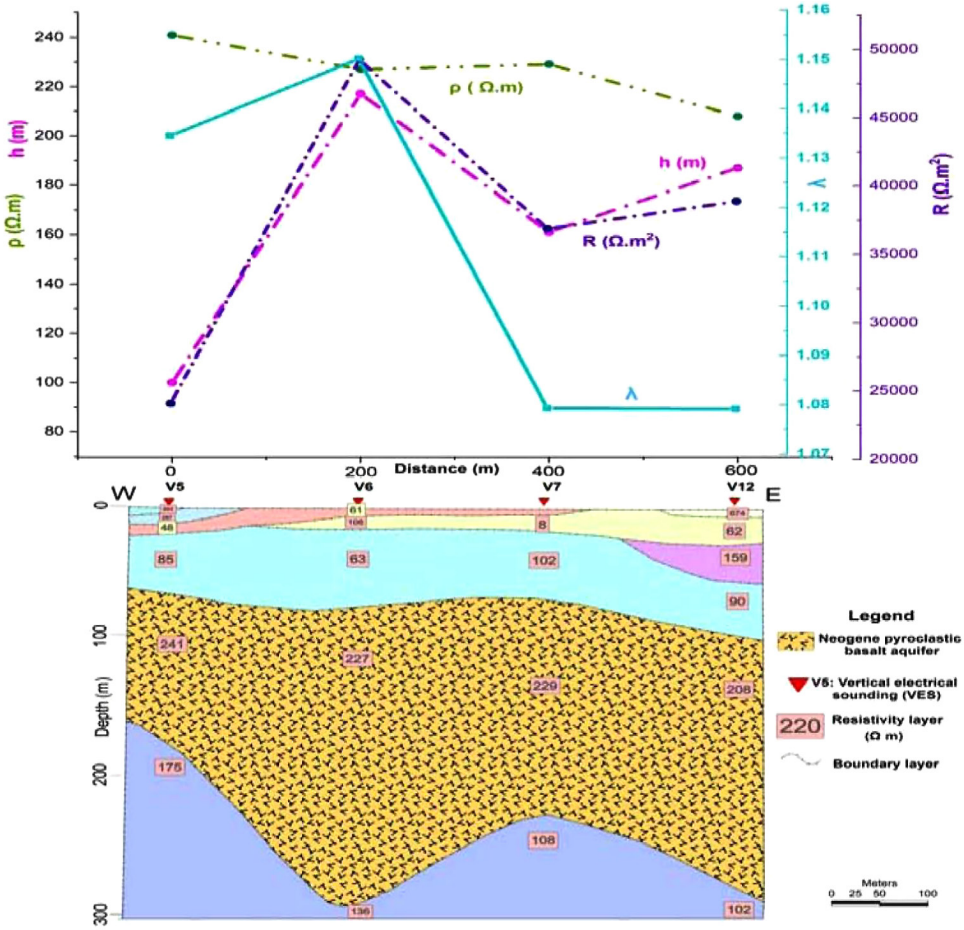

Figure 11. Geoelectrical cross section of the W-E profile (B) and the lateral variations of the h, ρ, R, and λ parameters along this profile.

The main confined fractured Neogene pyroclastic basalt aquifer in the drilled Kodana well has a thickness varying between 8 and 10 m, with an average of 5 m, and it is localized at a depth of 186 m. The static water level (*S.W.L*) is found at a depth of 122 m, whereas the dynamic water level (*D.W.L*) is found to be at a depth of 153 m (Figure 13). The discharge of 20 m^3/h corresponds to an hydraulic conductivity of 3.09 *m/day*, and a transmissivity (*T*) of 15.46 m^2/day is obtained for that well, according to the pumping test (Asfahani, 2017-a). Kodana well is of a pressure type, where the drastic descent of the water column is of about 31 m. Another seasonal free water-bearing horizon exists, which is localized at the depth interval of 100–110 m, and depends on the rainy annual periods.

The range of the hydraulic conductivity parameter established

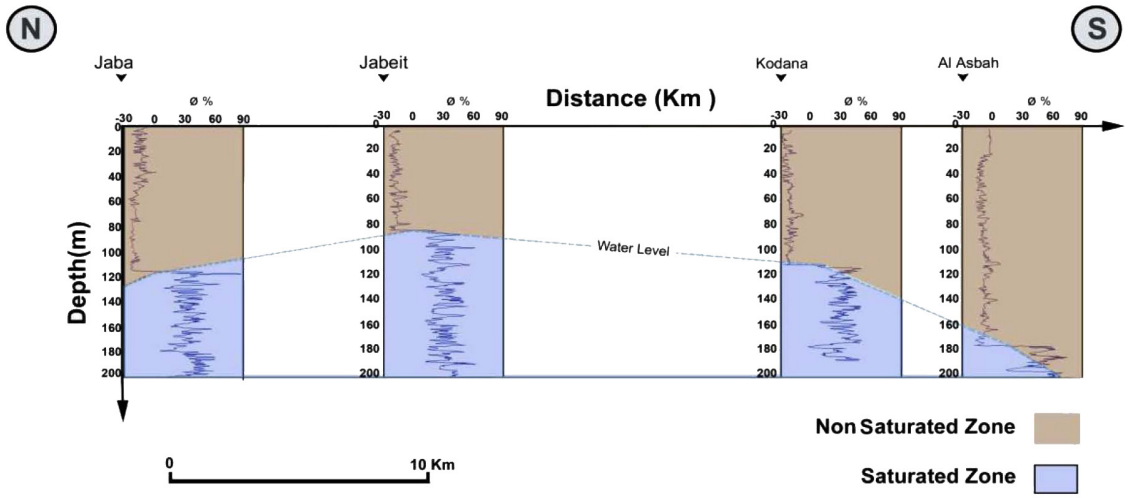

Figure 12. Water level and contact between saturated and non saturated zones in different wells in Southern Syria (particularly Kodana well), (Asfahani, 2011).

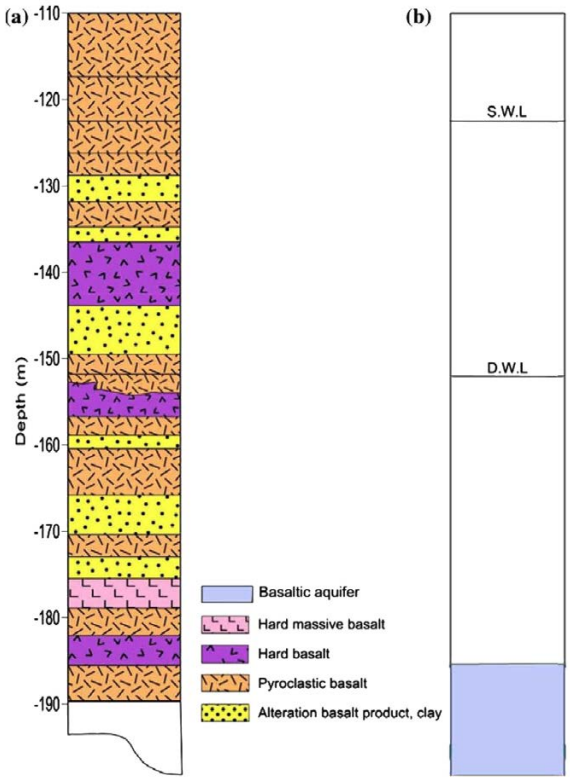

Figure 13 (a). Lithological characteristics of the saturated zone of the Kodana well, (b): Hydro-geological characteristics of the Kodana well (Asfahani 2017-a).

for the Kodana well of less or equal 8.8 m/day for the pyroclastic basalt is in an excellent agreement with that obtained (from 1.97 m/day to 8.97 m/day) for the Quaternary basaltic aquifer in Deir Al-Adas area, Yarmouk Basin, Southern Syria, (Asfahani and Al-Fares; 2021).

Asfahani., 2012, 2013 has already developed an alternative *VES* approach, in which, it has been found a positive empirical relationship between the transverse resistance (*R*) and the transmissivity (*T*) for the Quaternary aquifer in the Khanasser valley region, Northern Syria. Asfahani and Al-Fares, 2021 have already also found a similar positive empirical relationship between the hydraulic conductivity (*K*) and the transverse resistance of the Quaternary fractured basalt aquifer (*B1Q1*) in Deir Al-Adas region, Southern Syria. Those two mentioned findings justify the reason behind which we were looking for the Neogene pyroclastic basalt aquifer of optimum high transverse resistance (*R*) as represented for the *VES* location at *V6*, where the Kodana well was successfully drilled.

Asfahani, 2017-b has already also classified four types of basalt in the study area by adapting the non linear statistical fractal technique with using the concentration-number model (*C-N*) and log-log graphs, and applying it on resistivity long normal well logging data as follows (Table 4):

1. Hard massive basalt is characterized by a resistivity of bigger than 347 Ωm.
2. Massive basalt is characterized by a resistivity ranged between 204 and 347 Ωm.
3. Pyroclastic basalt is characterized by a resistivity ranged between 117.5 and 204 Ωm.
4. Alteration basalt product, and clay are characterized by a resistivity of less than 117.5 Ωm.

Table 4. Basalt characterization by long normal resistivity well logging technique (Asfahani, 2017-b).

ROCK TIPE	Long Normal Resi (Ωm) 200 400
Hard massive basalt	
Hard basalt	
Pyroclastic basalt	
Alteration basalt product, clay	

One can therefore interpret the geoelectrical results obtained in this research study in lithological description term by calibrating the resistivity range values obtained already by WinResist as documented above, with those values obtained by fractal long normal resistivity well logging technique.

Different methodological researches have been already carried out in this successful drilled well at *V6* location (Asfahani, 2011, 2014, 2017; Asfahani, 2017-a; Asfahani and Abdul Ghani, 2012; and Asfahani *et al.*, 2015), that concentrated only on the saturated zone in that well (from a depth of 115m).

This paper shows the importance of the surfacial geoelectrical study with the proposed integrated approach, in which the efficacy of the *VES* technique is increased, and the high failure in locating and drilling a successful groundwater borehole is considerably decreased. It is a successful case study in a hard basaltic environment characterized by sharp lithological variations laterally and vertically, applied widely in Syria, and could be practiced in other worldwide similar basaltic areas.

4. Conclusions

Geoelectrical integrated approach is proposed in this paper to support and increase the application efficacy of the vertical electrical sounding (*VES*) technique, oriented towards locating and drilling successful groundwater boreholes in basaltic environments. This approach is essentially based on analyzing Dar-Zarrouk (D-Z) parameters with constraining several specific conditions that insure to get the optimum hydro-geophysical model. The advantage of such a *VES* proposed approach is the possibility to apply it solely in comparing with other geophysical techniques that require basically the combination of *VES* technique with another available geophysical technique as documented in this paper.

Schlumberger configuration is adapted while carrying out the *VES* measurements to locate and drill a successful borehole for groundwater extraction in the Kodana station for the Shami goats, Southern Syria.

The geoelectrical cross section of the basaltic environment and the Neogene pyroclastic basalt aquifer established for profile. B in the study area are well characterized by the use of both the *1D* inversion technique and the different Dar-Zarrouk-parameters of transverse resistivity, longitudinal resistivity, and anisotropy. Similar geoelectrical cross sections could be obtained for profiles A and C.

The optimum and favorable conditions for locating and drilling a successful groundwater borehole are well documented and determined in the Kodana station, where the *VES* point (*V6*) was decided to be the best location for this purpose.

The *1D* geoelectrical results obtained in this paper could be easily transferred to be expressed in lithological description term, through calibrating the resistivity range values obtained already by WinResist with the resistivity values obtained by fractal concentration-number model (C-N), applied on long normal resistivity well logging data at Kodana well (Asfahani, 2017-b).

The different hydro-geophysical parameters of the Neogene

pyroclastic basalt aquifer related to Kodana well, drilled at the *V6* point were well characterized. Although the study area is too small of (1Km.1Km), however, it was geoelectrically shown the presence of different geoelectrical curve types, indicating the complexity, and the difficulty of such basaltic regions.

The geoelectrical survey presented in this paper is an interesting case study for engineering geophysists to show them how we can deal easily with such difficult basaltic environments, that sharply change laterally and vertically, through proposing an integrated *VES* approach, establishing and combining integrally the different discussed hydro-geophysical parameters. Such a proceeding reduces the uncertainties and the failures in locating and drilling a successful borehole.

The *VES* technique within the proposed approach is therefore recommended to be applied worldwide for groundwater investigations, and for determining the suitable favorable locations for drilling successful boreholes in basaltic environments.

5. Acknowledgements

The author would like to thank Dr. I. Othman, General Director of Syrian Atomic Energy Commission, for his permission to publish this paper. The two reviewers are thanked for their professional comments, remarks and suggestions that considerably improve the quality of the final version. The Editor in Chief of Geofisica Internacional is cordially thanked for his (her) assistance during the different stages of this paper.

6. Funding

This work is part of a scientific research under the No.266-2001, which is totally funded by the authority of the Atomic Energy Commission of Syria.

7. Data availability

The datasets related to this research paper are available with the author, however accessing to these data or making them available to others requires special permission from the Syrian Atomic Energy Commission.

8. Declaration of competing interest

The author declares that he has no known competing financial interests or personal relationships that could have appeared to influence the work reported in this paper.

9. References

Asfahani, J. (2011). Basalt characterization by means of nuclear and electrical well logging techniques. Case study from southern Syria. *Appl. Radiat. Isot.* 69, 641-647.

Asfahani, J. (2012). Quaternary aquifer transmissivity derived from vertical electrical sounding measurements in the semiarid Khanasser Valley Region, Syria. *Acta Geophysica*, 60(4), 1143-1158, doi: **http://dx.doi.org/10.2478/s11600-012-0016-x**

Asfahani, J. (2013). Groundwater potential estimation using vertical electrical sounding measurements in the semi-arid Khanasser Valley region, Syria. *Hydrological Sciences Journal*, 58:2, 468-482, doi: **http://dx.doi.org/10.1080/02626667.2012.751109**

Asfahani, J. (2014). Statistical factor analysis technique to interpret nuclear and electrical well logging measurements for basalt characterization. Case Study South. *Syr. Appl. Radiat. Isot.* 84, 33-39.

Asfahani, J. & Abdul Ghani, B. (2012). Automated interpretation of nuclear and electrical well loggings for basalt characterization. Case Study South. *Syr. Appl. Radiat. Isot.* 70, 2500-2506.

Asfahani, J., Abdul Ghani, B. & Ahmad, Z. (2015). Basalt identification by interpreting nuclear and electrical well logging measurements using fuzzy technique (case study from southern Syria). *Appl. Radiat. Isot.* 105, 92-97.

Asfahani, J. (2017-a). Porosity and hydraulic conductivity estimation of the basaltic aquifer in Southern Syria by using nuclear and electrical well logging techniques. *Acta Geophys*. doi: **https://doi.org/10.1007/s11600-017-0056-3**

Asfahani, J. (2017-b). Fractal theory modeling for interpreting nuclear and electrical well logging data and establishing lithological cross section in basaltic environment (case study from Southern Syria). *Appl. Radiat. Isot.* 123, 26-31.

Asfahani, J. & Al-Fares, W. (2021). Alternative vertical electrical sounding technique for hydraulic parameters estimation of the quaternary basaltic aquifer in Deir AlAdas area, Yarmouk Basin, Southern Syria. *Acta Geophysica*. doi: **https://doi.org/10.1007/s11600-021-00646-x**.

Chakravarthi, V., Shankar, GBK., Muralidharan, D., Harinarayana, T. & Sundararajan, N . (2007). An integrated geophysical approach for imaging sub basalt sedimentary basins: case study of Jam river basin, India. *Geophysics* 72(6):141-147.

Dobrin, M B., 1976. *Introduction to geophysical prospecting*. Mc Graw-Hill, New York.

Ebong, DE., Akpan, AE. & Onwuegbuche, A.A. (2014). Estimation of geohydraulic parameters from fractured shales and sandstone aquifers of Abi (Nigeria) using electrical resistivity and hydrogeologic measurements. *J. Afr. Earth Sci.* 96:99-109.

Flathe, H. (1955). Possibilities and limitations in applying geoelectrical methods to hydrogeological problems in the coastal area of northwest Germany. *Geophysical Prospecting*, 3:95 110.

Keller, G.V. (1988). Rock and mineral properties. (In: Nabighian, M.N. ed.) *Electromagnetic Methods in Applied Geophysics, 1: Theory*. Society of Exploration Geophysicists, pp. 13-51, Tulsa.

Kumar, D., Rai, SN., Thiagarajan, S. & Kumari, R. (2014). Evaluation of theterogeneous aquifers in hard rocks from resistivity sounding data in parts of Kalmeshwar taluk of Nagpur district, India. *Curr. Sci.* 107(7), 1137-1145.

Lordon, A., Agyingi, C., Manga, V., Bukalo, N. & Beka, E. (2017). Geo-Electrical and Borehole Investigation of Groundwater in Some Basalts on the South-Eastern Flank of Mount Cameroon, West Africa. *Journal of Water Resource and Protection*, 9, 1526-1546. doi: **https://doi.org/10.4236/jwarp.2017.912097**

Mailet, R. (1947). *The Fundamental equations of electrical prospecting*. Geophy, 1974, 12, 529-556.

Muchingami, I., Hlatywayo, D.J., Nel, J.M. & Chuma C. (2012). Electrical resistivity survey for groundwater investigations and shallow subsurface evaluation of the basaltic-greenstone formation of the urban Bulawayo aquifer. *Physics and Chemistry of the Earth* 50-52, 44-51.

Orellana, E.& Mooney, H.M. (1966). Master Tables and Curves for Vertical Electrical Sounding Over Layered Structures: *Interciencia*, Madrid.

Ponikarov, V.P. (ed.) (1966*). The Geological Map of Syria, scale 1:200000, sheets I-37-XIX and I-36-XXIV*, Ministry of Industry, Damascus.

Rustadi, Darmawan., IGB, Haerudin., N. & *et al.* (2022). Groundwater exploration using integrated geophysics method in hard rock terrains in Mount Betung Western Bandar Lampung, Indonesia. *Journal of Groundwater Science and Engineering*, 10(1): 10-18. doi: **https://doi.org/10.19637/j.cnki.2305-7068.2022.01.002**

Velpen, B.A. (2004). Win RESIST Version 1.0. M. Sc Research Project. ITC, Deft, Netherlands.

Zohdy, A. A. R., Eaton, G. P, & Mabeym, D.R. (1974). Application of surface geophysics to groundwater investigations: in *Tech. of water sources investigations of the U.S. Geol. survey book 2*, chap, Dl. U.S. Dept. of the Interior, Geological Survey: U.S. Govt. Print.

Zohdy, A.A.R. (1989). A New Method for the Automatic Interpretation of Schlumberger and Wenner Sounding Curves. *Geophysics*, 54, 245-253.

Zohdy, A.A.R., & Bisdorf, R.J. (1989). *Schlumberger Sounding Data Processing and Interpretation Program*: U. S. Geological Survey, Denver.

Geofísica Internacional (2024) **63-2**: 851 - 864

The use of *in situ* Gamma-Ray Spectrometry to Assess the Environmental Impacts of Intensive Agriculture in terms of Geochemical Mobility in soil and waters

Matheus Felipe Stanfoca Casagrande[1*], César Augusto Moreira[1], Lucas Moreira Furlan[1] and Vania Rosolen[1]

Abstract

The concentration and mobility of metals in the lithosphere and hydrosphere are led by many physical-chemical parameters and processes from natural and anthropogenic origins, the last one resulting in impacts over many ecosystems around the World, including wetlands. These transitional zones, often characterized by the presence of hydric soils, adapted vegetation, and seasonal or permanent presence of surface water, are commonly under human pressure in terms of land use conversion and contamination, notably in agricultural production areas, where excess of nutrients/organic matter, pesticides, salts, sediments, heavy metals and radionuclides (originated from inorganic fertilizers) can substantially alter the ecological balance of those ecosystems. Thus, this study aimed to evaluate the agricultural impact over a tropical geographically isolated wetland in the Brazilian Cerrado by the analysis of geochemical mobility and interaction between surface and groundwater through in situ gamma-ray spectrometry and hydraulic conductivity measurements. The results demonstrated that the margins of this diabase-derived soil wetland are one of the most important and critical compartments due to its capacity of metal immobilization and surface water infiltration, indicated especially by uranium concentrations. Thorium, in turn, was most related to colluvial transport from slopes to the center of wetland. It was also corroborated by low hydraulic conductivity zones as a result of soil compaction due to heavy agricultural machinery and increase in runoff fluxes. Thus, this methodology could be used as an initial fast screening method in wetlands under other climatic and geological/pedological contexts to evaluate the local hydrogeochemical dynamics and impacts of agriculture.

Key words: uranium, thorium, hydrology, wetland, contamination, hydraulic conductivity.

Resumen

La concentración y movilidad de metales en la litosfera y la hidrosfera están influenciadas por muchos parámetros físico-químicos y procesos de origen natural y antropogénico, siendo este último responsable de impactos en muchos ecosistemas alrededor del mundo, incluyendo los humedales. Estas zonas de transición, a menudo caracterizadas por la presencia de suelos hídricos, vegetación adaptada y presencia estacional o permanente de agua superficial, suelen estar bajo presión humana en términos de conversión de uso del suelo y contaminación, especialmente en áreas de producción agrícola, donde el exceso de nutrientes/materia orgánica, pesticidas, sales, sedimentos, metales pesados y radionúclidos (provenientes de fertilizantes inorgánicos) pueden alterar sustancialmente el equilibrio ecológico de estos ecosistemas. Por lo tanto, este estudio tuvo como objetivo evaluar el impacto agrícola en un humedal tropical geográficamente aislado en el Cerrado brasileño mediante el análisis de la movilidad geoquímica e interacción entre agua superficial y subterránea a través de espectrometría de rayos gamma in situ y mediciones de conductividad hidráulica. Los resultados demostraron que los márgenes de este humedal, con suelos derivados de diabasa, son uno de los compartimentos más importantes y críticos debido a su capacidad tanto de inmovilización de metales como de infiltración de agua superficial, indicado especialmente por las concentraciones de uranio. El torio, por su parte, se relacionó principalmente con el transporte coluvial desde las pendientes hacia el centro del humedal, corroborado también por zonas de baja conductividad hidráulica como resultado de la compactación del suelo debido al uso de maquinaria agrícola pesada y aumento del flujo de escorrentía. Por lo tanto, la metodología aplicada podría utilizarse como un método inicial de detección rápida en humedales bajo otros contextos climáticos, geológicos y edafológicos, con el fin de evaluar la dinámica hidrogeoquímica local y los impactos de la agricultura.

Palabras clave: uranio, torio, hidrología, humedal, contaminación, conductividad hidráulica.

Received: May 23, 2023; Accepted: December 13, 2023; Published on-line: April 1, 2024.

Editorial responsibility: Dr. Oscar C. Valdiviezo-Mijangos

* Corresponding author: Stanfoca Casagrande, Matheus Felipe, e-mail: matheus.fs.casagrande@unesp.br
[1] São Paulo State University (Universidade Estadual Paulista), Department of Geology, Av. 24A, 1515, CEP: 13506-900, Rio Claro (SP), Brazil.

Matheus Felipe Stanfoca Casagrande, César Augusto Moreira, Lucas Moreira Furlan, Vania Rosolen

https://doi.org/10.22201/igeof.2954436xe.2024.63.2.1711

1. Introduction

The mobility and accumulation of certain chemical elements in geological and hydrogeological environments are fundamental aspects in studies of mineral exploration and soil and environmental sciences (Boyle, 1982; Ridley, 2013; Kesler & Simon, 2015). The influence of natural and anthropogenic processes occurring in the critical zone determine the mobilization and segregation of certain chemical species over others. Such mechanisms have been active since the beginning of the planet's evolutionary history, demonstrated by the chemical heterogeneity of the Earth, where the diversity of lithotypes, soils, and occurrence of mineral deposits are some of its most notable products.

Within the context of environmental studies, specific patterns in the spatial distribution of some chemical elements or compounds in water, air, soil, and sediment often demonstrate the direct or indirect influence of human activities on the environment (Calabrese *et al.*, 2005), which have the power to trigger profound impacts on ecosystem equilibrium at various scales.

In the case of agriculture and livestock farming, both activities have the capacity to drastically alter the integrity of soils and hydrological systems through the release of pesticides, nutrients, salts, sediments, organic matter, pathogens, and metals/heavy metals into the environment (Mateo-Sagasta *et al.*, 2018). Thereby, the complexity of mobility of an specific element is given by physical-chemical conditions of soils and waters, whose values of pH, presence of clay minerals (texture), organic compounds, microorganisms, and the concentrations of other chemical species, play a profound role in the geochemical behavior of metals through the mechanisms of sorption/desorption, complexation, reaction and precipitation (Iaea, 1973; Becegato & Ferreira, 2005; Souza & Ferreira, 2005; Conceição & Bonotto, 2006a; Hussain & Hussain, 2011; Mazzilli *et al.*, 2013).

Additionally, natural environmental radioactivity can also be disturbed by the addition of radionuclides originated from the decay series of ^{232}U, ^{235}U, and ^{232}Th present in mineral fertilizers (NPK), where the main raw material for the production of phosphate concentrates, with P_2O_5 concentrations ranging from 32% to 38%, are phosphate-rich minerals rocks, especially the apatite group (Ulbrich *et al.*, 2009). According to Isherwood (2000), besides U and Th, other elements such as Cd, also contained in small amounts in phosphate minerals, are also present in fertilizers due to the inefficiency of industrial processes to totally remove them. This fact occurs due to the crystal structure of apatite, where Ca^{2+} can also be partially replaced by other elements, such as Pb and the rare earth group (ETR) members, in addition to the exchange of the PO_4^{3-} by other radicals such as UO_4^{2-}, AsO_4^{2-}, or SiO_4^{4-} (Loureiro *et al.*, 2005). In the case of Brazil, igneous rocks such as carbonatites account for approximately 95% of the raw material for apatite concentrate production in the country (Loureiro *et al.*, 2005), where the application and management of agrochemicals are a growing concern as the country takes one of the highest positions in food production in the world.

Due to its extensive territory, Brazil is also the custodian of some of the world's most biodiverse tropical biomes, while also being an important worldwide recognized agricultural hub. As a result, land use and management associated with environmental preservation practices on local and regional scales constitute actions of global interest, both in terms of ensuring the supply of agricultural goods such as food, fuel, and fibers, preserving the integrity of the environment and the quality of water and biological resources.

This issue is even more critical in specific environments, such as wetlands, where the interaction between surface water and groundwater is even more active and direct, especially when considering the regional influence of an entire group of wetlands (Maltby, 1988; Mclaughlin *et al.*, 2014; Hayashi *et al.*, 2016; Rains *et al.*, 2016). Wetlands cover 6% of Earth`s surface, and the agriculture is the main factor to wetlands degradation, such as pollution and eutrophication (Guo & Yang, 2016). Pollutants are retained through precipitation and/or adsorption processes in clay minerals and organic matter or released to water (Luko-Sulato *et al.*, 2012). Their role on water quality, storage, and aquifer recharge can be extremely important for the management of water resources and environmental protection, however those ecosystems are often excluded from environmental politics and social interest. Thus, understanding the hydrogeochemical dynamics of those ecosystems is an important factor in soil, water and agriculture management.

The present study aims to evaluate the impact of agricultural activities based on the mobility of radionuclides and in situ hydraulic conductivity in a small isolated wetland originally developed in the Brazilian Cerrado. The relevance of the study relies on the location, like much of the state, which is mainly dedicated to the cultivation of sugarcane and soybeans, one of the most important sectors of Brazilian agribusiness

2. Study area

The study area is located in the rural zone of the municipality of Cordeirópolis, at an altitude of 653 m and defined by the coordinates -22º 29' 22" S and -47º 29' 14" W, part of the Limeira Microrregion and Piracicaba Mesoregion, central portion of the state of São Paulo, Brazil (Figure 1).

The wetland itself is classified as geographically isolated due to its lack of superficial connection with nearby drainages and streams (Leibowitz, 2015; Tiner, 2003; Hayashi *et al.*, 2016; Furlan *et al.*, 2023). Its circular shape resembles a roman amphitheater, with the center (flooded during a certain period

of the year) at a lower level compared to the slopes, where the land was converted to agriculture in this specific case. Thus, the local hydrological connection occurs only through groundwater fluxes, probably recharging deep aquifers and nearby streams during most of the year (Casagrande *et al.*, 2021).

Due to the heavy agricultural machinery traffic in the area, unpaved roads were built around the entire perimeter of the area, as well as an area designated for high voltage power transmission lines that intercepts the study area in the approximate N-S direction, which corresponds exactly to the soybean cultivation zone (Figure 2).

The local climate is classified as "Cwa" (Köppen & Geiger, 1928), characterized by warm humid summer (from September to April) and dry mild winter (from May to August) with an average temperature of 21.1°C. In geological terms, the wetland is developed on a diabase sill of the Serra Geral Formation, a unit belonging to the Paraná Basin and associated with fissure magmatism caused by the breakup of the Gondwana megacontinent during the Cretaceous and the consequent evolution of the South Atlantic ocean (Milani *et al.*, 2007). This dike lies above the Perminan sedimentary rocks of Corumbataí Formation, whose maximum local thickness is about 130 m and predominantly composed of dark gray argillites and siltstones at its basal portion, while the top is described as reddish-purple argillites, shales, and siltstones with intercalations of carbonate banks and fine sandstones (Schneider *et al.*, 1974).

3. Environmental radioactivity

Radioactivity can be defined as the spontaneous decay of chemical elements, with the emission of alpha particles (positively charged as a helium nucleus) and beta particles (negatively or positively charged as electrons or positrons, respectively), and

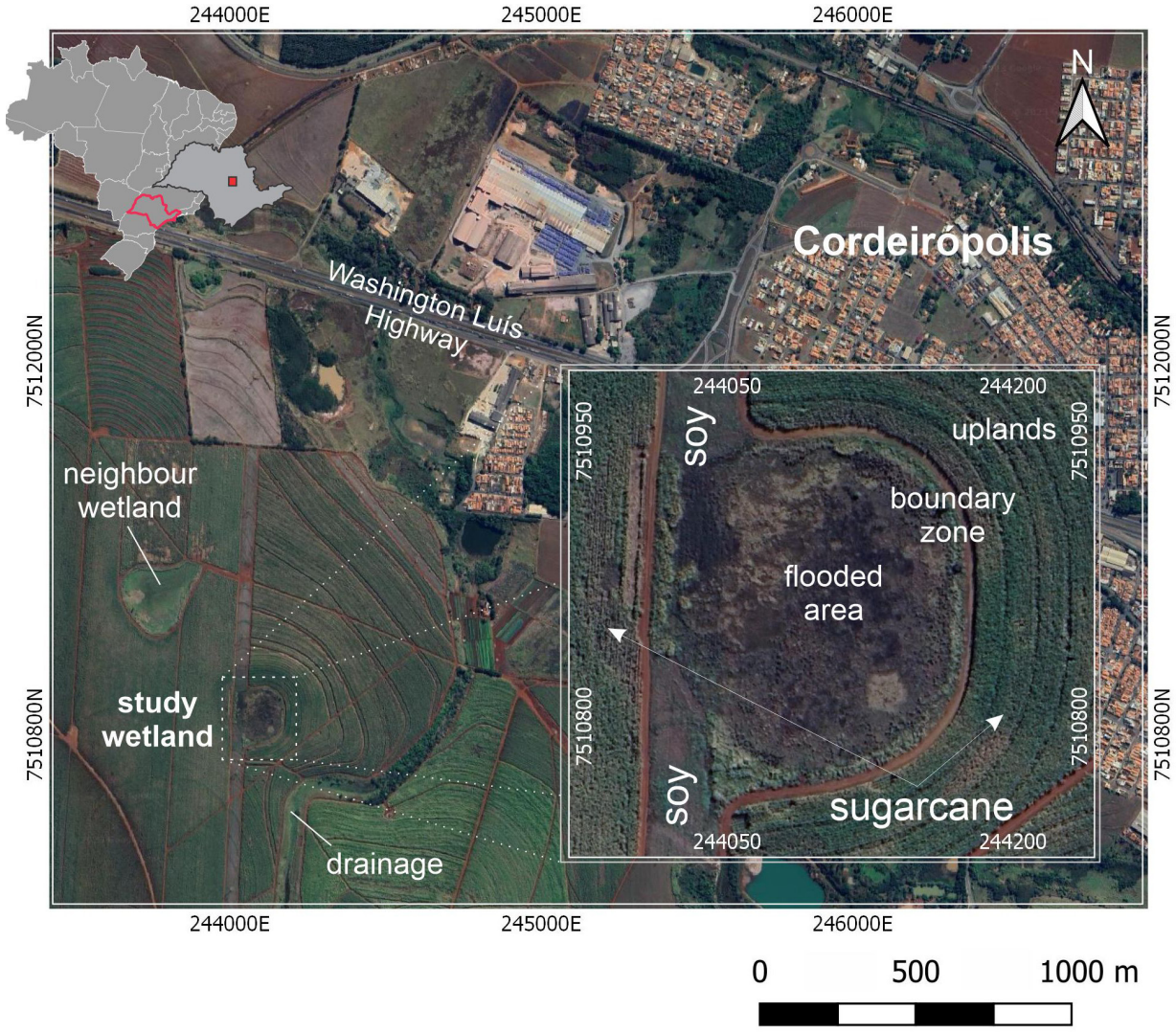

Figure 1. Location of the study area, with the indication of Cordeirópolis, access roads and highways.

Figure 2. North view of the wetland area (flat and lower terrain in the middle of the picture), with soybean (under the high voltage power transmission) and sugarcane cultivation. The yellow circle indicates the presence of surface water on the access road as a direct result of land conversion to agriculture.

the eventual release of energy in the form of gamma photons, which are highly penetrative. In the electromagnetic spectrum, gamma rays have the highest frequency (>1019 Hz) and the shortest wavelength (< 10-11 m).

Radionuclides tend to undergo spontaneous decay, where the atomic nucleus emits a radioactive particle or a gamma ray and ends up in a lower energy level and, therefore, relatively more stable. The decay of a number N of nuclei of any decaying radioactive element can be expressed by the general equation:

$$N=N_0e^{-\lambda t} \quad (1)$$

where N corresponds to the number of radionuclides at time t; N_0 is the initial number of radionuclides; and λ represents the decay constant.

Natural occurring radionuclides come from both cosmogenic (such as ^{14}C and ^{3}H) and lithospheric sources (such as ^{235}U, ^{238}U, ^{232}Th and ^{40}K) (Unscear, 2008), with the latter group being the most important source of environmental radioactivity, surface exposure, and mobilization into the hydrosphere and atmosphere, along with their associated radionuclides (Eisenbud & Gesell, 1997; Casagrande & Bonotto, 2018).

Unlike ^{40}K, which decays directly to stable nuclides such as ^{40}Ca through β- emission (89.3%) and to ^{40}Ar (10.7%) through the phenomenon of electron capture plus gamma emission of 1.46 MeV, the radioisotopes ^{238}U, ^{235}U, and ^{232}Th constitute primordial nuclides of the so-called decay series. In the case of uranium, its most abundant isotope is ^{238}U (93.3%), whose decay series includes 15 daughter radioisotopes with significantly shorter half-lives until its end as stable ^{206}Pb (Chu *et al.*, 1999). On the other hand, ^{235}U, of great interest in the nuclear industry for energy and military purposes, has a proportion of only 0.7% and its series, composed of 12 radioisotopic species, ends with the stable ^{207}Pb (Chu *et al.*, 1999; Unscear, 2008). Finally, ^{232}Th represents almost all the natural thorium (99.98%) and decays in a series down to ^{208}Pb (Chu *et al.*, 1999).

In terms of abundance, potassium is by far the most common element compared to uranium and thorium, commonly measured in parts per million (ppm). The first constitutes about 2.3% of the Earth's crust and is a major element in various rock-forming minerals, unlike the two other metals that have concentrations of approximately 2.4 ppm and 12 ppm, respectively, and are often found as minority elements associated with various resistate minerals (Emsley, 1998).

The three elements are unknown in natural settings as free metals and the most common oxidation states for uranium are U^{4+} and U^{6+}, whereas thorium often exhibits a 4+ oxidation state in nature. Both uranium and thorium are commonly associated with Zr, Hf, rare earth, Nb, and Ta in terms of geochemical aspects and mobility (Ulbrich *et al.*, 2009).

In soils, U and Th comprises concentrations as low as 1 ppm and 5 ppm in average, respectively, with a deep increase in soils derived from granitic, gneissic and alkalic igneous rocks (BOYLE, 1982). Otherwise, most mafic and ultramafic rocks generally exhibit low U and Th concentrations but in soils the A horizon is usually the richest in U, whereas C horizon is generally the most enriched just in vicinity of uraniferous deposits (Musset & Khan, 2000). The differential solubility of uranium and thorium can influence their mobility in natural environments as U^{6+} presents higher solubility, which can favor its release, for example, through liquid soil phase in oxidizing mediums (Boyle, 1982), allowing its migration. However, uranyl ion can be retained by neoformed substances, including colloids of organic origin.

Th^{4+}, in turn, has the opposite behavior compared to U^{6+}

under same environmental conditions (Ulbrich *et al.*, 2009). However, when released, thorium will certainly be immobilized with some ease, through its retention in secondary substances.

4. Materials and methods

Gamma detectors are widely used in geosciences due to the relative ease of detection and high penetrability of gamma emissions, as well as their ability to provide quantitative and qualitative information on radioactive elements in mineral samples, soils, and water. As such, their applicability, especially in portable or airborne equipment, includes research on undifferentiated intrusions and impact craters, mineral prospecting, oil exploration, aiding in the determination of geological boundaries and large structures (Hoff *et al.*, 2004; Vasconcelos *et al.*, 2012; Fianco *et al.*, 2014; Ferronsky, 2015), as well as in the environmental field, with applications in controlling areas impacted by radioactive leakage, medical geology, and studying the influence of fertilizer compounds in water systems and soils (Umisedo, 2007; Schuler *et al.*, 2011).

This tool is incorporated in geophysics as a passive, non-invasive radiometric method that involves detecting gamma emissions from various natural radioisotopes, including those from the decay series of ^{235}U, ^{238}U, ^{232}Th, and ^{40}K. In gamma spectrometry, it is common the use of photopeaks generated by daughter radionuclides in order to determine their respective initial decay series components, where energies of 1461 keV (^{40}K), 1765 keV (^{214}Bi), and 2615 keV (^{208}Tl) are used to estimate the concentrations of K, U, and Th, respectively (Erdi-Krausz *et al.*, 2003). However, this condition is theoretically valid only with the consideration of secular equilibrium in the sample or investigated medium (Ferronsky, 2015; Casagrande & Bonotto, 2018).

In order to determine the coefficient of soil hydraulic conductivity in the field and make a correlation with gamma signals distribution, a Guelph Permeameter was utilized (Reynolds *et al.*, 1983). The method is based on the measurement of saturated hydraulic conductivity in situ, by excavating boreholes up to a depth of 50 cm, where the equipment is set. When a constant hydraulic load is established inside the borehole, a "bulb" of water saturation is generated into the soil. The calculation of the hydraulic conductivity in situ is only possible after the stabilization of the water column, where graduate marks on the equipment and a chronometer are used in order to determine water infiltration rates (R1 and R2), followed by the equations of the double head method (Soil Moisture Corp., 2012):

$$K_{fs} = [(0.0041)(X)(R2) - (0.0054)(X)(R_1)] \quad (2)$$

$$K_{fs} = [(0.0041)(Y)(R2) - (0.0054)(Y)(R_1)] \quad (3)$$

where K_{fs} comprises the hydraulic conductivity (cm.$^{s\text{-}1}$); X and Y stand for the area of the reservoir tube section (35.22 cm^2 or 2,16 cm^2); R1 and R2 are the stabilized infiltration rates corresponding to H_1 (5 cm) and H_2 (10 cm), respectively, in cm.s^{-1}. Taking into account the physical properties of the study area, the dimensionless values of 0,0041 and 0,0054 are based on some important parameters such as soil type (texture-structure category related to the local clay and agricultural soils), water height in borehole, soil matric flux potential and borehole radius (Zhang *et al.*, 1998; Soil Moisture, 2012).

5. Data aquisition

In the study area, 507 surface reading points were obtained, covering all segments of the wetland, including its center and slopes (Figure 3). The focus of the analysis was on K, Th, and U elements, with a predefined acquisition time of 180 seconds, analogous to other studies (see Šimíček *et al.*, 2012; Nardy *et al.*, 2014). The conversion of counts per second in the energy windows defined for ^{40}K, ^{214}Bi, and ^{208}Tl to concentration units was automatically performed by the RS-332 gamma spectrometer model from Canadian Radiation Solutions, associated with a BGO scintillation crystal of 104 cm^3 and FWHM resolution less than 11.5%.

The analysis period was concentrated in the dry season, specifically in two field campaigns in August 2020, in order to minimize the effect of gamma signal attenuation in excessively wet soils, as expected for the central zone of the wetland. A second field campaign was carried out after one year, shortly after a fire of unknown causes consumed the entire area. The purpose of the new survey was to analyze possible temporal variations in K, Th, and U in the soil, as well as to serve as a qualitative comparative in determining the degree of gamma signal absorption caused by the natural substrate moisture, which was very low after the fire. Thus, the focus of the new acquisition stage was concentrated only inside the wetland, which included 157 reading points with the usual acquisition time of 180 seconds.

For data quality analysis, the coefficient of variation (CV) (Becegato *et al.*, 2008; Mikami *et al.*, 2015) of the obtained values was calculated, according to equation 4:

$$CV = (\sigma.100\%) / \mu \quad (4)$$

where μ represents the arithmetic mean of the values obtained at each analysis point and σ represents the associated standard deviation. The generation of maps of eU, eTh, Ke, and eU/eTh

distribution was performed through the Oasis Montaj (Geosoft) platform, where the data were interpolated using the kriging method, followed by the minimum curvature for central value smoothing over the edges.

The hydraulic conductivity tests, on the other hand, comprised 70 uniformly distributed points throughout the study area, both inside and on the slopes of the wetland (Figure 3). Data acquisition was performed over a period of 2 years (2020-2021) and was carried out only during the dry season due to the impossibility of conducting hydraulic conductivity tests in fully saturated soils, which occurs annually in the study area during the rainy period. Subsequently, the spatial data were interpolated to generate a hydraulic conductivity map of the area using the kriging method through Oasis Montaj (Geosoft) software.

6. Results and discussions

The results indicate that the concentrations of K varied from 0.03 to 0.2%, with a mean of 0.082% and a median of 0.078%. Approximately 8% of the analysis points resulted in values below the detection limit of the equipment (0.02%). On the other hand, eU and eTh did not present values below the detection limit, ranging from 1.28 pmm to 2.83 ppm and 6.94 ppm to 11.43 ppm, respectively. In this case, eU resulted in an average value of 2.02 ppm and a median of 2.01 ppm, while eTh indicated mean and median values of 9.55 ppm and 9.57 ppm, respectively. For comparison, in agriculture soil managed with phosphate fertilizer Souza Souza e Ferreira (2005) found average concentrations for eU as high as 6,87 ppm, whereas eTh showed lower values of around 4,3 ppm.

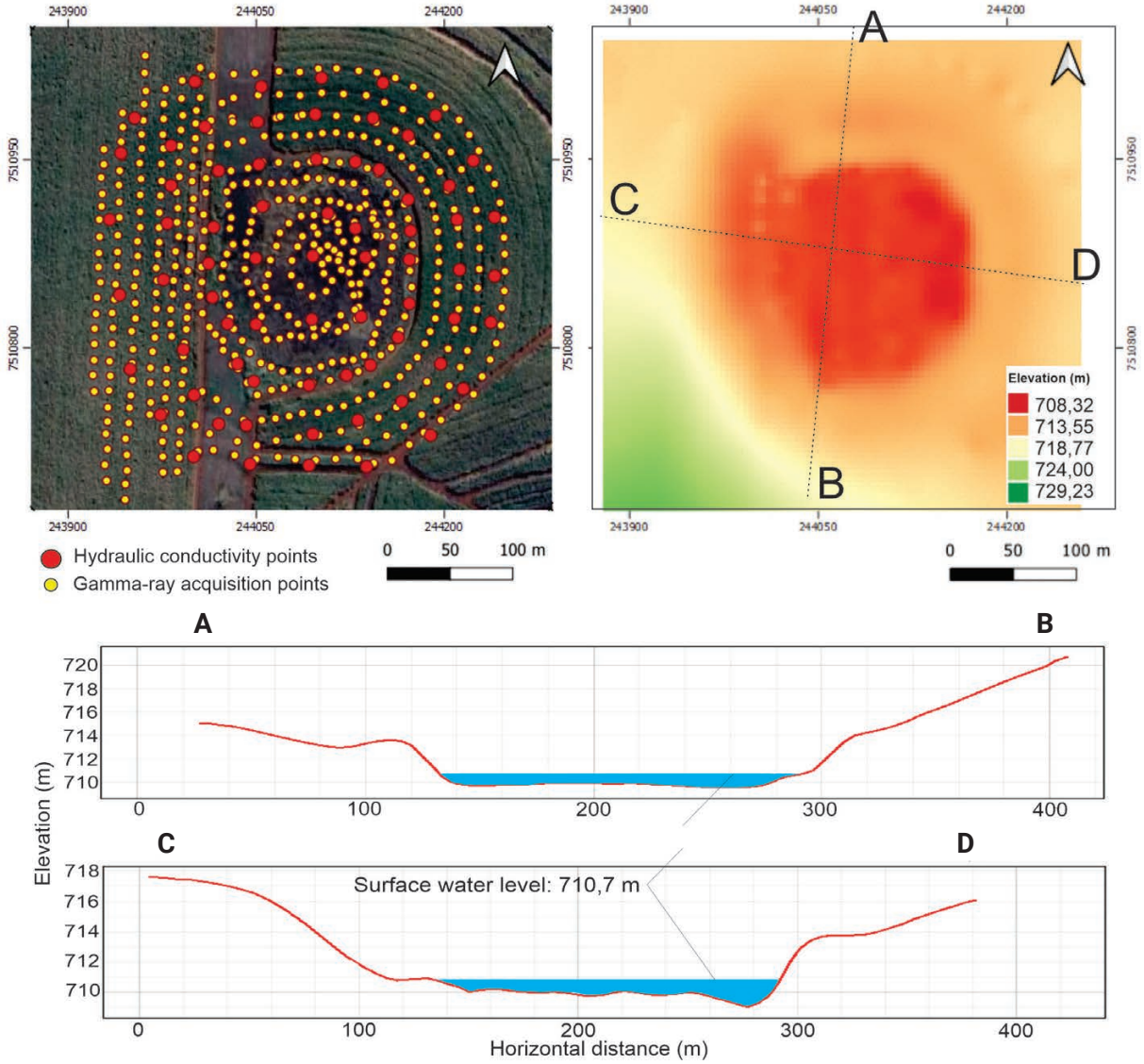

Figure 3. Distribution of hydraulic conductivity and gamma-ray acquisition points, covering all segments of the study wetland. The Digital Elevation Model (DEM) of the area was generated by multiple high precision GPS acquisitions, giving an idea of the local topography in terms of slopes around the wet center (geographically isolated wetland).

Although the use of coefficient of variation CV as a way of evaluating data dispersion in terms of precision and accuracy, its value is subjective and a maximum value of 10% was established for eU and eTh during the interpolation stage. Only five points exceeded this limit for eU (all of them discarded) and the boxplot diagrams (Figure 4) indicated extremely high CV values related to K, with minimum and maximum values of 14% and 100%, respectively.

Soils generated by the alteration of the Serra Geral Formation diabases are generally characterized by low concentrations of radionuclides (Conceição & Bonotto, 2006a), although several studies have pointed to the existence of radiometric anomalies in associated soils generated by the use of phosphate fertilizers in agriculture, especially for sugarcane (Souza & Ferreira, 2005; Conceição & Bonotto, 2006b). This fact may be related to the radiometric interest zones found in the study region, where presence of diabase-derived clay-rich soils and the occurrence of organic matter might lead to a geochemical sink for many elements and compounds, including radionuclides belonging to U and Th decay series originated from mineral fertilizers (Souza & Ferreira, 2005). However, Olivie Lauquet *et al.* (2001) emphysises that the dissolved organic carbon (DOC) concentrations play an important role in a wetland's behavior as a sink or source of trace elements and their transfer to water systems.

The spatial distribution of the element K showed strong heterogeneity throughout the study area, as observed in the map of Figure 5, where warmer shades correspond to higher concentration values (%) and cooler colors indicate relatively depleted regions in the element. The map allowed for the identification of anomalous concentration zones characterized by values close to 0.19 ppm, particularly in the northwest and southwest portions of the map, which correlate with areas of the slope covered with sugarcane. It is noteworthy that the SW-NE orientation of the anomaly located in the southwest region of the map is associated with the roads and the alongated soy plantation area, with visible propagation into the interior of the humid area.

Likewise, a large anomaly of relatively high concentration was identified along the northern and northeastern edges of the wetland, which also appears to follow the same orientation as the rural access road that borders the center of the humid area. In this case, the tendency of the anomaly to propagate into the central region of the study area is equally notable.

By comparing the maps of potassium CV distribution and K gamma-ray (Figure 5), it was possible to verify a clear correlation between low K anomalies and regions characterized by higher CV values, theoretically indicating low reliable data. In theory, this issue would be solved if longer acquisition times were applied, but according to tests performed in the field the chosen acquisition time of 300 seconds was the best option compared to other tests (600 and 900 seconds) where the slightly difference in results (less tha 10%) did not justify the large increment of acquisition time.

Methodologically, this relationship would point to a very low concentration of ^{40}K at the site, combined with the "short" acquisition time that is usually adopted in terrestrial gamma-ray acquisitions. However, in qualitative terms, such areas should not be disregarded because they represent potassium depleted zones. Thus, it was possible to indicate the presence of at least four low-K zones in Figure 5, especially along the soy plantation located in the east of the study area. The soil derived from weathering of diabase and constituted by low-activity clays. Thus, it is expected that K contents variation is mainly related to plant uptake or leaching losses of mobile K via fertilizers (Reinhardt and Herrmann, 2018).

On the other hand, the eU distribution map indicated a high contrast in the element concentration between the interior of the

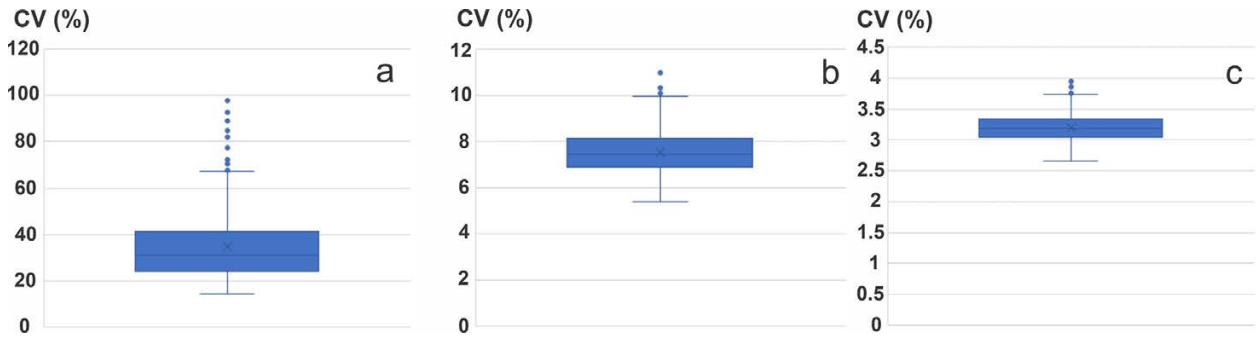

Figure 4. Boxplot diagrams for coefficient of variation related to K (a), U (b) and Th (c) data.

study area and its slopes, with its center anomalously depleted in U (~1.5 ppm) and its outer edges enriched in the metal (~2.8 ppm). From the perspective of the slopes, the northern portion is characterized by moderate eU values (~2 ppm), while further south there are zones of higher concentrations correlated with agriculture (~2.8 ppm).

In a less defined way, the variation in eTh concentration throughout the study area followed, to some extent, the same behavior observed for eU, but with a center that was not completely depleted in the element in question (Figure 5). There, eTh concentrations varied from 6.95 ppm to values greater than 11.40 ppm, mainly in the northeast and southeast edges of the central area.

It is worth noting the presence of a high concentration anomaly correlating to the point of water accumulation in the N-S oriented rural access road, where high eU values are also observed, as well as the southeastern portion of the study area already in agricultural land.

In this case, the eU/eTh ratio was used for mapping and examining patterns of uranium mobility relative to thorium, due to the observed average ratio of 0.21 between the two metals in the in the study area and the relatively immobile nature of Th compared to U. Therefore, lower eU values relative to eTh would indicate depletion, while higher values would indicate enrichment. The map shows warmer colors concentrated along the edges of the central area of the study region, suggesting relative enrichment of uranium in these zones. In contrast, the green and yellow shades distributed along the slopes and northwestern portions of the study region approach the obtained average value of 0.21, being also close to the average of approximately 0.25 discribed for the lithosphere. In addition, the study area shows several anomalies of high eU/eTh ratio (possibly due to accumulation of leached U) (BOYLE, 1982).

Another and more plausible possibility relies on the mobility of Th, and consequently its daughter radionuclides, through colluvial transport (Pickup & Marks, 2000; Ulbrich *et al.*, 2009). As long as Th can be adsorbed by solid fractions of soil (clay minerals, Fe-Mn-Al-Ti oxi-hydroxides, and organic compounds), the element might act as a good indicator of erosional and sediment accumulation processes, which are of profund interest in water and soil management. Thus, the spacial variability of Th over the study area follows almost the same pattern as observed for U, exept by the presence of a high-Th narrow elongated segment from the wet margins to the center of the wetland (NW-SE) where no fertilizer is directly applied, indicating an apport of sediments from the nearby slopes (Figure 5). Thus, the relationship between U and Th might be an complex influence of both processes: the geochemical lixiviation of U in relation to Th and the mobility of adsorbed Th by fine soil particles.

Another interesting characteristic relyes on the fact that the high-Th zones forming a ring around the wetland margin have some continuity into the flooded area, including the west portion along the N-S road and soy plantation, which might facilitate the input os sediments from higher levels to the lower zone, especially when the natural margin vegetation is impacted. Figure 2 shows the accumulation of water and sediments in the already mentioned pound formed along the unpaved road, right the same place where high values of eTh (and, in this case, eU as well) were observed (>11,40 ppm), a zone where a significative edge of the original wetland soil was converted into the access road and agriculture, as indicated by the elevation model and aerial imagery. Additionaly, K shows low concentration values in this exactly same spot probably due to plant uptake or leaching to groundwater.

The differences in the mobility of Th^{+4} and U^{+6} under an oxidizing environment may be the explanation of the existence of a well-defined uranium-rich ring over wetland margins in contrast to a similar less defined high-Th aureole.

All this complexity of geochemical mobilization of metals is especially because its different phases act through different retention and liberation mechanisms as a function of very specific physical-chemical paramethers that occur in the environment (Strawn *et al.*, 2020). From an ecological point of view, the fluxes between solid and liquid phases of soil are one of the basis of the maintenance of life on Earth, providing the disponibility of nutrients for primmary producers. Those mechanisms, however, might also act in the fixation of contaminnats of natural and human origins and are applied in many environemental projects (Uddin, 2017; Han *et al.*, 2019; Arif *et al.*, 2021), where the sorption mechanism work in the immobilization of ion on mineral surfaces, especially clay minerals, whose electrostatic behavior is controlled by chemical and cristalographical particularities.

After the fire in the following year, the K concentration values obtained were practically the same, while the spatial distribution of K in the center of the humid area showed certain changes, especially due to the absence of the elongated southwest anomaly that extended into its interior (Figure 6). In the case of eU, the range of values obtained during the second campaign was slightly lower, with the center of the study area still contrasting with its surroundings characterized by greater gamma response, but with values not as low as those observed during the acquisition prior to the fire. The eTh, in turn, also presented relatively higher concentration values in the second campaign, in addition to the extension of the high concentration anomaly (~11.3 ppm) from the northeastern edge to the center of the study area. As a result, the eU/eTh ratio was also affected in the same trend, although the contrast between the outer part and the edges of the study area persisted after the fire.

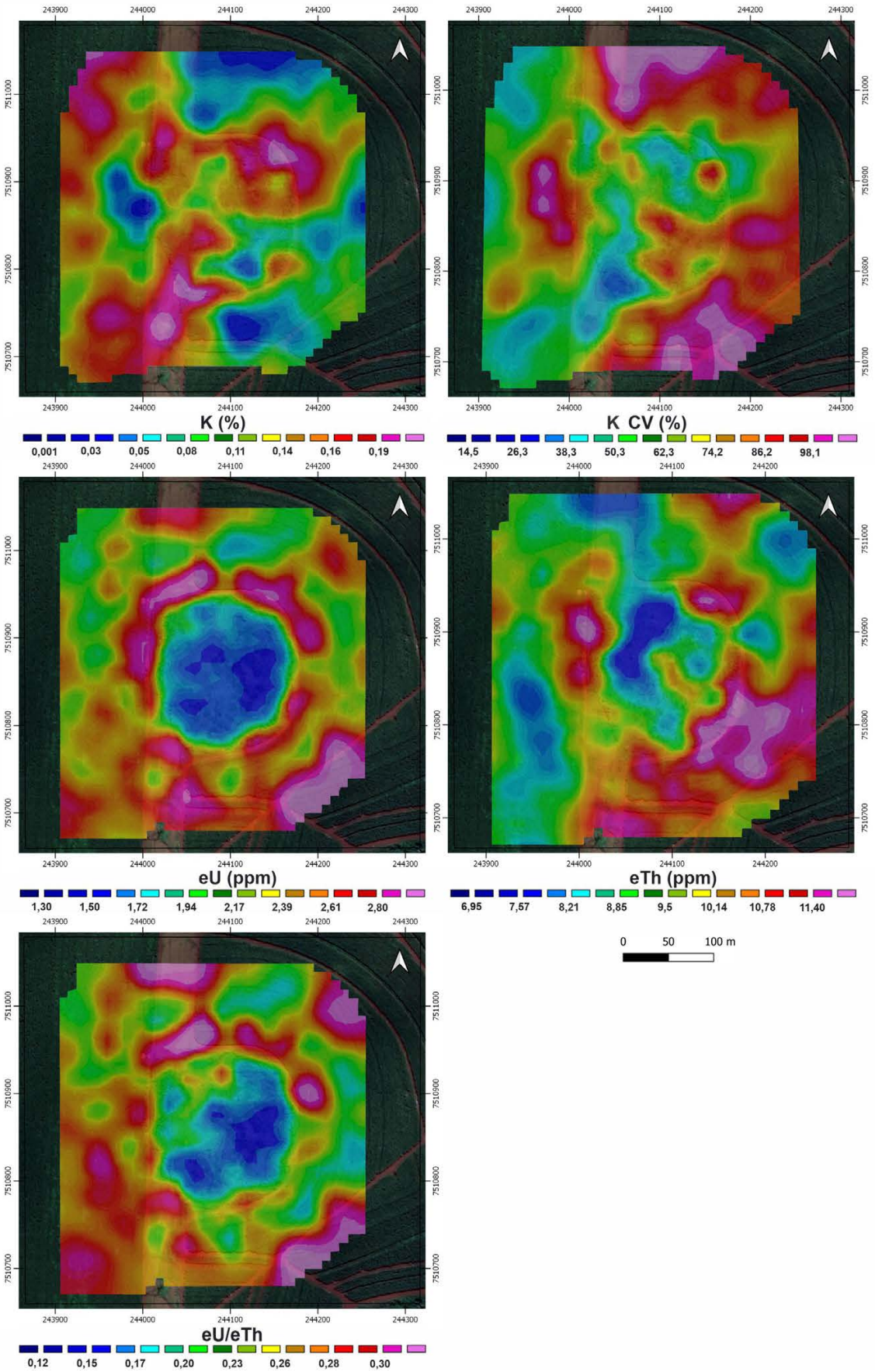

Figure 5. Maps of K (%), CV (K) (%), eU (ppm), eTh (ppm), and eU/eTh distribution obtained by gamma-ray acquisitions.

The slight variation in gamma response after one year is probably attributed to the reduction of the natural absorption effect due to low soil moisture and reduction of superficial organic matter in the weeks following the fire (Reinhardt & Hermann, 2018), when no precipitation was recorded in the area. However, the soil absorption effect was not intense enough to impair the qualitative evaluation of the spatial distribution of K, eU and eTh in the area, especially since the relative concentrations basically followed the same overall trend, particularly the contrast between the interior of the study area and its wet margins.

Other factors such as variations in fertilizer application over time and the presence of large amounts of mineral matter in the soil (ashes) can also have a subordinate influence on the surficial variability of the gamma response obtained after the fire. However, a more profound evaluation of element mobility from the soil to the water system must consider associated factors related to seasonal variations of hydrological and biochemical cycles, especially seasonal parameters such as temperature and water-table fluctuation over the year, which directly influences reducing conditions and organic matter decomposition (Olivie Lauquet *et al.*, 2001).

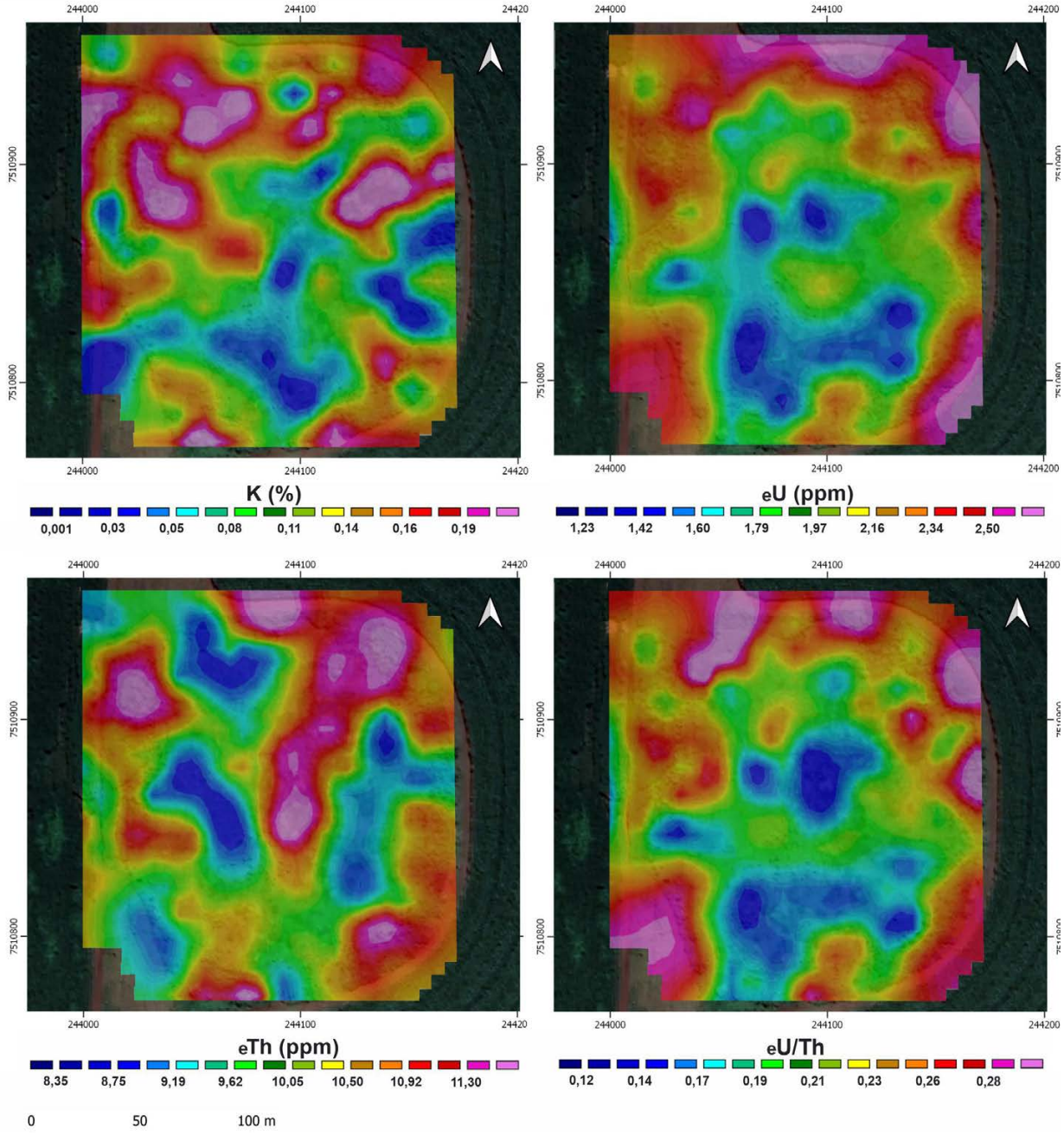

Figure 6. Maps of K (%), eU (ppm), eTh (ppm), and eU/eTh distribution obtained by gamma-ray acquisitions. (after the fire).

The hydraulic conductivity data acquired though Guelph Permeameter configure a shallow method to quantify the ability of water (or a given fluid) to pass through the pores and fractures in the geological environment. Thus, these surficial results can be compared with the spatial variability of K, U, and Th in order to describe the link between geochemical mobility and the local hydrogeological dynamics in terms of mass transfer. The relationship between soil and hydrosphere plays an important role in the geochemical dynamics of the system, since many reactions and ion mobility occur in aqueous medium.

The values of hydraulic conductivity were deeply variable, with a range in the order from 10^{-3} cm/s to 10^{-6} cm/s (Figure 7). The contrast between the center and the slopes around the wetland is very clear, specially by the low hydraulic conductivity values at its center ($<10^{-5}$ cm/s) and the variable, but frequently higher, values at the agriculture zones ($>10^{-4}$ cm/s). Some exceptions are observed as low conductivity zones over the slopes (blue areas, especially the one N-S oriented), which might be explained by the near surface soil compaction due to heavy machinery applied in the sugarcane plantation (Horn & Peth, 2011).

The reduction of pore space in the soil can impact not only the natural geochemical and biological dynamics, but also soil productivity in terms of food production (Tubeileh *et al.*, 2003; Blum, 2013). In addition, the increase of surface water flux resulted by the compaction of uppermost part of soils is often accompanied by a gain of erosion rates and consequent sedimentation, thereby causing the loss of arable land and soil nutrients, reduction of surface water quality, and siltation. Thus, this phenomenon might be a key factor for the occurrence the already mentioned high eTh concentration zones at the wetland center associated with colluvial transport, also evidenced by the same N-S alignment as observed for the long low conductivity zone in the slopes. This factor might be allied to the suppression of the natural margin vegetation, which acts as a natural barrier against solid particles (Mitsch & Gosselink, 2015)

Again, the wetland margins seem to be a very critical natural buffering zone, especially for its capacity to drain runoff water as a result of medium to high hydraulic conductivity values (~10^{-4} cm/s) compared to the center portion. This same compartment is also the responsible for the accumulation of U, probably by a combination of factors such as immobility as a result of a reduction front (at least during the surface water accumulation season), low hydraulic conductivity towards the central region of the wetland, and adsorption/complexation mechanisms in the fine textured diabase-derived soil.

During the dry season, it is possible that an alternation to aerobic conditions occur by the lowering of water-table level and the input of occasional oxygen-rich waters in the presence of electrons acceptors (Mn^{4+}, Fe^{3+} and NO^{3-}), which might lead to the mobilization of trace elements, in addition to a more efficient decomposition of organic matter (especially with medium to high temperatures even during winter), resulting in a higher DOC

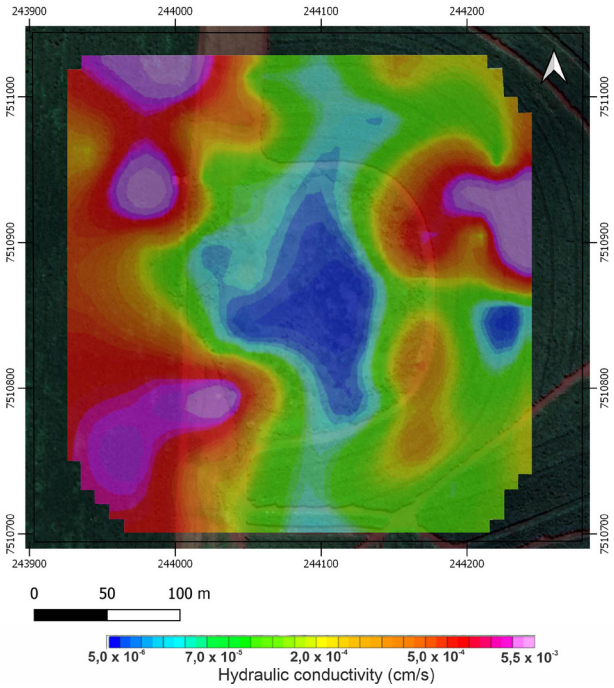

Figure 7. Hydraulic conductivity map acquired using a Guelph Permeameter.

concentration in waters (Strawn *et al.*, 2020; Olivie Lauquet *et al.*, 2001). Hence, the local wetland system might act as a source of chemical species for a short period of the year.

7. Conclusions

Based on gamma ray data and the hydraulic conductivity map, it was possible to assume the existence of a 20 meters wide strip zone around the wetland (from external and internal sides of the margins) where geochemical processes and hydrogeological factors play important role in the uptake, concentration, and immobilization of certain chemical elements, allied to the protection of wetlands's interior against heavy sedimentation uptake and surface water flow. Thus, the well-defined eU and eTh rings around wet margins represent clear evidences of the significance of wetlands as attenuation zones in the protection of surface and groudwater quality.

It is important to mention that even the higher values of eTh and eU found do not necessarily configure a contaminated site. However, the spatial distribution analysis based on gamma spectrometry method showed to be a very useful tool in order to establish an initial geochemical model and the definition of target areas for soil sampling in a such complex environment in terms of metal mobility, even though each specific element has its own behavior under different environmental parameters (pH, Eh, temperature, etc.) so other methods could be applied for a more detailed assessment, which includes regular soil sampling and chemical analysis that could lead to more expenses and longer field acquisitions. Thus, given the large variability of Brazilian wetlands in terms of size, geology, climate, vegetation, geochemistry and pedology, the use of gamma ray spectrometry as an initial fast low-cost screening method for hydrogeological characterization, soil management and evaluation of human impacts could easily be combine to other methods and applied to other similar environments.

The results corroborate the fact that wetlands are very distinct and important ecosystems with many environmental functions that must be considered in governmental policies, water resources management and public discussions. Thus, the results aim to contribute to highlight wetland importance and its wet margin zone in in terms of water infiltration (aquifer recharge and storage) and fixation of certain chemical species as natural "geochemical sponges". However, even though the accumulation of trace elements was observed, a profound study focused on local water samples collected over the hydroperiods should be performed in order to stablish the possible release of those elements to groundwater during periods of change in the parameters of pH, redox potential, water-table fluctuation and temperature.

8. Acknowledgements

This work was funded by the São Paulo Research Fundation (Fundação de Amparo à Pesquisa do Estado de São Paulo - FAPESP), through the project entitled "Hydrology and environmental function of upland wetlands in the Depressão Periférica Paulista (Brazil)" (Process n° 2020/03207-9).

I extend my sincere gratitude to the esteemed reviewers and the dedicated Associate Editor of Geofisica Internacional for their invaluable contributions to the enhancement of our manuscript. Their meticulous review and insightful comments have significantly enriched the quality and clarity of our work.

9. Author contributions

MFSC and CAM: Conceptualization, planning, data acquisition, data processing, interpretation and writing. VR: Planning, acquisition, critical data analysis and writing. LMF: Critical data analysis, writing and review.

10. References

Arif, M., Liu, G., Yousaf, B., Ahmed, R., Irshad, S., Ashraf, A., Zia-Ur-Rehman, M., Rashid, MS. (2021). Syn.thesis, characteristics and mechanistic insight into the clays and clay minerals-biochar surface interactions for contaminants removal-a review. *J Clean Prod.*; 310:127548. **https://doi.org/10.1016/j.jclepro.2021.127548**

Becegato, V.A., Ferreira, F.J.F. (2005). Gamaespectrometria, resistividade elétrica e susceptibilidade magnética de solos agrícolas no noroeste do estado do Paraná. *Revista Brasileira de Geofísica.* 23(4): 371-405. **http://dx.doi.org/10.1590/S0102-261X2005000400004**

Becegato, V.A., Ferreira, F.J.F., Cabral, J.B.P., Rafaelli Neto, S.L. (2008). Gamma-ray Spectrometry Sensor and Geochemical Prospecting in an Area of Sugar Cane Plantation. *Braz. arch. biol. technol.* 51:1, 1-10. **http://dx.doi.org/10.1590/S1516-89132008000100001**

Blum, W.E.H. (2013). Soil and Land Resources for Agricultural Production: General Trends and Future Scenarios-A Worldwide Perspective. *International Soil and Water Conservation Research.* 1;3, 1-14. **https://doi.org/10.1016/S2095-6339(15)30026-5**

Boyle, R.W. (1982). *Geochemical prospecting for thorium and uranium deposits.* Elsevier Scientific Publishing Company, Amsterdam, 498 p.

Calabrese, E.J., Kostecki, P.T., Dragun, J. (2005). Contaminated Soils, Sediments and Water: *Science in the Real World.* Springer, Boston. 611 p.

Casagrande, M.F.S., Bonotto, D.M. (2018). The use of γ-rays analysis by HPGe detector to assess the gross alpha and beta activities in waters. *Appl Radiat. Isot.* 137:1–11. **https://doi.org/10.1016/j.apradiso.2018.02.027**

Casagrande, M.F.S., Furlan, L.M., Moreira, C.A., Rosa, F.T.G., Rosolen, V. (2021). Non-invasive methods in the identification of hydro-

logical ecosystem services of a tropical isolated wetland (Brazilian study case). *Environ Chall.* 5:100233. **https://doi.org/10.1016/j.envc.2021.100233**

Chu, S.Y.F., Ekström, L.P., Firestone, R.B. (1999). *The Lund/LBNL Nuclear Data Search.* **http://nucleardata.nuclear.lu.se/nucleardata/toi/index.asp**

Conceição, F.T., Bonotto, D.M. (2006a). Dose de exposição radiométrica e composição das rochas sedimentares e ígneas na bacia do Rio Corumbataí. *Rev. Bras. Geof.* 24 (1), 37-48. **https://doi.org/10.1590/S0102-261X2006000100003**

Conceição, F.T., Bonotto, D.M. (2006b). Radionuclides, heavy metals and fluorine incidence at Tapira phosphate rocks, Brazil, and their industrial (by) products. *Environ. Pollut.* 139 (2): 232-243. **https://doi.org/10.1016/j.envpol.2005.05.014**

Eisenbud, M., Gesell, T. (1997). *Environmental Radioactivity from Natural*, Industrial, and Military Sources. 4th ed. Academic Press, San Diego, 688 p.

Emsley, J. (2001). *Nature's Building Blocks: An A-Z Guide to the Elements*. Oxford: Oxford University Press, 720p.

Erdi-Krausz, G., Matolin, M., Minty, B., Nicolet, J.P., Reford, W.S., Schetselaar, E.M. (2003). *Guidelines for radioelement mapping using gamma-ray spectrometry data*. International Atomic Energy Agency (IAEA),. 179p.

Ferronsky, V.I. (2015). Nuclear Geophysics: Applications in Hydrology, Hydrogeology, Engineering Geology. 1st ed. *Agriculture and Environmental Science*, 522p.

Fianco, C.B., Vidotti, R.M., Pires, A.C.B. (2014). Phosphorite porspection using ground gamma spectrometry in northeast Goiás state, Brazil. *Revista Brasileira de Geofísica*.; 32(4): 721-733. **http://dx.doi.org/10.22564/rbgf.v32i4.540**

Furlan, L.M., Ferreira, M.E., Moreira, C.A., Alencar, P.G., Casagrande, M.F.S., Rosolen, V. (2023). Satellite, UAV, and Geophysical Data to Identify Surface and Subsurface Hydrodynamics of Geographically Isolated Wetlands: Understanding an Undervalued Ecosystem at the *Atlantic Forest-Cerrado Interface of Brazil. Remote Sens*. 15, 1870. **https://doi.org/10.3390/rs15071870**

Guo, Y., Yang, S. (2016). Heavy metal enrichment in the Changjiang (Yangtze River) catchment and on the inner shelf of the East China Sea over the last 150 years. *The Science of the Total Environment*, 543 (Part A), 105-115. **https://doi.org/10.1016/j.scitotenv.2015.11.012**

Han, H., Rafiq, M.K., Zhou, T., Xu, R., Mašek, O., Li, X. (2019). A critical review of clay-based composites with enhanced adsorption performance for metal and organic pollutants. *Journal of Hazardous Materials*. 369, 780-796. **https://doi.org/10.1016/j.jhazmat.2019.02.003**

Hayashi, M., Van Der Kamp, G., Rosenberry, D.O. (2016). Hydrology of Prairie Wetlands: Understanding the Integrated Surface-Water and Groundwater Processes. *Wetlands.* 36, 237-254. **https://doi.org/10.1007/s13157-016-0797-9**

Hoff, R., Rolim, S.S.A., Bastos Neto, A.C. (2004). Mapeamento aerogamaespectrométrico da alteração hidrotermal associada à mineralização no distrito fluorítico de Santa Catarina, Brasil. *Revista Brasileira de Geofísica.* 22(1): 45-55. **https://doi.org/10.1590/S0102-261X2004000100004**

Horn, R., Peth, S. (2011). Mechanics of unsaturated soils for agricultural applications. In P. M. Huang, Y. Li & M. E. Sumner (Eds.), *Handbook of soil sciences*, 2nd. ed. (pp. 1-30). Boca Raton, FL; CRC Press.

Hussain RO, Hussain HH. (2011). Investigation the Natural Radioactivity in Local and Imported Chemical Fertilizers. *Braz. Arch. Biol. Technol.* 54(4): 777-782. **https://doi.org/10.1590/S1516-89132011000400018**

International Atomic Energy Agency. (1973). *Safe Handling of Radionuclides.* Safety Series. No.1. International Atomic Energy Agency, Viena.

Isherwood, K.E. (2000). *O uso de fertilizantes minerais e o meio ambiente*. IFA/UNEP/ANDA.

Kesler, S.E., Simon, A.C. (2015). *Mineral resources, economics and the environment*, 2nd. ed.: Cambridge, Cambridge University Press, 434 p.

Köppen W, Geiger R. (1928). *Klimate der Erde*. Gotha: Verlag Justus Perthes.

Leibowitz, S.G. (2015). Geographically Isolated *Wetlands*: Why We Should Keep the Term, *Wetlands*. 2015; 35, 997-1003. **https://doi.org/10.1007/s13157-015-0691-x**

Loureiro, F.E.L., Monte, M.B.M. 2005 , Nascimento, M. Fosfato. In: *Rochas e minerais industriais: usos e especificações*. Rio de Janeiro, RJ, Brasil: Centro de Tecnologia Mineral-Ministério da Ciência e Tecnologia,.

Luko-Sulato, K., Rosa, V.A., Furlan, L.M., Rosolen, V. (2021). Concentration of essential and toxic elements as a function of the depth of the soil and the presence of fluvic acids in a wetland in Cerrado, Brazil. *Environ Monit Assess*, 193:157. **https://doi.org/10.1007/s10661-021-08945-y**

Maltby, E. (1988). Global *wetlands*-history, current status and future. In: Hook, D.D.; McKee, W.H.; Smith, H.K.; *et al. The Ecology and management of wetlands.* London: Croom Helm, v.1: 3-14.

Mateo-Sagasta, J., Marjani Zadeh, S., Turral, H. (2018). *More People, More Food, Worse Water? A Global Review of Water Pollution from Agriculture*. Roma: Food and Agriculture Organization of the United Nations.

Mazzilli, B.P., Máduar, M.F., Campos, M.P. (2013). *Radioatividade no meio ambiente e avaliação de impacto radiológico ambiental.* São Paulo: Instituto de Pesquisas Energéticas e Nucleares (IPEN).

Mckee, W.H., Smith, H.K., *et al.* (1988). *The Ecology and management of wetlands*. London: Croom Helm, v.1: 3-14.

Mclaughlin, D.L., Kaplan, D.A., Cohen, M.J. (2014). A significant nexus: geographically isolated wetlands influence landscape hydrology. *Water Resour. Res.* 50 (9), 7153-7166. **https://doi.org/10.1002/2013WR015002**

Mikami, S., Sato, S., Hoshide, Y., Sakamoto, R., Okuda, N., Saito, K. (2015). In Situ Gamma Spectrometry Intercomparison in Fukushima, Japan. Jpn. *J. Health Phys.*; 50 (3): 182-188. **http://dx.doi.org/10.5453/jhps.50.182**

Milani, E. J., Melo, J. H. G., Souza, P. A., Fernandes, L. A., França, A.

B. Bacia do Paraná. (2007). Bacia Parana Carta Estratigraf Simples. *Boletim de Geociências da Petrobras*, v. 15, n. 2, p 265-287.

Mitsch, W.J., Gosselink, G. (2015). *Wetlands.* 5th ed. pp 456.

Mussett, A.E.; Khan, M.A. Looking into the earth: an introduction to geological geophysics. *Nova Iorque:* Cambridge University Press, 2000, 470 p.

Nardy, A.J.R., Moreira, C.A., Machado, F.B., Luchetti, C.F., Hansen, M.A.F., Rossini, A.J., Barbosa Jr. (2014). Gamma-ray spectrometry signature of Paraná volcanic rocks: preliminar results. *Geociênc.,* [s.l.], 33, 216-227.

Olivie-Lauquet, G., Gruau, G., Dia, A., Riou, C., Jaffrezic, A., Henin, O. (2001). Release of trace elements in wetlands: role of seasonal variability. *Wat. Res.,* [s.l.], v. 35, n. 4, pp. 943-952. **https://doi.org/10.1016/S0043-1354(00)00328-6**

Pickup, G., Marks, A. (2000). Identifying large-scale erosion and deposit processes from airbone gamma radiometrics and digital elevation models in a weathered landscape. *Earth Surface Processes and Landforms*, v. 25, p. 535-557, **https://doi.org/10.1002/(SICI)1096-9837(200005)25:5%3C535::AID-ESP91%3E3.0.CO;2-N**

Rains, M.C., Leibowitz, S.G., Cohen, M.J., Creed, I.F., Golden, H.E., Jawitz, J.W., Kalla, P., Lane, C.R., Lang, M.W., Mclaughlin, D.L. (2016). Geographically isolated wetlands are part of the hydrological landscape. *Hydrol. Process*., [s.l.], 30, 153-160. **https://doi.org/10.1002/hyp.10610**

Reinhardt, N., Hermann, L. (2018). Gamma-ray spectrometry as versatile tool in soil science: A critical review. *J. Plant Nutr. Soil Sci.*, [s.l.], 1-19. 2018. **https://doi.org/10.1002/jpln.201700447**

Reynolds, W.D., Elrick D.E., Topp G.C. (1983). A reexamination of the constant head well permeameter method for measuring saturated hydraulic conductivity above the water table. Soil Sci., [s.l.], 136(4), 250–268.

Ridley, J. (2013). *Ore deposit geology*. 398 p. Cambridge University Press.

Schneider, R.L., Muhlmann, H., Tommasi, E., Medeiros, R. A., Daemon, R. F., Nogueira, A.A. (1974). Revisão estratigráfica da Bacia do Paraná. In: Congresso Brasileiro De Geologia, 28, Porto Alegre. Anais. Brazil, Porto Alegre: SBG, v. 1, p. 41-65.

Schuler, U., Erbe, P., Zarei, M., Rangubpit, W., Surinkum, A., Stahr, K., Herrmann, L. (2011). A gamma-ray spectrometry approach to field separation of illuviation-type WRB reference soil groups in northern Thailand. *Journal of Plant Nutrition and Soil Science*, [s.l.], 174, 536-544. **https://doi.org/10.1002/jpln.200800323**

Šimíček, D., Bábek, O., Leichmann, J. (2012). Outcrop gamma-ray logging of siliciclastic turbidites: Separating the detrital provenance signal from facies in the foreland-basin turbidites of the Moravo-Silesian basin, Czech Republic. *Sedimentary Geology,* [s.l.], v.261, 50-64,. **https://doi.org/10.1016/j.sedgeo.2012.03.003**

Soil Moisture Corp. (2012). Model 2800K1, *Guelph Permeameter: Operating Instructions*. Santa Bárbara, CA, 93105, 28p.

Souza, J.L., Ferreira, F.J.F. (2005). Anomalias aerogamaespectrométricas (K, eU e eTh) da quadrícula de Araras (SP) e suas relações com processos pedogenéticos e fertilizantes fosfatados. *Revista Brasileira de Geofísica*, [s.l.], 23(3): 251-274. **https://doi.org/10.1590/S0102-261X2005000300005**

Strawn, D.G., Bohn, H.L., O'connor, G.A. (2020). *Soil chemistry*. 5th ed. West Sussex, U.K.: John Wiley & Sons.

Tiner, R.W. (2003). Geographically isolated *wetlands* of the United States. Wetlands, [s.l.], 23, 494-516.

Tubeileh, A., Groleau-Renaud, V., Plantureux, S., Guckert, A. (2003). Effect of soil compaction on photosynthesis and carbon partitioning within a maize-soil system. *Soil Tillage Res.* 71:151-161.

Uddin, M.K. (2017). A review on the adsorption of heavy metals by clay minerals, with special focus on the past decade. *Chemical Engineering Journal*, vol. 308, pp. 438-462. **https://doi.org/10.1016/j.cej.2016.09.029**

Ulbrich, H.H.G.J., Ulbrich, M.N.C., Ferreira, F.J.F., Alves, L.S., Guimarães, G.B., Fruchting, A. (2009). Levantamentos gamaespectrométricos em granitos diferenciados. I*: revisão da metodologia e do comportamento geoquímico dos elementos K*, Th e U. Geologia USP, Série Científica, São Paulo, 9 (1), p. 33-53.

Umisedo, N.K. (2007). Dose de radiação ionizante decorrente do uso de fertilizantes agrícolas. [Tese de doutorado]. Faculdade de Saúde Pública da Universidade de São Paulo, São Paulo.

United Nations Scientific Committee on the Effects of Atomic Radiation. (2008). *Sources and effects of ionizing radiation*. UNSCEAR 2008 report. vol. 1. New York: United Nations Scientific Committee on the Effects of Atomic Radiation.

Vasconcelos, M.A.R., Leite, E.P., Crósta, A.P. (2012). Contributions of gamma-ray spectrometry to terrestrial impact crater studies: the example of Serra da Cangalha, northeastern Brazil. *Geophys. Res. Lett*., [s.l.], v. 39, L04306. **https://doi.org/10.1029/2011GL050525**

Zhang, Z.F., Groenevelt, P.H., Parkin, G.W. (1998). The well shape-factor for the measurement of soil hydraulic properties using the Guelph Permeameter. *Soil Tillage Res.*, [s.l.], 49:219-221.

Geofísica Internacional (2024) **63-2**: 865 - 879

Investigation of Salanda Fault Zone, between Yesiloz and Gumuskent (Nevsehir-Turkey) with PSInSAR

Ramazan Demircioğlu[*1] and Osman Oktar[2]

Abstract

In this study, the section of the Salanda fault zone between Yesiloz village and Gumuskent (Nevsehir, Turkey) was investigated by geodetic methods, and the amount of movement in this area was determined. We used a Persistent Scatterer Interferometric Synthetic Aperture Radar (PSInSAR) to determine the line of sight (LOS) movement. Previous studies using geological and geomorphological indices have shown that the Salanda fault zone is active. For the first time in this study, 36 synthetic aperture radar (SAR) images acquired between January 8, 2020, and November 29, 2022, were used in PSInSAR analysis. When the annual velocity values of the stud area in the LOS direction were analysed, annual subsidence values of up to 7.6 mm and annual uplift values of up to 7.2 mm were revealed. These movements indicate that the Salanda fault is active and normal fault characteristics. However, it also has a dextral strike-slip component.

Key words: Central Anatolia, active tectonics, Salanda fault zone, GNSS, PSInSAR.

Resumen

En este estudio, se investigó la sección de la zona de la falla de Salanda entre el pueblode Yesiloz y Gumuskent (Nevsehir, Turquía) mediante métodos geodésicos, y sedeterminó la cantidad de movimiento en esta zona. En este estudio, con este fin utilizamosun radar de apertura sintética interferométrico de dispersión persistente (PSInSAR) paradeterminar el movimiento de la línea de visión (LOS). Estudios anteriores realizados conínidces geológicos y geomorfológicos han demostrado que la zona de la falla de Salandaestá activa. Por primera vez en este estudio, se utilizaron en el análisis PSInSAR 36imágenes de radar de apertura sintética (SAR) adquiridas entre el 8 de enero de 2020 y el29 de noviembre de 2022. Cuando se analizaron los valores anuales de velocidad delárea de estudio en la dirección LOS, se revelaron valores anuales de subsidencia dehasta 7,6 mm y valores anuales de elevación de hasta 7,2 mm. Estos movimientosindican que la falla de es activa y tiene características de falla normal. Sin embargo,también tiene un componente de deslizamiento dextral.

Palabras clave: Anatolia Central, tectónica activa, zona de falla de Salanda, GNSS, PSInSAR.

Received: August 2, 2023; Accepted: January 9, 2024; Published on-line: April 1, 2024.

Editorial responsibility: Dr. Rakesh Dumka

* Corresponding author: Ramazan Demircioğlu. E-mail: ra.demircioglu@gmail.com
[1] Department of Emergency Aid and Disaster Management, Aksaray University, Aksaray, Turkey.
[2] Department of Geomatics Engineering, Aksaray University, Aksaray, Turkey. osman.oktar38@gmail.com

https://doi.org/10.22201/igeof.2954436xe.2024.63.2.1733

1. Introduction

The study area is located on the Kırşehir Block, one of the tectonic units of Turkey, approximately in the middle of Turkey and north of Nevşehir Province (Figure 1).

Palaeozoic to Quaternary age rocks are found in and around the study area, as shown in Figure 2. The basement of the study area is made up of Palaeozoic-Mesozoic metamorphic rocks from the Kırşehir Massif, which are cut by Late Cretaceous igneous rocks. These units are unconformably overlain by Palaeocene-Middle Eocene sedimentary units known as the Ayhan Group. Additionally, Middle Miocene-Quaternary units unconformably overlap these units. Polyphase deformation has occurred in the basement metamorphic rocks in the study area.

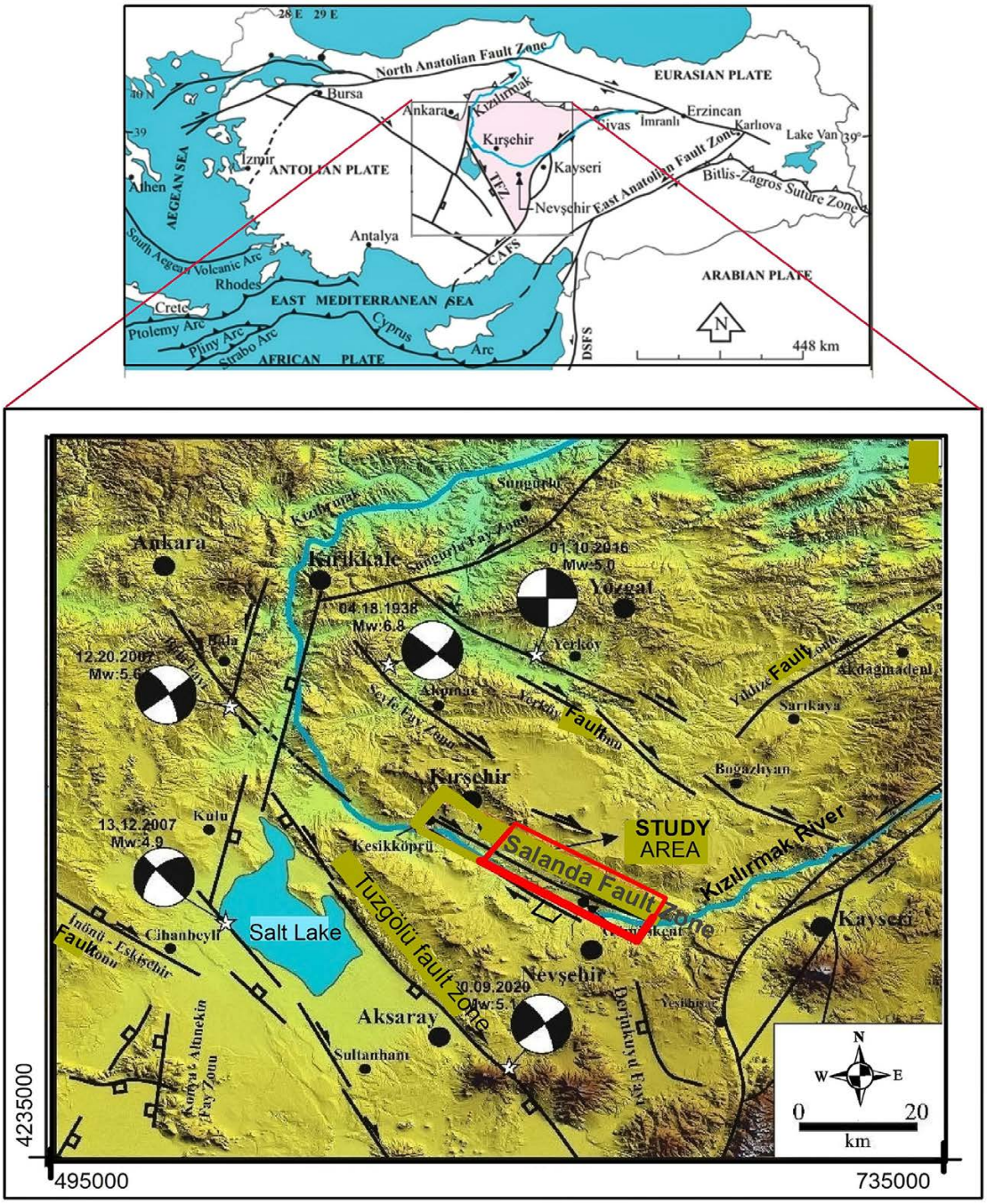

Figure 1. The study area location map.

Palaeozoic to Quaternary age rocks are found in and around the study area, as shown in Figure 2. The basement of the study area is made up of Palaeozoic-Mesozoic metamorphic rocks from the Kırşehir Massif, which are cut by Late Cretaceous igneous rocks. These units are unconformably overlain by Palaeocene-Middle Eocene sedimentary units known as the Ayhan Group. Additionally, Middle Miocene-Quaternary units unconformably overlie these units. Polyphase deformation has occurred in the basement metamorphic rocks in the study area. Palaeozoic to Quaternary age rocks are found in and around the study area, as shown in Figure 2.

The basement of the study area is made up of Palaeozoic-Mesozoic metamorphic rocks from the Kırşehir Massif, which are cut by Late Cretaceous igneous rocks. These units are unconformably overlain by Palaeocene-Middle Eocene sedimentary units known as the Ayhan Group. Additionally, Middle Miocene-Quaternary units unconformably overlie these units. Polyphase deformation has occurred in the basement metamorphic rocks in the study area. Due to the closure of the Inner Tauride Ocean, the basement units and the rocks of the Ayhan Group underwent polyphase deformation. The Palaeocene-Middle Eocene units unconformably overlying these basement units have undergone at least 3 stages of folding. In the study area, the extensional tectonic regime began in the Late Miocene according to field studies (Demircioglu, 2014).

In the Middle Miocene units, folds were formed due to a compressional tectonic regime. However, in the units formed after the Late Miocene-Pliocene period, no structures belonging to the compressional tectonic regime were observed. Instead, normal faults were formed due to the influence of the extensional regime.

In the study area, northeast-southwest-trending normal faults were formed due to the northeast-southwest-trending extensional tectonic regime. The most significant fault in this area is the Salanda fault zone, which consists of several segments. In this study, we analyzed the movements of this fault between Yesilöz and Gumuskent using the PSInSAR method. According to the studies of Şengör and Yılmaz (1981), the Salanda fault zone, which is the subject of this study, is located in the Central Anatolian Plain region. Central Anatolia was under an extensional tectonic regime during the Neotectonic Period (Şengör and Yılmaz (1981), Koçyiğit (1984, 2003). The resulting faults generally developed as normal and extensional strike-slip faults. Koçyiğit and Doğan (2016) conducted a study on the neotectonic faults of Central Anatolia (Figure 3).

The study area is located in the Central Anatolian region, east of the Tuzgölü fault zone and north of Nevşehir province (Figure 3). One of the most important fault zones in Central Anatolia in Turkey is the Salanda fault zone. A satellite-based study on this fault zone has been carried out for the first time in this study.

This study aims to investigate the characteristics of the Salanda fault zone between Yesiloz-Gumuskent in the study area. For this purpose, field and PSInSAR studies were carried out.

The Salanda fault, which is the focus of this study, is one of the normal faults that developed in Central Anatolia during

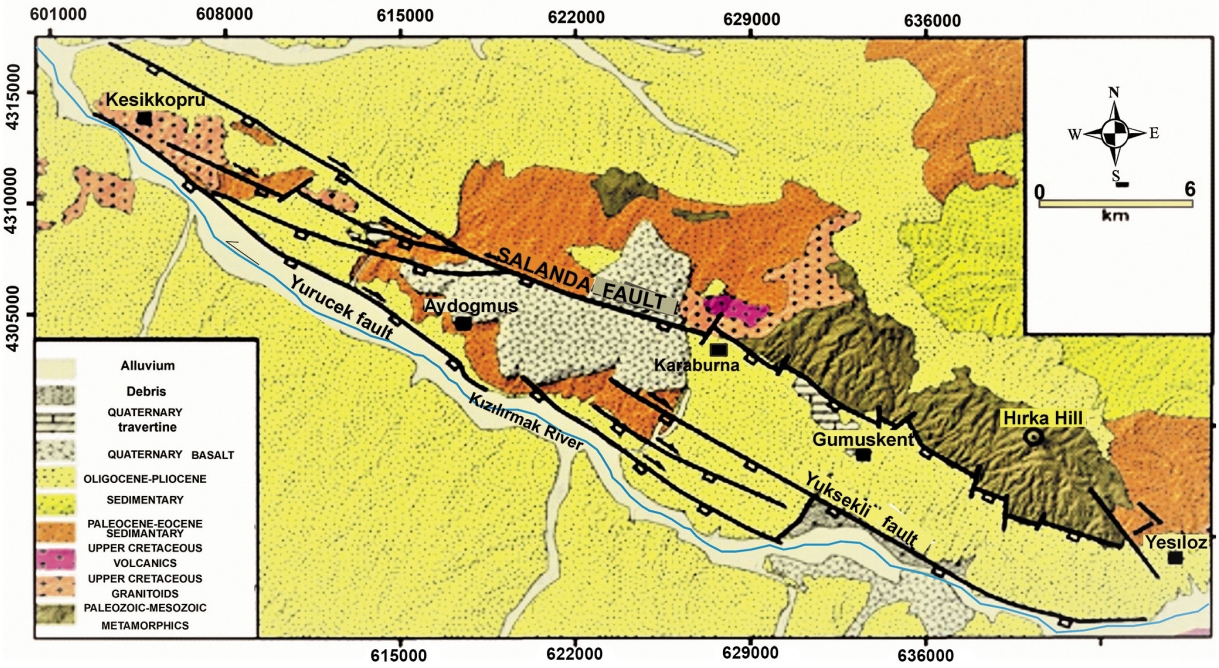

Figure 2. Geological map of the study area and the Salanda Fault (Modified from Demircioğlu and Coşkuner, 2022)..

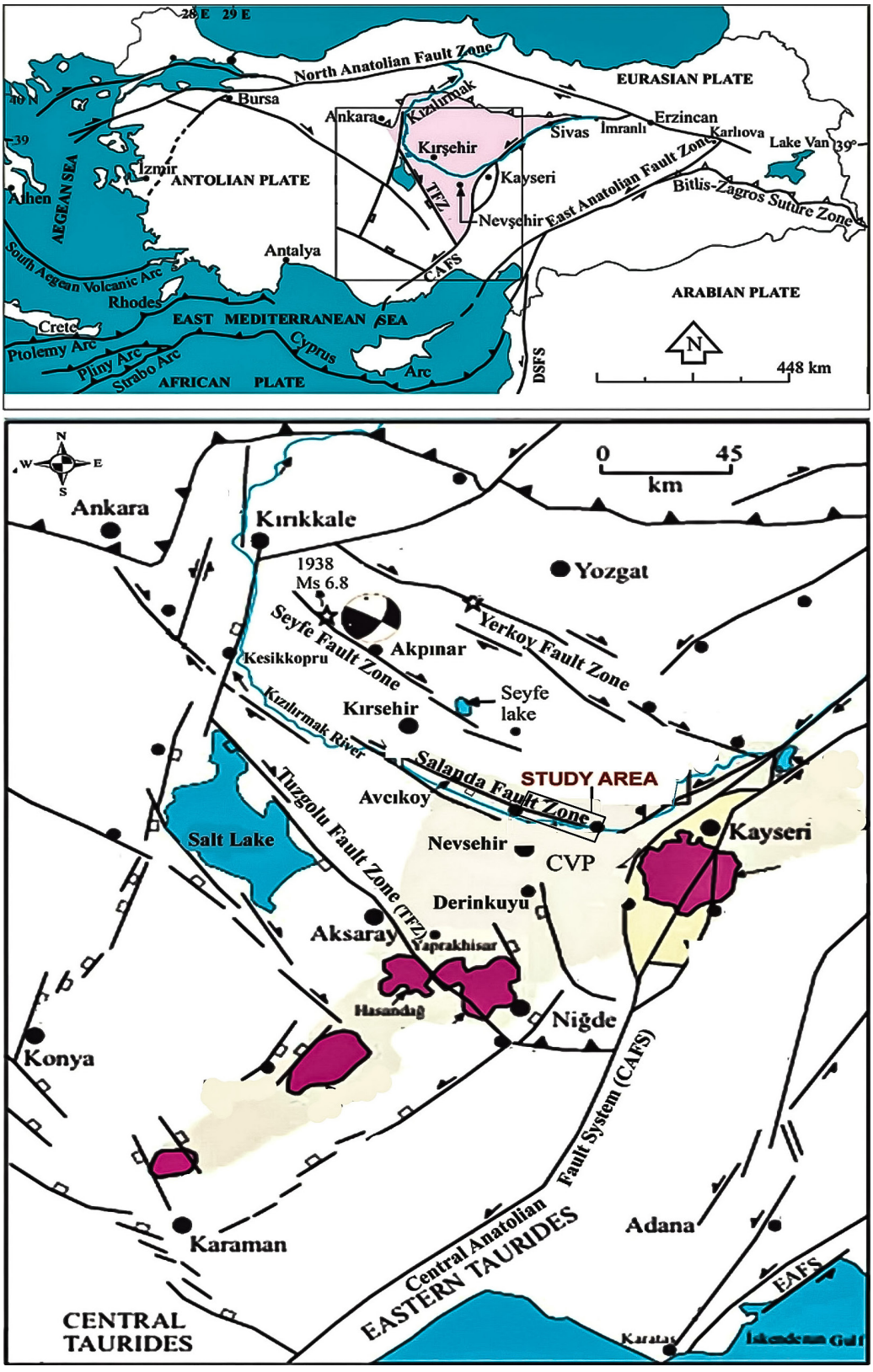

Figure 3. Simplified map showing plate tectonics and neotectonic faults of Turkey. CVP: Central Anatolian Volcanic Province (Modified from Koçyiğit and Doğan, 2016).

the Neotectonic period. This development was due to the northeast-southwest extensional tectonic regime. The Yerköy, Seyfe, Salanda, and Tuzgolu faults are examples of such normal faults, which also have lateral thrusts. The extensional tectonic regime created fault directions that run in a northwest-southeast direction, as shown in Figure 3.

The study area has Palaeozoic-Mesozoic age metamorphic rocks belonging to the Kırşehir Massif, and Late Cretaceous age igneous rocks cut these rocks. Palaeocene-Quaternary rocks unconformably overlie these units. The Salanda fault zone has travertines formed by it. Additionally, the fault cut the Quaternary basalts. These deformations are visible in the field, as shown in Figure 2. The Salanda fault, which is the focus of this study, is one of the normal faults that developed in Central Anatolia during the Neotectonic period. This development was due to the northeast-southwest extensional tectonic regime. The Yerköy, Seyfe, Salanda, and Tuzgolu faults are examples of such normal faults, which also have lateral thrusts. The extensional tectonic regime created fault directions that run in a northwest-southeast direction, as shown in Figure 3.

The study area has Palaeozoic-Mesozoic age metamorphic rocks belonging to the Kırşehir Massif, and Late Cretaceous age igneous rocks cut these rocks. Palaeocene-Quaternary rocks unconformably overlie these units. The Salanda fault zone has travertines formed by it. Additionally, the fault cut the Quaternary basalts. These deformations are visible in the field, as shown in Figure 2. The Salanda fault, which is the focus of this study, is one of the normal faults that developed in Central Anatolia during the Neotectonic period. This development was due to the northeast-southwest extensional tectonic regime. The Yerköy, Seyfe, Salanda, and Tuzgolu faults are examples of such normal faults, which also have lateral thrusts. The extensional tectonic regime created fault directions that run in a northwest-southeast direction, as shown in Figure 3.

The study area has Palaeozoic-Mesozoic age metamorphic rocks belonging to the Kırşehir Massif, and Late Cretaceous age igneous rocks cut these rocks. Palaeocene-Quaternary rocks unconformably overlie these units. The Salanda fault zone has travertines formed by it. Additionally, the fault cut the Quaternary basalts. These deformations are visible in the field, as shown in Figure 2. The Salanda fault, which is the focus of this study, is one of the normal faults that developed in Central Anatolia during the Neotectonic period. This development was due to the northeast-southwest extensional tectonic regime. The Yerköy, Seyfe, Salanda, and Tuzgolu faults are examples of such normal faults, which also have lateral thrusts. The extensional tectonic regime created fault directions that run in a northwest-southeast direction, as shown in Figure 3.

The study area has Palaeozoic-Mesozoic age metamorphic rocks belonging to the Kırşehir Massif, and Late Cretaceous age igneous rocks cut these rocks. Palaeocene-Quaternary rocks unconformably overlie these units. The Salanda fault zone has travertines formed by it. Additionally, the fault cut the Quaternary basalts. These deformations are visible in the field, as shown in Figure 2.The Salanda fault, which is the focus of this study, is one of the normal faults that developed in Central Anatolia during the Neotectonic period. This development was due to the northeast-southwest extensional tectonic regime. The Yerköy, Seyfe, Salanda, and Tuzgolu faults are examples of such normal faults, which also have lateral thrusts. The extensional tectonic regime created fault directions that run in a northwest-southeast direction, as shown in Figure 3.

The study area has Palaeozoic-Mesozoic age metamorphic rocks belonging to the Kırşehir Massif, and Late Cretaceous age igneous rocks cut these rocks. Palaeocene-Quaternary rocks unconformably overlie these units. The Salanda fault zone has travertines formed by it. Additionally, the fault cut the Quaternary basalts. These deformations are visible in the field, as shown in Figure 2. The Salanda fault, which is the focus of this study, is one of the normal faults that developed in Central Anatolia during the Neotectonic period. This development was due to the northeast-southwest extensional tectonic regime. The Yerköy, Seyfe, Salanda, and Tuzgolu faults are examples of such normal faults, which also have lateral thrusts. The extensional tectonic regime created fault directions that run in a northwest-southeast direction, as shown in Figure 3.

The study area has Palaeozoic-Mesozoic age metamorphic rocks belonging to the Kırşehir Massif, and Late Cretaceous age igneous rocks cut these rocks. Palaeocene-Quaternary rocks unconformably overlie these units. The Salanda fault zone has travertines formed by it. Additionally, the fault cut the Quaternary basalts. These deformations are visible in the field, as shown in Figure 2. Using the Persistent Scatterer Interferometric Synthetic Aperture Radar (PSInSAR) technique, surface deformation can be easily monitored spatially (Poyraz and Hastaoğlu 2020). PSInSAR is a widely used geodetic method that has been applied in recent years. The PSInSAR method has been widely used in deformation-observing scientific research focusing on tectonic movements (Arıkan *et al.* 2010; Poyraz and Hastaoğlu 2020; Dumka *et al.* 2020; Dumka *et al.* 2021; Suribabu *et al.* 2022a; Suribabu *et al.* 2022b; Dumka *et al.* 2023), in the determination of earthquake-induced surface movements (Yen *et al.* 2011; Suárez *et al.*, 2018; Famiglietti, 2022), landslide monitoring (Peyret *et al.* 2008; Hastaoğlu *et al.* 2014), volcanic (Hooper *et al.* 2004, 2007; Gündüz *et al.* 2023), geological and urban areas (Meisina *et al.* 2006; Rodríguez *et al.*, 2012; Gezgin 2022; Dumka *et al.* 2022), and subsidence in mining areas (Abdikan *et al.* 2014).

This study aims to determine the tectonic movements and surface deformations in the Salanda Fault Zone. To this end, PSInSAR was applied to the Salanda Fault Zone to determine movements in the line of sight (LOS) of the area. The PSInSAR analyses were performed using the Stanford Method for Persistent Scatterers (StaMPS)/MIT software (Hooper *et al.* 2018). The novelty of this study is the lack of any geodetic study related to the Salanda fault. The results of our study are important in that the velocity information obtained from the analysis results can be used by different disciplines, such as geology and geophysics.

1.1 Salanda Fault Zone

In the study area, the neotectonic period started during the Late Miocene-Early Pliocene (Demircioglu, 2014). Following this period, the study area and its surroundings were affected by the extensional tectonic regime which led to the formation of

normal faults. Even though these faults have strike-slip movements, they exhibit normal faulting characteristics. The strike-slip faults observed in and around the study area indicate that they were formed under the extensional tectonic regime.

The Salanda fault zone was first identified in the study of Koçyiğit (1984), and it has been determined that the length of the fault is 60 km. The Salanda fault has different segments, and its strikes vary between N40-800E and N450W-N820W. The dip of the fault plane is observed towards the southwest and southeast with values ranging from 58 to 72 degrees (as shown in Figures 2, 3, and 4). One of the best places to observe the fault is southeast of Gumuskent (Figure 5).

In the following years, studies were carried out on the Salanda Fault (Şaroğlu *et al.*, 1987; Atabey, 1989). Şaroğlu *et al.* (1987) mentioned in their study that the Salanda fault zone cuts the Quaternary units and causes deformation in them. Therefore, they considered the Salanda fault as an active fault. Doğan (2011) obtained Quaternary (1.9 my. to 96 ka) ages in his radiometric dating of the basalts observed in the study area. In the north of the field, it was observed during field studies that the Quaternary

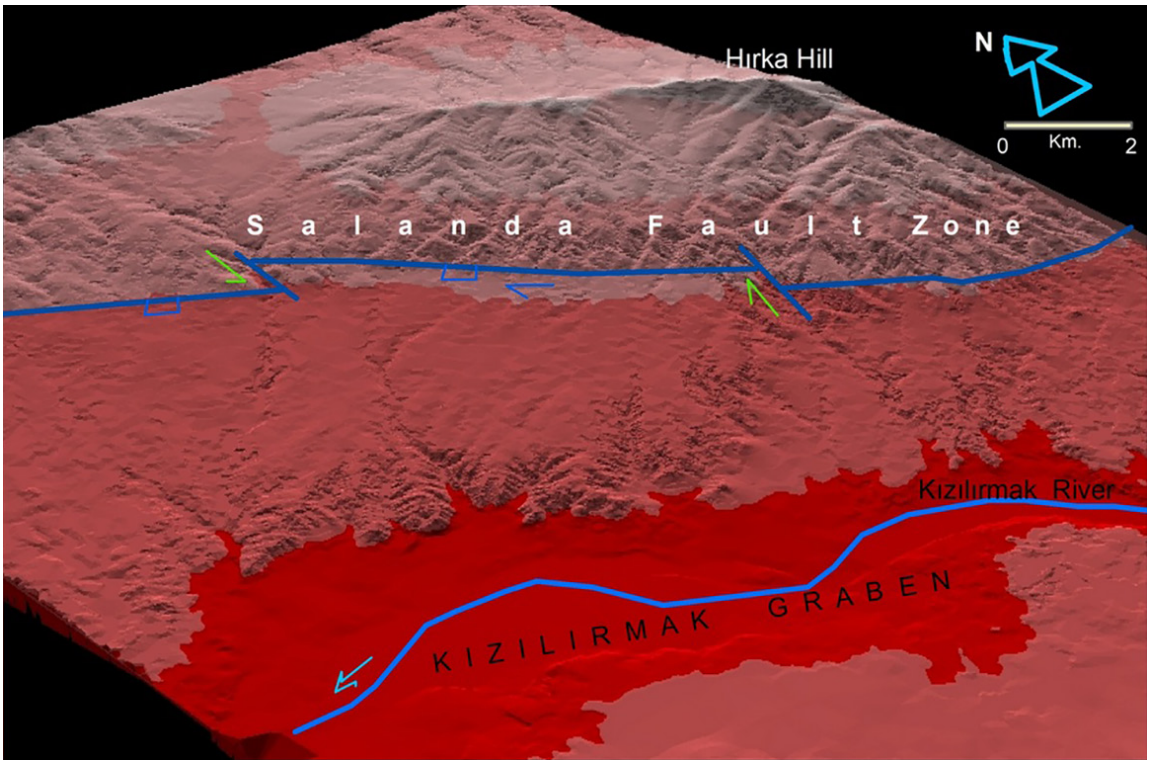

Figure 4. The Salanda fault zone and the Kızılırmak Graben (Between Yesıloz-Gumuskent village).

Figure 5. View of the Salanda fault zone from southeast of Gumuskent (Gumuskent-Yesıloz road).

basalts around Karaburna were cut by the Salanda fault. Temiz (2004) and Temiz *et al.* (2009) found 70145-96080 years (late Pleistocene) and 18040-8700 years old (late Pleistocene-Holocene) by uranium ageing method on travertines in the vicinity of Avcıkoy, northwest of the study area.

In Turkey, the neo-tectonic onset of each region is different. In the study area, the neo-tectonic period begins in the Late Miocene-Lower Pliocene (Demircioğlu, 2014). After this period, Central Anatolia came under an extensional tectonic regime. There are important faults in and around the study area. During the instrumental period, catastrophic earthquakes occurred on these faults (Figure 6).

In 1938, a magnitude 6.8 earthquake occurred on the Akpınar fault, which is the continuation of the Salanda fault (Figures 3, 6).

Non-instrumental period earthquakes are said to have occurred among the people. Demircioğlu and Coşkuner (2022) found that the fault showed medium-high tectonic activity in the geomorphic index studies of the Salanda fault zone between Yeşilöz and Kesikköprü. In the study of Koçyiğit and Doğan (2016), the annual right lateral offset was 4 mm since the Pleistocene, and they determined the length of the fault to be 66 km.

Along the Kızılırmak valley, where the Salanda Fault borders on one side, there are some studies on the fault (Koçyiğit, (2003), Doğan *et al.*, (2009), Doğan, (2011), Çiner *et al.*, (2015). In addition, with the development of satellite and measurement technologies in recent years, studies to determine the amount of movement on fault lines have intensified (Biggs *et al.*, 2007; Yavaşoğlu *et al.*, 2011; Shirzaei and Bürgmann 2013; Wang and Johnson 2015; Rosu *et al.*, 2015; He *et al.*, 2019; Gürsoy *et al.*, 2017; Liu and Zhao, 2020; Scott *et al.*, 2020; Peterson *et al.*, 2020; Howel *et al.*, 2020).

The Salanda fault zone is located in the northeastern part of the Kızılırmak graben, through which the Kızılırmak River flows. This is one of the faults that played an important role in the formation of the graben.

2. Materials and Methods

Geological and geomatic studies carried out in the area were evaluated together and new data on the Salanda fault zone were obtained. A geological map was produced from field studies in

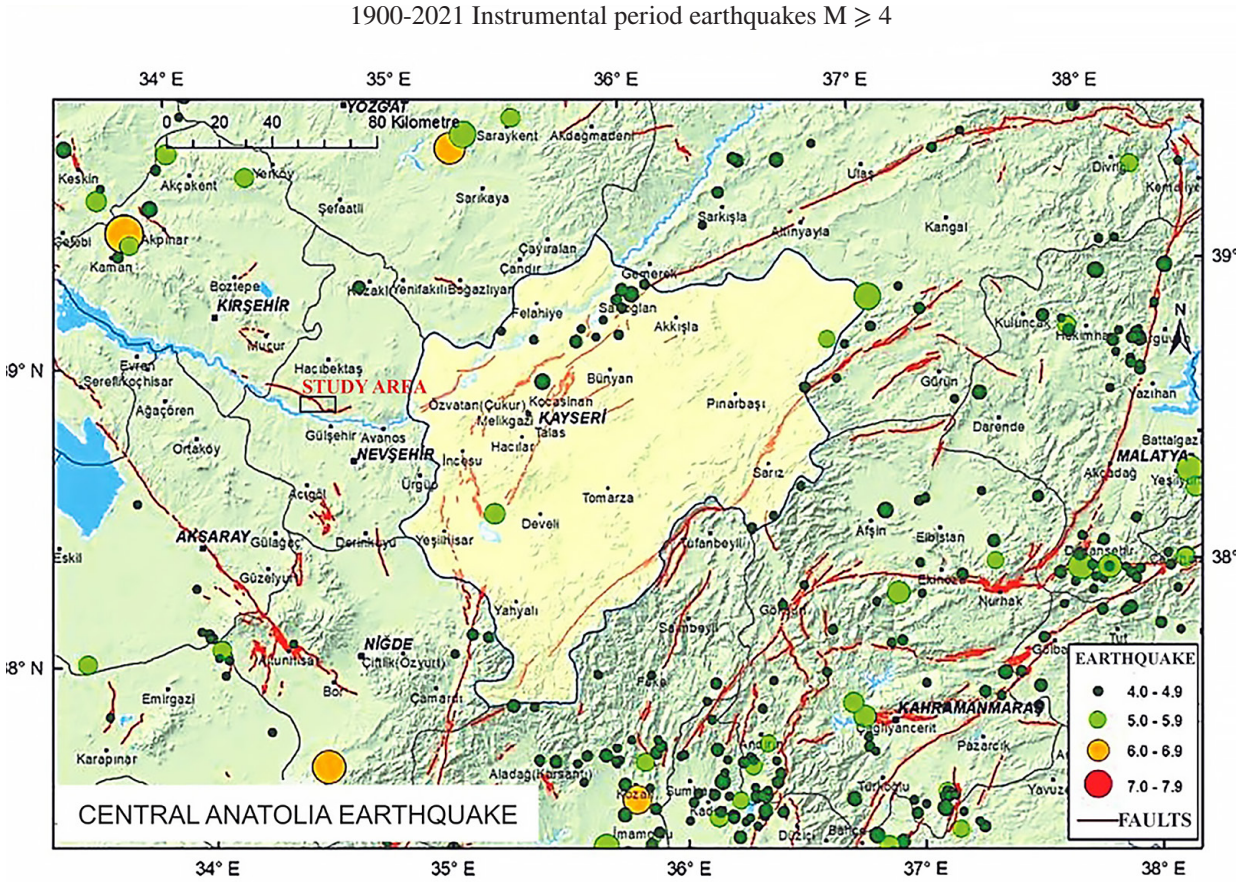

Figure 6. Earthquakes in and around the study area (Modified from Kandilli, 2022).

the area. The young units cut by the Salanda fault zone were analysed in detail. The fact that it cuts basalts that are radiometrically dated and determined to be of Quaternary age indicates that the fault is active. In addition to these field data, geomatic data were required, and 3 years of data were obtained for this area. The field and geomatics data obtained were analysed together to provide data on the extent of the fault zone's vertical and horizontal movement and activity These data were analysed using computer software. Plots of these data were produced.

2.1 Study Area Field dataset

Mapping investigations were conducted on the Salanda fault zone segments during the field survey of the research region. We spotted the young units that were severed by the fault. In the field, the fault planes' strike and dip values were measured, and the fault lines' variations were identified. Figure 6 displays the seismic data that was collected for the research region and its environs. In particular, faulting was shown to have altered the Kızılırmak River's bed.

We followed the river's ancient beds. Geological information was gathered on the degree of displacement, which was previously ascertained by other studies.Seismic activities are observed in and around the Salanda fault.

2.3 PSInSAR data acquisition

Images from the European Space Agency's Sentinel-1 satellite were used in the PSInSAR analysis. The data of the Sentinel-1A synthetic aperture radar (SAR) images are shown in Table 1.

The total SAR coverage (Track 14) is shown in Figure 7. In addition, these data have been added to the Google Earth image.

Table 1. Dates of the SAR images used.

Sentinel-1A		
2020.01.08	2021.01.02	2022.01.09
2020.02.01	2021.02.07	2022.02.02
2020.03.08	2021.03.03	2022.03.10
2020.04.01	2021.04.08	2022.04.03
2020.05.07	2021.05.02	2022.05.09
2020.06.12	2021.06.07	2022.06.02
2020.07.06	2021.07.01	2022.07.20
2020.08.11	2021.08.06	2022.08.01
2020.09.04	2021.09.11	2022.09.06
2020.10.10	2021.10.05	2022.10.12
2020.11.03	2021.11.10	2022.11.05
2020.12.09	2021.12.04	2022.11.29

This image shows the uplift and subsidence zones caused by the Salanda fault zone (Figure 8). The approximate boundaries of the uplift and subsidence zones also form fault lines.

36 Sentinel-1 SAR images have been used in this study. The SAR images are interferometric wide (IW), C-band, track number 14, and were acquired between 08.01.2020 and 29.11.2022. The Copernicus Open Access Hub (URL-1) provided the SAR images free of charge.

2.2 PSInSAR analysis

The StaMPS software has been developed to analyse movement over the continent (Hooper *et al.* 2007). In addition, the PSInSAR technique has been applied, which brings a different approach. These methods use the spatial correlation of the interferometric phase to find pixels with low phase change. This makes it possible to analyse all types of terrain, excluding man-made objects. Fixed target points are determined using adaptation maps of the interferograms. The most basic technique in the evaluation is the determination of the correlation threshold. If a target gives a higher correlation value than the mean, it is designated as a permanent scatterer (PS) point. PSInSAR analyses with a minimum of 12 SAR images are suggested to increase the number of PS points (Hooper *et al.* 2007). The time series is generated from the amplitude values of the pixels in each image. Multiple sets of interferograms are generated to identify highly fitted targets. A single master image is used to produce a set of differential interferograms for this target. When producing interferograms, it is suggested that a DEM be used to remove the effects of topography.

3. Results

3.1 PSInSAR analysis

The process consists of three main steps: interferogram generation, PS selection, and atmospheric filtration. First, appropriate sub-swath and bursts are selected in the SAR dataset, and precise orbit files are applied to them. Then, the master image is selected considering the time interval, vertical baseline, and least atmospheric effect, and all dependent images are recorded using the master image with the help of the S-1 Back Geocoding operator. After the coregistration process, interferograms are produced and prepared for StaMPS analysis by removing the topographic phase component. The entire processing block has been performed using SNAP. The next steps of the processing block are performed in the StaMPS software, and in the first step, PS candidates are selected based on the amplitude distribution

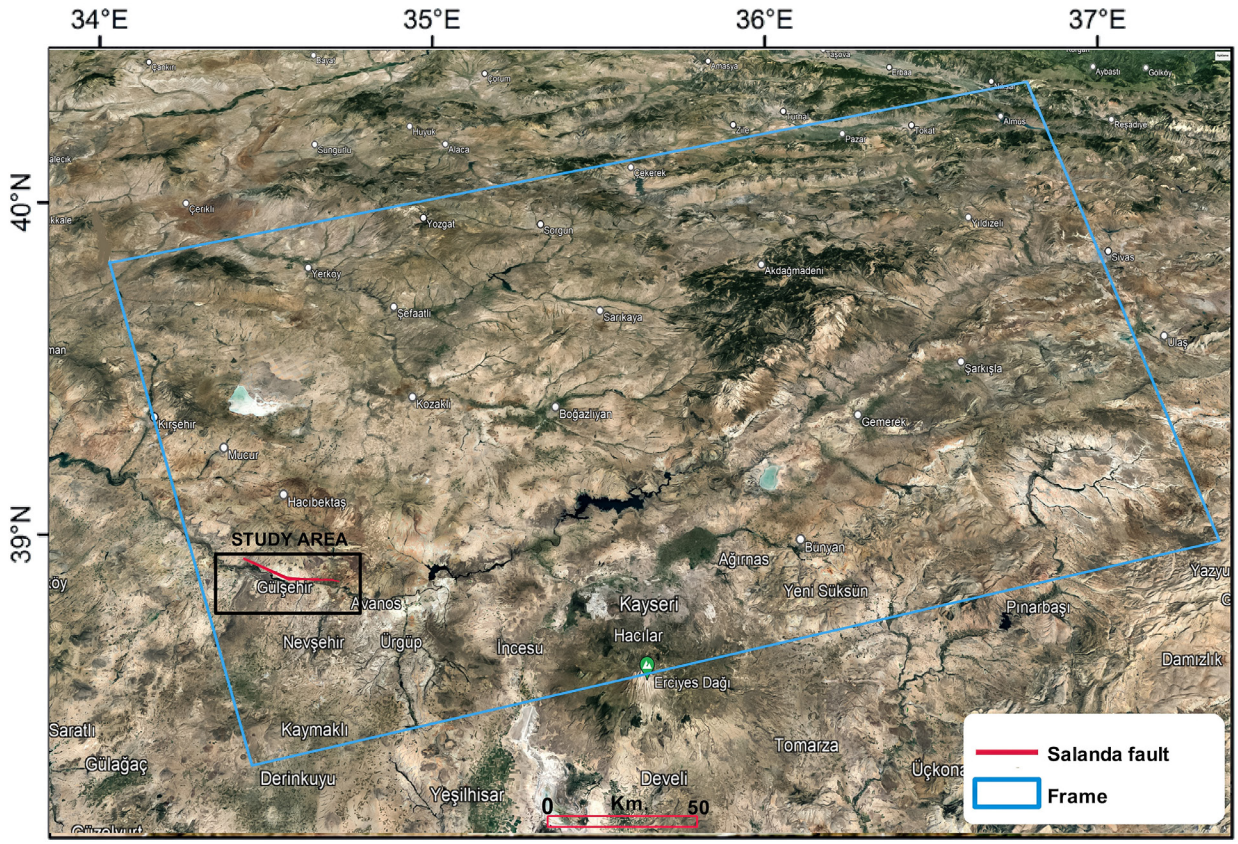

Figure 7. The blue box indicates the approximate coverage of the Sentinel-1A satellite radar images, track number 14. The red line represents the Salanda Fault (Emre *et al.* 2013).

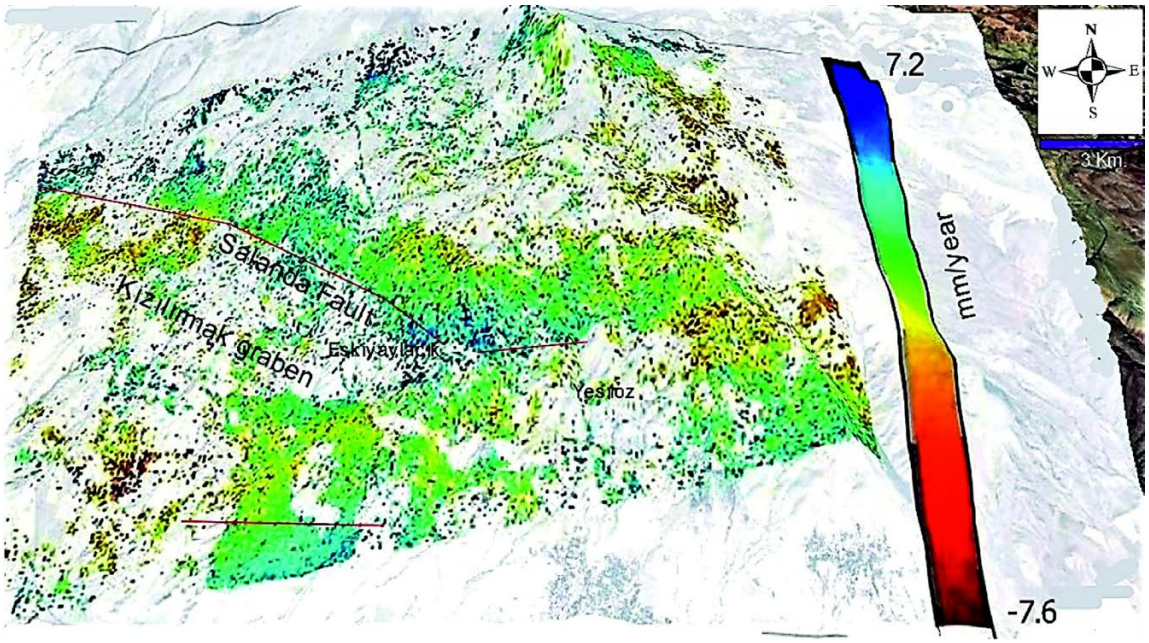

Figure 8. PSInSAR results of the study area with Google Earth image and Salanda fault.

index. The amplitude distribution index is defined as the ratio of the standard deviation of each pixel to the average amplitude value and is calculated using Equation (1) (Hooper *et al.* 2007 and Ferretti *et al.* 2001):

$$D_A \frac{\sigma_A}{\mu_A}$$

where D_A defines the amplitude dispersion value and σ_A and μ_A define the standard deviation and mean of the amplitude values (Hooper *et al.* 2007). The threshold value used is typically between 0.4 and 0.42. After determining the candidate pixels according to the amplitude distribution, the phase noise is estimated and removed for each candidate pixel using phase analysis. The residual phase of the xth pixel and the ith interferogram is given by Equation (2) (Hooper *et al.* 2007):

$$\psi_{x,i}=W\{\phi_{D,x,i}+\phi_{A,x,i}+\Delta\phi_{S,x,i}+\Delta\phi_{\theta,x,i}+\phi_{N,x,i}$$

where W{·} defines the wrapping operator, $\psi_{x,i}=W\{\phi_{D,x,i}+\phi_{A,x,i}+\Delta\phi_{S,x,i}+\Delta\phi_{\theta,x,i}+\phi_{N,x,i}$, represent the general terms for phase change due to movement of the pixel in the satellite LOS direction, phase change due to atmospheric delay between satellite passes, residual phase change due to satellite orbital error, phase change due to viewpoint, and phase noise, respectively (Hooper *et al.* 2007, Lu *et al.* 2020). Then, candidate PS points are filtered according to the noise features estimated and extracted in the previous step so that PS points in the time series are determined based on the amplitude and phase analysis for each pixel in each interferogram. After filtering the PS points, the wrapped phase is corrected for spatially uncorrelated look angle (SCLA) error, and then the phase unwrapping step is performed. In the last step, SCLA errors mostly caused by digital elevation model (DEM) errors are predicted and removed, after this step atmospheric filtering is performed, and the LOS direction velocities for the region of interest are obtained (Gündüz *et al.* 2023). The processing workflow of the study is given in Figure 9.

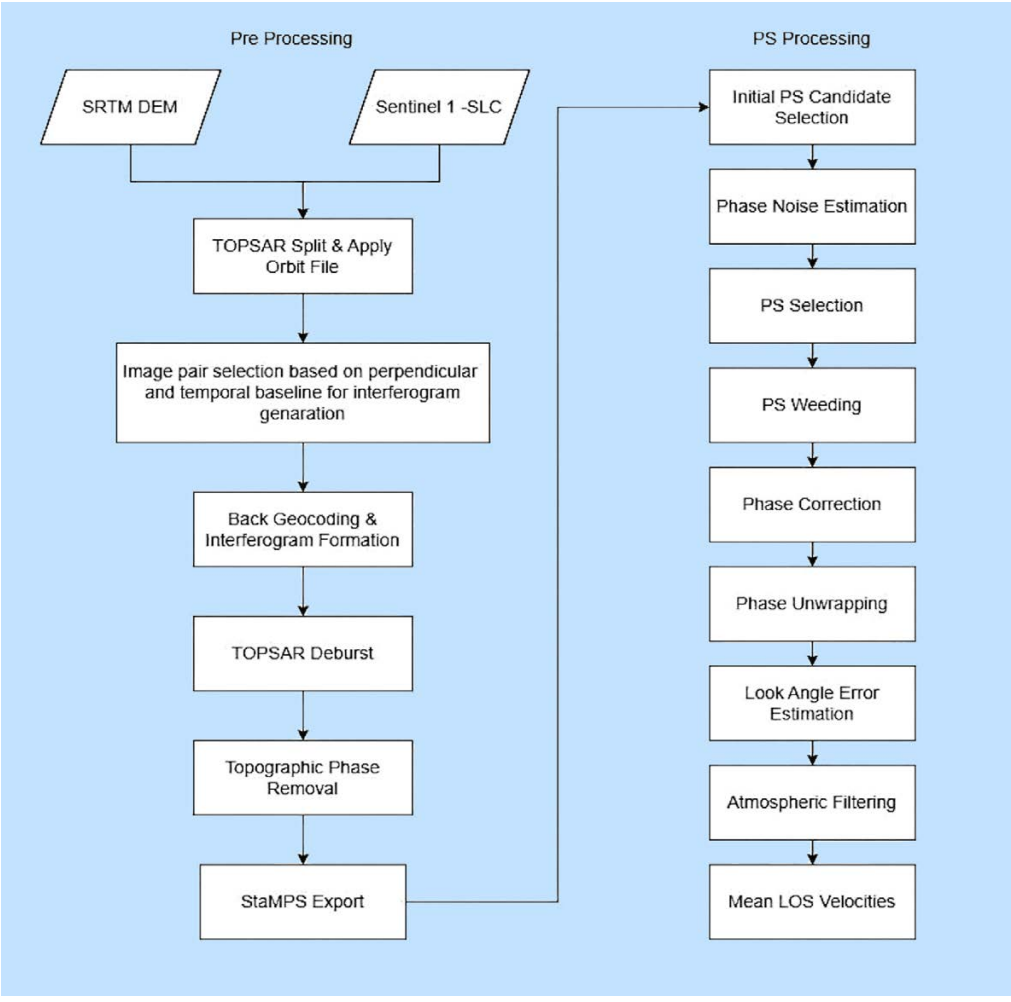

Figure 9. Processing workflow of the study.

Shuttle Radar Topography Mission (SRTM) data were used to remove the effect of topography on the interferograms. The master image was chosen to be the temporal and spatial centre of all images in the PSInSAR analysis. The 07 June 2021 image was used as the master image in the SAR image analysis. Figure 10 shows the baseline perpendicular values and the baseline temporal values with the master images.

A total of 323111 PS points were generated for the study area. The annual velocities in the study area in the LOS direction and their standard deviations are shown in Figure 11a. The vertical axis represents the latitude value while the horizontal axis represents the longitude value in Figure 11b.

In Figure 11, red indicates an uplift in the LOS direction, while blue indicates subsidence in the colour scale of the figure. The annual velocities in the study area range from -7.6 mm (lowest) to 7.2 mm (highest), while the standard deviation of the annual velocities in the LOS direction ranges from 0.4 mm to 2.7 mm (Figure 11).

4. Discussion

According to the results of the PSInSAR analysis, when the annual velocities in the LOS direction obtained for the study area are examined, annual subsidence values up to -7.6 mm and annual uplift values up to 7.2 mm were determined. Doğan *et al.* (2009), based on field observations, determined the erosion rate of the river along the Kızılırmak valley to be 0.08 mm/year during the last 2 million years. The highest rate of erosion was found to be 0.11 mm/year. In addition, Koçyiğit and Doğan (2016) determined the annual right lateral displacement as 4 mm since the Pleistocene and the length of the fault as 66 km. This study determined the average uplift values obtained from the SAR images for the last 3 years as 7.2 mm/year.

This is considerably higher than the data obtained in previous studies. According to the investigations carried out at these points along the Kızılırmak Graben, the Salanda fault zone shows high uplift values due to the normal fault character. The fault has both vertical and horizontal movement components. However, it will not be called an oblique fault as it has much less horizontal slip. According to the study of Scholz *et al.* (1987), the amount of movement and the risk of generating earthquakes, higher movement values are observed compared to intra-continental faults. It poses a risk in terms of earthquake potential. The characteristics of the segments of the Salanda fault zone are different. In particular, the larger segments should be studied in more detail, including paleoseismology.

5. Conclusions

Through the utilization of the PSInSAR methodology, this study analyzed the Salanda Fault Zone and accurately identified movements in the LOS direction. The PSInSAR data enabled a comprehensive determination of the number of movements that occurred on the Salanda Fault Zone, producing detailed information about the area with 323111 PS points. These points provided crucial insights into the magnitude of movement, field observations, and uplifts in the fault zone, particularly in areas where the fault passes, indicating significant activity. Additionally,

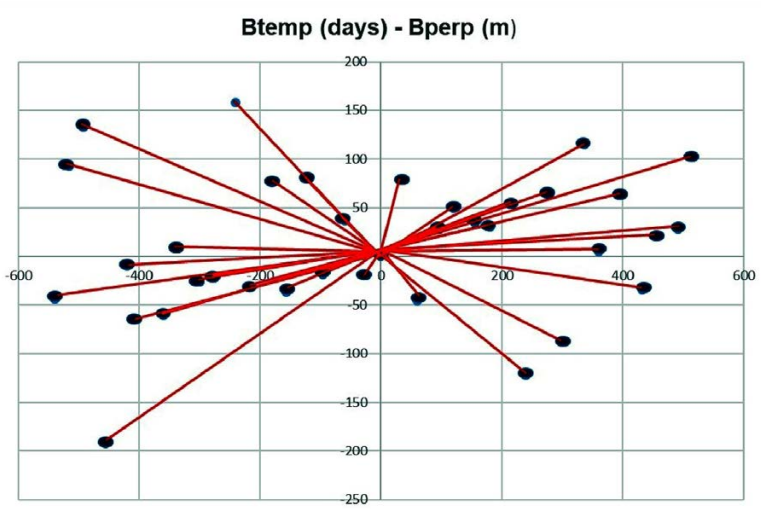

Figure 10. Temporal and spatial distribution of 36 ascending Sentinel-1 images, track number 131, based on the master image (red lines indicate interferogram pairs).

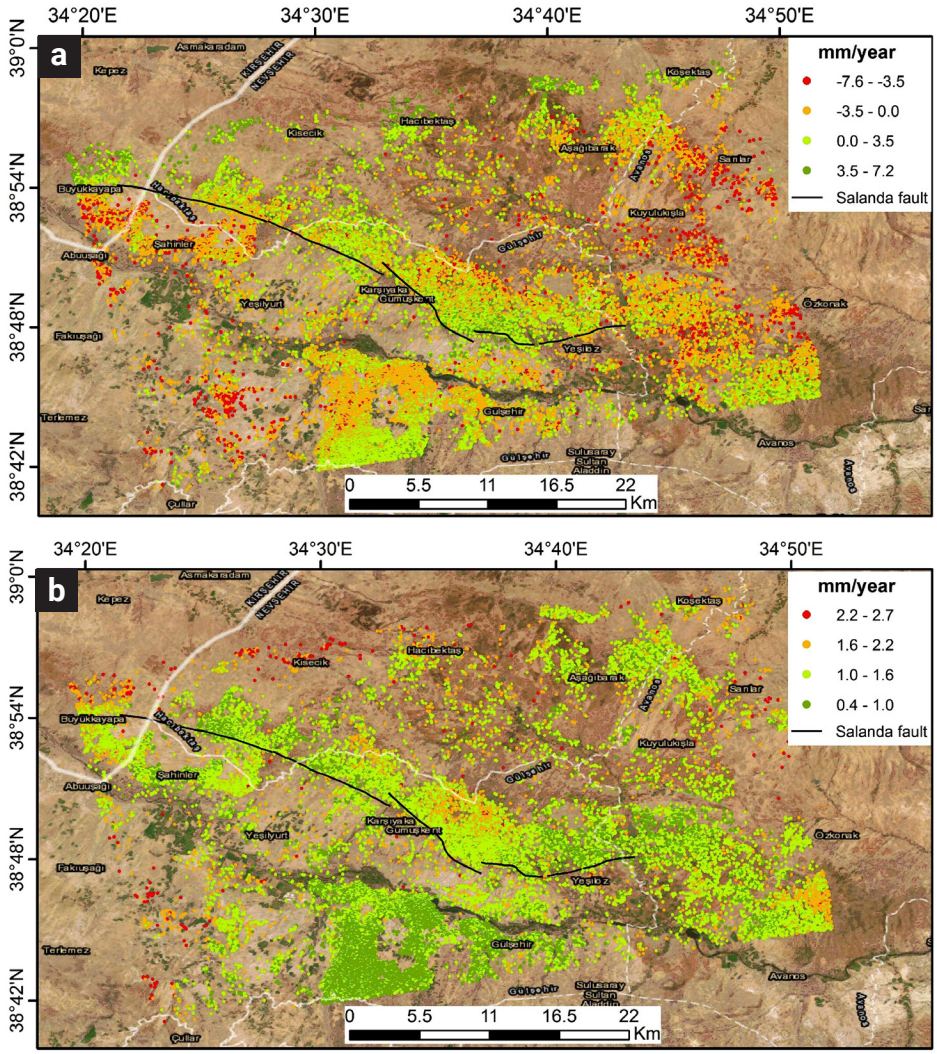

Figure 11. PSInSAR results of the study area. (a) Annual velocity in the LOS direction. (b) Standard deviations of the annual velocities in the LOS direction.

the study employed geomorphic indices (Demircioğlu and Coşkuner, 2022), revealing medium to high levels of tectonic activity.

Upon examining the historical earthquake data (Figure 6), it is evident that an earthquake measuring 6 on the magnitude scale occurred in the northwestern region of the Salanda fault zone, which is located outside of the study area. Seismic activity has been detected in and around the Salanda fault. The combined findings of PSInSAR results, field observations, and geomorphic indices studies strongly suggest the presence of an active fault. When analyzing movement values, the geomorphic indices and PSInSAR methods yield higher results compared to field studies. Interestingly, the uplift and subsidence values align closely with the fault lines. Palaeoseismological studies on this fault segment will be useful. Thus, the frequency of earthquake generation can be determined approximately. The high amounts of movement obtained indicate that it has the potential to produce earthquakes. A possible earthquake will significantly affect the neighbouring provinces. The fault zone is in a position to affect several neighbouring cities.

6. Author contributions

The authors declare that they contributed to the paper in an equal way.

7. Declaration of competing interest

The authors declare that they have no known competing financial interests or personal relationships that could have appeared to influence the work reported in this paper.

8. Data availability

Data can be provided upon request.

9. Acknowledgements

As authors, we would like to thank the editor and the associate editor for their efforts. We thank reviewers who contributed to the development of the manuscript. We thank the European Space Agency (ESA) for providing SAR images (Sentinel-1).

10. References

Abdikan, S, Arıkan, M., Sanli, F.B. (2014). Monitoring of coal mining subsidence in a peri-urban area of Zonguldak city (NW Turkey) with persistent scatterer interferometry using ALOS-PALSAR. *Environ. Earth Science*, 71:4081-4089.

Arikan, M., Hooper, A., Hanssen, R. (2010). *Radar time series analysis over West Anatolia*. European Space Agency (Special Publication) ESA, SP-677.

Atabey, E. (1989). *Aksaray-H18 Quadrangle, 1:100,000 Scale Geological Map and Explanatory Text.* Ankara, Türkiye, Maden Tetkik Arama Yayınları.

Biggs, J., Wright, T., Lu, Z., Parsons, B. (2007). Multi-interferogram method for measuring interseismic deformation: Denali Fault, Alaska. *Geophysical Journal International*, 170(3), 1165-1179. doi: **https://doi.org/10.1111/j.1365-246X.2007.03415.x**

Colesenti, C., Ferretti, A., Prati, C., Rocca, F. (2001). Comparing GPS, optical levelling, and persistent scatterers. *Proceedings of IGARSS*, 2622-2624.

Çiner, A., Doğan, U., Yıldırım, C., Akçar, N., Ivy-Ochs, S., Alfimov, V., Schlüchter. C. (2015). Quaternary uplift rates of the Central Anatolian Plateau, Turkey: insights from cosmogenic isochron-burial nuclide dating of the Kızılırmak River terraces. *Quaternary Science Reviews*, 107, 81-97. doi: **https://doi.org/10.1016/j.quascirev.2014.10.007**

Demircioğlu, R. (2014). *Gülşehir-Özkonak (Nevşehir) Çevresinde Kirşehir Masifi ve Örtü Birimlerinin Jeolojisi Ve Yapisal Özellikleri.* Doktora Tezi, Selçuk Üniversitesi, Konya, Türkiye.

Demircioğlu, R. and Coşkuner, B. (2022). Salanda Fay Zonu'nun Kesikköprü (Kırşehir) ve Yeşilöz (Nevşehir) arasında kalan kesiminin göreceli tektonik aktivitesinin jeomorfik indislerle incelenmesi. *Pamukkale Üniversitesi Mühendislik Bilimleri Dergisi*, 8(3),464-482. doi: **https://dergipark.org.tr/tr/pub/pajes/issue/70618/1136992**

Doğan, U., Koçyiğit, A., Wijbrans, J. (2009). *Evolutionary history of the Kızılırmak River, Cappadocia Section: implication for the initiation of Neotectonic regime in Central Anatolia*, Turkey. 62nd Geological Congress of Turkey, Ankara, Türkiye, 13-17 Nisan.

Doğan, U. (2011). Climate-Controlled river terrace formation in the Kızılırmak Valley, Cappadocia section, Turkey: inferred from Ar-Ar dating of Quaternary basalts and terraces stratigraphy. *Geomorphology Journal*, 126, 66-81. doi: **https://doi.org/10.1016/j.geomorph.2010.10.028**

Dumka, R. K., SuriBabu, D., Malik, K., Prajapati, S. and Narain, P. (2020). PS-InSAR derived deformation study in the Kachchh, Western India. *Applied Computing and Geosciences*, 8, 100041. doi: **https://doi.org/10.1016/j.acags.2020.100041**

Dumka, R. K., Suribabu, D., Narain, P., Kothyari, G. C., Taloor, A. K. and Prajapati, S. (2021). PSInSAR and GNSS derived deformation study in the West part of Narmada Son Lineament (NSL), western India. *Quaternary Science Advances*, 4, 100035.

Dumka, R. K., Suribabu, D. and Prajapati, S. (2022). PSI and GNSS derived ground subsidence detection in the UNESCO Heritage City of Ahmedabad, Western India. *Geocarto International*, 37, 25, 7639-7658. doi: **https://doi.org/10.1080/10106049.2021.1980618**

Suribabu, D., Dumka, R. K., Paikray, J., Kothyari, G. C., Thakkar, M., Swamy, K. V., Taloor, A. K. and Prajapati, S. (2022). Geodetic characterization of active Katrol Hill Fault (KHF) of Central Mainland Kachchh, western India. *Geodesy and Geodynamics*, 13, 247-253. doi: **https://doi.org/10.1016/j.geog.2021.05.003**

Suribabu, D., Dumka, R. K., Kothyari, G. C., Swamy K. V. and Prajapati, S. (2022c). Identification of crustal deformation in the Saurashtra region, western India: insights from PSI and GNSS derived investigation. *Acta Geodaetica et Geophysica*, 57, 639-659. doi: **https://doi.org/10.1007/s40328-022-00399-z**

Dumka, R. K., Prajapati, S., SuriBabu, D., Swamy, K. V., Kothyyari, G. C. and Malik, K. (2023). GPS and InSAR derived evidences of intra-basin stress and strike-slip tectonics in the vicinity of 2001 (M7.7) earthquake, Kachchh, western India. *Geological Journal*, 58, 683-699. doi: **https://doi.org/10.1002/gj.4618**

Emre, Ö., Duman, T.Y., Özalp, S., Elmacı, H., Olgun, Ş., Şaroğlu, F. (2013). *Açıklamalı Türkiye Diri Fay Haritası Ölçek 1/1.125.000:* Maden Tetkik ve Arama Genel Müdürlüğü Özel Yayın Serisi 30. ISBN: 978605531056.

Famiglietti, N.A., Golshadi, Z., Vallianatos, F., Caputo, R.; Kouli, M., Sakkas, V., Atzori, S., Moschillo, R., Cecere, G., D'Ambrosio, C. *et al.* (2021). Greece Central Crete ML 5.8 Earthquake: An Example of Coalescent Fault Segments Reconstructed from InSAR and GNSS Data. *Remote Sensing, 14*, 5783. **https://doi.org/10.3390/rs14225783**

Ferretti, A., Prati, C. and Rocca, F. (2001). Permanent scatterers in SAR interferometry. *IEEE Transactions on Geoscience and Remote Sensing*, 39, 8-20. doi: **http://dx.doi.org/10.1109/36.898661**

Gezgin, C. (2022). Using the PS-InSAR technique, the influence of groundwater levels on land subsidence in Karaman (Turkey). *Advances in Space Research, 70*, 3568-3581. doi: **https://doi.org/10.1016/j.asr.2022.08.003**

Gündüz, H. İ., Yılmaztürk, F. and Orhan, O. (2023). An Investigation of Volcanic Ground Deformation Using InSAR Observations at Tendürek Volcano (Turkey). *Applied Sciences*, 13, 6787. doi: **https://doi.org/10.3390/app13116787**

Gürsoy, Ö., Kaya, Ş., Çakir, Z., Tatar, O., Canbaz, O. (2017). Determining lateral offsets of rocks along the eastern part of the North Anatolian Fault Zone (Turkey) using the spectral classification of satellite images and field measurements. *Geomatics, Natural Hazards, and Risk*, 8(2), 1276-1288. doi: **https://doi.org/10.1080/19475705.2017.1318794**

Hastaoğlu, K.Ö., Poyraz, F., Türk, T., Koçbulut, F., Şanlı, U., Yılmaz, I., Şanlı, F.B., Kuçak, R.A., Demirel, M., Gürsoy, Ö., and Duman, H. (2015). GPS ve PS-InSAR yöntemleri kullanılarak Koyulhisar (Sivas) heyelanlarının izlenmesi: ilk sonuçlar. *Gümüşhane Üniversitesi Fen Bilimleri Enstitüsü Dergisi*, 4, 2, 161-175. doi: **https://doi.org/10.17714/gufbed.2014.04.013**

He, P., Wen, Y., Xu, C., Chen, Y. (2018). High-quality three-dimensional displacement fields from new-generation SAR imagery: application to the 2017 Ezgeleh, Iran, earthquake. *Journal of Geodesy*, 93. doi: **https://doi.org/10.1007/s00190-018-1183-6**

Hooper, A., Zebker, H., Segall, P., Kampes, B. (2004). A new method for measuring deformation on volcanoes and other natural terrains using InSAR persistent scatterers. *Geophysical Research Letters*, 31(23):5. doi: **https://doi.org/10.1029/2004GL021737**

Hooper, A, Segall, P, Zebker, H. (2007). Persistent Scatterer InSAR for crustal deformation analysis with application to Volcán Alcedo. *Galápagos Journal of Geophysical Research*, 112: B07407. doi: **https://doi.org/10.1029/2006JB004763**

Hooper, A., Bekaert, D., Hussain, E., and Spaans, K. (2018). *Stamps/Manual, VeStamps4.1b*, School of Environment, University of Leeds, LS2 9JT Leeds, UK.

Howell, A., Nissen, E., Stahl, T., Clark, K., Kearse, J., Van Dissen, R., Jones, K. (2020). Three-dimensional surface displacements during the 2016 MW 7.8 Kaikōura earthquake (New Zealand) from photogrammetry-derived point clouds. *Journal of Geophysical Research: Solid Earth*, 125(1), e2019JB018739. doi: **https://doi.org/10.1029/2019JB018739**

Kandıllı. (2022). *Observatory Regıonal Earthquake-Tsunami Monıtorıng And Evaluatıon Centre*. 18 January 2022 Sarıoglan-Kayserı Earthquake. Press Release.

Koçyiğit, A. (2003). Orta Anadolu'nun genel neotektonik özellikleri ve depremselliği. *Türkiye Petrol Jeologları Derneği Bülteni*, 5(Özel Sayı), 1-26.

Koçyiğit, A., Doğan, U. (2016). The strike-slip neotectonic regime and related structures in the Cappadocia region: a case study in the Salanda basin, Central Anatolia, *Turkey. Turkish Journal of Earth Sciences*, 25(5), 393-417. doi: **https://doi.org/10.3906/yer-1512-9**

Liu, J., and Zhao, X. (2020). GNSS Fault Detection and Exclusion Based on Virtual Pseudorange-Based Consistency Check Method. *Chinese Journal of Electronics*, 29(1), 41-48. doi: **https://doi.org/10.3390/s20030590**

Lu, P., Han, J., Hao, T., Li, R. and Qiao, G. (2020). Seasonal deformation of permafrost inWudaoliang basin in Qinghai-Tibet plateau revealed by StaMPS-InSAR. *Marine Geodesy*, 43, 248-268. doi: **https://api.semanticscholar.org/CorpusID:213881589**

Meisina, C., Zucca, F., Fossati, D., Ceriani, M., Allievi, J. (2006). Ground deformation monitoring by using the permanent scatterers technique: the example of the Oltrepo Pavese (Lombardia, Italy, *Engineering Geology*, 88(3-4):240-259.

Oktar, O., Erdoğan, H., Poyraz, F., and Tiryakioğlu, İ. (2021). Investigation of deformations with the GNSS and PSInSAR methods. *Arabian Journal of Geosciences*, 14, 2586. doi: **https://doi.org/10.1007/s12517-021-08765-x**

Florian, P., Heidrun, K., Dietrich, L., Katrin, H., Morelia, U. (2019). Measuring tectonic seafloor deformation and strain-build up with acoustic direct-path ranging, *Journal of Geodynamics*, 124, 14-24. doi: **https://doi.org/10.1016/j.jog.2019.01.002**

Peyret, M., Rolandone, F., Dominguez, S., Djamour, Y., Meyer, B. (2008). Source model for the Mw 6.1, 31 March 2006, Chalan-Chulan earthquake (Iran) from InSAR. *Terra Nova* 20(2):126-133. doi: **https://doi.org/10.1111/j.1365-3121.2008.00797.x**

Poyraz, F., Hastaoğlu, K.Ö. (2020). Monitoring of tectonic movements of the Gediz Graben by the PSInSAR method and validation with GNSS results. *Arabian Journal of Geosciences*, 13:844. doi: **https://doi.org/10.1007/s12517-020-05834-5**

Rodríguez, R., Lira, J., & Rodríguez, I. (2012). Subsidence risk due to groundwater extraction in urban areas using fractal analysis of satellite images. *Geofísica Internacional*, 51(2),157–167. doi: **https://doi.org/10.22201/igeof.00167169p.2012.51.2.605**

Rosu, A.M., Pierrot-Deseilligny, M., Delorme, A., Binet, R., Klinger, Y. (2015). Measurement of ground displacement from optical satellite image correlation using the free open-source software MicMac. *ISPRS Journal of Photogrammetry and Remote Sensing*, 100, 48-59. doi: **https://doi.org/10.1016/j.isprsjprs.2014.03.002**

Scott, C., Bunds, M., Shirzaei, M., Toke, N. (2020). Creep along the Central San Andreas Fault from surface fractures, topographic differencing, and InSAR. *Journal of Geophysical Research: Solid Earth, 125*, e2020JB019762. doi: **https://doi.org/10.1029/2020JB019762**

Shirzaei, M., and Bürgmann, R. (2013). Time-dependent model of creep on the Hayward fault from joint inversion of 18 years of InSAR and surface creep data. *Journal of Geophysical Research: Solid Earth*, 118(4), 1733-1746. doi: **https://doi.org/10.1002/jgrb.50149**

Suárez, G. ., Jaramillo, S. H., López-Quiroz, P., & Sánchez-Zamora, O. (2018). Estimation of ground subsidence in the city of Morelia, Mexico using Satellite Interferometry (INSAR)s. *Geofísica Internacional*, 57(1), 39-58. doi: **https://doi.org/10.22201/igeof.00167169p.2018.57.1.1821**

Şaroğlu, F., Emre, Ö., Aydoğan, B. (1987). Türkiye'nin diri fayları ve depremsellikleri. Maden Tetkik ve Arama Genel Müdürlüğü, Ankara, Türkiye, 394.

Şengör, A.M.C., Yılmaz, Y. (1981). Tethyan evolution of Turkey: a plate tectonic approach. *Tectonophysics*, 75(3-4), 181-241. doi: **https://doi.org/10.1016/0040-1951(81)90275-4**

Temiz, U. (2004). Kırşehir Dolayının Neotektoniği ve Depremselliği. PhD, Ankara University, Ankara, Turkey.

Temiz, U., Gökten, E., Eikenberg, J. (2009). U/Th dating of fissure

ridge travertines from the Kırşehir region (Central Anatolia Turkey): structural relations and implications for the Neotectonic development of the Anatolian block. *Geodin Acta 22*: 201-213. doi: **https://doi.org/10.3166/ga.22.201-213**

Wang, T., and Jónsson, S. (2015). Improved SAR amplitude image offset measurements for deriving three-dimensional coseismic displacements. *IEEE Journal of Selected Topics in Applied Earth Observations and Remote Sensing*, 8 (7), 3271-3278. doi: **https://doi.org/10.1109/JSTARS.2014.2387865**

Yavaşoğlu, H., Tarı, E., Tüysüz, O., Çakır, Z., Ergintav, S. (2011). Determining and modelling tectonic movements along the central part of the North Anatolian Fault (Turkey) using geodetic measurements. *Journal of Geodynamics*, 51(5), 339-343. doi: **https://doi.org/10.1016/j.jog.2010.07.003**

Yen, J.Y., Lu, C.H., Chang, C.P., Hooper, A., Chang, Y.H., Liang, W.T., Chang, T.Y., Lin, M.S., Chen, K.S. (2011). Investigating active deformation in the northern longitudinal valley and City of Hualien in Eastern Taiwan using persistent scatterer and small-baseline SAR interferometry. *Terrestrial Atmospheric and Oceanic Sciences*, 22(3):291-304. doi: **https://scihub.copernicus.eu/dhus/#/home**

Geofísica Internacional (2024) **63-2**: 881 - 907

La erupción del volcán Irazú 1917-1921 (Costa Rica): dinámica y entorno social

Mauricio M. Mora[*1, 3], Giovanni Peraldo Huertas[2] and Gerardo J. Soto[1, 4]

Abstract

This study reconstructs and analyzes, from a volcanological and historical approach, the 1917-1921 eruptive phase of the Irazú volcano based on newspaper, documental, technical-scientific and historical sources. The results are consistent with the known tephrostratigraphy and new aspects of the eruption are given, such as: the description of strombolian eruptions, tephra fall reconstructions for relevant eruptions and the detail analysis of the November 30, 1918 (VEI~3) vulcanian eruption. The convergence of this natural event with the dictatorship of "the Tinoco" between 1917 and 1919 is analyzed as well as how both events abruptly burst into the life of Costa Rican society, especially in San José, the capital of Costa Rica. The impact of the eruptive phase 1917-1921 was minor compared to that of 1963-65, but not negligible, and the adverse political climate of the time contributed to overshadow it. All this made a deeper analysis and quantification of its impact difficult. The study of the eruptive phase of 1917-1921 is fundamental to evaluate risk scenarios based on the characteristics of Costa Rica in the 21st century and thus contribute to an adequate risk management.

Key words: Irazú volcano, eruption, San José, eruptive phases, Tinoco.

Resumen

En este trabajo se reconstruye y analiza, desde un enfoque vulcanológico e histórico, la fase eruptiva de 1917-1921 del volcán Irazú con base en fuentes hemerográficas, documentales, técnico-científicas e históricas. Los resultados son coherentes con la tefroestratigrafía conocida y se agregan elementos nuevos, tales como: la ocurrencia de erupciones estrombolianas, las reconstrucciones de caídas de tefra para algunas erupciones relevantes y especialmente la erupción vulcaniana del 30 de noviembre de 1918 (VEI~3). Se analiza la convergencia de este acontecimiento natural con la dictadura de “los Tinoco” entre 1917 y 1919 y cómo ambos sucesos irrumpieron abruptamente en la vida de la sociedad costarricense, sobre todo en San José, la capital de Costa Rica. El impacto de la fase eruptiva 1917-1921 fue menor en comparación con la de 1963-65, pero no despreciable, y el clima político adverso del momento contribuyó a opacarla, lo que dificultó el análisis más profundo y su cuantificación. El estudio de la fase eruptiva de 1917-1921 es fundamental para valorar escenarios de riesgo construidos a partir de las características de la Costa Rica del siglo XXI y con ello contribuir con una adecuada gestión del riesgo.

Palabras clave: Volcán Irazú, erupción, San José, fases eruptivas, Tinoco.

Received: August 2, 2023; Accepted: January 9, 2024; Published on-line: April 1, 2024.

Editorial responsibility: Dr. Juan Manuel Espíndola-Castro

* Corresponding author: Mauricio M. Mora. E-mail: mauricio.mora@ucr.ac.cr
[1] Universidad de Costa Rica, Escuela Centroamericana de Geología, Sede Rodrigo Facio Brenes, Montes de Oca, San José, Costa Rica. E-mail: mauricio.mora@ucr.ac.cr.
[2] Universidad de Costa Rica, Escuela Centroamericana de Geología, Sede Rodrigo Facio Brenes, Montes de Oca, San José, Costa Rica. E-mail: marino.peraldo@ucr.ac.cr.
[3] Universidad de Costa Rica, Red Sismológica Nacional (RSN), Sede Rodrigo Facio Brenes, Montes de Oca, San José, Costa Rica.
[4] Universidad de Costa Rica, Escuela Centroamericana de Geología, Sede Rodrigo Facio Brenes, Montes de Oca, San José, Costa Rica. Consultor geológico. E-mail: katomirodriguez@yahoo.com.

https://doi.org/10.22201/igeof.2954436xe.2024.63.2.1736

1. Introducción

Los doce años transcurridos entre 1910 y 1921 fueron particularmente difíciles para Costa Rica. Eventos naturales, políticos y epidemiológicos fueron puntos de quiebre en la cotidianidad del país. El 25 de enero de 1910 el volcán Poás produjo una erupción freatomagmática importante; entre abril y mayo del mismo año las crisis sísmicas de Desamparados y Cartago culminaron con el desastroso sismo del 4 de mayo (Ms 6,4), que destruyó casi la totalidad de la ciudad de Cartago y produjo cerca de 600 fallecidos. La Primera Guerra Mundial, entre 1914-1918, afectó severamente la economía, y en medio de ella, la dictadura militar de los hermanos Federico y José Joaquín Tinoco Granados ("los Tinoco"), entre 1917 y 1919, sembró incertidumbre y terror. Concomitante con esta dictadura tuvo lugar un nuevo periodo eruptivo del volcán Irazú entre 1917 y 1921 que generó asombro, temor y pérdidas económicas en el sector agropecuario. Entre 1914 y 1918 ocurrieron también epidemias sucesivas de sarampión y tosferina, así como la parte final de la pandemia de "gripe española" que llegó al país en 1920.

En este trabajo se analiza la evolución e impacto de la fase eruptiva del volcán Irazú de 1917 a 1921, con el propósito de brindar nuevas luces sobre su dinámica eruptiva e incorporar nueva información a los análisis de riesgo volcánico, de modo que sirva como antecedente para la prevención de desastres en Costa Rica. Cualquier esfuerzo para reducir el riesgo volcánico debe estar sustentado en bases sólidas del conocimiento del comportamiento a largo plazo de los volcanes activos y potencialmente activos (Tilling, 2009). Por ello el enfoque multidisciplinario, desde la historia y la vulcanología, permiten la generación de conocimiento para completar el registro histórico de actividad de un volcán, en el contexto de los hechos políticos, económicos y sociales de la época en la que ocurrió la actividad eruptiva de interés. Por ello nos interesamos en la convergencia de la fase eruptiva de 1917-1921 del Irazú con la dictadura de "los Tinoco" y cómo ambos acontecimientos irrumpieron abruptamente en la vida de la sociedad costarricense, particularmente en la capital, San José, y trastocaron su cotidianidad. Se analiza cómo los acontecimientos políticos, sociales y económicos influyeron en la documentación histórica de dicho periodo eruptivo, y se pone de relieve la labor encomiable de los científicos de la época, quienes hicieron lo posible por documentar un proceso natural que duró cinco años, en un momento histórico donde el conocimiento relativo a los procesos geológicos y vulcanológicos era incipiente en Costa Rica y en el que la ciencia se encontraba limitada por la clausura del *Instituto Físico-Geográfico Nacional (IFG)* en 1910.

1.1 Volcán Irazú: ubicación, contexto geológico y vulcanológico

La subducción de la placa del Coco bajo la placa del Caribe, sobre la que se encuentra el territorio de Costa Rica, es muy compleja debido a las variaciones del ángulo, morfología, edad y características petrológicas de la primera (p. ej., Gazel *et al.* 2021). Este proceso da origen al arco volcánico cuaternario, que tiene una orientación noroeste-sureste, y se ubica unos 150 km tierra adentro de la Fosa Mesoamericana. Este arco está dividido en tres segmentos (Fig. 1a): la cordillera volcánica de Guanacaste (CVG) en el extremo noroeste, la cordillera volcánica de Tilarán (CVT) y la cordillera volcánica Central (CVC) en el extremo sureste. El volcán Irazú (9,979°N y 83,852° O, 3432 m s.n.m) se ubica en este último segmento, unos 25 km al este del centro de la ciudad de San José, capital de Costa Rica y 15 km al noreste de la ciudad de Cartago. Ambas conforman, junto con las ciudades de Heredia y Alajuela el Gran Área Metropolitana (GAM), el centro socio-económico y la zona más densamente poblada de Costa Rica (Figura 1a y b).

El Irazú es un amplio complejo estratovolcánico andesítico basáltico (aunque también presenta basaltos, andesitas y raramente dacitas) con varios cráteres y conos piroclásticos cuspidales y adventicios, así como también varios anfiteatros de avalancha (Soto & Sjöbohm, 2015; Alvarado *et al.*, 2021) (Figura 1c). Las principales erupciones históricas del Irazú ocurrieron en 1723-26 (estromboliana violenta, freatomagmática y freática), varias dudosas en el siglo XIX, 1917-1921 (freatomagmática a magmática), 1924 (posiblemente freatomagmática), 1928-1930 (freatomagmática), 1933 (freatomagmática), 1939-1940 (freatomagmática) y 1963-65 (freática, freatomagmática y estromboliana a vulcaniana) (Barquero, 1976; Alvarado, 1993). Luego de la última fase eruptiva de 1963-1965 el Irazú ha mantenido una tenue actividad fumarólica en el flanco norte, muy cerca de la cima, variaciones del nivel y color de la laguna intracratérica, enjambres sísmicos ocasionales y la generación de megadeslizamientos en el flanco norte del macizo, uno de los cuales se asoció con una erupción freática en 1994 al noreste del cráter principal, en el sitio conocido como volcán Nuevo (Fallas *et al.*, 2018) (Figura 1b).

Los eventos eruptivos históricos más importantes, de origen magmático y freatomagmático e Índice de Explosividad Volcánica (VEI, siglas en inglés, Newhall & Self, 1982) de 3 se dieron separados por 240 años (1723 y 1963). Hay referencias indirectas de que los españoles llegaron al valle de El Guarco y lo encontraron cubierto de cenizas y árboles desprovistos de follaje, y por esto se especuló que podría haber habido una erupción

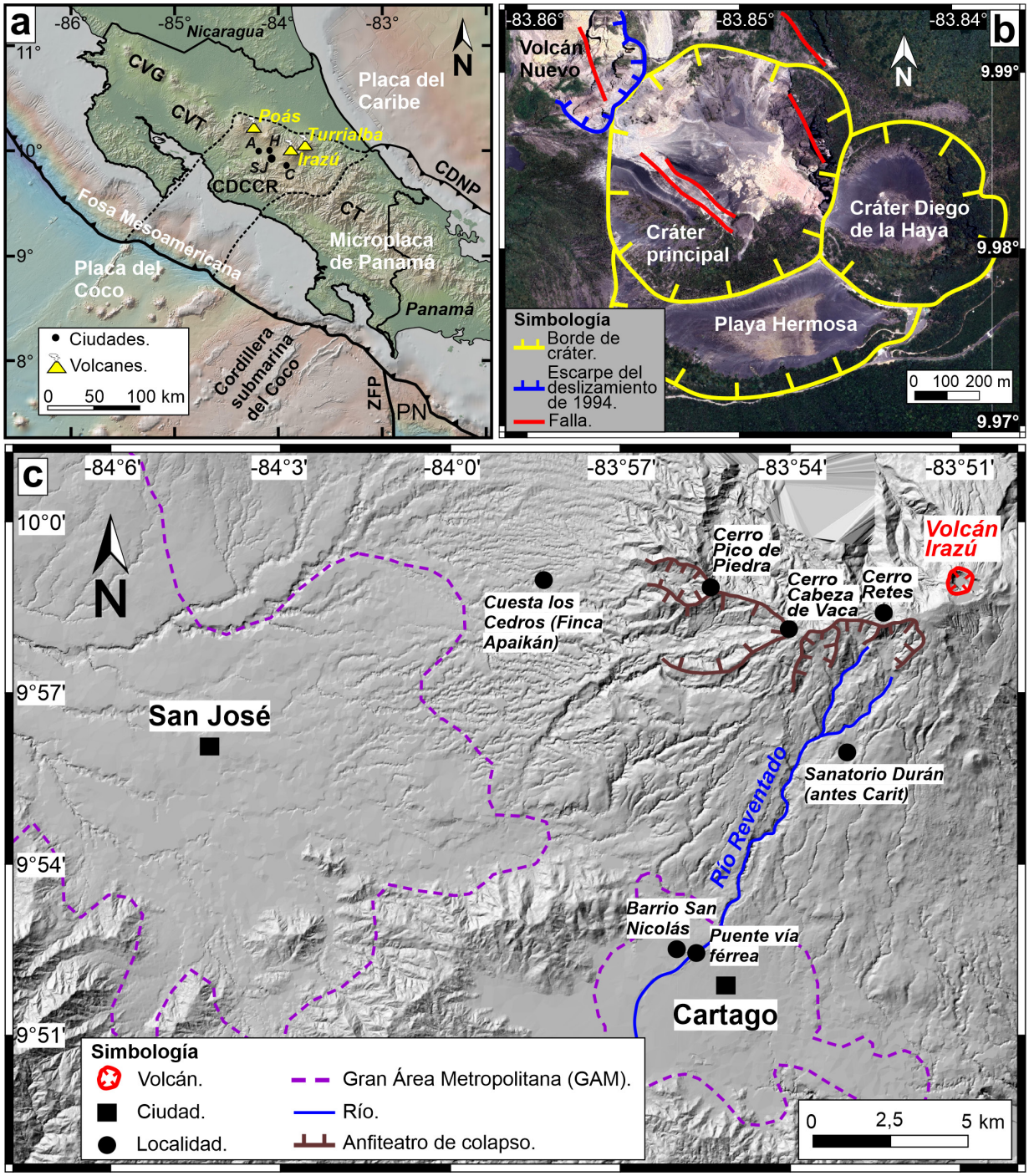

Figura 1. a) Contexto tectónico simplificado de Costa Rica en el que se muestran los volcanes activos (triángulos amarillos) de la Cordillera Volcánica Central (CVC) y principales ciudades (círculos negros). Las abreviaturas de los rasgos tectónicos son: Cordillera Volcánica de Guanacaste (CVG), Cordillera Volcánica de Tilarán (CVT), Cordillera de Talamanca (CT), Cinturón Deformado del Centro de Costa Rica (CDCCR, región dentro de la línea punteada con base en Denyer *et al.*, 2013), Cinturón Deformado del Norte de Panamá (CDNP), Zona de Fractura de Panamá (ZFP) y la placa Nazca (PN). Los triángulos negros pequeños indican movimiento inverso y apuntan hacia la placa cabalgante. La batimetría y topografía se obtuvieron de Ryan *et al.* (2009). Las ciudades son: Alajuela (A), Heredia (H), Cartago (C) y San José (SJ). b) Detalle de la cima del volcán Irazú con base en una imagen de *Google Earth* CNES/Airbus, Maxar Technologies de abril de 2023. Las fallas se indican según el trabajo de Ulloa *et al.* (2018). c) Detalle del área del volcán Irazú, parte de San José y Cartago en el que se muestra el río Reventado y algunas localidades mencionadas en el texto. El modelo de elevación digital fue elaborado con base en curvas de nivel a escala 1:25 000, suministradas por el Instituto Geográfico Nacional (IGN).

alrededor de 1560 (Alvarado 1989, 2000). Algunas dataciones sugieren que cerca de 1561 ocurrió una erupción importante del Irazú (Clark *et al.*, 2006). Clark *et al.* (2006) le asignaron un VEI de 3, similar a la de 1963-65, pero especulan que pudo haber sido de menor duración y de mayor altura de columna eruptiva. El poco conocimiento histórico y prehistórico de la actividad eruptiva explosiva del Irazú permite sugerir que las erupciones magmáticas-freatomagmáticas con VEI ≥ 3 suceden con periodos de retorno del orden de 200-400 años, mientras que los episodios con VEI < 3 suceden con recurrencias pluridecadales (Soto & Sjöbohm, 2015), pero luego de periodos de calma eruptiva de varias décadas posteriores a las paroxísmicas, como fue el caso pos 1723-26 y es el caso pos 1963-65. De hecho, la erupción más trascendente posterior a 1723 no se dio sino hasta 1917, lo cual sería evidente en los depósitos en la cima del volcán (Figura 2).

Los depósitos finales de 1723 (Figura 2) son escorias de caída con mediana granoselección con clastos balísticos gruesos, que alcanzan varios metros de espesor, seguidos por un hiato erosivo. Los depósitos de 1917-21 son de color claro, de caída, ricos en líticos en la base y con más juveniles hacia el centro (erupciones estrombolianas), y cierran la erupción una serie de corrientes piroclásticas diluidas de color claro a gris, bien laminadas, que ilustran las fases que se discutirán luego. Un delgado paquete de escorias y corrientes piroclásticas diluidas separados por hiatos erosivos de los depósitos sobre y subyacentes, se interpreta como los productos de las erupciones menores de 1939-40. Finalmente, los depósitos de 1963-65, se componen de corrientes piroclásticas diluidas y eventos de caídas de escorias de un espesor pluridecimétrico a métrico en este sitio. Esta secuencia proximal ilustra las diferencias texturales que conllevan a las interpretaciones dinámicas, así como el tamaño, intensidad y volumen de las diferentes erupciones.

1.2 Breve contexto político y socio-económico de San José, capital de Costa Rica, a finales del siglo XIX e inicios del siglo XX

La fundación de la ciudad de San José se remonta a 1737, cuando el Cabildo de León ordenó la erección de una ermita en la Boca del Monte del Valle de Aserrí, en un sitio muy cercano al centro de la ciudad actual, con el fin de concentrar las familias que se habían establecido de forma dispersa en esa región (González Víquez *et al.*, 1987). A finales del siglo XIX, San José ya era la capital de Costa Rica y los liberales imprimieron en ella su concepto de modernidad, al dotar a la ciudad de arquitecturas europeas, lo que se reflejó también en las demás ciudades del

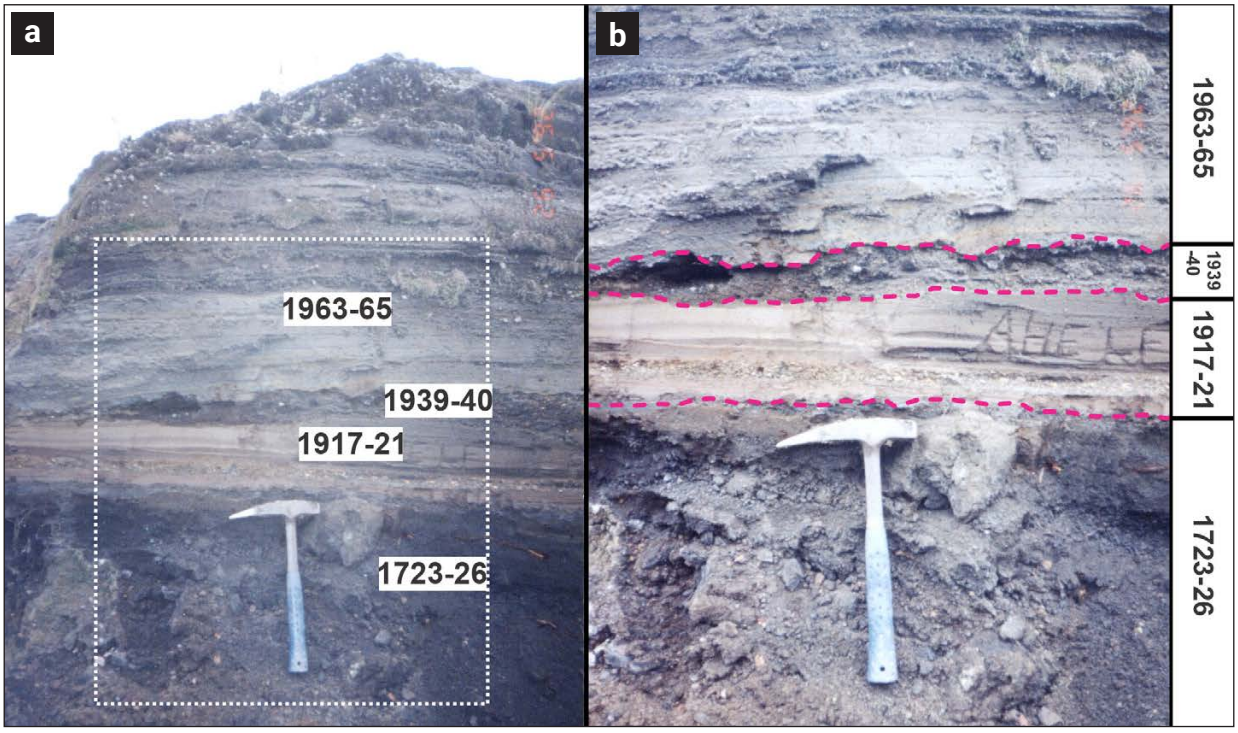

Figura 2. Tefras de las erupciones históricas del Irazú que afloran en el sector occidental del cráter activo, interpretadas a partir de las características dinámicas, estratigráficas, composicionales y texturales. a) Vista general del afloramiento. La línea punteada indica la zona agrandada en la imagen derecha. b) Acercamiento de los depósitos de las erupciones. Fotografías de Gerardo J. Soto tomadas en 1992.

centro del país (Fumero, 2000). A inicios del siglo XX, este clima liberal también era favorable a la educación secundaria de alcance universal, pero restrictivo con la educación superior a la que tenían acceso solo las élites dominantes al asistir a universidades extranjeras, pues no habían universidades locales. Sin embargo, la ciencia pasaba por un mal momento con el cierre definitivo del *Instituto Físico-Geográfico Nacional (IFG)* en 1910, a lo que se sumaron cambios desfavorables en los medios de difusión científica, pues los *Anales del IFG*, uno de los principales, ya no se publicaban (Solano & Díaz, 2009). Por otro lado, las actividades culturales y deportivas florecían (Fumero, 1996), y la cultura impresa (libros, revistas y periódicos) se tornó cada vez más notable (Fumero, 2005). La elección presidencial de 1914 puso en evidencia la crisis política del momento (Oconitrillo, 1982; Bonilla Castro, 2008). Al mismo tiempo, la economía estaba en franco deterioro por la Primera Guerra Mundial (1914-1918) y el dominio del pensamiento liberal poco favorable a la producción nacional y que perjudicaba a una población con bajo poder adquisitivo (Fernández Morales, 2010). Por esta razón, el gobierno de Alfredo González Flores (1914-1917) impulsó un nuevo modelo económico a partir de una reforma tributaria y del sistema bancario, que no cayó bien a los sectores poderosos (Murillo, 1981; Oconitrillo, 1982; Fernández Morales, 2010). Esto abriría las puertas a la ulterior dictadura de "los Tinoco" en enero de 1917. Este escenario arquitectónico y social en el centro socioeconómico de Costa Rica sería testigo de la convergencia de un acontecimiento político-social y otro natural, que irrumpirían abruptamente en la sociedad y trastocarían su cotidianidad.

2. Método y fuentes de información

El análisis de la dinámica de la fase eruptiva de 1917-1921 del volcán Irazú y su impacto se realizó con base en las siguientes fuentes de información:

a) Artículos científicos publicados por José Fidel Tristán y Ricardo Fernández Peralta y sus apuntes originales que nutrieron esos artículos, así como también los reportes de actividad volcánica contenidos en cartas y telegramas. Esta información se encuentra, en su mayor parte, en el Fondo José Fidel Tristán del Archivo Histórico del Archivo Nacional de Costa Rica. También se consultaron informes técnicos de fuentes oficiales como el *Diario Oficial La Gaceta*, accesible a través del portal de la Imprenta Nacional de Costa Rica, así como de otras publicaciones periódicas como la *Revista de Costa Rica* y la *Revista del Colegio Superior de Señoritas*, accesibles desde el portal del Sistema Nacional de Bibliotecas de Costa Rica (SINABI).

b) Fuentes hemerográficas que informaron sobre la actividad eruptiva y que se encuentran disponibles de manera digital y física, en la Hemeroteca Nacional de la Biblioteca Nacional de Costa Rica. Los periódicos consultados son: *La Información, El Renacimiento, La Acción Social, El Comercial, La Verdad, El Heraldo de Puntarenas y Guanacaste, La Prensa, El Hombre Libre* y *Diario de Costa Rica.* Las noticias de interés fueron transcritas y sistematizadas cronológicamente en una base de datos de 160 noticias que contiene: periódico, página, autoría, título de la noticia, día, mes, año y la transcripción. También se creó una base de datos específica sobre los lahares ocurridos en el río Reventado en 1919 (Figura 1c) compuesta por 22 noticias.

Las transcripciones de los documentos históricos y las noticias mantienen, en gran medida, los rasgos gramaticales y ortográficos originales; solo se corrigieron algunos errores tipográficos de imprenta y elementos menores como los acentos. La información relativa a la actividad eruptiva y su impacto se extrae y se analiza desde el prisma de la percepción permeada por el contexto cultural e histórico del momento. Se identifican sesgos y distorsiones a partir de la comparación de los discursos, lo que resalta los elementos consistentes sobre la actividad volcánica. Las interpretaciones se calibran, al menos en parte, cuando se cuenta con información científica obtenida durante la misma época. Finalmente, se interpretan los hechos a la luz del conocimiento científico actual, lo que obliga a generar hipótesis y suposiciones con respecto a la información localizada. La contextualización histórica se basó en periódicos, revistas, obras literarias y publicaciones relativas al contexto histórico, social y económico de la época, accesibles desde el portal del Sistema Nacional de Bibliotecas de Costa Rica (SINABI), bibliotecas institucionales y colecciones privadas.

3. Reconstrucción de la fase eruptiva de 1917 a 1921 del Irazú

Se identificaron 71 erupciones reportadas entre diciembre de 1917 y 1921. Se consideró una erupción cuando se cumplía al menos una de las siguientes condiciones: 1) certeza de la caída de ceniza en una o varias localidades; 2) que la descripción permitiera diferenciar entre la emanación de vapor de agua y gases de las emanaciones de ceniza. La mayoría de las erupciones apenas se mencionan o su descripción es muy escueta en las noticias de los rotativos de la época, otras fueron sujeto de mayor atención y se describieron con más detalle, proporcionalmente a su energía e impacto.

El catálogo de erupciones no es exhaustivo, ya que solo se tienen reportes discretos en un momento histórico cuando no se tenían instituciones científicas calificadas, y cuando además, había una efervescencia política que debe haber enmascarado, o al menos reducido parcialmente, la cobertura periodística y la atención ciudadana al fenómeno volcánico, tal y como se verá en la sección 6.

A continuación se describe la evolución de la actividad eruptiva de la siguiente manera: 1) 1917: el inicio; 2) 1918: el clímax; 3) 1919 a 1921: el epílogo.

3.1 Actividad eruptiva de 1917: el inicio

El primer reporte de actividad fumarólica en los cráteres antiguos del Irazú se atribuye a Juan Gómez, Paula Gómez y Rubén Sánchez, peones de la finca de Alfredo Volio, quienes comunicaron que el 29 de setiembre "vieron los chorros de humo saliendo de las bocas [cráteres viejos]" cuando iban para el sitio conocido como Volcán Nuevo (Figura 1b), pero que al ver esa actividad se devolvieron (Tristán & Fernández, 1917). Juan Gómez manifestó que algunos días antes de esa fecha había visto el Volcán Nuevo como siempre, "echando humo", pero solo en la "parte de abajo" (Tristán & Fernández, 1917). Una semana después, el periódico *La Información* se adjudicó la primicia sobre la nueva actividad en el volcán Irazú gracias a un reporte que recibió desde Tierra Blanca:

"Anoche a las diez tuvimos noticia de fuente fidedigna, de que de Tierra Blanca habían comunicado a Cartago que el volcán Irazú estaba echando grandes columnas de humo y llamas... el Agente de Policía de Tierra Blanca, pueblo situado en las faldas y muy contiguo al Irazú, avisaba por telégrafo que ese Volcán estaba arrojando columnas de humo y llamas y que con ese motivo había gran pánico entre los habitantes de la pequeña población... Es de notar que el almanaque de don Pedro Nolasco, anuncia para hoy «día crítico»" (La Información, 1917a).

El 5 de octubre de 1917 salió de Tierra Blanca una comisión integrada por Raúl Cordero (director de la escuela), Froilán Gómez (agente de policía), los señores Alfredo Solano, Romano Orlich, Fabián Ortega y un corresponsal del periódico *La Información*. Al día siguiente, este último publicó sus apreciaciones en las que describió que los cráteres viejos "exhalaban violentamente grandes columnas de humo" que "parece ser vapor de agua" y se elevaban hasta unos 75 m (La Información, 1917c). Fabián Ortega, uno de los integrantes de esa excursión, envió una carta a José Fidel Tristán con un reporte en el que detalló los cambios observados en el volcán Irazú (Ortega, 1917a) y aseguraba que muchos datos publicados por *La Información* en su edición del 5 de octubre (La Información, 1917b) eran exagerados. Dicho reporte fue publicado en el periódico *La Información* (Ortega, 1917b). José Fidel Tristán y Ricardo Fernández Peralta visitaron la cima del Irazú el 19 y 20 de octubre y aunque observaron la actividad fumarólica en los cráteres antiguos, constataron que el volcán no había hecho erupción (Figura 3a); sin embargo, dudaron si la actividad volcánica se debía a un nuevo despertar del volcán o simplemente a un aumento en la actividad fumarólica y tampoco sabían cuándo inició (Tristán, 1917; Tristán & Fernández, 1917).

El 4 de noviembre se observó una profusa desgasificación desde el llamado cráter G, acompañada de un fuerte sonido (Tristán, 1923). Entre el 8 y el 16 de diciembre la desgasificación se mantuvo con altos y bajos hasta que el 17 de diciembre en la noche, la actividad se intensificó y culminó con la primera erupción (Tristán, 1917; Tristán & Fernández, 1921; Tristán, 1923). Ese mismo día, José Fidel Tristán recibió un telegrama que decía:

"Tengo informes obtenidos hoy de vecinos que viven en las faldas del Irazú [ha] entrado de nuevo en actividad. [En la] noche hubo lluvia de ceniza en gran cantidad quedando las hojas de los árboles cubiertas y las aguas de un color claro de las mismas cercanías de ahí, retumbos con frecuencia y se oía al lado del volcán un ruido como de una fogata y se notaba mucha claridad…" (Ortega, 1917c).

También se informó de caída de ceniza en Curridabat (La Información, 1917g). Desde Sabanillas (un lugar cercano al cráter del Irazú) un testigo indicó:

"En la madrugada del martes me despertó un ruido sordo y prolongado que parecía venir del centro de la tierra y que no se parecía a los que frecuentemente oímos aquí y que son los retumbos corrientes del Volcán. Salí asustado y noté que llovían cenizas y escorias volcánicas en gran cantidad y cuando amaneció pude apreciar que todos los lugares cercanos estaban cubiertos de cenizas y escorias del volcán" (La Información, 1917h).

La ceniza de esta erupción se dispersó hacia el oeste-suroeste y llegó hasta el sector oriental de San José (Tabla 1, figura 4). Esta ceniza fue descrita de color gris claro: "capa gruesa de un polvo fino como cemento romano y de un color gris perla uniforme cubría todo el lomo de burro en toda su extensión… en la lejanía se ven bosques cubiertos completamente de polvo y escorias volcánicas, que hacen el efecto de bosques nevados" (La Información, 1917k).

José Fidel Tristán reportó que la erupción del 17 de diciembre de 1917 también eyectó balísticos hacia el noreste del cráter:

"La pendiente del Volcán Nuevo presentaba un aspecto extraño: los mirtos y arrayanes estaban todos más o menos mutilados con las ramas rotas y desgajadas, en el suelo varias piedras cubiertas de ceniza y fragmentos de otras más grandes. En partes el camino había quedado

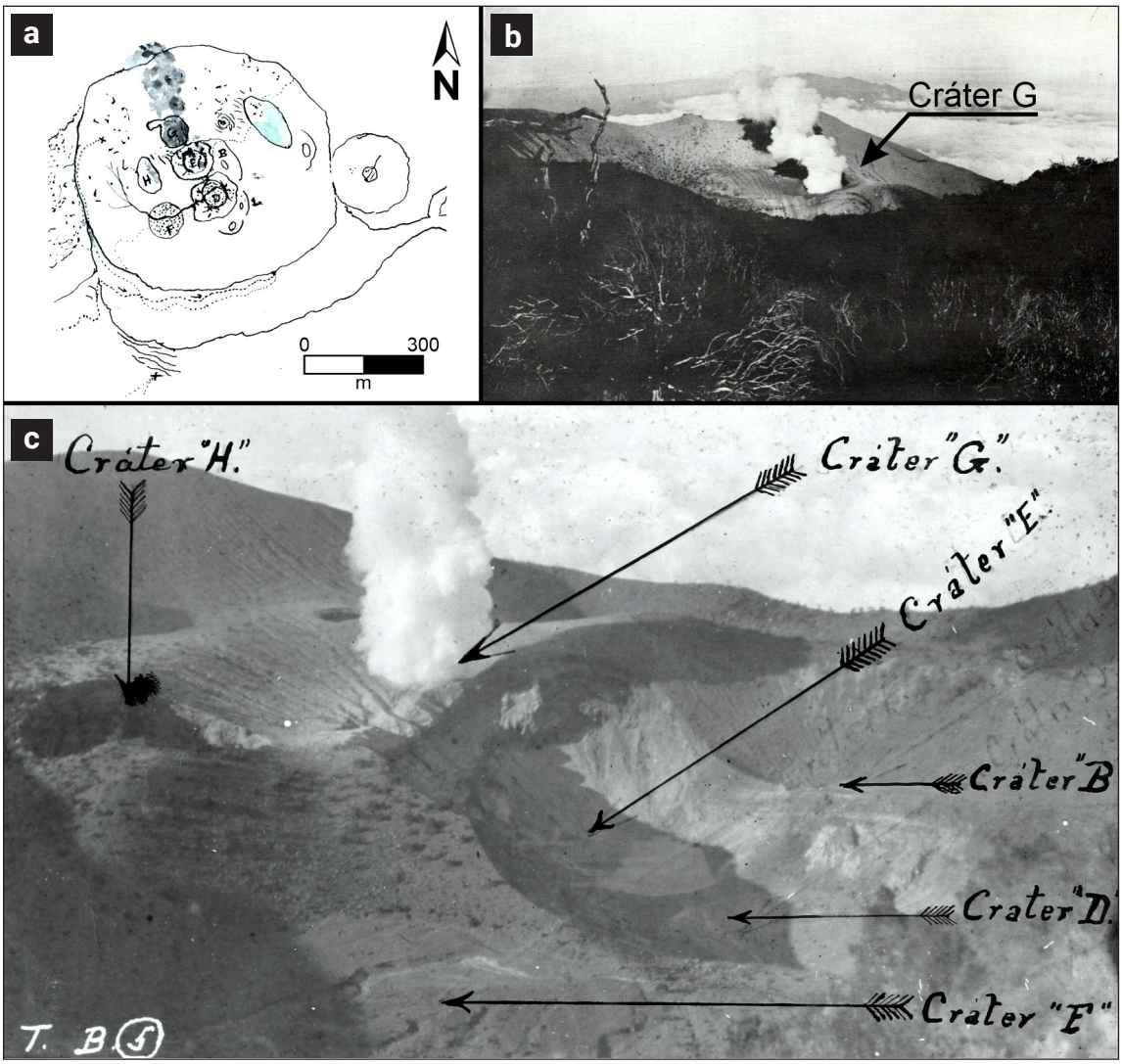

Figura 3. Actividad del volcán Irazú en 1917: a) Esquema elaborado por José Fidel Tristán en octubre de 1917, donde resalta la profusa actividad en el cráter G, así como también algunas fumarolas en los cráteres E y H (Tristán, 1917). b) Fotografía de Manuel Gómez Miralles (Vargas Chaves, 1967). c) Fotografía tomada por José Fidel Tristán el 20 de diciembre de 1917, donde indica los cráteres y los etiqueta con base en la nomenclatura de Sapper (1901) (Tristán, 1917). Nótese en ambas imágenes la actividad en el cráter G.

Tabla 1. Reportes de caída de ceniza de las principales erupciones de la fase eruptiva de 1917-1921 del volcán Irazú.

Localidades	**Distancia (km) y rumbo con respecto al cráter principal)**	**Erupciones y referencias**				
		17/12/1917	**06/01/1918**	**16 y 17/08/1918**	**09/10/1918**	**30/11/1918**
Parte alta de la cuenca del río Reventado	3 (SO)	1				
Cerro Cabeza de Vaca	4 (O)	1				
Sanatorio Carit (actual Sanatorio Carlos Durán, ubicado en Potrero Cerrado de Oreamuno, Cartago)	7 (SO)				6	
Tierra Blanca (Cartago, Cartago)	9 (SO)	1, 3, 4			2, 7, 8	
Cot (Oreamuno, Cartago)	9 (SO)		2, 3			
Capellades (Alvarado, Cartago)	10 (SE)					2, 10
Cervantes (Alvarado, Cartago)	11 (SE)					2, 10
Rancho Redondo (Goicoechea, San José)	11 (SO)		2			

Continúa...

Santa Cruz (Turrialba, Cartago)	13 (SE)					2
Cartago (ciudad)	15 (SO)				5, 6, 7, 8	2, 10
Vista de Mar (Goicoechea, San José)	15 (O)		2			
Finca Apaikán (cerca de la actual cuesta Los Cedros camino a las Nubes de Coronado)	16 (O)					10
Coronado (ciudad cabecera de cantón de Vásquez de Coronado, San José)	18 (O)		2	2		10
Tres Ríos (ciudad cabecera de cantón de la Unión, Cartago)	18 (SO)	1, 3, 4	2, 3			
Montes de Oca (Cantón)	20 (SO)		2			
Sabanilla (Montes de Oca, San José)	20 (SO)	1				
Moravia (ciudad)	22 (SO)		2			
Curridabat (ciudad cabecera del cantón, San José)	22 (SO)	1, 3, 4				
San Isidro (ciudad cabecera de cantón, Heredia)	23 (NO)			2		2
Tibás (ciudad cabecera del cantón, San José)	25 (O)		2			
San José (ciudad capital de Costa Rica)	25 (SO)				9	
Desamparados (ciudad cabecera de cantón, San José)	26 (SO)			2		
Santo Domingo (ciudad cabecera de cantón, Heredia)	27 (O)		2	2		10
San Rafael (ciudad cabecera de cantón, Heredia)	27 (NO)			2		
La Sabana (parque metropolitano de San José)	28 (SO)					10
Heredia (ciudad)	29 (NO)		2, 3			
Alajuelita (ciudad cabecera de cantón, San José)	29 (SO)			2		
Barva (ciudad cabecera de cantón, Heredia)	30 (NO)					2, 10
Aserrí (ciudad cabecera de cantón, San José)	30 (SO)		2, 3			
San Joaquín de Flores (ciudad cabecera de cantón, Heredia)	33 (NO)			2		
Escazú (ciudad cabecera de cantón, San José)	33 (SO)			2		
Santa Bárbara (ciudad cabecera de cantón, Heredia)	35 (NO)					2
San Antonio (ciudad cabecera del cantón de Belén, Heredia)	37 (SO)		2, 3	2		
Santa Ana (ciudad cabecera de cantón, San José)	37 (SO)		2	2		
Dota (cantón)	39 (SO)				9	
Alajuela (ciudad)	40 (NO)			2		
Sabanilla (distrito del cantón de Alajuela, Alajuela)	41 (NO)					11
Villa Colón (actual Ciudad Colón, distrito del cantón de Mora, San José)	44 (SO)		3, 2	2		
San Pedro (distrito del cantón de Poás, Alajuela)	45 (NO)			2		2, 10
Grecia	52 (NO)			2		2
Puriscal (cantón de San José)	53 (SO)		3, 2	2		
Atenas (ciudad cabecera de cantón, Alajuela)	58 (NO)			2		2
Naranjo (ciudad cabecera de cantón, Alajuela)	59 (NO)			2		10
Orotina (ciudad cabecera de cantón, Alajuela)	74 (O)					10
San Mateo (ciudad cabecera de cantón, Alajuela)	74 (O)					9
Miramar (ciudad cabecera del cantón de Montes de Oro, Puntarenas)	97 (NO)					10
Puntarenas (ciudad)	100 (O)					12

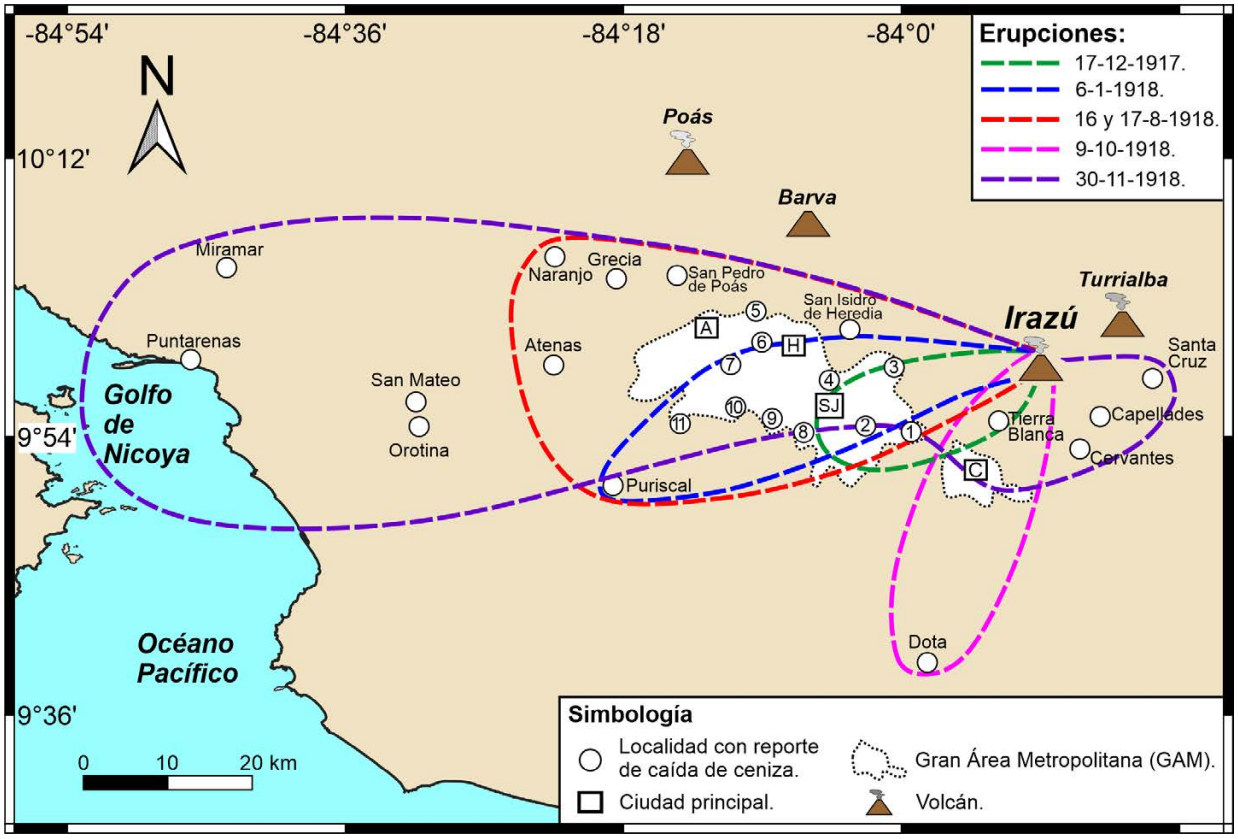

Figura 4. Dispersión de la tefra de caída de las erupciones más notables y con mayor cantidad de reportes de la fase eruptiva de 1917-1921 del volcán Irazú. Los números corresponden con las siguientes localidades: 1) Tres Ríos, 2) Curridabat, 3) Coronado, 4) Tibás, 5) Santa Bárbara de Heredia, 6) San Joaquín de Flores, 7) San Antonio de Belén, 8) Alajuelita, 9) Escazú, 10) Santa Ana, 11) Villa Colón (actual Ciudad Colón). Las ciudades principales son: A. Alajuela, C. Cartago, H. Heredia y SJ. San José.

obstruido por las ramas de los arbustos destruidos. Por todas partes había señales evidentes de que había caído por este lado una verdadera LLUVIA DE PIEDRAS" (Tristán, 1917).

Y también describe algo muy peculiar:

"Continuamos hacia el Oeste [de la cima del Irazú] hasta alcanzar las profundas pendientes del REVENTADO. En todos estos lugares cayó la ceniza en verdaderas masas. Había sobre las hojas no una capa sino verdaderas pelotas. Los tallos de los arbustos tenían encima gruesa capa de barro gris. Algunos árboles recibieron tanto de este lodo que las ramas habían sedido [sic] al peso y estaban inclinadas. Por este lado había pasado gran manga de agua lodosa" (Tristán, 1917).

En el artículo científico, lo anterior se describe de la siguiente forma: "Un gran torbellino de barro había pasado sobre toda la vegetación, dejando los árboles y arbustos con sus ramas dobladas por el peso de una gruesa capa de lodo oscuro" (Tristán & Fernández, 1921); y agregan: "Este lodo siguió en línea recta y fue después esparcido a grandes distancias por los vientos superiores" (Tristán & Fernández, 1921). Estas descripciones sugieren la ocurrencia de corrientes piroclásticas diluidas y lapilli acrecional, tal y como veremos más adelante en la discusión. Luego de esa erupción habría seguido un periodo de calma durante el resto de diciembre de 1917, caracterizado por una columna blanca de vapor de agua y gases que se observaba regularmente (La Información, 1917e; Tristán & Fernández, 1921) (Figura 3b y c). Esto marcaría el inicio de una nueva fase eruptiva del Irazú que se prolongaría, de forma intermitente y con magnitud variable, hasta el año de 1921.

3.2 Actividad eruptiva de 1918: el clímax

En enero se constataron siete erupciones. Entre ellas destaca la del 6, entre las 7:00 y las 8:00 p.m.:

"Como a las 7 pasadas de la noche me avisaron algunas personas que se veía una erupción muy grande... la cual me sorprendió bastante por el tamaño y el color oscuro rojizo, y se veía que tomaba una dirección noreste a sureste poco más o menos. La mayor parte de los

vecinos se alarmaron pues nunca habían visto erupción igual. Es de notarse que en el norte de Cartago no cayó ceniza y en San José si" (Vicente, 1918).

La ceniza de esta erupción se dispersó hacia el oeste-suroeste y alcanzó mayor distancia con respecto a la del 17 de diciembre de 1917 (Tabla 1, figura 4). Otra erupción, ocurrida el 14 de enero a las 7:30 a. m., es descrita con bastante detalle desde Guápiles:

"...la erupción que presencié esta mañana a las 7 y 30 ha sido una de las mayores del periodo de actividad del Volcán. Una gran columna de humo completamente negro subía y al tomar dirección Oeste, parte de esa masa negra se iba desprendiendo y cayendo verticalmente sobre el mismo cerro formando así como un fleco o barbas de pañón. No hay duda que este fenómeno se debe a la cantidad de pequeñas piedras y arenas y otras escorias que revueltas con el humo iban" (Expediente sobre actividad del volcán Irazú, 1918).

Entre febrero y julio continuaron las erupciones de magnitud variable. A partir de agosto la energía y tamaño se fue incrementando paulatinamente y las "lluvias de ceniza" se tornaron cada vez más profusas, duraderas y alcanzaban mayor distancia. También se tienen reportes de cenizas con tonos amarillentos, como es el caso del 8 de enero de 1918 o el 31 de julio de 1918 (Tristán & Fernández, 1921).

En agosto la ceniza causaba gran escozor en Llano Grande (El Renacimiento, 1918b) y San José (La Verdad, 1918b) y las columnas eruptivas se describían oscuras o negras (La Verdad, 1918d) (Figura 5a y b). Las erupciones del 16 y 17 de ese mes habrían sido las más energéticas (El Renacimiento, 1918c) y sus cenizas se dispersaron hasta unos 60 km de distancia en dirección oeste-noroeste (Tabla 1 y figura 4). El 30 de agosto se reportó caída de ceniza en Santa Bárbara de Heredia "por primera vez y en cantidad suficiente que puede notarse bien" (Expediente sobre actividad del volcán Irazú, 1918). En septiembre solo hay dos erupciones documentadas el 19 y el 25 (Figura 5c), lo que podría sugerir un breve descenso en la actividad eruptiva, aunque se continuaba reportando ceniza oscura (Expediente sobre actividad del volcán Irazú, 1918).

En octubre la actividad eruptiva se incrementó: "El cráter arrojaba con fuerza negras columnas de humo que se perdía a gran altura, presentando un espectáculo realmente admirable"

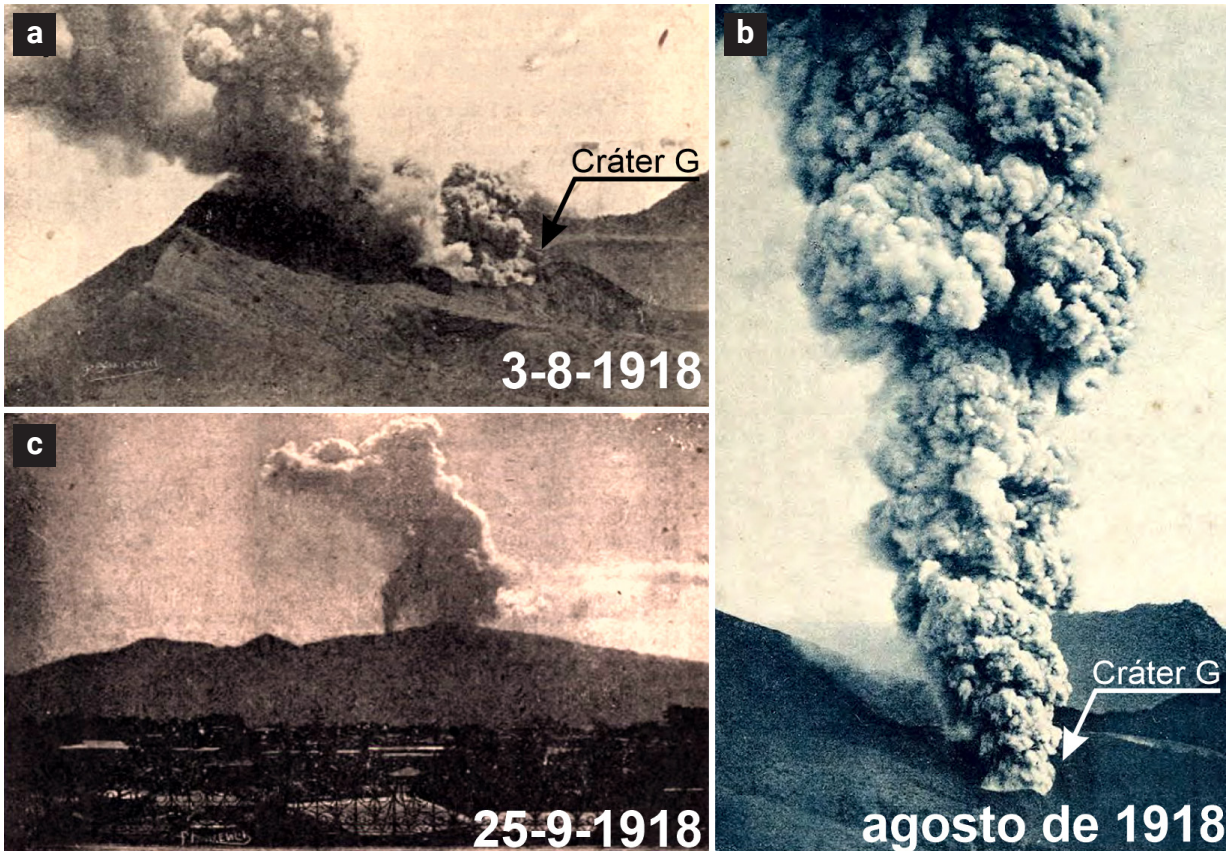

Figura 5. Fotografías de la actividad del volcán Irazú en 1918 tomadas por: a) Ricardo Fernández Peralta (Tristán, 1929), b) Manuel Gómez Miralles (Tristán, 1923), y c) José Fidel Tristán desde la azotea del Colegio Superior de Señoritas en San José (Tristán, 1929).

(La Información, 1918a). La ceniza nuevamente se hacía sentir: "Creíamos que vueltas las lluvias, la ceniza del Irazú no caería más, pero resulta que ahora flota en el aire con más abundancia. Y se ha notado que está cayendo no solo blanquecina ceniza sino escorias en forma de granitos de carbón, que molestan demasiado, pues se introduce en los ojos, produciendo escozor" (La Verdad, 1918e). La noche del 9 de octubre de 1918, a eso de las 7:00 p. m., ocurrió una erupción cuya ceniza se dispersó principalmente hacia el sur-suroeste (Figura 4) y tuvo algunas características particulares:

a) Fue abundante (La Información, 1918b) y prolongada: "Desde las 8 de la noche, ayer en esta ciudad [Cartago], se notaba la caída de ceniza en nuestras calles. La lluvia arreció conforme avanzaban las otras y a la de cerrar nuestra edición, a la 1 a. m. de hoy, continuaba en gran cantidad. Muchas personas hubieron de liberarse de esa lluvia por medio de paraguas, para evitarse el deterioro de trajes" (El Renacimiento, 1918d).
b) Caía aún caliente (La Información, 1918d; El Renacimiento, 1918d) y quemaba la piel y la ropa (El Renacimiento, 1918d); también causaba pequeñas quemaduras a los animales "que bramaban y corrían por todas partes" (La Información, 1918c).
c) Se describió como "arena gruesa" (El Renacimiento, 1918e; Tristán & Fernández, 1918).
d) Durante esa erupción se observó incandescencia: "una claridad continua en los cráteres del volcán" (El Renacimiento, 1918d); o bien como "una intensa actividad producida por llamas" (La Información, 1918b). También se escucharon retumbos (La Información, 1918c).

Las erupciones continuaron al menos hasta casi finales de octubre y se caracterizaron por "gruesas y negras columnas de humo" (La Información, 1918j) con cenizas que caían casi en "estado candente" (La Verdad, 1918g; La Información, 1918f, 1918d, 1918k). También se observó incandescencia (La Información, 1918g). El 20 de octubre unos excursionistas que visitaron la cima del Irazú describieron: "eso sí, adentro oíanse [sic] a cada instante dilatadas explosiones, algo así parecido a lentas descargas de fusilería; a nuestro alrededor caía algo y al amanecer del día siguiente, notamos que eran pequeñas piedras calcinadas" (La Información, 1918h). Otra descripción detalló:

> "las erupciones del volcán se suceden cada dos o tres minutos y en esos momentos óyense [sic] formidables ruidos en el interior, como también explosiones de gran intensidad que se perciben tan fuertes como el retumbar de cañones. Cuando ocurre este fenómeno, es que trepida la tierra tanto más fuertemente cuanto más violentas sean esas explosiones. En el momento de algunas de las erupciones más fuertes, yo observé que entre la densa columna de humo negro flotaban objetos calcinados de diferentes tamaños y que los más grandes volvían a caer dentro de la bocaza del cráter" (La Información, 1918i).

En los periódicos se manifestaba que la actividad se había incrementado bastante lo que trastocó nuevamente la cotidianidad, ya que la gente se había acostumbrado a la actividad eruptiva:

> "El público ha podido apreciar que durante estos últimos días, las erupciones del volcán Irazú han aumentado notablemente y que cada vez son más grandes. Todo eso, sin embargo, con motivo de que hace ya tiempo está en al [sic] actividad, no había alarmado a las gentes que viven en las inmediaciones de aquel volcán, a pesar de que fuertes retumbos se han dejado oír, aún a gran distancia. Ahora, según noticias, se trata de algo que sí ha causado mucha alarma..." (La Información, 1918c).

En los periódicos se insiste en que "El Irazú --agregó el informante-- aumenta cada día en actividad; sus erupciones son más frecuentes y potentes y las lluvias de ceniza y arcillas [probablemente ceniza muy fina mezclada con gotículas de lluvia], más copiosas que antes" (La Información, 1918e).

En noviembre el Irazú entró en un periodo de calma (El Renacimiento, 1918g, 1918h; La Información, 1918l). Una noticia, en particular, detalla lo siguiente: "El volcán en relativa calma. Son vapores, no humo precisamente, lo que arroja por sus dos grandes cráteres. No se perciben ruidos internos ni tiembla como antes en la cúspide de la montaña" (La Información, 1918m). Esa calma se prolongó al menos unas cuatro semanas: "Casi un mes había transcurrido sin que el Irazú, el coloso del este, interrumpiera su reposo" (La Información, 1918n).

Sin embargo, el 30 de noviembre de 1918 tuvo lugar, según José Fidel Tristán, "la erupción más formidable del Irazú" a eso de la 1:30 p. m. (Tristán & Fernández, 1921; aunque los periódicos la reportaron a las 2:30 p. m). Fue una explosión violenta y se escuchó en un radio de al menos unos 15 km e incluso a mayor distancia (Tabla 2, figura 6).

En la finca "El Roble", ubicada cerca de la cima del Irazú, al momento de la explosión del 30 de noviembre de 1918 unos testigos narraron lo siguiente:

> "En momentos de la erupción venían con dos bestias cargadas de palmitos precisamente en las playas del volcán, y fue tal el susto y el pánico que de ellos se apoderó al oír aquellos retumbos y aquellas bocanadas de humo y cenizas, que corrieron a quitar las cargas de las bestias echándolas en un barranco, para montar a caballo y salir de aquel lugar a todo escape como alma que lleva el diablo" (El Renacimiento, 1918k).

Desde la ciudad de Cartago se observó cómo la columna eruptiva se elevó varios kilómetros de altura: "Como impulsada a golpes de intensa presión la columna de humo negruzco

Tabla 2. Retumbos y vibraciones asociadas con la erupción del volcán Irazú del 30 de noviembre de 1918.

Localidad	Distancia (km) y rumbo con respecto al cráter principal	Descripción y referencias
Capellades (Alvarado, Cartago)	10 (SE)	"A las 2:00 p.m. se oscureció todo, un gran ruido se oyó dentro de la tierra y se observaron como relámpagos sobre el Irazú" (1). "Hubo un ligero temblor como a las 2:30 p. m." (2)
Cervantes (Alvarado, Cartago)	11 (SE)	"Primero sentimos un pequeño temblor y oímos ruidos fuertes y prolongados debajo de la tierra. Vino después la oscuridad". (1). "un prolongado trueno se oyó debajo del suelo" (Brenes, 1918).
Santa Cruz (Turrialba, Cartago)	13 (SE)	"Se ha sentido temblor pequeño" (2).
Cartago (ciudad)	15 (SO)	"El admirable fenómeno se produjo segundos después de haberse percibido débiles ruidos subterráneos" (1).
Finca Apaikán (cerca de la actual cuesta Los Cedros camino a las Nubes de Coronado)	16 (O)	"notamos también fuertes retumbos que en ocasiones parecían estremecer la tierra" (1).
Barva (ciudad cabecera de cantón, Heredia)	30 (NO)	"El Sr Gregorio Alfaro a quien sorprendió la tempestad en el norte dice que al norte se oyó un fuerte retumbo y se vio levantarse una negra columna" (2).
Sabanilla (distrito del cantón de Alajuela, Alajuela)	41 (NO)	"Pero sí se percibieron allí formidables retumbos subterráneos en el momento en que se produjo la erupción" (1).

Fuentes: (1) La Información (1918n); (2) Expediente sobre actividad del volcán Irazú (1918).

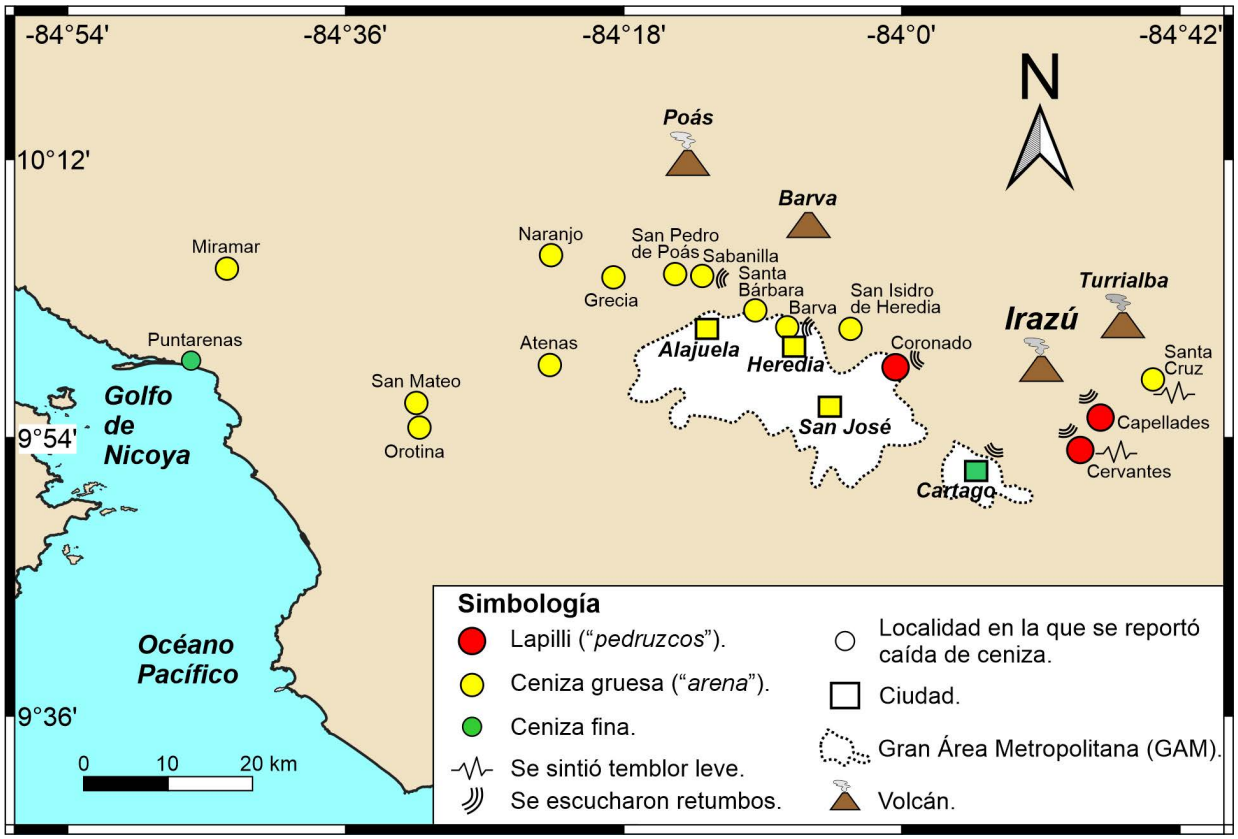

Figura 6. Reportes de caída de ceniza de la erupción del 30 de noviembre de 1918 y otros fenómenos asociados.

fue ascendiendo hasta alcanzar verticularmente [sic] una altura incalculable" (La Información, 1918n). O en esta otra descripción:

"El volcán estaba cubierto por una densa nube blanca, gigantesca, que no dejaba ver la cordillera y que se remontaba a una altura considerable sobre la cresta del coloso. Y, sobre esa gran nube se destacaba, dominando el espacio hasta llegar al fondo del firmamento, hasta rozar perfectamente el cénit, la columna monumental de cenizas" (El Renacimiento, 1918j).

También se describe la fuerza de la explosión: "vimos alzarse una gigantesca columna de humo de espesor nunca visto... Esas escorias debieron ser lanzadas con una fuerza espantosa, pues pocas veces las hemos visto igual" (El Renacimiento, 1918i). En muy corto tiempo, la alta densidad de la columna eruptiva oscureció el firmamento (El Renacimiento, 1918j; La Información, 1918n). La ceniza se describió oscura o negra, pero también se hace mención a una fracción más clara, incluso rojiza (Tabla 3, figura 6).

La ceniza fue dispersada hacia el oeste-noroeste hasta unos 110 km (ya que alcanzó el golfo de Nicoya) y también hacia el sureste hasta unos 11 km (Figuras 4 y 6). La ceniza gruesa (tamaño arena, < 2 mm) alcanzó unos 90 km hacia oeste-noroeste y material aún más grueso, quizás lapilli muy fino, de unos 2 a 4 mm, habría alcanzado hasta ~18 km hacia Coronado y ~11 km hacia Cervantes y Capellades (Figura 6). En Cervantes se reportó que: "comenzó a caer arena negra gruesa como si fueran garbanzos [sic, lapilli fino < 8 mm] y más menudita mucha ceniza" (Expediente sobre actividad del volcán Irazú, 1918). Mientras que, en Capellades, se reportó lluvia de "arena y pedruscos" (La Información, 1918n). En la finca Apaikán (Coronado, figura 1c) se reportó: "Al fijar la atención nos sorprendió que no era agua lo que llovía sino arena" (La Información, 1918n). Otro reporte de Coronado describe que hubo: "lluvia de pedruscos" (La Información, 1918n).

Algunas noticias aludieron a una posible actividad del volcán Poás concomitante con la erupción del 30 de noviembre. Sin embargo, esto obedece a una confusión, ya que la nube de ceniza pareció provenir del norte como lo evidencia un reporte desde Barva (Tabla 2). Esto último es un problema de percepción, del sitio en donde se observó la nube y achacar la ceniza al volcán más cercano, que para el caso de San Pedro de Poás y de Barva, es el Poás.

En diciembre se reportaron 5 "erupciones grandes" (Tristán & Fernández, 1921) de las cuales, la del día 15 habría generado caída de ceniza gruesa en San José (La Información, 1918p).

3.3 Actividad eruptiva de 1919 a 1921: el epílogo

A partir de 1919 los reportes sobre la actividad eruptiva se tornaron escasos y cada vez más escuetos en la prensa. En ese año se constataron 18 erupciones que generaron caídas de ceniza principalmente hacia el oeste y, ocasionalmente, hacia el suroeste en dirección a la ciudad de Cartago. El 13 de febrero de 1919, particularmente, se describió una "formidable erupción" que hizo llover sobre dicha ciudad "gruesos fragmentos de ceniza" (El Renacimiento, 1919a). Los informes de las excursiones de José Fidel Tristán y Ricardo Fernández Peralta al Irazú durante 1919 ofrecen algunos detalles que sugieren que la actividad eruptiva se prolongaba durante varios días en los que ocurrían emisiones de ceniza sostenidas pero poco explosivas y, ocasionalmente, ocu-

Tabla 3. Descripciones de la ceniza generada por la erupción del volcán Irazú del 30 de noviembre de 1918.

Localidad	Distancia (km) y rumbo con respecto al cráter principal	Descripción y referencias
Santa Cruz (Turrialba, Cartago)	13 (SE)	"La arena tiene reflejos también como plata" (3).
Cartago (ciudad)	15 (SO)	"En algunos puntos de ella, se apreciaba un color rojizo muy marcado, y en otros, el color negro era acentuadísimo" Más adelante: "En el fondo del espacio, una gran mancha semi-roja a especie de una gran cauda, precedía el tinte negro del cielo". (1).
Finca Apaikán (cerca de la actual cuesta Los Cedros camino a las Nubes de Coronado)	16 (O)	"La primera arena que cayó era muy negra; más luego cayó otra cenicienta y húmeda, que empañaba todos los objetos". (2).
San José (ciudad capital de Costa Rica)	25 (SO)	"Sobre esta capital llovieron dos clases de arenas: una rojiza húmeda y otra muy morena, seca". (4).
Barva (ciudad cabecera de cantón, Heredia)	30 (NO)	"la primera oscura, segunda limpia, fina y clara". (2).
San Mateo (ciudad cabecera de cantón, Alajuela)	74 (O)	"lluvia arena fina con partículas blanquecinas". (2).

Fuentes: (1) El Renacimiento (1918j); (2) La Información (1918n); (3) Expediente sobre actividad del volcán Irazú (1918); (4) La Información (1918o).

rrían episodios explosivos superpuestos, de magnitud variable, como es el caso de lo observado entre el 14 y el 16 de febrero de 1919 en la cima del volcán (Figura 7):

"salía por este cráter una gruesa y compacta columna de humo, renegrido, ya en grandes porciones que se iban desemvolviendo [sic] en otras tantas más pequeñas, torciéndose y retorciéndose en todas las formas imaginables"... "De pronto oímos un ruido formidable; mil piedras parecen chocar unas con otras y segundos después salen del cráter, abriendo la espesa humareda, grandísima columnas [sic] de un barro negro y reluciente. Pude observar dos de estas columnas, una más gruesa que la otra. Momentos después tuvimos la suerte de ver una gran lluvia de piedras. Casi todas se dirigieron hacia el lado O, después de describir en el aire grandes curvas. Evidentemente estas piedras fueron arrastradas por las erupciones de barro. Calculamos que habían llegado a una altura de 100 a 150 metros. Vimos rodar varias piedras y caer de nuevo en el cráter" (Tristán, 1919).

Luego de la erupción anterior continuó la emisión de ceniza pero, después:

"...violentamente salió de nuevo una nueva erupción de humo negro que se elevó a mucha altura. Casi al mismo tiempo se produjo el fuerte ruido de piedras mucho más fuerte que la primera vez y las elevadas y lucientes [sic] columnas de barro volvieron a manifestarse en todo su esplendor" (Tristán, 1919).

En marzo de 1919, José Fidel Tristán, Ricardo Fernández Peralta y David Sutherland describieron algunas erupciones poco explosivas que salían del nuevo cráter: "Momentos después salía por dicho cráter X [el nuevo] una pequeña erupción de humo algo negruzco, pero floja, es decir sin violencia y sin mayor ruido (Figura 7). Duró esta erupción unos 10 minutos" (Tristán, 1919). En 1920 solo se obtuvieron reportes de 8 erupciones que afectaron San José con caída de ceniza (Figura 7). Finalmente, en 1921, solo una erupción se constató.

4. Cambios geomorfológicos del cráter principal del volcán Irazú durante la fase eruptiva de 1917 a 1921

Antes de la fase eruptiva de 1917-1921, el volcán Irazú presentaba al menos 8 cráteres denominados: A, B, C, D, E, F, G y H (Sapper, 1901; figura 8a). Esta nomenclatura fue luego utilizada por José Fidel Tristán y Ricardo Fernández Peralta como base para sus descripciones y esquemas elaborados durante sus excursiones (Figura 8b-h).

Conforme la actividad eruptiva evolucionaba, los cráteres se ensanchaban progresivamente, particularmente los cráteres G, D y E (Figura 8c-e). Entre agosto y octubre de 1918 se formó un nuevo cráter que ocupó parte del espacio de los cráteres E, D y L. Ese cambio habría ocurrido el 9 de octubre (Fernández, 1920), pero no es seguro, ya que no hubo excursiones entre el 3 de agosto y el 20 de octubre de 1918, cuando unos excursionistas ascendieron y tomaron fotos cuyo análisis permitió verificar la formación del nuevo cráter (Tristán & Fernández, 1918). Es posible que ese cráter se hubiese gestado en algún momento durante ese lapso por una o varias erupciones. En noviembre de 1918 se observaba una profusa desgasificación desde el cráter G y el nuevo cráter (Tristán & Fernández, 1918). Durante la erupción del 11 de noviembre de 1918 el nuevo cráter se ensanchó y fue denominado M (Figura 8f-h). También se describió lo que podrían ser anillos de tobas o pequeños conos piroclásticos: "Algo más de nuevo; se han formado en diferentes direcciones promontorios de arenas calcinadas que obstaculizan el paso para llegar al borde del segundo de los cráteres en actividad; quiero decir, al de más reciente formación" (La Información, 1918i). Al respecto José Fidel Tristán y Ricardo Fernández notaron que: "Las fotografías tomadas el 20 indican muy claramente que se ha formado un cono dentro del cráter que irá aumentando poco a poco" (Tristán & Fernández, 1918). En marzo de 1919 ambos científicos reportaron lo que habría sido un lago de lava en el fondo del nuevo cráter M: "se ve una capa negra que se mueve lentamente formando ondas grandes. De la superficie sale el humo azul que sube lentamente" (Tristán, 1919). Esto sería similar a lo reportado por el gobernador Diego de la Haya Fernández, en su diario, para la erupción de 1723: "…el fuego se mantenía en el plano bajo, sobre la parte del norte, á manera de cuando una paila de brea ó alquitrán se pega fuego, con continuados esfuerzos é impulsos, como si en aquel fuego echasen algunas partes tenuas de aguas y que echava por instantes cenisas, arenas y piedras menudas…" (Alvarado, 2021) y que es atribuido por Alvarado y Schmincke (2013) a un laguito de lava.

La actividad volcánica posiblemente también aumentó el proceso de inestabilidad de laderas: "…hacia el lado noroeste de la cima de la cordillera, esto es, en dirección a Coronado, grandes derrumbes; allí se han desplomado no menos de diez manzanas de montaña y en cada gran erupción que hace el coloso, se observa de lejos cómo caen continuamente los grandes bloques de los perfiles de las montañas" (La Información, 1918i). Otro reporte menciona que: "El 30 de noviembre [por contexto sería 1917] durante la noche hubo un derrumbo [sic] de consideración en el Reventado" (Tristán & Fernández, 1921).

Figura 7. Imágenes de la actividad del volcán Irazú tomadas por José Fidel Tristán en febrero y marzo de 1919 (Tristán, 1919) y en agosto de 1920 (Tristán, 1920). Durante estos años la actividad cesó en el cráter G y se concentró en el nuevo cráter denominado "X" (que luego fue denominado M en Fernández, 1920) y que abarcó parte de los cráter E y D, tal y como se observa en el esquema del recuadro de Tristán (1919).

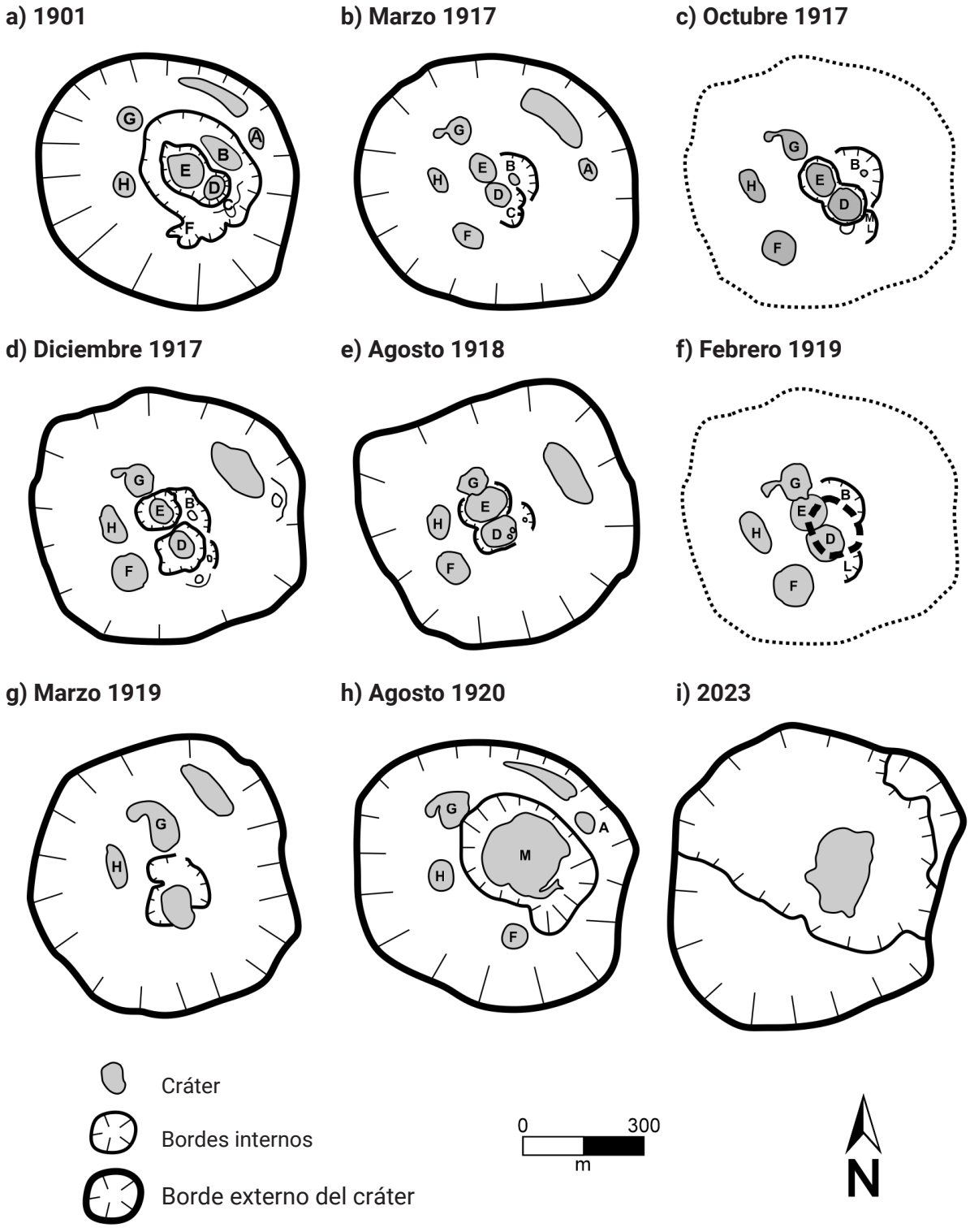

Figura 8. Evolución de los cráteres en el volcán Irazú entre 1901 y 1920. Las fuentes de los esquemas son: a) Sapper (1901), b) Fernández (1920), c) Tristán & Fernández (1917), la línea punteada indica el borde externo del cráter como referencia; d) Tristán (1917); e) Tristán (1918); f) Tristán (1919), la línea discontinua indica el lugar del nuevo cráter formado luego de la actividad eruptiva ocurrida entre agosto y octubre de 1918, la línea punteada indica el borde externo del cráter como referencia; g) Tristán (1919); h) Fernández (1920). i) Esquema basado en una imagen de *Google Earth* CNES/Airbus, Maxar Technologies del 17 de abril de 2023.

5. Impactos de la fase eruptiva de 1917-1921 del volcán Irazú

5.1 En la producción agropecuaria

La producción agropecuaria fue impactada desde la primera erupción en diciembre de 1917: "Los potreros de esa localidad [Tierra Blanca] están cubiertos de una espesa capa de ceniza y escorias volcánicas, a tal extremo que el ganado no puede comer y está seriamente amenazado" (La Información, 1917i). Muy pronto se hizo necesario llevar el ganado a un lugar seguro: "El señor Sánchez ha dispuesto trasladar inmediatamente su ganado a otros potreros pues está seguro de que si no lo hace el frío y la ceniza lo van a matar" (La Información, 1917i). Otra noticia indica: "…antes que perecieren de hambre, debido a que las cenizas exhaladas por el coloso, se amontonan en los potreros y aniquilan por completo los pastos" (El Renacimiento, 1918a). En algunos fue necesario incluso trasladar el ganado a fincas lejanas, hacia el sur y sureste del volcán, hasta unos 50 km:

"En previsión de males mayores y para salvar sus ganados en caso apurado, algunos finqueros forman fincas en la región alta de Navarro, la Estrella, Muñeco y Palo Seco, parajes de clima frío; esta región es la comprendida en el Cerro de la Muerte y Cartago; son la mayoría de esos terrenos muy accidentados, aunque la naturaleza allí es exuberante" (La Información, 1918e).

La necesidad de traslado del ganado prevaleció durante 1919: "Numerosos finqueros se han visto en la necesidad de trasladar los animales a pastizales más distantes donde no cayere ceniza" (El Renacimiento, 1919i). Otra complicación fue la disminución de la mano de obra en las fincas por temor a las erupciones: "… han abandonado las fincas muchos peones contándose ya en ellas, la falta de brazos para las faenas agrícolas" (La Información, 1918g). Al impactarse las fincas y el ganado, la producción de leche y sus derivados también se afectó:

"Muchas familias que se proveen diariamente de leche traída por expendedores del lado Este de la capital, han notado en ella un sabor amargo y bastante desagradable. Tratándose de inquirir el motivo de ese sabor tan detestable, los expendedores explican que él se debe a las cenizas volcánicas que las vacas ingieren al pastar en los potreros que recibieron con alguna abundancia en días pasados las escorias del Irazú" (La Acción Social, 1918a).

Lo anterior coincide con el aumento del 100% en el precio del queso durante el segundo cuatrimestre de 1918 (Barrantes *et al.*, 2011). Al respecto el periódico La Verdad publicó que dicho aumento se debía al uso de la leche para elaborar queso de exportación, motivados por los buenos precios del producto en el extranjero (La Verdad, 1918a). Sin embargo, la actividad volcánica pudo influir, al menos en parte, en el faltante de leche y queso y, consecuentemente, en la volatilidad de los precios de esos productos:

"En las fincas donde llueve cenizas volcánicas, nótase [sic] al instante, en la producción de leche, los efectos perjudiciales; por ejemplo, en la finca del señor Gutiérrez, se hacen de ordinario hasta tres quintales de queso, cuando cae cenizas, esa producción baja al instante a un quintal y medio, cuando mucho. En igual cantidad exactamente, y por la misma circunstancia, queda reducida en aquella y todas las fincas de la misma región, la producción de leche". También se comenta que "…el problema de las subsistencias en San José, desde que los pobladores de esta ciudad son principalmente abastecidos de leche y quesos procedentes de aquellas fincas" (La Información, 1918e).

La época lluviosa en 1919 dio una tregua a los productores de leche (La Información, 1919b). En mayo de ese año el precio bajó a 25 céntimos y se atribuía a las lluvias que lavaban las cenizas (La Información, 1919g). Pese a ello, también había especulación, por cuanto algunos lecheros la continuaban vendiendo a 30 céntimos (La Información, 1919g).

También el ganado enfermaba y moría por la ingesta de la ceniza que cubría el pasto: "La intoxicación del ganado al comer la yerba cubierta de ceniza era terrible y estaba causando grandes perjuicios y como consecuencia de ello, el ganado moría rápidamente" (La Información, 1919c). En una finca ubicada en Coronado se informó que: "han muerto en esa finca más de cuarenta reses intoxicadas por las sustancias que contiene la ceniza volcánica" (La Información, 1919c). Otra noticia advertía:

"Sabemos de lecherías que se han visto reducidas a un 40 por ciento de su producción corriente, y de finqueros que cuentan por docenas sus pérdidas de ganado, entre grandes y pequeños"... "Las vacas lecheras son las que más sufren esas entoxicaciones [sic], porque su secreción láctea se reduce notablemente, amén de la pérdida paulatina en carnes, quedando--las más contaminadas--en estado cadavérico, siendo imposible en la mayoría de las veces, salvarlas de la muerte" ... "…que la industria lechera cuente hoy con tan implacable enemigo, que seguirá produciendo sin duda alguna, alza justificada en el precio de la leche, y perjuicios incalculables al ganado lechero" (La Verdad, 1919d).

También la actividad agrícola se vio impactada por la actividad del Irazú, por ejemplo los cultivos de papa y cebolla. José Fidel Tristán reportó que: "Las fincas situadas al oeste del cráter y a una distancia de varios kilómetros están sufriendo mucho con la constante caída de ceniza que destruye los pastos y sembrados" (La Verdad, 1918c). Otras fincas al noroeste de

Cartago fueron afectadas: "...principalmente los sembrados de ceboyas [sic], frijoles y papas. Todo un plantío de papas, que tenía yo en aquellas regiones, se dañó grandemente, debido a que en ese lugar, fue mucha la ceniza que cayó. Las hojas de las ceboyas [sic] se han secado por completo" (La Acción Social, 1918b). En otra noticia se comenta que: "…en una plantación de papas hacia la parte noroeste del volcán, tanto se ha acumulado la ceniza, que bien pude tener esa capa un pie de espesor" (La Información, 1919a). También se comenta sobre las pérdidas en los cultivos de trigo: "Pero resulta que en esta época, en que mayor cantidad de ceniza ha estado cayendo en todos aquellos lugares, tanto el trigo como otros cultivos que allí posee, se han perdido casi por completo debido a la acción de esas escorias volcánicas, que tanto perjuicio están causando a todos los agricultores y propietarios de fincas ganaderas" (La Información, 1919a). Resulta también significativo el efecto que la ceniza generó en las milpas, lo que podría haber dejado un portillo abierto para la acción de plagas:

"…vemos este año que gran parte de las matas del maíz cultivado se han desarrollado de modo conveniente, y sin embargo dentro del zurrón formado por las tusas que han de envolver la mazorca, no se ha cuajado el producto; y, en muchas, ni aun el olote en que han de salir pegados los granos… para que se piensen otras causas, a las cuales se pueda atribuir la plaga" (El Renacimiento, 1919h).

Ante la perspectiva de que la actividad volcánica no terminara, los agricultores, algunos calificados como pobres por la noticia, se vieron en la incertidumbre de volver a sembrar, lo que pudo aumentar el problema del abasto de alimentos agrícolas: "Ahora se encuentran ellos privados de la siembra temerosos de regar la semilla, por cuanto que con una sola erupción no más todo queda perdido, tal es la acción de la ceniza. No encuentran qué camino tomar" (El Renacimiento, 1919b). La papa blanca tuvo fluctuaciones de precios entre 1905 y 1925 posiblemente por el impacto climático y de las plagas (Barrantes *et al.*, 2011). La actividad del Irazú podría sumarse como otra causa de dicha fluctuación. Los precios más altos se alcanzaron en 1916, 1918 y septiembre de 1919, cuando el saco de ocho cajuelas llegó a costar 25 colones (Barrantes *et al.*, 2011). Al menudeo, el cuartillo de papas costaba 0,50 colones en enero de 1918, y para junio de ese año había aumentado a 0,75 colones (Barrantes *et al.*, 2011). Aunque la actividad del Irazú no se contempla como la causa directa de las fluctuaciones en la producción y los precios de los productos agrícolas como la papa, es claro que podría haber jugado un papel importante, como se desprende de la siguiente noticia:

"Un agricultor cartaginés, persona seria y de respeto, dice refiriéndose a los perjuicios que reciben los finqueros de la región norte de la ciudad de Cartago a propósito de las constantes erupciones de cenizas del Irazú: Esos daños son mucho mayores de lo que la mayoría de las gentes sospechan; ascienden esos perjuicios a millones, con la ruina casi total de numerosos agricultores" (La Información, 1918e).

En 1919, prevalecía la preocupación por la producción de papa: "La inutilización de los terrenos que se encuentran situados en las faldas del volcán Irazú, ha hecho que los propietarios abandonen toda clase de sembrados que allí tenían. Las tierras de estas regiones eran fertilísimas y especialmente las papas se daban con una frondosidad digna de admirarse" (El Renacimiento, 1919f). Al cabo de dos años de actividad eruptiva, la angustia por los efectos adversos de la ceniza en la actividad agropecuaria y agrícola era palpable: "La constante actividad de nuestro 'coloso', que, dicho sea de paso, lleva ya cerca de dos años de interminable 'humarera', tiene convertidos a los mejores sitios de ganado lechero, situados en la cadena del Este, en campos de desolación y ruina" (La Verdad, 1919d).

5.2 En la salud

Sobre las consecuencias en la salud se tienen pocas noticias y las que existen se relacionan con malestar e irritación en los ojos en San José: "Ayer durante el día fue muy perceptible la caída de ceniza volcánica en esta capital. Causaba gran escozor en los ojos de los transeúntes" (La Verdad, 1918b); o en Puntarenas: "Los ojos en los hermosos rostros de las bellas sí fueron los verdaderamente perjudicados con el escozor que les produjo la caída en ellos de aquella sustancia volcánica" (El Heraldo, 1918).

5.3 Los lahares de 1919 en el río Reventado

Los lahares en el Irazú son originados por lluvias intensas durante o después de períodos eruptivos intensos, que arrastran gran cantidad de lodo, arenas y rocas métricas, en particular hacia el sector sur del volcán, que son las áreas más vulnerables (Soto & Sjöbohm, 2015).

Los lahares a lo largo del río Reventado suelen ser concomitantes con los periodos eruptivos del volcán Irazú durante la época lluviosa que tiene lugar entre mayo y noviembre en la vertiente del Pacífico (Manso *et al.*, 2005). Entre los que se han reportado resaltan aquellos que ocurrieron en 1724 (Peraldo, 1996) y 1963 (ICE, 1965). Para la fase eruptiva de 1917-1921, una descripción de un periodista mexicano refiere que las lavas invadieron los pueblos cercanos, sin embargo, esto ha sido interpretado como lahares (Peraldo & Mora, 2008).

En este trabajo se extrajo de las fuentes hemerográficas alguna información, a veces ambigua, respecto a la generación de lahares en el río Reventado (Figura 1c), por ejemplo: "También en Car-

tago el río Reventado está aumentando de manera extraordinaria su caudal de aguas. Los vecinos temen que, como 29 años ha, se desborde e inunde algunas casas" (La Verdad, 1919a). Se puede resaltar en este texto la referencia a las inundaciones de 1891.

En otra noticia se asocia la acumulación de material volcánico con las crecidas: "…han cesado las grandes crecientes del Río Reventado, que se atribuían a la acumulación de escorias que se encontraban haciendo presa en las faldas del volcán, que es donde nace este río. Ha llovido fuerte y el vecindario de San Nicolás, dichosamente, no se ha vuelto a ver amenazado por dicho río" (El Renacimiento, 1919g). Asimismo, otra noticia describe lo que podría ser el arrastre de ceniza acumulada durante las crecidas: "Es tan grande la cantidad de arena que ha arrastrado, que formó un inmenso montón hacia el puente" (El Renacimiento, 1919c). Esta descripción hace referencia al puente en el barrio de San Nicolás de Tolentino. El Barrio de San Nicolás (Figura 1c), es donde se ubica el actual dique noroeste dentro de la ciudad de Cartago y es interesante una propuesta para contener la corriente de agua dentro del cauce: "Para evitar cualquier daño, lo que cabe hacer en este caso, es una especie de cortina a la orilla del río, en una distancia bastante grande, a fin de que las aguas no se desborden e inunden las casas de aquel barrio" (La Información, 1919h). Otras noticias refuerzan la tesis de que lahares bajaron por el río y afectaron las áreas circunvecinas (Tabla 4).

6. Convergencia de los acontecimientos políticos y la fase eruptiva del volcán Irazú de 1917 a 1921

El 27 de enero de 1917, Federico Tinoco Granados y su hermano José Joaquín Tinoco Granados propinaron un golpe de Estado que derrocó al presidente Alfredo González Flores (Figura 9). Poco tiempo después Federico Tinoco se erigió como presidente constitucional con amplio apoyo popular, que pronto disminuyó, entre otras causas, por una pésima administración de las finanzas públicas que afectaba a los sectores populares y, sobre todo, por instaurar un cuerpo policial represivo y cruel, compuesto por esbirros leales a la dictadura y de restringir la libertad de expresión a todo nivel (Fernández Morales, 2010). En julio de 1917 se cerró el periódico *El Imparcial* y en agosto se reforzó la represión con la entrada en vigencia de la "Ley del Candado" (Fernández Morales, 2010). Las palabras de Eduardo Oconitrillo resumen el sentimiento de muchas personas de la época: "Decían que los Tinoco habían adoptado como lema de buen gobierno: Para los amigos: plata. Para los enemigos: plomo, y para los indiferentes: palo. Porque eran tiempos en que se repartía plata, plomo y palo" (Oconitrillo, 1985).

Mientras la dictadura de "los Tinoco" seguía su curso, a partir del 4 de octubre de 1917 el volcán Irazú también irrumpiría en la vida de la población costarricense, especialmente la del Valle Central (La Información, 1917a) (Figura 9). Esto lo aprovechó el periódico *El Lábaro*, crítico del régimen de los Tinoco, que contribuyó a crear una atmósfera de "mala suerte":

"El volcán Irazú está en actividad. Son síntomas de mal agüero. Siempre ha existido una relación sumamente directa entre los volcanes terrestres y los sociales. Cuando hizo erupción el Pichincha, fusilaron a

Tabla 4. Síntesis de los reportes sobre lahares durante la fase eruptiva del Irazú de 1919 a 1921.

Día	Daños	Comentarios y referencias
10 de mayo de 1919	No hay información.	En la noche hubo una creciente por fuertes lluvia. Se escuchó un ruido atronador por el arrastre de rocas de gran tamaño y troncos. Sin embargo no salió de su cauce (1).
14 de mayo de 1919	7 viviendas (2). Estas casas parece que estaban ubicadas en la parte norte de ese barrio [San Nicolás]; casas fueron inundadas sin pérdidas apreciables (3). Lavado de terrenos cultivados (4). Pérdidas en cultivos de papa y maíz; animales de corral ahogados (4, 5). Pérdida de muebles, ropa y otros (5). Puentes dañados, uno de ellos ya estaba en malas condiciones (6).	Otra crecida que se desbordó inundando parte del barrio de San Nicolás. La corriente arrastraba piedras enormes (2). Se dice que en otros lugares a lo largo del cauce dado lo plano del terreno la inundación se ha extendido hasta 100 metros. Una noticia refiere que las cuadrillas del ferrocarril, se han llegado "…donde se encuentra el desbordamiento del río por el lado de la línea…"; no se indica el nombre del río pero se infiere que es el Reventado, que causa problemas en la línea férrea (7) (Figura 1c).
24 de mayo de 1919	No hay información.	Se escuchó ruido de la creciente, sin que se saliera del cauce (8).
16 de octubre de 1919	Inundó el barrio San Nicolás (9) (Figura 1c).	Nuevamente pánico entre los vecinos. Se sugiere ensanchar el cauce. No fue grave (10).

Fuentes: (1) La Información (1919d); (2) La Información (1919e); (3) El Renacimiento (1919c); (4) La Información (1919f); (5) La Verdad (1919b); (6) El Renacimiento (1919e); (7) El Renacimiento (1919d); (8) La Información (1919h); (9) La Prensa (1919); (10) Diario de Costa Rica (1919).

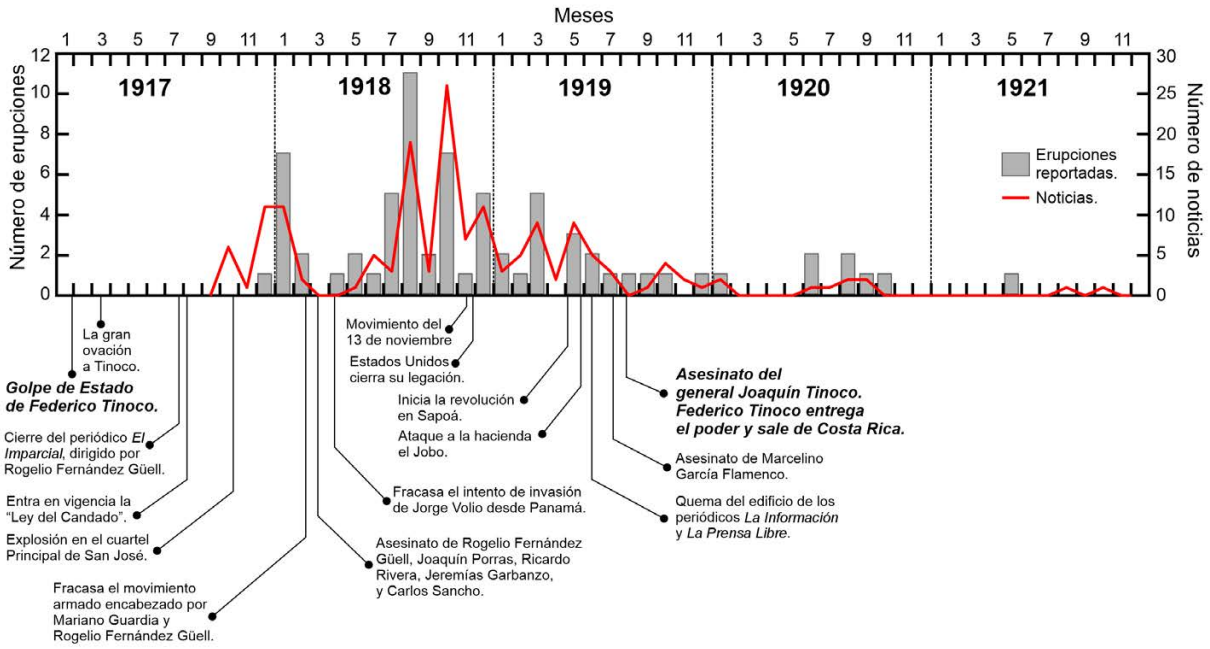

Figura 9. Convergencia de los acontecimientos políticos y la fase eruptiva del volcán Irazú de 1917 a 1921, dada en el número de erupciones reportadas y la cantidad de noticias aparecidas en los periódicos.

los Alfaro, cuando rugió el Momotombo dieron los despachos a Zelaya; cuando el Izalco se alborotó mandaron a los Ezetas a cenar a ultratumba; cuando se embarcaba don Porfirio al ostracismo, el Popocatepelt parecía un Vesubio… y así sucesivamente. ¡Y que no ruja en la Yankilandia ningún volcán para que haga temblar al Tío Sam!" (El Lábaro, 1919).

El 23 de octubre de 1917, explotó una parte del Cuartel Principal (La Información, 1917d), ubicado en lo que fue la Penitenciaría Central y actual Museo de los Niños y aunque se daba por un hecho que había sido accidental, el gobierno no tardó en atribuirlo a sus enemigos políticos (Fernández Morales, 2010). Casi dos meses después, el 17 de diciembre de 1917 por la noche, el Irazú hizo su primera erupción y ensombreció aún más el ambiente que ya estaba enrarecido por los sucesos políticos y sociales: "EL COLOSO DESPIERTO: Nuestro viejo coloso, el Volcán Irazú, que parecía dormido y que no daba más trazas de vida que las solfataras y alguna boca secundaria humeante en las pendientes del lado noreste, parece haber despertado ahora de su sueño ancestral" (La Información, 1917f).

De modo que, volvió a llover ceniza en San José, después de la vertida por el Turrialba en 1864-1866 (Soto, 2012): "También en esta capital [San José] ha habido algunas manifestaciones de la lluvia de cenizas. En la parte Sur de la ciudad notaron las personas que dejaron tendida ropa algunas pequeñas cantidades de cenizas que dejan una mancha bien perceptible" (La Información, 1917g). Este nuevo fenómeno despertó la curiosidad en la población: "Había muchas personas que observaban el volcán desde que apareció la primera luz del día y que daban cuenta hasta del número de erupciones que había hecho y que ellos habían tenido la paciencia de contar" (La Información, 1917j). La profesora Ester de Tristán describió la actividad eruptiva desde la azotea del Colegio Superior de Señoritas:

"… las alumnas que frecuentaban el Colegio en aquella época, vieron con frecuencia grandes erupciones, a veces blancas, formadas por vapor de agua condensado; a veces oscuras y negras por la gran cantidad de lodo gris---llamado ceniza--- que arrastraban en su salida por la chimenea. Espectáculo verdaderamente imponente fue ver desde aquí las sucesivas erupciones, cuando la luz de la mañana apenas principiaba a alumbrar la cumbre del volcán" (Tristán, 1929).

El mismo José Fidel Tristán, desde su prisma científico, también describió el espectáculo:

"Imponente aspecto del Volcán IRAZU [sic] al amanecer el día 18 de Enero de 1918. A las 5 y 10 minutos de la mañana el cielo un bello color rosado y la gran columna se veía casi completamente negra. A las 5 y 30 el cielo se puso rojo y la elevada columna de un color negro se elevaba magestuosa [sic] produciendo un extraordinario contraste. El fenómeno más hermoso que he visto. Todavía a las 6 de la mañana tenía el cielo un tinte rosado muy hermoso" (Expediente sobre actividad del volcán Irazú, 1918).

La actividad eruptiva del volcán Irazú extrañó a los habitantes de la época y, ya sea por lo prolongado del periodo de calma del volcán (casi dos siglos, y cuando la ciudad capital aún no existía), olvido o poco o ningún conocimiento de la historia, lo interesante es que no se tenía recuerdo de una erupción anterior similar: "No registra la historia erupciones más potentes y más continuas que las de esta época. Siempre se le tuvo por volcán muerto y próximo a no ocupar lugar en la geografía. Pero ya estamos presenciando potentes erupciones que mueven a cuidado; ruidos sordos interiores que se acentúan más durante las noches y más que todo, lluvias casi constantes de ceniza" (El Renacimiento, 1918f).

La dictadura y la actividad del Irazú transcurrieron en paralelo, aunque no necesariamente imbricados. Lo que hacía el volcán no parecía preocupar a "los Tinoco", quienes estaban más ocupados en mantenerse en el poder y, sobre todo, lograr el reconocimiento del presidente de Estados Unidos, Woodrow Wilson, quien no simpatizada con la dictadura, y de hecho, nunca lo reconoció (Oconitrillo, 1982). El único vínculo entre la erupción del Irazú y el gobierno, se halló en los telegramas que contenían los reportes de la actividad volcánica y que fueron enviados por las autoridades de distintas jurisdicciones del país por orden directa del presidente de la República, ante la solicitud de José Fidel Tristán. Sin embargo, Tristán comentó que el resultado no fue el esperado, ya que algunos se extraviaron y sobre todo "Muy poco interés tomaron en estos asuntos las personas que pudieron haber hecho algo. San José 31 de diciembre de 1918" (Expediente sobre actividad del volcán Irazú, 1918). Por esta razón la documentación del impacto por caída de ceniza es escaso, lo que limita el análisis volcanológico. Las noticias no evidencian alguna preocupación del gobierno por la actividad volcánica y sobre todo su impacto. Por el contrario, en varios comentarios periodísticos se hacía explícito cómo los acontecimientos políticos, sociales y económicos del país eran más importantes que las erupciones del Irazú. En 1918, durante el apogeo de la actividad volcánica se escribió en un rotativo:

"Por un lado el "escándalo" de la inesperada y enorme baja de los cambios; por otro, el "bombazo" terrible de don Julio [Julio Sánchez], el de Heredia, fijando el precio del café a un tipo inconcebible, lo que no ha dejado de producir conmoción general; luego, los "noticiones" de Europa; la polémica establecida entre los gruñones apóstoles de la enseñanza para probar quién ha servido mejor a la juventud estudiosa y ha enseñado más, resultando que ninguno ha hecho bien su tarea; los proyectos económicos de don Enrique el de Hacienda, encaminados a establecer nuevas contribuciones no obstante las muchas que ya nos ahogan; los rumores políticos que no faltan, a cual más alarmista; las picardías de ciertos comerciantes que aprovechando la situación explotan criminal y alevosamente al sufrido pueblo; el dengue; las fechorías de la plaga de rateros y ladrones que invaden esta capital; los escándalos del juego y de la prostitución; y mil pestes, desgracias y molestias más que desde hace tiempo traen a los josefinos a tan mal traer, nos hacen olvidar la actividad del formidable coloso del Este, el Irazú que al decir de las gentes que han visitado últimamente sus cráteres, ha entrado en tranquilidad casi absoluta. Buena noticia...? No tal; porque, cuando el León duerme..." (La Información, 1918l).

De manera explícita, el siguiente texto también refiere cómo los acontecimientos políticos ensombrecían la actividad volcánica, aun cuando esta ya venía en descenso en 1919:

"Los acontecimientos políticos últimos, que mantienen la atención del público en todas sus manifestaciones, no han permitido que se observen las grandes erupciones que desde hace más de cinco días está haciendo el Irazú. En la mañana de ayer el volcán amaneció completamente despejado y de su cráter salía una gruesa columna de humo negro que en forma de espirales le daba un aspecto muy hermoso. Durante toda la mañana pudieron admirarse estas grandes erupciones, que posiblemente ocasionaron en los contornos del cráter lluvias de cenizas" (La Verdad, 1919c).

Incluso, de vez en cuando, se publicaba algún texto peculiar, que convertía al Irazú en personaje de chistes o de sátiras poéticas: "Mr. Sittenfeld, Presidente de la Comisión de Fiestas, ha entrado en arreglos con el volcán Irazú para la iluminación del Parque de Morazán del día 1° de Enero. Desde que se instaló la Comisión de Fiestas los dos colosos, el Irazú y Mr. Sittenfeld, están dando muestras de la mayor actividad" (Crispín, 1918). O bien, esta otra graciosa gacetilla mordaz contra la policía:

"El paisaje es gracioso y atractivo / cuando el volcán está en actividad, / y es lo que no concibo / que el "monstruo enorme" sea más "activo" / que el "cuerpo policial" de esta ciudad. / La vista es atrayente en grado sumo, / desde aquí bien se ve, / y sin embargo yo, en verdad, presumo que / humeante el "Irazú" / echa menos humo que algunos "dandys" que hay en San José" (El Duende Rojo, 1918).

Durante un lapso de baja actividad eruptiva, entre febrero y abril de 1918, se gestaron los primeros movimientos armados en contra de "los Tinoco", encabezados por Rogelio Fernández Güell, pero él y otros líderes serían brutalmente asesinados en marzo de ese año (Oconitrillo, 1982). El 27 de noviembre de 1918 Estados Unidos cerró su legación en San José (Oconitrillo, 1982) y el 30 de noviembre ocurrió la erupción de mayor magnitud de la fase eruptiva (Tristán & Fernández, 1921). Luego de este evento, la actividad se mantuvo intensa hasta agosto de 1919. En junio de ese año, una gran manifestación contra el régimen, impulsada principalmente por estudiantes, culminó con el incendio al edificio de los periódicos progobiernistas *La Información*

y *La Prensa Libre*, lo que sería un importante catalizador a la salida de "los Tinoco" del poder (Bonilla Castro, 2008), pero también dejaría un importante vacío de información sobre la actividad del Irazú (Figura 9). Finalmente, el 9 de agosto de 1919 el General José Joaquín Tinoco fue asesinado y al día siguiente Federico Tinoco, familia y amigos cercanos abandonaron Costa Rica (Oconitrillo, 1982).

7. Discusión

Con la información disponible y la reconstrucción histórica efectuada, se pueden definir las siguientes etapas de la fase eruptiva del Irazú entre 1917 y 1921 (Figura 10):

- **Etapa 1. Intranquilidad y despertar (antes del 16 de diciembre de 1917):** Se observaron cambios en áreas que casi una década antes no presentaban actividad, principalmente fumarolas en los cráteres viejos D, E, F, G, H (más profusamente en G). Esto se vio, fortuitamente, a finales de setiembre de 1917. No se sabe cuándo inició el despertar real.
- **Etapa 2. Freática a freatomagmática posiblemente vulcanianas menores (17 de diciembre de 1917 a julio de 1918):** Tristán (1917) explicó que la erupción del 17 de diciembre se habría originado por un taponamiento del cráter G, primero por derrumbes que pudieron ocurrir a finales de octubre (lo que produjo su ensanchamiento), seguido de la formación de una "masa pastosa" producto de distintas reacciones químicas con el material del cráter por acción del agua caliente, vapor de agua y gases sulfurosos. Según Tristán (1917), este taponamiento obstruyó la salida de los gases y condujo a una explosión violenta en la que los materiales más pesados salieron inclinados hacia el lado norte, en tanto que otros materiales salieron en línea recta por la pared sur. Lo

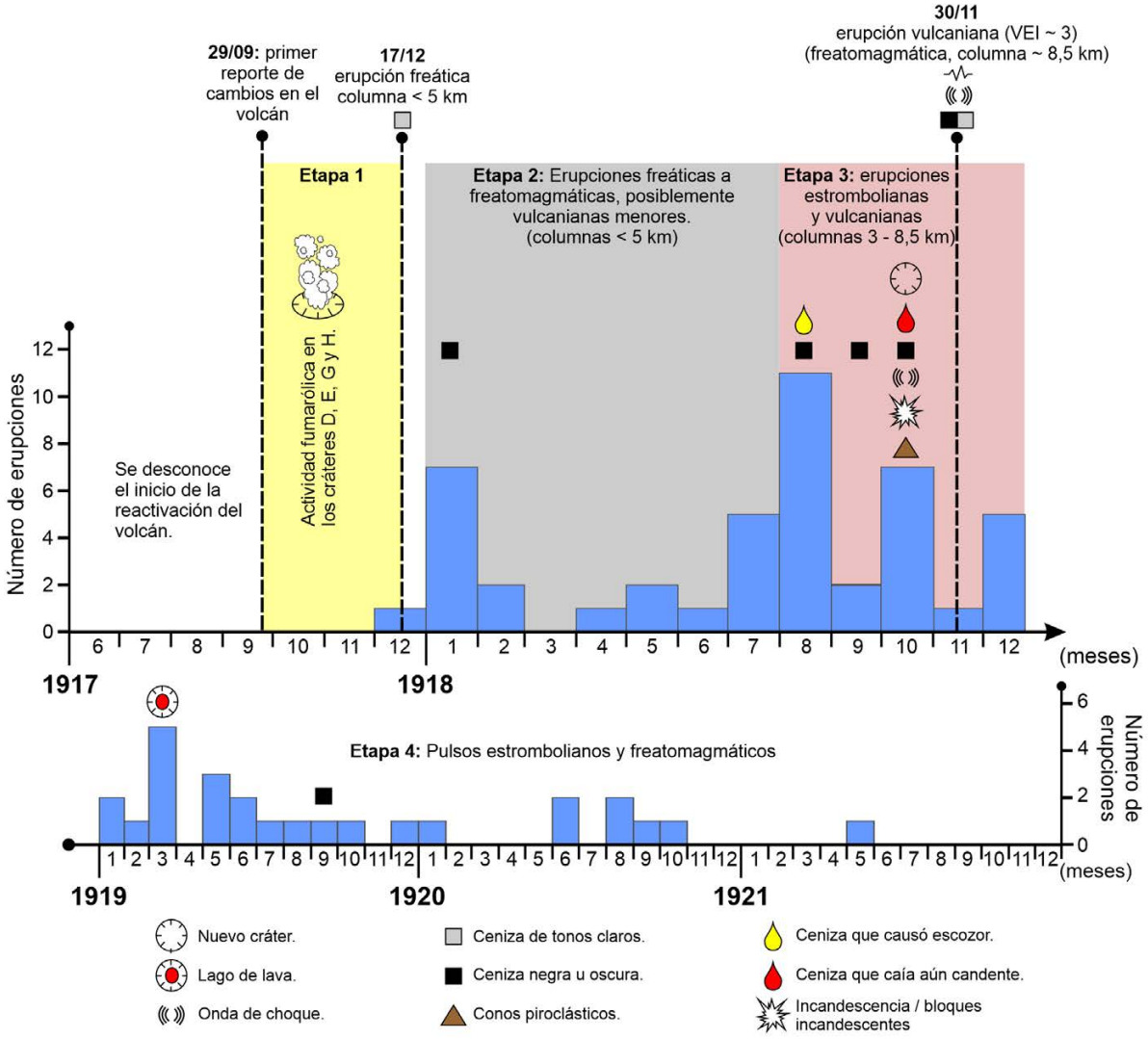

Figura 10. Esquema de la evolución de la fase eruptiva del volcán Irazú de 1917 a 1921 y principales reportes.

expuesto por Tristán describe un mecanismo freático para el origen de la primera erupción ocurrida el 17 de diciembre de 1917, congruente con cenizas emitidas gris claro que sugiere el predominio de componentes no juveniles. Esta explosión fue dirigida, por la proyección de balísticos hacia el noroeste. También pudo ocurrir una corriente piroclástica de densidad húmeda hacia el suroeste, con generación de lapilli acrecional ("pelotas de barro"). Progresivamente, las erupciones se tornaron más energéticas y la ceniza poco a poco alcanzó lugares más remotos. Ocasionalmente, se reportaron "velos de ceniza" amarillentos y, más frecuentemente, columnas negras y densas de ceniza o escorias, lo que sugiere actividad entre freática, freatomagmática y vulcaniana.

- **Etapa 3. Actividad estromboliana y vulcaniana (agosto a diciembre de 1918):** Desde agosto se incrementó la actividad y en octubre se reportaba ceniza de tamaño arena, incluso posiblemente lapilli, a distancias de hasta unos 30 km. Pero, más importante aún, se indicaba que esa ceniza caía "todavía ardiendo". También se reportó incandescencia en el cráter, en ocasiones "como chispas", esto aunado al carácter repetitivo de las explosiones (entre 2 o 3 minutos). Adicionalmente, se describe lo que podría ser la formación de anillos de tobas o conos piroclásticos bajos, lo cual también fue observado durante la fase de 1963-1965 (Alvarado *et al.*, 2021). Esto refleja un mecanismo eruptivo típicamente estromboliano a freatomagmático. Para ese momento el sistema volcánico ya habría estado abierto y, posiblemente la columna de magma se encontró, a pocos metros de la superficie, con agua subterránea y superficial intermitentes. Entre finales de octubre y todo el mes de noviembre la actividad disminuyó y luego de este impasse, el 30 de noviembre de 1918 ocurrió la erupción más explosiva de toda la fase eruptiva. La columna habría tenido dos fases, una de material grueso que alcanzó unos 18 km hacia el oeste y unos 11 km hacia el sureste, así como otro menos grueso que alcanzó hasta unos 60 km hacia el oeste-noroeste. Las fases más finas llegaron hasta el golfo de Nicoya, hasta unos 110 km hacia el oeste. Esto implica que la altura de la columna eruptiva tendría que oscilar entre los 5 y los 8,5 km sobre el nivel del cráter, teniendo como referencia las proyecciones y simulaciones numéricas (Soto & Sjöbohm, 2015). La explosión generó una onda de choque que se percibió claramente hasta unos 15 km de distancia pero que pudo incluso escucharse más lejos, correspondiente con una explosión vulcaniana importante. La ceniza habría tenido componentes de color oscuro pero también de tonos claros, incluso rojizos, lo que refleja que habría un componente juvenil dominante, pero también un componente no juvenil en proporción apreciable, o bien con un grado de oxidación sineruptivo, posiblemente durante dos fases de la erupción. Muy posiblemente el mecanismo explosivo pudo haber sido vulcaniano-freatomagmático con VEI~3, que habría abierto finalmente el nuevo cráter M. Luego de esa erupción la actividad se mantuvo relativamente alta hasta enero de 1919, aunque tal parece que no con la misma intensidad que en 1918.
- **Etapa 4. Pulsos estrombolianos-freatomagmáticos (enero de 1919 hasta 1921):** Los informes se tornaron más escasos y escuetos, lo que denota que la actividad había dejado de ser preponderante para la prensa y la población, aunque hubo reportes de interés en febrero y marzo de 1919. De las descripciones realizadas durante las excursiones científicas se constata que la actividad había disminuido y se caracterizaba por emisiones de ceniza de duración variable con ocasionales explosiones, que en conjunto, podrían corresponder con un mecanismo dominantemente estromboliano menor con pulsos freatomagmáticos. Durante esta etapa se observó un laguito de lava en marzo de 1919.

Hasta la fecha solo se conocen dos niveles delgados de depósitos de tefra ubicados entre los correspondientes a las erupciones de 1723-1726 y 1963-1965, que son atribuidos a las erupciones de 1917-1921 y 1939-1940 (Alvarado, 1993; Soto & Sjöbohm, 2015) (Figura 2). Estos depósitos están conformados por corrientes piroclásticas de densidad diluidas y húmedas, así como piroclastos de caída con colores amarillentos a rojizos pálidos desde 0,5 hasta 4 cm de espesor, separados por discordancias erosivas locales (Alvarado *et al.*, 2021). Las erupciones de 1917-1921 se han interpretado como de un inicio freático, predominantemente freatomagmáticas con un índice de explosividad volcánica (VEI) igual a 1-2, aunque la mayor explosión de noviembre de 1918 habría alcanzado un VEI igual a 3. Puesto que la erupción de 1939-40 parece ser menor, y no se ha estudiado con detalle, se especula que la secuencia interpretada como 1939-40 en la figura 2, podría ser principalmente del depósito de las etapas 3 y 4 de esta erupción de 1918-19.

La morfología de la cima varió sustancialmente entre 1917 y 1921. La evolución de los cráteres mantuvo una orientación noroeste-sureste coherente con una zona de falla que tendría ese rumbo y que atravesaría el macizo volcánico (Ulloa *et al.*, 2018) (Figura 2b). Esto podría haber condicionado los mecanismos explosivos de las erupciones del 17 de diciembre de 1917 y la del 30 de noviembre de 1918. La primera al dirigir los balísticos hacia el noreste desde el cráter G (Figura 8d) y la segunda, al proyectar material más grueso hacia el sureste desde el cráter M (Figura 8h).

La fase eruptiva de 1917-1921, aunque menor que otras que ha tenido el Irazú (Soto & Sjöbohm, 2015; Alvarado *et al.*, 2021), generó un impacto en las actividades agropecuarias y, quizás, en otras actividades económicas. No obstante, parece haber pasado inadvertido en la historia de Costa Rica quizás por haberse diluido

en la muy grave crisis económica que atravesaba por la Primera Guerra Mundial y el momento político convulso de la época, o por falta de información y estudio de dicha fase eruptiva, o una combinación de esos factores. La etapa más intensa de la actividad eruptiva acompañó a "los Tinoco" durante casi todo el bienio en que estuvieron en el poder y el análisis de las noticias deja ver un ápice de preocupación gubernamental por la situación generada por el volcán. La quema del edificio donde se publicaba *La Información* dejó un gran vacío informativo, y *El Renacimiento* dejó de informar sobre el Irazú casi al mismo tiempo, lo cual llama la atención, siendo un periódico regional cartaginés y del cual se esperaría mayor preocupación por las consecuencias de las erupciones. De hecho ambos rotativos aportan, casi equitativamente, el 62% de las noticias de la fase eruptiva. En lo posible se abarcó la mayor cantidad de periódicos y, aunque prevalecen algunos vacíos hemerográficos, el conjunto de noticias obtenido permitió hacer una reconstrucción coherente de la fase eruptiva de 1917-1921 del Irazú que incorpora elementos novedosos tales como: los mapas de dispersión de ceniza, descripciones con cierto grado de detalle de algunas erupciones, sobre todo de la actividad estromboliana y la erupción del 30 de noviembre de 1918, así como el impacto de la actividad en general. El presupuesto de este análisis es limitado para dirimir las razones que opacaron la actividad del Irazú entre 1919 y 1921 y se requeriría de un análisis historiográfico más profundo para ello.

Finalmente, José Fidel Tristán y Ricardo Fernández Peralta dejaron, sin duda, un legado invaluable para la vulcanología de Costa Rica. Ellos documentaron una de las fases eruptivas del Irazú que ha sido poco estudiada por la vulcanología moderna, aunque no por ello es menos importante, ya que fue el primer episodio eruptivo conocido posterior a la gran erupción del Irazú de 1723 -que no se llegó a presenciar en San José ya que no existía en ese momento-, y que solo llegó a experimentar de manera no tan intensa con las erupciones del Turrialba de 1864-66 (Soto, 2012). Su aporte es aún más notorio, en tanto no había ninguna institución de investigación que los acuerpara, financiara o proveyera de presupuesto de investigación.

8. Conclusión

La fase eruptiva de 1917 a 1921 fue considerablemente menor a otras que ha tenido el Irazú, y es normal que muchos de los depósitos hayan sido rápidamente erosionados, o bien, aún puede quedar mucho trabajo tefroestratigráfico por hacer que permita detallarlos en el área cuspidal del volcán. La información que se tiene con base en los discursos hemerográficos y científicos son coherentes con la tefroestratigrafía conocida, aunque agregan algunos elementos nuevos, tales como: la actividad estromboliana, las reconstrucciones de caídas de tefra para algunas erupciones relevantes, el detalle de la erupción más energética ocurrida el 30 de noviembre de 1918 y la evolución de la dinámica eruptiva desde la etapa de intranquilidad y despertar hasta la etapa de conducto abierto. En todo caso, esta fase eruptiva fue la más grande, y de hecho la primera que viera el Valle Central después de la de 1723, así como la más duradera, con una fase claramente magmática -estromboliana a vulcaniana a fines de 1918 y un poco a principios de 1919.

Se analizó la convergencia de este acontecimiento natural con la dictadura de "los Tinoco" entre 1917 y 1919 y cómo ambos irrumpieron abruptamente en la vida de la sociedad costarricense, sobre todo en la capital, San José. El impacto y la molestia generada en los derredores inmediatos al volcán como en el Valle Central, de El Guarco y el resto del territorio nacional fueron menores en comparación con la ulterior erupción de 1963-65, pero no despreciables, y el clima político adverso del momento habría contribuido a opacarla, lo que dificulta la valoración y cuantificación adecuada de su impacto. Por lo tanto, se requiere de una investigación orientada a cuantificar, de ser posible, las pérdidas generadas por la actividad eruptiva. Una actividad del Irazú, similar a la de 1917-1921 podría generar un impacto significativo bajo las condiciones de desarrollo y vulnerabilidad de Costa Rica en el siglo XXI, en particular por la extensión actual de la mancha urbana en el Valle Central Occidental hacia las faldas del Irazú.

9. Agradecimientos

Este trabajo es producto de los proyectos de investigación: Caracterización de los edificios volcánicos por medio de estudios de geomorfología para la gestión del riesgo volcánico en Costa Rica (113-C3-011), Auscultación de los volcanes de Costa Rica basada en la Sismología Volcánica (113-C3-722), Sismicidad histórica de Costa Rica durante el siglo XIX (830-C3-158) y del Programa de Investigación, Red Sismológica Nacional (B9911), todos de la Universidad de Costa Rica. Se agradecen los aportes y sugerencias de la revisora, Dra. Ana Lillian Martin Del Pozzo y otro revisor anónimo, que contribuyeron a la mejora del manuscrito.

9. Referencias

Alvarado, G. E. (1989). *Los volcanes de Costa Rica*, Costa Rica. Editorial de la Universidad Estatal a Distancia (UNED). 179 p.

Alvarado, G. E. (1993). *Volcanology and Petrology of Irazú Volcano*, Costa Rica [Tesis de doctorado]. Universidad Christian Albrechts. Kiel, Alemania. 289 p.

Alvarado, G. (2000). *Volcanes de Costa Rica: Geología, historia y riqueza natural.* Editorial de la Universidad Estatal a Distancia (UNED). 386 p.

Alvarado, G. E. (2021). *Costa Rica y sus volcanes*. Editorial de la Universidad de Costa Rica, Editorial de la Universidad Nacional y Editorial Tecnológica de Costa Rica. 933 pp.

Alvarado, G. E., Schmincke, H.U. (2013). The 1723 A.D. violent strombolian and phreatomagmatic eruption at Irazú volcano, Costa Rica. *Revista Geológica de América Central*, 48, 41-61. doi: **https://doi.org/10.15517/rgac.v0i48.12212**

Alvarado, G. E., Campos-Durán, D., Brenes-André, J., Alpízar, Y., Núñez, S., Esquivel, L., Sibaja, J. P., & Fallas, B. (2021). Peligros volcánicos del Irazú, Costa Rica. Unidad de Investigación y Análisis del Riesgo, *Comisión Nacional de Prevención de Riesgos y Atención de Emergencias (CNE).* 407 pp.

Barquero, J. (1976). El volcán Irazú y su actividad [Tesis de licenciatura]. Escuela de Ciencias Geográficas, Universidad Nacional. Heredia, Costa Rica.

Barrantes, E. A., Bonilla, H. M., & Ramírez, O. M. (2011). *Las subsistencias en una coyuntura de crisis: producción, consumo y nivel de vida*, Costa Rica 1905-1925. Editorial de la Universidad de Costa Rica. 520 p.

Bonilla Castro, A. (2008). Movimientos sociales y represión del Estado en la dictadura de Tinoco. 1918-1919. *Diálogos: Revista de Historia, 9*, 1512-1538. doi: **https://doi.org/10.15517/dre.v9i0.31250**

Clark, S. K., Reagan, M. K., & Trimble, D. A. (2006). Tephra deposits for the past 2600 years from Irazú volcano, Costa Rica. *The Geological Society of America. Special Paper* 412 (pp. 225-234): The Geological Society of America.

Crispín. (1918). Crónicas Alegres. Lecturas, Año 1(12), 182.

Denyer, P., Aguilar, T., & Montero, W. (2013). *Cartografía Geológica de la Península de Nicoya, Estratigrafía y Tectónica.* Editorial de la Universidad de Costa Rica. 216 p.

Diario de Costa Rica. (1919, 17 de octubre). Otras noticias alarmantes de Cartago. Diario de Costa Rica. p. 1.

El Duende Rojo. (1918). Los viajes al Irazú. *Lecturas*, 1(2), 112.

El Heraldo. (1918, 3 de diciembre). Lluvia de ceniza*. El Heraldo*. p. 1.

El Lábaro. (1917, 14 de octubre de 1917). Sección Polémica. *El Lábaro*. p. 2.

El Renacimiento. (1918a, 31 de julio). Las erupciones del Irazú. *El Renacimiento*. p. 2.

El Renacimiento. (1918b, 7 de agosto). De todo un poco. *El Renacimiento*. p. 4.

El Renacimiento. (1918c, 17 de agosto). De todo un poco. *El Renacimiento*. p. 4.

El Renacimiento. (1918d, 10 de octubre). De última hora. *El Renacimiento*. p. 3.

El Renacimiento. (1918e, 11 de octubre). De todo un poco. *El Renacimiento*. p. 1.

El Renacimiento. (1918f, 16 de octubre). Y...continúa el Irazú. *El Renacimiento*. p. 2.

El Renacimiento. (1918g, 20 de noviembre). Lo que pasa. *El Renacimiento*. p. 1.

El Renacimiento. (1918h, 30 de noviembre). El volcán Irazú y la guerra europea. *El Renacimiento*. p. 3.

El Renacimiento. (1918i, 1 de diciembre). El Irazú y la nunca imponderable erupción de ayer que fue inmensísima. *El Renacimiento*. p. 1.

El Renacimiento. (1918j, 1 de diciembre). La impresión de un suscriptor: una erupción fenomenal. *El Renacimiento*. p. 3.

El Renacimiento. (1918k, 5 de diciembre). Lo que traen las erupciones del Irazú. *El Renacimiento*. p. 3.

El Renacimiento. (1919a, 14 de febrero). La erupción de ayer en la mañana. *El Renacimiento*. p. 3.

El Renacimiento (1919b, 9 de mayo). Consecuencias de las cenizas del volcán. *El Renacimiento*. p. 2.

El Renacimiento (1919c, 16 de mayo). Parece que el Río Reventado amenaza con una gran creciente. *El Renacimiento*. p. 2.

El Renacimiento. (1919d, 17 de mayo). De todo un poco. *El Renacimiento*. p. 1.

El Renacimiento. (1919e, 17 de mayo). Continúan las crecientes del Río Reventado. *El Renacimiento*. p. 3.

El Renacimiento. (1919f, 22 de mayo). Los terrenos situados en las faltas del Irazú. *El Renacimiento*. p. 3.

El Renacimiento. (1919g, 26 de junio). Con respecto al volcán Irazú. *El Renacimiento*. p. 2b.

El Renacimiento. (1919h, 14 de noviembre). Fenómeno que desconsuela. *El Renacimiento*. p. 1.

El Renacimiento. (1919i, 16 de noviembre). Noticias. *El Renacimiento*. p. 2.

Expediente sobre actividad del volcán Irazú. (1918). [Telegramas al Presidente de la República]. Archivo Nacional de Costa Rica, Archivo Histórico, Fondo José Fidel Tristán Fernández, (CR-AN-AH-FITRIS-000020), San José Costa Rica.

Fallas, M., Prado, A., Mora, M. M., Ruiz, P., Alfaro, E. J., & Soto, G. J. (2018). El deslizamiento del 8 de diciembre de 1994 en el volcán Irazú (Costa Rica): aspectos históricos y geomorfología con base en fotografías aéreas históricas y recientes. *Revista Geológica de América Central*, 58, 55-83. doi: **https://doi.org/10.15517/rgac.v58i0.32844**

Fernández Morales, J. M. (2010). *Las presidencias del Castillo Azul*. Litografía e Imprenta Lill. 512 pp.

Fernández Peralta, R. (1920). Una visita al volcán Irazú*. Revista de Costa Rica*, 2(2), 42-47.

Fumero, P. (1996). Las diversiones públicas en Costa Rica: 1850-1950. *Temas de Nuestra América Revista de Estudios Latinoamericanos*, 12(25), 17-30. **https://www.revistas.una.ac.cr/index.php/tdna/article/view/9447**

Fumero Vargas, P. (2000). Vida cotidiana en el Valle Central: 1850-1914. Los cambios asociados con la expansión del café. En A.M., Botey Sobrado (Coord.), *Costa Rica desde las sociedades autóctonas hasta 1914* (pp. 303-338). Editorial de la Universidad de Costa Rica, Cátedra de Historia de las Instituciones.

Fumero Vargas, P. (2005). *El advenimiento de la modernidad en Costa Rica*; 1850-1914. Editorial de la Universidad de Costa Rica, Serie cuadernos de Historia de las Instituciones de Costa Rica. 64 pp.

Gazel, E., Flores. K. E., Carr, M. J. (2021). Architectural and Tectonic Control on the Segmentation of the Central American Volcanic Arc. *Annual Review of Earth and Planetary Sciences*, 49,495-521. doi: **https://doi.org/10.1146/annurev-earth-082420-055108**.

González Víquez, C., Núñez, F. M., Tinoco, L. D. (1987). *San José y sus comienzos: documentos fundamentales*. Comisión Nacional de Conmemoraciones Históricas. 60 pp.

Instituto Costarricense de Electricidad (ICE). (1965). *Informe sobre el problema del río Reventado* [Informe interno]. Instituto Costarricense de Electricidad. 126 pp.

La Acción Social. (1918a, 29 de enero). La leche y las cenizas volcánicas. *La Acción Social*. p. 3.

La Acción Social. (1918b, 6 de febrero). Perjuicio del a ceniza del Irazú. *La Acción Social*. p. 3.

La Información. (1917a, 4 de octubre). De última hora. *La Información*. p. 1.

La Información. (1917b, 5 de octubre). Las Manifestaciones de Actividad del Irazú. *La Información*. p. 5.

La Información. (1917c, 6 de octubre). Ultima hora. *La Información*. p. 1.

La Información. (1917d, 23 de octubre). La espantosa catástrofe de esta madrugada en el Cuartel Principal. p. 1.

La Información. (1917e, 4 de noviembre). El Irazú de nuevo en tranquilidad. *La Información*. p. 1.

La Información. (1917f, 18 de diciembre). El volcán Irazú en actividad. *La Información*. p. 4.

La Información. (1917g, 19 de diciembre). La actividad volcánica. *La Información*. p. 4.

La Información. (1917h, 19 de diciembre). De la noche. *La Información*. p. 4.

La Información. (1917i, 20 de diciembre). Las erupciones del Irazú pudieron verse ayer desde esta capital. *La Información*. 20 de diciembre de 1917. p. 4.

La Información. (1917j, 21 de diciembre). Los volcanes Irazú y Poás hicieron en la mañana erupciones conjuntamente. *La Información*. p. 4.

La Información. (1917k, 22 de diciembre). Llegan a la cima del Irazú los primeros excursionistas. *La Información*. p. 4.

La Información. (1918a, 2 de octubre). En la cima del Irazú. *La Información*. p. 2.

La Información. (1918b, 10 de octubre). De la noche. *La Información*. p. 5.

La Información. (1918c, 11 de octubre). Las erupciones del Irazú en estos días. *La Información*. p. 2.

La Información. (1918d, 11 de octubre). "Nota de última hora", *La Información*, 11 de octubre de 1918. p. 3.

La Información. (1918e, 12 de octubre). Las furias del Irazú y sus consecuencias sobre la agricultura. *La Información*. p. 2.

La Información. (1918f, 12 de octubre). Otros informes sobre los daños que están causando las erupciones volcánicas. *La Información*. p. 3.

La Información. (1918g, 15 de octubre). El coloso de Cartago. *La Información*. p. 4.

La Información. (1918h, 22 de octubre). Se observan durante las noches fenómenos luminosos en los cráteres del Irazú? *La Información*. p. 4.

La Información. (1918i, 22 de octubre). Visita al Irazú. *La Información*. p. 5.

La Información. (1918j, 27 de octubre). En la mañana de ayer hubo grandes erupciones en el Irazú y en el Poás. *La Información*. p. 5.

La Información. (1918k, 27 de octubre). Lo que cuentan los excursionistas que fueron al volcán Irazú. *La Información*. p. 8.

La Información. (1918l, 8 de noviembre). El Irazú. *La Información*. p. 3.

La Información. (1918m, 19 de noviembre). Los temblores de anoche. *La Información*. p. 5.

La Información. (1918n, 1 de diciembre). El "Poás" y el "Irazú" hicieron ayer formidables erupciones de cenizas y arenas. *La Información*. p. 4.

La Información. (1918o, 3 de diciembre). Los dos colosos de nuevo en reposo en los cráteres del Poás y del Irazú. *La Información*. p. 5.

La Información. (1918p, 18 de diciembre). Las erupciones del Irazú. *La Información*. p. 2.

La Información. (1919a, 6 de febrero). Lo que nos dice un agricultor de Cartago. *La Información*, 6 de febrero de 1919. p. 2.

La Información. (1919b, 25 de abril). Las lluvias y sus beneficios. *La Información*. p. 2.

La Información. (1919c, 9 de mayo). La ceniza volcánica ha causado considerables pérdidas. *La Información*. p. 2.

La Información. (1919d, 14 de mayo). El río Reventazón alarmó al vecindario de Cartago. *La Información*. p. 3.

La Información. (1919e, 17 de mayo). El río Reventazón se sale de su cauce e inunda varias casas del barrio de San Nicolás de Cartago. *La Información*. p. 2.

La Información. (1919f, 18 de mayo). Más detalles de la inundación. *La Información*. p. 4.

La Información. (1919g, 22 de mayo). El precio de la leche ha bajado. *La Información*. p. 2.

La Información. (1919h, 25 de mayo). Sigue la alarma en Cartago por las crecientes del Reventado. *La Información*. p. 5.

La Prensa. (1919, 17 de octubre). Se desbordó el Reventado. *La Prensa*. p. 4.

La Verdad. (1918a, 10 de julio). La Leche. *La Verdad*. p. 1.

La Verdad. (1918b, 8 de agosto). Noticias y comentarios. *La Verdad*. p. 1.

La Verdad. (1918c, 10 de agosto). Noticias y comentarios. *La Verdad*. p. 3.

La Verdad. (1918d, 23 de agosto). Noticias y comentarios. *La Verdad*. p. 3.

La Verdad. (1918e, 3 de octubre). Noticias y comentarios. *La Verdad*. p. 3.

La Verdad. (1918f, 11 de octubre). Noticias y comentarios. *La Verdad*. p. 1.

La Verdad. (1918g, 17 de octubre). Noticias y comentarios. *La Verdad*. p. 1.

La Verdad. (1919a, 16 de mayo). Noticias y comentarios. *La Verdad*. p. 1.

La Verdad. (1919b, 17 de mayo). Noticias y comentarios. *La Verdad*. p. 1.

La Verdad. (1919c, 6 de septiembre). El Irazú de nuevo en acción. *La Verdad*. p. 3.

La Verdad. (1919d, 11 de octubre). Lluvias de ceniza del Irazú. *La Verdad*. p. 3.

Manso, P., Stolz, W., Fallas, J.C. (2005). El régimen de precipitación en Costa Rica. *Ambientico*, 144, 7-8.

Murillo, H. (1918). *Tinoco y los Estados Unidos*. Editorial de la Universidad Estatal a Distancia. 191 pp.

Newhall, C. G., & Self, S. S. (1982). The volcanic explosivity index (VEI) an estimate of explosive magnitude for historical volcanism.

Journal of Geophysical Research: Oceans, 87(C2), 1231-1238. doi: **https://doi.org/10.1029/JC087iC02p01231**

Oconitrillo, E. (1982). *Los Tinoco* (1917-1919). Editorial Costa Rica. 254 pp.

Oconitrillo, E. (1985). *Memorias de un telegrafista*. Editorial Costa Rica. 211 pp.

Ortega, F. (1917a, 10 de octubre). [Carta a José Fidel Tristán]. Archivo Nacional de Costa Rica, Archivo Histórico, Fondo José Fidel Tristán Fernández, (CR-AN-AH-FITRIS-000019), San José, Costa Rica.

Ortega, F. (1917b, 15 de octubre). Mis impresiones recogidas en los cráteres del volcán Irazú. *La Información*. p.3.

Ortega, F. (1917c, 18 de diciembre). [Telegrama a José Fidel Tristán]. Archivo Nacional de Costa Rica, Archivo Histórico, Fondo José Fidel Tristán Fernández, (CR-AN-AH-FITRIS-000020), San José, Costa Rica.

Peraldo, G. (1996). Desastre natural y planificación urbana. *Reflexiones*, (43), 13-23.

Peraldo, G., & Mora, M. (2008). Enseñanzas de la actividad histórica de los volcanes Irazú y Turrialba, Costa Rica, América Central. En V. García (Coord.), *Historia y desastres en América Latina III* (pp. 115-162). Centro de Investigaciones y Estudios Superiores en Antropología Social/Red de Estudios Sociales en Prevención de Desastres en América Latina (La Red).

Ryan, W. B. F., Carbotte, S. M., Coplan, J. O., O'Hara, S., Melkonian, A., Arko, R., Weissel, R. A., Ferrini, V., Goodwillie, A., Nitsche, F., Bonczkowski, J., & Zemsky, R. (2009). Global Multi-Resolution Topography (GMRT) synthesis data set. *Geochemistry, Geophysics, Geosystems*, 10(3),1-9. doi: **https://doi.org/10.1029/2008GC002332**

Sapper, K. (1901). Die südlichsten Vulkane Mittel-Amerikas. *Zeitschrift der Deutschen geologischen Gesellschaft*, (53), 24-51.

Solano, F. & Díaz, R. (2009). Las revistas científicas de Costa Rica (1883-1910). En C. Lértora (ed.), *Geografía e Historia Natural: Estudio a través de Argentina*, México, Costa Rica y Paraguay (pp. 173-213). Editorial FEPAI.

Soto, G. J. (2012*). Preparación de mapas de peligros volcánicos y restricción de uso de la tierra en el volcán Turrialba* [Informe para la Comisión Nacional de Prevención de Riesgos y Atención de Emergencias]. FUNDEVI, Universidad de Costa Rica. **https://www.researchgate.net/publication/316146333_Preparacion_de_mapas_de_peligros_volcanicos_y_restriccion_de_uso_de_la_tierra_en_el_volcan_Turrialba**

Soto, G. J. &, Sjöbohm, L. (2015). *Escenarios de amenaza del volcán Irazú (Costa Rica): Una aproximación preliminar [Informe de consultoría para el Banco Interamericano de Desarrollo (BID)]*. FUNDEVI, Universidad de Costa Rica. **https://www.researchgate.net/publication/329170347_Escenarios_de_amenaza_del_volcan_Irazu_Costa_Rica_Una_aproximacion_preliminar**

Tilling, R. I. (2009). El Chichón's "surprise" eruption in 1982: Lessons for reducing volcano risk. *Geofísica Internacional*, 48(1), 3-19. doi: **https://doi.org/10.22201/igeof.00167169p.2009.48.1.96**

Tristán, E. (1929). En la azotea del Colegio de Señoritas: descripción del panorama. *Revista del Colegio Superior de Señoritas*, 1(6), 1-23.

Tristán, J. F. (1917). *Datos sobre el volcán Irazú hasta el 31 de diciembre de 1917*. Archivo Nacional de Costa Rica, Archivo Histórico, Fondo José Fidel Tristán Fernández, (CR-AN-AH-FITRIS-000030), San José, Costa Rica.

Tristán, J. F. (1918). *Excursión al Irazú. Agosto 2, 3 y 4*. Archivo Nacional de Costa Rica. Archivo Histórico, Fondo José Fidel Tristán Fernández (CR-AN-AH-FITRIS-000031), San José, Costa Rica.

Tristán, J. F. (1919). *Excursiones al Irazú, Año de 1919.* Archivo Nacional de Costa Rica, Archivo Histórico, Fondo José Fidel Tristán Fernández (CR-AN-AH-FITRIS-000037), San José, Costa Rica.

Tristán, J. F. (1920*). Excursión al volcán al Irazú*, agosto 26 y 27 de 1920. Archivo Nacional de Costa Rica, Archivo Histórico, Fondo José Fidel Tristán Fernández (CR-AN-AH-FITRIS-000032), San José, Costa Rica.

Tristán, J. F. (1923). The activity of volcano Irazú in Costa Rica. *Zeitschrif für Vulkanologie*, 7(2), 93-113.

Tristán, J. F. & Fernández, R. (1917, 4 de diciembre). Informe presentado al Sr. Ministro de Instrucción Pública sobre la actividad del volcán Irazú. *La Gaceta Diario Oficial*. p. 662-664.

Tristán, J. F., & Fernández, R (1918, 3 de noviembre). Actualidad científica. *La Información*. p. 4

Tristán, J. F., & Fernández, R. (1921). La actividad del Volcán Irazú. *Revista del Colegio Superior de Señoritas*, A(7), 1-18.

Ulloa, A., Gázquez, F., Sanz-Arranz, A., Medina, J., Rull, F., Calaforra, J. M., Alvarado, G. E., Martínez, M., Avard, G., de Moor, M., & De Waele, J. (2018). Extremely high diversity of sulfate minerals in caves of the Irazú Volcano (Costa Rica) related to crater lake and fumarolic activity. *International Journal of Speleology*, 47(2), 229-246. **https://doi.org/10.5038/1827-806X.47.2.2198**

Vargas Chaves, J. M. (1967). Belleza y Amenaza del Volcán Irazú. *Efemérides Costarricenses*, 1(3), 1-17.

Vicente, E. (1918, 16 de enero). [Carta a José Fidel Tristán]. Archivo Nacional de Costa Rica, Archivo Histórico, Fondo José Fidel Tristán Fernández, (CR-AN-AH-FITRIS-000020), San José Costa Rica.

Sección especial

Vulcanismo Monogenético, medio ambiente y sociedad

Special section

Monogenetic volcanism, environment and society

Introduction

This number includes two new publications on the issue that was first introduced in the January 2024 volume as a contribution to improve the preparation and management of the risks of future monogenetic eruptions, as well as the preservation of the associated natural and cultural heritage.

The first paper of this volume addresses the origin of the recent seismic swarms that have occurred in the Parícutin-Tancítaro area in Michoacán (Mexico) and have caused significant concern to the local population. This study supports a magmatic origin for this phenomenon, and relates it to the stalling of magma within the crust. The results of this paper have great relevance for the study of the precursors of new monogenetic eruptions and related magmatic processes.

The second paper herein included makes a significant contribution to the characterization of an important intangible heritage in Michoacán, which is the manufacture of milling stones (metates). This paper addresses the relationship of this centuries-long practice with the local volcanic landscape and associated resources, and their evolution with time. Results contribute to a better understanding of the relationship between people and their environment in an active monogenetic field.

Looking forward to unveiling more papers in the next-coming issues of ***Geofísica Internacional***, we wish you a pleasant and instructive read.

Introducción

Este volumen contiene dos nuevas publicaciones de esta sección especial que se inició en el volumen de enero de 2024 y tiene como objetivo contribuir a mejorar la preparación y gestión de riesgos de futuras erupciones monogenéticas, así como a la preservación del patrimonio natural y cultural en regiones de vulcanismo activo.

El primer artículo aborda el origen de los recientes enjambres sísmicos ocurridos en el área del Parícutin-Tancítaro en Michoacán (México) y que han causado inquietud en la población local. Este estudio apoya un origen magmático para este fenómeno y lo relaciona con el estancamiento del magma dentro de la corteza. Los resultados de este artículo tienen gran relevancia para el estudio de los precursores de erupciones monogenéticas y procesos magmáticos asociados.

El segundo artículo incluido hace un aporte significativo sobre la caracterización de un importante patrimonio intangible en Michoacán, como es la fabricación de piedras de molienda (metates). A través de un estudio multidisciplinario, este artículo aborda la relación de esta práctica centenaria con el paisaje volcánico y los recursos asociados, y su evolución en el tiempo. Los resultados contribuyen a mejorar la comprensión de la relación entre las poblaciones y su entorno en un campo monogenético activo.

Esperando revelar más artículos en los próximosnúmeros de ***Geofísica Internacional***, les deseamos una agradable e instructiva lectura.

Marie-Noëlle Guilbaud
Coordinadora de la sección especial
Doi: **https://doi.org/10.22201/igeof.2954436xe.2024.63.2.1792**

Special Section
Monogenetic volcanism, environment and society

Geofísica Internacional (2024) **63-2**: 913 - 927

The 2020 and 2021 Seismic Swarms in the Tancítaro-Paricutín Area (Uruapan-Michoacán, México) Evidence Magma Intrusion in an Area with High Density of Monogenetic Cones

Gema V. Caballero-Jiménez[1], Ma. Cristina Zarazúa-Carbajal[2], Ana Teresa Mendoza-Rosas[3] and Servando De La Cruz- Reyna[4]

Abstract

The Michoacán-Guanajuato Volcanic Field (MGVF) in central-western Mexico, with more than 1,000 monogenetic volcanoes, has been well known since 1943 when an eruption formed the Paricutín volcano, 11 km to the NW of the summit of Tancítaro stratovolcano. In the highly fractured zone around Tancítaro, referred to as the Paricutín-Tancítaro region (PTR), two major seismic swarms have been recorded, the first between January 5 and February 22, 2020, and the second between May 30 and July 22, 2021. The Mexican National Seismological Service (SSN) reported a total of 4,956 earthquakes with coda magnitudes between 2.6 and 4.2. With the aim to determine the causes of the swarms and the potential hazard they may pose on the region, we first analyze their spatial distributions by relocating all of the events using the Double Difference method and testing different 1-D velocity models to select the one with the lowest residual errors. Secondly, we analyze the temporal distributions finding that their temporal occurrence fits a Mogi's type 3 volcanic seismic swarm. We conclude that each swarm is due to stresses induced by dike-fed intrusions of moderate volumes of magma in a pre-existing temporal magma reservoir, probably a sill.

Key words: Paricutín-Tacítaro, earthquake swarm, monogenetic volcano, distributed volcanism hazards, magma intrusion.

Resumen

El Campo Volcánico Michoacán-Guanajuato (MGVF) ubicado en el centro-oeste de México y con más de 1,000 volcanes monogenéticos, en su mayoría conos de escoria, es frecuentemente citado desde 1943 cuando nació el volcán Paricutín en un maizal ubicado a 11 km al NO de la cumbre del Tancítaro, el estratovolcán más grande del campo. En una zona altamente fracturada alrededor de Tancítaro, denominada región Paricutín-Tancítaro (PTR), recientemente se han registrado dos importantes enjambres sísmicos, el primero entre el 5 de enero y el 22 de febrero de 2020, y el segundo entre el 30 de mayo y el 22 de julio de 2021. El Servicio Sismológico Nacional (SSN) de México ubicó y reportó un total de 4,956 sismos con magnitudes de coda entre 2.6 y 4.2. Con el objetivo de determinar las causas de los enjambres y los peligros que pueden representar para la región en primer lugar analizamos sus distribuciones espaciales, reubicando todos los eventos registrados con el método de Dobles Diferencias y probando diferentes modelos de velocidad para seleccionar aquel con los menores errores residuales, y en segundo lugar, analizando sus distribuciones temporales, encontrando que los histogramas de ocurrencias por fecha tiene formas aproximadas de campana, correspondientes al tipo 3 de Mogi. Concluimos que cada enjambre probablemente ha sido causado por esfuerzos inducidos por intrusiones de volúmenes moderados de magma alimentadas a través de diques hacia un depósito temporal preexistente de magma, probablemente un sill.

Palabras clave: Paricutín-Tancítaro, enjambre sísmico, volcán monogenético, riesgo del volcanismo disperso, intrusión magmática.

Received: November 28, 2023; Accepted: February 26, 2024; Published on-line: April 1, 2024.

Editorial responsibility: Dr. Roberto Carniel

* Corresponding author: Gema Victoria Caballero-Jiménez, gema.caballero.jimenez@gmail.com
[1] Centro Nacional de Prevención de Desastres (CENAPRED), Avenida Delfín Madrigal No. 665, México 04510, CDMX.
[2] Research Assistant program. SNI-CONAHCYT / Instituto de Geofísica, Universidad Nacional Autónoma de México, C. Universitaria, México 04510, CDMX.
[3] CONAHCYT - Instituto de Investigaciones en Ciencias de la Tierra, Universidad Michoacana de San Nicolás de Hidalgo, Santiago Tapia 403, 58000 Morelia, Michoacán, México.
[4] Instituto de Geofísica, Universidad Nacional Autónoma de México, C. Universitaria, México 04510, CDMX.

Gema Victoria Caballero-Jiménez, Ma. Cristina Zarazúa-Carbajal, Ana Teresa Mendoza-Rosas, Servando De La Cruz-Reyna

https://doi.org/10.22201/igeof.2954436xe.2024.63.2.1759

1. Introduction

The Trans-Mexican Volcanic Belt (TMVB) is associated with the subduction of the Cocos and Rivera plates beneath the North American plate (Figure 1). Along TMVB, calderas, stratovolcanoes, and monogenetic fields characterize the landscape. The Michoacán-Guanajuato monogenetic field (MGVF) is located in the central-western portion of the TMVB and represents one of the world's largest fields covering an area of about 40,000 km^2 and hosting more than 1,000 volcanic vents. MGVF includes 901 scoria cones, 43 domes, 13 young shield volcanoes with surmounting cones, 22 maars or tuff rings, and 61 lava flows with hidden vents (Hasenaka and Carmichael, 1985b).

Two scoria cones were formed in recent times: Jorullo (1759-1774) and Paricutín (1943-1952) (Luhr and Simkin, 1993; Becerril *et al.*, 2021). Eruptions from these cones caused significant economic damage, mostly by lava flows flooding arable lands and burying two villages (Alonso-Núñez and Marín-Tello, 2009; Rees, 1970). This type of scoria cone-forming eruptions tends to be long-lived, ejecting relatively large volumes of magma, at relatively low rates, for extended periods. For example, the Jorullo volcano eruption lasted fifteen years (Rasoazanamparany *et al.*, 2016) ejecting about 1.25 km^3 of magma (Yokoyama and De la Cruz-Reyna, 1990). Guilbaud *et al.* (2011) conclude that the Jorullo eruption is the latest of 26 monogenetic events that occurred during the past 1 Ma in a relatively small area (333 km^2) of the southern part of the MGVF, producing ca. 10 km^3 of dominantly andesitic magma. Similarly, 80 km NW of Jorullo, the Paricutín eruption ejected 1.3 km^3 of magma (Yokoyama and De la Cruz-Reyna, 1990). In both cases the eruptions were preceded by felt local seismicity having the characteristics of seismic swarms, i.e. moderate magnitude (M<5) and frequent earthquakes usually not following Omori's law (lack of a clear mainshock-aftershock behavior).

Seismic swarms may occur in different geological environments. They may be caused by tectonic processes, magma and/or fluid intrusions, or by karstic phenomena related to pore pressure variations. Hydrothermal activity and glacier instabilities may also produce a swarm-like seismicity. Several of these sources may lead to potentially hazardous outcomes of the source phenomena causing the seismicity. When a seismic swarm characterized by a significant increase in the occurrence rate of earthquakes develops in a region in which more than one of the above sources is present, a challenge is posed to identify its causes and possible consequences.

In the Paricutín area, a clear precedent is represented by the seismicity recorded 45 days before the volcano's birth, with some of the events reaching Ms 4.5 (Yokoyama and De la Cruz-Reyna, 1990). The Paricutín eruption began on 20 February 1943 and lasted for 9 years with lava flows flooding an area of about 25 km^2. Then, after 54 years of relative quietness in the region, a seismic swarm was recorded in 1997 between Tancítaro, a large (3840 m a.s.l.) currently inactive Pleistocene stratovolcano, and Paricutín located 11 km NE of the Tancítaro summit. The 1997 swarm was characterized by 230 events with duration magnitude between 1.5 and 3.5, at depths between 10 and 18 km, with at least 5 events exceeding magnitude 3.9. At that time, that swarm was attributed to the regional tectonic seismicity related to the San Juanico-Buenavista Fault (Pacheco *et al.*, 1999). Later, similar earthquake swarms were reported in 1999, 2000, and 2006, the latter with more than 730 events with duration magnitude between 2.4 and 3.7. Unlike the 1997 seismicity, these more recent swarms were associated with magma intrusions near Tancítaro (Pinzón *et al.*, 2017) and, in particular, with the emplacement of a dike in the shallow crust, at a depth around 4-5 km, that extended as a sill-like short horizontal migration (Gardine *et al.* 2011). More recently, between 5 January 2020, and 22 July 2021, the largest seismic swarms ever recorded in the region producing a maximum Md of 4.2 (Figure 2) caused considerable concern in the authorities and population. Here, we discuss and interpret the causes and possible consequences of the swarms in light of their time evolution and detailed relocation of the events using different velocity models.

2. Geology and Tectonics of the Area

Carbon 14, K–Ar ages as well as geomorphic age estimates define a late Pliocene to Holocene age for the TMVB cinder cones (Hasenaka and Carmichael, 1985 a,b). The tectonics of the area is complex and some authors suggest that the crust in the southern part of the TMVB is divided into different blocks moving independently among them and with respect to the North American plate. Those movements are evidenced through complex systems of active faults (Luhr *et al.*, 1985; Pacheco *et al.*, 1999). Some relate to alignments of monogenetic cinder cones with a N35°E strike parallel to the direction of plate convergence, while other cones align approximately N60W, roughly parallel to the Middle America Trench (MAT) (Connor, 1987; Connor, 1990; Hasenaka and Carmichael, 1985b). Some small volcanoes (mostly cinder cones) show local alignments striking E-W in the northern part of the volcanic field, ENE-WSW in the middle part, and NE-SW in the south (Hasenaka and Carmichael, 1985a).

Most volcanoes are located between 200 and 440 km from the MAT, with nearly 75% between 200 and 300 km and with the highest cone density at 250 km. Small volcanoes tend to form clusters, but the probably older medium-sized volcanoes, more abundant and degraded than the small ones in the northern part of the volcanic field, do not show clustering (Hasenaka *et al.*, 1994). Small monogenetic volcanoes are located between

medium-sized volcanic centers, either on their lower flanks or in the surrounding alluvial plains (Ban et al; 1992). The volcanism migrated southwards from the northern part of the MGVF around 1 Ma and in the last 40,000 yr, and the average magma output rate in the field has been about 0.8 km^3/1,000 years (Hasenaka and Carmichael, 1985a; Hasenaka and Carmichael, 1985b).

In the notch between the limits of the North American plate and some of the crustal blocks, the Michoacán Triangle occurs. This is a region of normal faulting without a preferred orientation and with a predominance of small monogenetic volcanoes, and absence of large volcanoes. These features suggest a high degree of crustal fragmentation and extension (Johnson and Harrison, 1989; 1990). This region is limited by three large fault zones, the Chapala-Tula fault zone to the north, the San Juanico-Buenavista fault zone to the south, and the Guerrero block to the east. Adjacent to the central part of the San Juanico-Buenavista lies the Tancítaro stratovolcano, the abovementioned large (~100 km^3) andesitic composite volcano. ^{40}Ar/^{39}Ar ages indicate that Tancítaro became active at ≥793±22 ka and that the most recent effusive activity occurred at 237± 34 ka (Ownby *et al.*, 2007).

Around Tancítaro and extending between 19° and 20° and -102.0° and -102.7° is the Paricutín-Tancítaro region (PTR), a complex, highly fractured and tectonically active region including part of the Michoacán Triangle hosting the highest volcanic vent concentration in MGVF.

3. The 2020-2021 seismic swarms in the Tancítaro- Paricutín Area.

Between 5 January 2020 and 5 November 2021, the National Seismological Service of Mexico (SSN) reported 4,956 earthquakes with duration magnitude between 2.6 and 4.2 and depths between 2 and 63 km. These events occurred in a region located between 102°30' W to 101°54' W and 19°12' N to 19°40' N. Ninety-six percent of that seismicity was recorded in two main periods: From 5 January to 22 February 2020 and from 30 May to 22 July 2021. With maximum magnitude of Md 4.2, in each swarm. Hereafter, we shall refer to those seismic swarm episodes as the PTRS-1 and the PTRS-2, respectively.

To locate these earthquakes, the National Seismological Service used data from several stations of its national broadband seismometer network (SSN), from accelerometers of the UNAM Institute of Engineering network (IIN), from Jalisco Seismic and Accelerometric Network (RESAJ), and from stations of the Colima volcano seismic network (RESCO-CUEV) (Figure 2). More

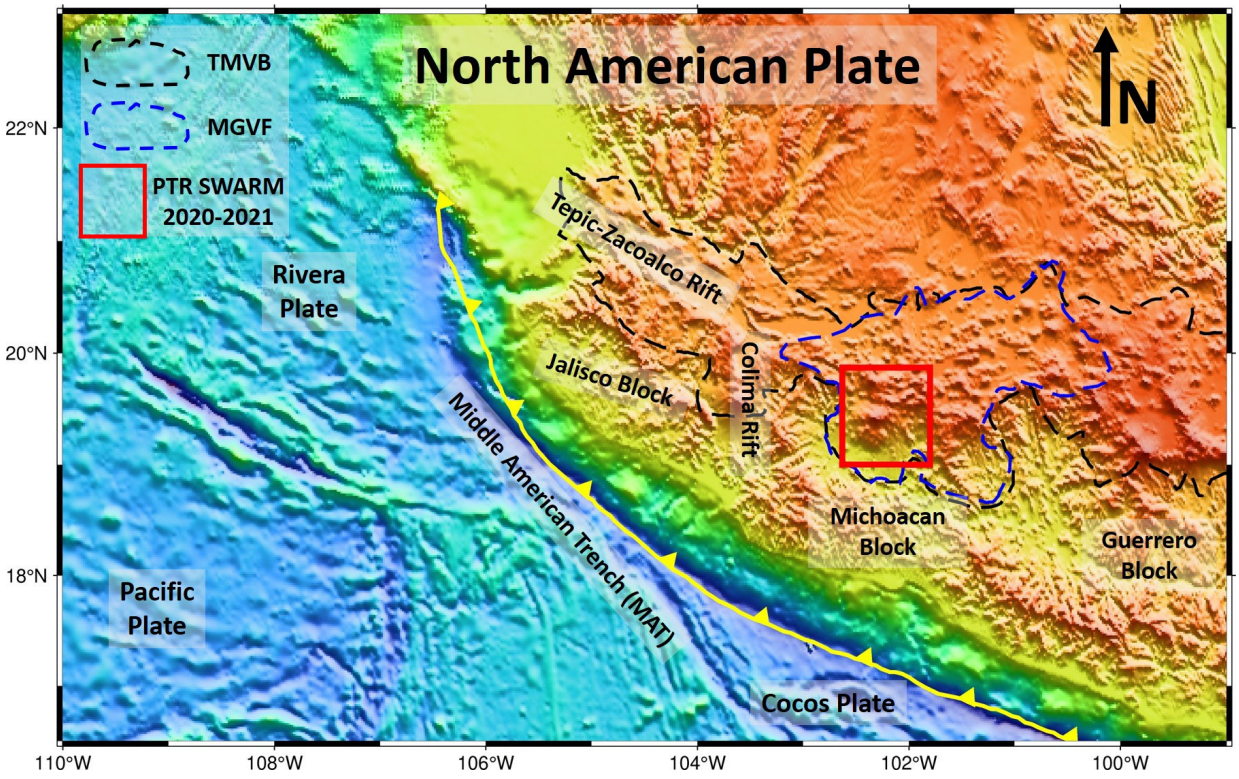

Figure 1. Tectonic map. MAT, Middle American Trench; TMVB, Trans-Mexican Volcanic Belt (black dashed line), MGVF Michoacán-Guanajuato volcanic field (blue dashed line).

seismic stations were gradually added as they were temporarily positioned near the seismic zone. Therefore, not all of the events were located with the same number of stations, and the number of stations used for each location depended upon the magnitude of each event. We remark that the temporary stations operated by SSN and the Institute of Engineering (Temporary Network) only recorded events of the PTRS-1 swarm between February 8 and December 15, 2020. The SSN original hypocentral locations are displayed in Figure 3.

3.1 Relocated seismicity

From the catalog data, we have relocated the events with HypoDD (double-difference earthquake location algorithm; Waldhauser and Ellsworth, 2000), which minimizes the travel-time residuals between pairs of events recorded at common stations. The algorithm adjusts the difference of vectors between the hypocenters canceling the common errors, mainly those related to the crustal velocity structure in the earthquakes' sites. When there is a dense distribution of seismicity and the distance between events is much smaller than the distance to seismic stations, hundreds or thousands of earthquakes can be linked through a chain of close neighbors and it is then possible to obtain higher-resolution hypocenter locations over longer distances (Waldhauser and Ellsworth, 2000).

Three different 1-D velocity models have been tested (Table 1 and Figure 4):

1. Espíndola (2009) model. This 8-layer model was obtained by receiver functions using teleseismic recordings to determine the crustal characteristics and to obtain shear-wave velocity models under the recording stations to improve focal determinations.
2. Pacheco *et al.* (1999) model. This 6-layer model was adapted from Fuentes (1997), who determined an average crustal structure from a surface wave dispersion analysis. Pacheco *et al.* (1999) also included a 1.5 km thick, 2.5 km/s, low-velocity layer to model the pronounced arrivals of P and S waves and to account for the low-velocity of the volcanic deposits.
3. Gardine *et al.* (2011) model. The authors developed this 8-layer velocity model using travel time tomographic inversions generalized for all of western Mexico (Gardine 2010).

The models have Vp/Vs ratios of 1.78 for Espíndola (2009) and Pacheco *et al.* (1999), and 1.76 for Gardine *et al.* (2011).

To select the most proper model, ten events with magnitudes 4.1 or higher were manually located, nine of these occurred during the 2020 PTRS-1 swarm and one was recorded during the 2021

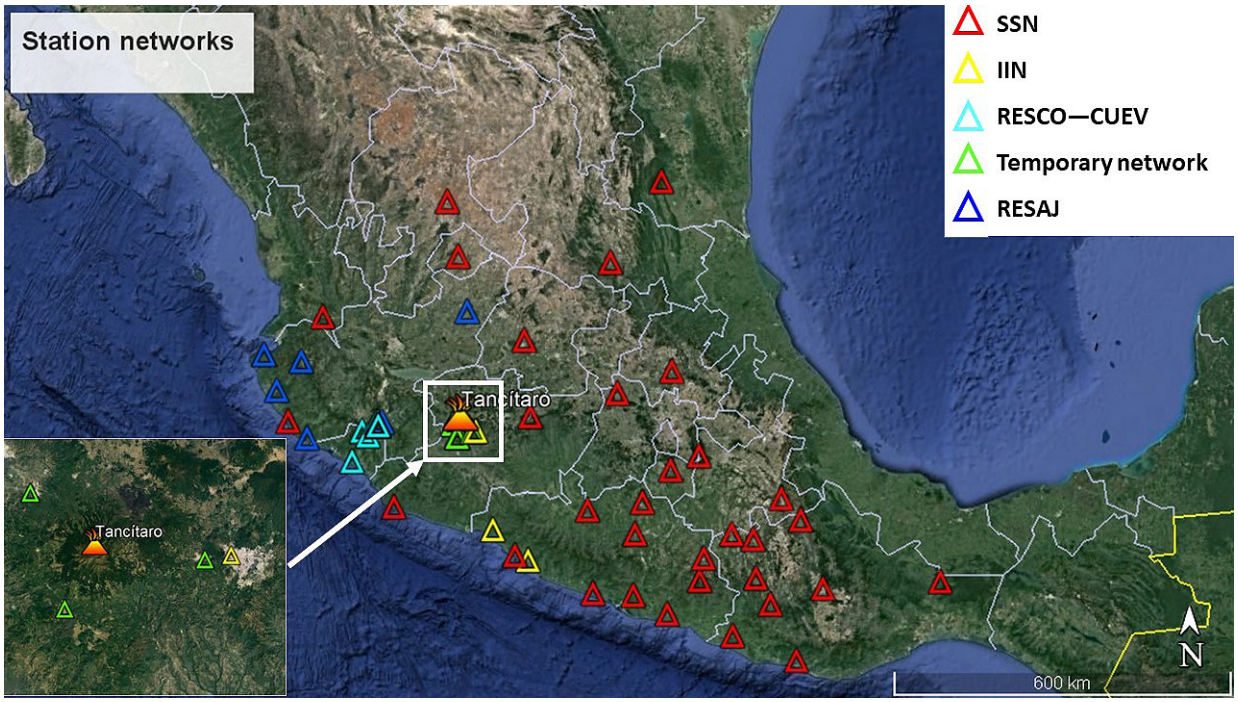

Figure 2. Stations used by SSN to locate the swarm earthquakes.

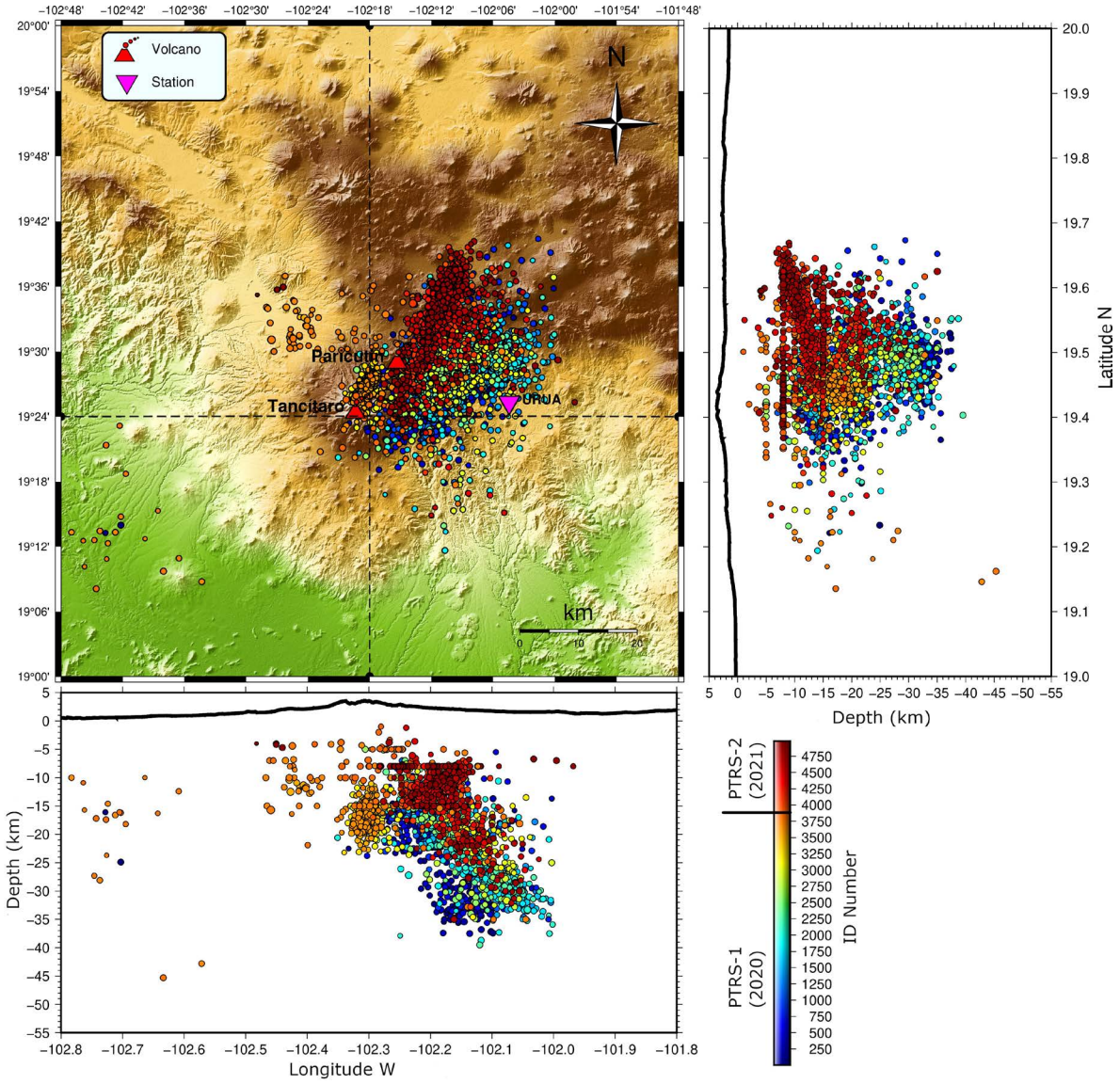

Figure 3. SSN hypocenter distribution of the PTR earthquake swarms recorded in 2020 and 2021.

Table 1. Tested velocity models. (From Pacheco *et al.*, 1999, Gardine *et al.*, 2011 and Espíndola, 2009).

Pacheco *et al.*		**Espíndola**		**Gardine *et al.***	
Depth	**P velocity (km/s)**	**Depth**	**P velocity (km/s)**	**Depth**	**P velocity (km/s)**
1.5	2.5	0	3.34	0	5.26
3	5	2	5.82	3	5.56
6	5.5	4	6.7	6	5.87
13	5.7	9	6.73	9	6.07
37	6.3	15	7	12	6.41
∞	7.4	21	7.61	15	6.71
		33	8	18	7.01
		400	8.5	30	7.41

PTRS-2 swarm. Once the 10 events were located the errors associated with their respective locations were compared with the errors provided by SSN (Figure 5). Based on the manual relocation results for the selected ten largest events, the velocity model with the lowest location errors was that of Gardine *et al.* (2011).

To explore whether the location errors could be further reduced to improve the hypocentral locations, small velocity variations were tested on the upper two layers of the Gardine *et al.* (2011) model. The variations were made by decreasing each velocity by 0.5 km/s, first individually, and then in pairs looking for the lowest errors and more constrained locations with respect to the previous locations made for this analysis. The best results, yielding slightly lower errors and less dispersed locations, have been obtained by adjusting only the first layer of the Gardine *et al.* (2011) model to 3.26 km/s (Figure 6), which will be referred as "*Gardine-mod*" model hereafter (Figure 7). Also in figure 7 the RC velocity model used by Legrand *et al.* (2023) is graphed.

Of the 4,956 swarm earthquakes, 4,310 were relocated.

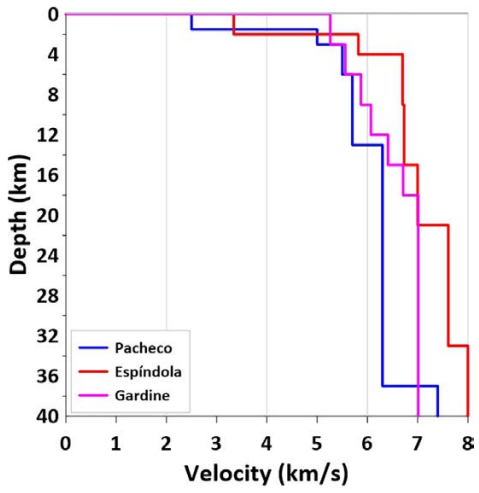

Figure 4. Tested velocity models.

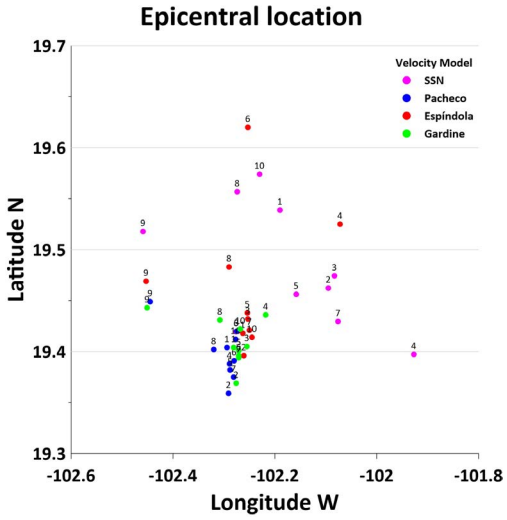

Figure 5. Epicentral localizations using different velocity models.

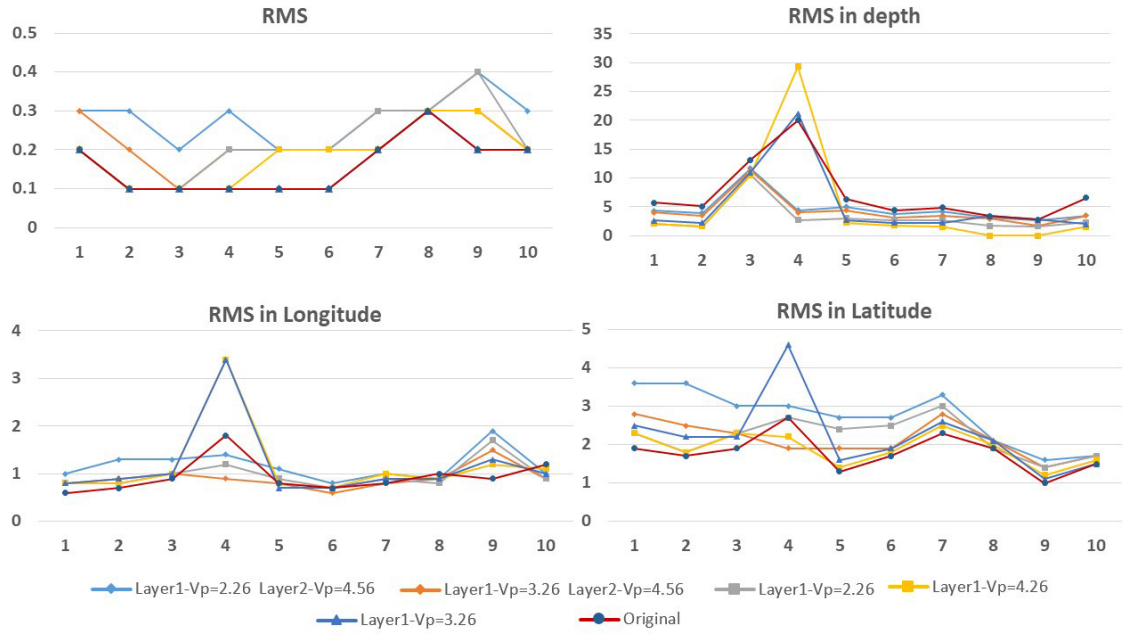

Figure 6. Errors associated with locations using different velocity variations and combinations.

4. Time evolution of the Swarm Seismicity

For the 2020 PTRS-1 swarm, SSN located a total of 3,688 earthquakes between January 5 and February 22 with a mean occurrence rate of approximately 68 events/day. The seismicity began with a relatively low rate since only 18 events were recorded during the first 18 days, but as time passed, the rate increased and the number of events gradually increased reaching a peak of 265 localized events on February 4. After that day, the seismicity progressively decreased returning to the background values (Figure 8).

For the PTRS-2 swarm occurred between May 30 and July 22, 2021, SSN located 1,114 earthquakes. The rate of occurrence of these events was lower than that of the PTRS-1 swarm (Figure 8) with 181 events between May 30 and June 3 and peaking on May 31 with 76 earthquakes.

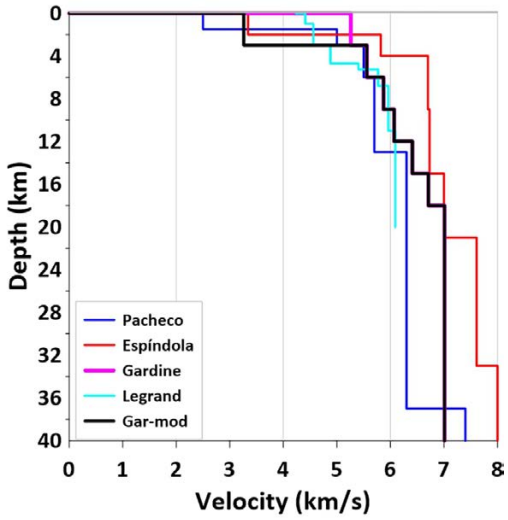

Figure 7. Tested velocity models and Gardine-mod model used in the swarm earthquakes relocation with HypoDD.

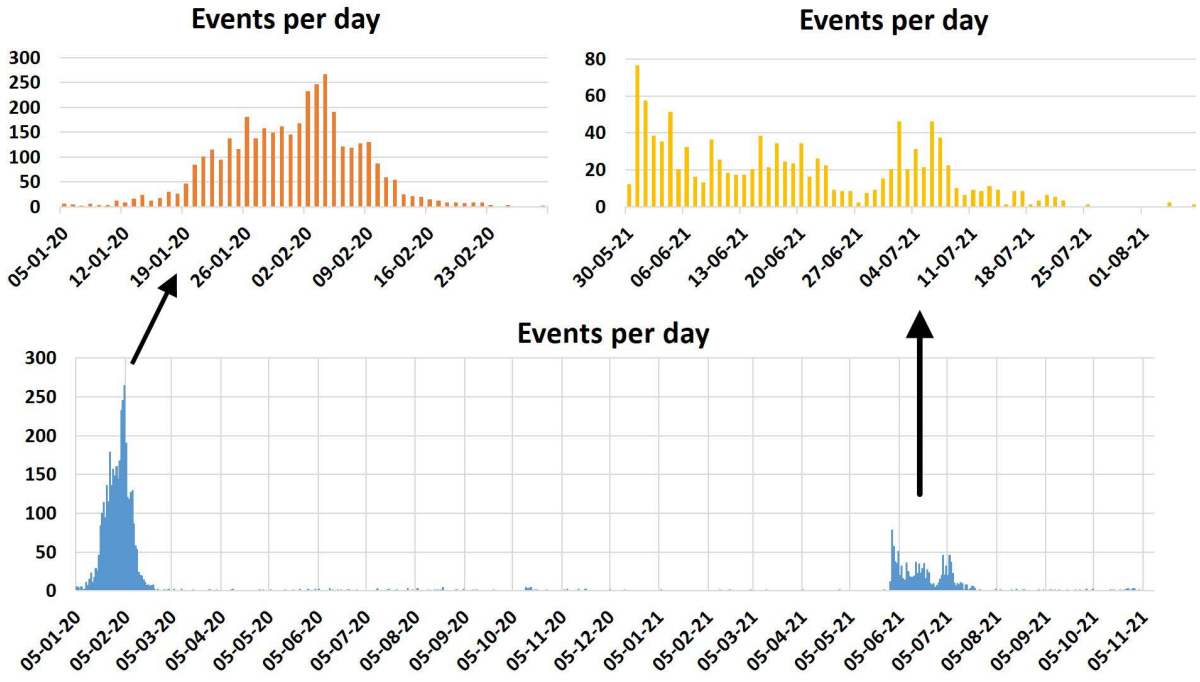

Figure 8. Number of events per day of swarms recorded in 2020 and 2021.

The frequency plots illustrated in Figure 8 hint that the PTRS-1 swarm shows a very characteristic bell-shaped type 3 Mogi earthquake sequence pattern (Mogi 1963a,b). This pattern is distinctive of highly fractured regions under concentrated stress such as magma intrusions. The PTRS-2 swarm is less clear with some mixed characteristics of the Mogi's type 2 and 3 and with a peak near the swarm onset followed by a slow, irregular decay, a feature more frequently observed in fractured regions under more distributed stresses (Mogi 1963a,b).

5. Analysis of the Hypocenter Distribution

Using the Gardine-mod 1-D velocity model (Figure 7), we relocated 3230 and 1010 earthquakes from the PTRS-1 and PTRS-2 swarms, respectively. In PTRS-1, the epicenters were distributed towards the east-northeast of Tancítaro and Paricutín, over an approximate extension of 30×40 km, and the hypocenters are vertically distributed around a plane dipping at approximately 45° to the NE, in the depth range 5 to 35 km below sea level (Figure 9a).

Starting on 8 February 2020, the earthquakes appear to migrate toward Tancítaro and concentrate below the Stratovolcano for the duration of the swarm. However, that date coincides with the day three temporary seismic stations began operating within 20 km from the Tancítaro volcano. Figure 10a-d shows how new stations were incorporated between 8 February and December 2020, reducing the average distance to the Tancítaro volcano and causing a slight increase in the number of stations used to localize the events. This hints that the apparent migration may be an artifact resulting from a higher location precision caused by the addition of nearer stations (Figure 10e-g). We relocated the events, removing data from the nearby stations to verify if there was a significant apparent migration of events caused by the additional stations. The addition of nearby stations reduced the dispersion of the events, especially on the latitude. Conse-

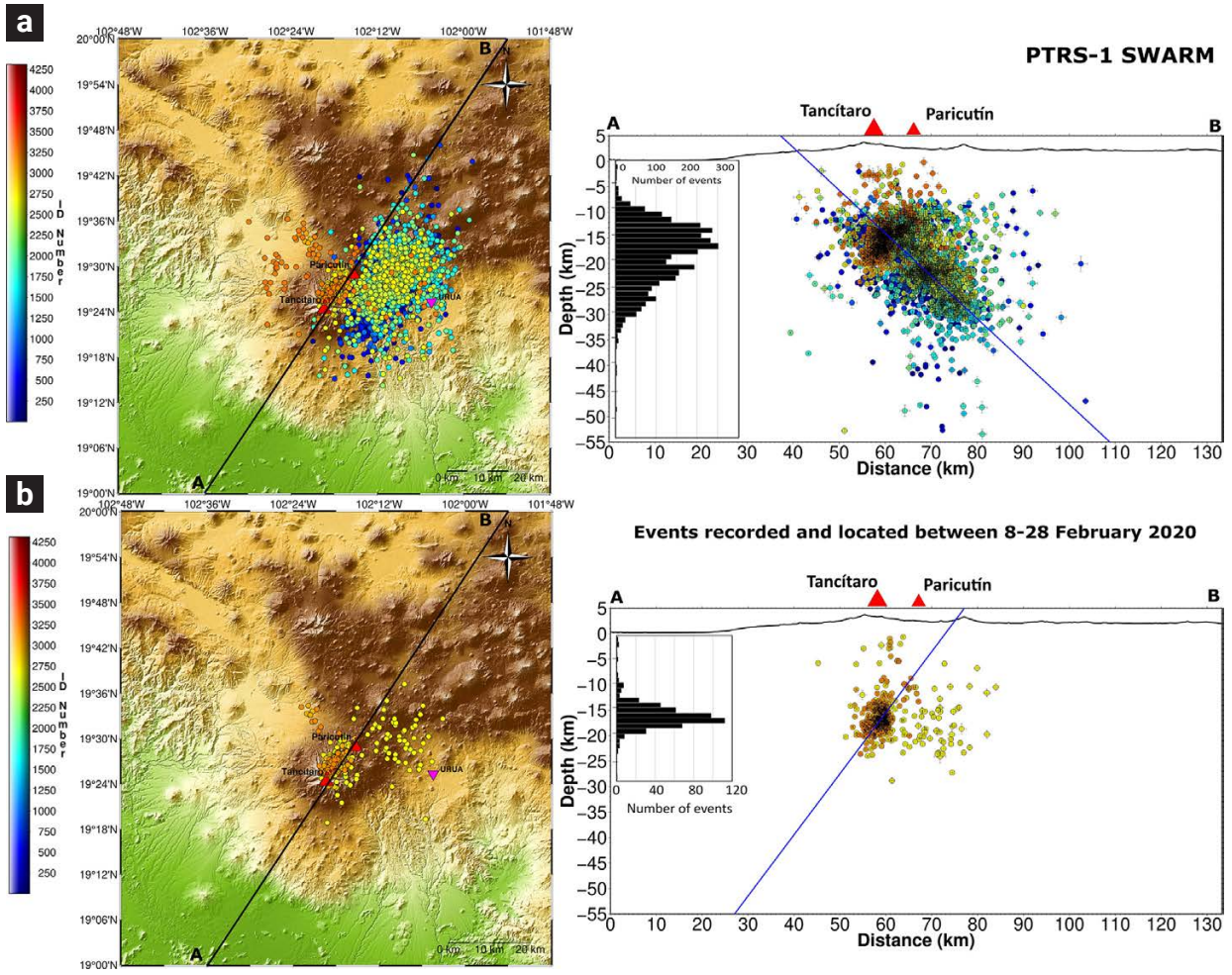

Figure 9. Hypocenter distributions: a) of the PTRS-1 swarm, b) of selected events recorded between February 8 and 28, 2020. Sections along the profile AB.

quently, the distance between the swarm epicentral center and its borders was reduced by a factor of ca. 0.12. Furthermore, this concentration of events coincides with the locations reported by Legrand *et al.* (2023) and Perton *et al.* (2024) using an independent temporary network. This coincidence supports the belief that a significant spatial migration of the swarms towards the SW did not take place, at least not during February, when the most intense swarm activity was detected. The epicentral locations (from 8 February) extend over an area of about 50 km^2, and in the vertical profile, concentrate under the Tancítaro at depths between 9 and 20 km (Figure 9b, orange hypocenters).

The first earthquakes of the PTRS-2 swarm were located below Tancítaro, further developing with an NE trend towards and beyond Paricutín with the hypocenters distributed in two main depth ranges: between 5 and 19 km and between 19 and 32 km (Figure 11). Most events (66%) concentrate in the shallower depth range and appear to migrate low angle fault plane towards the NE. We attribute the dispersion of the epicenters to the lack of nearby stations for localization (Figure 10b). By contrast, the apparent migration towards the Paricutín may be caused by the larger number of stations located at the NW of Tancítaro volcano (Figure 10c).

6. Discussion

The *Gardine-mod* velocity model and the hypocenter location analysis based on the number and distance to temporary seismometers allow us to obtain well-constrained locations. In particular, the events recorded when three stations within 20 km of Tancítaro volcano were operating (February-December 2020) conveyed results supporting the conclusions of Legrand *et al.* (2023) about a constrained extent of the first swarm seismicity, evidencing the location of a magma intrusion under the NE flank of Tancítaro, similar to previous cases reported between 1999 and 2006.

Here, we provide additional evidence supporting the magmatic origin of the concentrated stress source causing the swarm through the analysis of the temporal evolution of the swarm earthquakes since, as mentioned above, both PTRS-1 and PTRS-2 comply with the empirical criteria of Mogi (1963a,b). Aside from the roughly bell-shaped histograms of the earthquake counts as a function of time in Figure 8, these are: the total number of events in each swarm should exceed 10, and $n_m/\sqrt{t} > 2$, this is the maximum daily number of earthquakes n_m divided by the square root of the duration t of the swarm (in days) exceeding a value of 2. They are 30 and 9.5 for PTRS-1 and PTRS-2, respectively, and the number of events exceeds 10 by two orders of magnitude).

Therefore, assuming that the swarms are caused by magma intrusion-induced stresses in a highly heterogenous medium, and using the magnitudes reported by the SSN for the swarm events, we estimated the intruded volumes using the relationship between cumulative seismic moment and intruded volume of White and McCausland (2016, 2019), and estimate the cumulative seismic moment from the body-wave magnitudes m_b with the best-fit relationship of Das *et al.* (2019),

$$\log M_0 = 1.36 m_b + 10.24 \quad (1)$$

We obtained about 96×10^6 m^3 of magma for PTRS-1 (calculated cumulative seismic moment of 5.45×10^{18} Nw-m of 3230 earthquakes recorded between 5 January and 28 February 2020) and about 45×10^6 m^3 for PTRS-2 (cumulative seismic moment of 1.85×10^{18} Nw-m for the earthquakes of the second swarm recorded between 30 May and 22 July 2021). These results are independent of the location of the hypocenters.

The adequacy of volume estimation from cumulative seismic moment relies on the diffusive behavior of the induced seismicity. Indeed, the spatio-temporal evolution of the PTRS-1 epicenters (Figure 12a) shows a diffusive behavior, as described by Eq. 8 from Shapiro *et al.* (1998), which relates the distance r from the intrusion to an event that occurred at time t as $r = \sqrt{4\pi \mathrm{Dt}}$ where D is the medium pore-pressure relaxation diffusivity. For the PTRS-1, a value of D in the range of 0.2 to 0.3 m^2/s describes the distance-time evolution of the swarm well. These values are similar to those reported by Shapiro *et al.* (1998) for swarms generated after liquid injections. In contrast, epicenters from the PTRS-2 do not show a clear diffusive behavior: events do not appear first near the assumed stress source and increase their spatial dispersion as a function of time (Figure 12b), suggesting the influence of an additional stress source, probably of tectonic origin. Consequently, the estimated volumes for the PTRS-2 may be less accurate than those of the PTRS-1.

The use of the White and McCausland relationship in this case may be questioned since it was obtained primarily with data from "distal" (within 30 km from the volcano) earthquakes preceding eruptions in dormant polygenetic volcanoes. Notwithstanding, we consider that it is also applicable to seismic activity caused by new magma intruding into brittle crust or in pre-existing dikes or sills filled with cooling magma from previous intrusions. In fact, the relationship was in part formulated from deformation and cumulative seismic moment observations made during experimental water injections in deep holes (McGarr, 2014), confirming that it may be applied to any similar configuration.

When the swarm seismicity precedes the eruption of polygenetic volcanoes, the volumes of magma intrusions calculated with the cumulative seismic moment-volume relationship are

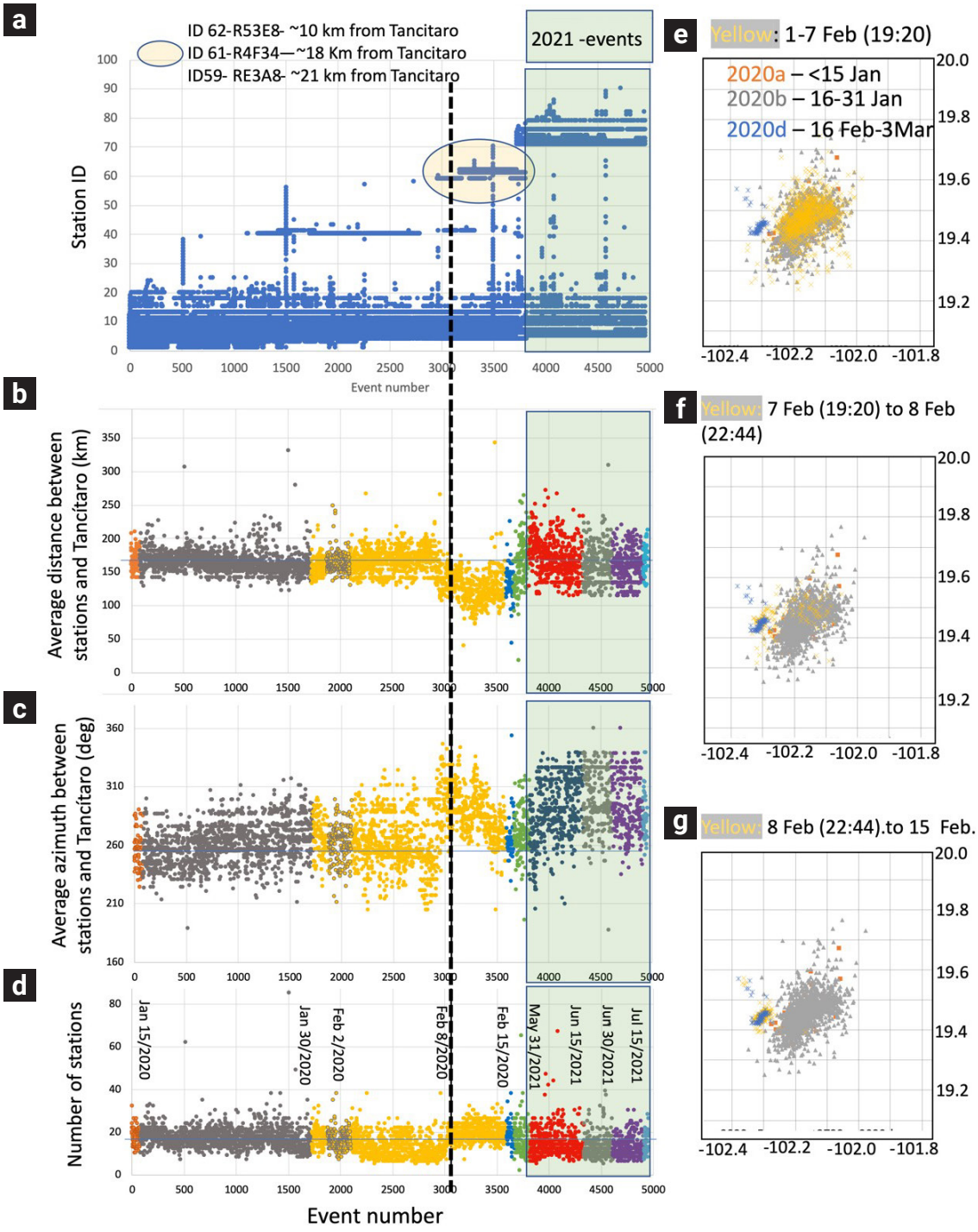

Figure 10. Event apparent migration resulting from changes in the number and distribution of seismic stations used for locations. In a) to d), seismic events are identified by a number according to occurrence order. Event 3056, the first event registered on 8 February 2020, is marked by a dotted line, and events that occurred in 2021 are highlighted and encompassed with a green area. a) Displays the ID of active seismic stations during each seismic event. b) Displays the average distance between all active seismic stations and the Tancitaro volcano during each seismic event. c) Displays the average azimuth of the location of seismic stations with respect to Tancítaro volcano. d) Displays the number of active stations during each seismic event. e)-g) Illustrate the effect of the introduction of nearby stations on February 8, 2020, on the location of the seismic events by comparing the locations around that day to those obtained before February 1 (gray and orange) and after February 16 (blue). e) Location of events before February 7, 2020 (yellow). f) Location of events on February 7, 2020, between 19:20 and 22:40 (yellow). g) Location of events between February 8 and February 15, 2020 (yellow).

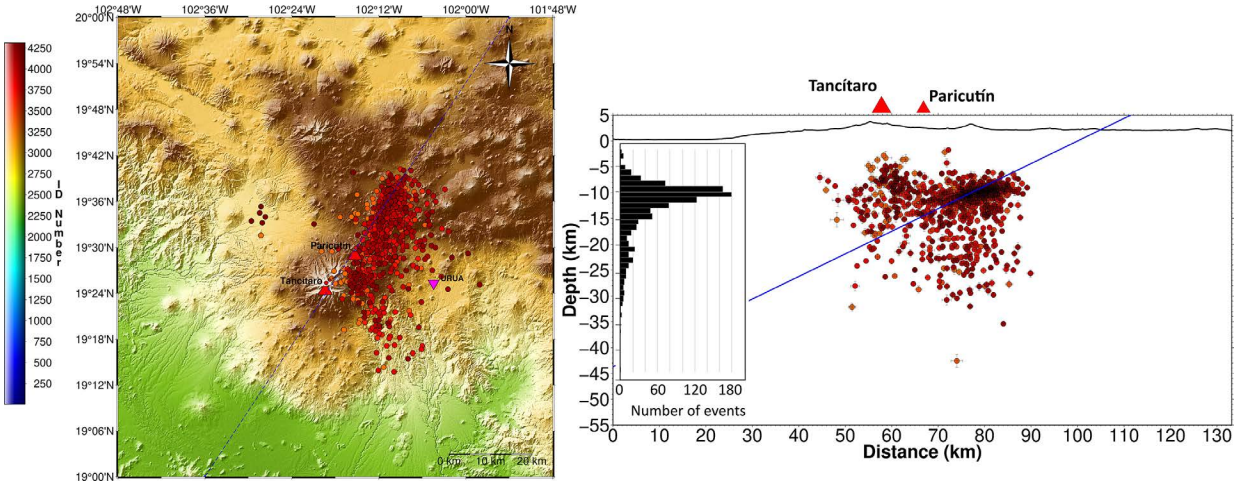

Figure 11. Location of the events that occurred during the PTRS-2 swarm, recorded in 2021.

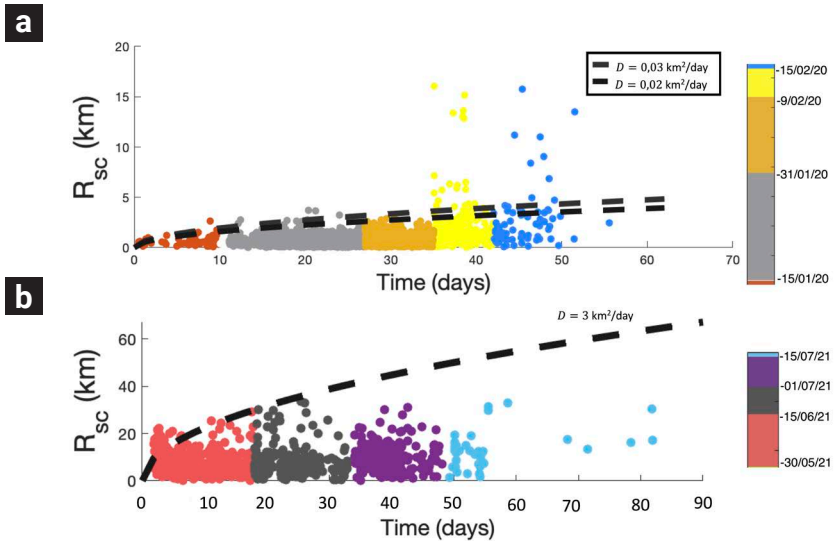

Figure 12. Distance from epicenters to the center of the swarm as a function of time. a) Events from PTRS-1. Radial distance from events before 9 February (when closer stations were added) have been corrected by a factor of 0.12, as described in section 5. b) Events from PTRS-2. Dotted lines are plots of the equation $r = \sqrt{4\pi Dt}$ (Shapiro *et al.* 1998) for different diffusivity values.

much smaller than the erupted volumes (White and McCausland, 2016). This also seems to be valid when eruptions open new vents. To test this, we estimated the cumulative seismic moment of the seismic swarm preceding the 2021 eruption of Tajogaite on La Palma (Canary Islands, Spain), which opened a volcanic vent complex on the western flank of the Cumbre Vieja rift, an N-S extended volcanic ridge, producing extensive lava flows and building scoria cones (Martí *et al.*, 2022). Using the public data of the IGN (Instituto Geográfico Nacional de España, Catálogo de terremotos, **https://doi.org/10.7419/162.03.2022**), we calculated the volume of the magma intrusion using the cumulative seismic moments of the events locally recorded between 17 June 2021 and 19 September 2021 (the eruption day), obtaining an intruded magma volume of 2.6×10^6 m^3, which is of the same order as the estimation of Suarez *et al.*, (2023) of 4.6×10^6 m^3 and as the 5.62×10^6 m^3 estimated from pre-eruptive DInsar analysis of the pre-eruptive ground deformations (DeLuca *et al.*, 2022), but significantly less than the erupted volume ~2×10^8 m^3 (Dayton *et al.*, 2023). As del Fresno *et al.* (2023) discussed, in the case of La Palma monogenetic basaltic volcanism, the pre-eruptive seismic

activity only reflects the final and shallow intrusion. However, most magma erupted from a deeper source (25-40 km). Thus, the volume intruded during the pre-eruptive activity is a minor part of the real amount of magma under the volcanic area. Then, the seismicity-inferred volume of a magmatic intrusion may be used as a lower threshold of the total intruded volume. In the case of our approximation for La Palma-2021 eruption, it was lower by a factor of two.

On the other hand, we obtained the strain release by Eq. 20 from De la Cruz-Reyna and Reyes-Dávila (2001) to describe the behavior of the PTRS-1 and PTRS-2 swarms. We divided the PTRS-1 into periods A and B. Period A corresponds to the events registered between January 5 and February 8, 2020 (Fig 13a). Period B corresponds to the events recorded in the period February 9 - 23, 2020 (Fig 13b). For period A of PTRS-1 and PTRS-2, we calculated the cumulative strain release of the epicenters every 2.5 km. For period B of PTRS-1, we calculated the cumulative strain values every 1 km because the epicenter distribution is constricted by the closer stations.

We interpret all of the above arguments as a piece of evidence that, in most cases, the swarm-causing magma-intrusion-induced stresses extend over sizable areas when the intrusion reaches a pre-existing magma reservoir, namely a large magma chamber in the case of polygenetic volcanoes, or a temporary elongated reservoir like a dike or a sill in the case of monogenetic eruptions. Even intrusions significantly smaller than the stored magma may generate pressure fluctuations that can activate fractures around any type of reservoir. This is consistent with the model of Albert *et al.* (2016) based on the felt seismicity of historic monogenetic eruptions and magma petrological analysis of eruptions in the Canary Islands (Albert *et al.*, 2015). They propose a magma ascent model in different stages: 1. Ascent of small magma batches intruding into the crust, accumulating at depths between 5 to 10 km and forming a temporal magma reservoir. This process can develop over years or months before an eruption. 2. The accumulated magma may mix, degas and crystallize. 3. When a new magma batch intrudes into the pre-existing temporary reservoir, mixing with the older magma can modify its rheology and density, allowing it to ascend and erupt. This last process is usually faster, developing over a timescale of days to weeks. This model entails the notion that for monogenetic eruptions to occur, a series of seismic swarms or 'failed eruptions' (De la Cruz-Reyna and Yokoyama, 2011) may arise before magma can reach the surface (Albert *et al.*, 2016).

In summary, our modified velocity model *Gardine-mod* permitted reducing the event location errors, helping to improve the delimitation of the swarm hypocentral region and to set more reliable boundaries on the region where the magmatic intrusion occurred. Secondly, the variation in the location of hypocenters of the PTRS-1 as a function of the distance of seismometers to the location of the hypocenters strongly supports what is stated by Legrand *et al.* (2023), that the primary source of error generally stems from the velocity model plus the number and spatial distribution of the seismometers. As a consequence, the events between 8 February and 15 December 2020 are more accurately located, when three stations placed within 20 km of Tancítaro volcano were operating.

In particular, hypocentral locations obtained for events recorded between 8 and 28 February 2020 overlap those reported by Legrand *et al.* (2023) for the swarms that occurred on 2 February 2020, confirming that most of the seismic swarm concentrated in the region at -102.29 E, 19.43 W, and at depths between 9 and

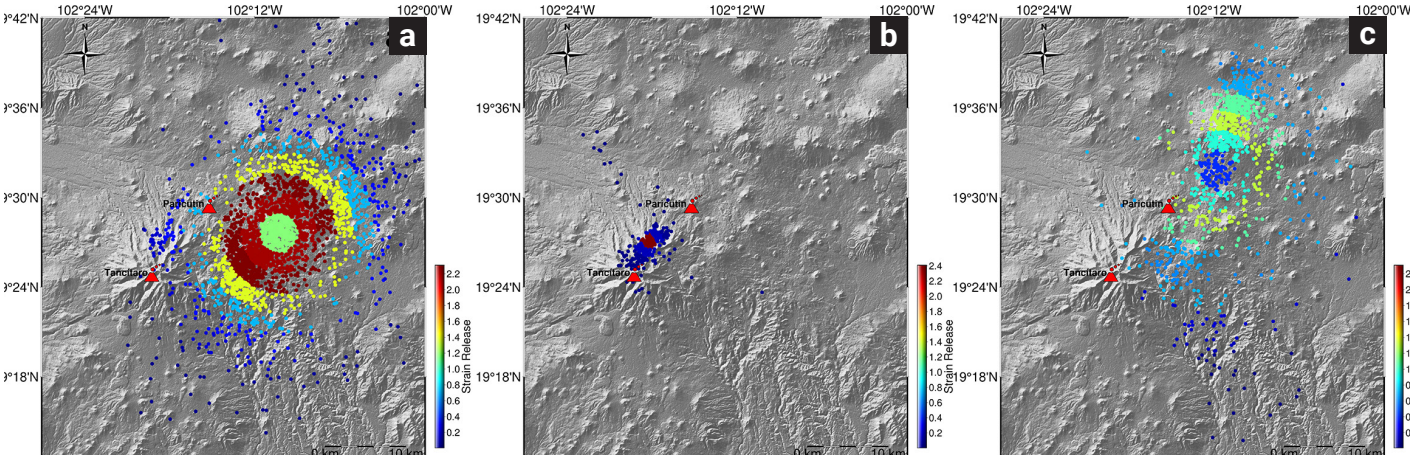

Figure 13. Strain release for PTRS-1 and PTRS-2. a) strain release between January 5, 2020 to February 8, 2020. b) strain release between February 9 - 23, 2020, and c) strain release during PTRS-2.

20 km below sea level, and that the neighboring seismicity was distributed in an elliptical shaped volume with the semi-major and semi-minor axis of approx. 5 km (~0.05 deg) and 3 km (~0.03 deg), respectively, and about 10 km thick.

Most of the PTRS-2 is distributed over an area to the NNE of the PTRS-1 towards the Paricutín volcano. However, this also may be an effect of the incorporation of seismic stations in the N and NW of Tancítaro volcano in January 2021. It is thus highly probable that the PTRS-2 was also located at, or very near, the location of the previous swarm.

7. Conclusions

We conclude that the PTRS-1 and PTRS-2 were probably caused by new magma intrusions of about 96 million cubic meters in 2020 and about 45 million cubic meters in 2021 into a pre-existing temporal magma reservoir at a depth below about 9 km, according to the model by Perton *et al.* (2024), and seemingly not yet large enough to trigger an eruption. The magma was probably fed through a dike or a system of spatially closed dikes and ascended until it encountered a horizontally extended older, cooled magma body, probably a sill that we speculate may be related to the system that fed the Paricutín eruption. The fresh magma injections pressurized the older magma deposit and nearby aquifers, and when the pressure pulses efficiently propagated through those fluid or viscoelastic media intersected tectonically pre-stressed faults, induced the seismicity (White and McCausland, 2016). The proportion between the pre-existent tectonic stress and the magma pressure-induced stresses probably controls the shape of the number of shocks per day histogram with a predominance of pressure-induced stresses in 2020 and an increased influence of more distributed tectonic stresses in 2021.

It is not possible to predict the size and time of a possible future magma intrusion and whether it may trigger an eruption, forming a new monogenetic volcano. The experience in polygenetic volcanoes, and more recently, the case of La Palma volcano, shows that the volume of magma intrusion triggering an eruption is a small fraction of the erupted magma. Therefore, even a moderate (in number and magnitude) earthquake swarm could represent a significant volcanic hazard for the region, with an added seismic hazard component for the case of swarms increasing in intensity with time. This calls for the densification of the volcanic monitoring infrastructure in the region, including more permanent telemetric seismic stations and continuous geodetic and geochemical studies. Early detection and diagnosis of developing seismicity would provide decision-makers with sufficient decision factors and time to develop efficient preventive actions.

8. Acknowledgments

The authors would like to express their gratitude to the National Seismological Service (SSN México) for providing the seismic data. The authors are indebted to the Editors and to both reviewers whose comments greatly helped to improve this contribution.

9. References

Albert, H., Costa, F., and Martí, J. (2015). Timing of magmatic processes and unrest associated with mafic historical monogenetic eruptions in Tenerife Island. *Journal of Petrology*, v. 56, p. 1945–1966. doi: **https://doi.org/10.1093/petrology/egv058**

Albert, H., Costa, F., and Martí, J. (2016). Years to weeks of seismic unrest and magmatic intrusions precede monogenetic eruptions. *Geology*, v. 44; no. 3, p. 211–214. doi: **https://doi.org/10.1130/G37239.1**

Alonso-Núñez M.C., Marín-Tello M.I. (2009). Impacto social y económico de la erupción del volcán Jorullo, Michoacán, 1759. *Tzintzun*, 49: 53-78.

Ban, M., Hasenaka, T., Delgado -Granados, H., and Takaoka, N. (1992). K-Ar ages of lavas from shield volcanoes in the Michoacan-Guanajuato volcanic field, Mexico. *Geofísica Internacional,* 31(4), 467–473. doi: **https://doi.org/10.22201/igeof.00167169p.1992.31.4.1367**

Becerril, L., Larrea, P., Salinas, S., Mossoux, S., Ferrés, D., Widom, E., Siebe, C., Martí, J. (2021). The historical case of Paricutin volcano (Michoacán, México): challenges of simulating lava flows on a gentle slope during a long-lasting eruption. *Natural Hazards* 107, pp. 809–829.

Connor, C. B. (1987). Structure of the Michoacán-Guanajuato volcanic field, Mexico. *Journal of Volcanology and Geothermal Research*, 33(1-3), 191-200. doi: **https://doi.org/10.1016/0377-0273(87)90061-8**

Connor, C. B. (1990). Cinder cone clustering in the TransMexican Volcanic Belt: implications for structural and petrologic models. *Journal of Geophysical Research: Solid Earth, 95*(B12), 19395-19405.

Das, R., Sharma, M. L., Wason, H. R., Choudhury, D., & Gonzalez, G. (2019). A seismic moment magnitude scale. *Bulletin of the Seismological Society of America*, 109(4), 1542-1555. Doi: **https://doi.org/10.1785/0120180338**

Dayton, K., Gazel, E., Wieser, P., Troll, V. R., Carracedo, J. C., La Madrid, H., ... and Pérez-Torrado, F. J. (2023). Deep magma storage during the 2021 La Palma eruption. *Science advances*, 9(6), eade7641.

Del Fresno, C., Cesca, S., Klügel, A., Domínguez Cerdeña, I., Díaz-Suárez, E.A., Dahm, T., García-Cañada, L., Meletlidis, S., Milkereit, C., Valenzuela-Malebrán, C. and López-Díaz, R. (2023). Magmatic plumbing and dynamic evolution of the 2021 La Palma eruption. *Nature Communications*, 14(1), p.358.

De la Cruz-Reyna, S., and Reyes-Dávila, G. (2001). A model to describe precursory material-failure phenomena: applications to short-term forecasting at Colima volcano, Mexico. *Bull. Volcanol*, 63:297-308. doi: **https://doi.org/10.1007/s004450100152**

De la Cruz-Reyna, S., and Yokoyama, I. (2011). A geophysical characterization of monogenetic volcanism. *Geofísica Internacional,* 50(4), 465-484. doi: **https://doi.org/10.22201/igeof.00167169p.2011.50.4.157**

De Luca, C., Valerio, E., Giudicepietro, F., Macedonio, G., Casu, F., & Lanari,R. (2022). Pre- and co-eruptive analysis of the September 2021 eruption at Cumbre Vieja volcano (La Palma, Canary Islands) through DInSAR measurements and analytical modeling. *Geophysical Research Letters*, 49, e2021GL097293.

Espíndola, V. H. (2009). Modelos de velocidad cortical en México, utilizando funciones de receptor en las estaciones de la red nacional de banda ancha. *Tesis de Doctorado (Ph.D. tesis)* UNAM.

Fuentes, C. (1997). Determinación de la Estructura Cortical en el Sur de México Utilizando Dispersión de Ondas Superficiales. *Tesis de Maestría (MSc tesis)*, UNAM, México D.F.

Gardine M. (2010). Tracing the movement and storage of magma in the crust through seismology: examples from Alaska and western Mexico. *Dissertation, University of Alaska* Fairbanks.

Gardine, M., West, M. E., Cox, T. (2011). Dike emplacement near Paricutín volcano, México in 2006. *Bull. Volcanol*, 73:123-132.

Guilbaud, M. N., Siebe, C., Layer, P., Salinas, S., Castro-Govea, R., Garduño-Monroy, V. H., and Le Corvec, N. (2011). Geology, geochronology, and tectonic setting of the Jorullo Volcano region, Michoacán, México. *Journal of Volcanology and Geothermal Research*, 201(1-4), 97-112. Doi: **https://doi.org/10.1016/j.jvolgeores.2010.09.005**

Hasenaka, T., Carmichael, I. (1985a). A compilation of location, size, and geomorphological parameters of volcanoes in the Michoacan–Guanajuato volcanic field, Mexico. *Geofísica Internacional,* 24, pp. 577-608. doi: **https://doi.org/10.22201/igeof.00167169p.1985.24.4.2179**

Hasenaka, T., Carmichael, I. (1985b). The cinder cones of Michoacán-Guanajuato, Central México: their age, volume and distribution, and magma discharge rate. *Journal of Volcanology and Geothermal Research*, 25: 105-124. **https://doi.org/10.1016/0377-0273(85)90007-1**

Hasenaka, T., Ban, M., and Delgado Granados, H. (1994). Contrasting volcanism in the Michoacán-Guanajuato Volcanic Field, central Mexico: Shield volcanoes vs. cinder cones. *Geofísica Internacional,* 33(1), 125–138. doi: **https://doi.org/10.22201/igeof.00167169p.1994.33.1.544**

Johnson, C.A., Harrison, C.G.A. (1989). Tectonic and volcanism in Central Mexico: a Landsat Thematic Mapper Perspective. *Remote Sens. Environ.* 28, 273-286. doi: **https://doi.org/10.1016/0034-4257(89)90119-3**

Johnson, C.A., Harrison, C.G.A. (1990). Neotectonics in Central Mexico. *Phys. Earth and Planet. Int*. 64, 187-210. doi: **https://doi.org/10.1016/0031-9201(90)90037-X**

Legrand, D., Perton, M., Macías, J. L., Siebe, C., Pacheco, J., Chacón, F., Lermo, J., Quintanar, L., Cisneros, G. (2023). Repeated seismic swarms near Paricutin volcano: precursors to the birth of a new monogenetic volcano in the Michoacán-Guanajuato volcanic field, México?. *Bulletin of Volcanology*, 85(5), 30. doi: **https://doi.org/10.1007/s00445-023-01645-0**

Luhr J., Nelson, F., Allan, J., Carmichael, I. (1985). Active rifting in southwestern Mexico: Manifestations of an incipient eastward spreading-ridge jump. *Geology*, 1985; 13 (1): 54–57. doi: **https://doi.org/10.1130/0091-7613(1985)13<54:ARISMM>2.0.CO;2**

Luhr J., Simkin T. (1993). Paricutin. The volcano born in a Mexican cornfield. *Geoscience Press & the Smithsonian Institution*, Phoenix, Arizona. 427 pp.

Martí, J., Becerril, L., and Rodríguez, A. (2022). How long-term hazard assessment may help to anticipate volcanic eruptions: The case of La Palma eruption 2021 (Canary Islands). *Journal of Volcanology and Geothermal Research*, 431, 107669. doi: **https://doi.org/10.1016/j.jvolgeores.2022.107669**

McGarr, A. (2014). Maximum magnitude earthquakes induced by fluid injection. *J. Geophys. Res. Solid Earth* 119 (2), 1008–1019.

Mogi, K. (1963a). Some discussions on aftershocks, foreshocks and earthquake swarms-the fracture of a semi-finite body caused by an inner stress origin and its relation to the earthquake phenomena. *Bull. Earthq. Res. Inst*., 41, 615-658.

Mogi, K. (1963b). Experimental study on the mechanism of the earthquake occurrences of volcanic origin. *Bulletin of Volcanology*, 26, 197-208.v

Pacheco, J. F., Valdés-González, C., Delgado, H., Singh, S. k., Zuñiga, R. F., Mortera-Gutiérrez, C. A., Santoyo, M. A., Domínguez, J., Barrón, R. (1999). Tectonic implication of the earthquake swarm of 1997 in the Michoacan Triangle, Mexico. *Journal of South American Earth Science*, 12, 567-577. doi: **https://doi.org/10.1016/S0895-9811(99)00040-1**

Perton, M., Legrand, D., Macías, J. L., Cisneros, G., Yañez-Sandoval, R. (2024). Magma migration below Tancítaro and Paricutin volcanoes revealed by seismology. *Geophysical Journal International,* 236(3), 1699–1715. doi: **https://doi.org/10.1093/gji/ggae015**

Pinzón J.I., Núñez-Cornú F.J., Rowe C.A. (2017). Magma intrusion near Volcan Tancítaro: Evidence from seismic analysis. *Physics of the Earth and Planetary Interiors*, 262, 66-79. **https://doi.org/10.1016/j.pepi.2016.11.004**

Rasoazanamparany, C., Widom, E., Siebe, C., Guilbaud, M. N., Spicuzza, M. J., Valley, J. W., ... & Salinas, S. (2016). Temporal and compositional evolution of Jorullo volcano, Mexico: implications for magmatic processes associated with a monogenetic eruption. *Chemical Geology*, 434, 62-80. doi: **https://doi.org/10.1016/j.chemgeo.2016.04.004**

Rees, J. D. (1970). Paricutin revisited: A review of man´s attempts to adapt to ecological changes resulting from volcanic catastrophe. *Geoforum*, 1(4), 7-25. doi: **https://doi.org/10.1016/0016-7185(70)90055-2**

Shapiro, Sergei A., J.J. Royer, and Pascal Audigane. (1998). Estimating the permeability from fluid-injection induced seismic emission. *Poromechanics.* CRC Press, 301-305.

Suarez, E.D., Domínguez-Cerdeña, I., Villaseñor, A., Aparicio, S.S.M., del Fresno, C. and García-Cañada, L. (2023). Unveiling the pre-eruptive seismic series of the La Palma 2021 eruption: Insights through a fully automated analysis. *Journal of Volcanology and Geothermal Research*, 444, p.107946. doi: **https://doi.org/10.1016/j.jvolgeores.2023.107946**

Waldhauser, F., Ellsworth, W. (2000). A double-difference earthquake location algorithm: method and application to the northern Hay-

ward fault. Bull Seismol Soc Am 90, 1353–1368. Doi: **https://doi.org/10.1785/0120000006**

White, R., McCausland, W. (2016). Volcano-tectonic earthquakes: A new tool for estimating intrusive volumes and forecasting eruptions. *Journal of Volcanology and Geothermal Research*, 309. pp. 139-155. doi: **https://doi.org/10.1016/j.jvolgeores.2015.10.020**

White, R. A., and McCausland, W. A. (2019). A process-based model of pre-eruption seismicity patterns and its use for eruption forecasting at dormant stratovolcanoes. *Journal of Volcanology and Geothermal Research*, 382, 267-297. doi: **https://doi.org/10.1016/j.jvolgeores.2019.03.004**

Yokoyama, I., De la Cruz-Reyna, S. (1990). Precursory eathquakes of the 1943 eruption of Paricutin volcano, Michoacan, Mexico. *Journal of Volcanology and Geothermal Research*, 44, 265-281. doi: **https://doi.org/10.1016/0377-0273(90)90021-7**

Data references:

Instituto Geográfico Nacional de España (2023). Catálogo de terremotos. España: Centro Nacional de Información Geográfica. **https://www.ign.es/web/sis-catalogo-terremotos**

Universidad de Colima (2022). Red Sísmica Telemétrica del Estado de Colima perteneciente al Centro Universitario de Estudios Vulcanológicos. México: Universidad de Colima. **https://portal.ucol.mx/cueiv/infraestructura.htm**

Universidad Nacional Autónoma de México (2023). Servicio Sismológico Nacional, México: UNAM, Instituto de Geofísica, SSN. URL: **http://www.ssn.unam.mx**

Universidad Nacional Autónoma de México (2023). URAII-UNAM: La red acelerográfica del Instituto de Ingeniería. México: UNAM, Instituto de Ingeniería. **https://aplicaciones.iingen.unam.mx/AcelerogramasRSM/RedAcelerografica.aspx**

Special Section
Monogenetic volcanism, environment and society

Geofísica Internacional (2024) **63-2**: 929 - 948

Quarrying volcanic landscapes: territory and strategies of *metate* production in Turícuaro (Michoacán, México)

Caroline Hamon[1], Gregory Pereira[2], Laurent Aubry[1], Oryaëlle Chevrel[3, 4, 5], Claus Siebe[6], Osiris Quezada[7] and Nanci Reyes-Guzmán[6]

Abstract

In the Purhépecha region of Michoacán in central-western Mexico, the village of Turícuaro has been for centuries a centre for the artisanal production of metates. There, these milling stones are crafted from andesite rocks exploited on the slopes of Hoya Urutzen and El Metate volcanoes. Surveys aimed at reconstructing the strategies adopted through time to extract the andesite were conducted in this volcanic territory with the help of some of the last *metateros* that still remain in Turícuaro, the Vidales family. This has allowed us to draw a map and propose a relative chronology of the quarry areas. Different types of exploitation could be recognized, from ancient quarries possibly related to Prehispanic occupations to those currently active. We observe that the morphology of the outcrops (walls, isolated blocks) partly conditioned the distribution of the quarries (flat areas, terraces, etc). From the observation of blocks, debitage, and roughouts at abandoned quarries, it was possible to reconstruct the different exploitation schemes and work organisation, offering a new perspective on Mesoamerican metate quarrying strategies.

Key words: Michoacán, volcano, andesite, quarries, archaeology, techniques, crafts.

Resumen

En la región purhépecha de Michoacán, en el centro-occidente de México, el pueblo de Turícuaro ha sido durante siglos un centro de producción artesanal de metates. Ahí, estas piedras de molienda son elaboradas a partir de rocas de andesita que se han explotado en las laderas de los volcanes Hoya Urutzen y El Metate. Con la finalidad de reconstruir las estrategias adoptadas a lo largo del tiempo para extraer la andesita, se realizaron prospecciones en este amplio territorio volcánico con la ayuda de algunos de los últimos *metateros* de Turícuaro, la familia Vidales. Esto ha permitido elaborar un mapa y proponer una cronología relativa de las diferentes zonas de extracción. También se han reconocido diferentes tipos de explotación, desde las canteras antiguas relacionadas con las ocupaciones prehispánicas, hasta las actuales. La morfología de los afloramientos rocosos (paredes, bloques aislados) condicionó en gran medida la organización de las canteras (áreas planas, terrazas, etc.). También se pudieron reconstruir las diferentes estrategias de extracción y organización del trabajo a través de la observación de los bloques, residuos y desbastes en canteras abandonadas, ofreciendo una nueva perspectiva sobre las estrategias de explotación en las canteras de metate mesoamericanas

Palabras clave: Michoacán, volcán, andesita, canteras, arqueología, técnicas, artesanía.

Received: November 29, 2023; Accepted: February 24, 2024; Published on-line: April 1, 2024.

Editorial responsibility: Dra. Marie-Noëlle Guilbaud

* Corresponding author: Caroline Hamon, caroline.hamon@cnrs.fr
[1] CNRS (French National Center for Scientific Research), UMR 8215 Trajectoires, 9 rue Mahler 75004 Paris, France.
[2] CNRS (French National Center for Scientific Research), UMR 8096 ARCHAM, 9 rue Mahler 75004 Paris, France.
[3] Université Clermont Auvergne, CNRS, IRD, OPGC, Laboratoire Magmas et Volcans, 63000 Clermont-Ferrand, France.
[4] Observatoire Volcanologique du Piton de la Fournaise, Institut de Physique du Globe de Paris, 97418 La Plaine des Cafres, France.
[5] Université Paris Cité, Institut de Physique du Globe de Paris, CNRS, 75005 Paris, France.
[6] Universidad Nacional Autónoma de México, Departamento de Vulcanología, Instituto de Geofísica, C.P. 04510 Coyoacán, Ciudad de México, México.
[7] Universidad Nacional Autónoma de México, Posgrado en Estudios Mesoamericanos, FFyL.

https://doi.org/10.22201/igeof.2954436xe.2024.63.2.1760

1. Introduction

The history of volcanic environments is structured around a strong dichotomy marked by alternating phases of profound landscape upheaval: brief eruptive episodes are followed by longer phases of recovery, occasionally accompanied by rapid anthropization motivated by the attractiveness of fertile land and abundant mineral resources (De Bélizal *et al.*, 2011; Sheets and Grayson, 1979). In Mesoamerica volcanic rocks (e.g., obsidian, andesite, basalt, etc.) were intensively used for construction (Robles 1992; Barba and Cordoba 2010; Quezada *et al.*, 2015; Quezada 2016), but also for more skilled crafts (Fujita and Poyatos 2007; Darras *et al.*, 2017; Quezada and Darras 2023; Gillespie 1994) that were highly valued for millennia. To address this duality over the long term, the METATE project aims to reconstruct the evolution of a volcanic territory organized around a specific activity: the exploitation of andesite for the production of *metates* (milling stones) and *molcajetes* (mortars). Emblematic of traditional Mesoamerican food preparation, these tools are part of the cultural expression of Mesoamerican groups, and their production constitutes a craft in its own right that has helped to define the identity of some villages.

Seminal ethnohistorical and ethnoarchaeological studies have shed fundamental light on the organization of grinding-stone production worldwide (Alonso 2019; David, 1998; Hamon and Le Gall, 2013; Roux, 1985), and more specifically in Mesoamerica, from Guatemala to Mexico (Cook, 1982; Hayden, 1987; Nelson, 1987, Rodríguez-Yc, 2013). Some studies have also explored the social context in which *metates* were used (Katz, 2006; Searcy, 2013), as well as their diffusion over shorter and longer distances (Abramiuk and Meurer 2006). These studies have also documented technical traditions that are presently in the process of being abandoned, and have provided archaeologists with clues for recognizing areas of ancient millstone quarries in Mesoamerica (Searcy and Pitezel, 2018).

In the Michoacán region of central-western Mexico, 'El Metate' volcano has been the subject of recent volcanological research (Chevrel *et al.*, 2016a, b; Mahgoub *et al.*, 2017): the morphological and geochemical characterization and dating of the various lava flows allow us to consider their potential impact on past and present settlers of the region, be it by exerting a repulsing or attracting effect. El Metate formed during a single eruption that began around AD 1250 and lasted more than 35 years (Chevrel *et al.*, 2016a), just prior to the emergence of the Tarascan civilization (Pollard, 1993, 2008). The present work highlights the exploitation of andesite lava flows from this volcano to produce high-quality metates, an activity that probably dates back to pre-Hispanic times (Hamon *et al.*, 2023). In the village of Turícuaro, located at the foot of the volcano on the Meseta Purépecha, a number of families still make and use these tools today (Figure 1). This very special configuration provides a unique opportunity to study the long-term territorial and chronological relationships between the exploitation of volcanic resources, anthropization linked to a targeted economic activity, and the evolution of a territory. In the last decades, the introduction of electronic devices has generated important changes, in terms of andesite selection and exploitation, organization of the work and social recognition at the regional scale.

The highest quality metate and molcajete production has tended to disappear, except for the cases in which some craftsmen produce masterpieces for the tourists. Today, most of the metates and molcajetes sold in the Purépecha region are imported from other villages, which exploit softer rocks to produce large -if not to say industrial- quantities of cheaper and lower quality tools. In this context, our study was aimed at reconstructing the impact of the long-term grinding tool activity on the territory and landscape around the El Metate volcano (Michoacán, Mexico), based on the memories of the last metateros (metate craftsmen) of Turícuaro.

By adopting a multi-disciplinary approach that combines volcanology, archaeology, and the anthropology of techniques, we seek to understand how these lava rocks have become a resource for the nearby inhabitants over time, how their exploitation has structured their environment and what role this exploitation has played on the anthropization of the landscape. We have centered our efforts on understanding the territorial organization of the grinding tool industry, from production to distribution, with the aim of proposing keys for recognizing such operations in ancient time periods. This paper focuses on the organization of the territory of metate exploitation, at its various spatial scales (from the quarries and workshops where the *metates* have been initially produced to the villages where they have been used) and temporal scales (from the 13th century to the present day).

Figure 1. Typical metate and molcajete produced by the Vidales in Turicuaro.

2. Eruption dynamic and raw material selection

'El Metate' volcano is an extinct andesitic volcano located in the middle of the "Meseta Purépecha" in the Michoacán-Guanajuato volcanic field (CVMG) of central Mexico (Chevrel *et al.*, 2016a and b; Mahgoub *et al.*, 2017). It is 900 m high, culminating at an altitude of 2,500 m, and extends over a circumference of 10 km in diameter. Due to its morphology and its gently sloping flanks, it can be catalogued as a shield volcano (Hasenaka *et al.*, 1994). The volcano is also considered to be monogenetic, meaning that it was formed by one single eruption that lasted between 35 and 270 years. The eruption was purely effusive (evidence of explosive activity was not found) and successively produced fifteen voluminous lava flows (up to 200-m-thick, 2-km-wide, and 15-km-long). The start of the eruption has been dated by the radiocarbon method at ~AD 1250, which shortly precedes the emergence of the Tarascan civilization and poses the question of the possible causal relationship between these two historical events (Chevrel *et al.*, 2016a).

The emitted lava was estimated at 9 to 10 km^3, which makes this one of the most voluminous eruptions of the Holocene in the Trans-Mexican Volcanic Belt. Knowledge of the physical characteristics and age of the lava flows allow to evaluate their potential impact, between repulsion and attraction, on past and present settlements in this region. Because the lava flows were only 950-1000°C and viscous, they advanced at low velocities (2 to 30 m/day). Chevrel *et al.* (2016b) estimated that the longest lava flows took ~2 years, while the thickest flows ~7 years to become emplaced. These so-called "block flows" are characterized by a surface that displays large angular blocks (1 to 2 m^3) with smooth faces. The andesitic rocks are partially crystallised (50 to 60 Vol.% crystals) and are mostly dense (less than 10 Vol.% vesicles), except for the last flow, which contains 30 Vol.% vesicles (Chevrel *et al.*, 2016b).

Chevrel *et al.*, 2016a were the first to report the intensive exploitation of the latest lava flow from El Metate for the production of high-quality metates by the inhabitants of Turícuaro. While andesites that were too dense were excluded from the outset because they were too hard to cut, vesicular materials were favored because of their roughness, which is better suited for grinding maize. Since the beginning of the 20th century, the lava flow near the summit of the volcano has been exploited exclusively by quarrymen from Turícuaro. The rare and distinctive micro-porosity of the rock at this site makes it suitable for sculpting. It is also rough enough for grinding maize and compact enough for cleaning the surface of the metate after use, e.g., after mixing tortilla dough on its surface (Hamon *et al.* 2023). Knowledge of the combination of these diagnostic criteria enabled us to better identify lava flows likely to have been exploited in Prehispanic times, and to pinpoint potential areas for archaeological prospection.

The porosity within a lava flow is heterogeneous. Pores are formed from the voids left by gas bubbles or by the difference in volume when crystals form during cooling (diktytaxtic cavities). Porosity is also the result of microfracturation during cooling and flow advance (brittle failure). Heterogeneity is hence found at the scale of the flow as well as at the scale of a single block. The porosity may change longitudinally along the lava flow due to degassing, vesiculation, crystallization and fracturing during emplacement. The porosity may also vary from the base to the top of the flow, where scoriaceous texture are often found (e.g. Fink *et al.* 1992) and from the core to the margins of a single block. Rocks are usually more porous near the vent in comparison to denser distal lava margins (e.g. Riker *et al.* 2009). Finding the right area for exploitation and the optimal blocks is hence not an easy task for the metateros.

A highly porous rock (scoriaceous texture) is often more altered due to the ease at which water percolates through the material. Such rocks are usually too friable to make good metates. Denser blocks may be to too hard to cut and have a smooth surface and hence are inefficient for grinding maize. The right porosity and the right vesicle shape must be found (Hamon *et al.*, 2023). One large block (1 or 2 m^3) may have a scoriacious carapace that the metateros need to remove to get to a denser core, but other parts of the block may be too dense and also need to be removed in order to obtain a roughout.

During emplacement and cooling of this type of block-lava flow, the lava surface becomes highly fractured while the core is massive. Large fractures divide the rock into blocks while smaller fractures and microfractures extend across the blocks. The *metateros* may use those fractures to cut down a block, however, they must be careful not to direct a blow at the wrong place which could fracture the roughout and destroy the emerging metate.

3. Studying the long-term evolution of metate quarrying around Turícuaro

Within the volcanic territory of the Meseta Purépecha, the production of metates from andesites has been the main craft activity in the village of Turícuaro since at least the 19th century (Leon, 1906; West, 1948, map 20); the village is located to the north-east of the Hoya Urutzen and El Metate volcanoes. But changes in food habits and the widespread development of mechanical mills (which sell masa at low prices in the village) have contributed to the decline of manual milling (Hamon *et al.*, 2023). Today, metates are mainly used as tables for mixing maize paste, and much more rarely for grinding hard grains,

while *molcajetes* are still used for preparing sauces and spices. Although there were almost 200 metateros in the village at the beginning of the 20th century, only 5 extended families currently make a living from this activity, and the know-how is no longer passed on to the younger generations due to the low profitability of this difficult and strenuous activity.

Our surveys were conducted in 2018 and 2019 with the invaluable help and knowledge of one of the last metateros families, the Vidales, who live in the village of Turícuaro. Most of the knowledge regarding the volcanic territory and the techniques of metate production was related by the men of the family: Don Pedro Vidales, his son Nicolás Vidales and, on particular aspects, his grandsons especially Tino and Héctor Vidales. Information regarding the use of metates and the organization of food preparation was mainly provided by Doña Livia Vidales, wife of Don Pedro, as this activity remains exclusively women's work. With their invaluable help, we felt it important to document the past and present metate quarries and production areas on the two nearby volcanoes: Hoya Urutzen and the north-eastern flanks of El Metate (Figure 2).

We present here the mapping of four areas of grinding stone quarries in the natural volcanic landscape: the East Hoya Urutzen, the West Hoya Urutzen (within the Tzintzicátaro area), the El Metate Taleminichi and El Cerro quarries. We acquired geographical data using Geographic Positionning System (GPS) with an accuracy of 3 to 5 m to map the paths used by the metateros to reach the various quarries. A differential GPS (Trimble) with decimetric accuracy was used for the quarry areas themselves. A data dictionary was defined for the differential GPS in order to harmonize and simplify data collection in the quarries. To complement the GPS surveys, the quarry areas were surveyed in 3D using photogrammetry, with ground acquisition for all areas. Four of these areas (A, B, C and D) were also surveyed by drone. The data acquired by GPS was projected into the UTM 14N (WGS84) cartographic system in order to be processed in a Geographic Information System (GIS). The base maps used in the GIS were taken from the INEGI E14A21 map base in vector format and the Digital Elevation Model (DEM) used was taken from the ASTER base interpolated to a spatial resolution of 40m.

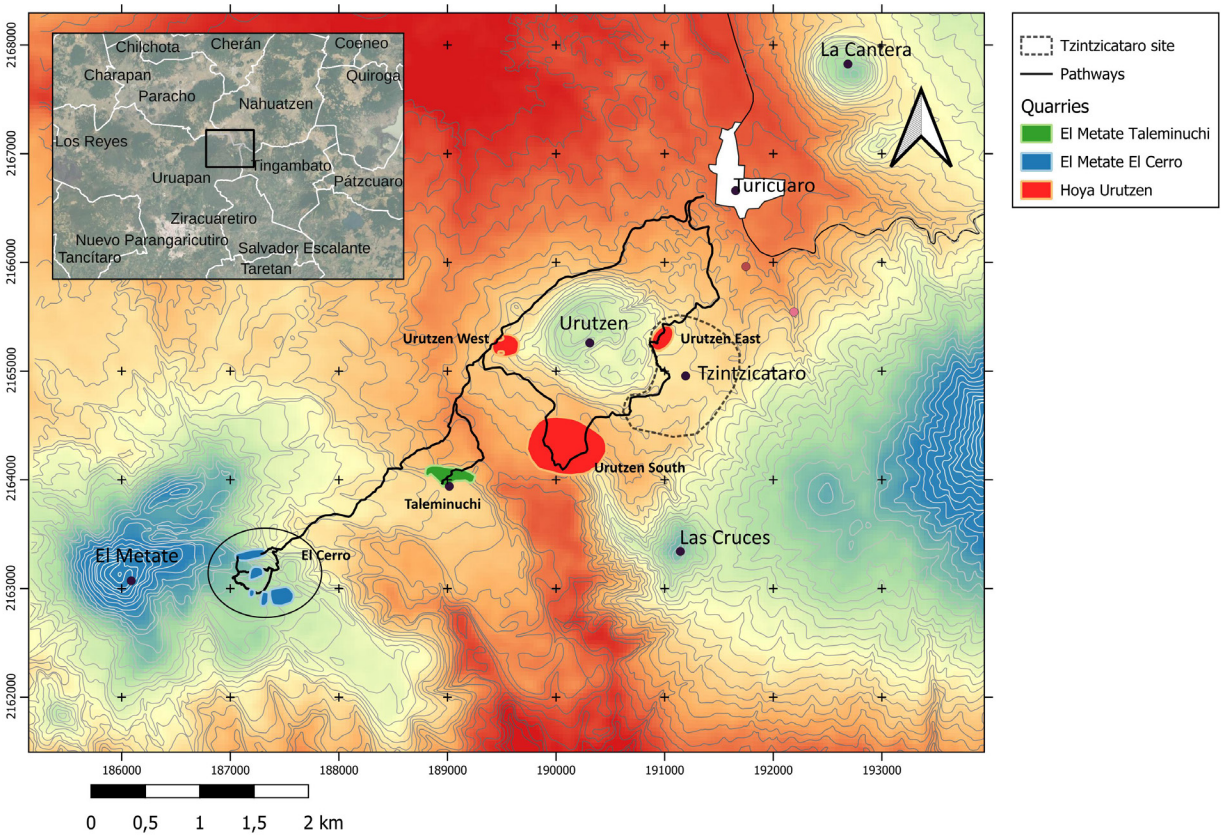

Figure 2. Map showing the quarries at Hoya Urutzen and El Metate, near Turícuaro.

Precise walking distances between the villages and the quarry areas were calculated from GPS surveys. By projecting the data onto the DEM, we obtained a first elevation profile between the start and end of the route (Table 1).

Coupling the path data with the DEM enabled us to establish more precise movement profiles, highlighting the constraints associated with the topography and the effort required to reach the quarry areas (Figure 3).

For each quarry, we measured the surface of the explored extraction and workshop areas (Table 2). However, due to the difficulties of access and the presence of extensive vegetation, we are unable to offer a precise estimation of the extent of the quarry areas.

The values presented therefore only correspond to the surfaces observed and documented as part of the study, but do not represent the total surface area of quarrying operations.

Considering the difficulty of finding elements to date these quarries, we relied on several clues, first and foremost the memory of the metateros, but also the type of tools produced and their location (proximity to the archaeological site, access, etc.).

Table 1. Main pathways from Turícuaro to the quarrying areas, with estimations of distance and overall altitude variation.

Pathways	Distance	Global variation of altitude
Turicuaro - Hoya Urutzen west	2.2 km	130 m
Turicuaro - Hoya Urutzen east	2.7 km	160 m
Turicuaro - El Metate Taleminuchi	4.5 km	100 m
Turicuaro - El Metate El Cerro	6.4 km	310 m

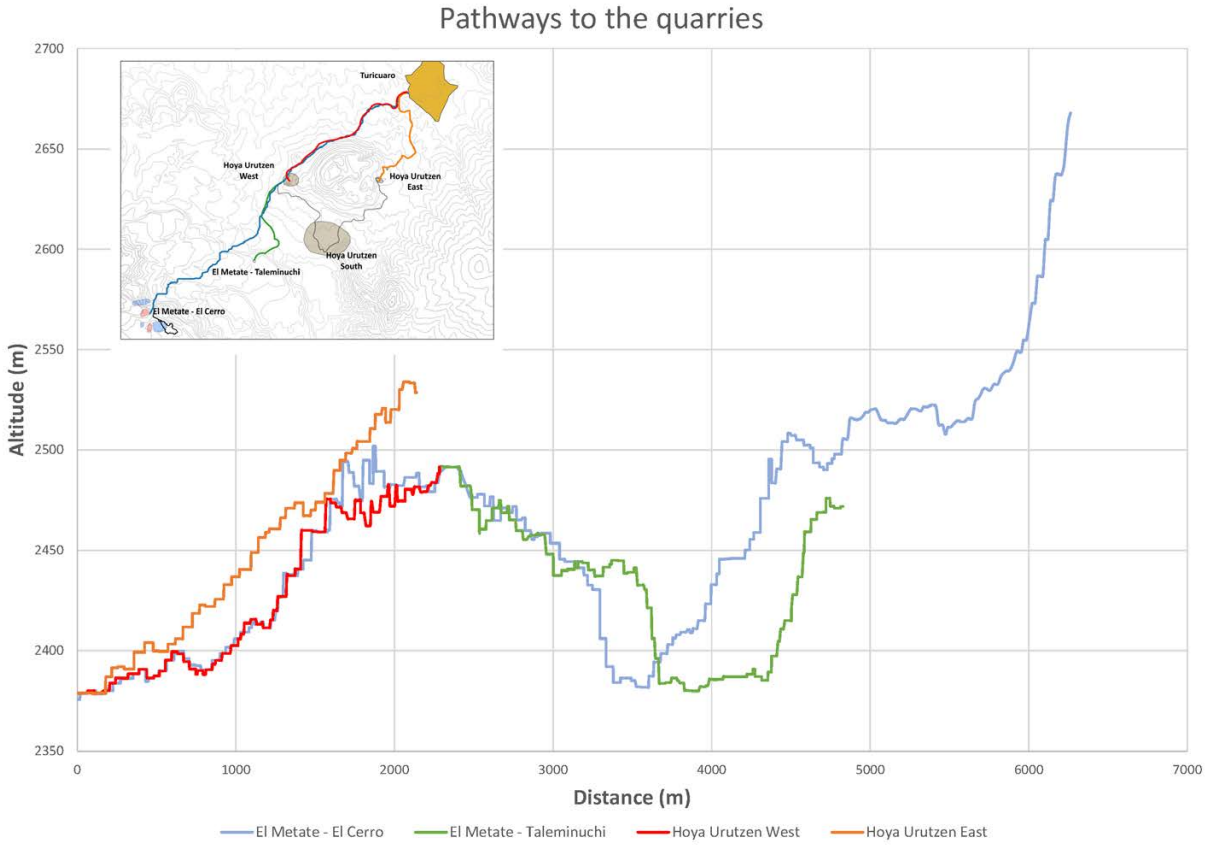

Figure 3. Altitudinal profiles of the pathways (in meters) from the Vidales workshop in Turícuaro to the different quarries.

Table 2. Main quarrying areas on Hoya Urutzen and El Metate, with estimations of the surface explored during our surveys.

Quarries	Explored Area
Hoya Urutzen west	40 000 m2
Hoya Urutzen east	8000 m2
El Metate Taleminuchi	1500 m2
El Metate El Cerro	< 70 000m2

4. Results for the Tzintzicátaro and the Hoya Urutzen quarries

In the vicinity of the present-day village of Turícuaro, our surveys uncovered an archaeological site. This settlement, known locally as Tzintzicátaro (Figure 4), has been partially surveyed, mapped and documented. It has revealed remains dating from the Late Postclassic (14th-early 16th century) and Early Colonial periods (16th century).

Located 500 m south of the present-day village, the Tzintzicátaro site ("built place" in Purépecha) occupies the eastern foothills of the Hoya Urutzen volcano. In this area, we observed archaeological concentrations of artefacts (sherds, obsidian) on the surface of cultivated plots, as well as a number of architectural remains preserved in the southern part of the surveyed area. As far as we know, the site extends over a strip at least 1200 m long (north-south) and 300 m wide (Figure 5). Observable archaeological remains can be dated to the Prehispanic period (potsherds, obsidian), and more specifically to the Middle/Recent Postclassic period (AD 1200-1522),

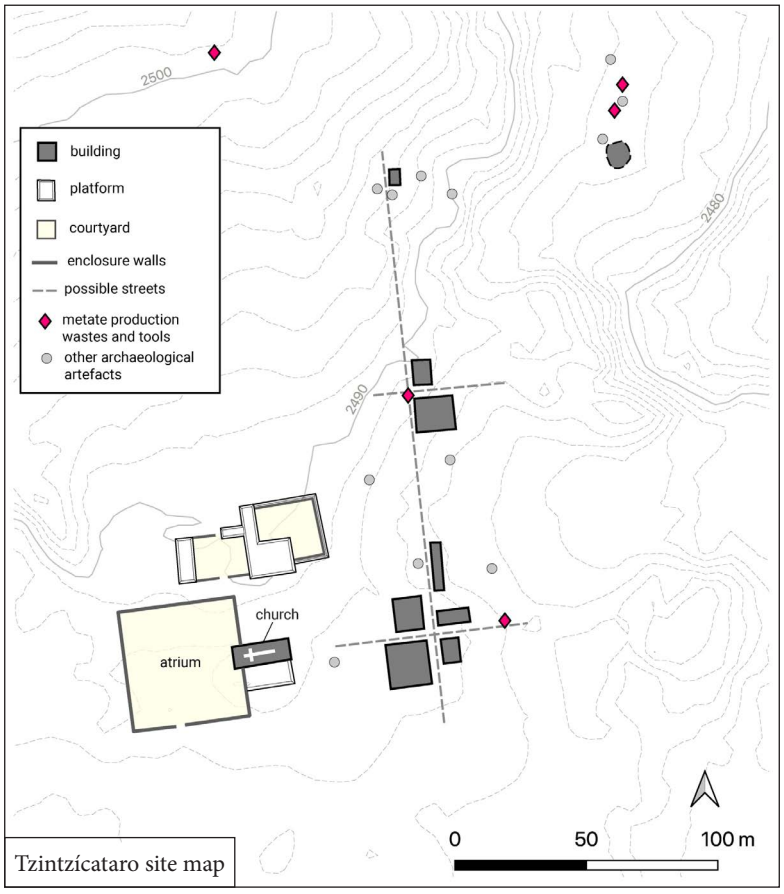

Figure 4. General map of the archaeological site of Tzintzicátaro.

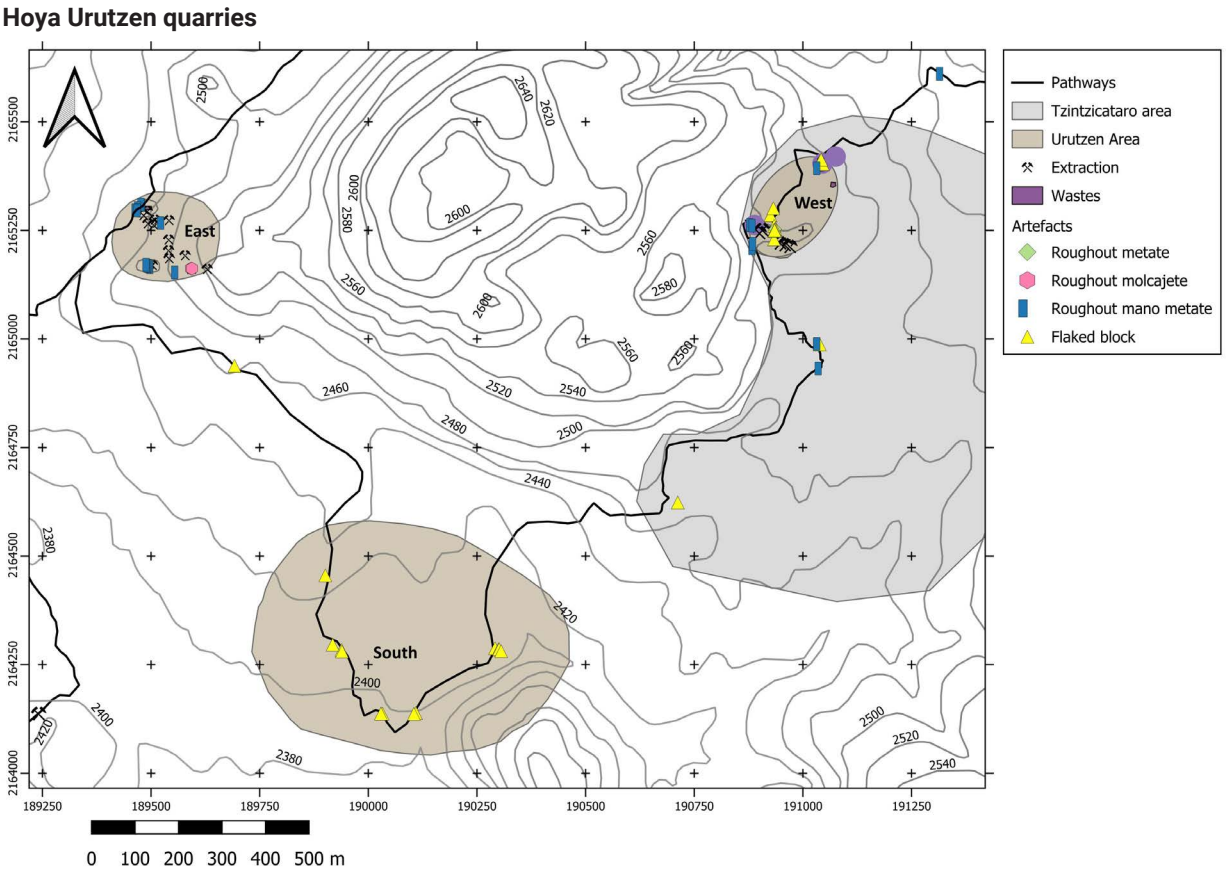

Figure 5. Map showing the quarry areas around Hoya Urutzen.

but also to the Early Colonial period (Romita-type ceramics). The southern part of the site, also contains clear evidence of a settlement from this period. A monumental area features a 45 m square plaza surrounded by a wall and bordered on the east by a rectangular stone building some 18-m-long (E-W) and 9-m-wide. This layout clearly corresponds to a colonial religious complex consisting of a church and its atrium, as documented elsewhere in the region (Lefebvre *et al.*, 2023). The rectangular building is still referred to locally as "tioxtacua", the Purépecha term for church, showing that the memory of this now-abandoned settlement is still alive. The structures located around the religious complex are organized on a grid pattern, another typical feature of the colonial period. To the north of the complex, there are buildings (residential platforms?) organized around two courtyards. Forty meters east of the church, there is a group of five residential structures organized around the crossroads of two perpendicular streets oriented north-south and east-west.

During our surveys, mano and metate roughouts and manufacturing wastes were found in association with archaeological structures of the dwelling type, in areas where both Prehispanic and Colonial remains are present (Figure 6). They were made from highly vesicular andesite. The metateros quickly interpreted these remains as the remains of a metate producer's workshop, comparable to the organization of their own work area. This evidence suggests that this craft activity must have been present from these early periods, allowing us to assume that Turícuaro's craft tradition dates back at least to the 15th - 16th centuries and has been maintained over a period of more than 500 years.

At least three ancient quarry zones were detected on the eastern, western and southern flanks of Hoya Urutzen (Figure 5). Highly vesicular andesites were extracted here, either as massive flow fronts or in the form of erratic boulders, depending on the sector. Though their dating is debatable, the exploitation of vesicular basalt would fit with archaeological exploitations, as these qualities of rocks were not exploited anymore during the 20th century according to the Vidales.

On the western slope, early quarries, hereafter called the West Hoya Urutzen quarries, were identified along the current pathway from Turícuaro to El Metate that passes along the Hoya

Figure 6. Tzintzicátaro: a) mano roughouts ; b) hammerstones found in the Tzintzicátaro area. Scale = 10 cm.

Urutzen volcano (Figure 7). This area is no longer exploited by the metateros, with the exception of some abandoned roughouts that are frequently recycled to produce small implements. Along the pathway, the lava flows front has been exploited in several areas. They are organized as follows: just in front of the extraction wall (Figure 8), a cleaned area served as a workshop to produce roughouts. Interestingly, production waste (larges flakes and mano roughouts) was piled to the side or downslope, depending on the topography. Some flaked blocks were put aside too. In other places, extracted blocks were reused to build terrace walls. On the flanks of the volcano, moving up towards the summit, extensive areas of quarrying sometimes yielded large quantities of flakes and waste, fragments of blocks and metate and molcajete roughouts (Figure 9).

On the East of Hoya Urutzen, quarries were detected on a lava flow directly overhanging the archeological site (Figure 10). Approaching the quarries from the site, more flakes and hammerstones (some are massive, 0.8 to 2 kg) were found in a ploughed plot. Manos and metate roughouts were found in this location. Among dense vegetation, quarry fronts of massive blocks were observed on the lava flow front. Depressions, with diameters of 6 to 7 m, contained blocks while waste material was dumped on the peripheries.

To the south, towards San Angel and the Las Cruces volcano, more random exploitations were identified (Figure 5). The metatero Nicolás Vidales recalls that he visited this area with his grand-parents but had no memory of when it was exploited. Several zones of activity, centered on small groups of blocks with random wastes, are visible in this area at the very south of the Hoya Urutzen volcano. No real extraction zone or roughouts have been recorded in this sector.

Among living metateros, the absence of any memory of mining at quarries that surround Hoya Urutzen, and the regular presence of andesitic hammerstones rather than metallic picks, both suggest a fairly early date. This is particularly true for the zone at the south-east of Hoya Urutzen where quarries could be directly connected to activities at the archaeological site. The archaeological site itself is said to produce metates Although their dating still needs to be precised, the close spatial relationship suggests that these quarries could have been exploited as far back as in the Postclassic period.

5. Results for the El Metate quarries

On the slopes of the El Metate volcano, several quarrying areas were identified, and at least two flows were exploited (Figure 2).

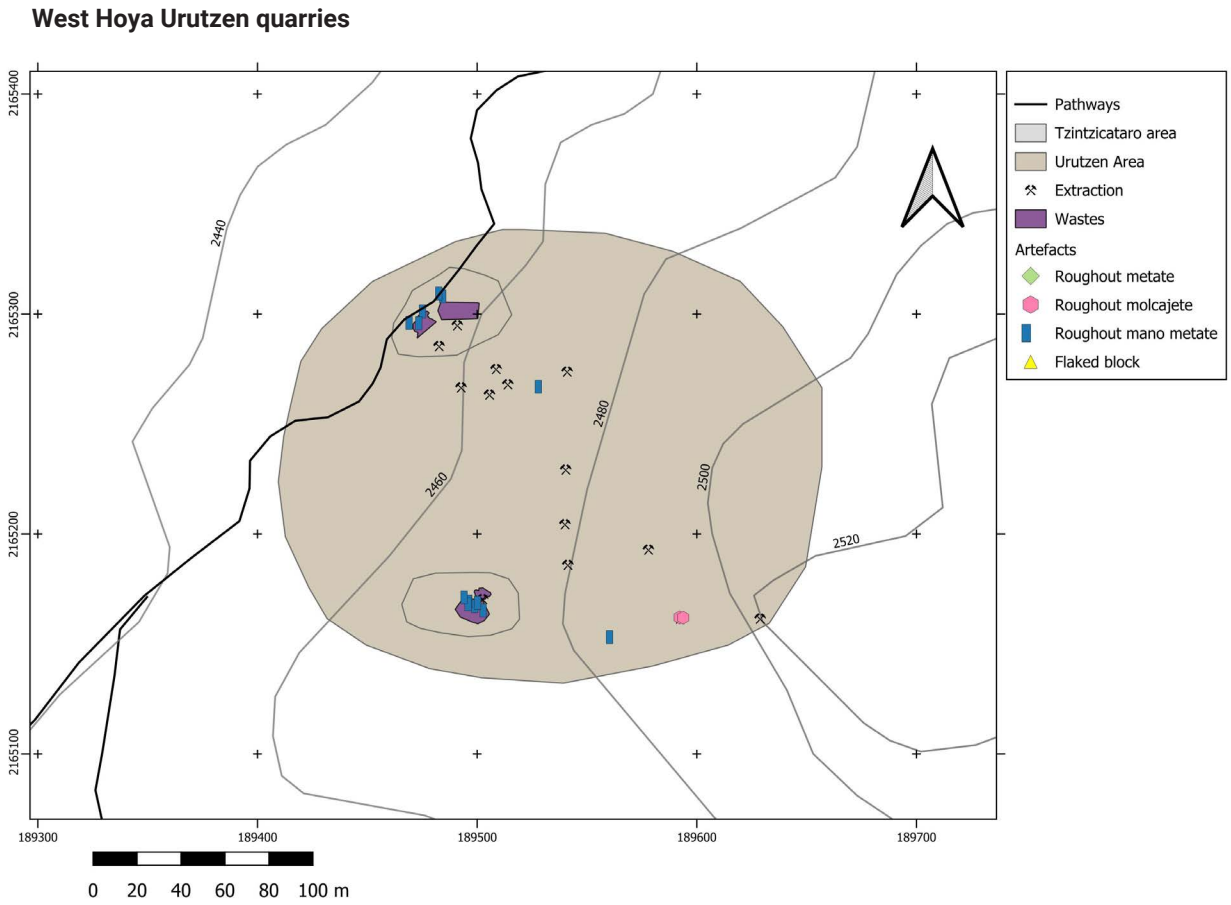

Figure 7. Detailed map of the West Hoya Urutzen quarry area

Figure 8. Front wall of andesite-block extraction at West Hoya Urutzen quarry. Scale = 50 cm.

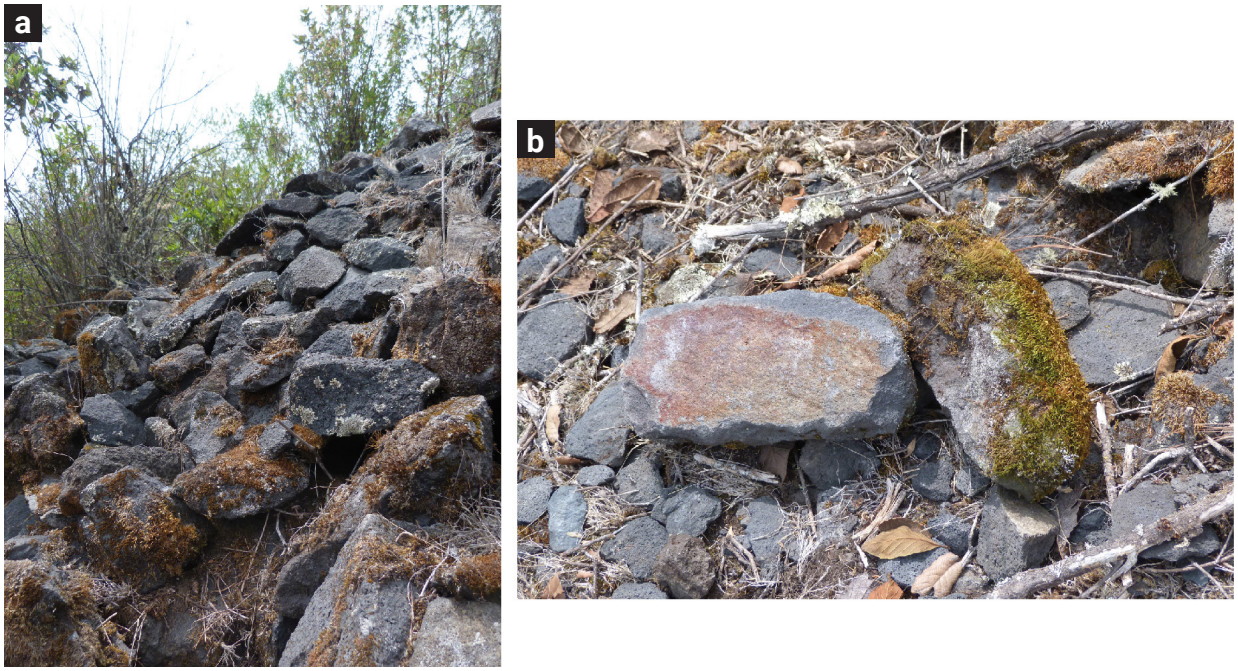

Figure 9. Exploitation debitage (a, scale = 50 cm) and mano roughouts (b; scale = 10 cm) on the slopes of West Hoya Urutzen

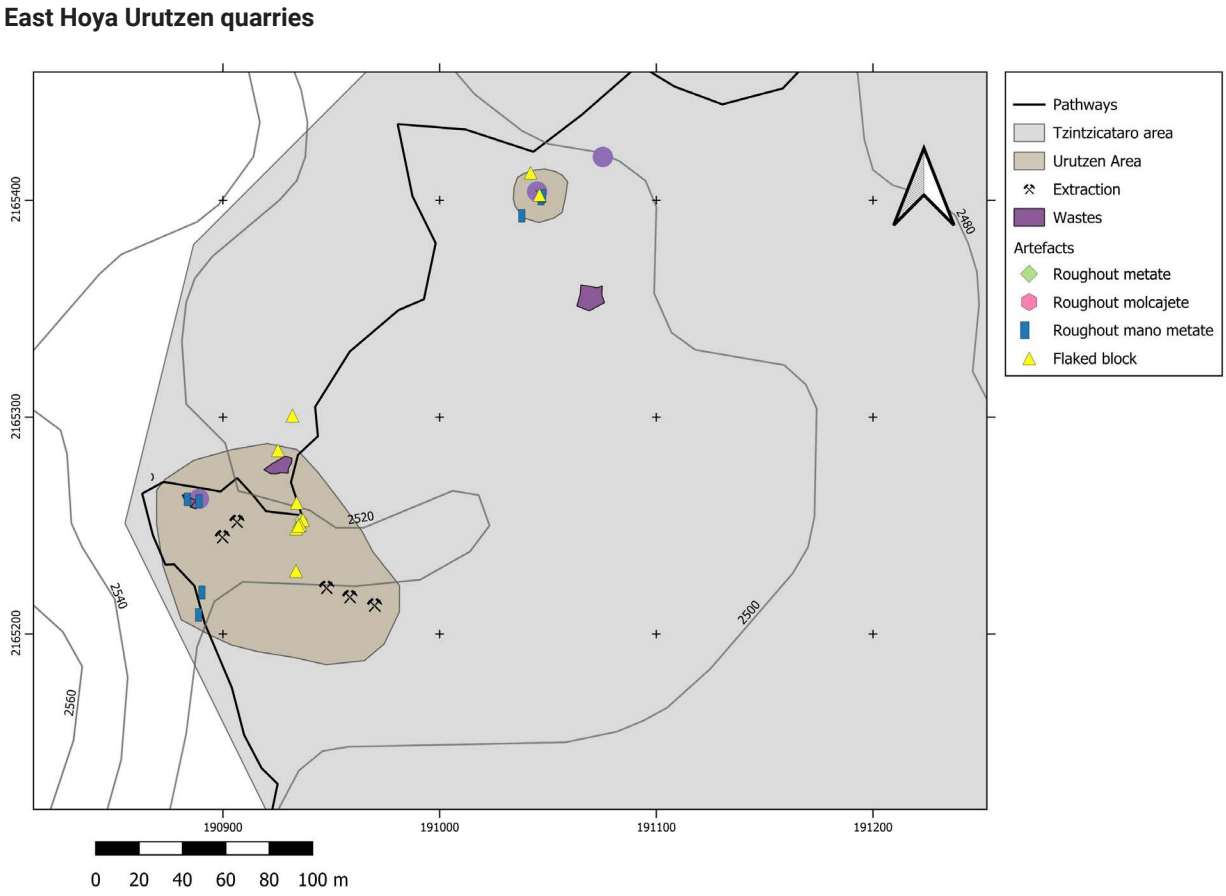

Figure 10. Detailed map of the quarry areas around East Hoya Urutzen.

5.1 "Taleminuchi"

The first area, called Taleminuchi or the «Cantera de los Abuelos» (Figure 11), is located at the foot of El Metate volcano, on lava flow n°7 as defined by Chevrel *et al.* (2016a). It is around 4 km south-east of the village of Turícuaro and is the smallest defined quarry area (7500 m^2, Table 2). Don Pedro learned quarrying from his uncles at the age of 9 in this area. Although easy to access and holding good rock quality, Don Pedros' brothers abandoned this area in the mid 20th century because of the exhaustion of unfractured blocks (Figure 12). They then decided to continue further away where blocks are bigger in size and less fractured.

5.2 "El Cerro"

The bulk of the quarrying area is located on lava flow n°12, as defined by Chevrel *et al.* (2016a), near the summit of El Metate, 6.5 km from Turícuaro (Figure 2). It was not possible to determine the exact extent of the quarrying area within this *malpaís* zone, which is particularly difficult to access due to the abundance of large boulders, the virtual absence of paths, and the presence of dense vegetation. According to our surveys, this zone close to the summit of El Metate appears to have been quarried over several hectares, and possibly over the whole surface of this lava flow.

The various past and present pathways from Turícuaro to the quarries on top of El Metate were mapped. Today, this area and the paths are shared with the timber harvesters. Directly installed on the chaotic malpaís, the quarry areas are only accessible on foot after a 3-hour walk, with heavy loads being carried by donkeys (Figure 13). Nicolás mentioned the existence of older paths, which are faster and more direct, but also steeper and more dangerous, especially with loads. Unfortunately, we could not map them.

A detailed study of the organization of the quarry zones was undertaken in 5 windows considered to be representative of the different morphologies of the flow and the associated andesite block mining strategies. Systematic recording was conducted, with standardized descriptive sheets, combined with a geo-ref-

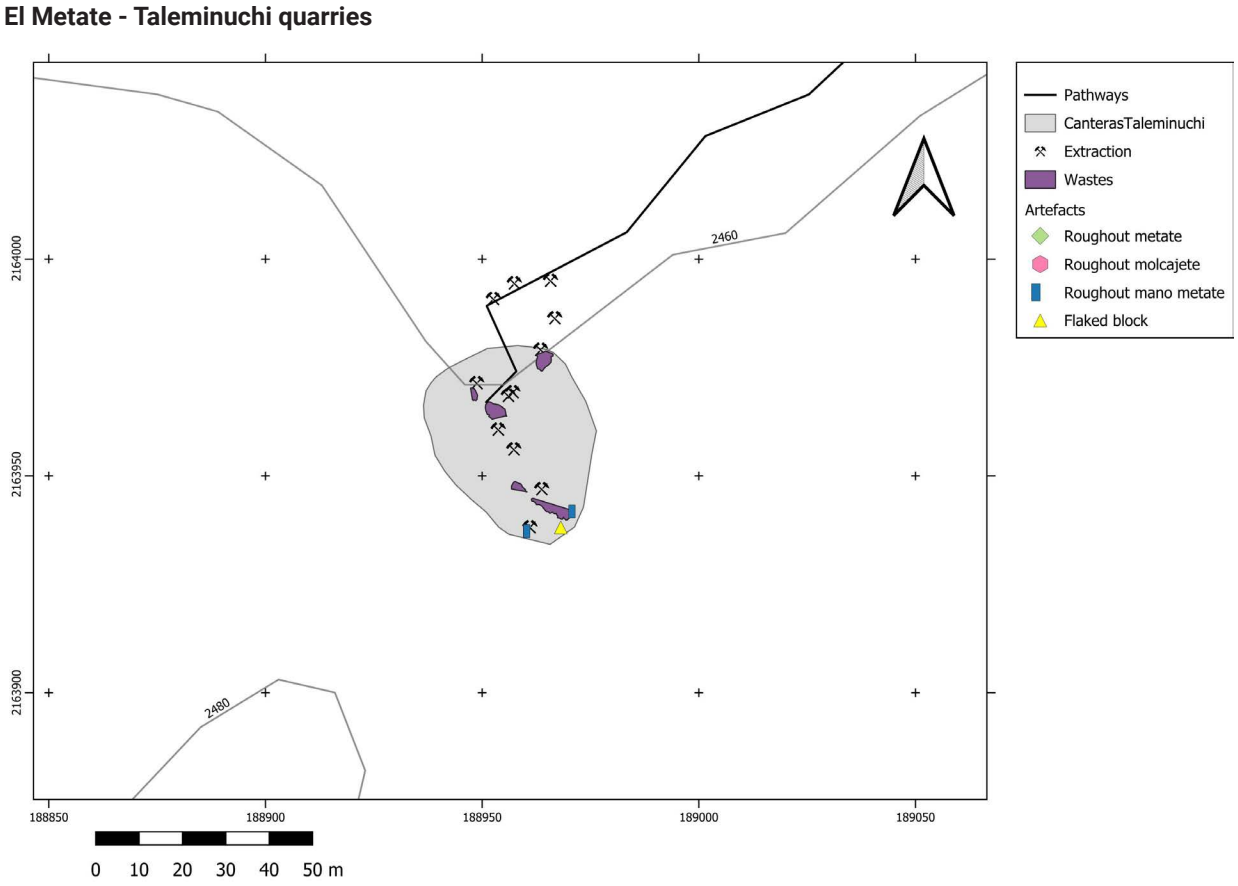

Figure 11. Detailed map of the quarry areas at El Metate "Taleminuchi".

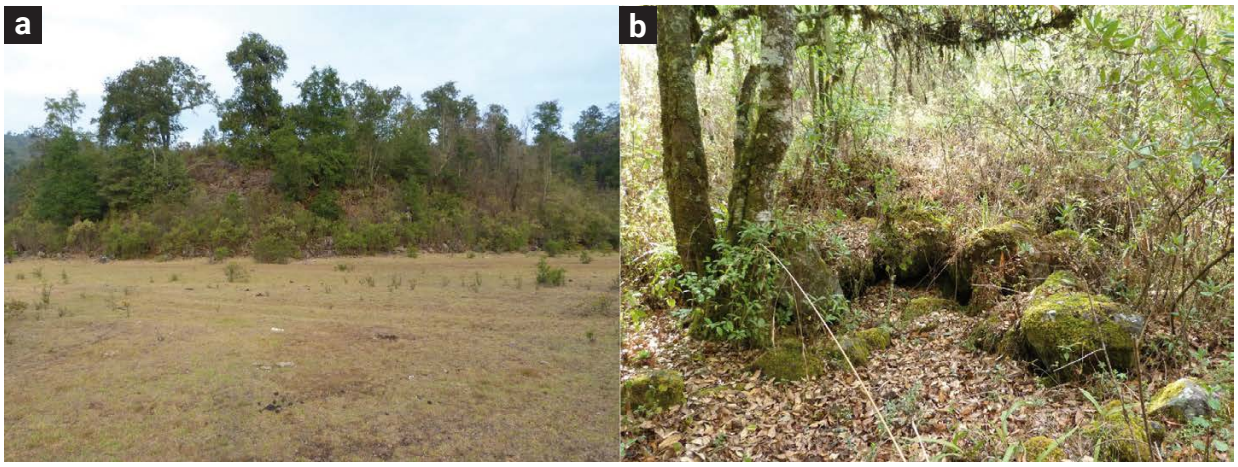

Figure 12. El Metate "Taleminuchi" quarry area: a) view of the lava-flow front; b) view of a former quarry area (scale = 50 cm).

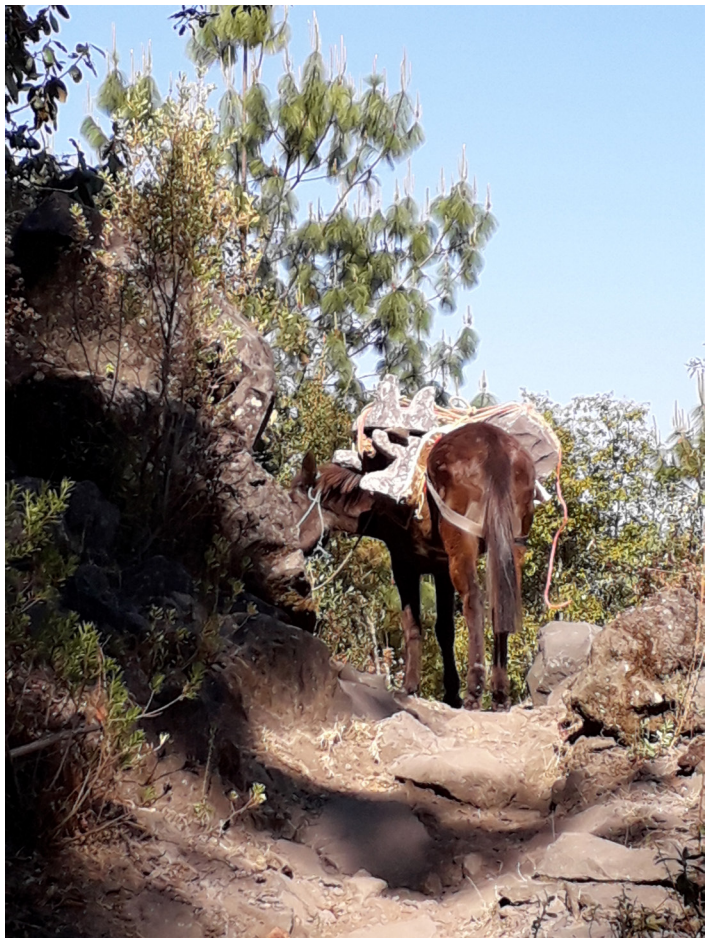

Figure 13. Transportation of metate roughouts by a horse on the main pathway to El Metate quarries.

erenced photogrammetric survey, on the ground and also by drone to provide a better idea of the topography of the extraction area and the organization of the various work areas (Figure 14).

Several forms and periods of exploitation were recognized at the summit of El Metate. They probably correspond to different periods of exploitation, to different groups of metateros, or to different strategies of adaptation to the configuration of the blocks and flows. The dating of these different sectors remains tricky in the absence of dates for associated characteristic material elements. Don Pedro explained to us that his brothers were the first to discover this area. But in fact, the area was already exploited before the mid-20th century. The abandoned roughouts evoke different types of metate: tripod forms that correspond to types still produced today in the village, but older types with shorter feet and of which the current metateros have no memory, were also produced (Figure 15a). Some of the areas identified by the village metateros as "old" also show much greater levels of sedimentation than others, both in the area closest to the summit and at the base of the lava flow (Figure 15b).

A strong spatial segmentation observed between the different stages of exploitation reflects on the organization of the quarry areas. The entire quarry zone is composed of a series of work areas linked to each other by a network of small paths. Each work area corresponds to a stage in the sequence of metate or molcajete production, from the natural block to the roughout. During work, roughouts may be abandoned for different reasons (breakage, problems of symmetry, etc.). Depending on the configuration of the quarry area, the organization of each workshop varies.

On a flat topography, quarry areas are generally organized into three components (Figure 16):

- one or several areas of block extraction, displaying broken blocks, natural blocks and depressions where former blocks were removed,
- an area of roughout shaping, where most of the roughouts are abandoned, and generally located in the middle of a group of extracted blocks,
- one or several areas for receiving wastes after cleaning of the workshop. This waste is generally located on the periphery of the shaping areas. Waste piles can be "sorted", with large and smaller flakes being separated,

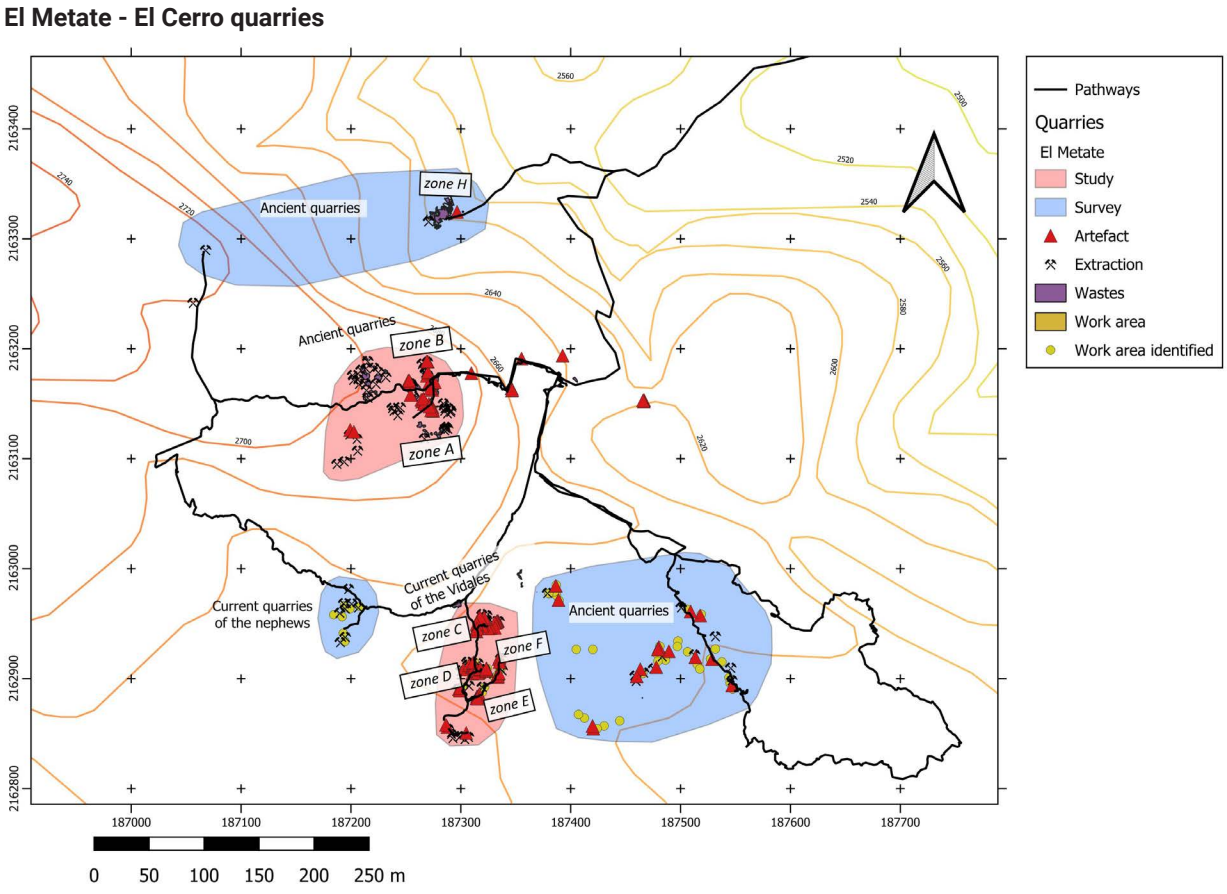

Figure 14. Detailed map of the quarry areas at El Metate "El Cerro".

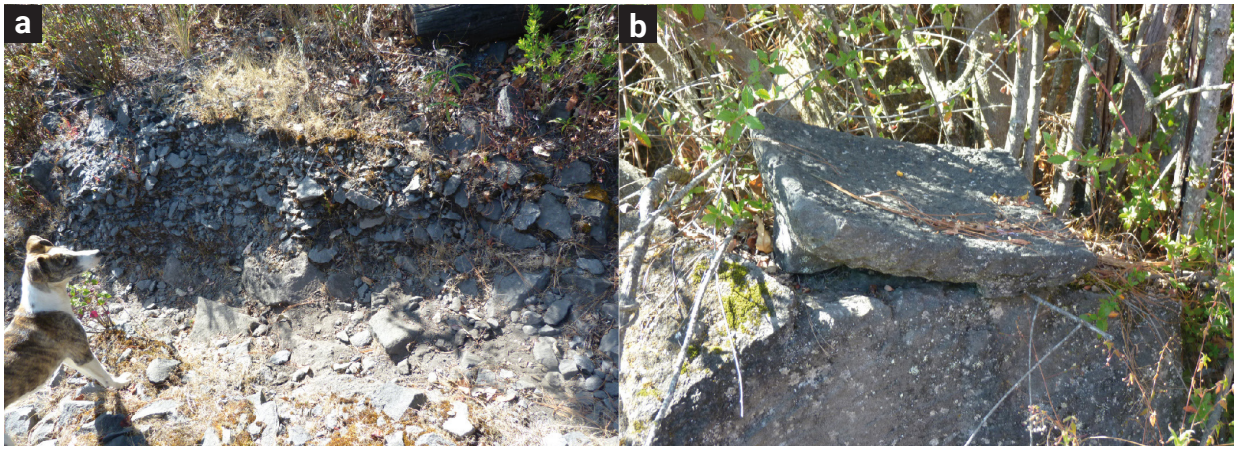

Figure 15. El Metate "El Cerro": old quarries from zone A-B with a) piles of andesitic debitage covered by humus and cut by a more recent pathway (scale = 50 cm), b) metate roughout with short feet and curved grinding surface (ancient type). Length of the roughout = 45 cm.

Figure 16. El Metate "El Cerro": recent quarries on the path to zones A and B, with blocks extracted in the back, and broken in the space toward the front that was formerly occupied by the andesite rock. The surface is occupied by debitage consisting of blocks and smaller flakes (Scale = 50cm).

if the cleaning of the workshop was carried out in several episodes during the roughing out process. They can also be shared by several shaping areas.

The distance between workshops can be very short, sometimes only separated by a group of blocks. This spacing is determined by the distribution of the blocks on the lava flow surface.

On a more sloping topography, quarrying areas may be organized into terraces, as follows (Figure 17):

- an area of block extraction,
- an area for block splitting (into cubic forms) with fragments of blocks and large sized flakes,
- an area for the coarse shaping stages of metate roughouts (step 1),
- an area for the fine shaping stages of metate roughouts (step 2),
- a resting area around a tree, both for the quarryman and the donkeys; that is also where roughouts will be loaded onto the donkeys

Blocks are rolled from one place to another at each stage of production. The last stage of production in the quarry corresponds to a cubic block, around 40 kg, featuring a table and three feet. Roughouts are then transported to the Vidales' house where a large area in the courtyard serves as a dedicated workshop used for all stages of metate shaping and finishing carried out over approximately a week.

This last configuration is the one observed in the quarry area exploited by Nicolás and Don Pedro Vidales for one year in 2019 (Figure 18). Contrary to other regions, dynamite is not used. Only metallic picks of various forms, weights and handle-length are used, together with long wooden sticks (up to 2 m) and stabilization blocks. According to Don Pedro, one day is necessary to find blocks of good quality (less fractured, possibly less dry), and one or two further days are necessary to split a block and shape a roughout from it. The entrance to a quarry area is materialized by abandoned metate and molcajete roughouts that serve as a sign of «ownership» of the areas within the framework of competition between village families. Continuing on the pathways to the current quarries, another area was exploited by Francisco Ruíz, Andrés y Santiago Vidales, nephews of Don Pedro Vidales. There, the strategy of exploitation appears to be slightly different (Figure 19). Soil is removed around and between groups of blocks which are left at the center before being exploited. This type of extraction

Figure 17. El Metate "El Cerro": workshop terraces from zone C exploited today by the Vidales family. Note the larger size of the flakes on top, the rolled roughout in the centre, and the second workshop for the finishing of the roughout below with smaller-sized flakes (Scale = 50cm).

Figure 18. El Metate "El Cerro": workshops on terraces from zone C exploited today by Nicolás Vidales, here shaping a metate roughout with an iron pick.

Figure 19. El Metate "El Cerro": quarry of Don Pedro's nephews, where the covering earth (humus) was removed prior to the breaking of the andesite blocks (Scale = 50cm).

leaves deep depressions and crescent-shaped waste areas in the direct vicinity.

On the steeply sloping areas, workshops sited downslope of extraction areas are generally covered by large amounts of flakes originating from the exploitations above. This is notably the case in Zone H (Figure 20), located at the foot of lava flow 12, in quite an isolated area adjacent to the ancient pathways to the summit quarries.

6. Discussion and comparisons

Grinding stone quarrying has left a strong imprint on the volcanic landscape. Andesite exploitation for the production of metate implies a close relationship between the configuration of lava flows, the accessibility of andesitic blocks of good quality, and the quarrying strategies adopted by metateros. It requires a perfect knowledge of the volcanic landscape and of the rock properties on the part of the metateros. In the vicinity of Turícuaro, the volcanic landscape has considerably evolved since the start of the El Metate eruption in AD 1250. Shortly after the volcanic eruption, it seems that new people settled at the foot of the Hoya Urutzen, in Tzintzincátaro, and began exploiting the andesite from this small volcano for the production of metates. Later on, the current town of Turícuaro was settled and, at an unknown date, its inhabitants started to exploit the slopes of El Metate volcano for the production of metates and molcajetes. Today the forest that took centuries to grow is intensively exploited for wood-based crafts, and fewer and fewer large trees are left, especially at the summit of the volcano. This intense exploitation of the volcanic resources in the current territory of Turícuaro has left important scars on the landscape, with quarrying creating holes and piles of extraction waste covering hectares of the lava flows. It is striking that the impact of human activities on the volcanic landscape has shifted within the territory and over time, in a dynamic trajectory.

The andesite exploitation strategies documented in Turícuaro echo those documented for other areas of Mesoamerica, such as Oaxaca (Cook, 1973, 1982) and Guanajuato (Rodriguez-Yc, 2013) in Mexico, and in the Maya Highlands of Guatemala (Hayden, 1987; Nelson, 1987; Searcy, 2011). Strongly determined by the configuration of the lava flows, the quarrying strategies differs significantly from the exploitation of other materials such as granite (Cook, 1973). In the Mayas area in Guatemala,

Figure 20. El Metate "El Cerro": quarry zone H, with large amounts of debitage and roughouts accumulated on a steep slope at the base of lava flow No. 12

extraction of large blocks from 1 or 2 meters underneath the *malpaís* soil is a strategy often chosen to access less fractured blocks (Searcy, 2011, p. 39; Hayden, 1987). Given the large size of the blocks, the goal is always to break them into smaller pieces that can be moved to the closest workshop within the quarry area (Searcy and PItezel, 2018). While the use of dynamite seems to have spread during the 20th century (Cook, 1973), this technique has not been documented in Turícuaro and in the Maya highlands, probably because it generates too much breakage of the rock for "traditional" production. Extraction is therefore mainly carried out with stone picks, and where these have been abandoned, by massive steel and iron picks; in all cases the quarrymen take advantage of the natural cleavage of the blocks. Documented extraction areas share many common points in terms of the organization of the work and the spatial segmentation of the stages of production (see also Nelson, 1987, p. 142). Depending on the slopes of the quarry, the workshops are generally located close to the extraction area, on a single flat surface or on a terrace system with spatial organization directly reflecting the technical sequence of shaping. These sites feature large pits surrounded by piles of waste material. In both contexts, quarries are organized on a personal or group basis, with no personal claim on the land (the land belongs to the municipality or *ejido*), contrary to what has been documented, for example, in Oaxaca (Cook,1973); however, implicit rules are respected, as expressed by the distance maintained between current extraction zones exploited by the Vidales family and those operated by their nephews. Working days are generally intense, stretching from early morning to late evening. However, in the Maya Highlands, for example, the exploitation of streambed blocks only occurs during the dry season, which implies different organizations of the work according to each region (Nelson, 1987).

7. Conclusions

Metate production in Turícuaro offers an example of the attractivity of volcanic areas, which can be seen as a source of economic development. Through the study of a plurisecular andesite quarrying activity, it has been possible to highlight the close relationship between men and volcano, and their invaluable knowledge of the volcanic resources as well as of the modeling of the landscape. Current metate production also offers a unique opportunity to define keys for the identification of ancient andesite exploitation. We sincerely hope that this study will be of great help for recognizing archaeological metate quarries in the near future.

Our study of the distribution networks for these products shows that Turícuaro's renowned products, made to order from the surrounding villages, are becoming less and less resistant to competition from mass-produced molcajetes from the La Piedad region, 120 km north of Turícuaro. The last remaining metateros in the village are now turning to the production of metates that are more decorative than functional. The metates thus contribute to retain a strong sense of identity and culture in one of the most traditional Purépecha villages, as part of wedding dowry. However, this will not preserve Turícuaro's centuries-old grinding stone industry. The disappearance of this activity also implies the loss of the memory and knowledge of the volcanic territory, which plays a central part in the intangible and cultural heritage of the Meseta Purépecha and beyond.

8. Acknowledgments

Our warmest thanks go to Nicolás, Don Pedro and Doña Livia Vidales, and all the members of their family in the village of Turícuaro, for transmitting their knowledge of metate production and of the El Metate volcano territory. Their time, patience and warm welcome were invaluable during these many weeks of learning. We also thank Karine Lefebvre (CIGA-UNA, Morelia, Mexico) for her expertise on the archaeological site of Tzintzicátaro.

This work was financially supported by a Sardyn research grant from the Labex Dynamite (French National Agency of Research) and a research grant from Paris 1 Panthéon-Sorbonne University. It also benefited from the financial and scientific support of several laboratories within the CNRS (UMR 8215 Trajectoires, UMR 8096 Archam, CEMCA Mexico).

The work of O.M. Chevrel, N. Reyes, and C. Siebe was supported by *Dirección General de Asuntos del Personal Académico* through project UNAM-DGAPA IN-104221. C. Siebe also benefitted from a sabbatical stay at the Senckenberg Naturhistorische Sammlungen, Dresden and the kind hospitality of Jan-Michael Lange and Peter Suhr. O. Chevrel acknowledges the ClerVolc program of the University of Clermont Auvergne, this is the contribution number 642.

9. References

Abramiuk, M., William, A., Meurer, P. (2006). A preliminary geoarchaeological investigation of ground stone tools in and around the Maya Mountains, Toledo District, Belize. *Latin American Antiquity* 17(3), 335-354.

Alonso, N. (2019). First approach to women, tools and operational sequences in traditional manual cereal grinding. *Archaeological Anthropological Science* 11, 4307–4324.

Barba, L. A., Córdoba, J. L. (2010). *Materiales y energía en la arquitectura de Teotihuacán*, Universidad Nacional Autónoma de México, Instituto de Investigaciones Antropológicas, México. **http://ru.iia.unam.mx:8080/handle/10684/27**

Chevrel, M., Siebe, C., Guilbaud, M. N., Salinas, S. (2016a). The AD 1250 El Metate shield volcano (Michoacán): Mexico's most voluminous Holocene eruption and its significance for archaeology and hazards, *The Holocene*, October 2015, doi: **https://doi.org/10.1177/0959683615609757**

Chevrel, M., Guilbaud, M.-N., Siebe, C. (2016b). The AD 1250 effusive eruption of El Metate shield volcano (Michoacán, Mexico): magma source, crustal storage, eruptive dynamics, and lava rheology, *Bulletin of Volcanology 78*, 32. **https://doi.org/10.1007/s00445-016-1020-9**

Cook, S. (1982). Zapotec stone workers. *The dynamics of rural simple commodity production in modern Mexican capitalism*. M.D. Lanham, University Press of America.

Cook, S. (1973). Stone Tools for Steel-Age Mexicans? Aspects of Production in a Zapotec Stoneworking Industry. *American Anthropologist* 75, 1485–1503.

Darras, V., Mireles, C., Siebe, C., Quezada, O., Castañeda, A., y Reyes, N. (2017). The Other Stone. Dacite Quarries and Workshops in The Prehispanic Tarascan Territory, Michoacán, Mexico. *Journal of Archaeological Science:* Reports 12, 219-231. **https://doi.org/10.1016/j.jasrep.2017.01.034**

De Bélizal, E., Lavigne, F., Grancher, D. (2011). Quand l'aléa devient ressource : l'activité d'extraction des matériaux volcaniques autour du volcan Merapi (Indonésie) dans la compréhension des risques locaux. *Cybergeo: European Journal of Geography.* doi: **https://doi.org/10.4000/cybergeo.23555**

David, N. (1998). The ethnoarcheology of grinding at Sukur, Adamawa state, Nigeria. *African Review* 15(1),13-63.

Fink, J. H., Anderson, S. W., and Manley, C. R. (1992), Textural constraints on effusive silicic volcanism: Beyond the permeable foam model, *J. Geophys. Res.*, 97(B6), 9073–9083, doi: **https://doi.org/10.1029/92JB00416**.

Fujita, H., Poyatos de Paz, G. (2007). Prehistoric Quarrying and Stone Tool Production at El Pulguero, Baja California Sur, Mexico. Pacific Coast *Archaeological Society Quarterly* 39 (2–3), 23–36. **https://www.pcas.org/assets/documents/prehistoricquarryinga.pdf**

Gillespie, S. D. (1994). Llano de Jicaro. An Olmec monument workshop, *Ancient Mesoamerica*, 5, 231-242. doi: **https://doi.org/10.1017/S095653610000119X**

Hamon, C., Le Gall, V. (2013). Millet and sauce: the uses and functions of querns among the Minyanka (Mali), *Journal of Anthropological Archaeology*, 32,109-121. doi: **https://doi.org/10.1016/j.jaa.2012.12.002**

Hamon, C., Pereira, G., Chevrel O., Aubry, L., Siebe, C., Quesada, O., Reyes-Guzmán, N. (2023). Present Use and Production of Metates and Molcajetes in Turícuaro (Michoacán, Mexico): Deciphering the Evolution of Food Preparation Practices, *Ethnoarchaeology* 15 (2), 208-232. doi: **https://doi.org/10.1080/19442890.2023.2280379**.

Hasenaka, T., Ban, M., Delgado Granados, H. (1994). Contrasting volcanism in the Michoacán-Guanajuato Volcanic Field, central Mexico: Shield volcanoes vs. cinder cones. *Geofísica Internacional, 33*(1), 125-138. **https://doi.org/10.22201/igeof.00167169p.1994.33.1.544**

Hayden, B. (1987). Traditional metate manufacturing in Guatemala using chipped stone tools". In Hayden B., ed., *Lithic Studies Among Contemporary Highland Maya*. University of Arizona Press, Tucson, pp. 8–119.

Katz, E. (2003). Le metate, meule dormante du Mexique. In Barboff M., Sigaut F., Griffin-Kremer C., Kremer R., Meules à grains. *Actes du Colloque International de la Ferté-sous-*Jouarre (16–19 mai 2002), Ibis Press/ Maison des Sciences de l'Homme, Paris, pp. 32–50.

Lefebvre, K., Urquijo Torres, P., Dorison, A. (2023). Pueblos viejos-pueblos nuevos: transformación del paisaje en el norte de Michoacán (México) durante el período novohispano (siglo XIV)", *Ancient Mesoamerica*: 1-21. doi: **https://doi.org/10.1017/S0956536121000584**

León, N. (1906). Los Tarascos. Notas históricas, étnicas y antropológicas. Tercera parte. Etnografía pos-cortesiana y actual. *Anales Del Instituto Nacional De Antropología E Historia*, 2(3), 298-479.

Mahgoub, A.N., Böhnel, H., Siebe, C., Chevrel, M.O. (2017). Paleomagnetic study of El Metate shield volcano (Michoacán, Mexico) confirms its monogenetic nature and young age (AD 1250). *Journal of Volcanology and Geothermal Research*, 336, 209-218. **https://doi.org/10.1016/j.jvolgeores.2017.02.024**

Nelson, M. (1987). Site and content structure: metate quarries and workshops in the Maya Highlands, In Hayden B., ed., *Lithic Studies Among Contemporary Highland Maya.* University of Arizona Press, Tucson, pp. 8–119.

Pollard, H. (2008). A Model for the Emergence of the Tarascan State. *Ancient Mesoamerica*, 19 (2), 217-230.

Quezada, O., Pascal, G. C., González, L. A. (2015). De la Cantera a Tenochtitlán: presencia de rocas de origen volcánico en la construcción y la escultura del Templo Mayor. La explotación de andesita en la cantera de San Bartolo Tenayuca, una aproximación etnoarqueológica. En Maclung de Tapia E., Serrano C., coord., *Aportaciones antropológicas: 70 aniversario de la Sociedad Mexicana de Antropología (1937-2007)*. Universidad Nacional Autónoma de México, Sociedad Mexicana de Antropología, pp. 555-566.

Quezada, O. (2016). *El Templo Mayor de Tenochtitlan: Materiales, Técnicas y Sistemas Constructivos.* [Tesis de licenciatura en arqueología inédita], Escuela Nacional de Antropología e Historia, Ciudad de México, México.

Quezada, O., Darras, V. (2023). Caracterización espacial de un paisaje de extracción prehispánico: El yacimiento de dacita de Las Minas, Zacapu, Michoacán. *Ancient Mesoamerica,* 1-29. doi: **https://doi.org/10.1017/S0956536122000025**

Riker, J. M., K. V. Cashman, J. P. Kauahikaua, and Montierth, C. M. (2009). The length of channelized lava flows: Insight from the 1859 erup-tion of Mauna Loa Volcano, Hawai'i, *J. Volcanol. Geotherm. Res.*, 183, 139–156, doi: **https://doi.org/10.1016/j.jvolgeores.2009.03.002**.

Robles, G. N. (1992). La extracción y talla de cantera en Mitla, Oaxaca. Tecnología para la arquitectura monumental, *Arqueología*, 7, 85-112. **https://revistas.inah.gob.mx/index.php/arqueologia/article/view/12631**

Rodriguez-Yc, J. R. (2013). *La molienda en Mesoamérica, formas, fun-*

ciones, usos y manufactura de los Instrumentos: un estudio etnoarqueológico en México. Unpublished [Tesis doctoral inédita], Departamento de Prehistórica, Historia Antigua y Arqueología, Universitat de Barcelona, Barcelona, Spain.

Roux, V. (1985). *Le matériel de broyage. Etude ethnoarchéologique à Tichitt* (R.I) Mauritanie. Edition Recherches sur les civilisations, mémoire n°58, Paris.

Searcy, M. T. (2011). *The Life-Giving Stone: Ethnoarchaeology of Maya Metates*. The university of Arizona Press, Tucson, 168 p.

Searcy, M.T., Pitezel, T. (2018). An ethnoarchaeological perspective on ground stone production at the Santiago quarry in the casas grandes region of Chihuahua, Mexico, *Latin American Antiquity*, 29 (1), 169 -184.

Sheets, P. D., Grayson, D. K. (1979). *Volcanic Activity and Human Ecology.* Academic Press.

West, R. C. (1948). *Cultural Geography of The Modern Tarascan Area*, Cultural Geography of the Modern Tarascan Area (Institute of Social Anthropology Publication No. 7). Washington, DC: Smithsonian Institution.